Universitat Politècnica de València
Departamento de Máquinas y Motores Térmicos

Doctoral Thesis

Computational study of the Injection Process in Gasoline Direct Injection (GDI) Engines

Presented by:
Ms. María Martínez García

Supervised by:
Dr. Pedro Martí Gómez-Aldaraví

Valencia, July 2022

Universitat Politècnica de València
Departamento de Máquinas y Motores Térmicos

Doctoral Thesis

Computational study of the Injection Process in Gasoline Direct Injection (GDI) Engines

Presented by:
Ms. María Martínez García

Supervised by:
Dr. Pedro Martí Gómez-Aldaraví

in fulfillment of the requirements for the degree of
Doctor of Philosophy

Valencia, July 2022

Ph.D. Thesis

Computational study of the Injection Process in Gasoline Direct Injection (GDI) Engines

Written by: Ms. María Martínez García
Supervised by: Dr. Pedro Martí Gómez-Aldaraví

Thesis committee:

Chairman: Prof. Antonio José Torregrosa Huguet
Secretary: Dr. Pablo Fajardo Peña
Member: Dr. Marco Crialesi Esposito

Reviewing board:

Dr. Marco Crialesi Esposito
Dr. Mario Medina
Dr. Jacopo Zembi

Valencia, July 2022

Abstract

Concerns about climate change, air pollution and the availability of fuel resources, coupled with the high demand for automobiles and transportation vehicles, have led governments to regulate the level of pollution, including CO_2, emitted by engines into the atmosphere. Because of this, there is a strong desire to adopt renewable and more sustainable energy sources, including partial electrification (hybridization) or full electrification (BEVs). However, the substitution of liquid fuels derived from petroleum as a primary source of energy will not emerge easily, quickly or cost-effectively, and Internal Combustion Engines (ICE) transport will continue to excel in the industry for at least the next few years. Combustion efficiency and engine performance are strongly influenced by the complex fuel injection process. Gasoline Direct Injection (GDI) strategies have the potential to greatly increase fuel economy and meet pollutant and greenhouse gases emission requirements, although many challenges remain, which has therefore been one of the main research objectives in recent years and also of this Thesis.

The present research aims to provide a better understanding to the scientific community in the field of GDI about the phenomena that take place during the injection process. The transient nature of the injection coupled with the complexity of the injector dynamics makes the experimental study of GDI quite challenging. Therefore, Computational Fluid Dynamics (CFD) is proposed as a powerful alternative which has been adopted for this research. In this context, the main objective of the present Thesis is to develop a predictive methodology capable of being applied to current and future generations of GDI injectors, regardless of the injector features and the software employed, for the hydraulic characterization of the injector under steady and transient operating conditions. Once validated, the subsequent goal is to employ the obtained results from this predictive methodology to analyze the behavior of the spray downstream of the injector (external flow). The intention behind the approach is to follow in the footsteps of the research community in avoiding experimental practice as far as possible.

The predictive methodology has been validated through its application to two multi-hole solenoid GDI injectors with very different features. On the one hand, the Delphi injector belonging to the well-known Engine Combustion Network (ECN) and named Spray G. On the other hand, an industrial Denso injector of real applicability currently used by a car manufacturer and referred to as Production Injector Unit (PIU). In addition, the mentioned methodology has been evaluated in several contexts using diverse commercial software: CONVERGE™ and StarCCM+. This developed methodology focuses on the

study of the internal and near-field flow to hydraulically characterize the injector. So the problem to be addressed is defined on the basis of a multi-phase system, performed in an Eulerian framework, modeled through a single-fluid approach. The treatment of the multi-phase flow is carried out by means of the Volume-of-Fluid (VOF) approach. Homogeneous Relaxation Model (HRM) is employed to consider the mass exchange between liquid and vapor phases of the fuel inside the nozzle, due to cavitation and flash boiling. The turbulence treatment has been accomplished from both Reynolds-Averaged Navier-Stokes (RANS) and Large Eddy Simulations (LES) approaches. On the other hand, regarding the external flow study, one of the most extended schemes for the modeling of the atomization process, the Discrete Droplet Model (DDM), has been adopted. In addition, being aware that atomization and spray behavior is greatly influenced, among other factors, by the geometry of the nozzle, the coupling strategy of the internal and external flow complements the analyses. For this purpose, one-way coupling and mapping approaches have been adopted, using as input parameters the internal flow data obtained from the already validated methodology.

Accordingly, this Thesis provides a new and valuable predictive methodology, which has demonstrated a high accuracy in characterizing the flow behavior during the injection process through comparison with experimental data present in the literature. It has also been proved to be directly transferable to different CFD software and applicable to injectors with dissimilar geometrical characteristics without compromising the requirements of the model. The correct characterization of the internal flow has made it possible to employ the obtained data to analyze the spray patterns downstream of the injector, which eliminates the need to consider experimental data. The resulting outcomes from this study macroscopically capture the behavior of the jet with an accuracy comparable to experiments under different operating conditions, flashing and non-flashing. Although there are still many challenges to face, overall, the present Thesis brings a breakthrough in the field of GDI. The quantum leap arises from the development and use of a fully predictive methodology, allowing to avoid most experiments to contribute to a greater and broader vision of the injection process physics.

Resumen

La creciente preocupación por la contaminación y los problemas medioambientales y de salud, además de la limitada disponibilidad de combustibles fósiles unido a la gran demanda de automóviles y vehículos de transporte, han llevado a los gobiernos a regular los niveles de emisiones, incluyendo CO_2, que los motores de combustión emiten a la atmósfera. Además, existe un fuerte deseo y con ello numerosas propuestas de adoptar fuentes de energía renovables y más sostenibles, incluyendo la electrificación parcial (hibridación) o la electrificación total (BEV). Sin embargo, la sustitución de los combustibles líquidos derivados del petróleo como fuente primaria de energía no será llevada a cabo de forma fácil, rápida o rentable, y el transporte propulsado por motores de combustión interna (ICE) seguirá destacando en la industria durante los próximos años. La eficiencia de la combustión además del rendimiento del motor están fuertemente influenciados por el complejo proceso de inyección de combustible. Las estrategias de inyección directa de gasolina (GDI) tienen la capacidad de aumentar en gran medida el ahorro de combustible y cumplir con los requisitos de emisiones contaminantes y de gases de efecto invernadero propuestos, aunque a día de hoy aún queda mucho potencial por descubrir. Por ello, este ha sido uno de los principales objetivos de investigación en los últimos años y, en consecuencia, de la presente Tesis.

Este trabajo de investigación tiene como motivación proporcionar a la comunidad científica un mejor entendimiento acerca de los fenómenos que tienen lugar durante el proceso de inyección directa de gasolina. La naturaleza transitoria de la inyección, junto con la complejidad de la dinámica del inyector, hace que el estudio experimental sea bastante complejo. La Mecánica de Fluidos Computacional (CFD) surge como una potente alternativa a los experimentos, la cual ha sido adoptada para esta investigación. Bajo este mismo contexto, se propone como objetivo principal de la presente Tesis, el desarrollo de una metodología predictiva capaz de ser aplicada a las actuales y futuras generaciones de inyectores GDI, independientemente de las características del inyector y del software empleado para el estudio, para la caracterización hidráulica del inyector en condiciones de operación estacionarias y transitorias. Una vez validada, el objetivo posterior es emplear los resultados obtenidos de esta metodología predictiva para analizar el comportamiento del flujo aguas abajo del inyector. La intención de este enfoque es seguir los pasos de la comunidad científica sustituyendo, en la medida de lo posible, la práctica experimental.

La validación de la mencionada metodología predictiva ha sido llevada a cabo mediante su aplicación en dos inyectores GDI solenoides multi-orificio con características muy diferentes entre sí. Por un lado, un inyector Del-

phi perteneciente a la conocida Engine Combustion Network (ECN) y denominado Spray G. Por otro lado, un inyector industrial Denso de aplicabilidad real denominado Production Injector Unit (PIU). No solo esto, sino que también, dicha metodología ha sido evaluada en varios contextos utilizando dos diferentes códigos CFD comerciales: CONVERGE™ y StarCCM+. La metodología predictiva se centra en el estudio del flujo interno y de campo cercano para caracterizar hidráulicamente el inyector. El problema a tratar se define en base a un sistema multifásico, llevado a cabo en un marco Euleriano y modelado considerando un único fluido. El tratamiento del flujo multifásico se realiza mediante el enfoque Volume-of-Fluid (VOF). Además, se emplea el Homogeneous Relaxation Model (HRM) para considerar el intercambio de masa entre las fases líquida y vapor dentro de la tobera debido a cavitación y flash boiling. El tratamiento de la turbulencia se ha llevado a cabo a partir de los enfoques Reynolds-Averaged Navier-Stokes (RANS) y Large Eddy Simulations (LES). Por otro lado, en cuanto al estudio del flujo externo, se ha adoptado uno de los esquemas más extendidos para el modelado del proceso de atomización, Discrete Droplet Model (DDM). Además, siendo conscientes de que el comportamiento de la atomización y del chorro están muy influenciados, entre otros factores, por la geometría de la tobera, la estrategia de acoplamiento del flujo interno y externo complementa los análisis. Para ello, se han adoptado enfoques de acoplamiento unidireccional y mapeado, utilizando como parámetros de entrada los datos de flujo interno obtenidos a partir de la mencionada metodología predictiva ya validada.

Así pues, esta Tesis aporta una nueva y valiosa metodología predictiva, la cual ha demostrado una elevada precisión a la hora de caracterizar el comportamiento de flujo durante el proceso de inyección a través de la comparativa con datos experimentales presentes en la literatura. Por otro lado, ha sido probado que es directamente trasferible a distintos códigos de cálculo así como aplicable a inyectores con características geométricas dispares sin perjudicar las exigencias del modelo. La correcta caracterización del flujo interno ha permitido emplear los datos obtenidos para analizar el comportamiento del chorro aguas abajo del inyector lo que elimina la necesidad de emplear datos experimentales. Los resultados obtenidos de este estudio capturan el comportamiento macroscópico del chorro con una precisión comparable a los experimentos bajo diferentes condiciones de operación. Aunque todavía hay muchos retos que afrontar, en general, la presente Tesis supone un gran avance en el campo del GDI. El remarcable progreso se debe al desarrollo y uso de una metodología totalmente predictiva, que permite prescindir de la mayoría de los experimentos para contribuir a una mayor y más amplia visión de la física del proceso de inyección.

Resum

La creixent preocupació per la contaminació i els problemes ambientals i de salut, a més de la limitada disponibilitat de combustibles fòssils, unida a la gran demanda d'automòbils i vehicles de transport, ha portat el govern a regular els nivells d'emissions, incloent CO2, que els motors de combustió emeten a l'atmosfera. Addicionalment, existeix un fort desig per adoptar fonts d'energia renovables i més sostenibles, per la qual cosa existeixen nombroses propostes incloent l'electrificació parcial (hibridació) o la electrificació total (BEV). Tanmateix, la substitució dels combustibles líquids derivats del petroli com a font primària d'energia no es durà a terme de forma fàcil, ràpida o rentable, i el transport propulsat per motors de combustió interna (ICE) es mantindrà a la industria almenys durant els pròxims anys. L'eficiència de la combustió y el rendiment del motor són fortament influenciats pel complex procés d'injecció de combustible. Les estratègies d'injecció directa de gasolina (GDI) tenen la capacitat d'augmentar en gran mesura l'estalvi de combustible i permetre complir amb els requisits propostes d'emissions i gasos d'efecte hivernacle, encara que queda molt potencial per descobrir. Per això, aquest ha sigut un dels principals objectius d'investigació als últims anys i, com a conseqüència, d'aquesta Tesi.

Aquest treball d'investigació té com a motivació proporcionar la comunitat científica un millor enteniment sobre els fenòmens que ocorren durant el procés d'injecció directa de gasolina. La natura transitòria de la injecció, junt a la complexitat de la dinàmica de l'injector, fa que l'estudi experimental siga força complex. La Mecànica de Fluids Computacional (CFD) sorgeix com una potent alternativa als experiments, i ha sigut adoptada per aquesta investigació. Baix aquest mateix context, es proposa com a objectiu principal d'aquesta Tesi el desenvolupament d'una metodologia predictiva capaç de ser aplicada a les actuals i futures generacions d'injectors GDI (independentment de les característiques de l'injector i del software utilitzat per a l'estudi) per a la caracterització hidràulica de l'injector en condicions d'operació estacionàries i transitòries. Una vegada validada, el posterior objectiu és analitzar el comportament del fluid aigües avall de l'injector (l'esprai). La intenció d'aquest enfocament és seguir els passos de la comunitat científica substituint, en la mesura que siga possible, la pràctica experimental.

La validació de la citada metodologia predictiva ha sigut duta a terme mitjançant la seva aplicació en dos injectors GDI solenoides multi-orifici amb característiques molt diferents entre si. D'una banda, un injector Delphi pertanyent a la coneguda Engine Combustion Network (ECN) i anomenat Spray G. D'altra banda, un injector industrial Denso d'aplicabilitat reial nomenat

Production Injector Unit (PIU). No només això, sinó que també aquesta metodologia ha sigut avaluada en diversos contextos utilitzant dos diferents software CFD comercials: CONVERGE™ i StarCCM+. La metodologia predictiva se centra en l'estudi del flux intern i el camp proper per tal de caracteritzar hidràulicament l'injector. El problema a tractar es defineix en base a un sistema multi-fàsic, resolt en un marc Eulerià i modelat considerant un únic fluid. El tractament del fluid multi-fàsic es realitza mitjançant l'aproximació Volume-of-Fluid (VOF). Amés, s'utilitza el Homogeneous Relaxation Model (HRM) per tal de considerar l'intercambi de massa entre les fases líquida i vapor a l'interior de la tovera degut als fenòmens de cavitació i flash boiling, si escauen.

El tractament de la turbulència s'ha dut a terme a través dels enfocaments Reynolds-Averaged Navier-Stokes (RANS) i Large Eddy Simulations (LES). D'una banda, pel que fa a l'estudi del flux extern, s'ha adoptat uns dels esquemes més estesos per al modelat de l'atomització, Discrete Droplet Model (DDM). A més, sent conscients que el comportament de l'atomització i la polvorització estan molt influenciats per la geometria de la tovera (entre altres factors), l'estratègia d'acoblament del flux intern i extern complementa les anàlisis. Per això s'han adoptat els enfocaments d'acoblament unidireccional i mapejat, utilitzant com a paràmetres d'entrada les dades del flux intern obtingudes amb la citada metodologia predictiva, ja validada. Així doncs, aquesta Tesi aporta una nova i valuosa metodologia predictiva, la qual ha demostrat una elevada precisió a l'hora de caracteritzar el comportament del flux durant el procés d'injecció a través de la comparativa amb els dates experimentals presentats a la literatura. D'altra banda, ha sigut provat que és directament transferible a diversos codis de càlcul així com aplicable a injectors amb característiques geomètriques dispars sense perjudicar les exigències del model. La correcta caracterització del flux intern ha permès utilitzar les dades obtingudes per tal d'analitzar el comportament de l'esprai aigües avall de l'injector, la qual cosa elimina la necessitat d'emprar dades experimentals.

Els resultats obtinguts d'aquest estudi capturen el comportament macroscòpic de l'esprai amb una precisió comparable als experiments en diferents condicions d'operació. Encara que queden molts reptes per afrontar, en general, aquesta Tesi aporta un important avanç al camp del GDI. La ruptura prové del desenvolupament i ús d'una metodologia completament predictiva, que substitueix els experiments requerits i així contribueix a una millor i més ampla visió de la física del procés d'injecció.

"Para ser grande, sé entero: nada tuyo exageres ni excluyas.
Sé todo en cada cosa. Pon cuanto eres en lo mínimo que hagas."
Fernando Pessoa

A mi familia.
En especial a ti, Abuelo

Acknowledgements

Quisiera aprovechar estas líneas para mostrar mi agradecimiento a todas aquellas personas, que de alguna manera u otra, han contribuido al desarrollo de este trabajo. Ha sido un camino largo, sin embargo, durante este tiempo he tenido la gran suerte de coincidir con gente maravillosa, con quienes he compartido numerosos momentos y experiencias, ayudándome a crecer no solo profesionalmente sino también en el ámbito personal. A todos aquellos que decidieron compartir conmigo una parte de su tiempo, GRACIAS.

En primer lugar, agradecer y expresar mi admiración por mi tutor, director y amigo Pedro Martí. Su paciencia, temple y sabia orientación han sido de inestimable valor para el desarrollo de esta Tesis y mi formación como investigador y persona. Han sido muchas las charlas, reuniones y debates donde he podido tomar nota de sus valores, manera de trabajar, razonar y cuidar al detalle cada proyecto, por mínimo que fuera. Me siento inmensamente afortunada de haberme embarcado en esta aventura junto a ti.

Asímismo, expresar mi gratitud al director de línea y jefe, Raúl Payri, quien siempre mostró su apoyo y no dudó en confiar en mi. Gracias por estar en la cabeza del pelotón y ser guía. Agradecer también al Insituto CMT-Motores Térmicos, en especial a la dirección del mismo, por darme la oportunidad de formar parte de este prestigioso centro de investigación. Además destacar la inmensa ayuda recibida por parte del personal de secretaría e informática. Amparo, no hay palabras para describir lo que diariamente haces por nosotros, gracias.

I would also like to thank the team at the Aerothermal and Combustion Systems Laboratory, ETH Zurich, and especially Konstantinos Boulouchos, who gave me the opportunity to be part of his prestigious research group for a few months. Yuri M. Wright and Christos Altantzis, it has been a real pleasure to work with you, thank you for every minute shared, for considering me as a member of the team.

De igual manera, me gustaría agradecer a todo el equipo, o podría decir familia, de Inyección CMT. Desde los profesores, quienes en algún momento han tendido su mano en forma de ayuda: Javi, Jaime, Marcos, Gabriela y Joaquín, hasta los doctorandos y proyectandos quienes han amenizado estos años. Vincen y Abian, gracias por los innumerables momentos que hemos compartido, muchos de ellos para enmarcar. Kike, qué gran descubrimiento, gracias por hacerlo todo tan fácil, por estar siempre de manera desinteresada. Mary, ha sido un verdadero placer coincidir, gracias por todas tus enseñanzas. Armando, por enseñarme que a veces no podemos conseguir lo que queremos pero si lo intentamos, quizá consigamos lo que verdaderamente necesitamos.

Rami, te has pasado el juego, gracias por aceptar el mayor reto de todos, una convivencia nada fácil. Jesús, Tomás y César, la familia venezolana, gracias por ponerle un poco de sabor a la vida. Agradecer también al resto del equipo con quienes he tenido el placer de compartir esta experiencia: Lucas, Victor, Santi, Sebas, Dani, Omar, David, Javier y Carlos. No querría olvidarme de Jose Enrique, quien nos ha hecho reir y enfadar a partes iguales pero, sin duda, ha sido un gran apoyo, gracias JE. A lo largo de estos años, he tenido la gran oportunidad de ayudar a varios proyectandos, o podríamos decir panchos, en su etapa final de carrera. Jordi, Sergio, Laura, Saul, Víctor, Javier y Álvaro, gracias de corazón porque creo que el aprendizaje ha sido mútuo. Por último, me gustaría mencionar a Toñi quien de manera indirecta ha formado parte de este grupo, alegrándonos diariamente con su sonrisa.

Agradecer también a todos aquellos compañeros y amigos que me han acompañado esta etapa: Alberto, Ibrahim, Leo, Alba y Antonio. Por último pero no menos importante, saber que hay un bonito mundo lleno de gente maravillosa fuera de CMT. A las de siempre, Laura y Adriana, por ser esas amigas que hacen que tu sonrisa brille un poco más. A Paula y Luis, por valorar, respetar, apoyar y disfrutar junto a mi. A Inma, por acompañarme en este vuelo algo turbulento. Perdón de antemano a todos aquellos que no he podido citar en estas breves líneas, no queriendo decir que no hayan sido relevantes en esta etapa. Gracias a todo aquel con quien compartí cervezas, bailes, cenas y largas conversaciones que han servido de combustible para seguir avanzando.

De manera especial, y estando completamente segura de que no existen palabras suficientes para agradecerles el apoyo incondicional que he recibido, me gustaría dar las gracias a mi familia, quienes no dudaron, me apoyaron y caminaron a mi lado. A mi Madre, nuestro pilar fundamental, el motor de la familia, ese que nunca para y tampoco permite que los demás lo hagan. Gracias por todas y cada una de las palabras de aliento, por tus ganas y la fuerza que a menudo trasmites. A mi Padre y mi hermano, Rubén, de quienes he aprendido la constancia y superación diaria. Gracias por hacer cualquier obstáculo parezca más fácil. A mi Tía, a quien admiro y de quien aprendí que el esfuerzo es la magia que transforma los éxitos en realidad. Y por último a mi Abuelo, quien siempre nos acompañará en cada pequeño paso que demos. Gracias de todo corazón.

A todos vosotros, de nuevo, GRACIAS. Ojalá nuestros caminos vuelvan a converger en algún punto, porque como sabemos, the future is eclectic!

Funding acknowledgements

María Martínez García has been founded through a grant from the Government of Generalitat Valenciana with reference ACIF/2018/118 and financial support from The European Union.

These same institutions, Government of Generalitat Valenciana and The European Union, supported through a grant for pre-doctoral stays out of the Comunitat Valenciana with reference BEFPI/2020/057 the research carried out during the stay at Aerothermochemistry and Combustion Systems Laboratory, Swiss Federal Institute of Technology, ETH Zurich, Switzerland.

Special gratitude from the author to both institutions, Government of Generalitat Valenciana and The European Union, for making this dream possible.

Technical acknowledgements

Author would like to special thank the "Fundación del Centro de Supercomputación de Castilla y León (FCSCL)", "ACT now HPC Cloud Cluster", "Sabarcore HPC Cloud" and "Rigel Cluster" from Universitat Politècnica de València for allowing the use of their clusters to perform the simulations carried out in this work and the excellent attention and technical support received.

Last but not least, thanks to the team of CONVERGE™ Studio and CD-Adapco for allowing the author to use their software to carry out this Thesis and for the attention received from all the members and the technical support.

Contents

List of Figures

List of Tables

Nomenclature

Acronyms

AMG	Algebraic MultiGrid.
AMR	Adaptive Mesh Refinement.
API	American Petroleum Institute.
BDC	Bottom Dead Center.
BEV	Battery Electric Vehicles.
BMEP	Brake Mean Effective Pressure.
BTDC	Bottom Top Dead Center.
CAD	Crank-Angle Degrees.
CFD	Computational Fluid Dynamics.
CIS	Continuous Injection System.
CI	Compression Ignition.
CO2	Carbon Dioxide.
CO	Carbon Monoxide.
DBI	Diffused Back-light Illumination.
DDM	Discrete Droplet Model.
DISI	Direct Injection Spark Ignition.
DI	Direct Injection.
DNS	Direct Numerical Simulation.
DPM	Discrete Phase Model.
DSMC	Direct Simulation Monte Carlo.
ECN	Engine Combustion Network.

ECU	Electronic Control Unit.
EE	Eulerian-Eulerian.
EFI	Electronic Fuel Injector.
EGR	Exhaust Gas Recirculation.
ELMO	Eulerian Lagrangian Mixing Oriented.
ELSA	Eulerian Lagrangian Spray Atomization.
EL	Eulerian-Lagrangian.
ESA	Eulerian Spray Atomization.
EU	European Union.
FTP	Federal Test Procedure.
GDCI	Gasoline Direct Compression Ignition.
GDI	Gasoline Direct Injection.
GHG	Greenhouse Gases.
HCCI	Homogeneous Charge Compression Ignition.
HC	Hydrocarbon.
HEG	Hydro-Erosive Grinding.
HLC	Homogeneous Lean Combustion.
HOS	Homogeneous-Stratified combustion.
HPC	High Performance Computing.
HPP	High Pressure Pump.
HRIC	High Resolution Interface Calculation.
HRM	Homogeneous Relaxation Model.
ICE	Internal Combustion Engine.
IDI	Indirect Injection.
IMEP	Indicated Mean Effective Pressure.
KH	Kelvin-Helmholtz.
LBDI	Lean Boost Direct Injection.
LDV	Laser Doppler Velocimetry.
LES	Large Eddy Simulations.
LPG	Liquid Petroleum Gas.
LVF	Liquid Volume Fraction.
MPI	Multi-Poing fuel Injection.
NIST	National Institute of Standards and Technology.
NOx	Nitrogen Oxides.

NTC No Time Counter.
OME Original Equipment Manufacturer.
PCCI Pre-mixed Charge Compression Ignition.
PDA Phase Doppler Anemometry.
PDI Phase Doppler Interferometry.
PDPA Phase Doppler Particle Analyzer.
PFI Port Fuel Injection.
PISO Pressure Implicit with Splitting of Operators.
PIU Production Injector Unit.
PIV Particle Image Velocimetry.
PLIC Piecewise Liner Interface Calculation.
PLIF Planar Laser Induced Fluorescence.
PM Particle Matter.
PN Particle Number.
RANS Reynolds-Averaged Navier-Stokes.
RCCI Reactivity Controlled Compression Ignition.
RNG Renormalization Group.
ROI Rate of Injection.
ROM Rate of Momentum.
RT Rayleigh-Taylor.
SCCI Spark Controlled Compression Ignition.
SGDI Spray-Guided Direct Injection.
SGSC Spray-Guided Stratified-Charge.
SGS Sub-Grid Scale model.
SIMPLE Semi-Implicit Method for Pressure-Linked Equations.
SI Spark Ignition.
SMD Sauter Mean Diameter.
SOI Start-of-Injection.
SOR Successive Over-Relaxation.
SPFI Sequential Port Fuel Injection.
SST Shear Stress Transport.
TAB Taylor Analogy Breakup.
TBI Throttle-Body Injection.
TDC Top Dead Center.

USB	Unified Spray Breakup.
VCO	Valve Covered Orifice.
VOF	Volume-of-Fluid.
VVA	Variable Valve Actuation.

Dimensionless quantities

α	Void fraction.
$\bar{x}$	Instantaneous equilibrium vapor quality.
δ_{ij}	Kronecker delta function.
ϕ	Non-dimensional pressure ratio.
AR	Area reduction of the orifice.
C_a	Area coefficient.
C_d	Discharge coefficient.
C_m	Momentum coefficient.
C_v	Velocity coefficient.
CFL	Courant-Friedrichs-Lewy number.
CN	Cavitation number.
Ja	Jakob number.
$k-factor$	Conic shape factor of the orifice.
k_{fric}	Coefficient of friction.
Nu	Nusselt number.
Oh	Ohnesorge number.
Pr	Prandtl number.
R_p	Radial expansion.
Re	Reynolds number.
Sch	Schmidt number.
Ta	Taylor number.
We	Webber number.
X	Volume fraction.
x	Instantaneous non-equilibrium vapor quality.
Y	Mass fraction.
y^+	Non-dimensional wall distance.

Greek symbols

$\boldsymbol{\tau}$	Viscous shear stress [Pa].

Δ	Spatial filter cut-off width in LES [m].
μ	Dynamic viscosity [kg/(m s)].
ν	Kinematic viscosity [m^2/s].
ν_{num}	Numerical viscosity in LES [m^2/s].
ν_t	Turbulent viscosity in LES [m^2/s].
ω	Specific turbulent dissipation [1/s].
Ω_{ij}	Rotation rate [rad/s].
ρ	Density [kg/m^3].
σ	Surface tension [kg/m^2].
τ_p	Ratio of particle response time [s].
τ_η	Turbulence Kolmogorov time scale [s].
θ	Time-scale [s].
ε	Turbulent dissipation [m^2/s^3].

Latin symbols

$\boldsymbol{n}$	Normal unity vector to the surface [-].
$\boldsymbol{U}$	Velocity vector [m/s].
$\dot{m}_f$	Fuel mass flow [kg/s].
$\dot{m_{f,th}}$	Theoretical fuel mass flow [kg/s].
$\dot{M}_{th}$	Theoretical spray momentum [kg/s].
$\dot{M}$	Spray momentum flux [N].
A	Area of the system, surface [m^2].
A_{eff}	Effective area [m^2].
c	Speed sound [m/s].
C_p	Specific heat capacity [m^2/s^2K].
D	Outlet diameter of the system [m].
d	Inner diameter of the system [m].
D_{diff}	Difussion coefficient [kg/(m s)].
e	Specific internal energy [m^2/s^2].
e_r	Absolute wall roughness [m].
g	Gravitational acceleration [m/s^2].
h	Specific enthalpy, [m^2/s^2].
h_{fg}	Latent heat of vaporization [kJ/kg].
K	Conductivity [S/m].
k	Turbulent kinetic energy [m^2/s^2].

L	Length of the system [m].
m	Total mass [kg].
M_m	Mass of species in the cell [kg].
M_{tot}	Total mass in the cell [kg].
P	Pressure [Pa].
R	Counter-bore fillet [m].
r	Inlet corner radius [m].
R_g	Gas constant [$m^2/(s^2K)$].
S_{ij}	Mean strain rate tensor [1/s].
T	Temperature [K].
t	Time [s].
u	Fluid velocity [m/s].
u_{eff}	Effective velocity [m/s].
u_{th}	Theoretical velocity [m/s].
V	Volume [m^3].
z	Elevation [m].

Subscripts

a, amb	Ambient.
$b, back$	Back.
$crit$	Critical.
f	Fluid.
g	Gas phase.
i	Inlet.
i	Liquid phase.
inj	Injection.
l	Liquid phase.
mod	Modeled.
o	Outlet.
p	Particle.
res	Resolved.
s, sat	Saturation.
tot	Total.

Chapter 1

Introduction

"Making mental connections is our most crucial learning tool,
the essence of human intelligence; to forge links;
to go beyond the given; to see patterns, relationships, context."
—Marilyn Ferguson

1.1 General Context

Internal Combustion Engines (ICEs) have been one of the greatest developments of the last century, revolutionizing the transport and mobility sector and becoming essential to modern society. The mobility of passengers and transport of goods is mainly powered by liquid-fueled ICEs due to their availability, convenience and cost effectiveness. Its working principle is based on producing mechanical energy from the chemical energy extracted from fuels through a regulated combustion process. These types of engines are not only found in transport applications (automotive, naval and aeronautical propulsion, etc.) but are also present in industries and power generation equipment. The continuous increase in population is requiring more and more available energy, thus making combustion engines indispensable to date.

The increase in energy demand [1] coupled with the widespread use of engines has led to an increase in the emissions and harmful pollutants mainly from the chemical reactions produced in the combustion of fuel. Only in the European Union (EU), means of transport are responsible for 27% of carbon dioxide (CO_2) [2] considered one of the principal greenhouse gases (GHG).

Not only CO_2 emissions are a concern, but also pollutants such as carbon monoxide (CO), nitrogen oxides (NO_x), particle matter (PM) and unburned hydrocarbons (HCs). This is why governmental institutions around the world and specially in the EU (Euro VI [3]) are imposing increasingly stringent restrictions to improve air quality and attempt to contain the well-known climate change [4]. For these reasons, the automotive sector is constantly changing in order to improve day by day and to help our society to become more environmentally friendly. This has also created a new challenge for researchers to find advanced solutions that comply with the current regulations, improve fuel economy while reducing operating costs.

In recent times, the reputation of ICEs has been damaged by emissions scandals that threaten and cast doubt on the ability of this technology to reduce emissions [5]. In response, several proposals have been suggested to replace conventional ICEs, including partial electrification (hybridization) or full electrification, although only the latter (battery electric vehicles (BEVs)) completely eliminates the need for ICEs. Even though at first glance BEVs may appear to be cleaner, the energy required for electricity generation and distribution as well as the manufacture of the batteries must be taken into account. In addition, the extraction of the materials necessary for batteries and electric motors (cobalt, lithium, etc.) demands a high source of energy and water. All of this energy generation is associated with CO_2 emissions, so the true benefit of full electrification is significantly less than it might appear [1]. Furthermore, the extensive and complex electrical infrastructure needed to charge BEVs in record time, which again means energy consumption, cannot be overlooked. Finally, end-of-life disposal must also be taken into consideration due to the toxicity of some of the materials that make up the batteries. For all these reasons, the all-electric future will not emerge easily, rapidly, or economically, and ICE transportation will continue to outstand in the industry for at least the coming three decades [6]. Consequently, the future that is foreseen today is that on- and off-road transport will be characterized by a combination of conventional ICE, battery and hybrid propulsion systems [1].

In Europe, diesel engines have been the main propulsion system in transport for last years. They are more energy efficient than gasoline engines due to the higher mass density of the fuel and the possibility of achieving higher compression ratios. In addition, diesel engines have also been economically attractive due to the significant price difference, especially in the European market, between fuels. The problem arose a few years ago, in 2015, when the famous Dieselgate scandal came to light where original equipment manufacturers (OEMs) used a specific software capable of manipulating the results

when detecting the performance of the emissions test, returning the engines to their normal operation in real driving conditions and emitting illegal values of NO_x. For this reason, together with the increasing regulation of NO_x and soot particles, consumers believed that diesel engines were highly polluting, which made gasoline gain interest in the automotive market. Since then, OEMs' attraction to gasoline engines has been increasing due to greater simplicity and reduced costs associated with after-treatment systems. Gasoline engines also exhibit advantages on the way to engine hybridization. A direct conversion from gasoline to gasoline-hybrid can lead to an 11% reduction in CO_2 emissions, and a further 23% reduction when going full hybrid [7].

The combustion efficiency and engine performance are greatly influenced by the complex fuel injection process. Given the importance, the injection event has become an object of study and is therefore one of the main objectives of research in recent years. The first injection strategy, Gasoline Port Fuel Injection (PFI), was characterized by injecting the fuel into the intake manifold, thus forming the air-fuel mixture outside the combustion chamber. Later, with the aim of improving fuel economy, Gasoline Direct Injection (GDI) strategy was introduced. Unlike the PFI, it allowed fuel to be injected into the cylinder, thus avoiding the wall wetting effect of the intake port and valves. However, it was not until 1996, when Mitsubishi launched an electronic GDI system that OEMs began to implement this system in their designs, increasing the number of models by up to 50% in 2016 [8]. GDI injection has a number of advantages including the ability to more precisely control the amount of fuel injected into the cylinder which offers the potential for leaner combustion and lower emissions, as well as improved fuel economy. The fuel injection pressure in these systems is higher than in PFI systems, which improves the atomization of the fuel in the cylinder, increasing the vaporization rate and thus overcoming cold starting. Improved fuel evaporation helps to cool the air which increases knocking resistance, allows higher compression ratios and can even improve volumetric efficiency [9]. GDI systems also benefit the implementation of strategies such as turbocharging and downsizing thus enhancing fuel economy by up to 8% [10]. For all these reasons, in addition to the continued tightening of restrictions associated with passenger cars, it is expected to push GDI engines further into the market and overtake PFI systems.

Nowadays, GDI engines continue to evolve and face new requirements in terms of fuel consumption and pollutant production. Behind all this, it is automotive companies and researchers who are struggling to uncover the hidden potential in this type of engines. For years, research has been focused on injection in diesel engines where the control of auto-ignition and resulting

combustion due to the small time scale has been a challenge for the engine community. At that time, the use of PFI in gasoline engines was widespread, but their operation was not as demanding since injection pressures were much lower and atomization, among other processes, did not determine the performance of the process to a significant extent. As already mentioned, it has been in recent years that the change in injection strategy in gasoline engines from PFI to GDI has been promoted to a greater extent, thus making the injection process critical and therefore a subject of in-depth study. In this context, a breakthrough has been made thanks to new developments in hardware and software systems, allowing higher injection pressures (10-40 MPa) and faster injections, even enabling the introduction of the concept of multi-injection. It has to be said, however, that despite all these improvements and the numerous investigations, the GDI process involves small time- and length-scales which, together with the difficulty of controlling the real operating boundary conditions and the complexity of the atomization process, makes it still interesting and demanding to study.

Research applied to GDI engines can be approached in several ways. The first one is aimed at understanding the injection and combustion processes inside the engine, without making any modifications to it and addressing all relevant phenomena. However, this approach makes numerous assumptions and thus involves many uncertainties. The second approach, on which this Thesis is mainly based, focuses on separating the relevant processes within the engine with the aim of going more deeply into each of them. In this sense, it is proposed, for example, to study injection without taking into account the combustion phenomenon. In the same way it is suggested to study the injection process in several phases: in- and near-field of the injector and downstream of the injector.

Notwithstanding, it is important to highlight that the study of the flow inside the injector, as well as in the near-field, is a very complex task due to several factors:

- Reduced size of the orifices (in the order of few hundred microns).
- High values of pressure and velocity (up to 40 MPa and 300 m/s).
- Short duration of the injection event (few milliseconds or even less).
- Influence of the dynamic behavior of the injector on transient phenomena.

For all the reasons above, among others, experimental campaigns under realistic operating conditions focused on the study of the internal nozzle flow behavior are extremely complex, if not practically unfeasible today.

Despite the above mentioned, there are some experimental techniques aimed at the hydraulic characterization of the injector based on macroscopic parameters such as the rate of injection (ROI) [11] and momentum flux (ROM) [12]. Other advanced tools that have been developed and implemented to study the phenomena inside the injector are the transparent nozzles which allow to obtain local values and above all to create profiles inside the injector [13, 14]. Although this is a major advance in research, it must be said that most of the studies are carried out on simple geometries, which differ from the commercial ones, and under operating conditions that are far from the real environment. Only tomography and x-ray techniques [15, 16] seem to provide accurate information about the flow inside and near the nozzle.

Leaving aside the internal flow and focusing on the structure of the spray itself, many techniques address its characterization as it develops out of the nozzle. Among those focused on the study of macroscopic parameters of the jet (liquid and vapor penetration or spray angle) [17], the following stand out: Diffused Back-light Illumination (DBI) [18], Mie scattering [19] and Schlieren [20]. All these experimental techniques have a high degree of uncertainty in their results due to the many parameters that can influence the outcome: position of the installation and of the lights associated, intensity of the light beams, image resolution and acquisition time, and above all, the post-processing criteria. In addition to macroscopic studies, there are numerous investigations that deal with the analysis of microscopic jet parameters such as droplet size and velocity. For this purpose, the most important experimental techniques are Phase Doppler Anemometry (PDA) [21] and Particle Image Velocimetry (PIV) [22] limited both to certain particle sizes and velocities.

Currently, due to the high cost of experimental tests and the existing limitations, one of the main short and long-term objectives of researchers is to describe injection and combustion processes on the basis of predictive models so that experimental practice is reduced to a minimum and replaced by computational analysis. The Engine Combustion Network (ECN) was born out of this need [23]. The ECN is a group of institutions collaborating together, experimentally and computationally, with the aim of creating a comprehensive framework that improves Computational Fluid Dynamics (CFD) modeling and enables the understanding of phenomena that take place particularly at high temperature and pressure relevant engine conditions where quantitative experimental data are limited [23]. In order to facilitate the comparison of

results between institutions and thus provide reliable datasets for the development of CFD models, this network has focused on developing and establishing standard processing methodologies. The ECN network started in 2009 and, thanks to a generous donation from Robert Bosch LLC and Delphi Technologies, who provided two completely different injectors, the so-called "Spray A" for diesel and "Spray G" for gasoline, studies were conducted for the same target conditions. The gasoline spray-guided injector (Spray G) was established as a multi-orifice valve covered injector for which three operating conditions were initially defined as standard. Those conditions have been extended in recent years in order to adapt to new market requirements. Once the research baselines, hardware and operating conditions were set, several institutions started to work on identifying the main areas of development. Given the open access to both hardware and validation data, ECN injectors have become potential objects of study in all fields of research. This is the main reason why it is one of the subjects of analysis in this Thesis.

This Thesis seeks to be part of a growing trend in computational studies that began about 40 years ago. The use of two CFD software and two different GDI injectors has enabled the study of the flow behavior inside the nozzle as well as the development of the spray downstream of the nozzle outlet. The results and conclusions obtained from these studies are a depiction of the general behavior expected for multi-hole spray-guided GDI injectors. Therefore, creating a methodology for analysis applicable to new and future generations of GDI injectors valid in different CFD software has been one of the main challenges of this project.

The present investigation was carried out at *Departamento de Máquinas y Motores Térmicos* in the frame of the *Universitat Politècnica de València (Spain)*. The mentioned institution has extensive experience in the fuel injection and combustion fields, among other topics (air management, aftertreatment, noise and vibrations, etc). Over more than 40 years of experience, nearly 300 doctoral thesis have been completed, around 180 books have been written and more than 800 articles have been published in international conferences and high-impact journals. In these period of time, the main focus of research in the field of injection-combustion, where the present Thesis is framed, has been on diesel engines especially focused on the hydraulic behavior of the injector [24–26], as well as experimental and computational studies of the diesel spray patterns [27–31] and its implications on the combustion process [32, 33]. From a computational point of view, Salvador [34] focused his efforts on better understanding the influence of the operating and geometrical conditions of the injector nozzle on the hydraulic behavior as well as the macroscopic development of diesel spray, using a commercial CFD software

and validating the obtained results with experimental tools. This work was further developed by Martínez-López [35] whose studies were based on the influence of partial needle lifts on the internal flow and especially on the cavitation process using an open source code. Going even further, Martí-Aldaraví [36] went in-depth the prediction of the internal nozzle flow behavior together with the spray structure and break-up pattern using multiphase models in an open source software. Regarding fuel spray and combustion analysis, Pachano [37] combined CFD models to investigate the influence of the fuel injection in the combustion process and soot formation. The growing interest in GDI has led this institution to specialize in the research of this type of technology given its promising future possibilities. Only two thesis have been carried out in the department, both developed experimentally, based specifically on gasoline direct injection systems. Vaquerizo [38] was responsible for transferring the knowledge acquired over the years from diesel injection studies to GDI cases both internal nozzle flow and fuel spray studies. Bautista [39] took the previous thesis as a reference and broadened the study by focusing on phenomena that occur in the injection process such as flash boiling and spray collapse.

1.2 Objectives and Methodology

The purpose of this Thesis is to provide a better understanding to the scientific community in the field of gasoline direct injection (GDI) about the phenomena taking place in the injection process that directly affect combustion efficiency and thus the fuel consumption and generation of pollutants. Nowadays, more than one third of the light-duty vehicles manufactured worldwide are equipped with a GDI fuel system and further growth of more than 10% per year or even more is expected with the upcoming hybridization [40]. In this context, it is important to combine efforts in order to develop and establish a solid computational basis complementary to experiments for a better understanding, design and efficient optimization of today's highly complex injection systems.

The main objective of this research is to develop a predictive methodology for the hydraulic characterization of a GDI injector under steady and transient operating conditions capable of being applied to current and future generations of GDI injectors, regardless of the injector features and the software used. The developed methodology will be validated with experimental data available in the literature. Once validated, the final goal is to use the obtained results from this predictive methodology to analyze the behavior of the fluid downstream of the injector (external flow). The intention of this approach is to follow in

the footsteps of the research community in replacing experimental practice as far as possible, as it has been done in recent years.

This document presents the validity of the predictive methodology developed through its application to two GDI injectors with very different features. On the one hand, the Delphi multi-hole solenoid injector belonging to the well-known ECN and named as Spray G has been used as the basis for the analysis. On the other hand, and with the main objective of validating this methodology in an industrial injector of real applicability, another solenoid injector has also been studied, in this case belonging to the Denso brand, which is used to date by a car manufacturer and which will henceforth be referred to as the Production Injector Unit (PIU).

The strategy to be followed in this research is to separate the processes to be studied so that each one can be investigated in greater depth. In this sense, the injection process will be divided into two distinct parts, the in- and near-nozzle on the one hand and the development and structure of the spray on the other. The predictive methodology is focused on the study of the internal flow and near-field in order to hydraulically characterize the injector. The problem to be addressed is defined on the basis of a multi-phase system, carried out in an Eulerian framework, modeled through a single-fluid approach. The above-mentioned multi-phase system is a two-phase three-component mixture consisting of a liquid phase, a vapor phase and non-condensable gas, which requires an specific method to simulate the two-phase (liquid and gas) flow. For this purpose, the well-known and widely used Volume-of-Fluid (VOF) model will be employed [41]. There are many phenomena that can occur inside the nozzle, including the phase change from liquid to vapor either by cavitation or flash-boiling. The mass exchange between the liquid and vapor phases of the same species is based on the non-equilibrium homogeneous relaxation model (HRM) [42], which is one of the most widespread approach nowadays among all the existing ones such as Schnerr and Sauer or Kunz cavitation models.

The Discrete Droplet Model (DDM) is the most common approach to modeling liquid atomization or break-up [43] and therefore, it is chosen for the study of the spray in the current investigation. The hydraulic characteristics of the injector are parameters of high importance in the modeling as they are the basis for the initialization of the properties and characteristics of the spray. DDM model is developed under a Lagrangian framework and captures the liquid droplet dynamics, spray breakup, heat transfer, evaporation, collision, etc. However, it is necessary to complement the model with an Eulerian approach that computes the ambient gas as well as the vapor phase. Under this premise, some researchers have taken advantage of the Eulerian framework

by using only this model to study the dense part of the spray [36]. On the other hand, others have preferred to combine the advantages of both approaches by creating what is called the Eulerian-Lagrangian Spray Atomization (ELSA) model [44].

It is well known that atomization and spray behavior is greatly influenced, among other factors, by the geometry of the nozzle [45]. Therefore, the coupling strategy of the internal and external flow can complement the previous analyses and provide a better understanding of the physics and even a closer approximation to reality. The coupling is mainly supported by the temporal and spatial transfer of internal flow variables (velocity, turbulent kinetic energy, dissipation rate or void fraction) to a primary break-up model which uses them to initialize droplet properties such as size and velocity. Several ways of internal and external flow coupling are known [46]. For the present work, the One-Way coupling [47] and mapping [43] approaches have been adopted.

The computational tools used to carry out this research are: CONVERGE™ v2.4 and StarCCM+ v12.04. Both software are commercial solvers, which means that access is not free for any user but requires a license for use. The employ of two codes allows to validate the above methodology in diverse contexts using different solvers. CONVERGE™ from CONVERGE Studio group is a code that has increasingly grown in strength in recent years, especially in the field of Internal Combustion Engines [48–50]. It stands out for its autonomous meshing, state-of-the-art physical models, robust chemistry solver, and the way it deals to easily accommodate moving geometries. It is based on automatic mesh generation and adaptive mesh refinement algorithms allowing the study of complex geometries with moving parts. By comparison, Star CCM+ from CD-Adapco has a wider range of applications not only in the field of engines and transportation [51] but also in areas such as biotechnology [52] and renewable energies [53]. One of the main advantages of this code is the possibility of configuring different types of meshes, especially with polyhedral elements.

1.3 Thesis Outline

This Thesis attempts to provide a better understanding of the flow behavior inside gasoline direct injection (GDI) nozzles and the spray patterns, in addition to provide a broad overview of phenomena that take place during the injection process creating a methodology capable of being applied to industrial GDI injectors. The results of applying the aforementioned methodology

developed in the jet study are presented in this document throughout the nine chapters of which it is made up.

In the already read introductory section (*Chapter 1*), the reader is contextualized on the subject of the study and its objectives. Subsequently *Chapter 2* covers the basics of internal combustion engines. The different types of existing combustion engines, their evolution and operating principles are presented. All this is followed by an overview of the theory and concepts related to injection, closing the chapter with more specific terms to GDI.

Chapter 3 describes the different types of GDI injectors existing to date, at least until the time this Thesis is being written. It also focuses on defining the flow characteristics inside the nozzle (internal nozzle flow) and outside the nozzle (spray patterns including atomization and breakup, dispersion, mixing and evaporation) as well as the phenomena arising during the injection process such as cavitation and flash boiling in case of internal flow and spray collapse when the spray leaves the nozzle.

The state of the art, *Chapter 4*, brings together the experimental and computational efforts of numerous researchers to understand the behavior of gasoline direct injection using laboratory test rigs and CFD approaches. The methodologies employed in the researches are set out in this chapter together with the discussion of the advantages and disadvantages of each. The purpose of this review is to select the best or most suitable models to characterize the entire injection process, from the turbulence and fluid behavior inside the nozzle to the air-liquid mixture downstream of it.

Chapter 5 describes the computational methodology that forms the basis of the present Thesis. It includes the necessary models and sub-models, which have been selected in order to carry out the most realistic simulations feasible and accurately predict the characteristics of the fluid behavior. Not only does this chapter describe the solvers used, but also reflects the strategy to set up the corresponding case studies (pre-processing) as well as explains the post-processing tools that have been used and developed specifically for the analysis.

After establishing the fundamentals of the study, *Chapter 6* presents the first set of results. They are concerned with the internal flow and near-field performance. The purpose of this chapter is to hydraulic characterize both studied injectors in terms of rate of injection (ROI), rate of momentum (ROM), hydraulic coefficients, spray angle and plume direction. This characterization is conducted under different operating conditions both when the needle is in a fixed position at a certain lift and when the transient behavior

(opening, steady and closing) of the needle is reproduced. The results obtained throughout this section are compared and validated with experimental data from previous thesis in the department.

Chapter 7 addresses the analysis of the spray structure as well as on the process of spray break-up. The models and sub-models employed in this study have been calibrated and validated with experimental data, as in the internal flow obtained from previous works in the institution. In this case, the study has focused on macroscopic spray characteristic parameters such as liquid and vapor penetration, gas velocity and spray shape among others, under several density and temperature parametric variations.

Up to this point, the flow behavior both inside the nozzle and near-field and the evolution of the spray structure downstream of the injector have been studied separately. *Chapter 8* reports the results obtained from the coupling between internal and external flow using different methods such as the known one-way coupling and mapping. All these results obtained are compared with experimental data and the results from the spray analysis presented in the previous chapter.

Finally, the last *Chapter 9*, summarizes the main findings of the research and sets out possible directions for future studies on the GDI strategy, a field with much potential to be developed.

References

[1] Reitz, R. D. et al. "IJER editorial: The future of the internal combustion engine". In: *International Journal of Engine Research* 21.1 (2020), pp. 3–10. DOI: 10.1177/1468087419877990.

[2] Archer, G. et al. "CO2 Emissions From Cars: The facts". In: *Transport & Environment* August (2018), p. 53.

[3] EuroVI. "Regulation (EC) No 715/2007 of the European Parliament and of the Council of 20 June 2007 on type approval of motor vehicles with respect to emissions from light passenger and commercial vehicles (Euro 5 and Euro 6) and on access to vehicle repair and mai". In: *Official Journal of the European Union* (2007), pp. 1–15.

[4] Morfeldt, J. et al. "Carbon footprint impacts of banning cars with internal combustion engines". In: *Transportation Research Part D: Transport and Environment* 95.May (2021), p. 102807. DOI: 10.1016/j.trd.2021.102807.

[5] An, Q. et al. "Volkswagen's diesel emission scandal: Analysis of facebook engagement and financial outcomes". In: *Lecture Notes in Computer Science (including subseries Lecture Notes in Artificial Intelligence and Lecture Notes in Bioinformatics)* 10968 LNCS (2018), pp. 260–276. DOI: 10.1007/978-3-319-94301-5_20.

[6] Kalghatgi, G. "Is it really the end of internal combustion engines and petroleum in transport?" In: *Applied Energy* 225.February (2018), pp. 965–974. DOI: 10.1016/j.apenergy.2018.05.076.

[7] USCAR. "Summary Report on the Transportation Combustion Engine Efficiency Colloquium Held at USCAR, March 3 and 4, 2010". In: (2010).

[8] US Environmental Protection Agency. "Light-Duty Automotive Technology, Carbon Dioxide Emissions, and Fuel Economy Trends: 1975 Through 2016". In: November (2018).

[9] Chincholkar, S. P. et al. "Gasoline Direct Injection: An Efficient Technology". In: *Energy Procedia* 90.December 2015 (2016), pp. 666–672. DOI: 10.1016/j.egypro.2016.11.235.

[10] Saliba, G. et al. "Comparison of Gasoline Direct-Injection (GDI) and Port Fuel Injection (PFI) Vehicle Emissions: Emission Certification Standards, Cold-Start, Secondary Organic Aerosol Formation Potential, and Potential Climate Impacts". In: *Environmental Science & Technology* (2017), acs.est.6b06509. DOI: 10.1021/acs.est.6b06509.

[11] Payri, R. et al. "Internal flow characterization on an ECN GDi injector". In: *Atomization and Sprays* 26.9 (2016), pp. 889–919. DOI: 10.1615/AtomizSpr.2015013930.

[12] Payri, R. et al. "Momentum Flux Measurements on an ECN GDi Injector". In: *SAE Technical Paper 2015-01-1893*. 2015. DOI: 10.4271/2015-01-1893.

[13] Mamaikin, D. et al. "High Speed Shadowgraphy of Transparent Nozzles as an Evaluation Tool for In-Nozzle Cavitation Behavior of GDI Injectors". In: *ILASS - Europe 2017, 28th Conference on Liquid Atomization and Spray Systems* September (2017). DOI: 10.4995/ilass2017.2017.4639.

[14] Mamaikin, D. et al. "Experimental investigation of flow field and string cavitation inside a transparent real-size GDI nozzle". In: *Experiments in Fluids* 61.7 (2020), pp. 1–15. DOI: 10.1007/s00348-020-02982-y.

[15] Duke, D. J. et al. "Time-resolved X-ray Tomography of Gasoline Direct Injection Sprays". In: *SAE International Journal of Engines* 9.1 (2015), pp. 143–153. DOI: 10.4271/2015-01-1873.

[16] Allocca, L. et al. "Tomography of a GDI spray by PolyCO based x-ray technique". In: *SAE Technical Papers* 6.April 2020 (2013). DOI: 10.4271/2013-24-0040.

[17] Lazzaro, M. "High-Speed Imaging of a Vaporizing GDI Spray: A Comparison between Schlieren, Shadowgraph, DBI and Scattering". In: *SAE Technical Papers* 2020-April.April (2020), pp. 1–15. DOI: 10.4271/2020-01-0326.

[18] Payri, R. et al. "ECN Spray G external spray visualization and spray collapse description through penetration and morphology analysis". In: *Applied Thermal Engineering* 112 (2017), pp. 304–316. DOI: 10.1016/j.applthermaleng.2016.10.023.

[19] Montanaro, A. et al. "Flash Boiling Evidences of a Multi-Hole GDI Spray under Engine Conditions by Mie-Scattering Measurements". In: *SAE Technical Papers* 2015-Septe.September (2015). DOI: 10.4271/2015-01-1945.

[20] Lazzaro, M. "Characterization of the liquid phase of vaporizing GDI sprays from Schlieren imaging". In: *Measurement Science and Technology* 30 (2019). DOI: 10.1088/1361-6501/AB228D.

[21] Araneo, L. et al. "Analysis of PDA measurements in double injection GDI sprays". In: *ILASS - Europe 2017, 28th Conference on Liquid Atomization and Spray Systems* September (2017), pp. 6–8. DOI: 10.4995/ilass2017.2017.5007.

[22] Prosperi, B. et al. "PIV Measurement of Injection Pressure Influence on Gas Entrainment in GDI Engines". In: *ILASS - Europe 2007, 21st Conference on Liquid Atomization and Spray Systems* Table 1 (2007), pp. 1–6.

[23] Pickett, L. et al. "Engine combustion network special issue". In: *International Journal of Engine Research* 21.1 (2020), pp. 11–14. DOI: 10.1177/1468087419882247.

[24] Gimeno, J. "Desarrollo y aplicación de la medida de flujo de cantidad de movimiento de un chorro Diesel". PhD thesis. E.T.S. Ingenieros Industriales, Universtitat Politècnica de València, 2008. DOI: 10.4995/Thesis/10251/8306.

[25] Venegas, O. "Estudio del fenómeno de la cavitación en la inyección diesel mediante la visualización del flujo interno en orificios transparentes." PhD thesis. Universitat Politècnica de València, 2014. DOI: 10.4995/Thesis/10251/37375.

[26] Carreres, M. "Thermal Effects Influence on the Diesel Injector Perfomance through a Combined 1D Modelling and Experimental Approach". PhD thesis. Universitat Politècnica de València, 2016. DOI: 10.4995/Thesis/10251/73066.

[27] Peraza, J. E. "Experimental study of the diesel spray behavior during the jet-wall interaction at high pressure and high temperature conditions". PhD thesis. Universtitat Politècnica de València, 2020. DOI: 10.4995/Thesis/10251/149389.

[28] Crialesi-Esposito, M. "Analysis of primary atomization in sprays using Direct Numerical Simulation". PhD thesis. Universtitat Politècnica de València, 2019. DOI: 10.4995/Thesis/10251/133975.

[29] Viera, A. "Effect of multiple injection strategies on the diesel spray formation and combustion using optical diagnostics". PhD thesis. Universitat Politècnica de València, 2019. DOI: 10.4995/Thesis/10251/123954.

[30] Jaramillo Císcar, D. "Estudio experimental y computacional del proceso de inyección diésel mediante un código CFD con malla adaptativa". PhD thesis. Universitat politècnica de valència, 2017. DOI: 10.4995/Thesis/10251/92183.

[31] De la Morena, J. "Estudio de la influencia de las características del flujo interno en toberas sobre el proceso de inyección Diesel en campo próximo". PhD thesis. Universtitat Politècnica de València, 2011. DOI: 10.4995/Thesis/10251/11098.

[32] De la Garza, O. A. "Estudio de los efectos de la cavitación en toberas de inyección Diesel sobre el proceso de inyección y el de formación de hollín". PhD thesis. Universtitat Politècnica de València, 2012. DOI: 10.4995/Thesis/10251/18153.

[33] Garcia-Oliver, J. M. "Aportaciones al estudio del proceso de combustión turbulenta de chorros en motores Diesel de inyección directa". PhD thesis. Valencia: E.T.S. Ingenieros Industriales. Universitat Politècnica de València, 2004. DOI: 10.4995/Thesis/10251/55164.

[34] Salvador, F. J. "Estudio teórico experimental de la influencia de la geometría de toberas de inyección Diésel sobre las características del flujo interno y del chorro". PhD thesis. Valencia: E.T.S. Ingenieros Industriales. Universidad Politécnica de Valencia, 2003.

[35] Martínez-López, J. "Estudio computacional de la influencia del levantamiento de aguja sobre el flujo interno y el fenómeno de la cavitación en toberas de inyección Diesel". PhD thesis. Valencia: Universitat Politecnica de Valencia, 2013. DOI: 10.4995/Thesis/10251/29291.

[36] Martí-Aldaraví, P. "Development of a computational model for a simultaneous simulation of internal flow and spray break-up of the Diesel injection process". PhD thesis. Valencia: Universtitat Politècnica de València, 2014. DOI: 10.4995/Thesis/10251/43719.

[37] Prieto, L. M. P. "CFD Modeling of Combustion and Soot Production in". PhD thesis. 2020. DOI: 10.4995/Thesis/10251/142189.

[38] Vaquerizo, D. "Study on Advanced Spray-Guided Gasoline Direct Injection Systems". PhD thesis. Universitat Politècnica de València, 2017. DOI: 10.4995/Thesis/10251/99568.

[39] Bautista Rodriguez, A. "Study of the Gasoline direct injection process under novel operating conditions". PhD thesis. Universitat Politècnica de València, 2021.

[40] Piock, W. et al. "Delphi Technologies Next Generation GDi-System - improved Emissions and Efficiency with higher Pressure". In: *Internationales Wiener Motorensymposium*. 2019, pp. 1–21.

[41] Giussani, F. et al. "VOF Simulation of The Cavitating Flow in High Pressure GDI Injectors". In: September (2017). DOI: 10.4995/ilass2017.2017.4989.

[42] Saha, K. et al. "Investigation of homogeneous relaxation model parameters and their implications for gasoline injectors". In: *Atomization and Sprays* 27.4 (2017), pp. 345–365. DOI: 10.1615/AtomizSpr.2017016338.

[43] Nocivelli, L. et al. "Analysis of the Spray Numerical Injection Modeling for Gasoline Applications". In: *SAE Technical Papers* 2020-April.April (2020), pp. 1–13. DOI: 10.4271/2020-01-0330.

[44] Navarro-martinez, S. et al. "An investigation on the impact of small-scale models in gasoline direct injection sprays (ECN Spray G)". In: *International Journal of Engine Research* (2019), pp. 1–9. DOI: 10.1177/1468087419889449.

[45] Payri, R. et al. "The effect of nozzle geometry over the evaporative spray formation for three different fuels". In: *Fuel* 188 (2017), pp. 645–660. DOI: 10.1016/j.fuel.2016.06.041.

[46] Benra, F. K. et al. "A comparison of one-way and two-way coupling methods for numerical analysis of fluid-structure interactions". In: *Journal of Applied Mathematics* 2011 (2011). DOI: 10.1155/2011/853560.

[47] Mohan, B. et al. "Coupled in-nozzle flow and spray simulation of Engine Combustion Network Spray-G injector". In: *International Journal of Engine Research* 22.9 (2021), pp. 2982–2996. DOI: 10.1177/1468087420960612.

[48] Benajes, J. et al. "Computational assessment towards understanding the energy conversion and combustion process of lean mixtures in passive pre-chamber ignited engines". In: *Applied Thermal Engineering* 178.April (2020), p. 115501. DOI: 10.1016/j.applthermaleng.2020.115501.

[49] García-Oliver, J. et al. "Computational study of ECN Spray A and Spray D combustion at different ambient temperature conditions". In: *Transportation Engineering* 2.October (2020), p. 100027. DOI: 10.1016/j.treng.2020.100027.

[50] Payri, R. et al. "Modeling gaseous non-reactive flow in a lean direct injection gas turbine combustor through an advanced mesh control strategy". In: *Proceedings of the Institution of Mechanical Engineers, Part G: Journal of Aerospace Engineering* 234.11 (2020), pp. 1788–1810. DOI: 10.1177/0954410020919619.

[51] Galindo, J. et al. "Assessment of the numerical and experimental methodology to predict EGR cylinder-to-cylinder dispersion and pollutant emissions". In: *International Journal of Engine Research* (2020). DOI: 10.1177/1468087420972544.

[52] Weyand, B. et al. "Three-Dimensional Modelling inside a Differential Pressure Laminar Flow Bioreactor Filled with Porous Media". In: *BioMed Research International* 2015 (2015). DOI: 10.1155/2015/320280.

[53] Van Rij, J. et al. "Extreme load computational fluid dynamics analysis and verification for a multibody wave energy converter". In: *Proceedings of the International Conference on Offshore Mechanics and Arctic Engineering - OMAE* 10.July (2019). DOI: 10.1115/omae2019-96397.

Chapter 2

Fundamentals of the ICE and Fuel Delivery

"Success is neither magical nor mysterious. Success is the natural consequence of consistently applying the basic fundamentals."
—Jim Rohn

2.1 Introduction

The last few centuries have been characterized by continuous social, cultural, economic and technological changes, including the well-known Industrial Revolution that took place between 1760 and 1840. The Industrial Revolution represented a breakthrough in the history of humankind, particularly because its repercussions extended to all spheres of society. In short, it marked the emergence of technological and scientific developments that constituted a break with the socio-economic patterns that had prevailed up to the present time. The steam engine was the basis of all the innovations that evolved as a consequence of this movement.

Steam engines are considered the first machines capable of producing non-natural mechanical energy (not come from the use of energy existing in nature such as hydraulic or wind power) with acceptable efficiency. They are, undoubtedly, defined as the antecedents of ICEs which are considered the most revolutionary invention of the last century with a remarkable impact on society. The emergence of ICEs completely changed the concept of transport

and mobility and enabled numerous technological advances. The continued widespread use of these technologies is due to their low cost, high power-to-weight ratio, high efficiency and relatively simple and rugged operating characteristics.

The birth date of ICEs, as they are known nowadays, is the late 1870s when the German Nicolaus Otto applied for the patent of the first practical four-stroke engine with a compression ratio of 2.5, generating 2 hp at 160 rpm and a braking efficiency of 14% under the name *Gasmotor* [1]. Although the four-stokes concept as such had been patented earlier by A. de Rochas, it was Otto who first manufactured and marketed the working flame ignition engine. Despite his lack of academic training, Otto devoted his entire life to ICE development and in 1872 founded the first ICE manufacturing company for which he hired Gottlieb Daimler and Wilhelm Maybach. Daimler founded the Daimler Motor Company years after building the first four-wheeled automobile and it is therefore known as the forefather of the automobile industry. Within this field, it is worth mentioning Rudolf Diesel who was the first to inject liquid fuel directly into the combustion chamber of a four-stoke engine. Diesel focused his work on designing engines that replicated the thermodynamic Carnot cycle, which was not feasible in practice, and ended up adopting the strategy of combustion at constant pressure instead of at constant temperature, as was his initial idea. Diesel carried out several collaborations among them with Carl von Linde, professor at Munich Polytechnic, with whom he worked on the refrigeration of the Rankine cycle using ammonia, and with MAN company to develop compression ignition engines. One of the first advances that Diesel made was a single-cylinder engine that atomized the fuel with the assist of air injection, reaching an efficiency of 27% at full load, much higher than the steam engines and spark ignition engines of the time [2].

In addition to the aforementioned, there are many others who stand out at that time for their enormous advances in the transportation sector. Simultaneously with the breakthroughs in spark-ignition engines with carburetor, Carl Benz opened the way for the automobile industry in 1885 by registering the patent for the first automobile. The following decades, the industry began to grow exponentially with the appearance of new companies such as Peugeot, Citroën, BMW, Renault, Ford, Rolls-Royce and Austin, among others. One of the main problems was that the vehicles were not affordable for all users, as they were considered individually manufactured one-offs. It was in 1913 that the assembly line concept created by Henry Ford was introduced and exploded the car market with reasonable prices for all social classes.

Since the introduction of Otto and Diesel engines as well as the first ICE-

powered vehicles, the automotive industry and the concept of mobility has been in a permanent transformation. Over the years, designs have been adapted mainly to user needs and recently also to government restrictions. The establishment of the Kyoto Protocol, which aims to reduce emissions of six greenhouse gases (GHG), has led vehicle manufacturers to change and improve its systems in order to comply with the limitations of harmful NO_x exhaust gases and pollutants. From this need arose the idea of adopting gasoline direct injection (GDI) aimed primarily at reducing fuel consumption and minimizing pollutant emissions. Although, in addition to GDI, new concepts such as hybridization or electrification are being introduced as alternatives to minimize pollutants. The characteristics that made internal combustion engines so popular remain their strong point today. However, it is important for vehicle manufacturers as well as researchers in the field to make efforts to achieve cleaner vehicles that offer the same or even better performance.

2.2 Description and Classification of ICEs

As a general definition, a motor is considered to be a device that allows the transformation of any type of energy into mechanical energy. Within this broad field, this energy can be obtained directly from the power source such as solar radiation, from thermal energy contained in a compressible fluid, or from the chemical energy available in materials, among many other options. In the last case, a process called combustion is needed to convert the chemical energy into mechanical energy. Depending on where this process takes place, engines can be classified into external combustion engines and internal combustion engines, which are the focus of this Chapter.

There are several classifications within ICEs that distinguish one engine from another. This involves differences in the operating cycle between 2-stroke and 4-stroke engines, for example. These two types of engines differ mainly in the exhaust and intake stages. In a two-stroke cycle, the piston produces power each downward stroke whereas the four-stroke cycle generates power every other downward stroke or which is the same two revolutions of crankshaft. The first type mentioned are usually simpler and lower cost engines used in applications that do not require large sizes such as motorbikes or light vehicles. Their use is decreasing due to poor emissions characteristics. In contrast, 4-stroke engines are more attractive and have a wider range of application due to their lower fuel consumption, longer range, better emission control and lower vibrations.

Another of the most widespread classifications among ICEs is according to the thermodynamic cycle, divided into Otto and Diesel engines, named after their developers. The main difference between these engine types is the ignition process of the air-fuel mixture, and the subsequent evolution of combustion. Diesel cycles are characterized by the self-ignition of the mixture when suitable pressure and temperature conditions are reached. Engines that operate on this principle are known as Compression Ignition (CI) engines. In contrast, Otto cycles are typified by the ignition of the mixture through an external energy source, usually a spark generated by a suitable plug. In this case, engines are also known as Spark Ignition (SI).

There are certain variations in the four-stroke cycle (Figure 2.1) between the two engine types. CI engines are governed by the following principles:

- Intake: the piston has a downward movement from top dead center (TDC) to bottom dead center (BDC) generating a vacuum in the in-cylinder that favors the entry of fresh air through the intake valve, which is open during this phase.
- Compression: at this stage both the intake and exhaust valves are closed. The piston starts an upward movement from BDC to TDC, compressing the air inside the cylinder which increases the pressure and temperature in the chamber.
- Combustion: at the end of the compression stroke when the piston reaches TDC, fuel is injected into the chamber. At this point, the temperature and pressure conditions are suitable for self-ignition of the air-fuel mixture. In this process, a large amount of energy is released, increasing the pressure and temperature and pushing the piston towards the BDC.
- Exhaust: the exhaust valve opens to let out the products of combustion pushed by the upward movement of the piston. The cycle is completed when the piston reaches TDC.

One of the distinguishing features of the CI engines is that only fresh air is introduced into the cylinder in order to control the timing of ignition. Fuel is delivered into the compression stroke when the piston is reaching TDC so that it has time to evaporate and mixing with air. At this point, the conditions are appropriate and ignition takes place in such a way that a diffusion flame is created around the spray which lasts until all the fuel is injected into the combustion chamber. In CI engines, combustion takes place mainly in areas

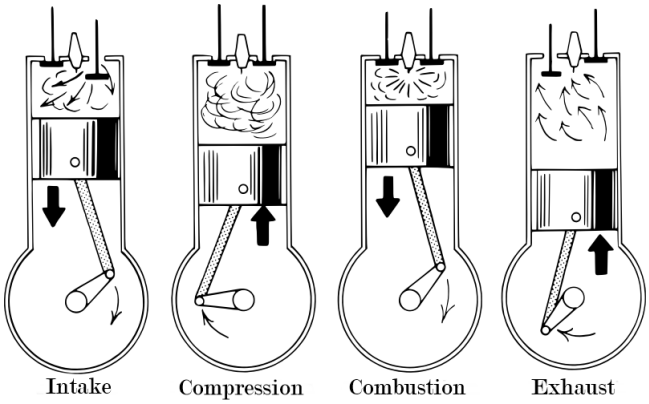

Figure 2.1: Four-stroke engine operating cycle.

where the air-fuel mixture is rich, usually in the surrounding of the spray, as the overall mixture in this type of engine is considered homogeneous. The combustion process is highly dependent on the jet behavior as well as on the air movement inside the cylinder. For this reason, spray atomization, evaporation and mixing are very important processes in this type of engine.

The ideal Diesel cycle is characterized by combustion at constant pressure whereas the Otto cycle develops this process at a constant volume, this being the simplified principle of operation in an SI engine. Apart from this nuance in combustion, the SI engine differs from the CI engine in that no fresh air is introduced into the cylinder during the intake phase, but an air-fuel mixture. In SI engines, combustion begins with a spark from a spark plug that produces the ignition. The timing of this extra energy input is controlled according to engine load and speed so that combustion occurs as optimally as possible. The mixture introduced in the intake phase is homogeneous charge close to the stoichiometric ratio. To achieve this specific condition over the entire operating range, the procedure is to control the amount of air introduced. For this purpose, a throttle valve is used in the intake duct upstream of the intake valve. It is therefore the valve itself that controls the power in an Otto cycle as the fuel is metered in proportion to the air flow rate introduced. In contrast to Diesel cycles where fuel is still being injected at the same time as combustion takes place, in Otto cycles the mixing takes place before combustion starts.

To summarize, the four-stroke cycle in both concepts is similar but differs in how the mixture is formed and how the ignition and combustion process take place and develop. These differences in operating cycle lead to discrepancies in engine design and geometry [1].

2.3 Fuel Injection Systems

2.3.1 Diesel engines

As mentioned above, the ignition and subsequent combustion in CI engines take place when the optimum temperatures and pressures to support these processes are reached. At this time, the air-fuel mixture has to be appropriate so that the highest possible efficiency and performance is achieved. Therefore, the fuel supply system must be capable of injecting the fuel into the cylinder at high pressures in order to promote the atomization and mixing phenomena. These are the main reasons why the injection system is considered a critical part of the design and have led researchers to study it in more detail [3]. In Diesel engines, there are two main ways of delivering the fuel into the cylinder. On the one hand, what is known as indirect injection (IDI), which consists of initially injecting the fuel into a pre-chamber where it is mixed with the air and then transferring this mixture into the combustion chamber. On the other hand, a more innovative technique is to inject fuel directly into the combustion chamber, known as the direct injection (DI) approach. Both techniques are explained in more detail in the following paragraphs.

Indirect injection

Indirect injection in Diesel engines is characterized by having, as shown in Figure 2.2a, two chambers of different sizes connected by a conduit. The smaller one located at the top, before the intake valve, corresponds to the pre-chamber while the lower one located between the piston and the cylinder head represents the main combustion chamber. This system is typified by the fact that combustion starts in the pre-chamber and extends into the main combustion chamber. The pre-chamber is designed in such a form that, during the compression stage, the air entering the cavity is sufficiently turbulent to promote mixing and atomization of the fuel as well as delivery of the air-fuel mixture to the main combustion chamber. The injection system developed for the IDI is simpler and therefore less demanding as the injection pressures involved are not as high (20-40 MPa) and the injector orifices are much larger (1 mm) compared to the DI. The reason for this is that the atomization and mixing process depends to a great extent on the turbulence and air movements generated by the pre-chamber.

The main weaknesses of this injection system include lower thermal efficiency of the engine due to heat loss to the cylinder walls, lower compression ratios and less stable operation. In addition, there are higher pumping losses due to the larger air flow path through both combustion chambers. The need to increase the efficiency of the engine gave rise to DI systems, which have

gradually gained an important place in the market, thus displacing the IDI systems.

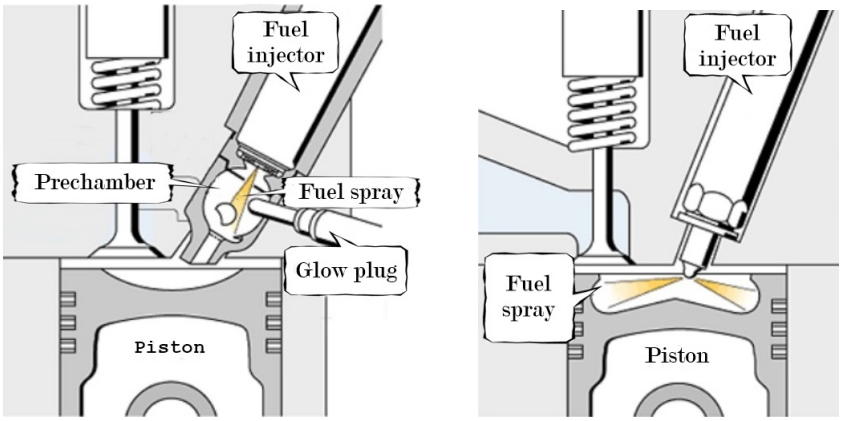

(a) Indirect injection (b) Direct injection

Figure 2.2: Sketch of an indirect and direct injection in Diesel engines.

Direct injection

Figure 2.2b illustrates the operation of the DI system where the fuel is directly supplied into the cylinder. One of the main differences at first sight is the shape of the piston, which differs from one system (IDI) to another (DI). In the case of DI, the turbulence generated in the cylinder is low due to the reduced velocities of the incoming air through the intake valve (in the order of 25 m/s). Therefore, like the pre-chamber in the case of the IDI, the piston head is designed with geometries that favor air movement within the combustion chamber, thus enhancing the air-fuel mixture. However, although piston design plays an important role, the convective field of the fuel is primarily responsible for the mixture. For this reason, injection systems are becoming increasingly advanced and complex so that their primary function is to improve fuel atomization. To achieve this, some of the employed strategies are to reduce the size of the nozzle orifice to the order of microns (0.1 mm), use multi-hole injectors and deliver fuel at high pressures which can be even higher than 200 MPa, and systems are being studied to double this injection pressure to 400 MPa [4]. The importance of the injection system in Diesel engines has led to its continuous evolution in order to extend its use within the required standards and requirements. The most common systems employed for fuel delivery are briefly mentioned in the following lines: the rotary pump, also known as direct acting system, where a high pressure pump introduces

the fuel into the cylinder while the injector only atomizes it; the unit injector which combines a pump and an injector into a single unit with the injection being controlled by a high speed solenoid valve; the unit pump, an alternative to the previous system with a modular design that allows control of the start-of-injection (SOI) and the total mass injected; and finally, the common-rail, considered an accumulative system, where the high pressure pump is only responsible for increasing the fuel pressure and the injector is responsible for fuel delivery and atomization.

The common rail was patented by Denso in 1995 and is currently the most widely used injection system in Diesel engines. This system has been improving and adapting to the market requirements over the years, and nowadays fulfills most of them. The diversity of working conditions requires a high degree of flexibility in the injection system, which is provided by the common-rail system [5].

2.3.2 Gasoline engines

Fuel and mixture formation requirements

Engine power is mainly regulated by the amount of fuel injected and the method of control depends on the type of engine. In CI engines, the regulation is of a qualitative nature in which the quantity of fuel injected varies, changing the quality of the mixture by varying the ratio between masses of fuel and air. On the contrary, in the case of SI working in a homogeneous mixing regime, the regulation is quantitative. This means that the quantity of mixture is controlled by the throttle valve in such a way that it is adjusted to the required needs. Through this valve the pressure drops, while the temperature remains practically unchanged, thus limiting the air flow. Pumping losses are a phenomenon to be taken into account as they greatly reduce the mechanical performance of the engine. The pressure losses in the intake ducts are much higher when the air flow is regulated from the throttle valve. This is the main reason for favoring the use of direct injection systems [6], as will be addressed in the forthcoming sections. Since the combustion efficiency as well as the products of combustion, differ significantly for fuel-lean and fuel-rich mixtures, and because the stoichiometric fuel-air ratio is highly dependent on the components that make up the fuel, the ratio between the current fuel-air ratio and the stoichiometric ratio (or its inverse) is a better descriptive variable for evaluating the mixture composition. The relative air-fuel ratio λ

is expressed as Equation 2.1.

$$\lambda = \frac{Current\ air\ mass}{Stoichiometric\ air\ mass} \tag{2.1}$$

The inverse of λ, fuel-air equivalence ratio ϕ, is presented in Equation 2.2.

$$\phi = \frac{m_{fuel}/m_{air}}{(m_{fuel}/m_{air})_{st}} = \frac{1}{\lambda} \tag{2.2}$$

From these two equations the characteristics of the mixture are defined: fuel-lean mixture presents $\lambda > 1$ or $\phi < 1$, stoichiometric mixture equals to $\lambda = 1$ or $\phi = 1$ and fuel-rich mixture reflects $\lambda < 1$ or $\phi > 1$.

The variables ratios previously outlined are of great relevance as they contribute to defining the flammability limits of the mixture and thereby the possible operating points. The character of combustion makes flammability limits more critical for SI engines than for CI engines. In order to ensure stable combustion, the ϕ should be between 0.6 and 1.6. Depending on the characteristics that are being sought in the operation, the equivalence ratio within this range varies. For maximum performance with moderately low consumption, it is appropriate to work in lean mixtures, $\phi < 1$. If, on the other hand, maximum power is desired, the recommended operating point is $\phi \approx 1.15$, which means rich mixtures. It is important to note that the working ranges vary depending on multiple variables including cylinder pressure and temperature, which in turn depend on the working load and engine speed, or the degree of opening of the throttle valve [1]. In addition, the use of three-way catalysts is widespread in SI engines to reduce pollutant gases such as CO, NO_x and HC. This method is associated with working close to the stoichiometric condition ($\phi = 1$) in order to achieve the best emission performance.

Over the years, several systems have been developed in SI engines to deliver the exact amount of fuel in order to create a mixture according to the needs of the operation. Among these developments are the well-known carburetors, which were the first to come into use, followed by the Port Fuel Injector (PFI) systems. Later, in order to reduce pumping losses, increase volumetric efficiency and avoid phenomena such as wall wetting, the use of direct injection (DI) was introduced.

Carburetor

The carburetor has been the device most widely employed to regulate the flow of fuel into the intake manifold. This device is attributed to Karl Benz who patented it in 1886 as a result of his numerous researches focused on the

development and improvement of ICEs and their components. The carburetor operates by drawing air through a convergent-divergent channel resembling a Venturi and acting on the Bernoulli principle. This system is dependent on the throttle valve located downstream of the carburetor that regulates the flow of air, and hence the mixture into the cylinder. The incoming air flow passes through the Venturi of the carburetor, thus generating a pressure drop due to the acceleration of the air. The mentioned depression acts to draw the fuel into the Venturi axis, incorporating to the air flow in the form of droplets which travel along the manifold into the cylinders, while evaporating. Fuel droplet size is a function of pressure drop and partly determines the quality and homogeneity of mixtures in carburetor systems. This system became popular in passenger cars and was improved over time until it was replaced by gasoline injectors.

The first applications of the aforementioned new injection systems were in the aviation sector due to the need to pressurize the fuel. For a long period of time, the carburetors and gasoline injectors coexisted side by side in the market. It was in the 1970s that the improvement of carburetor systems began to stagnate, as it became increasingly difficult to meet accuracy requirements over the air-fuel mixture. This was compounded by concerns about emissions, leading to the introduction of mandatory catalyst technology. These reasons together with the great advances in electronic injectors resulted in the disuse of carburetors by the 1990s.

The carburetor was replaced by fuel injection systems mainly because of the advantages they offered in terms of ease and manageability of fuel delivery and atomization. Nowadays, gasoline injection systems are divided, as in CI engines, into direct injection and indirect injection depending on where the fuel is delivered and thus where the mixture takes place. DI systems will be treated more extensively in a different section (Section 2.4) since it is the topic of the present Thesis.

Indirect injection

Since the implementation of indirect injection systems in the automotive industry, their use has increased. In fact, to this day, many SI engines still use this type of injection system. The fuel delivery is regulated by means of an injector and is supplied directly upstream of the opening valve, in the intake manifold. The basic scheme of operation of these systems is illustrated in Figure 2.3.

Bendix Corporation used its experience in aircraft fuel injection systems to introduce the Electrojector concept known as the first electronic fuel injector (EFI) in 1956 [7]. In many respects it was far ahead of its time.

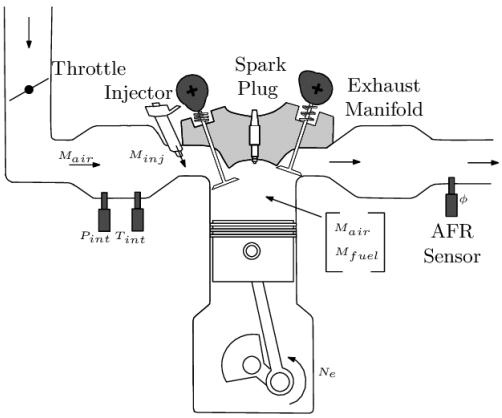

Figure 2.3: Scheme of a Spark Ignition engine equipped with indirect injection [6].

However, during this time fuel injection systems were complex, costly, and fitted to only the most expensive vehicles. Years later, in 1965, the system would be licensed to Bosch, who was able to make roadworthy in various German manufacturers as Bosch D-Jetronic. This system was characterized by pressure regulation in the intake manifold. The energy consumption became an important issue, so the L-Jetronic models with air flow measurement were developed, as well as the K-Jetronic with mechanical-hydraulic control (a system that also measures the intake air flow). In 1976, Bosch developed the lambda sensor and thus made the controlled catalytic converter possible. Subsequently, the Motronic, which combines the L-Jetronic with a program-map control for the ignition, was launched on the market. In 1981, the LH-Jetronic was offered for the first time with a thermo-wire air mass meter. A year later, the KE-Jetronic was introduced, which consisted of the K-Jetronic system extended by an electronic control circuit and the Lambda sensor. With the aim of extending the use of this type of injection, the Mono-Jetronic was born in 1987, a particularly economical central injection system which made it possible to equip small vehicles with electronic fuel supply systems [8]. It is at this point that the use of the carburetor becomes obsolete as the advantages of indirect injection systems (fuel consumption, emissions, efficiency, etc.) eclipse the performance of carburetors. These technologies have undergone improvements such as the implementation of the three-way catalyst to adapt to the new requirements, especially in terms of emissions. It has already been mentioned that these systems are still in use today, but only Motronic engine-management technology coupled with multi-point injection meets current fuel consumption and emission standards [5].

It is important to note that indirect injection systems have also been characterized by their configuration scheme.

- Single-point or Throttle-Body injection (TBI): the more primitive and less developed injection system which occupied the position of the carburetor with one or two fuel-injector nozzles in the throttle body. It

provided better fuel control than the carburetor at lower cost and was easier to operate. Single-point injection paved the way for the more complex multi-point systems.

- Continuous injection (CIS): unlike other fuel injection systems, the nozzles do not open and close in short pulses, but supply fuel continuously. The injector has the purpose of atomizing the continuous flow of fuel, the quantity of which is regulated according to the incoming air.
- Multi-point fuel injection (MPI) or port fuel injection (PFI): allocates a different injector nozzle for every cylinder, just outside the intake port. Discharging the fuel vapor close to the intake port nearly assures that it will be carried directly over the cylinder. This system stands out from the others mainly because of its precision in fuel delivery. Typical injection pressures at which they operate are in the range of 2 to 5 bar.
- Sequential Port Fuel Injection (SPFI): the basic MPFI adopts several injectors, all of which spray their fuel at the same time or in groups. SPFI activates each injector nozzle independently in a way that prevents fuel from sitting in the duct for a while when the engine is idling.

Of all the types presented above, the PFI was the most widespread due to its many advantages over the others. It offers lower exhaust emissions, higher power and torque through improving volumetric efficiency, lower fuel consumption, more rapid engine response and driveability, less noise than carburetors and more accurate control of the equivalence ratio during cold-start and engine warm-up [2]. In SI engines operating on PFI, the injector is generally oriented so that it hits the back of the intake valve (the hottest surface in the manifold) in order to improve the evaporation of the fuel and the mixture. In that way, the mixture enters the combustion chamber at high velocity, achieving a high degree of homogeneity when the spark plug is triggered. This injection system allows the option of staggered fuel injection which can be performed during the valve open period or when the valves are closed [9]. Although the fuel spray will impact with other surfaces increasing the wall wetting and generating unwanted fuel film puddles, these phenomena are much smaller compared to systems such as TBI as the air-fuel mixture travels much less through the ducts to the cylinder. In addition, PFI systems allow inlet ducts to be designed for optimal airflow, rather than enhanced mixing. By contrast, the PFI systems guarantee injection pressures between 2 and 5 bar but has to precisely control the quantities of fuel injected, especially during short injection periods such as when the engine is idling. The type of injector used to meet the requirements is a pintle nozzle where its upward movement involves the flow

of fuel. While the engine load is regulated by the throttle valve, a mass flow sensor and ECU calculate the required amount of fuel to be injected. Then, the ECU sends a signal to the injector, which opens by means of a solenoid. Port fuel injectors must meet a set of different criteria, including effective fuel metering, fast opening and closing, strong atomization, limited leakage, small pulse-to-pulse differences, large flow range, and resistance to deposits, among others. This makes them challenging hardware that is still being investigated and optimized for future developments including hybrid engines [10].

2.4 Gasoline Direct Injection

2.4.1 Introduction

Gasoline engines have been, since the invention of vehicle engines and for years, the main form of propulsion for passenger vehicles. Their elevated specific power, manoeuvrability and low cost are the main reasons for the high demand generated. As cited throughout the document, over the years, governmental pressures to reduce carbon dioxide emissions and fuel consumption have grown exponentially. The main reductions in average CO_2 levels in Europe are due to the prompt introduction to the market of high speed direct injection Diesel engines which accounted for more than 50% of sales in recent years. However, it is mainly due to the inherent nature of the crude oil refining process that preference is given to the production and use of gasoline fuels. Moreover, Diesel engines require much higher injection pressures, which makes the injection systems more complex. They also face problems with soot and NOx emissions which have to be neutralised with expensive aftertreatment devices if they want to comply with legislation. At this point, there is a growing need for increased efforts to develop more efficient gasoline engines that have the ability to compete with direct injection Diesel engines with the advantage of higher specific power output, more simplified aftertreatment devices and relatively economical fuel injection systems [11].

Gasoline Direct Injection (GDI) arose from the need to minimise fuel consumption, pollutant and noise emissions at the exit of the engine as a result of the hike in petrol products and the tightening of emission standards worldwide. This innovative injection system is associated with improved fuel energy conversion efficiency and higher specific power output as well as the reduction in knocking at high loads and lower pumping losses at part load conditions together with less NO_x and HC emissions [12]. GDI is characterized by injecting the fuel directly into the cylinder, which evaporates due to its high volatility, generating lower mixture temperatures and resulting in a reduction of NO_x

and possible knocking phenomenon. The improvement offered in emissions with regard to HC production is mainly due to the elimination of the wall wetting phenomenon in the intake port both in the ducts (carburetors) and in the intake valve (gasoline indirect injection). Another way to minimize such emissions, mainly during cold starts, is the use of split injections. The GDI system also helps to reduce pumping losses as, at part loads, the engine may work with stratified mixtures and unthrottled operation, which means that the areas close to the spark plug are rich while the overall mixture remains stoichiometric. However, this stratified waych of working has seen its expansion slowed down as it has certain limitations such as the need to implement new aftertreatment devices to control NO_x emissions, as conventional three-way catalyst systems do not operate properly in lean mixtures, as well as the possible formation of PM emissions. The implementation of GDI systems in gasoline engines has brought other advantages such as the introduction of downsizing, the use of turbocharging or the increase of the compression ratio. Not only that, but it has also allowed the investigation of other combustion modes which were impossible to implement with previous fuel injection systems: HCCI (Homogeneous Charge Compression Ignition), GDCI (Gasoline Direct Compression Ignition), RCCI (Reactivity Controlled Compression Ignition), SPCCI (Spark Controlled Compression Ignition), Homogeneous Lean Combustion (HLC), etc [13].

2.4.2 Overview of direct injection gasoline engines

The idea of direct injection in gasoline engines is not recent, but it was in the 1930s that these systems began to be used in two-stroke engines for the aviation sector. Although many automakers try to take credit for it, Goliath and Gutbrod were the first to implement this injection system manufactured by Bosch in automotive applications. These were the Goliath GP700 E and the Gutbrod Superior 600 models, two-cylinder two-stroke gasoline engines. The aforementioned landmarks took place years before the first four-stroke engine with this direct petrol injection system, from the prestigious Mercedes-Benz brand, came onto the market. The introduction of direct injection at this time was driven by the main objective of increasing vehicle performance through the charge cooling effect of direct fuel injection.

In the years thereafter, the 1970s, there was limited research activity concerning the development of direct injection gasoline engines. The few projects that were carried out were soon canceled due to inefficient progress, the extreme cost of development and the lack of flexibility of the injection system. Since traditional solutions were effective for much of the 1980s, it was not

until the mid-1990s that electronic direct injection systems emerged and revolutionised the automotive market with a new generation of engines. It was in 1996 that Michubishi introduced the first modern gasoline direct injection automotive engine to the Japanese market under the name Galant. A year later, it arrived in Europe in the Mitsubishi Carisma model [14]. Considering the success of this new technology, other manufacturers did not want to be left behind. Toyota introduced, at the same time in Europe and Japan, its model engine running on DI gasoline and designed to work in stratified modes at low loads and low to medium speed operation and with homogeneous mixtures at high loads and speed operation [15]. Subsequently, all OMEs introduced GDI systems in their engines, although they preserved the PFI systems in parallel.

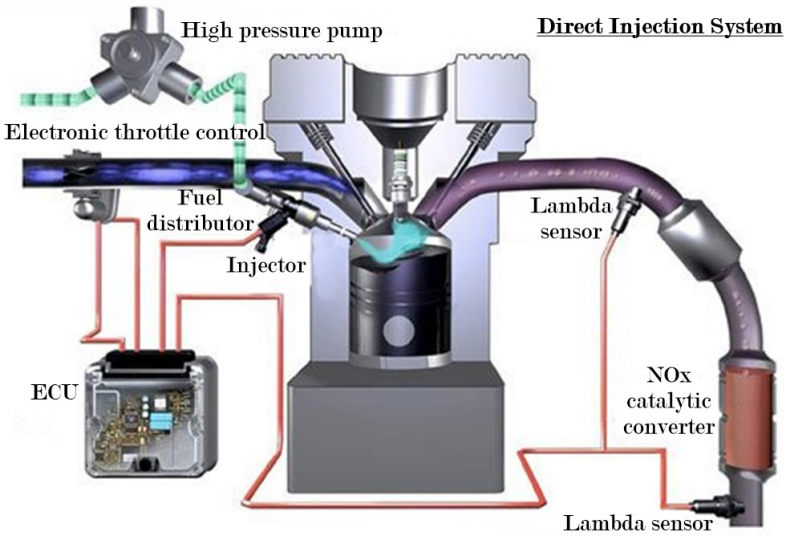

Figure 2.4: Scheme of the components which conform a GDI engine. Adapted from [16].

Figure 2.4 captures the basic components that make up a gasoline direct injection engine. The injector is mounted in such a way that the high-pressure fuel coming from the common rail enters directly into the combustion chamber. There are different arrangements of the injector in the cylinder, in this case on the side. The air passing through the intake valve and being subsequently mixed with the fuel is regulated by the electronic throttle valve. In this particular case, there are two lambda sensors in the exhaust duct, at the inlet and outlet of the aftertreatment system. They operate in a closed-loop, which engages the ECU, so that by measuring the amount of oxygen in the

products of combustion, the amount of fuel to be injected at each operation point is determined [16].

Despite all this progress, fuel efficiency in GDI engines under real operating conditions was not as high as expected. Operating in stratified combustion modes entailed numerous challenges [17], in combination with increasingly stringent emissions legislation. They generally have a tendency to produce high particulate emissions, reduce combustion stability and interfere with exhaust aftertreatment. With reference to the latter concern, almost no lean combustion is compatible with conventional three-way catalytic converters because lean combustion produces exhaust gas mixtures containing an excess of oxygen. Therefore, the aftertreatment system needs to be more complex and thus more bulky [18]. For all these reasons, during 20th century, GDI engines were designed and modified to operate at maximum performance under homogeneous charging mode. Nonetheless, some manufacturers chose to combine two strategies: direct in-cylinder injection and port injection. DI is used to provide the maximum power while the combination of both approaches are used to achieve smooth operation in a stoichiometric mode at part load conditions [11].

In spite of all the inconveniences and difficulties encountered in the use of this stratified combustion mode, many efforts and researches have been carried out with the aim of improving little by little this operating method due to the enormous potential it has in enhancing the fuel economy and emissions [9, 19].

2.4.3 Operating strategies in GDI engines

The operating combustion mode of GDI engines is typically determined by the degree of in-cylinder charge stratification and the strategy employed to accomplish it. Traditional gasoline engines are designed to operate at homogeneous charges close to the stoichiometric condition. In this type of operation, as mentioned above, the working load is governed by the throttle valve, which means that at low and part loads, the most frequent operating conditions, it is necessary to reduce the pressure in the intake manifold, thus generating pumping losses and decreasing the volumetric efficiency. Minimizing these losses can lead to, among many other benefits, a significant improvement in fuel consumption. The implementation of stratified charge mode during engine operation is one of the existing strategies along with variable valve actuation (VVA), cylinder deactivation or downsizing to reduce the losses due to throttling. It has been discussed in previous paragraphs that gasoline engines have to operate within specific equivalence ratio ranges, thus respecting the flammability limits of the fuel. Considering this, the mixture stratification

strategy works in such a way that in the area close to the spark plug there is a rich air-fuel mixture that allows ignition with the extra energy supply while maintaining a globally lean air-fuel mixture inside the cylinder. This mode of operation not only helps to reduce pumping losses but also decreases heat losses and NO_x generation due to lower cylinder temperatures, and improves thermodynamic efficiency by increasing the ratio of specific heats [19].

The air-fuel ratio determines the operating mode and the engine management system is responsible for its selection. Compared to the air-fuel ratio of a stoichiometric air-gasoline mixture (14.7:1), the leaner mode GDI engine can operate with an air-fuel ratio of up to 65:1. The operating modes of a GDI engine are mainly divided into homogeneous or stratified strategy and are described in detail in the following lines. Figure 2.5 illustrates schematically the differences between the two mentioned strategies on the basis of fuel-air mixture distribution as well as indicating at which point of combustion the fuel injection takes place.

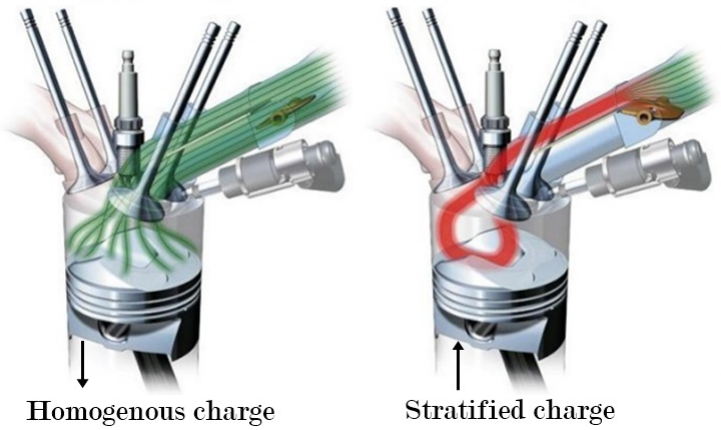

Figure 2.5: Schematic representation of the homogeneous and stratified modes.

- Homogeneous mode: operates on stoichiometric fuel-air mixture and is suitable for all loads and speeds. It requires fuel injection during the intake stroke, at around 270-300 crank-angle degrees (CAD) before top dead center (BTDC) [9]. It is such an early injection so there is enough time to form a homogeneous mixture before spark plug ignites, resulting in a higher degree of complete combustion and reduced emissions. Early fuel injection cools the charge as the spray droplets absorb the heat due to the ambient vaporizing air in the combustion chamber, thus enhanc-

ing the volumetric efficiency of the engine. Lower charge temperature enables a higher compression ratio and a higher tolerance to knocking.

- Stratified mode: operates under leaner mixture and is suitable for use under low load and low speed conditions. Fuel is supplied on the compression stroke, around 60-70 CAD BTDC [9]. In this form, stratified charge layers of widely ranging equivalence ratios are generated inside the combustion chamber, with a rich fuel mixture close to the spark plug and a leaner mixture further away from the spark plug. The shape of the piston used in this type of combustion is toroidal or ovoid and is arranged according to the position of the injector in such a way as to generate a greater swirl during fuel injection and to promote optimum ignition conditions in the areas close to the spark plug. This mode of operation is characterized by generating and sustaining flames and burning the overall lean mixture, providing better fuel efficiency. To a great extent, air and residual gases surround the stratified charge layers, thus minimizing heat loss during combustion by keeping flames away from the walls and reducing emissions due to the lower combustion temperature [20].

If the possible operating modes of a GDI engine were represented in a graph, it would look like the one shown in the Figure 2.6. The operating mode shown in zone A generally corresponds to high load and speed ranges, where the amount of fuel to be introduced into the engine is the highest corresponding to the air admitted and there are no appreciable advantages compared to the same engine with indirect injection. For lower load ratings and engine speeds, it is more advantageous for the engine to run with gradually leaner mixture (zone B), to have the benefits of better performance and lower pollutant emissions (CO, HC, NO_x). However, as the mixture becomes leaner, in order for combustion to start and progress, the mixture must be within the flammability limits, forcing the mixture to be stratified (zone C), with mixtures close to stoichiometry near

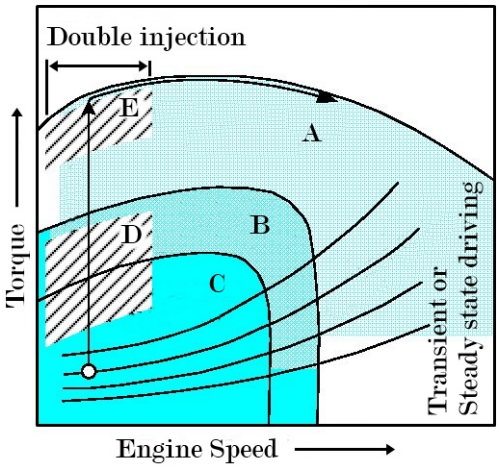

Figure 2.6: Engine operating modes in a GDI Engine. Adapted from [20].

the spark plug and lean mixtures or just air in the other regions of the combustion chamber. The mentioned basic modes of operation are also compatible with the existence of exhaust gas recirculation (EGR) for further emission control as well as supporting second injection for additional fuel and acceleration requirements (zone D) or cold starting, additional catalyst heating for regeneration or enrichment to prevent detonation (zone E), where detonation means rapid and violent combustion of the air-fuel mixture after ignition.

Getting the right mixture is a complex process that depends on several variables and even more so in stratified modes where reaching the right fuel-air concentration around the spark plug and layering it in the following levels is more challenging than it seems. For this purpose, both homogeneous- and stratified-mixture GDI engines can operate with different combustion systems: air-guided, wall-guided and spray-guided. These strategies differ mainly according to the position of the injector and the piston cavity for in-cylinder displacement as can be discerned from the Figure 2.7.

- Wall-guided: the injector is away from the spark plug and the piston cavity is off-centre. This design causes the fuel injection to be directed into the piston cavity so that the fuel impinges on the walls of it, encouraging evaporation and mixing with the ambient air. The mixture is transported to the spark plug electrodes by a strong reverse tumble movement.
- Air-guided: the injector and the spark plug are normally widely spaced. In this case the mixture is formed by air movements such as swirl and tumble that promote the mixing of air and fuel. These air movements also bring the mixture closer to the spark plug so that the ignitable mixture is present at the time of spark when the spark is ignited. In case of adequate air movement, the combustion chamber walls will be prevented from wall wetting phenomenon, resulting in stable operation of the stratified charge over a wide engine operating range.
- Spray-guided: the injection characteristics control the formation of the mixture and the stratification of the mixture. The spark plug is positioned close to the injector and thus to the spray to ensure the flammable mixture at the moment of ignition. At high loads, the formation of an efficient mixture is more complex and combustion is, therefore, very sensitive to spray characteristics. The proximity between the injector and the spark plug electrodes can cause the spark plug to be wetted by liquid fuel involving frequent fouling.

Figure 2.7: Different combustion systems in a GDI Engine. Adapted from [21].

The first GDI engines were mainly based on the wall-guided strategy, which proved to be inefficient on its own. The impact of the fuel on the piston surface meant that evaporation was not complete, resulting in pollutant emissions such as HC and CO, as well as being inefficient in terms of fuel consumption [22]. In the beginning of the 2000s, Volkswagen was the first to introduce a combustion system based on a combination of wall-guided and air-guided strategies which proved to have potential advantages at both homogeneous and stratified modes. This system is complemented by the piston geometry which has two cavities, one in the intake area to guide the fuel towards the spark plug electrode zone and the other in the exhaust part to generate such air movement as to bring the remaining fuel closer to the ignition region. This combination is considered to be less sensitive against the cyclic variations of airflow. The efficient operation of these strategies is highly dependent on the air movement inside the cylinder, as well as on the piston head geometries, both of which contribute to heat losses and thus to a reduction of the thermal efficiency and performance of the engine [23]. Despite their improvements over predecessor systems, their design tends to inherently lead to wetting of the piston head walls and thus result in HC and soot emissions. The system most recently implemented by Mercedes and BMW is the spray-guided direct injection (SGDI) and is classified within the second generation of gasoline DI engines, which has a wider operating range [24]. In this particular case, the responsibility for proper operation does not lie with the piston geometry, but with the injector. Of those mentioned, this approach has the highest theoretical efficiency and is the subject of current research for new combustion concepts [25, 26]. This combustion system allows wider stratification regions, less flow variations inside the cylinder, reduces the wall wetting phenomenon and thus HC emissions. Despite these advantages, there are certain performance

improvements that can be implemented and are therefore still under study. The proximity of the injector to the spark plug coupled with low combustion temperatures can lead to a coking and fouling phenomena at the injector tip which can be avoided with careful design of the holes and specific geometries such as counter-bore [27]. On the other hand, this system is highly dependent on injection efficiency and injection timing.

The development of these new systems favored the implementation of charge stratification which has a limited time for mixture formation and could result in overly rich zones leading to HC emissions, misfiring and unstable combustion. Therefore, with the introduction of this operating system, Europe was forced to limit emissions, in particular PM, by applying the Euro VI standard. This has led in recent years to research aimed at meeting the new standards. Among them is the so-called Homogeneous-Stratified (HOS) combustion system which proposes a multi-injection strategy with one injection during intake to provide a lean homogeneous charge and a second injection during the compression stroke to ensure a rich mixture around the spark plug [22]. This particular concept among many others has demonstrated the potential to overcome shortcomings of stratified charging. However, even today and after much research, the potential of a GDI engine has not yet been fully exploited and therefore remains a challenge worth investing effort in [22, 28].

2.4.4 Advances in GDI engine technology

As mentioned in previous paragraphs, GDI engine technology has evolved significantly over the recent decades. Much effort has been spent by researchers and engineers on improving mainly critical areas of development, such as optimization of the fuel injection system, mixture preparation, combustion system, etc., in order to improve performance and reduce emissions. Some of the improvements made to date are outlined in the following lines.

- **Dual-Fuel Injection.** The SI dual-fuel engine merges the advantages of direct and indirect injection and relies on the combined injection of a low knock resistance and high knock resistance fuel to dynamically adjust the resistance of the fuel mixture to knock as appropriate [29]. These engines are capable of running into gasoline as the main fuel and use as alternative fuel natural gas, meanly methane, liquid petroleum gas (LPG) like propane or butane, hydrogen, or some alcohols like ethanol or methanol. This strategy is considered to be promising for achieving the highest power output among engines of similar displacement, improving

fuel economy and reducing HC emissions in gasoline engines. Furthermore, the use of the PFI allows for better mixture homogeneity under high load and low speed conditions [30]. However, the challenges related to multiple deposits and multiple fuels are challenging researchers to find ways to make the technology more feasible.

- **Multi-Injection Strategy.** The multi-injection strategy is based on splitting the injection into several shots in order to obtain a lean homogeneous stratified charge at the start of ignition. In general, the first injection is conducted during the intake stroke to allow enough time to form a lean homogeneous mixture. Subsequently, secondary injection is performed on the compression stroke in order to achieve a stratified mixture [22]. The possibility of controlling the injection timing and thus the combustion characteristics allows for higher combustion efficiency and lower pollutant emissions.
- **New Combustion Concepts.** Researchers and manufacturers are putting efforts into improving the combustion modes and from this requirement arises the concept of GDCI. It is based on the use of a GDI system operating in stratified mixture with a reduction in fuel consumption, NO_x and PM emissions through the use of multiple-late injections [31]. This system may use in a new generation of engines that take advantage of the benefits of SI and CI approaches and overcome the shortcomings of stratified combustion. In addition, it appears to be less complex than the dual-fuel system.

  The approach of this strategy is to use fuels with low cetane numbers, so that they self-ignite in a similar way to diesel in CI engines and have a longer ignition delay, thus allowing more time to achieve a better mixture, reducing emission levels such as soot and HC [9]. The parameters that mainly control the correct operation are injection timing and the mixing process. By varying the above mentioned, the GDCI combustion mode can work as HCCI, PCCI or conventional combustion modes used in CI engines, where premixed diffusion combustion takes place initially in the combustion process and then diffusion combustion follows [32].
- **Downsizing and turbocharging.** The downsizing technique emerges as an important way to improve the fuel economy of SI engines by enabling the unthrottle operation while allowing the application of the economical and robust three-way catalytic converter for exhaust emission control. This type of engine has a smaller displacement and therefore smaller friction surfaces, in addition to a reduction in pumping losses. They are optimised to operate on the same vehicle and in the same

driving cycle with a higher mean effective pressure. Reducing the displacement means increasing the Brake Mean Effective Pressure (BMEP) to obtain the same engine torque [33]. Normally, the implementation of this technique is associated with the use of supercharging, considering turbocharging as the best solution to adopt. Turbocharging is the selected technique to provide the downsize engine with the mass of air needed to keep the engine performance ensuring a highly efficient and clean combustion. In addition, the combination of these two strategies allows for increased resistance to knocking. Another feature to highlight is the possibility of modifying the compressor map by increasing the scavenging, a strategy that can only be carried out on DI engines by introducing fuel up to after the exhaust valve closes.

The advantages of turbocharged SI have led to its widespread implementation. However, these systems also have certain weaknesses such as being prone to knock combustion and high exhaust gas temperatures at high loads due to the high power density [34]. This increase in exhaust temperatures usually leads to a higher level of NO_x emissions. On the other hand, there is also the case of SI engines designed to work in lean or even ultra-lean mixtures where the use of the three-way catalyst to eliminate NO_x emissions is unfeasible. It is therefore proposed to use the EGR system together with other advanced technologies to mitigate the disadvantages they present [35].

- **Exhaust Gas Recirculation.** Engine EGR is the technique of reintroducing exhaust gases into the intake ducts. This operating strategy is divided into two: exhaust gases directly recycled to the intake is called hot EGR while exhaust gases recycled after cooling is called cooled EGR. Each approach is focused on a different objective. The engine running hot EGR uses the high-temperature exhaust gases to heat the intake, promoting combustion and thus increasing thermal efficiency. Meanwhile, cooled EGR increases the intake density, thereby increasing the volumetric efficiency of the engine. Moreover, the lower temperature can further reduce NO_x emissions, but HC emissions and cycle-to-cycle variations increase in comparison to those of hot EGR [36].

As a summary of this chapter on advances in GDI engine technology, one of the main elements common to all the technologies presented is the direct injection system, where the injector plays an important role in the behavior and development of the spray inside the cylinder. Therefore, as this element is so important in the development of the correct operation of the engine,

it deserves special attention. Technological requirements are becoming more and more demanding and with stricter limitations, especially in terms of pollutants. This also applies, of course, to both GDI and PFI injection systems. Whereas PFI injectors are complex systems, those used in GDI go a step further as the time for injection, mixing and atomization is much shorter, leading them to be more precise and with even higher performance requirements. Not only the amount of fuel injected or the atomization of that fuel influences the performance of the engine but there are other parameters, which partly depend on the injector, such as the shape of the spray, spray direction, opening angle of the spray, penetration, etc. which can be considered as critical for the correct functioning of the engine in the different operating conditions. Due to the importance of these systems, researchers have devoted and continue to dedicate efforts to the study, understanding and improvement of the performance of these devices. For this reason, this Thesis is mainly focused on the study of spray-guided multi-hole injectors, which will be further discussed in the following chapters.

References

[1] Payri, F. et al. *Motores de combustion interna alternativos*. Editorial Universitat Politecnica de Valencia, 2011.

[2] Kirkpatrick, A. T. et al. *Internal Combustion Engines: Applied Thermosciences*. John Wiley & Sons, 2015, pp. 1–635.

[3] Salvador, F. J. et al. "Computational assessment of temperature variations through calibrated orifices subjected to high pressure drops: Application to diesel injection nozzles". In: *Energy Conversion and Management* 171 (2018), pp. 438–451. DOI: 10.1016/j.enconman.2018.05.102.

[4] Payri, R. et al. "The effect of nozzle geometry over ignition delay and flame lift-off of reacting direct-injection sprays for three different fuels". In: *Fuel* 199 (2017), pp. 76–90. DOI: 10.1016/j.fuel.2017.02.075.

[5] Reif, K. *Gasoline Engine Management*. 2014, p. 354. DOI: 10.1007/978-3-658-03964-6.

[6] Spicher, U. et al. "Gasoline Direct Injection (GDI) engines - Development potentialities". In: *SAE Technical Papers* 724 (1999). DOI: 10.4271/1999-01-2938.

[7] Winkler, A. et al. "ELECTORJECTOR. Bendix Electronic Fuel Injection System". In: (1957).

[8] Bosch Extranet Service. “Sistemas de Inyección Electrónica”. In: (2018), p. 72.

[9] Pham, P. et al. “Development of fuel metering techniques for spark ignition engines”. In: *Fuel* 206 (2017), pp. 701–715. DOI: 10.1016/j.fuel.2017.06.043.

[10] He, L. et al. “Numerical study on combustion and emission characteristics of a PFI gasoline engine with hydrogen direct-injection”. In: *Energy Procedia* 158 (2019), pp. 1449–1454. DOI: 10.1016/j.egypro.2019.01.348.

[11] Zhao, H. *Overview of gasoline direct injection engines*. Di. Woodhead Publishing Limited, 2020, pp. 1–19. DOI: 10.1533/9781845697327.1.

[12] Chincholkar, S. P. et al. “Gasoline Direct Injection: An Efficient Technology”. In: *Energy Procedia* 90.December 2015 (2016), pp. 666–672. DOI: 10.1016/j.egypro.2016.11.235.

[13] Johnson, T. et al. “Review of Vehicle Engine Efficiency and Emissions”. In: *SAE Technical Papers* 2017-April.April (2017). DOI: 10.4271/2020-01-0352.

[14] Iwamoto, Y. et al. “Development of gasoline direct injection engine”. In: *SAE Technical Papers* 412 (1997). DOI: 10.4271/970541.

[15] Harada, J. et al. “Development of direct injection gasoline engine”. In: *SAE Technical Papers* 412 (1997). DOI: 10.4271/970540.

[16] Erjavec, J. *Automotive Technology : A systems approach.* 5th. Cenga. 2009, p. 1665.

[17] Whitaker, P. et al. “Measures to Reduce Particulate Emissions from Gasoline DI engines”. In: *SAE International Journal of Engines* 4.1 (2011), pp. 1498–1512. DOI: 10.4271/2011-01-1219.

[18] Johansson, A. N. *Challenges and advantages of stratified combustion in gasoline direct-injected engines challenges and advantages of stratified combustion in gasoline direct-injected engines*. 2017.

[19] Fansler, T. D. et al. “Combustion instability in spray-guided stratified-charge engines: A review”. In: *International Journal of Engine Research* 16.3 (2015), pp. 260–305. DOI: 10.1177/1468087414565675.

[20] Kalwar, A. et al. *Overview, Advancements and Challenges in Gasoline Direct Injection Engine Technology*. April. 2020, pp. 111–147. DOI: 10.1007/978-981-15-0368-9_6.

[21] Marchitto, L. "Characterization of air/fuel mixture and combustion processes in a DISI engine through advanced optical and X-ray based diagnostics". PhD thesis. 2015.

[22] Costa, M. et al. "Split injection in a homogeneous stratified gasoline direct injection engine for high combustion efficiency and low pollutants emission". In: *Energy* 117.2016 (2016), pp. 405–415. DOI: 10.1016/j.energy.2016.03.065.

[23] Zeng, W. et al. "The role of spray-enhanced swirl flow for combustion stabilization in a stratified-charge DISI engine". In: *Combustion and Flame* 168.x (2016), pp. 166–185. DOI: 10.1016/j.combustflame.2016.03.015.

[24] Price, P. et al. "Particulate Matter and hydrocarbon emissions measurements: Comparing first and second generation DISI with PFI in single cylinder optical engines". In: *SAE Technical Papers* 724 (2006). DOI: 10.4271/2006-01-1263.

[25] Smith, J. K. et al. "Thermodynamic modelling of a stratified charge spark ignition engine". In: *International Journal of Engine Research* 21.5 (2020), pp. 801–810. DOI: 10.1177/1468087418784845.

[26] Firat, M. "Investigation of multistage injection strategies in a DISI engine fueled with methane under stratified charge lean combustion conditions". In: *Environmental Progress and Sustainable Energy* 39.5 (2020), pp. 5–7. DOI: 10.1002/ep.13402.

[27] Zhou, J. et al. "Characteristics of near-nozzle spray development from a fouled GDI injector". In: *Fuel* 219.92 (2018), pp. 17–29. DOI: 10.1016/j.fuel.2018.01.070.

[28] Gong, C. et al. "Assessment of ultra-lean burn characteristics for a stratified-charge direct-injection spark-ignition methanol engine under different high compression ratios". In: *Applied Energy* 261.December 2019 (2020), p. 114478. DOI: 10.1016/j.apenergy.2019.114478.

[29] Kassa, M. et al. "Dual-Fuel Combustion". In: *The Future of Internal Combustion Engines*. 2018, pp. 1–17. DOI: 10.5772/intechopen.80570.

[30] Cando Comino, J. C. "Investigation of Knock Limits of Dual Fuel Engines". PhD thesis. 2013.

[31] Kalghatgi, G. et al. "Gasoline compression ignition approach to efficient, clean and affordable future engines". In: *Proceedings of the Institution of Mechanical Engineers, Part D: Journal of Automobile Engineering* 232.1 (2018), pp. 118–138. DOI: 10.1177/0954407017694275.

[32] Agarwal, A. K. et al. "Evolution, challenges and path forward for low temperature combustion engines". In: *Progress in Energy and Combustion Science* 61 (2017), pp. 1–56. DOI: 10.1016/j.pecs.2017.02.001.

[33] Police, G. et al. "Downsizing of SI engines by turbo-charging". In: *Proceedings of 8th Biennial ASME Conference on Engineering Systems Design and Analysis, ESDA2006* 2006.January (2006). DOI: 10.1115/esda2006-95215.

[34] Fontana, G. et al. "Experimental analysis of a spark-ignition engine using exhaust gas recycle at WOT operation". In: *Applied Energy* 87.7 (2010), pp. 2187–2193. DOI: 10.1016/j.apenergy.2009.11.022.

[35] Fathi, M. et al. "The influence of Exhaust Gas Recirculation (EGR) on combustion and emissions of n-heptane/natural gas fueled Homogeneous Charge Compression Ignition (HCCI) engines". In: *Applied Energy* 88.12 (2011), pp. 4719–4724. DOI: 10.1016/j.apenergy.2011.06.017.

[36] Wei, H. et al. "Gasoline engine exhaust gas recirculation - A review". In: *Applied Energy* 99.X (2012), pp. 534–544. DOI: 10.1016/j.apenergy.2012.05.011.

Chapter 3

Fuel Injectors in GDI Engines

"Without the influence of experience
we would be in total ignorance of all matters of fact,
beyond what is immediately present to the memory and the senses."
—David Hume

3.1 Introduction

Direct injection in gasoline engines is one of the most innovative technologies of recent years that has a lot of potential to offer. This method has established itself over existing systems due to higher fuel energy conversion efficiency and greater specific power output as well as reductions in pollutants such as HC and NO_x. However, by definition, the fuel is injected directly into the cylinder and has to be mixed and ignited inside the combustion chamber. The efficient development of this process has been the main challenge of the system, which has led to continuous innovation in technology and strategies.

This chapter describes the main characteristics and the technological evolution over time of the GDI injectors, element belonging to the injection system considered as one of the most important parts of the equipment. Furthermore, the following paragraphs also discuss the phenomena concerning the flow inside the injector nozzle that define the jet behavior (internal flow) and, the dynamics of the spray formation including liquid core break-up, droplet formation and evaporation (external flow). Understanding the physics behind these processes helps to improve the quality of the air-fuel mixture and the

efficiency of combustion. Spray formation is a highly challenging phenomenon that represents the real weakness of gasoline fuel injection. The turbulent structure of the atomization process and the transient characteristics of the spray formation (very small length and time scales) further increase the complexity and understanding of the aforementioned event.

3.2 Common-rail Gasoline Injection System

Most of the design and manufacturing know-how acquired in the field of diesel direct injection systems has been transferred to the development of new technologies for gasoline engines. The fuel injection system is considered a critical element as it must be able to deliver fuel efficiently and accurately over a wide range of operating conditions, high pressure in late injection strategies and lower pressure under early injection strategies. In order to meet these requirements, the most commonly used injection system associated with GDI engines is known as common-rail.

The common-rail system is based on the strategy of accumulating fuel at high pressure in a volume between the pump and the injector, where it is stored until it is delivered. Figure 3.1 represents a typical fuel rail pressure control system schematic consisting mainly of the low pressure circuit, the high pressure pump (HPP), the fuel rail, the injectors, the rail pressure sensor and the electronic control unit (ECU). The system has a low-pressure pump, usually located in the fuel tank, whose purpose is to supply fuel to the high-pressure pump. This second pump, mechanically coupled to the engine (the crankshaft), delivers a certain mass flow of fuel well in excess of the average quantity demanded by the engine. The pressure control valve is installed on the HPP allowing effective control of the fuel quantity. The check valve installed at the exit of the high pressure pump is to prevent unwanted backflows, and the pressure limiting valve installed at the outlet of the HPP prevents the rail from being damaged by excessive pressure, when the pressure is higher than the maximum set. The fuel is injected directly into the combustion chamber via the injectors. The fuel injection commands are given by the ECU. The pressure in the fuel rail increases when the fuel is pumped and the pressure decreases when injection takes place [1].

The fundamental advantage of this injection system is the accurate electronic control it has over the rail pressure and the opening and closing of the injectors depending on the engine operating conditions. The ECU plays a very important role as it is not only connected to the pressure rail but also communicates with numerous sensors that allow the exact engine working conditions

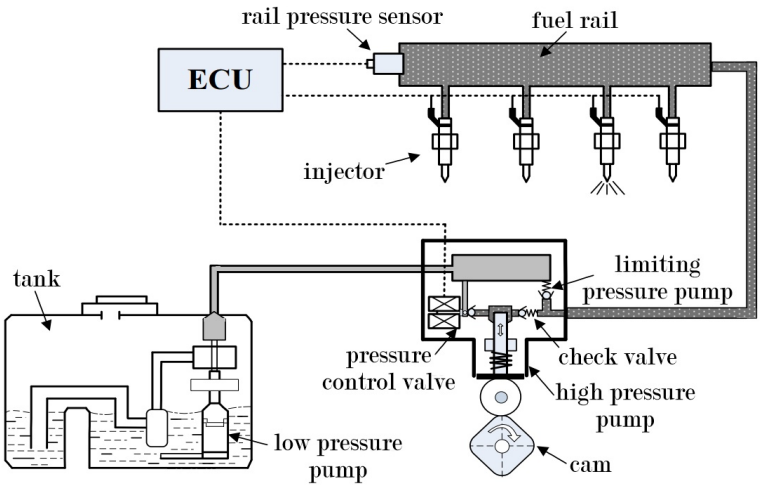

Figure 3.1: The structure diagram of the common rail system of GDI engines. Adapted from [1].

to be known at all times. Moreover, the capability to independently control injection timing and injection pressure enables different operating strategies to be adopted for each driving condition. In summary, this common-rail system allows, compared to other technologies, greater control of the start and duration of the injection process and greater precision and control of the amount of fuel injected [1].

3.3 Evolution and Types of GDI Injectors

Similarly to the technology used in direct injection systems, the injectors in particular have also taken over details and characteristics from the ones used in CI engines. The injector has the important purpose of correctly atomizing the fuel so that in homogeneous operations it achieves a uniform mixture perfectly distributed throughout the chamber while in stratified operating conditions it has to provide a cloud of fuel around the spark plug where ignition takes place. Compared to PFIs, the injectors used in GDI systems have shorter mixing time and therefore reduced injection time, which is the reason that justifies the current strategy of increasing the fuel injection pressure. In order to meet the demanding requirements, GDI injectors operate at injection pressures between 30 to 300 MPa [2] although several vehicle manufacturers and researchers are now focusing on the advantages that the use of higher injection pressures could offer such as positive effects on emissions and engine-efficiency.

Johansson et al. [3] used an injector capable of reaching 350 bar and observed how it reduced particle matter (PM) emissions and the soot formation. This effect is likely to be due to the fact that the increased fuel injection pressure favors atomization and evaporation of the fuel, which in turn decreases the non-premixed part of the combustion that is considered to be a significant contributor to soot emissions. Other researchers such as Piock et al. [4] and Peer et al. [5] corroborated these claims by testing injection systems with 400 and 500 bar of injection pressures respectively. The Delphi technologies team [6] studied the feasibility of increasing the pressure not only in the injector but also in the fuel pump and other components in order to make way for a new generation of GDI injection systems. In 2016, Delphi announced the launch of the first commercially available GDI injector capable of reaching 350 bar of injection pressure, leaving the door open for the development of injection systems that could go even further [7]. This new market opportunity led to further research focusing on the mechanisms responsible for the beneficial effects including the injector nozzle shape. Postrioti et al. [8] analyzed the spray evolution and atomization process at injection pressures between 50 and 600 bar using a prototype side-mounted 5-hole GDI injector, observing the biggest improvements in the atomization process in termns of both mean diameter and sauter mean diameter (SMD) when the injection pressure was increased up to 200 bar, thereafter the improvement was minimal. Husted et al. [9] ensured that increasing the fuel pressure generates a slight benefit in fuel economy despite the greater energy demand of the fuel pump. Given the number of benefits in engine performance that can be achieved by increasing injection pressure, manufacturers of injectors such as Bosch, Delphi and Continental, among others, are investing in technologies that can reach up to 800 bar [7]. Note that BorgWarner already has a high-efficiency 500+ bar solution on the market that is designed to minimize the load on the engine valvetrain while delivering class-leading performance and Magneti Marelli has the prototype injector and fuel pump ready to reach 800 bar.

As discussed in the subsection 2.4.3, the first injection strategies used were wall-guide systems which typically operated in the injection pressure range of 50 to 100 bar. The injectors associated with this operation are swirl-type and their main features are a single outlet orifice and an inwardly opening pintle [10]. The operating concept of this type of injector is based on a rotational movement of the fuel at the outlet nozzle by means of tangential holes or slots in such a way that the liquid exits the single discharge orifice as an annular sheet extending radially outwards to constitute a hollow cone spray. This approach has a number of disadvantages, including high variability of the spray pattern with changes in injection pressure, ambient pressure or density,

and nozzle operating temperature [11]. As a result, the spray structure of the swirl injector changes substantially over the operating range leading to significant difficulty in optimizing performance over a wide range of operating conditions. On the other hand, the use of specific geometries to benefit the in-cylinder charge motion (tumble or swirl), reduces volumetric efficiency and thus torque performance. In order to reduce the variability of first generation DI systems, the high-pressure split-injection concept was introduced. This system incorporates a single rectangular orifice and its slit is positioned to produce a fan-shaped spray on- or off- axis which enhances the torque curve [12]. Despite these advances, a new generation of injectors was developed, mainly focused on spray-guide applications, which extended the operating ranges and improved operation in stratified conditions. To this end, multi-orifice solenoid and piezoelectric injectors were developed.

The principle of operation of both types of injectors, solenoid-actuated and piezo-electrically actuated, is divided into several phases as explained in Figure 3.2. First of all, the fuel from the high-pressure pump flows through the rail and enters the injector where, after passing the filter, it splits into two separate lines. One of them is directed to the lower part of the injector, in charge of feeding the nozzle, while the other part of the fuel supplies the control volume, at the top of the connecting rod. The control volume is provided with two calibrated orifices: one connected to the injector intake and the other to the low pressure return line; the fuel flow through this second channel is governed by the solenoid/piezoelectric valve. Solenoid injectors rely on the electromagnetic force generated in a copper coil to initiate the opening and closing movement of the needle (against the injection pressure), whereas piezoelectric injectors use the dimensional change of certain ceramics after a voltage is applied to them. The size difference of a piezoelectric material is very narrow, so to provide enough displacement to allow the needle opening, the injectors are equipped with a stack of crystals, often referred to as a piezoelectric stack [13]. The first phase of operation is when the system is at rest, which means it is not energized, so that the control volume is closed and no fuel flow is allowed. In this state, the fuel pressure in the control volume is equal to the fuel pressure in the supply line, causing the orifices to be closed. Even without applying pressure, the connecting rod is held in this locking position by a pre-loaded spring. As the solenoid/piezoelectric crystal is energized and thus activated, fuel begins to flow to the control volume outlet. The specific design of the bores causes a depression to be generated in this region of the injector, with the pressure at the top of the connecting rod being lower than at the bottom of the needle. This effect causes the connecting rod and needle to lift allowing the fuel to pass through and the injection to start.

When the system is de-energized, the fuel flow stops, the pressure increases again and the system returns to the initial state.

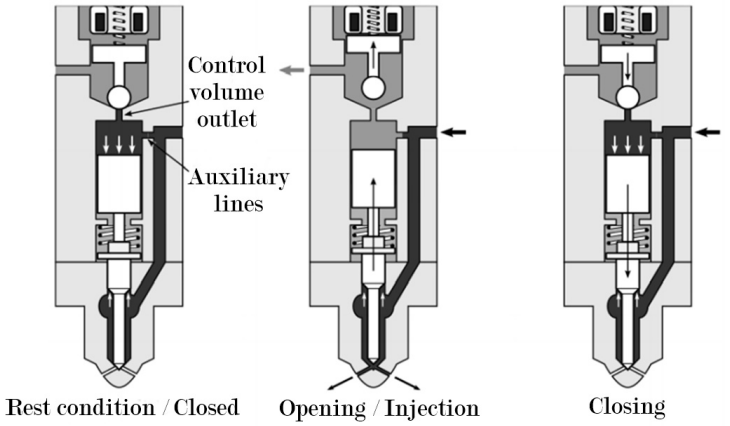

Figure 3.2: Operating principle of an injector in a common rail system. Adapted from [14].

Solenoid driven injectors

The essential components of a solenoid type injector are depicted in Figure 3.3a. They are the solenoid valve, the injector holding including the high-pressure fitting, the fuel return line, the filter, the body, the spring and the connecting rod, and finally, the injector nozzle. The injection duration as well as the injected mass is defined through the width of an electric pulse sent by the ECU.

Piezoelectric driven injectors

Figure 3.3b describes the different parts that make up a piezoelectric injector. It is divided into three completely different parts: on the one hand the piezoelectric valve consisting of the actuator, the hydraulic amplifier and the control valve; on the other hand the injector holder comprising the high pressure fitting, the filter, the return line, the spring and the body; and finally the injector nozzle. The opening shape of the piezoelectric injectors largely determines the shape of the spray. As the needle is pushed outwards, it leaves a radial slit that forms a thin hollow-cone spray cone. This opening shape benefits the operation of the injector in a way that largely prevents deposits on the injector tip and thus the formation of cocking. In addition to this advantage, there are many others, such as the speed in the opening and closing phases and the arrangement of the control volume directly over the needle,

which allows multi-injection strategies that minimize emissions and noise, the high precision that enables the needle to move in orders of nanometers and, finally, the absence of deterioration after cycles of operation.

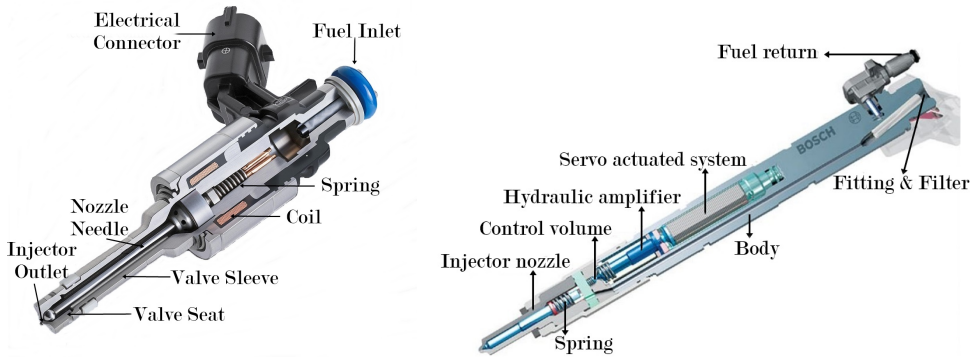

(a) Solenoide (b) Piezoelectric

Figure 3.3: Main components of solenoide and piezoelectric driven Bosh high-pressure injectors [15, 16].

Piezoelectric technology makes it possible to replace the moving parts of the injector and the connecting rod by the aforementioned piezoelectric crystal which compresses or expands depending on the applied electric field. Other mechanical characteristics that differentiate it from the solenoid type injector is that instead of having two orifices, it is equipped with three, two inlets and one outlet, although this can also operate as an inlet.

Dahlander et al. [17] carried out comparisons between solenoid- and piezoelectric- actuated GDI injectors by measuring the rate of injection of both. From this research it was concluded that the piezoelectric injector was more robust at short energization times and could accurately deliver fuel doses of less than 1 mg while the multi-orifice solenoid injector dispensed at least 1.8 mg, almost twice as much. These disadvantages of solenoid injectors compared to piezoelectric injectors have been overcome by continuous improvements in the new models of GDI solenoid injectors. The combined use of precise metering of the injected fuel and an advanced electronic management system which allows the electronic drive signals to be adjusted in real-time means that the new generation of injectors can also achieve small injection mass quantities.

In GDI engines, the mixing process is greatly influenced by the spray penetration velocity. A higher penetration speed can promote the mixing and atomization process but has the disadvantage that the spray could impact with the piston head or cylinder walls which results in unburned HC, soot

formation and thus increased particulate emissions. Mercedes' BlueDirect technology [18] was directly developed to improve fuel atomization while reducing spray penetration in order to mitigate the disadvantages but the cost of these systems meant that they were only applicable to high-end vehicles. Figure 3.4 represents a comparison of the jet characteristics using different types of injectors, the BlueDirect system on the one hand and a multi-orifice solenoid type on the other hand. It can be clearly seen, and therefore corroborated the above statement, that the distance at which the jet penetrates is shorter in the piezoelectric type injector.

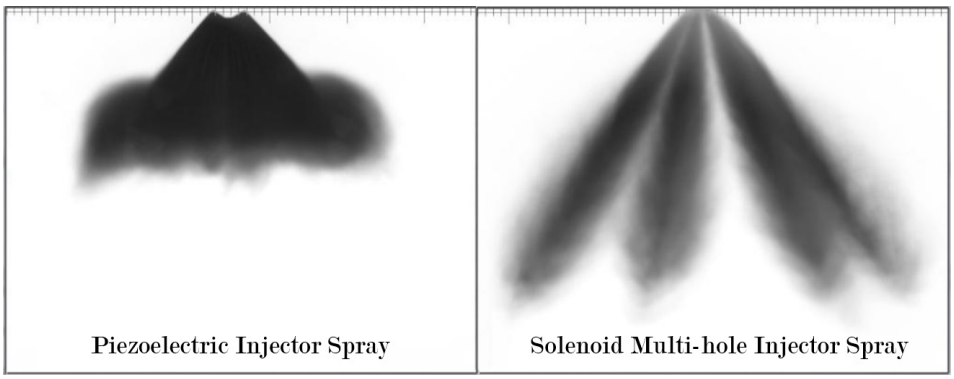

Figure 3.4: Spray structure and penetration resulting from a GDI piezoelectric injector and a solenoid multi-hole injector. Adapted from [18].

Despite all the above mentioned advantages of using the piezoelectric injector that make it attractive in GDI engines for both homogeneous and stratified operations such as resistance to deposit formation, fast response time and spray characteristics, among others, it is important to note that these benefits are not always reproduced in actual engine operation. This statement was substantiated by Smith et al. [19] through his research where compared the performance in spray-guided stratified-charge (SGSC) approach using a piezoelectric injector and a multi-hole solenoid injector. After developing a Federal Test Procedure (FTP) cycle, the multi-hole solenoid injector was found to have lower consumption, which had a positive impact on 15% less HC and 18% less CO_2 emissions. In addition to this, solenoid type injectors are quite versatile so that the number of orifices and their position on the nozzle can be optimally modified to avoid, as far as possible, the impact of sprays on walls and valves [11]. Despite this, the manufacturing cost of this type of injectors is much lower than piezoelectric injectors and, therefore, they are more in demand by manufacturers and researchers, with many more studies

of multi-hole solenoid-actuated injectors being found in the literature. Such is the widespread use of solenoid injectors that the ECN collaborative network, discussed in Chapter 1, took this hardware as a reference model for the topic focusing on gasoline direct injection.

3.4 Internal Nozzle Flow

Once the parts that conform the injector and the technology used nowadays for these components have been defined, it is necessary to understand how the air-fuel mixing process in gasoline engines occurs in detail. For this purpose, it is important to characterize the flow inside the nozzle as it has a great influence and can therefore be said to define the spray structure [20]. The investigation of the internal flow involves not only the analysis of the flow inside the nozzle but also in the near field, which means the first millimeters at the outlet of the injector. The hydrostatic energy of the liquid accumulated in the rail allows the fuel to flow easily through the injector and subsequently reach the combustion chamber through the nozzle orifices. Fuel flow can be defined as forced internal flow. In this type of operation, it is a pressure difference that drives the fluid through the injector cavities and valves. This process is associated with certain transformations mainly related to changes in fluid pressure and velocity or energy dissipation. In some cases, the alterations are produced by the sudden formation of vapor due to the presence of areas with extremely low pressures, phenomena known as cavitation or flash boiling.

3.4.1 Forced internal flow

A convenient starting point to introduce the problems in forced internal flow is to define Bernoulli's equation (Equation 3.1), which is considered as a formulation of the energy transport equation dealing with non-viscous flows of incompressible fluids.

$$\frac{p}{\rho} + \frac{u^2}{2} + gz = constant \tag{3.1}$$

The terms that characterize the Equation 3.1 are: the pressure (p/ρ), the dynamic pressure ($u^2/2g$) and the elevation gz, term that could be excluded as in vehicle applications the elevation differences are minimal. It should be noted that the transformation from potential to kinetic energy is associated with viscous dissipation (Φ_{visc}), which cannot be disregarded in realistic operations. Energy losses when a fluid flows through a pipe are unavoidable. On the one

hand, these losses are due to friction between the pipe wall and the fluid. On the other hand, they are due to friction within the fluid due to the viscosity of the fluid. The term Φ_{visc} encompasses the total viscous flow losses and, as pressure can also be understood as volume-specific energy, an energy loss translates into a pressure loss. Therefore, it can be said that this term is responsible for the pressure losses when a real fluid flows through a pipe. The complexity in determining this term has meant that it has been studied and characterized for years [21, 22]. In a real fluid, the term Φ_{visc} is divided into minor losses ($\Phi_{visc,m}$) and major losses ($\Phi_{visc,M}$). The fluid in a typical piping system passes through various fittings, valves, bends, elbows, tees, inlets, exits, enlargements, and contractions in addition to the pipes. These components interfere with the smooth flow development by causing additional losses because of the flow separation of the boundary layer they induce. This separation leads to the presence of a recirculation zone and constrains the flow in a narrower area known as *vena contracta*. The fluid in this section behaves by initially accelerating and then slowing down around the *vena contracta* causing energy dissipation and potentially pressure losses. Although they are known as minor losses, the complexity of the flow geometry can make such types of losses noticeable [22]. The pressure drop across a pipe component associated with the minor losses may be expressed as a function of the dynamic pressure and the loss coefficient defined by the variable ξ which ranges between a value of 0, no loss, and a value of 1, meaning that the pressure drop has the same value as the dynamic pressure (Equation 3.2). The minor loss coefficient may take a value greater than unity for some specific cases such as a partially closed ball valve or a open or partially open diaphragm valve.

$$\Delta p_{visc,m} = \xi \rho \frac{u^2}{2} \tag{3.2}$$

The flow regime affects the behavior of the fluid so it is necessary to identify the operating regime in order to predict the pressure losses with a high degree of precision. Two principal operating regimes are distinguished: laminar and turbulent, which are identified from the Reynolds number. The Reynolds number is expressed from Equation 3.3, where L is a typical length of the system to be studied. The variable is a dimensionless parameter that expresses a relationship between inertial and viscous forces.

$$Re = \frac{\rho u L}{\mu} = \frac{u L}{\nu} \tag{3.3}$$

At a high Reynolds number (turbulent values above $Re \approx 4000$ for wall-bounded flows), the inertia forces, which are proportional to the density of

the fluid and the fluid velocity, are great compared to the viscous forces, so that the viscous forces cannot counteract the random and rapid fluctuations of the fluid. Nevertheless, at small or moderate Reynolds numbers (values below $Re \approx 2300$), the viscous forces are great enough to overcome these fluctuations and keep the fluid "stable". These ranges define the flow regime, being turbulent in the first case and laminar in the second case. The transition between one regime and the other ($Re \in [2300, 4000]$) allows both regimes to operate according to the roughness of the pipe, pipe vibrations and fluctuations in the flow. Notwithstanding, special consideration should be given to the definition as it does not necessarily apply to all flows, but it can be assured that it is met under fully developed flow conditions. For each operating regime (laminar or turbulent) the distance required to consider stabilized flow is different and, therefore, specific equations or coefficients are required for each particular situation.

Once the minor losses have been defined, it is necessary to determine the major losses, which are due to the friction of the fuel on the walls and depend mainly on the length of the pipe under study. Equation 3.4 represents the pressure drop that occurs due to the major losses where, in this particular case, the friction coefficient is defined by the variable k_{fric} and L is the pipe length. It is considered that major losses are directly a function of the Reynolds number and the relative wall roughness.

$$\Delta p_{visc,m} = k_{fric} \frac{L}{D} \rho \frac{u^2}{2} \tag{3.4}$$

In the same way as mentioned before, to estimate the coefficient of friction, it is necessary to know the operating regime. In case it is defined within the laminar regime, the roughness of the wall would be neglected and Equation 3.5 would apply. On the contrary, if the working regime is turbulent, the interaction between the fluid and the wall as well as the velocity profile are modified and it is essential to consider the effect of the surface roughness as indicated in Equation 3.6.

$$k_{fric} = \frac{64}{Re} \tag{3.5}$$

Equation 3.6 is known by the name of its creator, Colebrooke [21], and presents the analytical solution to determine the coefficient of friction in turbulent flow cases where e_r/D refers to the relative roughness.

$$\frac{1}{\sqrt{k_{fric}}} = -2log\left(\frac{2.51}{Re\sqrt{k_{fric}}}\right) + \frac{e_r/D}{3.72} \tag{3.6}$$

The theory presented in these lines is defined for circular sections although it can be further applied to other shapes using the principle of equivalent diameter (D_{eq}).

3.4.2 Geometry of the injector nozzle

The fuel stored in the rail travels through many parts of the injection system before it reaches the injector nozzle, including the high pressure feeding line and the injector hydraulics themselves (see Section 3.2 and Section 3.3). Along this path, the energy undergoes transformations from potential to kinematic and, although it is certain that the fluid does not suffer significant pressure losses, the design of the injection system must be precise in order to favor the dynamics of the system [22]. One of the parts to be highlighted in the correct design is the feeding line where, although the pressure drop during the injection process is small compared to the injection pressure, it must be taken into account that the propagation time of the pressure waves is of the order of magnitude of the duration of the injection process; furthermore, this phenomenon of waves inside the injection system could have consequences on the fuel injection, especially in the case of the application of multiple injections.

The characterization of the flow inside the injector is an important part of the design phase, especially when deciding on injector specifications such as the size and number of orifices in the control volume. For this reason, it is typical to carry out computational studies with 1D models in order to estimate the fuel flow [23]. Fast injector response is one of the main features to be considered when carrying out the hydraulic design of the injector system. In addition, the reduction in moving parts also benefits the speed of response. Another factor to be taken into account is the design of the inner channels through which the flow passes, as certain pressure waves can be generated in the interior, resulting in oscillations in the mass flow rate [24].

Needle seat

The needle is one of the moving parts of the injector that can interfere with the development of the jet. Nevertheless, such interference is limited or negligible for long injection times since the injector is in a stationary state most of the time when it is actuated, which means that the needle is fully raised and cross-sectional area with respect to the needle seat is relatively large. The current trend in GDI engines is to introduce new strategies, most notably multiple injection. Although the transient phases of needle opening and closing are short, the use of several injections makes the intermediate needle positions important and therefore requires more attention. For this

reason, several specific studies have been carried out to determine the influence of the needle position on the spray characteristics [25]. In addition, efforts were also made to find out how the type of needle seat [26]. The needle not only has vertical displacement (lift) but can also move laterally (wobble), a movement that has a significant effect on the fluid in a way that prevents it from being evenly distributed in all orifices. Therefore, the three-dimensional needle movement has been the subject of study in recent years [27].

At the present time, there are two principal types of needle seat used in commercial injectors designed in such a manner that the nozzle must have a high purge capacity: micro-sac and valve-covered-orifice (VCO). Figure 3.5 illustrates the shape of these two geometries and reveals the differences between them. VCO type injectors have the inlet orifices located on the needle-nozzle contact surface, whereas in micro-sac nozzles, the needle sealing is performed upstream of the orifices, meaning that the inlet of the holes is located in a particular volume referred to as a sac.

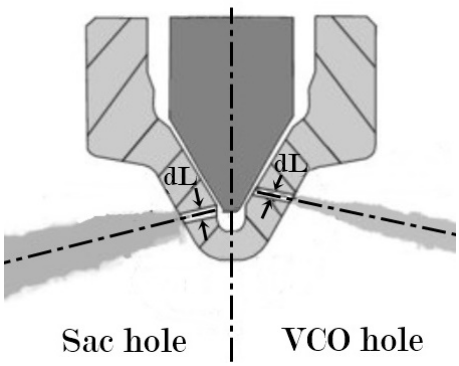

Figure 3.5: Geometries representing the main needle set types. Adapted from [28].

One of the advantages of using VCO type injectors is that, the needle covers the holes when it closes, so the fuel stops flowing sharply at the end of injection and there is no boils off or flows at low pressure as in the sac-type. Furthermore, the VCO nozzle has a faster reaction time and improved accuracy in the amount of fuel delivered. On the contrary, as a shortcoming, the VCO type is more sensitive to the position or eccentricity of the needle strongly influencing the fuel flow and thus resulting in an asymmetric fuel flow and an irregular mass concentration surrounding the nozzle [29].

Sac nozzles are designed to minimize the asymmetry problem, but the presence of the sac leads to the generation of residual fuel inside the cavity when the needle is closed, resulting in an increase in unburned hydrocarbons and soot. For this purpose, the design preference is to limit and reduce the sac volume as much as possible resulting in micro-sac nozzles.

Nozzle orifice

In the injector nozzle there are certain openings called orifices which provide a pass-through for the fuel to enter the combustion chamber. This process is associated with a change of potential energy from the pressure exerted on the fuel to kinetic energy causing the flow to accelerate before entering the cylinder. The microscopic features of the holes have a great influence on the characteristics of the GDI jet and thus on the atomization and mixing processes [30, 31].

Figure 3.6 presents the most relevant microscopic features for the characterization of the orifices of a modern GDI nozzle: hole inlet diameter (d) and hole outlet diameter (D), hole length (L_1), counter-bore length (L_2), hole inlet corner radius (r), counter-bore fillet (R). Although the image represents a counter-bore orifice geometry, the definitions are applicable to other types of geometries such as divergent, convergent or convergent-divergent. For a better characterization of the geometry, certain adimensional variables are defined from the above-mentioned dimensions:

- length to outlet diameter ratio: L_1/d or L_2/D;
- hole inlet corner radius to hole inlet diameter ratio: r/d;
- hole inlet to hole outlet diameter ratio: d/D.

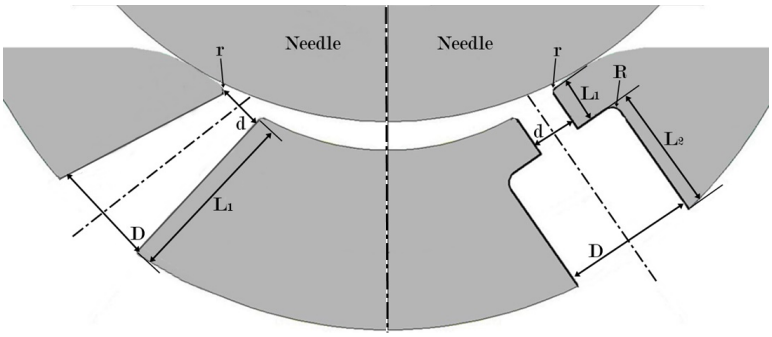

Figure 3.6: Geometries parameters to define the nozzle orifice.

The last parameter ratio defines the conical shape or convergence/divergence of the orifice, if equal to unity it refers to a cylindrical nozzle. In the literature, although much more widespread for Diesel injectors, there are other correlations that determine the convergence of an orifice such as the *k-factor* (Equation 3.7), and the area reduction AR (Equation 3.8).

$$k - factor = \frac{d - D}{10[\mu m]} \tag{3.7}$$

$$AR = \frac{A_d - A_D}{A_d} = \frac{d^2 - D^2}{d^2} \tag{3.8}$$

In the case of GDI injectors, it has been more common among researchers to define the orifice shape by the Conicity Factor (CF) shown in Equation 3.9 [32].

$$CF = \frac{100(d - D)}{L} \tag{3.9}$$

Not only the above mentioned parameters have a great influence on the development of the jet, but also other geometrical characteristics such as the number of orifices, the arrangement of the orifices as well as the spacing between them, which significantly affect the internal flow and the spray pattern [33]. It is well known that the investigation of the flow inside the nozzle involves significant challenges due to the reduced orifice and nozzle size and the highly transient character of the injection process. Consequently, special attention has to be given to inherent uncertainties/defects of manufacturing or processes such as hydro-erosive grinding (HEG) because of the possible influence on the flow development. Numerous efforts have been made by the research community to develop non-invasive experimental techniques in order to obtain accurate nozzle geometry. On the one side, Macian et al. [34] developed a novel technique that included the creation of a silicon-based nozzle mold, by using a Scanning Electron Microscope and CAD software they generated the images of the injector and measured the main geometrical parameters of the images. This technique is extremely accurate, providing errors of less than 1% in the measurements. On the other side, Duke et al. [27] employed phase-enhanced high-energy x-rays to determine the internal structure of the injector nozzle, enabling the visualization of defects and irregular features that cannot be observed by any other non-destructive technique. In addition, this x-ray method can also be employed to determine the spatial movements of the needle as demonstrated by the same group.

Influence of nozzle geometry on the internal flow

Length to outlet diameter ratio (L/D)

Li et al. [30] demonstrated in a counter-bore injector type that the decrease of L_1/d ratio through increasing the orifice diameter (d) accelerates the flow velocity at the nozzle outlet, shortens the transition period, and accelerates the stability of the fuel injection rate. In addition, a linear increment in mass flow rate was observed with increasing diameter. Tu et al. [31] observed from the variation of the L_1/d ratio of the inner hole that this ratio of dimensions

was more influential on the spray characteristics than the counter-bore length to outlet diameter variation. In addition, they also asserted, supporting the previous statement, that the reduction of the L_1/d ratio effectively increases the mass flow rate, velocity, spray angle and reduces droplet size and breakup length. Increasing the spray angle causes wall impingement inside the counter-bore, particularly for $L_1/d = 1$, which potentially lead to further deposit accumulation in the injector. Jiang et al. [35] investigated the influence of the length to outlet diameter ratio in a converging cross-sectional area injector where it was observed that under atmospheric conditions a lower L/D ratio (larger hole diameter) led to a greater mean droplet size. This behavior was sustained when changing the ambient conditions to instantaneous boiling conditions. The bigger droplet size led to a reduced level of droplet break-up, due to the decreased fluid velocity in a larger orifice. This contributed to preserve the morphology of the spray plume and to avoid collapse between sprays.

Hole inlet corner radius (r)

The HEG process previously mentioned is a technique commonly used on Diesel injectors that allows the radius of an edge to be increased by flowing an abrasive fluid through it. On the contrary, care must be taken when using it on GDI injectors, as several studies have proven that lower injection pressures coupled with a rounded edge at the nozzle inlet due to HEG technique increase the wall film in the injector [36]. Moreover, this is not the only negative effect, but the rounding of the hole inlet allows deposits to form at the entrance of the cavity. Increasing the hole inlet radius seemingly decreases cavitation effect and turbulence inside the orifice eliminating some of the cleaning mechanisms and allowing deposits to form.

Hole inlet to hole outlet diameter ratio (d/D)

The convergence of the orifice is the ratio between the inlet and outlet area. A convergent geometry is characterized by having the outlet diameter smaller than the inlet one. This reduction in area results in an acceleration of the velocity for subsonic flows [37]. In terms of the influence of geometry on phenomena that typically occur in GDI injectors such as flash boiling and spray collapse, the diverging orifice offeres higher resistance against spray collapse than the converging orifice, as its droplet size is less affected by variations in ambient conditions, whereas the droplet size of the converging orifice is significantly reduced under flash boiling conditions, creating higher levels of spray collapse [35]. Concerning injectors with counter-bore geometry, Tu et al. [31] further focused their efforts on quantifying the effects of varying the counter-bore diameter and thus the d/D ratio. The effects of these vari-

ations were more pronounced as the smaller the L_1/d ratios were. Injectors with narrower counter-bore diameters have greater mass flow rates. This observation can be attributed to the effect that a liquid flowing through the counter-bore generates a positive circulating air flow inside the orifice cavity which reduces the flow resistance and increases the total mass flow rate of the inner hole. However, the increase in counter-bore diameter is associated with an additional air entrainment in the cavity, decreasing the recirculation velocity and its positive effect on the mass flow rate. In a general overview, increasing counter-bore diameter (D) has an overall adverse effect on spray characteristics. Mass flow rates and spray angles decrease and droplet size increases for larger L_1/d ratios.

3.4.3 Hydraulic characterization of the nozzle

The flow entering the orifice sharply changes direction so that it could flow away from the surface at the orifice inlet and thus generate recirculation zones between the wall and the lines followed by the flow, narrowing the cross-section of the fluid passage (*vena contracta*). Generally in commercial applications, as mentioned above, GDI engines have a tendency to use multi-orifice injectors for offering the much sought-after flexibility of spray pattern adaptation and reduced penetration, so the pattern of this phenomenon is shown in Figure 3.7. As it is appreciated, the orifice forms an angle with respect to the geometrical axis of the injector so that the recirculation only appears in the upper part of the orifice. Nevertheless, Salvador et al. [38] demonstrated that at low needle lifts this effect can also be observed in the lower part of the orifice.

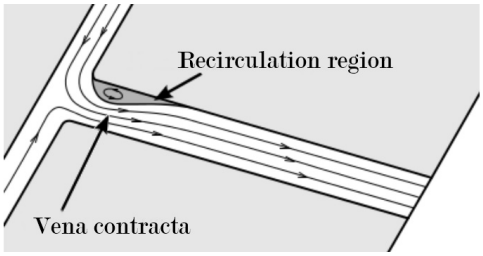

Figure 3.7: Detached flow inside the orifice forming recirculation zones and narrowing in the cross-section of the fluid passage (*vena contracta*) in multi-orifice injectors. Adapted from [14].

One of the main consequences of the flow detachment is the pressure losses in the orifice, which characterizes the flow inside the nozzle to a large extent. In addition, there is friction between the liquid and the walls, which aggravates pressure losses and also contributes to viscous dissipation. For the calculation of the above-mentioned losses, special attention has to be paid as the working regimes may vary according to the operating conditions. When a fluid running

through a pipe encounters an abrupt change of section, it tends to detach, causing local disturbances. This flow needs a certain time or, in other words, a specific length in order to stabilize again. The stabilization distance is commonly defined in terms of diameters and depends, to a large extent, on the working regime or, in short, on the Reynolds number. In the case of laminar defined flows, the stabilization distance can be calculated from Equation 3.10 [39] with the given coefficient ranging from 0.03 to 0.06 according to the literature [40].

$$L/D = 0.03Re \qquad if Re < 2300 \tag{3.10}$$

On the other hand, if the case is turbulent, owing to the mixing intensity induced by the turbulence itself, the length required to have a developed flow is shorter, and can be defined by Equation 3.11 [40].

$$L/D = 4.4Re^{\frac{1}{6}} \qquad if Re > 4000 \tag{3.11}$$

If the Diesel orifices were not long enough (L/D $\approx$ 4 - 10) to stabilize the flow, those present in GDI nozzles and especially the counter-bore type are even smaller (L/D $\approx$ 0.5 - 3). For this reason, the following should be taken into account when analyzing internal flow:

- The geometry of the orifice inlet directly determines the flow behavior and thereby the flow characteristics, i.e. the size of the boundary layer or the local pressure losses among others.
- The Reynolds number is not sufficient to characterize the flow regime and thus the turbulence intensity because the theoretically stipulated limits for the calculation of the regime (laminar or turbulent) are not valid due to the fact that the fluid is not fully developed.
- The lack of full flow development prevents the application of the associated theory to the calculation of the regime. Therefore, the velocity profiles at the orifice exit cannot be considered to be constant as in a fully developed flow but neither can they be described under the Hagen-Poiseuille law for laminar regime [37].

For all that, the most widespread and consistent way to analyze the internal nozzle flow is by mean parameters measured at the orifice outlet and dimensionless flow coefficients such as discharge, velocity or area coefficients, among others [20]. In order to carry out the calculation of these dimensionless coefficients, it is necessary to define some previous concepts such as instantaneous mass flow or momentum flux. Starting with the discharge coefficient,

this is defined as the ratio of the real total mass flowing through the orifice and the theoretical mass flow rate. The mass flow rate is estimated from Equation 3.12, requiring knowledge of the density and velocity profiles in the orifice.

$$\dot{m}_f = \int_A \rho(\mathbf{U} \cdot \mathbf{n}) dA \tag{3.12}$$

Considering the velocity perpendicular to the orifice exit the above expression might be reformulated as Equation 3.13.

$$\dot{m}_f = \int_A \rho u dA \tag{3.13}$$

As it has been stated in previous paragraphs, the small length- and time-scales of the problem make accurately calculating the axial velocity and density profiles involved in Equation 3.13 a highly difficult and imprecise process. However, there are ways to simplify the study, including considering the fluid incompressible and inviscid (which implies no boundary layer). This allows the integral Equation 3.13 to be transformed into a simpler one as presented in Equation 3.14, where u_{th} (Equation 3.15) is the theoretical velocity obtained from Bernoulli's theorem (Equation 3.1) and A_o is the cross-section area of the outlet orifice.

$$\dot{m}_{f,th} = \rho u_{th} A_o \tag{3.14}$$

$$u_{th} = \sqrt{\frac{2\Delta p}{\rho_f}} \tag{3.15}$$

Once the terms that make up the discharge coefficient calculation for a particular condition have been established, the dimensionless coefficient that determines specific flow characteristics is given in Equation 3.16.

$$C_d = \frac{\dot{m}_f}{\dot{m}_{f,th}} = \frac{\dot{m}_f}{A_o \sqrt{2\rho_f \Delta p}} \tag{3.16}$$

The expression encompassing the discharge coefficient reflects the efficiency of the nozzle in supplying the fuel and emphasizes the dependence between the mass flow rate and the pressure difference in the interior of the nozzle. The cavitation phenomenon affects the behavior of the nozzle (see Section 3.4.4) so that if it operates under non-cavitating conditions, the mass flow depends linearly on the $\sqrt{\Delta p}$. On the contrary, if the nozzle is under cavitating conditions, the mass flow is limited in its growth, stabilizing its value and thus causing the discharge coefficient to be affected with a decrease in its value.

The behavior of the discharge coefficient in orifices has been the subject of extensive research during the last few decades as it not only characterizes the flow but also the pressure losses in the nozzle and orifices in fluid systems [42]. This dimensionless coefficient is mainly a function of Reynolds number and orifice geometry, in particular length-to-diameter ratio and diameter ratio. Other geometrical factors that may influence it are the shape of the pipe section in which the nozzle is placed, and the sharpness of the upstream edge of the nozzle orifice [43]. Figure 3.8 represents the above mentioned dependence, showing how the evolution of the discharge coefficient with the Reynolds number can be considered as asymptotic. The curves also allow to distinguish the operating flow regime being laminar when the dependence on the Reynolds number is linear and turbulent in case of losing this dependence. Furthermore, it is clear from the illustration how the geometry of the orifice has a strong influence on the shape of the curves.

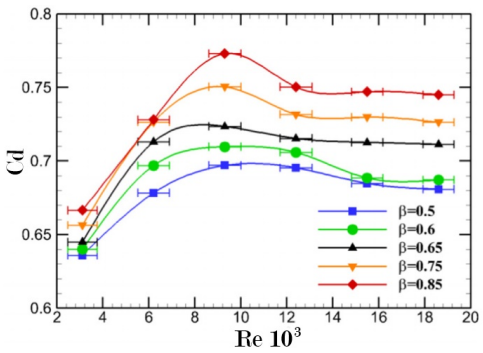

Figure 3.8: Discharge coefficient evolution as function of Reynolds number for different $\beta = d/D$ ratios in an orifice with a sharp-edged of 30° angle. Adapted from [41].

In order to determine the degree of relationship between the discharge coefficient and the geometrical parameters described in Section 3.4.2, many empirical correlations have been developed [44]. Some of them, such as the one implemented by Salvador, J. [45] were specifically aimed at Diesel injectors. Nevertheless, to date and to the best of the author's knowledge, no researcher has developed a specific correlation to characterize the discharge coefficient in GDI injectors.

As mentioned in previous paragraphs, the discharge coefficient is a dimensionless way of reflecting the efficacy of the orifice in supplying any particular type of fluid. It reflects the pressure losses in the nozzle due to many different reasons including wall friction losses and the non-uniformity of the velocity pattern at the orifice outlet. In addition, it also takes into account the cavitation phenomenon when it occurs (see Figure 3.9a). However, the study of these different types of pressure losses is complex and therefore tends to be simplified as shown in Figure 3.9b. This simplification assumes that all the fluid inside the nozzle is liquid and flows through an effective area considering

its movement at a constant effective velocity. These assumptions lead to the calculation of the actual mass flow through the orifice from Equation 3.17.

$$\dot{m}_f = \rho_f A_{eff} u_{eff} \tag{3.17}$$

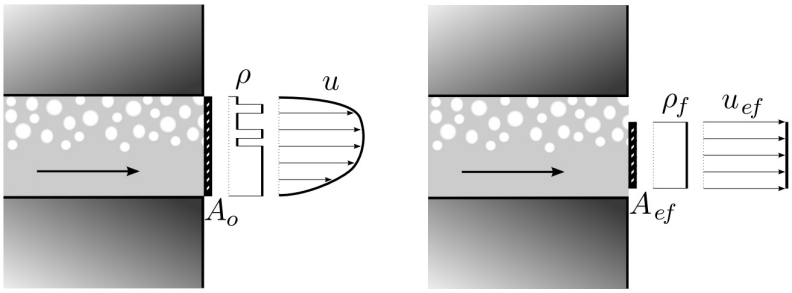

(a) Real flow (b) Effective flow

Figure 3.9: Graphical representation of the definitions of effective area and effective velocity. Adapted from [24].

The equation defining the discharge coefficient can also be expressed as shown in Equation 3.18, as a direct function of the pressure or energy losses represented by the velocity coefficient (C_v) and of the section losses associated with different phenomena such as cavitation, non-uniform velocity pattern effects and flow detachment from the wall which are reflected from the area coefficient (C_a). In accordance with the defined concept, the velocity coefficient can be expressed, as shown in Equation 3.19, as the ratio between the effective velocity and the theoretical velocity (Equation 3.15) while the area coefficient is described as the relationship between the effective and the geometric area, and it is simplified by using the effective and geometric diameters, as indicated in Equation 3.20 [20].

$$C_d = C_v C_a \tag{3.18}$$

$$C_v = \frac{u_{eff}}{u_{th}} \tag{3.19}$$

$$C_a = \frac{A_{eff}}{A_o} = \frac{D_{eff}^2}{D_o^2} \tag{3.20}$$

The momentum of a moving object is defined as the product of its mass flow rate and squared velocity. The spray formed in the injection process is

composed of numerous droplets of different sizes and each moving at different velocities. That being said, the definition of the momentum flux of a GDI spray is expressed by Equation 3.21.

$$\dot{\mathbf{M}} = \int_A \rho \mathbf{U}(\mathbf{U} \cdot \mathbf{n}) dA \tag{3.21}$$

In the same way as for mass flow rate, considering the fluid velocity perpendicular to the outlet area of the orifice under study, the above Equation 3.21 can be reformulated as shown in Equation 3.22.

$$\dot{M}_x = \int_A \rho u^2 dA \tag{3.22}$$

Again, assuming the fluid to be incompressible and inviscid, the integral form of the flux momentum equation can be simplified as presented in Equation 3.23. In addition, from this definition arises another dimensionless coefficient, the momentum coefficient (C_M), which relates the theoretical momentum obtained from the Bernoulli velocity to the actual measured momentum (Equation 3.24).

$$\dot{M}_{x,th} = \rho u_{th}^2 A_o \tag{3.23}$$

$$C_M = \frac{\dot{M}}{\dot{M}_{x,th}} \tag{3.24}$$

The momentum flux can also be expressed as a function of area and effective velocity by Equation 3.25.

$$\dot{M} = \rho_f A_{eff} u_{eff}^2 \tag{3.25}$$

The behavior of the spray jet has a strong dependence on the momentum flux and can therefore be considered as a fundamental measure for the characterization of the jet. Several researchers such as Naber and Siebers [46] have tried to experimentally understand the relationship between this parameter and the spray penetration under different operating conditions. Gimeno [20] also joined this common objective by carrying out an extensive experimental analysis of the momentum flux of various injectors, demonstrating the existing relationship between momentum flux and spray penetration. In addition, he took into account and analyzed the effects of the cavitation phenomenon on the spray performance. Knowledge of the mass flow rate and momentum flux associated with an injector allows parameters such as effective velocity and

area as well as dimensionless coefficients to be calculated without knowing the geometrical details of the internal nozzle such as the size of the outlet orifice. Thus, if the values of mass flow rate (Equation 3.17) and momentum flux (Equation 3.25) are experimentally obtained, the effective velocity can be defined by Equation 3.26 and the effective area as presented in Equation 3.27.

$$u_{eff} = \frac{\dot{M}}{\dot{m}_f} \tag{3.26}$$

$$A_{eff} = \frac{\dot{m}_f^2}{\rho_f \dot{M}} \tag{3.27}$$

3.4.4 Cavitation phenomenon

As mentioned in Section 3.4.3, the abrupt changes in cross-section experienced by the flow inside the nozzle can lead to a recirculation area between the *vena contracta* and the wall in the form already presented in Figure 3.7. This effect is characterized by a pressure drop in the recirculation zone due to the acceleration experienced by the fluid. The value of this pressure drop can go even below the vapor pressure for a given operating temperature, leading to a rise to an instantaneous partial evaporation of the liquid, and causing the phenomenon known as cavitation, which is defined as the formation of small vapor bubbles within a moving fluid.

The structure of a GDI injection nozzle plays an important role in the formation of the cavitation phenomenon inside the orifices (incipient cavitation) [30]. In addition, the fluid velocity, in other words the injection and discharge pressures, has a high influence on the mentioned phenomenon. Li et al. [30] studied the influence of the injection pressure on the behavior of the fluid inside the nozzle, focusing mainly on the generation of cavitation, and concluded that the development of cavitation in the nozzle and the deflection of the fuel jet from the geometrical axis became more severe with increasing injection pressure. The importance of nozzle orifice flow and cavitation means that several studies in recent years have used injectors with optically transparent nozzles to directly examine orifice flow cavitation [47]. Another popular technique for the study of in- and near- nozzle flow characteristics is the x-ray imaging technique; method employed by Moon et al. [48] to analyze the influence of the nozzle geometry on the flow behavior and particularly on the cavitation formation. In this experiment they evaluated three different geometries in which the main variation was the inclination of the geometry with respect to the geometrical axis of the injector, concluding that nozzle

hole inlet angle less than 90° generated cavitation, the smaller the angle, the more pronounced the cavitation. Not only the presence of cavitation was observed under certain geometries but also the existence of another phenomenon known as hydraulic flip. The hydraulic flip effect can be experienced when the detached flow is not added back to the wall but extends to the orifice outlet in such a way that the gas in the combustion chamber tends to enter inside the orifice and fills the space between the wall and the *vena contracta*. This phenomenon is quite widespread in GDI injectors and has been observed by numerous researchers in several investigations [49].

Cavitation is an interesting phenomenon to consider and plays an important role in GDI injectors. The combined effects of the particular GDI nozzle geometry, the low needle lift and the low vapor pressures of the fuels typically used are what prove the importance of this effect. Bergwerk [50] defined the appearance of cavitation from Equation 3.28, where p_{inj} refers to the injection pressure, p_{back} reflects the pressure downstream of the injector in the discharge chamber and p_v the vapor pressure of the fuel at operating temperature.

$$CN = \frac{p_{inj} - p_{back}}{p_{back} - p_v} \tag{3.28}$$

According to Chaves et al. [51], one of the most remarkable effects of cavitation is the increase of the spray angle at the nozzle exit. This result was also observed by Salvador [45] and De la Morena [52], who noticed an increase in the angle between 1.5° and 3° in a cylindrical mono-orifice nozzle for conditions in which cavitation bubbles were detected at the nozzle outlet. However, it is not necessary for cavitation to extend all the way to the orifice exit to find significant effects on the jet. In fact, authors such as Hiroyasu et al. [53] and Soteriou et al. [54] found evidence of a significant increase of the jet angle already during the first phase of cavitation (incipient cavitation).

It is important to mention that most of these studies as well as the obtained correlations related to cavitation are based on investigations with Diesel injectors, which have been the main object of analysis for years, while GDI nozzles are relatively new. Among all of them, some focused on the calculation of the critical cavitation number above which cavitation took place. Bode et al. [55] based their work on demonstrating the boundary between cavitating flow and non-cavitating flow (critical cavitation number) in real size Diesel injector holes by setting it to a value close to 5. In later work, Arcoumanis et al. [56] identified that the initiation of cavitation in Diesel injectors occurred for a cavitation number value of 2.

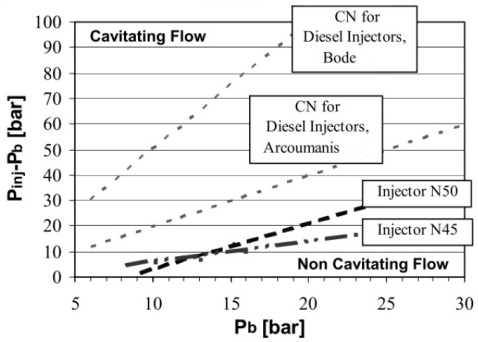

Figure 3.10: Cavitation number analysis as a function of discharge pressure and the pressure difference between injection pressure and discharge pressure for various types of injectors: two Diesel injectors from the studies of Bode et al. [55] and Arcoumanis et al. [56] and two multi-hole GDI injectors with drill angles of 45° (N45) and 50° (N50). Adapted from [57].

The scientific community adapted the definitions to the jet behavior of GDI injectors. However, Gilles-Birth et al. [57] proved that the critical cavitation number for GDI injectors was significantly lower and depended on the geometrical hole angle (drill angle), finding critical values of 0.81 for a 50° drill angle nozzle and 0.64 for a 45° drill angle nozzle. Figure 3.10 reflects the comparison of the critical cavitation numbers as a function of the operating conditions (injection pressure and discharge pressure) for two Diesel injectors of different authors and two DISI multihole injectors with cylindrical shaped orifices and different drill angles (45° and 50°). From the image, it is evident that the critical cavitation values for the analyzed GDI injectors are much lower than for Diesel injectors and it is stated that the cavitation phenomenon is present in the whole operating range of the studied GDI injectors, changing only the degree of cavitation existing in the injectors. Furthermore, similar to other researchers [48], it was deduced that the inclination of the orifice had a significant influence on vapor generation, being earlier and more severe for those nozzles with a lower drill angle.

Despite the difficulty associated with determining the presence of the cavitation phenomenon, there are two possibilities to experimentally observe it: from the hydraulic characterization of the cavitation flow or through direct visualization. The main difference between these two study methods is that hydraulic characterization is a non-invasive method that allows the study of real nozzles by obtaining details of the injector and the flow through it from the associated dimensionless coefficients, whereas the visualization option requires either transparent injectors, which are usually of more simplified geometries than the real ones due to the intricacies of the flow, or expensive visualization techniques such as x-ray image technique.

Bergwerk [50] proved the dependence of discharge coefficient on cavitation with pressure ratio defined as $(p_i - p_b)/p_b$ and demonstrated that discharge co-

efficient values tend to decrease under cavitating operating conditions. Spikes and Pennington [58] seconded these statements and trends as well as relating geometry features such as L/D ratio and hole entrance radius to the emergence of cavitation. Nurick [59] attempted to explain the behavior of the discharge coefficient under cavitating conditions in a clear and simplified form through a one-dimensional model (for more information on this model the reader is encouraged to consult [45]).

As it has been seen throughout this Section, the cavitation phenomenon has generated a lot of interest among researchers over the years, as the fluid behaves in a characteristic way in the presence of this phenomenon. Within this framework, Payri et al. [60] pointed out that although the mass flow collapsed with the onset of cavitation, the momentum flux continued to grow as a function of Reynolds due to the reduction of friction with the wall owing to the presence of vapor. An additional finding is the affirmation of the increase in the flow velocity at the outlet that occurs with cavitation, and the reduction of the effective area available for liquid phase fuel outlet. These results were corroborated by authors such as Suh y Lee [61] who used the PDPA (Phase Doppler Particle Analyzer) visualisation technique to measure the velocity at the nozzle outlet and Winklhofer et al. [62] who relied on the LDV (Laser Doppler Velocimetry) technique for the same purpose.

3.4.5 Flash boiling phenomenon

During the injection process, in addition to cavitation, other phase change phenomena such as flash boiling may occur. Both cavitation and flash boiling induce small discontinuities and cavities in a liquid. The difference between these processes is that the vapor generated in cavitation bubbles may be unsaturated. Hydrodynamic cavitation results from a pressure drop in the liquid flow as a consequence of high local velocities and usually appears at low temperatures where the vapor density is sufficiently small that the latent heat flow does not affect the event [63]. As a result, the time scale of the heat transfer is much faster than the time scale of the bulk motion; and hence, the dynamics is basically controlled by the inertia of the liquid. On the other hand, flash boiling takes place at slightly higher temperatures where the vapor density is much greater; and therefore, the liquid must provide more energy per unit volume of vapor. In this case, the time scale cannot be considered negligible, and thus dynamics are controlled by finite heat transfer rather than inertia. Therefore, the transition from cavitation to flash boiling is due to a reduction in static pressure or an increase in liquid temperature. This explanation can

also be supported by the Jakob number,

$$Ja = \frac{\rho_l C_p \Delta T}{\rho_v h_{fg}} \tag{3.29}$$

where ρ represents density, C_p the specific heat at constant pressure, ΔT the amount of superheat, and h_{fg} the latent heat of vaporization.

If the value of the Jakob number is above unity, it means that more energy per unit volume is required for vaporization than is available in the form of sensible heat. An increase in temperature is associated with an increase in the denominator of Equation 3.29 ($\rho_v h_{fg}$). Therefore, at high temperatures the energy demanded for vaporization rises, increasing the time required for heat transfer between phases, even approaching the transit time of the flow through the nozzle [65]. Contrarily, in cavitating flows, the time required for vaporization is quite short, making absolutely instantaneous. To sum up, Figure 3.11 illustrates in a pressure-volume diagram the different conditions of occurrence of flash boiling, phenomenon in which the fluid enters a metastable superheat condition either by a rapidly heating of the liquid or by rapidly depressurizing it (lines OA and OB, respectively).

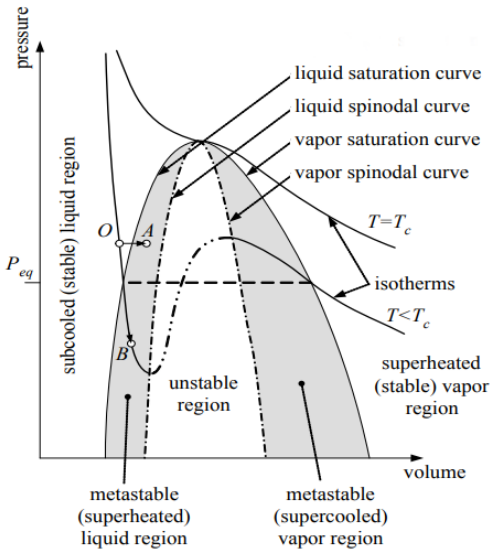

Figure 3.11: Pressure-volume phase diagram that identifies the conditions of appearance of the flash boiling phenomenon. Adapted from [64].

Many researchers have focused for years on the study of the flash boiling phenomenon and its characteristics because of its importance and influence on spray behavior and its widespread use in areas such as coating industries, agriculture, combustion, turbine, sensing, desalination, energy storage, refrigeration, pharmaceutical, and even in household sprays [66]. All these studies together concluded that the formation of the flash boiling phenomenon is constituted by three stages: bubble nucleation, bubble growth and two-phase flow.

Bubble nucleation

A superheated liquid is a particular case of metastable system with respect to the phase equilibrium condition defined by equality of chemical potential (represented between the binodal and the spinodal curve in Figure 3.11). The faster this process is, the more superheating of the liquid can be achieved, and the more violent the subsequent vaporization. The nucleation and vaporization processes allow the conversion of metastable systems into stable or relaxation systems. The nucleation process can be classified into two groups depending on the degree of superheat: homogeneous and heterogeneous nucleation.

- **Homogeneous nucleation**. It is also known as continuous phase transition which means that the transformation from one phase to another takes place smoothly. This kind of nucleation in which nucleation sites form within the liquid itself, in the absence of bubble nuclei, becomes predominant when the liquid pressure is significantly reduced.
- **Heterogeneous nucleation**. It initiates with the appearance of gas and solid phases at an interface or a boundary rather than in the liquid. The nucleus can manifest itself in different forms, as a gas dissolved in the liquid, as small dust particles or as irregularities present on a solid surface such as the walls of an injector.

During the nucleation phase, one of the most important variables is the nucleation flux density, which is described as the number of bubbles generated during a unit of time per unit volume. Heterogeneous nucleation flux is evidently lower than in homogeneous nucleation as it requires a lower effective activation energy (or energy barrier) for the formation of a critical nucleus [66]. Another interesting parameter is the R_p, which refers to a widely used indicator for measuring the fuel superheated degree from the ratio of ambient pressure to vapor saturation pressure at operating temperature (Equation 3.30).

$$R_p = \frac{P_{sat}(f(T_f))}{P_{amb}} \tag{3.30}$$

The parameter R_p was additionally employed to relate the radial expansion of the spray to the flashing regimes. The flashing regimes are mainly divided according to the position of the radial expansion as internal and external flashing [63]. Authors such as Lin et al. [67] and Cleaty et al. [68] reported after their numerous studies that external flashing takes place at relatively low R_p numbers while internal flashing develops for high R_p numbers.

Despite the abovementioned, Guo et al. [69] demonstrated in one of their many research works that this statement was not always accurate, as under certain operating conditions the jet did not behave as stipulated. They realized from the analysis that for sub-cooled and transitional regions where the pressure ratio (R_p) is below 3.3, the relationship between this parameter and the radial expansion or, in other words, the spray width is correct and adequately predicted. However, for higher R_p ($R_p > 3.3$), the behavior of the jet is not adequately predicted, resulting in disparate radial expansions for similar R_p ratios. Their research did not end there, but went further in determining a correlation for the calculation of the spray width. Furthermore, they concluded that during the first stage the radial expansion was governed by the nucleation rate while in the second stage it is the thermal energy for vaporization that controls the radial expansion.

The importance of correctly determining the radial expansion is because of its close relationship to the phenomenon of spray collapse, which will be explained in detail in later sections. The spray collapse phenomenon is mainly attributed to the pressure drop in the central area of the jets and usually occurs at high levels of superheat. The opening of the flashing jets generates a strong interaction between them causing them to deflect towards each other, which finally generates a single spray in the central axis, leading to the collapse of the jet.

Bubble growth

Once bubble nucleation stage has been generated and developed, pressure fluctuations in the environment can cause the bubbles to collapse or grow. From a spray atomization point of view, the growth phase plays a fundamental role due to the direct impact it has on the jet characteristics both inside the injector and in the atomization phase. Plesset et al. [70] explained in detail the stages of bubble growth in superheated liquids based on physical terms, listed below.

- In the early stages, when the bubbles are still too small, the growth rate is very low and depends to a large extent on the surface tension of the bubble.
- As the bubble size increases, the growth rate can reach a maximum if the superheating degree is high enough.
- The thermal energy required for evaporation causes the liquid adjacent to the bubble to cool down due to the heat transfer effect. Thereby, the vapor pressure decreases and the bubble growth rate is controlled and limited by inertia and thermal diffusion.

- The growth rate of the bubble decreases more and more and the inertial effects become less important so that the growth rate is controlled by thermal diffusion. The pressure and temperature inside the bubble approach the ambient values until they are reached and once this occurs, the bubble growth stops.

Just as several researchers focused their efforts on studying the bubble nucleation phase, many others analyzed the growth of bubbles [71]. It is generally considered that the growth rate of the cavitation bubble is controlled by hydrodynamics forces and Rayleigh-Plesset equation [72] (Equation 3.31) describes its growth process.

$$R\ddot{R} + \frac{3}{2}\dot{R}^2 = \frac{1}{\rho}(P_w - P_r) \tag{3.31}$$

where ρ is the liquid density and P_r is the pressure around bubble. Equation 3.32 reflects the definition of the fluid pressure at bubble surface, P_w.

$$P_w = P_{sat} + \left(P_{r0} + \frac{2\sigma}{R_0}\right)\left(\frac{R_0}{R}\right)^{3n} - \frac{2\sigma}{R} - \frac{4\mu_l\dot{R}}{R} - \frac{4k\dot{R}}{R^2} \tag{3.32}$$

where P_{sat} is the saturation pressure of fuel, P_{r0} corresponds to the initial fluid pressure around the bubble, R_0 represents the initial bubble radius, μ_l is liquid viscosity and k reflects the surface viscosity coefficient proposed by Scriven [73].

The assumptions generally made for the study of bubble growth are the following:

- The temperature of the bubble should be equal to that of the liquid fuel. On the other hand, the temperature and pressure inside the bubbles are uniform.
- The bubbles grow in a spherical shape.
- The growth of cavitation bubbles inside the nozzle orifice and fuel droplets causes the phase change from liquid to vapor to occur continuously.
- The frequency of coalescence between the bubbles is altered and, in this case, increased due to Marangoni convection [74].

Bubble disruption. Two-phase flow

Bubble growth within the droplet is limited by a number of parameters, such as droplet diameter, surface tension, liquid viscosity, number density of bubble nuclei and growth rate. The limit of the bubble growth rate within a droplet can be determined by Equation 3.33, which expresses the volume ratio between the vapor and liquid phases, known as the void fraction, α.

$$\alpha = \frac{V_{bubble}}{V_{bubble} + V_{liquid}} \tag{3.33}$$

being V_{bubble} the volume of bubbles and V_{liquid} the volume of liquid. Suma and Koizumi [75] noticed that the break-up of a fuel jet takes place at α ranging from 0.51 to 0.53. Once the limit is reached, it is assumed that the droplet breaks into small droplets twice as many as the number of bubbles, as depicted in Figure 3.12. This being known, both the number and the diameter of the droplets after the rupture caused by the disruption of the bubbles can be calculated. The momentum of the parent droplet must be considered to be evenly distributed among the smaller droplets. This process ends the flash boiling phenomenon and results in a *two-phase flow* consisting of liquid and vapor in equilibrium.

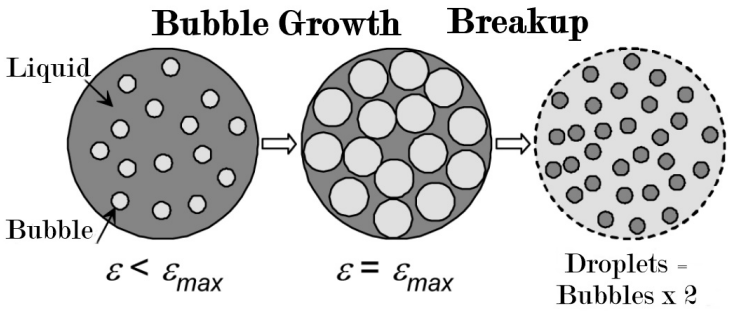

Figure 3.12: Breakup caused by bubble disruption. Adapted from [76].

Having explained the theory behind the flash boiling phenomenon and applied it to the present context, in the case of a direct injection gasoline engine, flash boiling of the injected fuel can appear under part-load operation, especially when late intake valve opening techniques are employed [77]. The stages of this process are as follows:

- The fuel during the injection event is at high temperature (60°C < T < 120°C) due to the heat received by the conduction process from the cylinder head.

- As the piston starts its downward movement and the intake valves are closed, a partial vacuum is created inside the cylinder, which can be up to about 0.1 bar.
- The boiling temperature of the fuel at in-cylinder pressure is lower than the temperature of the fuel inside the injector.
- Superheated liquid fuel is injected into the cylinder. Latent heat cannot be conducted by surface evaporation.
- Fast and explosive bubble growth takes place within the droplets and vaporizes the fuel.

The main governing factor of the flash boiling phenomenon is the temperature difference between the fuel leaving the injector nozzle and the boiling point of the fuel at the pressure condition at which the fuel tends to expand. This can be referred to as the "degree of superheat" and investigation has demonstrated that the atomization of a liquid jet is much greater when the degree of superheat is large enough to cause instantaneous flash boiling. It should be mentioned that the degree of superheat is also described as the difference between the ambient pressure and the vapor pressure of the fluid. Some previous work [70] have suggested that the jet and its structure will be significantly affected by flash boiling when the degree of superheat is at least 20°C. However, the particular degree of superheat necessary to induce flash boiling depends on several factors, including the surface finish of the nozzle orifice and the Weber number of the liquid.

Senda et al. [78] were some of the many drivers of flash boiling studies, conducting research on fuels with very low boiling points. For the study, the authors modified and controlled the physical processes in the spray such as fuel evaporation and vapor-air mixing by including additives in the main fuel. The investigation revealed that in the two-phase region, the vapor of the lower boiling fuel dominates, coexisting with the higher boiling fuel vapor. The vapor of the higher boiling fuel would not be present under the same conditions if it were the only constituent available in the system since this region is below

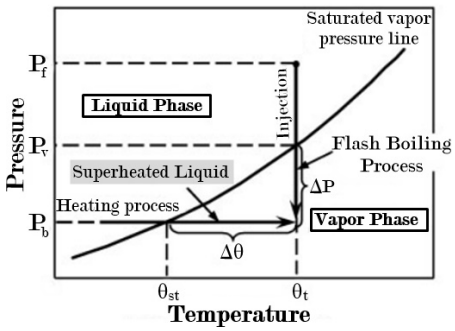

Figure 3.13: Explanation of the flash boiling phenomenon process. Adapted from [78].

the saturated fuel vapor pressure line, illustrated in Figure 3.13. This suggests that mixing a low-boiling element with a high-boiling component results in increased evaporation of the fuel and therefore, multi-component fuel, such as gasoline, are more prone to flash boiling than single-component fuels.

The flash boiling phenomenon changes the stipulated normal patterns of jet behavior and it is thereby recognized as one of the most successful methods of generating fully developed atomization and homogeneous mixtures. Some of the benefits of this phenomenon are the reduction in droplet size leading to smaller Sauter Mean Diameter (SMD) for lower pressure differences, larger surface area and improved vaporization. Flash boiling also leads to an increase in the spray angle (for better volume repartition) and a more uniform distribution. Finally, it is also characterized by a reduction in particle velocity which results in a lower spray penetration, thus reducing the risk of impact with the piston and the inconvenience this entails. The combination of these factors results in reduced spray wall impigement, improving the combustion thermal efficiency and reducing HC emissions from the engine [79]. However, despite the positive aspects of flash-boiling, this phenomenon may also lead to negatives ones such as longer spray penetration, piston wall wetting, and increased soot emissions, due to increased interactions among the spray plumes under certain operating conditions which can induce spray collapse and the aforementioned problems [80].

3.5 GDI Spray Formation

Spray formation is one of the most important aspects when talking about gasoline direct injection (GDI) as it depends to a large extent on providing a correct mixing of the fuel with the surroundings and the proper stratification of the mixture. Correctly predicting the spray behavior and understanding its internal structure is the basis for improving injection strategies, a fact that is directly related to the objectives of this Thesis. In recent years, the scientific community has increasingly focused its efforts on the study of GDI engines and specifically on the knowledge and understanding of the spray pattern. However, the atomization process still has several important features that need to be further investigated and fully comprehended.

The GDI spray is a complex structure resulting from the atomization process, the aim of which is to split the liquid nucleus first into ligaments and then into droplets. The different phases of the atomization process in the GDI jet are shown in Figure 3.14. The start of the spray is typically considered to be at the exit of the nozzle and, depending on the operating conditions, it will

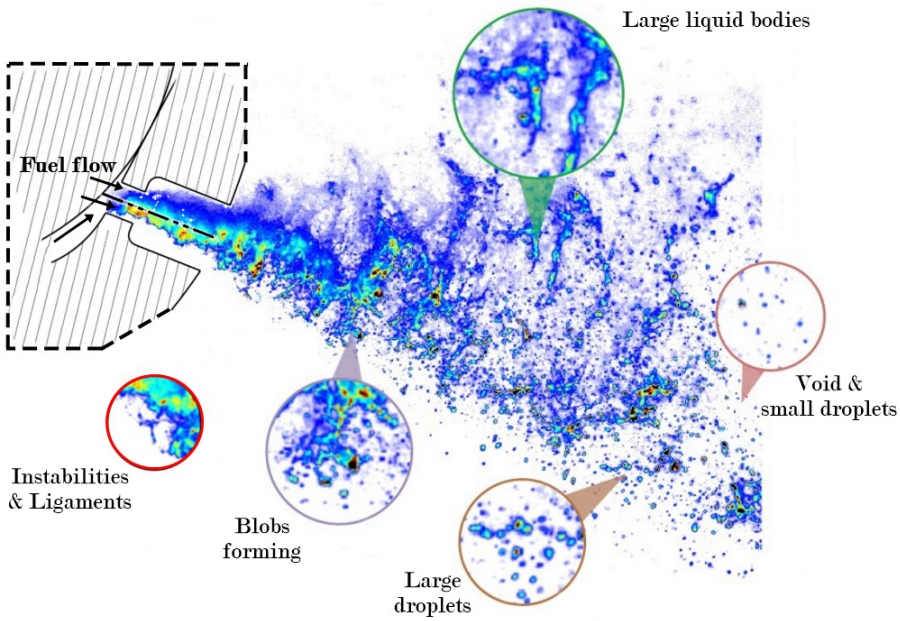

Figure 3.14: Structure of the GDI spray. Adapted from [81].

behave in different ways. In the case of Figure 3.14, it can be seen that there is a region of the spray (no more than 1-1.5 mm long) that remains intact without forming any droplets or ligaments and it is known as the liquid vein. Aerodynamic instabilities at the liquid-gas interface, coupled to the turbulent flow disturbances, lead to the detachment of the liquid core with the subsequent development of fairly large liquid structures named ligaments. Such structures have no particular profile pattern to follow and are characterized by originating directly in the liquid core. This formation procedure is referred to as primary atomization. After the ligaments separate out of the liquid core of the spray, the relative velocity of the ligaments with respect to the surrounding ambient gas and the corresponding viscous interaction induce a new aerodynamic instability that breaks the ligaments into smaller formations called droplets. This process is repeated, forming smaller and smaller droplets until the fluid surface tension is sufficient to counteract the existing aerodynamic forces. This process is known as secondary atomization or secondary breakup.

In addition to defining the GDI spray according to the atomization phases and the structures formed in each of them, it is also possible to characterize it in terms of the region being dense and dilute. This classification largely deter-

mines the optical requirements and experimental facilities required to study each part of the jet. The dense part of the jet, referred to as the near-field, corresponds to the area where the spray begins to be influenced by external phenomena and is made up of the liquid core and the ligaments associated with it. This part of the jet is, as its name suggests, too dense to be studied experimentally by conventional optical techniques such as shadowgraphy, although there have been some researchers who obtained interesting results [52]. Therefore, advanced experimental techniques are used to facilitate the analysis of this part of the jet and are mainly based on x-ray [27, 33, 49] or ballistic imaging [82]. Despite all the advances and research that has been done, this part of the spray remains difficult to study and sometimes controversial. On the other hand, the dilute part of the jet or also known as far-field collects and refers to the part where the first atomization is complete. The characteristics of this region do allow the use of conventional experimental techniques to obtain accurate results [83]. It is important to note that the discretization of the spray in these two areas is not a strict definition but rather for analytical reasons.

3.5.1 Atomization process

Liquid fuels have the advantage that they are convenient to transport and store, and a large and wide diversity of fuels are stable in liquid form. To burn stable liquid fuels in an engine, an intimate mixture must occur between the fuel and the oxidizer in a gaseous state. This gaseous mixing involves converting the liquid to vapor and promoting the mixing of the resulting gases. For this to take place easily, the liquid must break down into small particles, a process that is modeled by the mechanisms of atomization and breakup.

The atomization process takes place as soon as the spray leaves the nozzle and it is the result of the interaction that occurs at the microscopic scale liquid-gas interface. Several of these perturbations grow over time and space due to a variety of physical mechanisms such as inertial forces, surface instabilities, aerodynamic interactions and surface tension.

- Turbulence: radial velocities affecting the flow are different depending on the operating regime (see Section 3.4.3). As a consequence, the resulting inertia forces have a tendency to expand the liquid inside the discharge chamber.
- Surface instabilities: the liquid vein becomes unstable when the flow goes from being confined between walls to being injected into the discharge

chamber and considered free flow. This implies that the surface tension remains in equilibrium only if the shape of the liquid vein is conserved over time. Any disturbance that appears is quickly amplified, leading to the initial shape of the spray to disappear.

- Aerodynamic interactions: the relative motion between the liquid and the environment surrounding gas leads to the emergence of frictional forces which, among others, are highly influenced by the characteristic of the liquid vein.
- Liquid surface tension: the shape of the liquid vein is highly dependent on this phenomenon as the resultant force drives the spray to remain compact or to create droplets.

Primary atomization

The process of jet breakup in cylindrical orifices is governed and controlled by different forces and their influence depends mainly on the operating conditions under which they operate. For this reason, several regimes can be distinguished based on the operating characteristics. Following the research of Birouk and Lekic [84], Lefebvre and McDonell [85] and Reitz [86, 87], the breakup regime can be categorized as follows (see Figure 3.15):

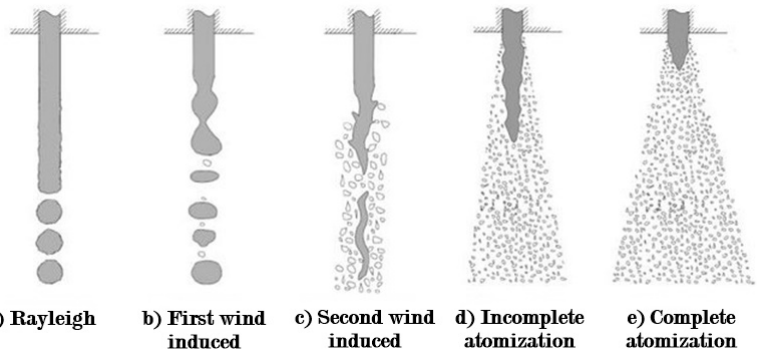

Figure 3.15: Graphical representation of the different atomization regimes. Adapted from [88].

- Dripping regime. The spray velocity is so low that the breaking process is governed by gravity, resulting in very large droplets.
- Rayleigh regime. Flow velocities remain low and disturbances on the spray surface cause small deformations. The physical mechanism of

surface tension magnifies the deformations up to the point where the liquid vein separates into droplets of the order of magnitude of the orifice.

- First wind-induced regime. In this regime, the first perturbations are amplified by the action of aerodynamic forces and the relative motion between the liquid and the environment surrounding gas. In this manner, the frictional forces act in a similar way to surface tension and thus facilitate the formation of droplets. In this regime the droplets are also formed from the liquid jet and, also in this case, the size is equivalent to the diameter of the outlet orifice.
- Second wind-induced regime. As the jet develops, the velocity increases, which favors the amplification of instabilities due to the action of aerodynamic forces. The growth of the instabilities is exponential with time, leading to the droplets formation of a dimension proportional to the wavelength of the initial perturbations. In this regime, droplets form close to the nozzle exit but need some spatial margin for their separation.
- Atomization regime. Two atomization regimes can be differentiated: incomplete and complete, depending on whether the liquid intact core is present or not. In the case of the full atomization regime, the initial disturbances together with the aerodynamic force mechanisms make droplets, similar in size to those obtained in the second wind-induced regime, to form close to the nozzle exit. This means that the intact liquid length is zero. However, it may also happen that the liquid core remains intact so that the atomization process is considered to be incomplete.

According to the numerous studies available in the literature, atomization processes and regimes are characterized by non-dimensional numbers and influenced by the following parameters: surface tension (σ), spray velocity (u_{eff}), effective orifice diameter (D_{eff}), gas density (ρ_g), liquid density (ρ_l), liquid viscosity (μ_l).

These six parameters displayed above are based on three fundamental quantities which are mass, length and time. Following Buckingham's π-theorem [89], the influence of the above parameters on the atomization process can be analyzed from three dimensionless groups. The most widespread dimensionless groups in the field of research are the density ratio ρ_g/ρ_l, the Reynolds number (Equation 3.3) and one of the following relationships:

$$\text{Ohnesorge number: } Oh = \frac{\mu_l}{\sqrt{\rho_l \sigma D_{eff}}} \tag{3.34}$$

$$\text{Weber number: } We = \frac{\rho_l u_{eff}^2 D_{eff}}{\sigma} \tag{3.35}$$

$$\text{Taylor number: } Ta = \frac{\rho_l}{\rho_g}\left(\frac{Re}{We_g}\right)^2 \tag{3.36}$$

Reitz and Bracco [87] studied the limits of each of the atomization regimes according to the three dimensionless groups above. From this research, they observed how the density ratio affected atomization process at only modest values. Therefore, it is usual to classify the atomization regimes in terms of Reynolds and Ohnesorge number only, as shown in Figure 3.16, which also shows the main breakup regimes for the various fuel properties.

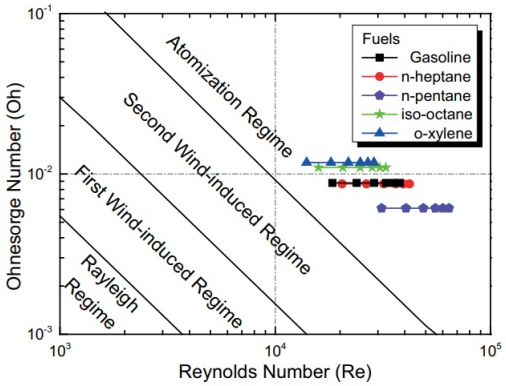

Figure 3.16: Ohnesorge diagram and primary breakup regimenes for high density ratios. Adapted from [89].

Continuing studies of the limits of the atomization regimes led to the determination of certain mathematical expressions shown in Table 3.1 which represent the boundaries between one regime and another. They are all expressed as a function of the We_g which is the Weber gas number, Equation 3.3 to which the gas density is applied. In the expression corresponding to the atomization range and proposed by Reitz [86], there is a constant called C which is calculated from the spray angle and has to be experimentally determined. In this way, the key internal flow parameters for determining the atomization characteristics at high Weber numbers [87] are included.

Regime	Expression	Ref.
Rayleigh to First wind-induced	$We_g = 0.4$ $We_g = 1.2 + 3.41Oh^{0.9}$	[90] [91]
First wind-induced to Second wind-induced	$We_g = 13$	[90]
Second wind-induced to	$We_g = 40.3$	[92]
Atomization	$\frac{\rho_g}{\rho_f} = \frac{\sqrt{C}-1.15}{744}\left(\frac{\sqrt{3}}{6}\left(1-e^{-10Ta}\right)\right)^{-2}$	[86]

Table 3.1: Transition ranges from one atomization regime to another.

Secondary atomization

The previously described process of disintegration (primary atomization) generates a collection of ligaments and droplets that are in continuous movement in a gaseous environment and, therefore, atomization continues to be governed by the same balance of forces explained in preceding paragraphs, giving rise to what is known as secondary atomization or secondary breakup. However, this breaking process is noticeably different owing to the shape of the droplets which tend to be spherical rather than cylindrical jet.

The aerodynamic interactions due to the relative motion between the liquid and the surrounding gas tend to break ligaments and droplets generated in smaller ones. On the other hand, and as an opposite effect, the forces related to surface tension favor the preservation of the original spherical shape of the droplet. The coexistence of these two physical mechanisms requires a high relative fluid velocity to counteract the surface tension effects due to the curvature of the droplets.

In a similar approach to primary atomization, the secondary breakup can also be quantitatively characterized from the dimensionless Weber number (Equation 3.35). It should be noted that in this case the definition is associated with the gas density and the relative velocity between the liquid droplets and the ambient gas (see Equation 3.37).

$$We_g = \frac{\rho_g u_{rel}^2 D_{eff}}{\sigma} \tag{3.37}$$

As with primary atomization, many researchers have also focused on conducting analyses of the different breakage mechanisms in secondary atomization. According to Wierzba [93], Krzeczkowski [94] and Pilch and Erdmann [95], among many others, the secondary breakup can be discretized into five different working regimes represented in Figure 3.17. The first regime to be

distinguished is known as vibrational and is classified for numbers $\mathrm{We_g} < 12$ where the aerodynamic forces are not large enough to break up the droplets and therefore only generate deformations in the shape of the liquid. In this region the particle oscillates with the characteristic frequency of the vortex tail that forms in the wake of the particle and a small increment in the relative velocity may lead to the splitting of the liquid. The next associated regime corresponds to $12 < \mathrm{We_g} < 50$ which is identified by a hollow bag-shaped membrane surrounded by an annular toroid. In this case, the rupture of the droplets starts with a bag-shaped deformation and ends with a fragmentation into numerous small droplets. The third known regime is between $50 < \mathrm{We_g} < 100$ and is called bag-sheet or multimode breakup. It has similar characteristics to the previous one but with the presence of a stamen in the middle of the bag which breaks into relatively large droplets. The next and fourth regime is known as the sheet or particle stripping regime and covers the $100 < \mathrm{We_g} < 350$ ranges. It is distinguished by the detachment of small fragments of the liquid boundary layer at the particle surface due to the continuous erosion to which it is subjected. It should be noted that it usually generates small droplets, although in some cases it creates a nucleus of comparable size to the parent droplet. Finally, the fifth regime is known as catastrophic rupture for $\mathrm{We_g} > 350$. The particle is fragmented by long wavelength amplitudes, creating several particle fragments which are usually undergo stripping.

The limits established between regimes and even the way of referring to each of them may vary according to the author who studies them. Those presented above are defined by Krzeczkowski [94] and Pilch and Erdmann [95] but an example of discrepancy is seen in the work of Arcoumanis et al. [44] or Wierzba [93] as presented in Table 3.2.

Regime	**Krzeczkowski [94]**	**Wierzba [93]**	**Arcoumanis et al. [44]**
Vibrational	$We_g < 12$	$We_g \approx 12$	$12 \leq We_g \leq 18$
Bag	$We_g < 50$	$We_g < 20$	$We_g \leq 45$
Bag-and-stamen	$We_g < 100$	$We_g < 50$	$We_g \leq 350$
Sheet stripping	$We_g < 350$	$We_g < 100$	$We_g \leq 2670$
Catastrophic	$We_g > 350$	$We_g > 100$	$We_g > 2670$

Table 3.2: Transition ranges from one secondary atomization regime to another depending on the author.

Despite all of the above and the many efforts put into the investigation of the different regimes and processes of atomization, there is still much uncertainty about the behavior of the atomization mechanisms at very high particle

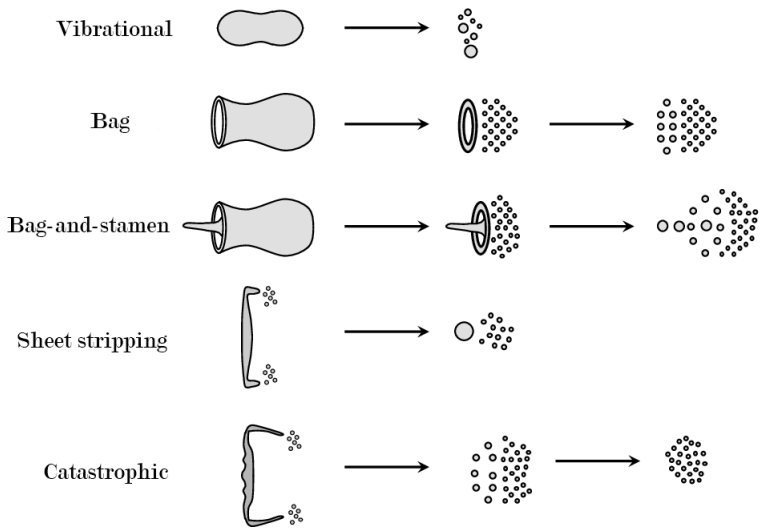

Figure 3.17: Sketch of the five existing regimenes of secondary atomization process. Adapted from [96].

velocities. This is because the higher the velocity at which one operates, the more noticeable the physical mechanisms of aerodynamic interactions, turbulence and viscous effects become, making the phenomena much more challenging to characterize. This suggests that further additional research on this topic is required. In fact, in order to increase knowledge in this field and to try to predict the behavior of the atomization process, many analytical models have been developed for this purpose. Among them, the following can be highlighted: Taylor Analogy Breakup (TAB) model [97], ETAB [98], Droplet Deformation Breakup Model [99], and the Unified Spray Breakup (USB) model [100]. Since this is not the basis of the study, more details about these analytical models can be found in the Ashgriz research [101].

Drop Drag and Deformation

A liquid droplet immersed in a steady stream of air is exposed to variations in spatial location, velocity and penetration, among others, affected by the variation of the air pressure distribution around the droplet. This variation of pressures can be translated into an influence of the acceleration experienced by the droplet, which in turn depends on the drop drag. These changes can also affect the ambient gas surrounding the droplet and in which it is embedded, so this phenomenon has to be considered when studying the atomization process in order to correctly predict the properties and characteristics of both the droplets and the ambient gas.

The equation that predicts the motion of the particle is based on the following expression (Equation 3.38) where gravity has been neglected.

$$\overrightarrow{F_D} = m_p \frac{dU_p}{dt} = m_p \frac{18\mu}{\rho_l D^2} \frac{C_D Re}{24} (U_g - U_p) \tag{3.38}$$

where m_p is total mass of the droplet, U_g corresponds to the ambient gas velocity, U_p reflects the droplet velocity and C_D the drag coefficient which quantified the drop drag.

Based on the assumption of the study of fine aerosols considering spherical droplets, there are numerous drag force coefficient (C_D) models in the literature which are listed in Table 3.3.

Equations of Drag Force Coefficient	**Ref.**
$C_{D,sphere} = \begin{cases} \frac{24}{Re_d}\left(1 + 0.15 Re_d^{2/3}\right), & Re \leq 1000 \\ 0.44, & Re \geq 1000 \end{cases}$	O'Rourke [97]
$C_D = \frac{24}{Re} 10^E$ $E = 0.261 Re^{0.369} - 0.105 Re^{0.431} - \frac{0.124}{1 + (log_{10} Re)^2}$	$Re < 3 \times 10^5$ Khan and Richardson [102]
$C_D = \frac{24}{Re}(1 + 0.173 Re^{0.657}) + \frac{0.413}{1 + 16300 Re^{-1.09}}$	$Re < 2.6 \times 10^5$ Turton and Levenspiel [103]
$C_D = \frac{24}{Re}(1 + 0.1806 Re^{0.6459}) + \frac{0.4251}{1 + 6880.95/Re}$	$Re < 2.6 \times 10^5$ Haider and Levenspiel [104]

Table 3.3: Different equations for calculating the drag force coefficient depending on the author.

Taking as a reference one of the most widespread, the model proposed by O'Rourke [105], the drop drag coefficient for thick sprays and $Re_d \leq 1000$ can be stated as:

$$C_{D,sphere} = \frac{24}{Re_d}\left(\alpha_g^{-2.65} + Re_d^{2/3} \alpha_g^{1.78}/6\right) \tag{3.39}$$

being α_g the local void fraction.

The oscillations and distortion of the droplets during the breakup process can greatly affect the development of the atomization resulting in much higher relative velocities. In these cases, the drag coefficient (C_D) can be expressed and calculated as:

$$C_D = C_{D,sphere}(1 + 2.632y) \tag{3.40}$$

known y and as the drop distortion from sphericity. The drop distortion can be calculated from the spring-mass equation (Equation 3.41) only if the process of atomization has begun.

$$\frac{d^2y}{dt^2} = \frac{2}{3}\frac{\rho_g u_{rel}^2}{\rho_l r^2} - \frac{8\sigma_l}{\rho_l r^3}y - \frac{5\mu_l}{\rho_l^2}\frac{dy}{dt} \tag{3.41}$$

where $\frac{dy}{dt}$ represents the oscillation velocity also known as $\dot{y}$ and $\ddot{y}$ is the rate change with time of $\dot{y}$.

It should be noted that in the limit of no distortion ($y = 0$), the obtained result will be the drag coefficient of a sphere and can be computed from Equation 3.40 whereas at maximum distortion ($y = 1$) the drag coefficient for a disc is derived.

Drop Turbulence Interactions

According to some authors, such as Lefebvre [85], turbulence is one of the primary contributors to atomization. This turbulence phenomenon is normally generated inside the orifices, in which the radial component of the perturbation velocity is confined by the walls. Once the fluid is outside the injector, the liquid is forced to separate from the vein by the action of this fluctuating component, which leads to atomization. The turbulence present in the environment not only favors the formation of droplets but also the interaction between them. This interaction is highly dependent on the properties of the turbulence which are affected by the movement of the particles and the inter-phase transport rates. A significant contribution of the turbulent gaseous kinetic energy is employed to dissipate the spray droplets. Nevertheless, wakes generated by large droplets (i.e. droplets larger than one tenth of the integral turbulent scale) normally act as a source of turbulent energy, leading to an increase in the gaseous turbulent kinetic energy [106]. Consequently, the variation of turbulence values is affected by opposing effects, and the magnitude of these two effects has to be evaluated in detail to determine the final result [107]. From experimental investigations, it was discovered that the rotational motion of the large structures could improve the dispersion of intermediate-sized particles. Such studies also revealed that small droplets tended to follow large-scale vortex structures, while larger droplets abandoned large eddies [106]. The inertia of particles in isotropic turbulence and, then, the significance of these characteristics is quantified by the Stokes number (S_t) under the Equation 3.42 [108].

$$St = \frac{\tau_p}{\tau_\eta} = \frac{\rho_p d^2\sqrt{\epsilon}}{18\nu^{3/2}\rho_f} \tag{3.42}$$

being τ_p the ratio of particle response time and τ_η the turbulence Kolmogorov time scale, ρ_p and ρ_f are the particle and fluid densities, respectively, and d is particle diameter.

The ratio of particle response time can be considered as an indicator of the capacity of a given droplet to react to a change in gas velocity. As a result, the Stokes number makes possible to analyze the effects of large-scale structures on particle dispersion as illustrated in Figure 3.18. Based on the image, it can be appreciated that particles with low Stokes numbers tend to follow the direction and streamlines of the surrounding fluid. On the contrary, particles with high Stokes numbers are driven by their own inertia because the time is not long enough for the large-scale vortices to influence them.

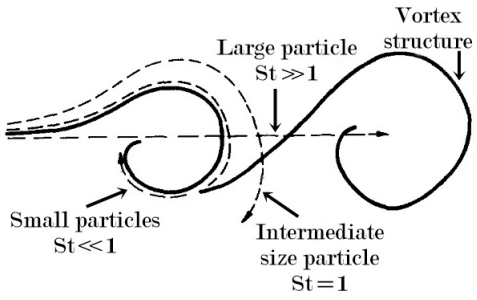

Figure 3.18: Effects of large-scale structures on particle dispersion based on Stokes number. Adapted from [106].

Drop Collision and Coalescence

During the atomization process, at the same time as it takes place, further secondary processes such as coalescence and collision or also known as bouncing of droplets (particle-to-particle interaction) occur. These phenomena significantly modify the spray characteristics in the dense regime. In fact, the literature reports that in cases of low ambient temperatures (non-evaporative aerosols), the droplet size is dependent on the phenomena of droplet breakup and droplet coalescence which compete with each other. The physical phenomenon of coalescence is defined as a process in which two or more droplets come into contact with each other, forming a single droplet. Particle contact and collision depends on the relative velocity between droplets, the droplet direction and the local fuel concentration. For this reason, the collision takes place most frequently in the near field and on the spray axis [109]. The outcome of the collision depends on many factors including the impact energy, the ratio of droplet sizes and environmental conditions such as gas density, gas viscosity and the air-fuel ratio of the gas surrounding the droplets. In addition, the collision frequency can be determined from kinetic theory considerations.

The collision phenomenon depends on four significant dimensionless parameters: the Reynolds number whose definition is based on Equation 3.3 where the diameter is the one of the largest particle being of the form of

Equation 3.43, the Weber number defined according to Equation 3.35 (Equation 3.44), the droplet diameter ratio (Equation 3.45) and the non-dimensional impact parameter B (Equation 3.46) [110].

$$Re_{coll} = \frac{\rho_l d_1 v_{rel}}{\mu_l} \tag{3.43}$$

$$We_{coll} = \frac{\rho_l d_2 v_{rel}^2}{\sigma_l} \tag{3.44}$$

$$\Delta_l = \frac{d2}{d1} \tag{3.45}$$

$$B = \frac{2X}{d_1 + d_2} \tag{3.46}$$

where X is the impact parameter and d_1 and d_2 the diameters of the large and small drops, respectively. The dimensionless parameter B ranges from 0 to 1 being $B = 0$ (head-on collision) the case where the relative velocity overlaps the center-to-center line and $B > 0$ when the collision occurs off-axis (tangential of grazing collision).

Ashgriz and Giv [111] organized the different types of drop collisions into four main categories: bouncing, coalescence, separation, and shattering collisions. In the bouncing collision, the existing gas film causes the contact of the droplet surfaces to be constrained so that the droplets rebound after contact. Coalescence, as mentioned before, makes two droplets to collide and merge each other creating a single particle. Additionally, separation collision can be divided into reflexing separation and stretching separation and refers to the phase in which droplets temporarily merge with later separation to form two or more droplets. Lastly, the shattering collision takes place in the context of high relative velocities resulting in the breakup of the interacting droplets into a group of numerous droplets which are ejected radially. It is also important to note that the number and size of the new droplets generated by the collision are highly influenced by the diameters of the parent droplets.

3.5.2 Evaporation process

Among all the processes that influence engine performance, such as atomization and air-fuel mixing, the evaporation of droplets also has a significant influence on ignition, combustion and thus on the production of pollutants

due to the impact it has on chemical reactions [112]. Droplets with low temperatures absorb the energy available in the combustion chamber due to the processes of convective, conductive and radiation heat transfer. This results in a diffuse and convective mass transfer of fuel vapor from its surface to the gas [113]. Therefore, ambient gas conditions including pressure, temperature and transport properties are closely related to evaporation rates.

Evaporation is a very challenging and multidisciplinary process from the microscopic perspective as it involves several fields of study such as chemical kinetics, fluid dynamics and, above all, heat and mass transport. Arguably, this process is even more difficult under real engine operating conditions, which is why many researchers prefer to approach the study of this particular macroscopically. In addition, for ease of study, the phases involved in the process (liquid and vapor) are usually assumed to be in equilibrium. This is accomplished by presuming that the transition between phases takes place much faster than the transport of vapor from the surface to the surrounding gas. Moreover, it is assumed that even if conditions vary either in the gas phase or in the interior of the droplet, phase equilibrium is always reached immediately. It is important to mention that these assumptions are not entirely correct and care should be taken when applying them [113]. One of the reasons for doubts about reaching the equilibrium phase is under conditions of high injection pressure and ambient properties close to the critical point. At this particular situation, the characteristic time scales of diffusion of both phases (ambient gas and fuel vapor) are similar so that the established quasi-steady surrounding gas assumption cannot be applied; and the thermodynamic properties have to be obtained from the equations of state due to the variability in pressure, temperature and fuel concentration.

Real fuels are made up of a variety of different components that determine and influence the evaporation process (the more volatile and less flammable components evaporate earlier, the higher molecular weight components evaporate later). In order to simplify this behavior and reduce the computational cost involved, the standard approach normally used for research is to employ a single component fuel. In general, tetradecane or dodecane are used to represent the relevant properties of Diesel, and octane for Gasoline, although other surrogate fuels such as ethanol, heptane, hexane and pentane are now being considered for the last mentioned [112].

Nevertheless, despite years of choosing simplicity over accuracy, research is increasingly focusing on the use of complex evaporative models, especially with regard to modeling more realistic component fuels, leaving aside single-component fuels. Gasoline is made up of numerous components so that a

simplified single-component approach does not accurately capture the details of certain sub-processes such as evaporation, combustion or ignition. Jin and Borman [114] investigated the influence of the fuel vapor composition on the overall mixture formation process, and thus also on ignition and combustion, and came to the conclusion that the multi-component character of the fuel could help the accuracy and quality of the above mentioned processes. Tamim and Hallett [115] focused on studying the possibility of using multicomponent fuels based on the behavior of continuous thermodynamics which describes the relevant fuel properties (boiling and critical temperatures, thermal conductivity, heat of evaporation, among others) as a function of a distribution variable. It may happen that the evaporation of the components occurs unevenly so that one evaporates before the other causing the distribution function and thus the properties of the fuel to change as well. This approach, while demanding more modeling effort, assures that the impact of different fuel components on the time-dependent evaporation process is taken into account at a lower computational cost.

3.5.3 Spray characterization

Throughout the document, spray has been described and mentioned from a physical point of view and based on the processes behind its formation. The spray pattern can be characterized from a macroscopic point of view which is based on the parameters that define the overall shape of the jet and from a microscopic perspective which focuses more on local parameters. It can also be said that they differ according to the scale of the studied parameter.

Macroscopic characterization

Macroscopic characterization of the spray provides a better understanding of the behavior of the fluid when interacting with the surrounding ambient gas. The parameters defined below are commonly studied in the literature from both computational and experimental points of view, although mainly from the latter since the determination of these variables is not overly challenging.

Spray penetration

Spray penetration, outlined in yellow in Figure 3.19, is defined as the maximum distance the spray tip reaches inside the combustion chamber. This parameter is one of the most important and characteristic parameters of injection as it not only provides a measure of the air-fuel mixture but also directly influences the wall-impingement phenomenon, which is critical to the correct combustion process and thus to emissions [116]. The definition of this variable is straightforward and easy to understand, but the calculation of it has

its peculiarities. It is important to note that penetration can be divided into liquid penetration and vapor penetration. Under non-evaporative conditions, both measurements will be similar as the liquid remains intact. In contrast, under evaporative conditions, when the liquid enters the combustion chamber it tends to progressively evaporate so that the liquid phase penetrates until it normally reaches a steady state value over time, in other words, it stabilizes, while the vapor phase continues to advance.

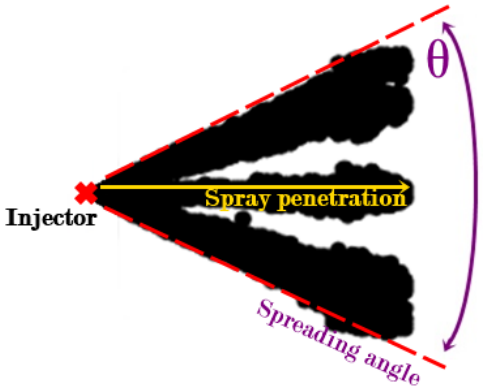

Figure 3.19: Macroscopic description of the spray: penetration and angle.

The knowledge of spray tip penetration is important in design of Diesel and GDI engines. For this reason, over the years, a great deal of research has been carried out in order to obtain certain correlations to predict the behavior of the spray, in terms of penetration, as a function of operating conditions such as injection pressure, ambient density and orifice size, among others. It is commonly noted that spray penetration depends largely on the spray momentum, the ambient density and the spray opening angle. Hay and Jones [117] and Dos Santos and Le Moyne [118] collected in their review papers the most important correlations to date respectively, highlighting the ones presented by Dent [103] and Wakuri et al. [104] as being the most accurate. It is important and curious to mention that despite the constants involved in the expression and other minor details, the calculation of penetration in most of the correlations, even the most recent ones, is expressed as presented in Equation 3.47. The exponents of each of the variables included in this expression are obtained directly from the dimensional analysis except for the one corresponding to the dimensionless component which considers the effect of the spray angle. The value of this exponent is extracted from a detailed study concerning the evolution of the spray where it is assumed that the shape of the spray is conical [46].

$$S(t) \propto \rho_g^{-\frac{1}{4}} \Delta p^{\frac{1}{4}} tan^{-\frac{1}{2}} \left(\frac{\theta}{2}\right) D_o^{\frac{1}{2}} t^{\frac{1}{2}} = \rho_g^{-\frac{1}{4}} \dot{M}^{\frac{1}{4}} tan^{-\frac{1}{2}} \left(\frac{\theta}{2}\right) t^{\frac{1}{2}} \tag{3.47}$$

Despite the importance and relevance of these correlations, they were all obtained using a single-hole Diesel injector and, therefore, cannot be said to

be in agreement with spray behavior in a multi-hole gasoline injector. For this reason, although based on the same premises, researchers in the field of gasoline injection developed new correlations. Zeng et al. [119, 120] focused their work on the characterization of a multi-hole spray by means of a dimensionless analysis. They used the Weber number (Equation 3.35), Reynolds number (Equation 3.3) and air-to-liquid density ratio (ρ_a/ρ_l) to represent the four main forces known to influence the spray. The correlations they obtained from their research are divided into two different groups depending on whether the operating conditions include the presence of flash boiling [120] or, on the contrary, are non-flashing [119]. One of the main limitations of this definition is that it was only intended for a specific injection time. For cases where the operating conditions are non-flashing, the penetration can be defined as a function of Reynolds number from Equations 3.48.

$$\begin{aligned} S = 0.076 \cdot (\rho_a/\rho_l)^{-0.268} \cdot We^{0.318} \cdot Re^{0.152}; \quad \text{if } Re < 12500 \\ S = 0.33 \cdot (\rho_a/\rho_l)^{-0.268} \cdot We^{0.318}; \quad \text{if } Re \geq 12500 \end{aligned} \tag{3.48}$$

On the other hand, for cases where the presence of flash boiling is expected, the penetration expression is dependent on ambient-to-saturation pressure ratio (Pa/Ps) and the air-to-liquid density ratio only, and lack dependence on the fuel type and fuel temperature.

$$\begin{aligned} S = (3.62 + 5.1 \cdot Pa/Ps) \cdot (\rho_a/\rho_l)^{-0.268}; \quad \text{if } 0.3 \leq Pa/Ps < 1 \\ S = (9.2 + 12.45 \cdot Pa/Ps) \cdot (\rho_a/\rho_l)^{-0.268}; \quad \text{if } Pa/Ps < 0.3 \end{aligned} \tag{3.49}$$

Years later, Zhang et al. [121] were motivated by the importance of developing an expression that determined the evolution of the macroscopic penetration parameter as a function of time and added this term to the existing equations. A peculiarity is that, in the same way as in Diesel, they divided the behavior into two parts, separating the initial stage of atomization and the stage where the jet is already atomized.

For the initial stage where $t < t_b$:

$$\begin{aligned} S = 0.022 \cdot (\rho_a/\rho_l)^{-0.142} \cdot We^{0.549} \cdot Re^{0.132} \cdot t; \quad \text{if } Re < 12500 \\ S = 0.072 \cdot (\rho_a/\rho_l)^{-0.142} \cdot We^{0.549} \cdot t; \quad \text{if } Re \geq 12500 \end{aligned} \tag{3.50}$$

Whereas, for $t \geq t_b$:

$$\begin{aligned} S = 0.076 \cdot (\rho_a/\rho_l)^{-0.268} \cdot We^{0.318} \cdot Re^{0.152} \cdot t^{0.638}; \quad \text{if } Re < 12500 \\ S = 0.33 \cdot (\rho_a/\rho_l)^{-0.268} \cdot We^{0.318} \cdot t^{0.638}; \quad \text{if } Re \geq 12500 \end{aligned} \tag{3.51}$$

where t_b is defined as Equation 3.52.

$$t_b = 1.642 \cdot (\rho_a/\rho_l)^{-0.268} \cdot Re^{-0.294} \tag{3.52}$$

Analyzing these expressions, penetration exhibits a dependence of $t^{0.683}$ while the classical Diesel spray penetration equations developed by Hiroyasu and Arai [122] show a dependence of $t^{0.5}$. This means that the gasoline jet is more time-dependent mainly because of the relatively slow atomization process compared to the Diesel spray. The dimensionless correlations in these mentioned works [120, 121] were developed under ambient temperature conditions, and evaporation due to the influence of the ambient gas temperature was not addressed. In addition, all these models were developed in an air environment for non-evaporative conditions and nitrogen (N_2) for evaporative conditions.

Spray angle

Another widely studied variable is the spray spreading angle (θ), which is defined as the angle that encompasses all the jets together and it is usually calculated as the space between the two lateral boundaries of the spray, as shown in Figure 3.19. This parameter is of high importance as it quantifies the air entrainment in the spray, and determines the fuel evaporation and combustion processes. The spray angle has high values in the first moments of the injection, then, after a short time after the start of the injection, the value stabilizes. This phenomenon is predominantly due to the fact that the environment where the fuel is being injected is quiescent prior to injection, putting up resistance to the incoming fluid and therefore increasing the spray angle. In addition, in the first instants of the injection, the liquid tends to occupy the entire volume of the orifice and the counter-bore, if present, which can also cause the spray angle to be larger initially. This effect is mitigated as the needle rises and the injection develops by the existing recirculation of the non-condensable gas into the nozzle.

In addition to developing correlations for spray tip penetration, Zhang et al. [121] presented expressions for defining the spray angle. As above, the spray angle is expressed as a function of Reynolds number and density ratio, as presented in Equation 3.53. The spray angle tends to stabilize and remain constant during most of the injection, so the authors considered this expression to be adequate to characterize the evolution of the spray angle as a function of time.

$$\begin{aligned} \theta &= A \cdot (\rho_a/\rho_l)^x \cdot We^{0.46} \cdot Re^{0.1}; \quad \text{if } Re < 12500 \text{ and } \rho_a/\rho_l \geq 0.002 \\ \theta &= B \cdot (\rho_a/\rho_l)^x \cdot We^{0.46}; \quad \text{if } Re \geq 12500 \text{ and } \rho_a/\rho_l \geq 0.002 \end{aligned} \tag{3.53}$$

Under standard conditions, the spray-plume angle increases with increasing air-to-liquid density ratio, thus assuming the constants appearing in Equation 3.53 to be the following values: A = 0.12, B = 0.0273 and x = 0.287. However, for vacuum conditions, a variation is required to account the opposite behavior, which means the increase of the spray column angle with decreasing air-to-liquid density ratio. Therefore, the values of the constants A and B are modified by taking the respective values of A = 0.002 and B = 0.0046. In addition, the exponent associated with the density ratio changes its sign and value being, consequently, x = -0.38.

Microscopic characterization

The microscopic characterization of the jet is concerned with what happens inside the spray boundaries. In recent years, the interest in the measurement of microscopic parameters has been driven by the need to help develop and validate spray models, especially for implementation in computational fluid mechanics (CFD). Unfortunately, the experimental techniques for the measurement of these parameters are very challenged and often have large uncertainties, as the time scales are very short, the spray has a high droplet density and the temperatures and pressures are critical. Even so, the results are usually presented in mean values because they have a lot of spatial and temporal variability.

Droplet size

Understanding the atomization process and the momentum transfer between the droplet and the environment can be done by measuring droplet size as it is an indication of whether this process is taking place properly or not. The actual droplet size provides a lot of information as the droplets have different sizes during the atomization process. These droplets, as they travel through the combustion chamber, become smaller and smaller due to the presence of the evaporation effect, which can take place even at ambient temperature. The difference in droplet size and the change in droplet dimensions over time means that droplet diameter cannot be treated as a deterministic measure and statistical approaches are needed to study and contextualize it. Therefore, the characterization of this parameter is usually carried out on the basis of histograms, which imply a discretization/mapping of the spray in both time and space. This type of study gives rise to what is known as a Probability Density Function (PDF), although it generally does not provide any relevant insights, apart from the non-uniformity of the spray. However, this characterization, although interesting, involves many assumptions and it requires complex outcomes and assessments, and is therefore only intended for very particular studies. The quality of atomization can be defined on the

basis of the characteristic diameter, which is a solution commonly adopted by the scientific community for its simplicity. This variable can be defined in several ways, so Mugele and Evans [123] have collected in their work the most commonly used expressions to date, presented in Table 3.4.

Notation	Factor	Pyshical meaning	Formulation
D_{10}	Diameter	Mean geometrical diameter	$\frac{\sum_i N_i D_i}{\sum_i N_i}$
D_{20}	Surface	Mean surface area	$\left(\frac{\sum_i N_i D_i^2}{\sum_i N_i}\right)^{\frac{1}{2}}$
D_{30}	Volume	Mean volume/mass	$\left(\frac{\sum_i N_i D_i^3}{\sum_i N_i}\right)^{\frac{1}{3}}$
D_{32}	Vol. / Surf.	Volume/Surface ratio	$\frac{\sum_i N_i D_i^3}{\sum_i N_i D_i^2}$

Table 3.4: Different definitions of the mean droplet diameter.

Despite all the definitions presented in Table 3.4, the most common expressions are the arithmetic diameter (D_{10}) and the SMD or D_{32}. The latter is known to be a direct representative of the relationship between drag forces (related to the droplet surface) and inertia forces (related to the droplet mass). One of its advantages is the direct acquisition of the value using experimental visualization techniques, such as Planar Laser Induced Fluorescence (PLIF) [123] and its derived techniques [124], which are based on a fluorescence signal, proportional to the volume of the droplet and relate it to the scattering signal, which is a function of the surface area of the droplet. Another commonly used technique for the determination of droplet size is the PDPA which not only allows to determine the droplet size but also the droplet velocity. Although the PDPA is more precise than the PLIF methods, it has the significant drawback of being a punctual measurement, which considerably increases the time required for testing.

Velocity distribution

The characterization of the spray velocity field enables the evaluation and comprehension of the air-fuel mixing process in addition to further understanding of the interaction mechanisms on GDI engines. For this reason, it is a parameter widely studied in the literature. Experimentally, there are numerous techniques for measuring velocity distribution. Angarita-Jaimes et al. [124] were the first to perform 3-component velocity measurements in a 2-phase system to quantify the interaction between the phases. For this

purpose, they used a single 3CCD color camera as a means of making simultaneous multi-constituent and multi-phase velocimetry measurements when combined with fluorescent tracers. Prosperi et al. [125] employed Particle Image Velocimetry with Fluorescent tracers (F-PIV) to allow measurements in the close vicinity of the spray-angle and obtain instantaneous velocity fields. Another commonly used technique is the PDPA which determines the velocity field; when it is intended only for particle velocity measurement it is referred to as LDV.

3.5.4 Spray collapse

Previous sections have discussed phenomena that occur during the injection process such as cavitation or flash boiling, among others. This section focuses on the phenomenon of spray collapse which is associated with the external flow phase as it takes place when the jet is developing or fully developed in the combustion chamber. The mentioned phenomenon can be defined as the interplay between spray plumes in multi-hole injectors which causes collapsed sprays to be misdirected and uncontrollable, and inhibits the mixing and evaporation processes. Spray collapse is an undesirable event because of the consequences it has on engine operation, such as promotion the developement of the spray which increases the penetration and therefore can lead to the impact of the droplets on the valves and the walls of the combustion chamber and the piston head, among others. Impingement of droplets on the walls of the chamber or the crown of the piston results in increased soot formation and aggravates particulate emissions [126].

Much research has been done in recent years to understand the phenomenon of spray collapse, both qualitatively and qualitatively. The findings indicate that spray collapse results from a combination of the nozzle geometry, the thermodynamic conditions of the fuel, and the ambient pressure. Spray collapse was detected in injectors with a narrow arrangement of the nozzle holes under extreme flash-boiling conditions with very low ambient or sub-atmospheric pressures under part-load operation and in cases of non-flash-boiling conditions with very high ambient pressures [83]. In addition to the above, fuel volatility is known to be a very influential and determining factor in spray behaviour [127].

Sphicas et al. [128] in their studies on the aerodynamics in an eight-hole GDI injector, states that an increase in momentum transfer between the ambient gas and the fuel results in the interaction between the plume and the spray, which subsequently leads to the collapse of the jet. The spray collapse phenomenon can be quantified from the existing collapse length. Figure 3.20

shows the spray collapse definition for a six-hole injector with two clearly differentiated zones: the collapsed region and the non-collapsed region. The collapse region is usually close to the injector tip and it obvious interaction is noticed between adjacent fuel plumes, whereas as the distance from the tip of the injector increases, gaps appear between the jets, so this is the non-collapse region.

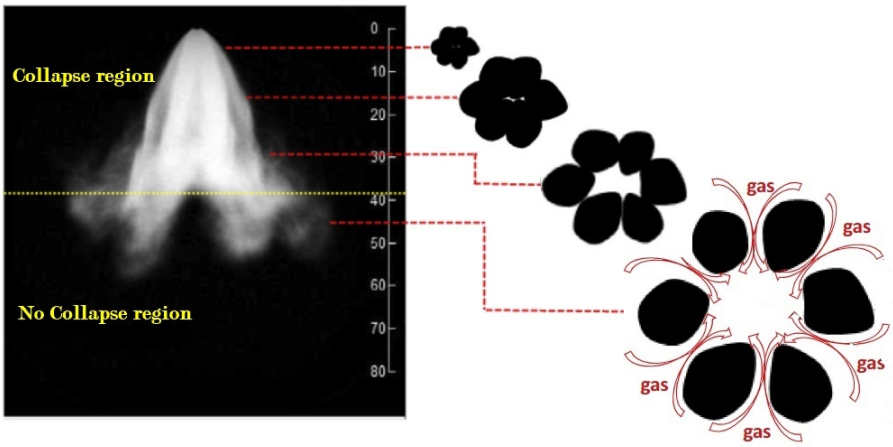

Figure 3.20: Schematic spray structure of the spray collapse phenomenon. Adapted from [129].

The collapse characteristics as well as the spray structure in the collapsed and non-collapsed regions are highly influenced by the air movements between the jets. Figure 3.20 represents such air movements in both regions, collapsed on the upper part and non-collapsed on the bottom right side. As the injection progresses in time and space, the ambient gas tends to move to the central zone of the spray. This causes the pressure inside the spray to be equal or similar to the ambient pressure, which results in the jet moving in the direction defined by the injector nozzle. In the case of spray collapse, the air cannot circulate around the jets as in the previous case because the sprays are in contact with each other and therefore no air can be transferred from the outside to the closed central region. This phenomenon causes a reduction in pressure in the center of the sprays as they develops downwards. The pressure difference between the central region of the jet and the ambient gas is the main reason why the sprays tend to collapse in the central region and also explains the reason for the spray collapse length to increase as the injection time elapses.

The injector geometry has a significant impact on spray collapse. Wu et al. [129] and Manin et al. [130] demonstrated in their work the influence

of nozzle geometry, aspect ratio and number of orifices on plume interaction under subcooling and superheated conditions. Li et al. [131] and Aori et al. [132] reached the same conclusions in the studies carried out based on injectors with different geometries under different injection pressures and ambient conditions. Lacey et al. [133] investigated the generalization of the behavior of multi-hole GDI fuel injectors in boiling conditions by relating the spray collapse to the distance between the farthest holes, the offset angle and the thermodynamic state of the fuel. According to Wu et al. [129], two factors govern the collapse characteristics of the spray: the injector cone angle and the degree of superheat. A larger injector cone angle results in faster separation of the fuel plumes, but a higher superheat conditions facilitates the connection of adjacent fuel plumes. The spray collapse length is driven by the competition effect between these two factors. Under transitional boiling conditions, it was observed that although the spray collapsed to the centerline within the collapse region, the fuel plumes separated again near the spray tip area; this is mainly due to the fact that, under these particular conditions, the effect of nozzle orientation on spray separation and direction is stronger than the effect of fuel flash boiling. However, under flare boiling conditions, the fuel plumes expanded further, filling the space between adjacent plumes even near the spray tip region.

Regarding the operating conditions and as mentioned above, the spray collapse phenomenon can take place under both flash boiling and non-flashing conditions. Guo et al. [134] reported two types of spray collapse for different operating conditions, both related to radial expansion. At high ambient pressure, the collapse of the jets tends to occur in the near field while under flash boiling conditions they occur in the far field. The collapse of the jets at high ambient pressures is attributed to the low pressures around the high speed jet whereas the collapse at flash boiling conditions is due to the low pressure resulting from the drop in temperature and the consequent condensation of vapor.

The investigation of plume interaction is complex but necessary for a better understanding of the intricate collapse process. Therefore, numerous experimental techniques are used to understand it. A number of experimental researchers have used the side view and volume illumination to study jet collapse (back-light imaging) [69, 134], Mie-scattering [135] or Schlieren [136]. These techniques have the benefit of capturing transient spray behavior, as well as cone angle or spray width, and provide direct information on whether or not the collapse of the spray occurs. In contrast, the overlapping of the plumes is unavoidable and is not possible to illuminate the internal structure of the spray and prove the interaction between the sprays. The front view

(ahead of the spray cone) becomes an attractive option to observe the transition from segregated to collapsed plumes, without the problem of overlaping between sprays mentioned above [137]. Finally, some works use a laser sheet illumination [120], applied to provide a cross-sectional view of the spray (either through the central plane showing the internal structure of the spray or perpendicular to the injector axis showing the cross-section of the plumes at a fixed distance from the nozzle).

References

[1] Statement, C. P. "Rail Pressure Control of Common Rail System for Gasoline Direct Injection Engines". In: 1 (2017), pp. 1–5.

[2] Lehnert, B. et al. "GDI Sprays with up to 200 MPa Fuel Pressure and Comparison of Diesel-like and Gasoline-Like Injector Designs". In: *SAE Technical Papers* 2020 (2020), pp. 1–11. DOI: 10.4271/2020-01-2104.

[3] Johansson, A. N. et al. "Reduction of Soot Formation in an Optical Single-Cylinder Gasoline Direct-Injected Engine Operated in Stratified Mode Using 350 Bar Fuel Injection Pressure, Dual-Coil and High-Frequency Ignition Systems". In: *SAE International Journal of Engines* 10.3 (2017). DOI: 10.4271/2017-01-9278.

[4] Piock, W. F. et al. "Fuel Pressure and Charge Motion Effects on GDi Engine Particulate Emissions". In: *SAE International Journal of Engines* 8.2 (2015), pp. 464–473. DOI: 10.4271/2015-01-0746.

[5] Peer, J. et al. "Development of a High Turbulence, Low Particle Number, High Injection Pressure Gasoline Direct Injection Combustion System". In: *SAE International Journal of Engines* 9.4 (2016), pp. 2301–2311. DOI: 10.4271/2016-01-9046.

[6] Hoffmann, G. et al. "Fuel System Pressure Increase for Enhanced Performance of GDi Multi-Hole Injection Systems". In: *SAE Technical Paper 2014-01-1209* (2014). DOI: 10.4271/2014-01-1209.

[7] Piock, W. et al. "Delphi Technologies Next Generation GDi-System - improved Emissions and Efficiency with higher Pressure". In: *Internationales Wiener Motorensymposium*. 2019, pp. 1–21.

[8] Postrioti, L. et al. "Experimental and Numerical Analysis of Spray Evolution, Hydraulics and Atomization for a 60 MPa Injection Pressure GDI System". In: *SAE Technical Papers* 2018-April (2018), pp. 1–17. DOI: 10.4271/2018-01-0271.

[9] Husted, H. et al. "The effects of GDi fuel pressure on fuel economy". In: *SAE Technical Papers* 1 (2014). DOI: 10.4271/2014-01-1438.

[10] Hentschel, W. et al. "Investigation of spray formation of di gasoline hollow-cone injectors inside a pressure chamber and a glass ring engine by multiple optical techniques". In: *SAE Technical Papers* 724 (1999). DOI: 10.4271/1999-01-3660.

[11] Zhao, H. *Overview of gasoline direct injection engines*. Di. Woodhead Publishing Limited, 2020, pp. 1–19. DOI: 10.1533/9781845697327.1.

[12] Kanda, M. et al. "Application of a new combustion concept to direct injection gasoline engine". In: *SAE Technical Papers* 2000.724 (2000). DOI: 10.4271/2000-01-0531.

[13] Motjabi, M. "Optical Analysis of Multi-Stream GDI Sprays under Various Engine Operating Conditions". In: (2011), pp. 1–331.

[14] Martí-Aldaraví, P. "Development of a computational model for a simultaneous simulation of internal flow and spray break-up of the Diesel injection process". PhD thesis. Valencia: Universitat Politècnica de València, 2014. DOI: 10.4995/Thesis/10251/43719.

[15] Bosh. *Bosch Premium Fuel Injectors*.

[16] Caika, V. et al. "Integrated 1D/2D/3D Simulation of Fuel Injection and Nozzle Cavitation". In: *SAE International Journal of Engines* 6.3 (2013), pp. 1544–1552. DOI: 10.4271/2013-24-0006.

[17] Dahlander, P. et al. "Measurements of Time-Resolved Mass Injection Rates for a Multi-Hole and an Outward Opening Piezo GDI Injector". In: *SAE Technical Paper 2015-01-0929* (2015). DOI: 10.4271/2015-01-0929.Copyright.

[18] Vent, G. et al. "The new 2.0 l turbo engine from the Mercedes-Benz 4-cylinder engine family". In: *2nd Aachen Colloquium China* (2012), pp. 137–160.

[19] Smith, J. et al. "A Comparison of Spray-Guided Stratified-Charge Combustion Performance with Outwardly-Opening Piezo and Multi-Hole Solenoid Injectors". In: *SAE International Journal of Engines* 4.1 (2011), pp. 1481–1497. DOI: 10.4271/2011-01-1217.

[20] Gimeno, J. "Desarrollo y aplicación de la medida de flujo de cantidad de movimiento de un chorro Diesel". PhD thesis. E.T.S. Ingenieros Industriales, Universitat Politècnica de València, 2008. DOI: 10.4995/Thesis/10251/8306.

[21] Colebrook, C. F. "Turbulent Flow in Pipes, With Particular Reference To the Transition Region Between the Smooth and Rough Pipe Laws." In: *Journal of the Institution of Civil Engineers* 12.8 (1939), pp. 393–422. DOI: 10.1680/ijoti.1939.14509.

[22] Salvador, F. J. et al. "Complete modelling of a piezo actuator last-generation injector for diesel injection systems". In: *International Journal of Engine Research* 15.1 (2014), pp. 3–19. DOI: 10.1177/1468087412455373.

[23] Payri, R. et al. "Virtual injection modelling for ECN Spray G". In: *ICLASS 2018*. Chicago, 2018, pp. 1–8.

[24] Vaquerizo, D. "Study on Advanced Spray-Guided Gasoline Direct Injection Systems". PhD thesis. Universitat Politècnica de València, 2017. DOI: 10.4995/Thesis/10251/99568.

[25] Saha, K. et al. "Numerical Investigation of Two-Phase Flow Evolution of In- and Near-Nozzle Regions of a Gasoline Direct Injection Engine During Needle Transients". In: *SAE International Journal of Engines* 9.2 (2016), pp. 1230–1240. DOI: 10.4271/2016-01-0870.

[26] Mouvanal, S. et al. "Numerical study of purging of a gasoline direct injection nozzle at the end of injection". In: *International Journal of Engine Research* 22.5 (2021), pp. 1670–1684. DOI: 10.1177/1468087420916658.

[27] Duke, D. J. et al. "Internal and near nozzle measurements of Engine Combustion Network "Spray G" gasoline direct injectors". In: *Experimental Thermal and Fluid Science* 88 (2017), pp. 608–621. DOI: 10.1016/j.expthermflusci.2017.07.015.

[28] Gramlich, R. et al. "Air Entrainment and Momentum Distribution in the Near Field of Diesel Sprays from Group Hole Nozzles". In: *ILASS Europe 2016, 27th Annual Conference on Liquid Atomization and Spray Systems* September (2016), pp. 4–7. DOI: 10.13140/RG.2.2.10584.90883.

[29] Lindström, M. "Injector Nozzle Hole Parameters and their Influence on Real DI Diesel Performance". In: (2009), pp. 1–45.

[30] Li, X. et al. "Sensitivity analysis of fuel injection characteristics of GDI injector to injector nozzle diameter". In: *Energies* 12.3 (2019). DOI: 10.3390/en12030434.

[31] Tu, P. W. et al. "Numerical Investigation of GDI Injector Nozzle Geometry on Spray Characteristics". In: *SAE Technical Papers* 2015-Septe.September (2015). DOI: 10.4271/2015-01-1906.

[32] Jiang, C. et al. "Impact of gasoline direct injection fuel injector hole geometry on spray characteristics under flash boiling and ambient conditions". In: *Fuel* 241 (2019), pp. 71–82. DOI: 10.1016/j.fuel.2018.11.143.

[33] Moon, S. et al. "Ultrafast X-ray study of multi-hole GDI injector sprays: Effects of nozzle hole length and number on initial spray formation". In: *Experimental Thermal and Fluid Science* 68 (2015), pp. 68–81. DOI: 10.1016/j.expthermflusci.2015.03.027.

[34] Macian, V. et al. "New technique for determination of internal geometry of a Diesel nozzle with the use of silicone methodology". In: *Experimental Techniques* 27.2 (2003), pp. 39–43. DOI: 10.1111/j.1747-1567.2003.tb00107.x.

[35] Jiang, C. et al. "Impact of gasoline direct injection fuel injector hole geometry on spray characteristics under flash boiling and ambient conditions". In: *Fuel* 241.November 2018 (2019), pp. 71–82. DOI: 10.1016/j.fuel.2018.11.143.

[36] Fischer, A. et al. "Methodology and Tools to Predict GDI Injector Tip Wetting as Predecessor of Tip Sooting". In: *SAE Technical Papers* 2018-April (2018), pp. 1–10. DOI: 10.4271/2018-01-0286.

[37] Anderson, J. D. J. *Fundamentals of Aerodynamcis*. Fifth edit. Vol. 1. 2015.

[38] Salvador, F. J. et al. "Study of the influence of the needle lift on the internal flow and cavitation phenomenon in diesel injector nozzles by CFD using RANS methods". In: *Energy Conversion and Management* 66 (2013), pp. 246–256. DOI: 10.1016/j.enconman.2012.10.011.

[39] Schlichting, H. *Boundary-Layer Theory*. McGraw-Hill, 1978.

[40] Gravensen, P. et al. "Microfluidics - A review". In: *Journal of Micromechanics and Microengineering* 3.4 (1993), pp. 168–182. DOI: 10.1088/0960-1317/3/4/002.

[41] Abd, H. M. et al. "Effects of varying orifice diameter and Reynolds number on discharge coefficient and wall pressure". In: *Flow Measurement and Instrumentation* 65.November 2018 (2019), pp. 219–226. DOI: 10.1016/j.flowmeasinst.2019.01.004.

[42] Kent, J. C. et al. "Nozzle Exit Flow Characteristics for Square-edged and Rounded Inlet Geometries". In: *Combustion Science and Technology* 30.1-6 (1983), pp. 121–132. DOI: 10.1080/00102208308923615.

[43] Hobbs, J. M. et al. "The effect of orifice plate geometry upon discharge coefficient". In: *Flow Measurement and Instrumentation* 1.3 (1990), pp. 133–140. DOI: 10.1016/0955-5986(90)90002-0.

[44] Arcoumanis, C. et al. "Effect of fuel injection processes on the structure of diesel sprays". In: *SAE Technical Papers* 41 2 (1997). DOI: 10.4271/970799.

[45] Salvador, F. J. "Estudio teórico experimental de la influencia de la geometría de toberas de inyección Diésel sobre las características del flujo interno y del chorro". PhD thesis. Valencia: E.T.S. Ingenieros Industriales. Universidad Politécnica de Valencia, 2003.

[46] Naber, J. D. et al. "Effects of Gas Density and Vaporization on Penetration and Dispersion of Diesel Sprays". In: *SAE Paper 960034*. Vol. 105. 412. Society of Automotive Engineers, Inc., Warrendale, Pennsylvania, USA, 1996, pp. 82–111. DOI: 10.4271/960034.

[47] Mamaikin, D. et al. "Experimental investigation of flow field and string cavitation inside a transparent real-size GDI nozzle". In: *Experiments in Fluids* 61.7 (2020), pp. 1–15. DOI: 10.1007/s00348-020-02982-y.

[48] Moon, S. et al. "High-speed X-ray imaging of in-nozzle cavitation and emerging jet flow of multi-hole GDI injector under practical operating conditions". In: *ICLASS 2015 - 13th International Conference on Liquid Atomization and Spray Systems* December (2015).

[49] Mamaikin, D. et al. "The effect of transient needle lift on the internal flow and near-nozzle spray characteristics for modern GDI systems investigated by high-speed X-ray imaging". In: *International Journal of Engine Research* (2021). DOI: 10.1177/1468087420986751.

[50] Bergwerk, W. "Flow Pattern in Diesel Nozzle Spray Holes". In: *Proceedings of the Institution of Mechanical Engineers* 173.25 (1959). DOI: 10.1243/PIME.

[51] Chaves, H. et al. "Experimental study of cavitation in the nozzle hole of diesel injectors using transparent nozzles". In: *SAE Technical Papers* 412 (1995). DOI: 10.4271/950290.

[52] De la Morena, J. "Estudio de la influencia de las características del flujo interno en toberas sobre el proceso de inyección Diesel en campo próximo". PhD thesis. Universtitat Politècnica de València, 2011. DOI: 10.4995/Thesis/10251/11098.

[53] Hiroyasu, H. et al. "Break-up length of a liquid jet and internal flow in a nozzle". In: *ICLASS-91, Gaithersburg, Maryland, July.* 1991.

[54] Soteriou, C. et al. "Direct injection diesel sprays and the effect of cavitation and hydraulic flip on atomization". In: *SAE Technical Papers* 412 (1995). DOI: 10.4271/950080.

[55] Bode, J. et al. "Fuel spray in Diesel engines. Part I: Spray formation". In: *ATA 92A065* (1992).

[56] Arcoumanis, C. et al. "Cavitation in real-size multi-hole diesel injector nozzles". In: *SAE Technical Papers* 724 (2000). DOI: 10.4271/2000-01-1249.

[57] Gilles-Birth, I. et al. "A study of the in-nozzle flow characteristic of valve covered orifice nozzles for gasoline direct injection". In: *SAE Technical Papers* 724 (2005). DOI: 10.4271/2005-01-3684.

[58] Spikes, R. H. et al. "Discharge coefficient of small submerged orifices". In: *Proceedings of the Institution of Mechanical Engineers* 173.1 (1959), pp. 661–674.

[59] Nurick, W. H. "Orifice cavitation and its effects on spray mixing". In: *Journal of Fluids Engineering* 98 (1976), pp. 681–687.

[60] Payri, R. et al. "Using spray momentum flux measurements to understand the influence of diesel nozzle geometry on spray characteristics". In: *Fuel* 84.5 (2005), pp. 551–561. DOI: 10.1016/j.fuel.2004.10.009.

[61] Suh, H. K. et al. "Effect of cavitation in nozzle orifice on the diesel fuel atomization characteristics". In: *International Journal of Heat and Fluid Flow* 29.4 (2008), pp. 1001–1009. DOI: 10.1016/j.ijheatfluidflow.2008.03.014.

[62] Winklhofer, E. et al. "Comprehensive hydraulic and flow field documentation in model throttle experiments under cavitation conditions". In: *Proceedings of the ILASS-Europe Conference, Zurich* August (2001), pp. 574–579. DOI: 10.13140/2.1.1716.4161.

[63] Oza, R. D. "On the Mechanism of Flashing Injection of Initially Subcooled Fuels". In: *ASME* 1.March 1984 (2016).

[64] Blander, M. et al. "Bubble nucleation in liquids". In: *AIChE Journal* 21.5 (1975), pp. 833–848. DOI: 10.1002/aic.690210502.

[65] Shields, B. et al. "Cavitation as Rapid Flash Boiling". In: *ILASS-Americas 23rd Annual Conference on Liquid Atomization and Spray Systems, Ventura, CA, May 2011 Cavitation*. May. 2011.

[66] Bar-Kohany, T. et al. "State of the art review of flash-boiling atomization". In: *Atomization and Sprays* 26.12 (2016), pp. 1259–1305. DOI: 10.1615/AtomizSpr.2016015626.

[67] Lin, T. C. et al. "Effects of superheat on characteristics of flashing spray and snow particles produced by expanding liquid carbon dioxide". In: *Journal of Aerosol Science* 61 (2013), pp. 27–35. DOI: 10.1016/j.jaerosci.2013.03.005.

[68] Cleary, V. et al. "Flashing liquid jets and two-phase droplet dispersion. I. Experiments for derivation of droplet atomisation correlations". In: *Journal of Hazardous Materials* 142.3 (2007), pp. 786–796. DOI: 10.1016/j.jhazmat.2006.06.125.

[69] Guo, H. et al. "Characterizing external flashing jet from single-hole GDI injector". In: *International Journal of Heat and Mass Transfer* 121 (2018), pp. 924–932. DOI: 10.1016/j.ijheatmasstransfer.2018.01.042.

[70] Plesset, M. et al. "Bubble Dynamics and Cavitation". In: (1974), p. 1974.

[71] Zanje, S. et al. "Development of generalized bubble growth model for cavitation and flash boiling". In: *Physics of Fluids* 33.7 (2021), pp. 1–15. DOI: 10.1063/5.0055744.

[72] Franc, J.-P. "The Rayleigh-Plesset equation: a simple and powerful tool to understand various aspects of cavitation". In: *Fluid Dynamics of Cavitation and Cavitating Turbopumps*. Vol. 496. Vienna: Springer, 2007, pp. 1–41. DOI: 10.1007/978-3-211-76669-9_1.

[73] Scriven, L. E. "Dynamics of a fluid interface Equation of motion for Newtonian surface fluids". In: *Chemical Engineering Science* 12.2 (1960), pp. 98–108. DOI: 10.1016/0009-2509(60)87003-0.

[74] Stralen van, S. J. D. et al. *Boiling phenomena : physicochemical and engineering fundamentals and applications*. Hemisphere, 1979.

[75] Suma, S. et al. "Internal boiling atomization by rapid pressure reduction of liquids". In: *Transactions of the Japanese Society of Mechanical Engineers* 43 (1977), pp. 4608–4617.

[76] Kawano, D. et al. "Numerical study on flash-boiling spray of multicomponent fuel". In: *Heat Transfer - Asian Research* 35.5 (2006), pp. 369–385. DOI: 10.1002/htj.20117.

[77] Mojtabi, M. et al. "The effect of flash boiling on break up and atomization in GDI sprays". In: *22nd European Conference on Liquid Atomization and Spray Systems* (2008), pp. 8–10.

[78] Senda, J. et al. "Improvement of combustion and emissions in diesel engines by means of enhanced mixture formation based on flash boiling of mixed fuel". In: *International Journal of Engine Research* 9.1 (2008), pp. 15–27. DOI: 10.1243/14680874JER02007.

[79] Dahlander, P. et al. "High-speed photography and Phase Doppler Anemometry measurements of flash-boiling multi-hole injector sprays for spray-guided gasoline direct injection". In: *10th International Conference on Liquid Atomization and Spray Systems, ICLASS 2006* (2006).

[80] He, X. et al. "Characteristics of spray and wall wetting under flash-boiling and non-flashing conditions at varying ambient pressures". In: *Fuel* 264 (2020). DOI: 10.1016/j.fuel.2019.116683.

[81] Berrocal, E. et al. "Two-photon fluorescence laser sheet imaging for high contrast visualization of atomizing sprays". In: *OSA Continuum* 2.3 (2019), p. 983. DOI: 10.1364/osac.2.000983.

[82] Rahm, M. et al. "Evaluation of optical arrangements for ballistic imaging in sprays". In: *Optics Express* 23.17 (2015), p. 22444. DOI: 10.1364/oe.23.022444.

[83] Payri, R. et al. "ECN Spray G external spray visualization and spray collapse description through penetration and morphology analysis". In: *Applied Thermal Engineering* 112 (2017), pp. 304–316. DOI: 10.1016/j.applthermaleng.2016.10.023.

[84] Birouk, M. et al. "Liquid jet breakup in quiescent atmosphere: a review". In: 19.6 (2009), pp. 501–528.

[85] Lefebvre, A. H. et al. *Atomization and Sprays*. 2nd Ed. Boca Raton, FL: CRC Press, 2017.

[86] Reitz, R. "Atomization and other breakup regimes of a liquid jet". In: 1978.

[87] Reitz, R. D. et al. "Mechanism of atomization of a liquid jet". In: *Physics of Fluids* 25.10 (1982), pp. 1730–1742. DOI: 10.1063/1.863650.

[88] Payri, R. et al. "Analysis of diesel spray atomization by means of a near-nozzle field visualization technique". In: *Atomization and Sprays* 21.9 (2011), pp. 753–774. DOI: 10.1615/AtomizSpr.2012004051.

[89] Bormashenko, E. "Generalization of the Buckingham Pi- Theorem". In: June (2016).

[90] Ranz, W. E. "Some experiments on orifice sprays". In: *Can. J. Chem. Engng, August* (1958), p. 175.

[91] Sterling, A. M. et al. "The instability of capillary jets". In: *Journal of Fluid Mechanics* 68.3 (1975), pp. 477–495. DOI: 10.1017/S0022112075001772.

[92] Miesse, C. C. "Correlation of Experimental Data on the Disintegration of Liquid Jets". In: *Industrial & Engineering Chemistry* 47.9 (1955), pp. 1690–1701. DOI: 10.1021/ie50549a013.

[93] Wierzba, A. "Deformation and breakup of liquid drops in a gas stream at nearly critical Weber numbers". In: *Experiments in Fluids* 9.1-2 (1990), pp. 59–64. DOI: 10.1007/BF00575336.

[94] Krzeczkowski, S. A. "Measurement of liquid droplet disintegration mechanisms". In: *International Journal of Multiphase Flow* 6.3 (1980), pp. 227–239. DOI: 10.1016/0301-9322(80)90013-0.

[95] Pilch, M. et al. "Use of breakup time data and velocity history data to predict the maximum size of stable fragments for acceleration-induced breakup of a liquid drop". In: *International Journal of Multiphase Flow* 13.6 (1987), pp. 741–757. DOI: https://doi.org/10.1016/0301-9322(87)90063-2.

[96] Kulkarni, V. et al. "Secondary atomization of newtonian liquids in the bag breakup regime: Comparison of model predictions to experimental data". In: *ICLASS 2012 - 12th International Conference on Liquid Atomization and Spray Systems* (2012), pp. 1–8.

[97] O'Rourke, P. J. et al. "The Tab Method for Numerical Calculation of Spray Droplet Breakup International Fuels and Lubricants Meeting and Exposition Toronto, Ontario". In: *SAE Technical Paper Series* 872089 (2018), pp. 2–10.

[98] Tanner, F. X. "Liquid jet atomization and droplet breakup modeling of non-evaporating diesel fuel sprays". In: *SAE Technical Papers* 412 (1997). DOI: 10.4271/970050.

[99] Ibrahim, E. A. et al. "Modeling of spray droplets deformation and breakup". In: *Journal of Propulsion and Power* 9.4 (1993), pp. 651–654. DOI: 10.2514/3.23672.

[100] Chryssakis, C. et al. "A unified fuel spray breakup model for internal combustion engine applications". In: *Atomization and Sprays* 18.5 (2008), pp. 375–426. DOI: 10.1615/atomizspr.v18.i5.10.

[101] Ashgriz, N. *Handbook of atomization and sprays: theory and applications*. Springer Science & Business Media, 2011.

[102] Khan, A. R. et al. "The Resistance to Motion of a Solid Sphere in a Fluid". In: *Chemical Engineering Communications* 62.1-6 (1987), pp. 135–150. DOI: 10.1080/00986448708912056.

[103] Turton, R. et al. "A short note on the drag correlation for spheres". In: *Powder Technology* 47.1 (1986), pp. 83–86. DOI: 10.1016/0032-5910(86)80012-2.

[104] Haider, A. et al. "Drag Coefficient and Terminal Velocity of Spherical and Nonspherical Particles". In: *Powder Technology* 58 (1989), pp. 63–70. DOI: 10.1021/ie50688a011.

[105] O'Rourke, P. J. "Collective Drop Effects on Vaporizing Liquid Sprays". PhD thesis. Princeton University, 1981.

[106] Crowe, C. T. et al. "Particle mixing in free shear flows". In: *Progress in Energy and Combustion Science* 14.3 (1988), pp. 171–194. DOI: 10.1016/0360-1285(88)90008-1.

[107] Yuan, Z. et al. "Turbulence modulation in particulate flows-A theoretical approach". In: *International Journal of Multiphase Flow* 18.5 (1992), pp. 779–785. DOI: 10.1016/0301-9322(92)90045-I.

[108] Dou, Z. et al. "Effects of Reynolds number and Stokes number on particle-pair relative velocity in isotropic turbulence: A systematic experimental study". In: *Journal of Fluid Mechanics* 839.716 (2018), pp. 271–292. DOI: 10.1017/jfm.2017.813.

[109] Reitz, R. D. et al. "Structure of high-pressure fuel sprays". In: *SAE Paper 870598* (1987).

[110] Ashgriz, N. et al. "Coalescence and separation in binary collisions of liquid drops". In: *Journal of Fluid Mechanics* 221 (1990), pp. 183–204. DOI: 10.1017/S0022112090003536.

[111] Ashgriz, N. et al. "Binary collision dynamics of fuel droplets". In: *International Journal of Heat and Fluid Flow* 8.3 (1987), pp. 205–210. DOI: 10.1016/0142-727X(87)90029-4.

[112] Baumgarten, C. "Mixture Formation in Internal Combustion Engine". In: *Mixture Formation in Internal Combustion Engine* (2006). DOI: 10.1007/3-5403-0836-9.

[113] Abramzon, B. et al. "Droplet vaporization model for spray combustion calculations". In: 32.9 (1988), pp. 1605–1618. DOI: 10.2514/6.1988-636.

[114] Jin, J. D. et al. "A Model for Multicomponent Droplet Vaporization at High Ambient Pressures". In: *SAE Technical Papers* (1985).

[115] Tamim, J. et al. "A continuous thermodynamics model for multicomponent droplet vaporization". In: *Chemical Engineering Science* 50.18 (1995), pp. 2933–2942.

[116] Montanaro, A. et al. "Wall impingement process of a multi-hole GDI spray: Experimental and numerical investigation". In: *SAE Technical Papers* (2012). DOI: 10.4271/2012-01-1266.

[117] Hay, N. et al. "Comparison of the various correlations for spray penetration". In: *SAE Technical Papers* (1972). DOI: 10.4271/720776.

[118] Santos, F. dos et al. "Spray atomization models in engine applications, from correlations to direct numerical simulations". In: *Oil and Gas Science and Technology* 66.5 (2011), pp. 801–822. DOI: 10.2516/ogst/2011116.

[119] Zeng, W. et al. "Macroscopic characteristics for direct-injection multihole sprays using dimensionless analysis". In: *Experimental Thermal and Fluid Science* 40 (2012), pp. 81–92. DOI: 10.1016/j.expthermflusci.2012.02.003.

[120] Zeng, W. et al. "Atomization and vaporization for flash-boiling multihole sprays with alcohol fuels". In: *Fuel* 95 (2012), pp. 287–297. DOI: 10.1016/j.fuel.2011.08.048.

[121] Zhang, G. et al. "Temporal investigations of transient fuel spray characteristics from a multi-hole injector using dimensionless analysis". In: *Experimental Thermal and Fluid Science* 66 (2015), pp. 150–159. DOI: 10.1016/j.expthermflusci.2015.03.011.

[122] Hiroyasu, H. et al. "Structures of Fuel Sprays in Diesel Engines". In: *SAE Technical Paper 900475*. 1990. DOI: 10.4271/900475.

[123] Mugele, R. A.; Evans, H. D. "Droplet Size Distribution in Spray". In: *Industrial & Engineering Chemistry,* 43.6 (1951), pp. 1317–1324. DOI: 10.1252/kakoronbunshu1953.33.357.

[124] Angarita-Jaimes, D. et al. "Three-component multi-phase velocimetry measurements on a GDI spray using optically efficient fluorescent tracers". In: *Experiments in Fluids* 52.4 (2012), pp. 949–962. DOI: 10.1007/s00348-011-1174-3.

[125] Prosperi, B. et al. "PIV Measurement of Injection Pressure Influence on Gas Entrainment in GDI Engines". In: *ILASS - Europe 2007, 21st Conference on Liquid Atomization and Spray Systems* Table 1 (2007), pp. 1–6.

[126] Schulz, F. et al. "The influence of flash-boiling on spray-targeting and fuel film formation". In: *Fuel* 208 (2017), pp. 587–594. DOI: 10.1016/j.fuel.2017.07.047.

[127] Aleiferis, P. G. et al. "An analysis of spray development with iso-octane, n-pentane, gasoline, ethanol and n-butanol from a multi-hole injector under hot fuel conditions". In: *Fuel* 105 (2013), pp. 143–168. DOI: 10.1016/j.fuel.2012.07.044.

[128] Sphicas, P. et al. "Inter-plume aerodynamics for gasoline spray collapse". In: *International Journal of Engine Research* 19.10 (2018), pp. 1048–1067. DOI: 10.1177/1468087417740306.

[129] Wu, S. et al. "Investigation of rapid atomization and collapse of superheated liquid fuel spray under superheated conditions". In: *Atomization and Sprays* 26.12 (2016), pp. 1361–1384. DOI: 10.1615/AtomizSpr.2016014231.

[130] Manin, J. et al. "Experimental Characterization of DI Gasoline Injection Processes". In: *SAE Technical Paper 2015-01-1894* (2015). DOI: 10.4271/2015-01-1894.

[131] Li, T. et al. "A comprehensive study on the factors affecting near-nozzle spray dynamics of multi-hole GDI injectors". In: *Fuel* 190 (2017), pp. 292–302. DOI: 10.1016/j.fuel.2016.11.009.

[132] Aori, G. et al. "Effect of Nozzle Configuration on Macroscopic Spray Characteristics of Multi-Hole Fuel Injectors Under Superheated Conditions". In: *Atomization and Sprays* 26.5 (2016), pp. 439–462. DOI: 10.1615/AtomizSpr.2015011990.

[133] Lacey, J. et al. "Generalizing the behavior of flash-boiling, plume interaction and spray collapse for multi-hole, direct injection". In: *Fuel* 200 (2017), pp. 345–356. DOI: 10.1016/j.fuel.2017.03.057.

[134] Guo, H. et al. "Comparison of spray collapses at elevated ambient pressure and flash boiling conditions using multi-hole gasoline direct injector". In: *Fuel* 199 (2017), pp. 125–134. DOI: 10.1016/j.fuel.2017.02.071.

[135] Kale, R. et al. "Experimental investigation on GDI spray behavior of isooctane and alcohols at elevated pressure and temperature conditions". In: *Fuel* 236.April 2018 (2019), pp. 1–12. DOI: 10.1016/j.fuel.2018.08.153.

[136] Araneo, L. et al. "Flash boiling in a multihole G-DI injector - Effects of the fuel distillation curve". In: *Fuel* 191 (2017), pp. 500–510. DOI: 10.1016/j.fuel.2016.11.104.

[137] Du, J. et al. "Study of spray collapse phenomenon at flash boiling conditions using simultaneous front and side view imaging". In: *International Journal of Heat and Mass Transfer* 147 (2020), p. 118824. DOI: 10.1016/j.ijheatmasstransfer.2019.118824.

Chapter 4

State of the Art

"To achieve anything you must first have ambition and then talent, knowledge, and finally the opportunity."
—Carlos Ruiz Zafón

4.1 Introduction

Multi-phase flows have been extensively studied over the years in various fields of application. Unlike diesel injection, the interest in GDI technology studies has only recently been grown and although many concepts can be transferred from one technology to another, there are still many uncertainties to be solved. These processes involve numerous complex phenomena such as turbulence, air-fuel mixing, heat transfer and atomization, among many others, which are still largely unknown to this day. In addition, the presence of a very wide spectrum of length- and time-scales makes the complete understanding of the injection process even more difficult. This Chapter presents the current state of the art concerning the subject of the document, GDI technology, with the objective of observing in which areas there are limitations and therefore further study should be carried out.

As stated in previous Section 1.2, the main objective of this Thesis is to provide a better understanding to the scientific community in the field of GDI in order to further comprehend the phenomena occurring in the injection process that directly affect combustion efficiency and thus fuel consumption and pollutant generation. For this purpose, the internal and external flow will

be analyzed separately in order to observe the phenomena that take place in each of the processes and, in addition, both studies will be coupled in order to appreciate the influence that the behavior of the flow inside the nozzle has on the subsequent development of the jet. The following paragraphs summarize the research carried out to date, both experimentally and computationally, based on the thematic area of interest.

4.2 Experimental Background on GDI Studies

A variety of fuel spray characteristics mentioned in Section 3.4 and 3.5 and phenomena derived from the injection process are measurable using well-established experimental diagnostic techniques. This section provides a brief overview of the main experimental work available in the literature on the GDI strategy from a few years ago to the present day.

4.2.1 Internal and near nozzle flow

4.2.1.1 Injector characterization

To understand the behavior of the complete injection process, one of the first steps is to characterize the injector, which means to know its main features in terms of geometry and internal and near nozzle flow behavior. This requires a multi-technique apporach and the participation of several institutions, as no single technique can provide the detailed information desired [1]. Manin et al. [2] combined several techniques, such as x-ray tomography and optical microscopy, to evaluate the internal nozzle geometry and orifice diameters of the injector used. X-ray computed tomography is typically used to identify the internal and external features in a non-intrusive way. In this case, the final resolution obtained was in the order of 5 µm. On the other hand, these researchers also employed the optical microscopy technique which, although it only allowed them to obtain details of the external part of the injector, the measurements had a higher precision, of the order of 1 µm or even less. This technique enabled them to characterize the peculiar shape of the orifice outlet accurately and with little margin for error. Later on, Duke et al. [3] used the x-ray tomography applying a 7-BM beamline of the APS at the Argonne National Laboratory facility where the study was not only focused on the characteristics of the orifices but also aimed to study the injector sac shape. The procedure followed was to acquire images with a spatial resolution of 1.17 µm per pixel and subsequently reconstructed. In doing so, they were able to obtain up to eleven key dimensions considered critical for the further

modeling of the domain (hole diameter, inlet and outlet radius and drill angle, among others). The precision of the technique in obtaining images is quite high, with the largest deviations, in the order of 2%, in the areas corresponding to the holes where the sizes are much smaller. The reconstruction clearly showed rough surface finish in addition to hole-inlet defects that match the optical microscopic metrology of the nozzle surface and bore region [2]. Both the surface roughness and these defects in the inlet orifice are expected to have a significant effect on the internal flow and therefore need to be taken into account in both modeling and analysis [4]. In the process of characterizing, the dynamics of the injector, in other words, the movement of the needle during the injection process, should be also included. Duke et al. [3] extended previous studies for the characterization and measurement needle dynamics from time-resolved x-ray phase contrast imaging at the APS 32-ID beamline. In these studies, both the vertical movement of the needle and the lateral displacements of the needle were obtained.

It is well known that the shape of the orifices that make up the GDI injectors alter the direction of the spray, so it is not only enough to know the geometric angle of the orifices from the aforementioned studies, but it is also interesting to determine how much the jets are deflected especially for the corresponding modeling and to carry out the necessary correction in the momentum flux measurements and spray validation. Computing the spray deflection can only be done once the jet has left the nozzle and, unlike typical diesel sprays which are better differentiated from each other, gasoline sprays are much closer together making it difficult to determine their characteristics. The determination of these angles could be done directly from experimental visualization techniques but the necessary set-ups are expensive just to obtain these characteristics. For this reason, Shahangian et al. [5] employed a method called "plastic deformation technique", which uses a deforming material to measure the footprint of the spray plumes on a surface at a given distance from the nozzle tip. To obtain the angle of each of the jets, they generated an in-house code based on trigonometric equations. The obtained results presented deviations of $\pm\ 2^{\circ}$ considered within the experimental uncertainty. The only limitation they reported is that the jets must have sufficient momentum to deform the material. Payri et al. [6] took advantage of the experimental momentum flux measurement campaign and used a high speed camera focused on the impact target to capture the amplitude of the sprays. The method offered was not very robust or consistent but it was useful to compare the results obtained between different configurations where 5° of error resulted in a deviation of 6% of the results.

Once the geometry and details of the injector are known, it is important to carry out a hydraulic characterization of the injector, which consists of determining the flow patterns in and near the injector field. Characterizing the injector behavior from mass flow rate measurements helped Costa et al. [7] to optimize the fuel economy in multiple injections of gasoline. Hoffman et al. [8], also measured mass flow in a very high pressure injector to evaluate its effect on the total mass injected and the fuel delivery form. These publications proved the relevance of mass flow rate as a major step in the investigation of GDI. Nevertheless, numerous literature publications on diesel [9, 10] indicates that not only mass flow rate is significant, but also momentum flux measurements are essential to characterize the hydraulic behavior of injectors and to model them successfully. The mass flow rate or also known as rate of injection (ROI) is commonly measured on the basis of specialized "long-tube" type rate meters [11] although there are many other methods also used. Among the employed approaches the most outstanding are Bosch method [12], Zeuch method [13], and momentum flux method [14]. The Bosch method is based on the measurement of the injection rate from the pressure wave generated when injecting fuel into the tube filled with the same fuel held at constant pressure by a check valve. In contrast, the Zeuch method uses the measurement of the rate of pressure increase inside a closed chamber when fuel is injected to calculate the injection rate from the fuel density. Bower and Foster [11] compared the performance of the two systems and concluded that both methods accurately measure magnitude and shape, except that the Bosch method produces a much smoother injection rate shape. Naber and Siebers [15], assuming that the injection rate follows the same profile as the momentum flux, used the momentum flux method to measure the ROI for the first time. In later years, this technique was used by several researchers to jointly measure mass flow and momentum flux for diesel [16] and urea injectors [17]. This method has been widely used because of the advantage of being able to visualize the hole-to-hole variation from transient measurements of injection rate and hydraulic coefficients [18]. On the other hand, the momentum flux or rate of momentum (ROM) measurement is more narrowly defined and is usually determined from a piezoelectric pressure sensor calibrated to measure force. When the spray from the injection event hits the sensor, the assumptions of perpendicular air entrainment and perpendicular projection of the spray upon impact are accepted, therefore, the force recorded by the sensor is the direct measure of the impulse given to the spray in the injection event.

Payri et al. [19] adapted the knowledge and experience gained applied diesel injection studies and used the Bosch method [12] on a commercial EVI rate meter to measure the ROI of a GDI injector. In this work, not only the

mass flow was measured for specific conditions, but also the injection pressure, discharge pressure, injection frequency and injector holder temperature were varied. Parametric pressure variations revealed the effect of the injection pressure on the injection rate The variation of the carrier temperature as well as the ambient pressure hardly influences the injection rate and the total injected mass. Payri et al. [6], in another of their articles, measured the momentum of a GDI injector allowing them to calculate hydraulic parameters of the injector such as area, velocity and discharge coefficients which enables to understand the internal nozzle flow and establish experimental validation for modeling gasoline injectors. In this study, two different configurations were used, one lateral and one frontal, and although differences between the two measurements were observed, they were reduced under low back pressure conditions. Cavicchi et al. [20] employed the Zeuch method to perform momentum and mass flow measurements which they combined with numerical simulations for different parameters such as target size, nozzle/target distance and ambient pressure. In doing so, they claimed that the combination of both study techniques can be a very useful tool to analyze in detail the behavior of the jet in GDI injectors. Finally, Ge et al. [21] compared the obtained results for mass flow and the influence of the same on liquid and vapor penetration lengths. They performed measurements with two different methods, Zeuch and momentum flux method, obtaining satisfactory results in comparison with the experiments for both techniques.

4.2.1.2 Injection process phenomena

Once the characteristics of the injector are determined, much research is focused on the study of phenomena that take place inside or in the near field of the injector during the injection process. As already mentioned in Section 3.4.4, cavitation plays a very important role in the behavior of the GDI jet due to a combination of effects from the geometry of the holes, the low needle lift, and the low vapor pressure of the fuels used in GDI nozzles. Experimental studies based on the search for this phenomenon are minimal as the experimental techniques needed to capture cavitation are complex and in many cases require, as was done many times in diesel injectors, a transparent prototype to observe the behaviour of the fluid inside the nozzle [22, 23]. Despite this, some researchers have accepted the challenge, such as Bornschlege et al. [24] who observed the presence of cavitation inside the orifices thanks to the optical access of a transparent injector and the use of the shadowgraph technique (see Figure 4.1). Chaves et al. [25] used a transparent three-hole injector that resembles the behavior of a real GDI multi-hole injector. For

this, under submerged conditions, they needed to change the orientation of the optical assembly and finally applied a beam splitter plate for illumination with the light from a Minilite NdYag laser. In this study they were able to observe that the occurrence of cavitation is dependent on the cavitation number (Equation 3.28) as well as on the composition of the mixture. Furthermore, they stated that due to the transient characteristics of the flow, the behavior is not expected to reach equilibrium thermodynamic conditions inside the orifices. Recently, Mamaikin et al. [26] employed a 2D micro PIV (Particle Image Velocimetry) technique in order to acquire the velocity field at the relevant injection conditions inside the nozzle. In addition, these velocity data were used for the evaluation of the pressure within the internal domain of the nozzle to determine the areas where cavitation could occur.

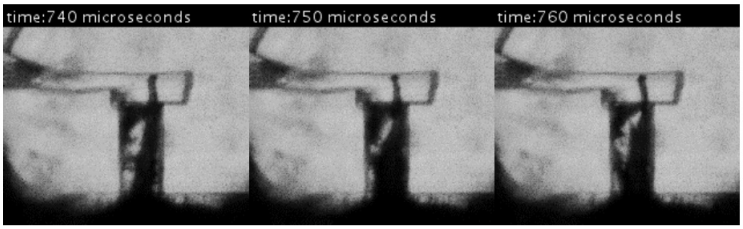

Figure 4.1: Series of high speed images of cavitation within the transparent nozzle. Adapted from [24].

A widely-studied phase change phenomenon is the well-known flash boiling (Section 3.4.5). Many researchers have taken up this branch of research because of the high influence this phenomenon has on the spray characteristics, improving the atomization process. Zhang et al. [27] employed a microscopic backlit imaging technique to obtain the near-field spray structure of flash boiling sprays. They clearly detected how the microscopic structure of the spray was critically dependent on the thermodynamic state of the injected liquid, observing a remarkable increase in the amplitude and angle of the plume under superheated conditions. The near-field angle under non-flashing conditions depends directly on the ambient-liquid density ratio, while the degree of superheat becomes dominant for flash boiling conditions. Accordingly, they developed a quantitative correlation to capture the respective importance of these factors at different superheat conditions. Yang et al. [28] were among the first researchers in more than 60 years to study the phenomena of cavitation and flash boiling together, interpreting the different bubble formations to attribute them to one phenomenon or the other. To this end, they employed a high-speed imaging system coupled with a series of two-dimensional transparent nozzles. The results indicated that cavitation at the upstream part of the

nozzle provides the nucleus for the onset of flash boiling at the downstream, which enhances the flash boiling effect. Low needle lift could improve the development of all kinds of internal bubbles. In addition, this study proposes the concept of cavitation boiling, which is defined as a phase change by both of the decrease of local pressure and the increase of vapor pressure due to the rise of fuel temperature.

Due to the continuous tightening of emission standards, some studies have been more focused on the investigation of phenomena that are the main contributors to the increase of these levels. Within these regulations, the one on particulate emissions stands out, which includes particulate matter (PM) mass limits and tends towards particle number (PN) criteria. Sources of particulate matter in engines are attributed to fuel-rich combustion regions formed during fuel-air mixing, liquid films created by fuel spray impact on walls, fuel trapped in crevice volumes and other mechanisms [29]. Several of these phenomena can be mitigated by improving the injection strategy, which will be discussed later on. However, the so-called tip wetting mechanism cannot be attenuated by such strategies and is not fully understood to date. Researchers such as Leick et al. [30] sought to contribute with their work to generate a complete and detailed experimental database for a better understanding of this type of mechanism. They concluded that the most influential parameters on tip wetting are flash boiling and injection pressure. Flash boiling tends to increase the amount of liquid coating on the injector tip at the end of injection whereas an increase in injection pressure consequently reduces the amount of fuel in the injector tip, which is in accordance with engine results presenting less deposit formation and lower particulate emission at higher injection pressures [31]. Medina et al. [32] also made efforts to further understand tip wetting and tip drying processes, that is, the evaporation of the fuel film deposited onto the injector tip. They attempted to identify trends from a broad range of experimental data on engine and fuel injector operating conditions and relate them to tip wetting and tip drying mechanisms. They concluded that tip wetting depended on both engine operating conditions and injector design parameters, which include injection pressure, chamber temperature and pressure, engine load, injector hole length, hole angle, and pre-hole size. In agreement with Leick et al. [30], they determined that increasing the injection pressure reduced the PN due to a reduction in tip wetting. They also observed that increasing the engine load from a longer injection duration generated a higher number of PM, suspecting that the main reason was a higher amount of tip wetting at the nozzle. With respect to the effects of geometry, they noted how increasing the holes length caused a net increase in tip wetting PN and divergent type holes reduced PN but, however, were suspected of increasing

deposits at the tip of the injector. As earlier mentioned, these researchers also analyzed tip drying and observed that the main parameters affecting tip drying were the time-scale and the injector tip temperature, which can change PN emissions by an order of magnitude. In last months, due to recent changes in emission regulations and the future of automobiles, Xiao et al. [33] have continued to study phenomena such as tip wetting in order to better understand how to reduce emissions and improve engine performance. They based their conclusions on measurements of film area and thickness as a function of time. They found that in sub-cooled conditions and long injections, the effect of hole position and hole structure on the film parameters was small. In contrast, under flashing conditions the nozzle configuration becomes significant and a configuration that benefits performance has to be found.

4.2.2 External flow

4.2.2.1 Spray pattern characterization

Once the injector is characterized and the flow behavior and phenomena taking place in- and near- field of the injector are known, research is based on understanding the behavior and characteristics of the spray once it leaves the injector due to its enormous contribution to fuel economy and emissions [34]. In recent years, the experimental scientific community has increasingly focused its efforts on the understanding of the spray pattern. However, the mixture formation and atomization processes still have many aspects that need to be further investigated and fully comprehended. Parrish [35] explored the influence of ambient conditions and fuel properties on the formation of liquid and vapor by high-speed imaging system capable of acquiring Schlieren and MIE-scattering images. He demonstrated how high ambient temperatures reduced liquid penetration and promoted shorter residence times while high ambient densities also reduced liquid penetrations but showed no effect on residence time. This research also made visible the differences in spray behavior with the use of different fuels. Finally, he pointed out how the near tip air entrainment and the plume-to-plume interactions are affected by diverse parameters such as the spray angle and the number of holes in the nozzle. Park et al. [36] obtained the spray pattern through the cross-sectional visualization of the fuel spray by a sheet-beam formed by a Nd:YAG laser, optic sets and high-speed camera. They focused on analyzing the movement of the spray plume center, spray area, and injection angle in addition to the uniformity of the individual spray plume and the spray dynamics. It was found that as the distance between the nozzle tip and the spray plume measurement cross-section increases, the deflection of the spray center becomes greater. On the other hand, it was

proven that an increase of the injection pressure enhanced the consistency of the individual spray due to the increase of the spray momentum. Finally, they highlighted how the GDI multi-hole injector exhibits different spray behavior for each hole depending on the arrangement of the orifices and that the injection strategy can be key to minimizing collisions with the combustion chamber and piston walls.

As with internal flow and because the expected spray behavior is not the usual, many researchers have put their efforts into investigating the spray pattern when the operating conditions are favorable for the occurrence of the phase change phenomenon known as flash boiling. In addition, as mentioned in Section 3.5.4, the behaviour of the plumes under the influence of this phenomenon can lead to the collapse of the jets. Bornschlegel et al. [37] prioritized the understanding of the physics behind these phenomena and therefore studied separately the effects of flash boiling and spray collapse on the spray pattern. They developed a single-orifice injector to isolate the jet and used a microscopic high speed setup to visualize the jet expansion at the outlet of the injector, the Schlieren visualization technique to determine macroscopic jet parameters such as liquid and vapor penetration and spray angle, and finally, they used the LDA/PDA technique to measure particle sizes and velocities. In this case and because the injector was a single orifice injector, the effects due to flash boiling were less significant than expected. It is true that higher penetrations, cone angles and spray volume were observed in those conditions favorable to flash boiling, but the improvement in primary atomization was not noticeable as the droplet size detected was similar in all the operating conditions tested. Wu et al. [38] considered a multi-orifice injector although their objective was to focus on the flash boiling phenomenon and the influence of the operating conditions on the characteristics of the spray structure and atomization droplet size distributions. In order to improve the insight into the flash boiling spray, three injectors with different spray characteristics were studied. The results proved the enormous influence of the operating conditions on the phase change, both lower ambient pressure and higher fuel temperature could accelerate the flash boiling process (Figure 4.2). They also noticed how the spray structure always turns from hollow cone into solid when flash boiling occurs. With regard to droplet size, they concluded that the higher the superheat degree of the droplet distribution, the smaller the droplet sizes tendto be, with SMD being reduced by up to 50% compared with cold spray. Finally, they also identified a close relationship between the collapsed flash-boiling spray target and the weighted geometric center of the injector, so spray collapse could be avoided by increasing the distance of the plumes.

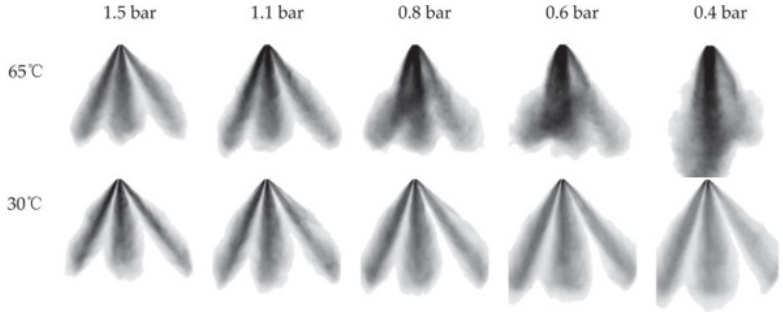

Figure 4.2: Spray pattern under various atmosphere pressure and fuel temperature. Adapted from [38].

Many other researchers study the phenomena of flash boiling and spray collapse together because, it has been mentioned several times, they are often linked. Payri et al. [39] used DBI and Schlieren visualization techniques to predict spray collapse formation patterns under high ambient temperature and density conditions. The presence of this phenomenon was detected by an increase in spray penetration and a decrease in spray aperture. Throughout the study, they found that the injection pressure did not directly affect the formation of the spray collapse. While varying the injection pressure does not change the liquid length under conditions that allow it to be achieved, under spray collapse conditions there is no stabilization of liquid penetration and the injection pressure has a similar effect on both liquid and vapor penetration. Lastly, after analyzing the trends in spray behavior with varying combustion chamber temperature and gas density, it was found that under certain conditions the spray did not follow the expected pattern, which led to the conclusion that further research on GDI spraying is needed to understand the phenomena described, especially considering the effects it can have on evaporation, fuel mixing and wall wetting, all of which are of critical importance for combustion and engine performance. Adding to the previous statement that the mechanism of spray collapse needs to be further understood, Sphicas et al. [40] set out to study the influence of injection duration and multiple injection use on the interaction between plumes. For this purpose, they used high-speed PIV and DBI techniques. These studies showed that the direction of the plume did not remain constant during the injection event but decreased over time without being influenced by the duration of the injection. Therefore, increasing the hydraulic injection promotes spray collapse. Another fact that came to light is that the collapse between jets is avoided by using small injections which seem to generate smaller and more dispersed droplets. Recently, Du et

al. [41] considered that the spray structure under flash boiling conditions was not well captured by the experimental techniques used to date. Therefore, they proposed the implementation of Structured Laser Illumination Planar Imaging (SLIPI) to visualize the occurrence and development of spray collapse behaviors under flash boiling conditions for the first time. Thanks to this visualization technique, they observed that for the injector studied, the spray collapse occurred at the center of the spray, leaving a hollow part inside the spray cone below the injector tip.

Several of the previous mentioned contributions have based a small part of their studies on the measurement of droplet size and particle velocity. Knowledge of these parameters gives a broad understanding of the quality of the atomization and the air-fuel mixture, important parameters for meeting stringent emission standards. Sharma et al. [42] focused on the measurement of droplet size and velocity distributions when the engine load is varied using Phase Droplet Interferometry (PDI). They also relied on Shadowgraphy techniques to determine primary and secondary spray breakup regimes. From these investigations they concluded that increasing the amount of fuel injection, while keeping the injection pressure constant, did not make a noticeable difference to the velocity or diameter distributions. However, it was noted that a smaller amount of injected fuel showed a larger droplet surface area in contact with the ambient air at constant pressure, resulting in a greater fuel-air mixture.

Just as time was spent on characterizing the injector geometry and analyzing its influence on the near-field characteristics, studies were also carried out investigating the influence of the geometry on the spray patterns. Furthermore, as many previous works have shown [38, 43], the geometrical arrangement of the orifices can mitigate the adverse effects of phenomena such as spray collapse. For these reasons, Medina et al. [44] carried out a study based on the influence of internal geometry in high-pressure gasoline sprays where they investigated five nozzles with different nozzle inlet rounding, conicity and outlet diameter. In addition, they also observed from imaging methods, the behavior of the spray under different operating conditions by varying the injection pressure and the discharge pressure. From the geometry comparison, large nozzle diameter, as well as the combination of a converging nozzle and hydro-erosion rounding, resulted in greater penetration distance and spray angle. However, the nozzle with the smallest diameter systematically resulted in the lowest spray angle, and the divergent nozzle produced the highest spray angle. Finally, the largest exit diameter had the longest penetration distance. Jiang et al. [45] determined the impact of hole diameter and conicity under flashing and non-flashing conditions. Most importantly, the research showed

that under flash boiling conditions the behavior of the spray was highly dependent on the type of geometry. Some orifice designs offered more resistance against spray collapse. In addition, a curious fact they noticed is that the orifice with a medium orifice size produced a jet-to-jet interaction more easily than smaller or larger orifice diameters and that the converging orifice was more prone to spray collapse.

4.2.2.2 Spray pattern influence on engine performance

The progressive trend towards downsizing GDI engines, the interest in improving fuel efficiency and performance, and regulatory requirements concerning combustion emissions have meant that one of the main interests of researchers has been and still is to focus on strategies to improve in-cylinder mixture formation and the identification and elimination of sources of combustion emissions, in particular the formation of in-cylinder particulate matter. For this reason, several works were focused on finding out about the influence of the injection pressure on the performance of the injection system and consequently of the engine. Hoffmann et al. [8] investigated the influence of increasing injection pressure, in this case reaching maximum pressures of 40 MPa. They employed the MIE-scattering technique. The images obtained showed a noticeable increase in light scattering by the spray plume, which is an indication of the reduction in droplet size associated with the increase in system pressure. They also observed, again, that the injection velocity increased with the injection pressure, however, the end of plume penetration length is nearly independent of the fuel pressure. The absence of a proportional increase in final spray penetration underlines the enhanced momentum exchange between spray and air (and hence air entrainment in the spray). This is a key mechanism, in addition to atomization, for the promotion of spray vaporization and spray mixing processes. The study by Hoffmann et al. [8] did not only remain here, but also tested the effect of injection pressure on particulate emissions. They observed a systematic improvement with increasing pressure both in the mass of the particles, reduced, and in the number of particles, which was also decreased. Increasing the injection pressure in order to improve engine performance has certain limits since, as mentioned above, the penetration length increases with injection pressure and can lead to wall wetting, which has a negative impact on emissions in GDI combustion. Against this, it is argued that the injector design is the most effective limiter of penetration length. To investigate the effect, Lehnert et al. [46] compared spray properties using a prototype GDI injector (100 MPa max. fuel pressure) and an injector with diesel-like design and came to the conclusion that the injector design affects

the penetration length and the transition to the vapor phase, due to different air entrainment rates. At higher fuel pressures, the diesel design leads to faster vaporization, so that mixture formation and phase change are also faster, especially in high temperature ambient conditions. Whereas a typical GDI design limits penetration more efficiently at moderate injection pressures and low to moderate ambient conditions.

As mentioned in previous paragraphs, the willingness to increase injection pressure in order to meet the new standards set by the authorities and the emergence of phenomena that change spray patterns (flash boiling and spray collapse) have led researchers in recent years to focus on a side effect caused by these new ways of operating, namely wall impingement. The impact of the spray on the cylinder or piston walls is a problem to be addressed as it favors the increase of emissions and therefore deteriorates the performance of the engine. For this reason, in the last years, Montanaro et al. [47] studied the influence of various factors on the development of the spray and the resulting wall impingement, including injection pressure and wall inclination at ambient conditions. One of the main conclusions they reached was that higher injection pressures promote higher radial penetration and spray height of the impinging jet (Figure 4.3). Years later and continuing with the idea of previous studies, Montanaro and Allocca [48] and Alloca et al. [49] set themselves the objective of studying in detail the interaction between the injected fuel and a flat wall which emulates the piston, focusing on the liquid and vapor phases. They used a wall at different temperatures to observe the influence of the temperature on the film formed during the impact. They combined MIE-scattering and Schlieren techniques with quasi-simultaneous timing to obtain simultaneous information from the liquid and gas phase. They confirmed the previous findings that the higher the injection pressure, the thicker the film formed and noticed that the thickness of the liquid film was reduced with higher wall temperature, but the opposite was true for the vapor phase. On the other hand, the curves show a well-scaled trend of both liquid and vapor length with respect to the wall temperature, the higher is the temperature and the faster the fuel slipping results. Liu et al. [50] also sought to understand in particular the behavior of the liquid film when the spray hits the wall and the wall is at a certain temperature although in this case they employed the LIF visualization technique. It was found that the fuel film volume increases almost linearly with injection duration when the surface temperature is low. The ratio of wall film volume to total injected volume is independent of injection duration, but gradually decreases with rising temperature.

Another fairly common way to improve spray performance is to modify the injection strategy, in this case by using multiple injections or by splitting

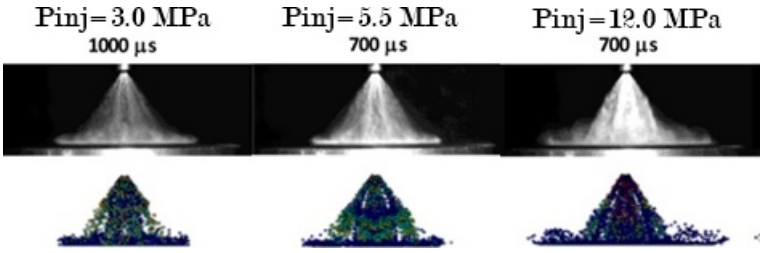

Figure 4.3: Experimental (top) and numerical (bottom) comparison, images of impinging spray for different injection pressures. Adapted from [47].

the main injection into several smaller ones. The split injection strategy can effectively reduce spray penetration by reducing the momentum of the liquid fuel, which decreases the potential for spray wall impingement. Wang et al. [51], based on high speed imaging and PDPA techniques, studied the effects of nozzle deposits on the macroscopic characteristics of the jet under flash boiling conditions. They reported how a single injection produced certain deposits that resulted in lower cone angle and higher penetration due to weaker atomization and dispersion. The deposition also resulted in a larger droplet size, as an increase in particle size caused a reduction of the breakup potential in small droplets. Because of this, and in order to mitigate these effects, split injection strategies were applied. Under non-flashing conditions, the effects of the deposits on the increased penetration and thus the high probability of impingement were mitigated, however, the negative effect on droplet size was enhanced. On the other hand, under flashing conditions, both adverse effects (increased penetration and droplet size) were attenuated. The authors concluded the research by stating that an optimal split injection strategy is important to overcome the adverse effect of deposits on spray characteristics and emissions. Shortly afterwards, Wang et al. [52] characterized the wall impingement effect under flash boiling conditions and analyzed the influence of the split injection strategy on this phenomenon. The studies reveal that under non-flashing conditions the spray has large secondary droplets and ligaments, thus having a greater impact against surfaces, effects that are reduced under flash boiling conditions. On the other hand, it was proven that the use of the split injection strategy could further reduce the deposited fuel. However, it was observed that the second injection in the multiple injection strategy generated a fuel film more quickly on impact with the surface due to the existence of remnants of the fuel film formed by the first injection. This effect could be overcome by increasing the degree of flash boiling as it would enhance evaporation and dispersion. Finally, one of the most recent investigations into

the influence of injection strategies was carried out by Sun et al. [53] using non-intrusive imaging techniques including micro-LIF-PIV, MIE-scattering, and flame chemiluminescence. The most relevant conclusion of this study was that the strong air-fuel entrainment under flash boiling condition contributed to better mixing performance using the split injection scheme, as the secondary injection will be more affected by the vortices generated by the primary injection, since the duration between the two injections is short enough before the vortices dissipate.

Recently, and with the new automotive scenario of hybridization and electrification, GDI has been progressively extended to improve the thermal efficiency of the powertrain. For this reason, not only is it important to know and understand the spray pattern under controlled conditions such as the vast majority of the studies mentioned above, which have been carried out in constant volume chambers (CVC), but it is also important to study the behavior of the spray during engine operation where the boundaries conditions are constantly changing (varying pressure, piston movement, valve opening and closing, etc.). Therefore, one clear example is the research of Serras-Pereira et al. [54] who studied the spray development, spark discharge and combustion in an optical engine under multiple injection strategies. More specifically, the authors employed single injection strategies from early to late intake stroke, as well as split multiple injection events with triple pulses on the early intake stroke or double pulses on the intake stroke and late compression stroke. The most relevant finding of the analysis was the potential to control the mixture formation and flow field in the early flame development stage of combustion by means of the early-late double injection strategy.

As a conclusion on the current state of experimental knowledge, the understanding of the dynamic spray pattern is crucial for the fulfillment of engine performance and pollutant emissions requirements. Despite all the research work that has been carried out over the years, the vast majority of the works cited, especially the more recent ones, come to the same conclusion; the complexity of the injection process including the formation of the spray mixture and atomization, as well as limitation of visualization techniques mean that the injection event remains partly unknown and therefore in need of further research. It is well recognized that CFD simulations are able to minimize research and development times as well as complement experimental findings by providing knowledge not available in the experiments. Therefore, a combination of both experimental and computational research would provide the scientific community with a better understanding of the injection process as a whole.

4.3 Numerical Background on GDI Studies

Throughout the previous section, numerous experimental works, which have been developed in the last few years concerning GDI, have been reported. Despite all the information that has been collected, the behavior of the spray pattern is still uncertain and not well understood, firstly because of the complex phenomena (turbulence, heat transfer and atomization, among others) involved, and secondly due to the presence of a very wide spectrum of length- and time-scales. Experimental approaches can be notoriously time-consuming and costly, whereas numerical simulations allow the number of experimental tests to be reduced, prevent the installation of complex diagnostic tools, and enable access to information in inaccessible locations for optical or sensor measurements. Accordingly, CFD simulations have arisen as a powerful additional research tool to provide a deeper insight into the complex unsteady dynamic processes involved in GDI systems. As said earlier, the combination of the numerical and experimental approaches makes it easier to more accurately and efficiently improve the performance of the GDI system under different operating conditions. In addition, the exponential increase in computing power and capability has also been used to further develop and test numerical submodels for in- and near- nozzle flow analysis and atomization process in more complex geometries. Thus, this section aims to provide a clear overview of the state of the art in computational research on GDI systems carried out in recent years.

In the last decades, a large number of numerical investigations on GDI systems have been conducted to study the behavior of the flow in the in- and near- nozzle region, spray breakup, droplet dispersion and mixing under different operating conditions. The GDI injection process is associated with high turbulence and instability that have to be modeled from CFD approximations. The Unsteady Reynolds-Averaged Navier-Stokes (U-RANS) turbulence modeling approach provides a basic analysis, without going into further detail, of the flow characteristics. U-RANS simulations, in which the field is decomposed into an ensemble mean and a fluctuating component, model the turbulence and only resolve statistically stable flow structures. For this reason, the aforementioned approach is not capable of accurately predicting the turbulence fluctuation statistics and therefore, depending on the purpose of the study, may be insufficient to represent the complexity of the GDI injection process. Contrary to this approach, Direct Numerical Simulation (DNS) turbulence approahc fully resolve all the scale structures of scalar and velocities fluctuations. Although the recent rapid development of numerical methods and computing power has enabled large-scale numerical simulations in other

fields of injection [55–57], the wide range of length scales involved in the injection and atomization of liquid fuel make the computational cost required to study the injection process in GDI engines prohibitive, even with today's computing power. Even so, it is still maintained that DNS remains very important for atomization research, as it can resolve interfacial multiphase flows much more accurately and can provide high-level details that are difficult to obtain in experiments or low fidelity simulations (LFS). In addition, the physical insights and high-fidelity simulation data obtained in DNS can be used to improve atomization models, which has received increasing attention and good progress has been made in the last decade [58]. Therefore, this field of knowledge remains open and may be explored in more detail in the not too distant future. Meanwhile, Large Eddy Simulation (LES) turbulence models have emerged as a realistic and affordable alternative and allows investigating the generation and evolution of fully transient coherent structures that take place during the injection process. It is therefore the direction that most researchers in the field of GDI are taking in order to go further in understanding and predicting the atomization of gasoline jets and spray characteristics. Yet, due to the high Reynolds and Weber numbers involved, they have to ensure that the mesh resolutions of these simulations are sufficient to faithfully resolve both the internal flow and the external turbulent sprays.

As seen in Chapter 3, as well as in the previous section (Section 4.2), the study of the injection process is normally divided into two broad and complex fields of analysis. On the one hand, the study of the internal and near flow of the injection nozzle which deal with the influence of the injector geometry on the flow pattern, the cavitation and flash boiling phenomena, the needle lift and wobble displacement, eccentricity and other manufacturing issues. On the other hand, the study of the external flow or also known as the observation of the spray patterns which, in this case, deal with fuel breakup, atomization, air-fuel mixing, evaporation and combustion processes. It is surprising how, knowing that the characteristics of the flow in and near the nozzle as well as the geometry of the injector through which the fuel flows significantly affect the patterns and development of the external flow, these processes are studied separately. Therefore, the trend is changing and there is an increasing tendency to analyze both processes together, although it is necessary to take into account the different phenomena that occur in the two fields and also the different time scales and duration of the two problems. For this reason, in addition to those corresponding to internal and external flow, an appropriate section has been added for those analyses dedicated to the study of both processes jointly.

4.3.1 Internal and near nozzle flow

The main challenges encountered in the description of multi-phase flow are associated with the following fundamental concerns: (1) liquid and gas flowing simultaneously in a pipe can adopt different geometrical arrangements, called flow patterns; (2) the flow mixture is compressible, so its density is continuously varying with changes in pressure and temperature; and (3) in addition to friction losses, a new type of energy loss occurs [59]. Multi-phase flow can be classified in a number of ways as Martí-Aldaraví [60] outlined: according to the combination of phases, on the basis of the type of distribution of the dispersed phase or depending on the geometry of the phase interfaces. Starting from the main objective of this thesis based on the study of the GDI injection process, the phases considered are only gas-liquid, the dispersed phase distribution is assumed to be heterogeneous and the interface is defined as dispersed.

The treatment of multi-phase fluids can be carried out under different approaches. Under the criteria of multi-phase models and focusing only on the study of internal flow, at least three approaches can be identified: the homogeneous Eulerian models, the multi-fluid Eulerian models and the interface tracking and capturing models.

4.3.1.1 Multi-fluid Eulerian models

The Eulerian multi-fluid model is the most complex of the multi-phase models which treats the phases as interpenetrating continua with independent velocity and temperature fields. In a gas-liquid combination phases, the gas phase is referred to as the primary phase, while the liquid phase is considered the secondary phase or also known as dispersed. The volume fraction is the distinguishing variable of both phases, the sum of which, by definition, must be unity. It should be mentioned that this model allows a more detailed description of the flow compared to the homogeneous Eulerian approaches.

The governing conservation equations of the multi-fluid model solved for each phase can be derived by conditionally averaging the local momentum conservation equations of the single-phase flow and coupling is achieved through the pressure and interphase exchange coefficients [61]. The approaches employed to compute these flows are analogous to those used for single-phase, but become more complex due to the addition of interaction terms and boundary conditions, without taking into account that twice as many equations have to be solved. It is true that the transfer processes of each phase are defined by their own equilibrium equations and are thus more accurate and detailed in

predicting phase changes than mixture or homogeneous approaches. For this reason, it is considered that multi-fluid models may be more suitable and useful for the analysis of transient phenomena, wave propagation and/or changes in the flow regime, as long as the dynamic and non-equilibrium interaction between phases is taken into account.

It should be noted that multi-fluid Eulerian models are computationally very expensive and demanding and the study of real cases of interest involves extremely challenging computational times. This, together with the experience acquired over the years of studies centred on the diesel spray, has led the scientific community to adopt more affordable models for the study of injection process. Therefore, there are few documented publications in the literature where multi-fluid models are used to study the flow behaviour during GDI injection.

Greif et al. [62] applied this two-fluid Eulerian model to the study of a gasoline-ethanol mixture where the five-phases injector flow was calculated with three different fractions of gasoline and ethanol. This was achieved by sharing the momentum field between the liquid phases of both fuels. The interfacial mass exchange was triggered independently and controlled by the properties of the fluid. Furthermore, air recirculation was introduced into the outlet planes, thus providing the fifth phase in the system. Mass transfer between the liquid and gaseous fuel fractions owing to cavitation phenomenon was addressed. The only drawback of this work was the impossibility to validate the results with experimental data, so although it is considered that the CFD tool applied through this new methodology offers a good basis for future studies, a validation of the aforementioned model should be carried out to affirm it.

Recently, Mishra et al. [63] developed a multi-fluid model integrated with the VOF interface tracking approach, model explained in more detail below, in order to capture the interface between liquid fuel, vapor fuel and de-gassed nitrogen. This approach is notably different from the available literature on degassing models for non-condensable gases, as these models assume that microbubbles that may not be physically stable already exist in the fluid stream and that the expansion of bubbles in low-pressure regions triggers cavitation. This new developed model made it possible to distinguish between the volume fraction occupied by vapor fuel and de-gassed nitrogen. Comparison of the predicted void fraction along the nozzle with available experimental data showed that this model significantly improved cavitation size/location predictions compared to existing single-fluid mixing models and multi-fluid simulation results. In addition, the appearance of cavitation patterns showed

the sensitivity that void fraction forecasts to model parameters. It suggested that monitoring the relationship between evaporation and condensation rate was essential.

4.3.1.2 Homogeneous Eulerian models

The homogeneous Eulerian flow approach is considered as the simplest multiphase CFD model. The fundamental concept of this approach is, unlike the multi-fluid model in which governing conservation equations are solved for each phase, to account for the mixture as a whole, so that the field equations should be expressed for the mass, momentum and energy balance in terms of the mixture properties. The two phases in the mixture are treated as a pseudo-single-phase flow by complementing the analysis with a diffusion equation that takes into account concentration changes. This approach assumes a local equilibrium between the continuous and dispersed phases, which share the same pressure. This means that at each point, the particles travel with the terminal slip velocity relative to the continuous phase. For this reason, the velocity components for the dispersed phases can be derived from algebraic formulations. In order to keep the approach comparatively simple, without compromising its generality, the following hypotheses can be applied to the model presented [64]: each of the two phases may consist of the same pure substance or, alternatively, each may consist of a different pure substance, both considered phases are supposed to be chemically inert, polar and electromagnetic effects are disregarded, all interfaces between phases are deprived of any physical properties including mass, surface tension, surface energy, etc.

This mixture model has been referred to in the literature in numerous ways: algebraic slip (mixture) model, diffusion model, suspension model, local-equilibrium model or drift-flux model. Among the advantages of this model are the reduced number of equations that need to be solved and, therefore, the speed of calculation; well-described particle size and other distributions; provides a clear description of the turbulence effect on the mixing of the dispersed phase. Despite the mentioned advantages, the implementation of this model also has certain disadvantages: even though the number of equations is small, the computing time can be significantly increased due to the use of small time steps; some difficulties in the convergence of the solution; only a few secondary phases are possible; and the consideration of processes such as mass transfer (evaporation) or chemical reactions, make the model much more complex. In addition, it has been proven that these apporaches can generate discrepancies, artificial discontinuities and numerical instabilities when applied to cases involving high-to-low pressure transients [61].

Unlike the two-fluid model explained above, the homogeneous Eulerian approach is simpler and more affordable even in complex applications. Moulai et al. [65] not only focused on studying the internal flow under flash boiling and non-flash boiling conditions but, in order to compare the results with experimental data, studied the behavior under submerged conditions. The calculation of the dimensionless flow coefficients exhibited a high consistency among the three conditions analyzed. Detailed observation of the cavitation formation in the nozzles reveals that vapor remains downstream and occupies a considerable volume of the counter-bore, suggesting that the counter-bore shape itself further expands the two-phase fuel flow. Downstream, large volume of vapor are generated under flashing conditions, although this vapor represents only a trivial quantity.

Strek et al. [66], under the assertion that prediction of spray behavior is particularly difficult due to the existence of cavitation, flash boiling, and plume/plume interaction, combined experimental diagnostics with an innovative in-house modeling capability in order to provide a multi-faceted vision of a multi-hole GDI injector. This new capability allowed to take into account cavitation and flash boiling by implementing a sub-model based on HRM concepts, in addition to considering compressibility and allowing for moving meshes. In these investigations, they reached similar conclusions to those of Moulai et al. [65] although they did reveal some differences in the mass flow compared to the experimental results, probably due to the assumption of a fixed needle position. Therefore, they proposed to extend the studies by including the needle movement in the simulation and a larger computational domain to be able to appreciate specific spray phenomena.

Chinmoy et al. [67] went further, not only taking into account the movement of the needle in the analysis but focusing specifically on the opening and closing phases of the injector. For this, they studied a mixture Eulerian approach with the well-known HRM sub-model for the phase change. One of the computational limitations encountered to faithfully study the transient phases of the injection is the impossibility to simulate the complete closure of the needle. For this purpose, the authors developed a sealing algorithm based on drag forces that halts the flow through the narrow gap between the needle and the nozzle. The study was carried out in evaporative but non-flashing conditions and observed the presence of vapor in both the opening and closing phases of the needle where the cross section is very narrow. They also witnessed fuel vapor in the injector sac at the end of injection and, after this time, liquid fuel dribble was captured leading to eventual jet disintegration. Residual liquid fuel was noticed to stick around the outlet wall of the counter-bore after the overall injection cycle was completed. Despite the fascinating advances made

with this study and the impressive results obtained, the authors left the door open for further research on the opening and closing transient phases due to their great potential and importance that they represent in the injection event.

Baldwin et al. [68] also included the transient character of the injection from not only the vertical movement of the needle but also took into account the lateral displacement called wobble. They demonstrated through the employment of the HRM model for phase change that a low needle lift results in vapor generation near the injector seat. In this research, the authors reaffirmed the complex nature involving the internal flow of the injector, as it contains many transient and interacting vortices, resulting in perturbations in the spray angle and fluctuations in the mass flow rate. The complexity of the internal flow also results in intermittent string flash-boiling when a strong vortex is injected and the resulting spray contains a thermal non-equilibrium vapor core (see Figure 4.4).

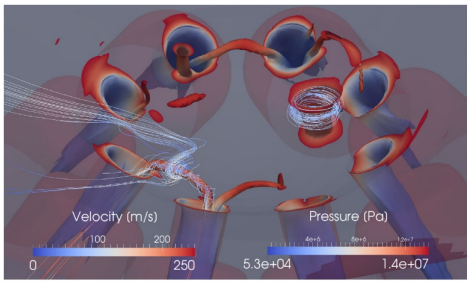

Figure 4.4: Transient and interacting vortices inside the injector sac which are unevenly distributed along the orifices. Adapted from [68].

Continuing with the previous objective, Jacobsohn et al. [69] set out to further investigate the complex and transient spray behavior associated with GDI technologies. For a better and more accurate understanding, they not only used RANS models for turbulence treatment but also employed LES approaches and included an accurate and unique sealing algorithm that allows to capture in detail the dynamics of the injector opening. After obtaining accurate results, the authors suggested studying the entire injection process using high-fidelity LES approaches, not only emphasizing the opening phase.

Although in recent years more interesting models have emerged to deal with multi-phase flows, which will be explained in the following paragraphs, recently Gärtner et al. [70] employed a homogeneous mixture Eulerian approach to study the problematic phenomenon of spray collapse that takes place under rapid evaporation conditions aimed at favoring fuel-oxidizer mixing and subsequent combustion. The work is focused on the study of severe spray collapse using a new solver developed by the authors, which was validated on a single-hole injector and data from commercial software studies carried out by Guo et al. [71]. In this research, they varied both the discharge

pressure and the injection temperature demonstrating how the position of the Mach disk is mainly influenced by the chamber

pressure, while the increase in velocity and also the extent of the shock wave were predominantly fixed by the injection temperature (see Figure 4.5). Thereby it was shown that the parameter R_p (Equation 3.30)normally used to define the superheat ratio and thus classify the flashing regimes, is not accurate in describing the behavior of the jet and subsequent spray collapse. The investigation also confirmed that an isolated region of low pressure in the center of the spray causes the jet to collapse. This work leaves the possibility of further investigations on the flow behind the shock system to obtain a holistic view of the spray behavior and to provide a quantitative prediction of the liquid penetration length. In addition, it is proposed to study in depth a criterion to determine the spray transition to plume collapse.

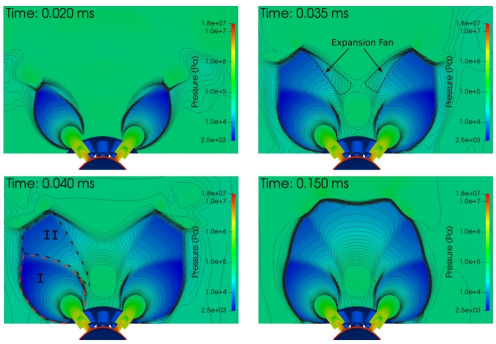

Figure 4.5: Spray evolution in the first step of the injection process showing the expansion of the jets, the Mach disk formation and the shape they adapt over time. Adapted from [70].

4.3.1.3 Interface tracking and capturing models

Flow problems with moving boundaries and interfaces include fluid-particle, fluid-object and fluid-structure interactions; free-surface and two-fluid flows; and flows with moving mechanical components. These problems present several computational challenges [72]. Among them, the boundary position is only identified at the starting time; its placement at subsequent times has to be determined as part of the solution [73].

Numerical simulations of free-surface flows involve the coupling between the equations governing the dynamics of the fluid and the free-surface. In general, there are two different approaches to the numerical simulation of free surface flows. Depending on the physical characteristics of the problem, the techniques used fall into two broad groups: interface-tracking or interface-capturing [74].

- Interface-tracking method: an approach that considers the free surface as a sharp interface whose motion is monitored. In the model, the flow

field is discerned by a conservative finite-difference discretization, and the interface is explicitly presented by a detached, unstructured mesh that travels through the steady mesh. The interface is continuously deforming and the application of moving mesh methods usually results in distortion of the elements, so it is necessary to generate a new grid as the simulation progresses and project the solution from the old mesh to the new one [75]. Although this method stands out for its high accuracy [76] and enables interface structures smaller than the mesh size to be solved, in complex 3D applications, this procedure is extremely difficult and time-consuming.

- Interface-capturing method: in this technique for two-fluid flows, the computations are based on fixed spatial domains, where an interface function, marking the location of the interface, needs to be computed to "capture" the interface. The form of the free surface is obtained by computing the fraction of each cell close to the interface that is partially occupied. There are different methods to carry out this process. Among the best known, are the VOF scheme, which focuses on solving a transport equation for the fraction of the cell occupied by the liquid phase, or the Level-Set formulation where the surface area is defined as that for which a level-set function is equal to zero. The accuracy of the interface-capturing techniques generally depends on how accurate the free-surface function is represented. Therefore, mesh resolution becomes a prime factor in determining the accuracy of this technique [77].

There is also the possibility of combining methods, known as hybrid techniques, which do not belong to either of the two categories previously discussed. These models borrow features from both interface-tracking and interface-capturing methods.

Volume-of-Fluid

The VOF approach [78] is based on the classical conservation of mass and momentum equations and, in addition, adds a transport equation to account for the existing volume fraction of the fluid in each cell, denoted by X. The value of the variable is $X = 1$ when the cell is full of liquid, while if the cell is full of gas and therefore empty of liquid, $X = 0$. Taking the continuity equation as a reference, the evolution of the variable X can be described from Equation 4.1. Under the assumption of incompressible flows, the equation is

invariant with respect to the exchange of X and 1-X; but for this the mass conservation has to be strictly fulfilled.

$$\frac{\partial X}{\partial t} + div(X\mathbf{U}) = 0 \tag{4.1}$$

One of the critical points in this approach is the way to discretize the convective term of Equation 4.1. Higher order schemes are usually given preference since lower order schemes (such as the first order accurate upwind method) daub the interface and involve a mixing of the two fluids that is considered artificial. The model must guarantee the non-generation of overshoots or undershoots since the variable X must satisfy the premise $0 \leq X \leq 1$. However, it is fortunately feasible to obtain schemes that preserve the sharp interface and result in monotonic patterns of X across it [79]. Actually, there are numerous interface reconstruction algorithms and high-resolution differencing schemes. Noh and Woodard [80], through the well-known simple line interface calculation (SLIC), represented the interface of each cell by vertical or horizontal lines. Seeking greater accuracy, Youngs [81] proposed the piecewise linear interface calculation (PLIC) method using, in this particular case, oblique lines to reconstruct the interface. However, it is well known that the application of the aforementioned models is not easy on unstructured meshes. That is why other approaches that combine high-resolution schemes with compressive schemes arose, such as High Resolution Interface Capturing (HRIC) [79] or Flux-Blending Interface-Capturing (FBICS) [82], among others [83].

One of the outstanding advantages of the VOF method is the fact that several algorithms can be employed to advance the interface so that the mass can be conserved while preserving a sharp depiction of the interface. However, a disadvantage of the VOF method is the point that it is difficult to estimate correct curvatures because it introduces a step discontinuity at the interface [84]. In addition to this, any changes associated with the breakup or coalescence of droplets or bubbles are barely noticeable unless the resolution of the mesh is extremely fine.

Another perspective can be given to this approach by treating both fluids as a single fluid whose properties change in space depending on the volume fraction of each phase [73]. To that end, it is not necessary to define boundary conditions for the interface because it is not considered as a boundary, but the interface is defined as the zone where the fluid properties change sharply. However, the solution of Equation 4.1 implies that the kinematic condition is met, and the dynamic requirement is also accounted. It may happen that the surface tension is meaningful at the free surface, and could be considered

by treating it as a body force [85, 86]. The surface tension force normally acts only in the interface region and can cause problems when surface-tension effects become dominant as may be the case for droplets or bubbles with small diameters and low velocities. If this were the case, the pressure term should be in accordance with the body force term representing the surface-tension effects [73].

This method is one of the most widely used in recent years in the study of GDI process, due to its excellent features and because it is a simple multi-phase model suitable for resolving sharp interfaces. It is important to mention that the studies presented in the literature where this model is used to address the multi-phase fluid are divided into two groups. On the one hand, those that adopt the VOF approach but sharp or nearly sharp interface between liquid and vapor phases is not expected, and therefore do not implement the interface-capturing function and, on the other hand, those that seek a higher accuracy in the interface and, therefore, use any interface-capturing scheme presented in the literature for it.

Within that group where interface-capturing function is not necessary, one of the first to use the VOF model to study in- and near-nozzle flow were Saha et al. [88] in their efforts to contribute to the ECN network in the creation of this extensive and comprehensive framework. The studies were carried out for a fixed needle position, regardless of the transient nature of the injection process. The authors accounted for turbulence effects using RANS approaches and captured the existing phase changes from the HRM model. They addressed different operating conditions: non-flashing and evaporative, non-flashing and non-evaporative, and flashing conditions. During this first contact with the models and domain, they observed slight cavitation-type phenomenon inside the nozzle orifices and flash boiling phenomenon in the region near the nozzle when the liquid fuel is

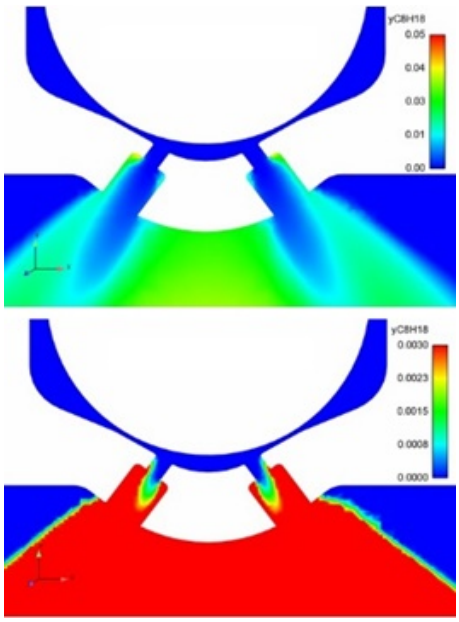

Figure 4.6: Flash boiling phenomenon in the region near the nozzle. Adapted from [87].

subjected to a superheated environment (see Figure 4.6). Furthermore, a remarkable hole-to-hole variation in mass flow rates was also observed for all orifices under all tested conditions. Given the success of the implementation of these models, the authors suggested extending the research by adding motion to the needle and treating turbulence from LES approaches. A short time later and based on the same assumptions, models and operating conditions, Saha et al. [87] extended the study reaching similar conclusions and highlighting the need for a larger computational domain in order to analyze in detail the near field and avoid the possible influence of the outlet in the holes.

Payri et al. [19] also joined to contribute to the ECN network, ventured not only to the experimental analysis but also to the computational study of the injection process. They used the VOF method without interface-capturing scheme to simulate the two-phase flow (liquid and vapor) inside the nozzle, the HRM approach for the phase change and treated the turbulence with RANS models. In this case, the needle was also considered in a fixed position. The added value of this work is the calculation not only of the mass flow rate in the orifices both in the inner orifice and in the counter-bore but also of the momentum flux. The implementation of the so-called Adaptive Mesh Refinement (AMR) allowed them to save computation time. The authors obtained fairly good agreement when comparing the results with the experimental injection rate data even though some values were outside the confidence range of the experiments. On the other hand, they highlighted the perfect agreement of the results obtained from the rate of momentum calculation, as this factor put more weight in deciding that the frontal configuration is the appropriate methodology to measure the spray momentum of a multi-hole GDI injector.

In later years, Saha et al. [89] gradually implemented and analyzed the improvements proposed in earlier work. Under the same framework, which means VOF model without activating interface-capturing option for two-phase flow, HRM for phase change and RANS for turbulence treatment, they studied the influence of the discharge volume on the jet development reaching the conclusion that for the study of macroscopic variables 9 mm of outlet plenum was enough, but if what is desired is to appreciate the vapor formation patterns or the full spray visualization, then it is necessary at least 18 mm. In addition to the computational domain, they performed a mesh independence in order to obtain the minimum size necessary to obtain accurate results. Not only that, but they also realized the influence of the mesh orientation on the development and shape of the plumes. This research also brought to light the existing deviation of the spray with respect to the geometrical axis of the injector, a phenomenon that the authors suggested to study further. In this work,

although the efficiency of AMR had already been proven in previous studies [19], the authors continued with the use of a fixed mesh. In addition, they used fixed needle lift but studied different positions, observing how low needle lifts significantly affected the flow pattern. Finally, the authors analyzed the liquid penetration in the early stages of injection using an Eulerian approximation. The closeness of the results to experimental results indicated that applying an Eulerian-Lagrangian Spray Atomization (ELSA) model could be both novel and potentially accurate.

Once the fundamentals for the study of in- and near- nozzle flow in GDi injectors had been established, in this particular case, Saha et al. [90] focused on studying the influence of the parameters that make up the HRM phase change model, in addition to the turbulence model, on the development of the spray. This study demonstrated the capability of HRM to predict non-flashing yet vaporizing, moderately flashing, and intensely flashing scenarios. It was found that the local pressure and physical properties as well as the time scale constant have a considerable effect on vapor production and are, therefore, dominant factors in vapor distribution. On the contrary, the void fraction also present in the HRM formulation is not an influential variable in the results. With respect to the comparison between turbulence models, the RNG k-ε turbulence model proves to be an economical, yet physically correct turbulence modeling approach for the GDI spray applications because it tends to minimize the physical vapor buildup in small outlet domains.

Torelli et al. [91] motivated to study the influence of fuel on atomization and spray characteristics and eventually on engine performance, analyzed the internal flow in a typical diesel injector using two gasoline-like naphtha fuels and compared the results with n-dodecane. In this particular case and based on the experience acquired in the literature, they employed the VOF model without interface-capturing, again the HRM for the phase change and RANS models to capture the turbulence phenomena. The results revealed that injector performance and tendency to cavitation are affected by the fuel properties. For all cases, the strong correlation between cavitation magnitude and saturation pressure was confirmed, which means that the higher the volatilities, the more cavitation is expected. It should be noted that these studies included the transient behavior of the injection and therefore the needle had an assigned lifting profile. This study demonstrated how cavitation has a tendency to appear in the needle seat and orifices when the space between the needle and the nozzle is very small. On the other hand, the authors also realized that the advantage presented by the low viscosity of a fuel becomes less effective at higher temperatures when the differences between relative viscosities are smaller.

The perseverance of Saha et al. [92] and the desire to understand in detail the GDI injection process led them to explore in this case three types of thermodynamic conditions: non-flashing, moderate flashing, and intense flashing. These studies led them to appreciate how aggravating the degree of flash boiling causes the plumes to have a greater tendency to interact and collapse with each other. In addition, and following the lines of the previously mentioned studies [91], different surrogate fuels other than iso-octane were analyzed, such as ethanol and two mixtures of both fuels at 30% and 85%. As a result, it was obtained that blends of isooctane and ethanol were more volatile than individual constituent species and therefore experienced enhanced flashing.

As noted and mentioned throughout the document, flash boiling is a topic of widespread interest among the scientific community. Guo et al. [71] joined the study of flash boiling using a single-hole GDI injector. Based again on a VOF model without interface-capturing and the HRM for the phase change, the authors varied the range of fuel temperatures and ambient pressure looking for different superheat conditions. The authors demonstrated in this study how the drastic vaporization increased the pressure inside the liquid core, so that the two-phase flow was under-expanded and a region of low pressure is generated, which is believed to be the starting zone of the spray collapse phenomenon.

Recently, since spray collapse and flash boiling phenomena, studied in the last few years, are still not fully understood, Guo et al. [93] applied the knowledge acquired in recent years to the study of spray collapse under flash boiling conditions in a multi-orifice injector. Not only this, but they also joined the study of spray behavior using different fuels such as n-hexane and propane. The obtained results closely matched the experimental data and exhibited how the models captured the near-nozzle shock structures witnessed in the experiments. The authors proved that the fuel properties had a significant influence on the spray behavior. Thus, iso-octane did not present under-expanded jets at the operating conditions tested, while in the case of n-hexane, this expansion was observed and even in propane the strong expansion made the flow become transonic and generated a unique shock structure near the nozzle outlet (see Figure 4.7). This study allowed to attribute the formation of the spray collapse under flash boiling conditions to the pressure decrease in the spray center induced by the low pressure cores and to the isolation effect caused by the interaction between plumes, which contributed to preserve the pressure differential between the spray center and the environment.

Of the latest work published in the literature under this framework is the one carried out by Jia et al. [94] who focused on studying something

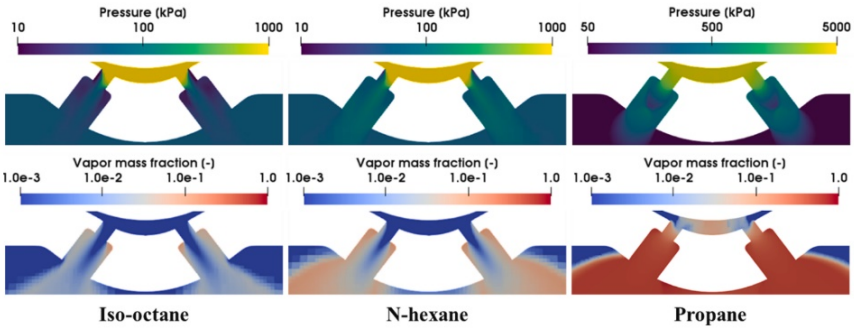

Figure 4.7: Pressure (top) and vapor mass fraction (bottom) distributions in orifices for iso-octane, n-hexane and propane at quasi-steady state conditions. Adapted from [93].

innovative in GDI injectors such as the application of divergent-convergent hole geometry. This convergent-divergent shape does not refer to the typical shape seen in diesel injectors [95] but it tends to be oval. In this work they studied 6 different types of geometries varying the medium diameter ratio and the position of the medium diameter. The results showed that cavitation was reduced with the increase of the medium diameter ratio while the discharge coefficient and orifice exit velocity increased. In addition, the average velocity at the outlet of the injector increases with the position of the medium diameter. Finally, turbulent kinetic energy at the nozzle exit decreases with the increase of the medium diameter ratio. This work opens the debate on which geometry is the most suitable to be applied in future GDI engines, which suggests the need for further research in this branch of knowledge.

Considering the work presented so far, all of them, apart from the use of the VOF approach to deal with the two-phase flow, and the use of RANS models for the treatment of turbulence, employ the Homogenoeus Ralaxation Model as phase change models. In recent years, the popularity of HRM has increased enormously due to the good results offered, but it must be said that there are also other models of phase change in the literature, which have also been used in the field of gasoline direct injection. An interesting example is the work carried out by Giussani et al. [96] who implemented a phase change model based on Schnerr and Sauer's [97] theory to study the flow behavior including the possible formation of cavitation inside the injector orifices during the first phases of injection. More recently, Mouvanal et al. [98] also left the phase change in the hands of the Schnerr and Sauer model, in this case, to study the fuel residues that remain in the injector sac and the orifices once

the injection has finished and to analyze the purging phenomenon with gas from the cylinder.

After presenting those works in which no sharp or near sharp interfaces between the liquid and vapor phases are expected and therefore the authors, in order to reduce computational cost, did not implement the interface-capturing function, it gives way to those research works in which added value and greater accuracy in the results, among other factors, were sought. For this purpose, the VOF model works together with an interface reconstruction algorithm, which increases the computational cost but offers a better precision in the detection of the interface.

As part of this scope, Befrui in collaboration with many different researchers [99–102] carried out one of the first studies based on high-fidelity simulations not only by employing interface reconstruction schemes but also by treating turbulence with LES approach. All their works, which were focused on the study not only of in- and near-nozzle flow but also on the characteristics and behavior of primary atomization, were encompassed in the same framework. They employed a VOF-LES as a tool to study the influence of nozzle design on key spray parameters. They justified the use of VOF as a simple and flexible method to simulate multi-phase systems with free surfaces, especially in cases where surface tension effects are not dominant. To avoid numerical dispersion and thus generate a diffuse interface, Befrui employed an advance method formulation in Open-FOAM, which incorporated the phase transport equation that includes a "compression velocity" term which acts to "compress" the VOF interface and maintain a sharp interface resolution. This technique was compared with alternative interface reconstruction techniques [103], obtaining satisfactory results and being close to experimental measurements and theoretical analysis.

One of their first works, Befrui et al. [99] combined internal nozzle flow analysis with specific models to study the development of the jet, the external flow. From the study corresponding to the internal flow, which is the subject of this section, it could be observed how the presence of the needle influences the non-uniform distribution of the fluid along the orifices (Figure 4.8). In addition, the flow direction was affected by the existing velocity gradients and the associated turbulence and vorticity, resulting in a separation of the flow with respect to the orifice entrance. This effect generates a pressure loss and a consequent reduction of the nozzle orifice discharge coefficient, but the advantage is that it favors the breakup of the liquid jet.

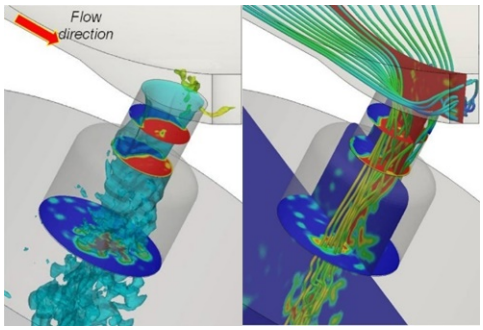

Figure 4.8: VOF-LES iso-surfaces and streamlines results. Adapted from [99].

Later on, Befrui et al. [100] focused on studying the influence of nozzle design and features (length-to-diameter ratio (l/d), counter-bore, and nozzle tapered geometry) on spray structure and primary atomization. The studies suggested the importance of hydraulic flip phenomena in the feature of the nozzle flow and the jet primary breakup process. The authors also noted how the greater discharge coefficients of the counter-bored and large l/d nozzles allow smaller nozzle sizes for the same static flow as the basic GDI nozzle geometry. This reduction in core jet diameter results in better jet breakup characteristics. Finally, in addition to highlighting the potential of VOF-LES simulations, the authors encouraged the use of more realistic geometries to observe in detail the actual spray behavior.

In their next contribution, Befrui et al. [101] and Shost et al. [104] introduced one of their earlier suggestions, the study of skew-angle orifices. In this case, they compared a counter-bore hole with a straight hole. The simulations demonstrated good predictability of the macroscopic characteristics of the spray in the near field and also highlighted the effect of the counter-bore nozzle on the primary atomization of the jet, through the influence on the instability of the jet interface and, most notably, the physical interaction with the atomization plume. Extending this last study and using only counter-bore orifices, Befrui et al. [102] compared with experimental images the spray structure at the nozzle outlet. In addition, they calculated the droplet size and velocity distribution in the near field in order to correctly initialize and enable a complete description of the plume initial conditions for Lagranagian spray simulation.

Not only did Befrui and colleagues rely on high-fidelity simulations to study in- and near-nozzle flow, but also researchers such as Tu et al. [105] used the VOF-LES approach in this case to study the effects of counter-bore geometry on near-field spray characteristics. The results revealed that varying the l/d ratio of the inner hole had a greater influence on the spray characteristics than the counter-bore. A reduction in l/d resulted in an increase in mass flow, velocity, spray angle and reduced droplet size and breakup length. Increasing the spray angle can result in impacts on the counter-bore wall depending on the l/d ratio of the counter-bore, which can form undesirable deposits. The air

entrainment inside the small counter-bore improves the mass flow rate from the inner hole. The presence of interconnected ligaments inside the counter-bore cavity and below it leads to deformation and secondary breakup.

Wang et al. [106] focused on studying the deposits generated in the nozzle which greatly affect the spray behavior and thus the combustion performance and associated emissions. In this case, the interface reconstruction model proposed by Befrui is left aside and instead a VOF-LES is applied with an interface-capturing scheme such as PLIC. Thanks to the accuracy provided by the model, the authors determined how the rough surface of deposit gave rise to additional cavitation inception inside the counter-bore and, therefore, restricted the passage area leading to losses in mass flow rate. The deposits inside the counter-bore act by restricting the phenomenon of recirculation and air entrainment which worsens the subsequent atomization of the spray and results in what is known as coked injector.

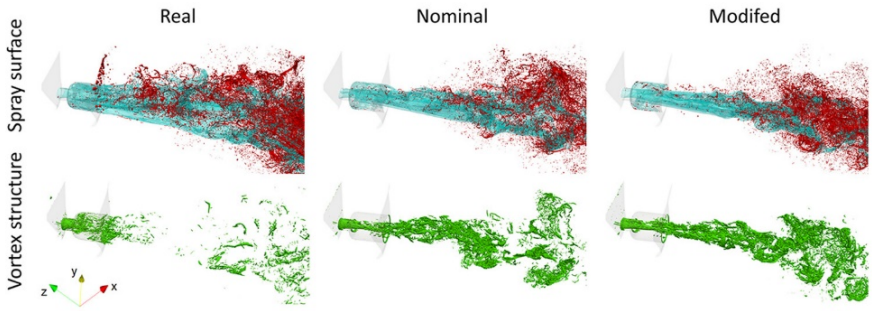

Figure 4.9: Spray and vortex structures in the upstream regions in the different nozzle geometries. Adapted from [107].

The most recent work in the literature under the same framework is that of Yue et al. [107] where they applied the same scheme as in the above mentioned work, a VOF-LES with interface reconstruction based on the PLIC method. This study was focused on the transient characteristics of the spray during the start of injection and the impact of imperfections and geometry details resulting from the manufacturing process. For this purpose, a nominal geometry and a modified geometry were considered. Significantly different near-field spray behaviors in terms of injection velocity, spray morphology and primary breakup mechanism were predicted using different nozzle geometries, which is mainly attributed to realistic surface finish and manufacturing defects (see Figure 4.9). The high-resolution geometry predicts a lower injection velocity, a larger spray opening and a slower breakup rate with an evident presence of tip wetting compared to the ideal geometry. Through this study

the authors bring to light the importance of injector manufacturing details, which are normally neglected in fuel injection studies and have a meaningful impact on the spray development process, so they must be taken into account for design optimization. In addition, this study suggested analyzing not only the transient phase of injector opening but also its closing, a study that may provide results of interest to the scientific community.

Despite all the work mentioned above, there are still many aspects to understand during the injection process. The complex nature of the jet in the first few millimeters of the near field means that it is often not possible to determine the characteristics of the spray experimentally. For this reason, and being the only work known to date, Zhang et al. [108] modeled in detail, using DNS approach, the effect of the internal flow on the primary atomization of the spray (Figure 4.10). The study of primary atomization from DNS techniques requires the resolution of sharp interfaces separating the gas and liquid phases so the mass and momentum conserving VOF method was employed. This study included the effects of inlet boundary condition, numerical method, and mesh resolution affirming that the proposed model is effective in resolving macro-scale and micro-scale breakup features. The study revealed spray behaviors of great interest to the scientific community such as the asymmetric behavior of the jet spray when introducing a nonzero injection angle which included an azimuthally varying velocity within the liquid jet. The authors wanted to emphasize that the study performed included only a short physical time compared to the entire duration of the injection of the operating conditions, thus not reaching a statistically steady state. For this reason, and with a view to measuring the properties of the time-averaged two-phase

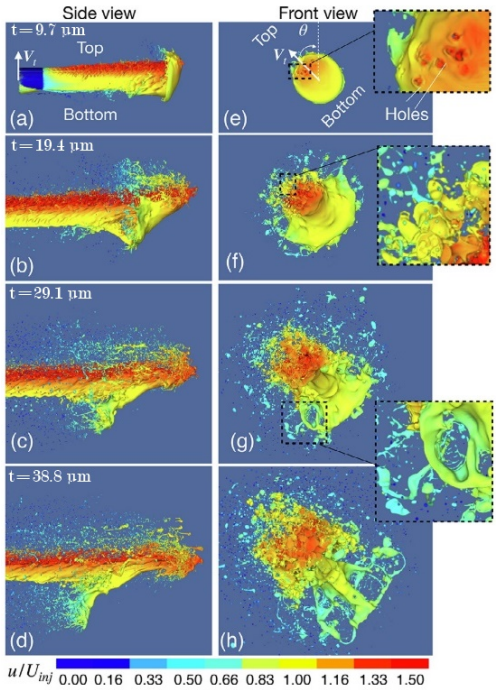

Figure 4.10: Temporal evolution of the jet head from the side (a-d) and front (e-h) views. The gas-liquid interfaces are colored by the streamwise velocity. Adapted from [108].

turbulent flow, they encourage running the simulation for a much longer time (twice or even more), which would provide a plus to the analysis.

Level-Set

Osher and Sethian [109] introduced another type of interface-capturing methods, which are grounded on the level-set (LS) formulation. The surface is specified as that on which a level-set function $\varphi = 0$. Other values of this function are unimportant and to be a smooth function, φ is characteristically initialized as the signed distance from the interface. Equation 4.2 then represents the evolved function as a solution of the transport equation.

$$\frac{\partial \varphi}{\partial t} + div(\varphi \mathbf{U}) = 0 \tag{4.2}$$

The advantage of this approach over the VOF method is that φ changes smoothly through the interface while the volume fraction X is discontinuous in there. However, in case function φ becomes overly complicated, it can be re-initialized.

In the field of GDI, the implementation of the level-set methods has not been widely accepted perhaps largely due to the lack of conservation of volume or mass even though it is considered a more accurate methodology in capturing the interface. Nevertheless, there are some works published in the literature in which this approach has been coupled with the VOF method to study not only the characteristics of the internal flow, but also to capture the bubbly flow in addition to the liquid breakup, thus being able to study the primary atomization or what is the same, the first droplets formation at the outlet of the injector. The coupling of these two interface-capturing methods combines the advantages and overcomes the disadvantages of both. The VOF method overcomes the disadvantage of nonconservation of mass in LS method whereas the level set function outweighs inaccuracy of curvature and bad smoothness of discontinuous physical quantities near interfaces, which makes it a powerful method to take into consideration. Arienti et al. [110] were among the first researchers to couple the mass conservation properties of the VOF approach with the accurate surface reconstruction properties of the level-set method to study the features of the early stages of atomization. Although the work carried out was not specifically focused on GDI studies, it is also interesting to mention it to see the possible scope of its application. The authors emphasize that the Eulerian-to-Lagrangian transformation achieved with this hybrid way of dealing with multi-phase flow can allow simulations on relatively large domains if carried out in the context of adaptive mesh refinement with block

structure. The limits of this hybrid approach are dictated by the mesh spacing and the number of refinement levels that can be allowed in the simulation. However, further work would be needed to improve the performance of the method to accelerate the convergence of the pressure equation in the mesh hierarchy.

Bode et al. [111] developed a new code called CIAO, which uses a highly accurate interfacial flow solver and combine the advantages in mass conservation and accuracy of different methods for multi-phase flows by approaches such as CLSVoF method (3D unsplit forward/backward Volume-of-Fluid approach that is coupled to a level set method [112]). They included in the in- and near- nozzle flow studies the phenomenon of cavitation and hydraulic flip, which have a crucial impact on the development of the spray, and to consider the influence of this phase on the primary breakup. Three clearly differentiated but combined zones are examined for the study, as depicted in Figure 4.11: Internal Nozzle Flow LES (INF LES) considering the exact injector geometry, highly resolved Primary Breakup DNS (PB DNS) in the vicinity of the nozzle, and Far-Field Lagrangian Particle-based LES (FF LP-LES) downstream. From these studies, it was concluded that taking into account the cavitation phenomenon made the simulation more realistic, thus predicting better penetration results, spray angle and velocity distribution. In addition, it was found that it was necessary to take into account the spray deflection due to the hydraulic flip phenomenon as it was the only accurate way to predict the droplet distribution. The authors noted some inaccuracies in predicting gas entrainment in the injector and suggest improving the hydraulic flip model to predict this effect correctly. In addition, they also suggest to investigate the change in cavitation and hydraulic flip along the transient injection since these presented works only take into account the steady state of the injection.

4.3.2 External flow

4.3.2.1 Introduction and basic descriptions

Once presented the works corresponding to the study of in- and near- nozzle flow whose studies are mainly based on analyzing the influence of the injector geometry on the flow characteristics, the phenomena of cavitation and flash boiling, the influence of needle lift and lateral movement (wobble) and other manufacturing issues, the research present in the literature is based on analyzing the behavior of the spray when it leaves the injector where the liquid fuel breakup process, atomization, air-fuel mixture formation, evaporation and combustion processes, among others, are taken into account. This division is carried out to study the processes separately in detail and because of

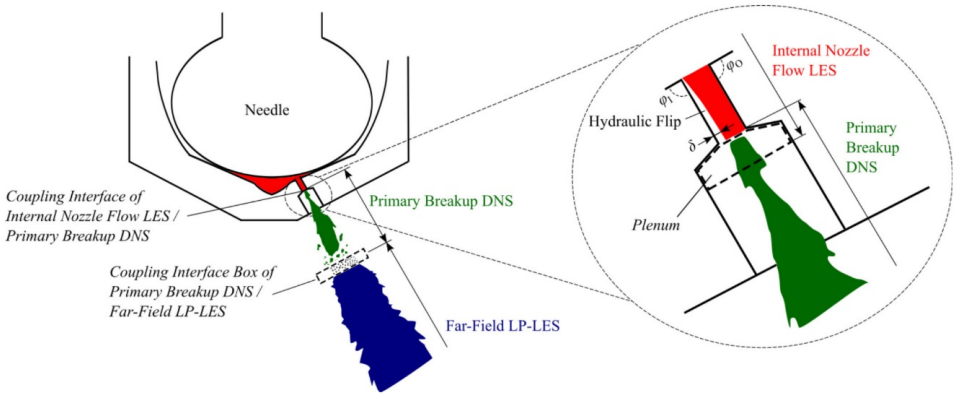

Figure 4.11: Schematic of the discretization carried out to study the hydraulic flip phenomenon and to couple the different phases of the spray to study the spray pattern characteristics. Adapted from [111].

the different nature of the flow. The internal flow is considered to be *continuous*, mono-phase liquid or multi-phase when cavitation and flash boiling are taken into account; while the external part, the flow is defined as *dispersed* multi-phase.

The present section gathers the state of the art of all those works based on the study of the spray behavior. This also includes those researches where internal and external flow are coupled in order to take into account the influence of the upstream flow behavior and to have a better representation of the reality. It should be noted that coupling internal and external flow is a very complex process that involves certain difficulties and high computational time and therefore, these investigations are not yet so widespread.

As it is already mentioned, the modeling of spray and associated phenomena refers to a subset of discrete phase particle modeling that describes the breakup of a liquid flow considered continuous in droplets. Most industrial processes and applications requiring this type of analysis, such as internal combustion engines, involve the transformation of liquid phases into vapor. The objective for effective combustion and engine performance is to obtain droplets as small as possible so that the resulting mixture between the liquid and the ambient gas is as efficient as possible. The disintegration of the liquid into smaller droplets, known as the atomization process, is divided into two main phases: primary atomization and secondary atomization. Primary atomization makes assumptions about the physics inside the nozzle and calculates an initial droplet size in the region near the nozzle. On the

other hand, secondary atomization models droplets that travel through the domain where they become hydrodynamically unstable and break into smaller droplets. These droplets can undergo different processes on their path such as collision or coalescence where they create larger droplets and thus change the dynamics of the spray plume. The treatment can be carried out under different schemes: Eulerian-Langragian or Discrete Droplet Model (DDM), Eulerian-Eulerian or Eulerian Spray Atomization (ESA) model and Eulerian-Langrangian Spray Atomization (ELSA) model.

Eulerian-Lagrangian. Discrete Droplet Model (DDM)

The Eulerian-Lagrangian (EL) model or also known as DDM is the conventional approach used in recent years in engine applications, not only because of its great effectiveness in predicting macroscopic and microscopic spray parameters, but also because of its high computational efficiency as well as its adaptability to all the processes taking place in a combustion chamber: evaporation, combustion, emissions and heat transfer, among others. One of the main assumptions of this model is that the liquid phase has a negligible volume fraction compared to the gas phase. Despite this, due to its reasonable efficiency, it is also widely used for dense jets.

The velocity and position of droplet or bubble parcels present in the main flow are calculated from the integration of the particle equation of motion. For this reason, these approaches are based on the use of two different numerical approaches; the carrier phase is described by means of an Eulerian description, while the disperse phase, composed of the so-called parcels, is represented by means of a Lagrangian description. It is important to clarify that when referring to parcels, it implies a group of identical droplets with the same properties (radius, velocity, temperature, etc.) that do not interact with each other. As mentioned above, this statistical treatment of droplets is also known as DDM and was originally developed by Dukowicz [113]. This model stands out for being mainly based on the resolution of the equations governing the liquid part of the spray from the Monte-Carlo method [114]. This implementation saves computational time when compared to other types of approaches such as the Continuum Droplets Model (CDM) where each droplet is represented and calculated individually.

Throughout the injection process and up to the moment of evaporation of the liquid, the droplets that make up the spray are subjected to numerous processes. The interaction between phases is taken into account by the inclusion of source terms, pondered by the void fraction, in the governing conservation equations. The source terms are defined from different sub-models, which play an indispensable role in the success of the Eulerian-Lagrangian model

since the interface cannot be solved directly mainly because of existing computational limitations. These types of simulations also base their accuracy on the mesh resolution, which is considered a key parameter in the models. The mesh should not be too refined due to the existence of limitations with the void fraction variable. To avoid numerical diffusion and thus a bad estimation of the spray evolution, the mesh should not be too coarse. To determine and clarify this dilemma, Abraham [115] demonstrated that a minimum two cells covering the orifice exit are required to successfully model a turbulent gaseous jet (the characteristic length of the problem is defined from the orifice exit diameter).

Eulerian-Eulerian model. Eulerian Spray Atomization (ESA) model

The Eulerian Spray Atomization (ESA) model is based on a homogeneous flow description, similar to the one described in the internal nozzle flow state-of-the-art section, under an Eulerian framework; in other words, the air-fuel mixture is considered as a single fluid and the mixing process is modeled by means of two new transport properties: the liquid mass fraction and the interfacial surface density. The density of interfacial area is typically denoted by Sigma (Σ) while the liquid mass fraction is denoted by Y. Hence, the literature refers to the strictly Eulerian model as a Σ-Y approach. It should be mentioned that this model does not include a transition to Lagrangian particle tracking and is commonly used to model internal and external flow together. The Σ-Y model, originally developed by Vallet and Borghi [116], is based on an Eulerian representation of the spray atomization and dispersion by means of a single-fluid variable density turbulent flow. The mentioned approach considers the liquid/gas mixture as a pseudo-fluid with a single velocity field. The assumption that injection takes place under large Reynolds and Weber numbers allows the separation of large scale flow features, such as mass transport, from processes occurring at smaller scales such as atomization. The scheme includes a transport equation for the interfacial surface density that allows capturing the rate at which the surface energy is created. This equation involves the production and destruction terms that account for the physical phenomenon of interface stretching and collapse. On the other hand, a new transport equation is added for the liquid mass fraction, which controls the dispersion of the liquid and models the turbulent mixing of the liquid. The liquid mass fraction is linked to the average density of the two fluids. The knowledge of the interfacial surface density, liquid mass fraction and mean density allows the determination of the droplet Sauter Mean Diameter (SMD) needed to define the primary atomization.

Eulerian-Langrangian Spray Atomization (ELSA) model

The Eulerian-Langrangian Spray Atomization (ELSA) model, originally developed by developed by Vallet et al. [116], is one of the schemes known for its ability to integrate the analysis of the two different fields of study mentioned above (internal and external flow). This approach not only deals with the different phenomena taking place in both fields but also with the different time- and length- scales of the problems. The dense region is near the nozzle with complex and irregular topology of the spray and the dispersed phase is a far-field of the spray with a collection of droplets (see Figure 4.12). In this approach, the dense spray region is modeled using an Eulerian-based homogenoeus mixture model while the disperse spray region is modeled using a Lagrangian droplet model. In particular, the dense spray region is accounted through the use of two additional scalar transport equations: an equation for the liquid mass fraction and liquid-gas interface area density. In the Eulerian phase, spray atomization is modeled by introducing source terms in the transport equations that depict the key physical mechanisms, such as primary breakup of the liquid film, secondary breakup of the droplets, as well as collision and coalescence of the droplets. Once the spray is considered to be sufficiently dispersed, the droplet distribution function (DDF) is estimated using the liquid mass fraction and the area density of the liquid-gas interface, and it is then used as input to the Lagrangian droplet model [118].

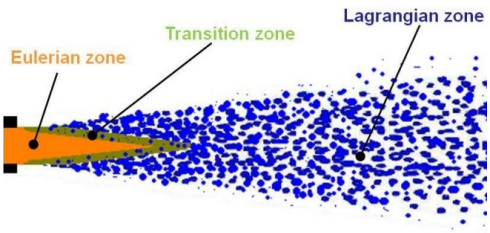

Figure 4.12: ELSA spray discretization depending on the treatment of each phase. Adapted from [117].

Despite the advantages of studying the combined internal and external flow spray, employing this type of model is computationally quite expensive. In addition, arguably a disadvantage of this model is that the resolution of the mesh near the nozzle is sensitive and difficult to adequately represent this dense near-field zone to capture the primary atomization, as well as a severe imbalance loading caused by the large droplets created near the near field. This type of approach is a growing alternative to DDM, but it is still under development and, therefore, there are few studies in the literature.

Having briefly explained the fundamentals of each of the schemes that can be employed for the investigation of spray behavior, the review of the state-of-the-art related to these works will be grouped according to whether the

study focuses only on the development of the jet or whether it also takes into account the phenomena inside the nozzle (coupling).

4.3.2.2 External flow analysis in gasoline nozzle flow applications

As previously commented, a significant part of the scientific community has opted for EL spray model for their research, although it has certain limitations such as the high mesh (size and structure) and the time-step dependence. An inadequate mesh resolution results in erroneous predictions of vapor and liquid velocity and fuel concentration values which induces some numerical diffusion. The position of the injector and its holes with respect to the mesh is another detail to take into account as it greatly influences the result. Despite the above, this model offers high accuracy in the results, which is the reason why it is so widely used in studies of spray behavior and development.

Malaguti et al. [119] were among the first to investigate the spray structure in the new generations of GDI multi-orifice injectors. They employed data obtained from experimental measurements to validate sub-models and numerical parameters such as grid density, numerical setup, primary and secondary fuel breakup and droplet to droplet interaction. Knowing that the grid is one of the key parameters in the analysis, the first thing the authors did was to carry out a sensitivity analysis of the grid size. Subsequently, they tested different atomization models and calibrated the corresponding constants. Tested breakup models obtained similar results although with some differences in terms of primary and secondary breakup contributions to the overall process. What became clear to them was that neither model was able to predict the existing jet-to-jet interaction so they implemented a routine to directly specify some initial characteristics of the droplets and thus reduce the deficiencies of the spray breakup models.

Nishad et al. [120] attempted to differentiate themselves from studies in the literature where most of them used RANS models to take into account the existing turbulence, therefore the authors used LES schemes. In addition, they included a particle collision model independent of the mesh size and type. In this way, they took into account different regimes, such as rebound, separation, stretching separation, reflection separation and droplet coalescence. The authors validated with experimental data two different operating conditions, evaporative and non-evaporative, accurately predicting the spray penetration depth, droplet size distributions and the important flow properties such as nozzle exit velocity.

Banerjee et al. [121] joined the study of atomization and preparation of air/fuel mixture under GDI conditions in a single-orifice injector where

the objective was to observe how the ambient pressure and temperature of the injected fuel affects on liquid and vapor penetration lengths. With this study the authors noticed how the liquid penetration length increased rapidly during the first instants, which results in the formation of a large number of liquid droplets due to droplet breakup. However, from a droplet size point of view, the reduction in size was mainly due to evaporation. Since this is a diffusion process, the rate of droplet diameter decrease was reduced much more than in the initial stages. The investigation revealed the significant effect of ambient pressure and temperature on the penetration length of the liquid. Nevertheless, the fuel injection temperature had little effect on the liquid penetration length, as it was in all cases significantly lower than the boiling temperature. After studying the injection process, the researchers completed the investigation by studying the air/fuel mixture in a simplified GDI engine operating under motored condition.

Over the years, understanding how the spray behaves has become one of the main objectives of researchers because of the great impact it has on fuel-air mixing, engine performance and, above all, emissions. As mentioned before, the first studies were mainly focused on observing the characteristics of the spray when varying the operating conditions, unlike them, the most advanced studies are focused on analyzing phenomena that take place in the GDI injection process due to its own nature. Such is the case of Sphicas et al. [122] who focused their study on the aerodynamic interaction between plumes and the complicated two-phase coupling of the evaporating spray as they are remarkably difficult processes to predict. The main objective was to develop an understanding of spray parameter sensitivities that suffer from many uncertainties and are difficult to prescribe exactly. For this study, they used experimental validation data paying attention to the prediction of the velocity field between plumes where the plume merging and complete spray collapse can be clearly seen. Thanks to this analysis, it was shown how, once the model was calibrated to provide good agreement between experiments and CFD, focusing on the degree of plume merging and interaction, it suggests that the recirculation rate is a key component for the physics of plume interaction.

As with internal nozzle flow, researchers began to consider the behavior of the spray under flash boiling conditions. To this end, Khan et al. [123] implemented a new spray injection model that would be able to reflect the rapid expansion of the flash boiling sprays in the near nozzle region. This new model allowed them to reasonably estimate the expansion of the spray plumes and axial penetration. They observed that air entrainment and vapor accumulation in the spray cone resulted in increased penetration values under

flash boiling conditions. In addition, once the collapse between jets occurs, penetration was also increased and the spray aperture was reduced.

Pursuing the same objective based on the adoption of combustion systems featuring high thermodynamic conversion efficiency and moderate pollutant emissions by increasing the injection pressure, Postrioti et al. [124] studied the spray evolution, hydraulics and atomization process over a wide range of injection pressures, reaching values up to twice the common injection pressure. The main conclusion obtained was that the trend of the SMD value with increasing pressure has an asymptotic tendency, suggesting a proper cost/benefit analysis in terms of soot reduction for further increases of the injection pressure level.

Seeking to increase the accuracy of the results without compromising too much the computational cost, Di Ilio et al. [125] proposed a hybrid URANS/LES scale-resolving turbulence modeling approach as a potential remedy for the numerical resolution mismatch. This type of modeling obtained consistent results in accordance with the experiments (see Figure 4.13) but was still at an early stage of research and the authors stressed the need for more in-depth analysis to asses its full validity and competitiveness.

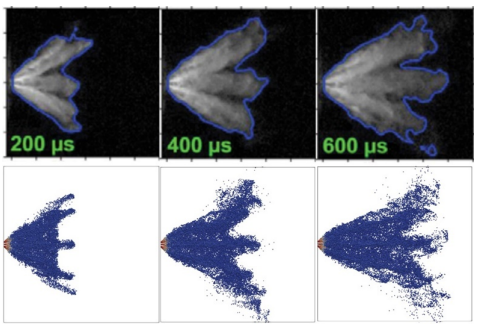

Figure 4.13: Liquid phase visualization in both experimental and computational approaches. Adapted from [125].

Sparacino with several of his colleagues [126–128] conducted a number of studies focused on the study of spray patterns under GDI operating conditions. The first two of them [126, 127] were focused on developing an atomization methodology that would allow to study the fuel spray under different operating conditions without having to tune too much the constants of the sub-models involved in the calculation. The remaining work was focused on the study of fuel distribution and atomization under flash boiling conditions using an alternative model for this type of operating environment. The new instantaneous boiling model consisted of three main parts: an atomization model capable of calculating the initial conditions of the droplets and the overall spray cone angle; an evaporation model; and finally a droplet breakup model. The numerical-experimental comparison they carried out yielded promising results in terms of liquid penetration, imaging,

and droplet sizing.

Despite all the work mentioned above, there are still many aspects to understand during the injection process. That is why researchers such as Payri et al. [129] continue to put efforts in studying the behavior of the spray under flash boiling conditions, which is the scenario that most concerns the scientific community. In the study, they used different fuels surrogates of gasoline and obtained very good agreement in terms of penetration and spray shape. However, they found certain deficiencies in the more volatile fuels to correctly predict the spray collapse phenomenon. Therefore, they suggested the need to investigate this issue more in depth.

Being aware of the limitations of the flash boiling and spray collapse models, Duronio et al. [130] developed a breakup model to capture the droplet shattering mechanism using linear stability analysis, bubble growth and conservation laws. The radial component of the velocity was added to the child parcel to account for the spray expansion under these conditions. The results obtained matched the experiments perfectly, adequately capturing the spray expansion due to flash boiling and the consequent spray collapse. These authors proposed as future work to consider in the model the phase change (cavitation and flash boiling) inside the nozzle in order to properly initialize the blob-method.

One of the major problems with the blob-method is the need to calibrate the sub-models involved in the analysis. At present, there is no standard configuration to obtain accurate results under different software codes and operating conditions. Therefore, Sciortino et al. [131] developed a novel calibration methodology that greatly reduced the required study times and test cases, accurately predicting the fundamental characteristics of high-pressure fuel GDI sprays. This was carried out by employing a half factorial design to reveal how the diverse model calibration factors influence the spray properties, leading to the selection of dominants. The results showed how the initial droplet size distribution was determinant in the results, in addition to the great importance of properly calibrating the secondary atomization model.

Following the lines of research highlighted in the previous works, the latest research in the literature in this field is that carried out by Berni et al. [132] who focused mainly on the secondary breakup atomization phase because of its great influence on air-fuel mixing. In this case and again due to the need for *ad-hoc* calibration of the atomization sub-models, the authors proposed a new alternative model for the secondary breakup model that reduced case-by-case tuning. This model mainly assumed that only stripping break-up can occur near the nozzle, while bag break-up only takes place sufficiently far from it.

The results revealed that the model parameters had a linear dependence on the ambient density. The developed breakup method was compared with typical atomization models, which deviated significantly from the experimental data, while the new approach perfectly matched the behavior of the experiments.

4.3.2.3 Coupling strategy in gasoline nozzle flow applications

Within the coupling scheme, a distinction can be made between what is known as one-way coupling or, on the other hand, the two-way coupling strategy. The one-way coupling strategy is based on the well-known DDM or blob-model procedure where, unlike the research described above, in-nozzle flow simulations are carried out from which the temporal distribution profiles of the variables of interest (velocity vector, fuel liquid volume fraction, temperature, turbulent kinetic energy or dissipation rate, among others) are obtained and introduced as input and initialization variables for the study of the spray behavior. In these cases, it is the internal flow that influences the solution downstream of the injector, the behavior of the spray, but at no time can the spray influence the performance upstream of the injector. On the contrary, the two-way coupling approach studies the complete computational domain, which means that the internal and external flow are coupled together so that, in this case, there can be an influence from the downstream flow on the internal flow characteristics.

One-way coupling

The well-known researcher Bizhan Befrui not only focused his studies on high fidelity simulations where only the internal flow was analyzed but wanted to go further and together with his colleagues [133] set out to develop a methodology capable of accurately predicting the spray structure in a multi-hole GDI injector. In this case, they transferred the volume fraction, mean velocity and turbulence distribution obtained from the internal flow simulations for prescription of the spray initial conditions in the Lagrangian DDM for stochastical spray simulation. In addition, by using a VOF-LES scheme for the analysis of the injector internal flow and near-field primary atomization, they estimated the size needed to initialize the "blob", thus providing greater accuracy to the computation. The authors highlighted as main aspects the deviation of the plumes with respect to the corresponding geometrical axes. A good precision of the individual direction of each plume and the spray angle was noticed. However, they recommended emphasizing simulations of this nature to improve the predictions.

Saha et al. [134] relied on the model published in [135] to perform the coupling of internal and external flows in a computationally affordable way.

They first calibrated the traditional ROI-based Eulerian-Lagrangian simulations and then applied this configuration to the one-way coupling scheme. Although both models adequately predicted macroscopic spray parameters such as liquid and vapor penetration, the one-way model showed promise in capturing plume-to-plume variations. In addition, some discrepancies in the calculated SMD values were also observed between the two approaches. Therefore, they suggested further study of this type of model due to its great potential and accuracy.

Years later, Nocivelli et al. [136] studied the spray behavior under different operating conditions (flashing and non-flashing) by three distinct approaches. The first one was the blob-model for which the parcel properties were defined according to semi-empirical models based on the nozzle properties. These results were compared with those obtained from the one-way coupling scheme where the properties of the injected parcel were obtained from high fidelity Eulerian multi-phase flow mixture simulations. Finally, the results obtained from the initialization of the primary atomization by droplet diameter probability functions were included in the comparison. While the blob-injector-based reasonably captured the spray behavior with a stronger liquid jet breakup mainly attributed to over-prediction of the tip ligament stripping phenomenon and leading to a smaller SMD in the far field, the one-way coupling routine proved to be a very promising approach without greatly penalizing the associated computational cost. This approach was able to adequately capture the spatial and temporal evolution of the spray with certain limitations in the opening and closing phases due to the lack of a sealing algorithm. Mohan et al. [137], parallel to the previous researchers, carried out a similar study where they employed the one-way coupling model to analyze the spray behavior under non-flashing and flashing conditions. The results predicted inter-plume interactions under flash boiling conditions.

Recently, Jia et al. [94] not only surprised with the study of the internal flow of an unusual geometry in GDI injectors such as the divergent-convergent nozzle, but also wanted to observe its influence on the development of the spray by means of a one-way coupling strategy. The results showed that penetration increased slightly as the medium diameter ratio increased. In addition, the cavitation density inside the nozzle decreases with the increase of the medium diameter ratio which causes the droplet diameter in the near field to increase. On the contrary, the mass flow rate and the average velocity at the nozzle exit increased with the increment of the medium diameter ratio so that the atomization in the far field was enhanced and with it the number of smaller particles increased.

Two-way coupling

In the field of diesel injection, such applications have been much more widespread than in gasoline injection [138], yet there are some works in the literature dedicated to the use and application of this approach. This is the case of Wang et al. [139] who used the ESA model with the interface area density to define local sub-grid distribution of the two phases in any CFD cell and determine the spray plume boundary. This study not only included the analysis of the spray plume cone angle in a single-orifice GDI injector but explored a new definition of spray plume boundary in an Eulerian two-phase flow CFD simulation by defining a line-of-sight integration of the interface area density being much more consistent with the experimental definition and predicting the spray plume cone angle trend more accurately.

Saha et al. [140] were one of the pioneers in implementing the use of the ELSA model for the study of internal and external flow in a coupled manner in GDI injector applications.This model proved to be computationally much more expensive than the basic Lagrangian blob model but more predictive in terms of spray penetration, and gas velocities. Despite providing comparisons between mesh sizes, ELSA model constants and atomization sub-models, the authors strongly requested further exploration of the prospect of ELSA for GDI applications as they believe this type of study can enhance the quality of academic research in automotive spraying.

Navarro-Martinez et al. [141] aimed to evaluate the impact of droplet size distribution (DSD) statistics using two modeling approaches: Eulerian-Lagrangian spray atomization with adaptive mesh refinement (ELSA-AMR) and a stochastic fields transported probability density function method (ELSA-PDF). Both resolution schemes simulated the small scales and sub-grid droplet physics based on the same concept of transport of liquid surface density. The results with both models obtained similar near-field liquid distributions comparable to the experimental data. The spray break-up patterns also

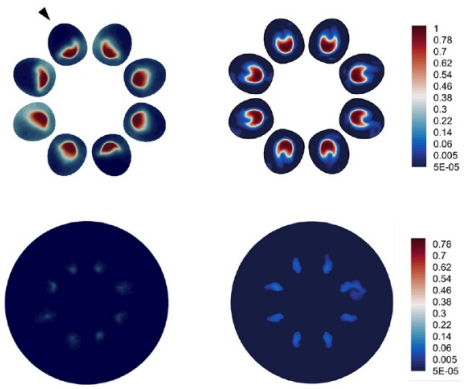

Figure 4.14: Time-averaged α parameter at: z=0 (top) and z=2mm (bottom). ELSA-PDF (left), ELSA-AMR (right). Adapted from [141].

exhibited successful approximations by correctly reporting quasi-log-normal droplet distributions with similar SMD. ELSA-PDF displayed a dissimilar breakup behavior between droplets coming from the dilute region and those coming from the dense core region. Both methods are efficient in providing a similar DSD below the filter width/mesh size resolution (see Figure 4.14).

Finally, and continuing with the improvements in the study of spray structure and behavior, Schmidt et al. [142] recently developed a model called Eulerian Lagrangian Mixing-Oriented (ELMO) based on ideas of thermodynamic and inertial equilibrium in the dense spray core, resulting in an approach that targets mixing-limited conditions. The model experiences full two-way coupling of mass, momentum, species, and energy and has the great advantage of using of relatively few modeling constants. Validation of the model showed applicability to both diesel and gasoline sprays and surprised with its reduced computational cost comparable to a traditional Lagrangian/Eulerian simulation. This new scheme is still under development and study is still required in this field but represents an initial foray into making a fully-coupled, mixing-limited, CFD computation.

4.4 Summary and Conclusions

Throughout this section an extensive state of the art of both experimental studies and computational calculations based on analyzing the behavior of the GDI injection process has been carried out.

With respect to the experimental part, numerous studies have been carried out, all of them very different from each other, using diverse techniques of experimental optical visualization and focusing on completely new and unique phenomena. Something important to note is that depending on the phenomenon to be studied there are more suitable visualization techniques than others. Numerous advances have been achieved thanks to all this research, in addition to a large data base needed for the validation of computational studies. There have been many published works but all of them agree on one thing, especially the most recent ones; the complexity of the injection process, which includes spray formation, mixture and atomization, the importance it has on engine performance and pollutants emission requirements and the existing limitations in the visualization techniques, make the injection event still an unknown process that needs further research. Within these limitations is where CFD studies are taken into great consideration, which have the ability to minimize research and study time and complement to a great extent most

of the experimental findings by providing knowledge not accessible experimentally.

In relation to the computational section, objective of the present Thesis, the first thing to be clear is that the study of the injection process can be treated from different points of view. The models used in the analysis depend to a large extent on the nature of the problem and the type of flow. The injection event is typically divided for computational analysis into two distinct but dependent fields: internal nozzle flow and external flow. It is true that given the enormous influence that the behavior of the flow inside the nozzle has on the development of the spray, in recent years the study of both fields together has been gaining importance.

Within the study of internal flow, many different models have been used to predict the phase change, both cavitation and flash boiling, and the turbulence inside the nozzle. However, it could be said that the most widely used schemes for the study of internal flow in GDI operations are the interface tracking methods (level-set/VOF), among which the VOF stands out. Commonly, those works that have adopted the VOF model do not make use of the interface-capturing algorithm since they do not expect sharp or nearly sharp interface between liquid and vapor phases and thus reduce computational cost by making it suitable for RANS simulations. However, the use of LES approach for the study of the internal flow is a viable alternative to be taken into account as it offers numerous details of the phenomena that take place during the injection process in the in- and near- field. The direct injection of gasoline is associated with the flash boiling phenomenon and to take into account this phase change together with the one produced by cavitation, several models have been implemented in the research software. The most popular for its wide use is the HRM, but most of the studies use the default parameters of the model. The phase change is highly dependent on the operating conditions so more consideration should be given to the influence of the parameters that make up the model.

On the other hand, the external flow is commonly studied from the Eulerian-Lagrangian approach despite its disadvantages. As mentioned above, there have been many efforts by the scientific community to reduce the mesh dependence (by adding new source terms to the classical equations and using the adaptive mesh refinement technique, among others) and to improve the sub-models and the large dependence and tuning work of the constants that conform them. However, with the proper selection of the models, the meshing strategy and the exact values of the constants of the sub-models, this Eulerian-Lagrangian approach gives very good results compared to experimental data.

In order to improve the approaches, alternatives such as one-way (mapping) or two-way (ELSA and ESA) coupling have proved to be a rising alternative to DDM, but are still under development.

References

[1] Sick, V. et al. "High-speed imaging for direct-injection gasoline engine research and development". In: *Experiments in Fluids* 49.4 (2010), pp. 937–947. DOI: 10.1007/s00348-010-0891-3.

[2] Manin, J. et al. "Experimental Characterization of DI Gasoline Injection Processes". In: *SAE Technical Paper 2015-01-1894* (2015). DOI: 10.4271/2015-01-1894.

[3] Duke, D. J. et al. "Internal and near nozzle measurements of Engine Combustion Network "Spray G" gasoline direct injectors". In: *Experimental Thermal and Fluid Science* 88 (2017), pp. 608–621. DOI: 10.1016/j.expthermflusci.2017.07.015.

[4] Medina, M. et al. "The effects of injector geometry and operating conditions on spray mass, momentum and development using high-pressure gasoline". In: *Fuel* 294.June (2021). DOI: 10.1016/j.fuel.2021.120468.

[5] Shahangian, N. et al. "Spray Orientation Assessment and Correction Method for GDI Momentum Flux Measurements". In: October (2019), pp. 231–241.

[6] Payri, R. et al. "Momentum Flux Measurements on an ECN GDi Injector". In: *SAE Technical Paper 2015-01-1893*. 2015. DOI: 10.4271/2015-01-1893.

[7] Costa, M. et al. "Multiple Injection in a Mixed Mode GDI Boosted Engine". In: *SAE Technical Paper* (2010), p. 15. DOI: https://doi.org/10.4271/2010-01-1496.

[8] Hoffmann, G. et al. "Fuel System Pressure Increase for Enhanced Performance of GDi Multi-Hole Injection Systems". In: *SAE Technical Paper 2014-01-1209* (2014). DOI: 10.4271/2014-01-1209.

[9] Payri, R. et al. "Using one-dimensional modelling codes to analyse the influence of diesel nozzle geometry on injection rate characteristics". In: *International Journal of Vehicle Design* 38.1 (2005), pp. 58–78. DOI: 10.1504/IJVD.2005.006605.

[10] Goldberg, J. H. "Worldview of High-Risk Juvenile Delinquents". In: *Criminal Justice and Behavior* 34.6 (2007), pp. 846–861. DOI: 10.1177/0093854807299413.

[11] Bower, G. R. et al. "A Comparison of the Bosch and Zuech Rate of Injection Meters". In: *SAE Technical Papers* (1991). DOI: https://doi.org/10.4271/910724.

[12] Bosch, W. "The fuel rate indicator: A new measuring instrument for display of the characteristics of individual injection". In: *SAE Technical Papers* (1966). DOI: 10.4271/660749.

[13] Zeuch, W. "Neue Verfahren zur Messung des Einspritzgesetzes und der Einspritz-Regelmäßigkeit von Diesel-Einspritzpumpen". In: *MTZ* 22.9 (1961), pp. 344–349.

[14] Naber, J. D. et al. "Effects of Gas Density and Vaporization on Penetration and Dispersion of Diesel Sprays". In: *SAE Paper 960034*. Vol. 105. 412. Society of Automotive Engineers, Inc., Warrendale, Pennsylvania, USA, 1996, pp. 82–111. DOI: 10.4271/960034.

[15] Naber, J. D. et al. "Effects of gas density and vaporization on penetration and dispersion of diesel sprays". In: *SAE Technical Papers* 412 (1996). DOI: 10.4271/960034.

[16] Yu, W. et al. "Macroscopic spray characteristics of kerosene and diesel based on two different piezoelectric and solenoid injectors". In: *Experimental Thermal and Fluid Science* 76 (2016), pp. 12–23. DOI: 10.1016/j.expthermflusci.2016.03.008.

[17] Payri, R. et al. "Spray Characterization of the Urea-Water Solution (UWS) Injected in a Hot Air Stream Analogous to SCR System Operating Conditions". In: *WCX SAE World Congress Experience*. 2019-01-0738. 2019, pp. 1–9. DOI: 10.4271/2019-01-0738.

[18] Luo, F. et al. "The development of a data acquisition system for measuring the injection rate of a multihole diesel injector". In: *Sensors and Actuators, A: Physical* 261 (2017), pp. 166–176. DOI: 10.1016/j.sna.2017.04.037.

[19] Payri, R. et al. "Internal flow characterization on an ECN GDi injector". In: *Atomization and Sprays* 26.9 (2016), pp. 889–919. DOI: 10.1615/AtomizSpr.2015013930.

[20] Cavicchi, A. et al. "Numerical and experimental analysis of the spray momentum flux measuring on a GDI injector". In: *Fuel* 206 (2017), pp. 614–627. DOI: 10.1016/j.fuel.2017.06.054.

[21] Ge, H. et al. "A comparison of computational fluid dynamics predicted initial liquid penetration using rate of injection profiles generated using two different measurement techniques". In: *International Journal of Engine Research* 20.2 (2019), pp. 226–235. DOI: 10.1177/1468087417746475.

[22] Manin, J. et al. "Transient cavitation in transparent diesel injectors". In: *ICLASS 2018 - 14th International Conference on Liquid Atomization and Spray Systems* (2020), pp. 1–9.

[23] Guo, G. et al. "Optical Experiments Of String Cavitation In Diesel Injector Tapered Nozzles". In: *Thermal Science* 24.1 Part A (2020), pp. 193–201. DOI: 10.2298/TSCI180405005G.

[24] Bornschlegel, S. et al. "Multi-hole gasoline direct injection:In-nozzle flow and primary breakup investigated in transparent nozzlesand with X-ray". In: *International Journal of Engine Research* 19.1 (2018), pp. 67–77. DOI: 10.1177/1468087417746860.

[25] Chaves, H. et al. "Binary cavitation in a transparent three hole GDI nozzle". In: September (2017). DOI: 10.4995/ilass2017.2017.5051.

[26] Mamaikin, D. et al. "Experimental investigation of flow field and string cavitation inside a transparent real-size GDI nozzle". In: *Experiments in Fluids* 61.7 (2020), pp. 1–15. DOI: 10.1007/s00348-020-02982-y.

[27] Zhang, G. et al. "A Study of Near-field Spray Structure under Superheated Conditions of a Gasoline Fuel Spray G". In: *ILASS Americas 26th Annual Conference on Liquid Atomization and Spray Systems* May (2014).

[28] Yang, S. et al. "In-nozzle bubble formation and its effect on fuel jet breakup under cavitating and flash boiling conditions". In: *Applied Thermal Engineering* 183.P1 (2021), p. 116120. DOI: 10.1016/j.applthermaleng.2020.116120.

[29] Chen, L. et al. "The influence of ethanol blends on particulate matter emissions from gasoline direct injection engines". In: *SAE Technical Papers* (2010), pp. 1–21. DOI: 10.4271/2010-01-0793.

[30] Leick, P. et al. "Experimental characterization of tip wetting in gasoline DI injectors". In: *ICLASS 2018 - 14th International Conference on Liquid Atomization and Spray Systems* July (2018).

[31] Schulz, F. et al. "Gasoline Wall Films and Spray/Wall Interaction Analyzed by Infrared Thermography". In: *SAE International Journal of Engines* 7.3 (2014). DOI: 10.4271/2014-01-1446.

[32] Medina, M. et al. “Mechanisms of fuel injector tip wetting and tip drying based on experimental measurements of engine-out particulate emissions from gasoline direct-injection engines”. In: *International Journal of Engine Research* (2020). DOI: 10.1177/1468087420916052.

[33] Xiao, D. et al. “Experimental investigations of injector internal parameters impact on tip wetting using Laser-induced Fluorescence”. In: *15thTriennial International Conference on Liquid Atomization and Spray Systems* (2021).

[34] Spiegel, L. et al. “Mixture formation and combustion in a spark ignition engine with direct fuel injection”. In: *SAE Technical Papers* (1992). DOI: 10.4271/920521.

[35] Parrish, S. E. “Evaluation of Liquid and Vapor Penetration of Sprays from a Multi-Hole Gasoline Fuel Injector Operating Under Engine-Like Conditions”. In: *SAE Technical Paper 2014-04-01* 7.2 (2014), pp. 1017–1033. DOI: 10.4271/2014-01-1409.

[36] Park, J. et al. “Study on the Spray Dynamics and Sectional Spray Distribution using Spray Pattern Measurement of Multi-Hole GDI Injector”. In: September (2019), pp. 2–4.

[37] Bornschlegel, S. et al. “Flash boiling atomization in nozzles for GDI engines”. In: *28th Conference on Liquid Atomization and Spray Systems* September (2017), pp. 6–8. DOI: 10.4995/ilass2017.2017.4750.

[38] Wu, J. et al. “Experimental study on flash-boiling spray structure of multi-hole gasoline direct injection injector in a constant volume chamber”. In: *International Journal of Spray and Combustion Dynamics* 12 (2020). DOI: 10.1177/1756827720932431.

[39] Payri, R. et al. “ECN Spray G external spray visualization and spray collapse description through penetration and morphology analysis”. In: *Applied Thermal Engineering* 112 (2017), pp. 304–316. DOI: 10.1016/j.applthermaleng.2016.10.023.

[40] Sphicas, P. et al. “Interplume velocity and extinction imaging measurements to understand spray collapse when varying injection duration or number of injections”. In: *Atomization and Sprays* 28.9 (2018), pp. 837–856. DOI: 10.1615/AtomizSpr.2018025956.

[41] Du, J. et al. “Study of spray structure under flash boiling conditions using 2phase-SLIPI”. In: *Experiments in Fluids* 62.1 (2021), pp. 1–17. DOI: 10.1007/s00348-020-03123-1.

[42] Sharma, N. et al. "Spray Behavior of a GDI Injector at Constant Fuel Injection Pressure and Varying Engine Load". In: *18th Annual Conference on Liquid Atomization and Spray Systems* - (2016).

[43] Wu, S. et al. "Experimental study of the spray collapse process of multi-hole gasoline fuel injection at flash boiling conditions". In: *Fuel* 242.Ic (2019), pp. 109–123. DOI: 10.1016/j.fuel.2019.01.027.

[44] Medina, M. et al. "High-Speed Imaging Study on the Effects of Internal Geometry on High-Pressure Gasoline Sprays". In: *SAE Technical Papers* 2020 (2020), pp. 1–14. DOI: 10.4271/2020-01-2111.

[45] Jiang, C. et al. "Impact of gasoline direct injection fuel injector hole geometry on spray characteristics under flash boiling and ambient conditions". In: *Fuel* 241 (2019), pp. 71–82. DOI: 10.1016/j.fuel.2018.11.143.

[46] Lehnert, B. et al. "GDI Sprays with up to 200 MPa Fuel Pressure and Comparison of Diesel-like and Gasoline-Like Injector Designs". In: *SAE Technical Papers* 2020 (2020), pp. 1–11. DOI: 10.4271/2020-01-2104.

[47] Montanaro, A. et al. "Wall impingement process of a multi-hole GDI spray: Experimental and numerical investigation". In: *SAE Technical Papers* (2012). DOI: 10.4271/2012-01-1266.

[48] Montanaro, A. et al. "Experimental analysis of a GDI spray impacting on a heated wall". In: *DIPSI Workshop 2018 on Droplet Impact Phenomena & Spray Investigation* May (2018), pp. 29–32.

[49] Allocca, L. et al. "Schlieren visualization of a GDI spray impacting on a heated wall: Non-vaporizing and vaporizing evolutions". In: *Energy* 108 (2016), pp. 93–98. DOI: 10.1016/j.energy.2015.09.107.

[50] Liu, Y. et al. "Investigation of the liquid fuel film from GDI spray impingement on a heated surface with the laser induced fluorescence technique". In: *Fuel* 250.February (2019), pp. 211–217. DOI: 10.1016/j.fuel.2019.03.120.

[51] Wang, Z. et al. "Influence of deposit on spray behaviour under flash boiling condition with the application of closely coupled split injection strategy". In: *Fuel* 190 (2017), pp. 67–78. DOI: 10.1016/j.fuel.2016.11.012.

[52] Wang, Z. et al. "Microscopic and macroscopic characterization of spray impingement under flash boiling conditions with the application of split injection strategy". In: *Fuel* 212.February 2017 (2018), pp. 315–325. DOI: 10.1016/j.fuel.2017.10.028.

[53] Sun, Z. et al. "Split injection flash boiling spray for high efficiency and low emissions in a GDI engine under lean combustion condition". In: *Proceedings of the Combustion Institute* 38.4 (2021), pp. 5769–5779. DOI: 10.1016/j.proci.2020.05.037.

[54] Serras-Pereira, J. et al. "An experimental database on the effects of single- and split injection strategies on spray formation and spark discharge in an optical direct-injection spark-ignition engine fuelled with gasoline, iso -octane and alcohols". In: *International Journal of Engine Research* 16.7 (2015), pp. 851–896. DOI: 10.1177/1468087414554936.

[55] Ling, Y. et al. "A two-phase mixing layer between parallel gas and liquid streams: multiphase turbulence statistics and influence of interfacial instability". In: *Journal of Fluid Mechanics* 859 (2019), pp. 268–307. DOI: 10.1017/jfm.2018.825.

[56] Hasslberger, J. et al. "Flow topologies in primary atomization of liquid jets: A direct numerical simulation analysis". In: *Journal of Fluid Mechanics* 859 (2019), pp. 819–838. DOI: 10.1017/jfm.2018.845.

[57] Shao, C. et al. "Detailed numerical simulation of swirling primary atomization using a mass conservative level set method". In: *International Journal of Multiphase Flow* 89 (2017), pp. 57–68. DOI: 10.1016/j.ijmultiphaseflow.2016.10.010.

[58] Duret, B. et al. "Improving primary atomization modeling through DNS of two-phase flows". In: *International Journal of Multiphase Flow* 55 (2013), pp. 130–137. DOI: 10.1016/j.ijmultiphaseflow.2013.05.004.

[59] Takacs, G. *A Review of Production Engineering Fundamentals*. 2015, pp. 13–56. DOI: 10.1016/b978-0-12-417204-3.00002-9.

[60] Martí-Aldaraví, P. "Development of a computational model for a simultaneous simulation of internal flow and spray break-up of the Diesel injection process". PhD thesis. Valencia: Universitat Politècnica de València, 2014. DOI: 10.4995/Thesis/10251/43719.

[61] Ishii, M. et al. *Thermo-Fluid Dynamics of Two-Phase Flow*. Vol. 51. 2. Heidelberg, Germany: Springer, 2013, pp. 535–535. DOI: 10.2514/1.j052026.

[62] Greif, D. et al. "Numerical study of transient multi component fuel injection". In: *SAE Technical Papers* 11.October (2013). DOI: 10.4271/2013-01-2550.

[63] Mishra, R. et al. "Three-component multi-fluid modeling of pseudo-cavitation phenomenon in diesel injector nozzles". In: *International Journal of Engine Research* (2021). DOI: 10.1177/1468087421993348.

[64] Bataille, J. et al. *Continuum modeling of two-phase flows*. Tech. rep. 1981, p. 35.

[65] Moulai, M. et al. "Internal and Near-Nozzle Flow in a Multi-Hole Gasoline Injector Under Flashing and Non-Flashing Conditions". In: *SAE Technical Paper 2015-01-0944* 2015-01-0944 (2015). DOI: 10.4271/2015-01-0944.Copyright.

[66] Strek, P. et al. "X-Ray Radiography and CFD Studies of the Spray G Injector". In: *SAE Technical Paper 2016-01-0858* (2016). DOI: 10.4271/2016-01-0858.

[67] Mohapatra, C. et al. "Modeling sealing in transient injector simulations". In: *American Society of Mechanical Engineers, Fluids Engineering Division (Publication) FEDSM* 1A-2017 (2017), pp. 1–10. DOI: 10.1115/FEDSM2017-69309.

[68] Baldwin, E. et al. "String flash-boiling in gasoline direct injection simulations with transient needle motion". In: *International Journal of Multiphase Flow* 87 (2016), pp. 90–101. DOI: 10.1016/j.ijmultiphaseflow.2016.09.004.

[69] Jacobsohn, G. L. et al. "Comparison of turbulence modeling methods for evaluating GDI sprays with transient needle motion". In: *SAE Technical Papers* 2019-April.April (2019), pp. 1–11. DOI: 10.4271/2019-01-0271.

[70] Gärtner, J. W. et al. "Numerical investigation of spray collapse in GDI with OpenFOAM". In: *Fluids* 6.3 (2021). DOI: 10.3390/fluids6030104.

[71] Guo, H. et al. "Numerical investigation on flashing jet behaviors of single-hole GDI injector". In: *International Journal of Heat and Mass Transfer* 130 (2019), pp. 50–59. DOI: 10.1016/j.ijheatmasstransfer.2018.10.088.

[72] Tezduyar, T. E. "Interface-tracking and interface-capturing techniques for finite element computation of moving boundaries and interfaces". In: *Computer Methods in Applied Mechanics and Engineering* 195.23-24 (2006), pp. 2983–3000. DOI: 10.1016/j.cma.2004.09.018.

[73] Ferziger, J. H. et al. *Computational Methods for Fluid Dynamics*. 3rd. Berlin, 2002.

[74] Tezduyar, T. E. "Finite Element Methods for Flow Problems with Moving Boundaries and Interfaces". In: *Archives of Computational Methods in Engineering* 8.2 (2001), pp. 83–130. DOI: 10.1007/BF02897870.

[75] Hayashi, K. et al. "Interface tracking simulation of mass transfer from a dissolving bubble". In: *ASME-JSME-KSME 2011 Joint Fluids Engineering Conference, AJK 2011*. Vol. 1. PARTS A, B, C, D. 2011, pp. 1593–1601. DOI: 10.1115/AJK2011-04007.

[76] Hayashi, K. et al. "Effects of shape oscillation on mass transfer from a Taylor bubble". In: *International Journal of Multiphase Flow* 58 (2014), pp. 236–245. DOI: 10.1016/j.ijmultiphaseflow.2013.09.009.

[77] Aliabadi, S. et al. "Stabilized-finite-element/interface-capturing technique for parallel computation of unsteady flows with interfaces". In: *Computer Methods in Applied Mechanics and Engineering* 190.3-4 (2000), pp. 243–261. DOI: 10.1016/S0045-7825(00)00200-0.

[78] Gueyffier, D. et al. "Volume-of-Fluid Interface Tracking with Smoothed Surface Stress Methods for Three-Dimensional Flows". In: *Journal of Computational Physics* 152.2 (1999), pp. 423–456. DOI: 10.1006/jcph.1998.6168.

[79] Muzaferija, S. et al. "Computation of free-surface ows using interface-tracking and interface-capturing methods Flows of two (or more) immiscible uids are often encountered in". In: November (1999).

[80] Noh, W. et al. *SLIC (simple line interface calculation)*. Tech. rep. Livermore, CA: Lawrence Livermore National Laboratory (LLNL), 1976. DOI: 10.2172/7261651.

[81] Youngs, D. L. "Time-dependent multi-material flow with large fluid distortion." In: January 1982 (1982).

[82] Tsui, Y. Y. et al. "Flux-blending schemes for interface capture in two-fluid flows". In: *International Journal of Heat and Mass Transfer* 52.23-24 (2009), pp. 5547–5556. DOI: 10.1016/j.ijheatmasstransfer.2009.06.026.

[83] Hui, D. et al. "Comparation with different interface capturing schemes based on gradient smoothing method using unstructured meshes". In: ().

[84] Antepara, O. et al. "A comparative study of interface capturing methods with AMR for incompressible two-phase flows". In: *Proceedings of the 7th International Conference on Coupled Problems in Science and Engineering, COUPLED PROBLEMS 2017* 2017-Janua (2017), pp. 981–992.

[85] Lafaurie, B. et al. *Modelling merging and fragmentation in multiphase flows with SURFER.* 1994. DOI: 10.1006/jcph.1994.1123.

[86] Sames, P. C. et al. "Application of a two-fluid finite volume method to ship slamming". In: *Journal of Offshore Mechanics and Arctic Engineering* 121.1 (1999), pp. 47–52. DOI: 10.1115/1.2829554.

[87] Saha, K. et al. "Modeling of internal and near-nozzle flow for a gdi fuel injector". In: *ASME 2015 Internal Combustion Engine Division Fall Technical Conference, ICEF 2015* 2 (2015), pp. 1–13. DOI: 10.1115/ICEF2015-1112.

[88] Saha, K. et al. "Numerical simulation of internal and near-nozzle flow of a gasoline direct injection fuel injector". In: *Journal of Physics: Conference Series* 656.1 (2015), pp. 1–6. DOI: 10.1088/1742-6596/656/1/012100.

[89] Saha, K. et al. "Numerical Investigation of Two-Phase Flow Evolution of In- and Near-Nozzle Regions of a Gasoline Direct Injection Engine During Needle Transients". In: *SAE International Journal of Engines* 9.2 (2016), pp. 1230–1240. DOI: 10.4271/2016-01-0870.

[90] Saha, K. et al. "Coupled Eulerian Internal Nozzle Flow and Lagrangian Spray Simulations for GDI Systems". In: *SAE technical paper 2017-01-0834*. 2017. DOI: 10.4271/2017-01-0834.

[91] Torelli, R. et al. "Internal Nozzle Flow Simulations of Gasoline-Like Fuels under Diesel Operating Conditions Internal Nozzle Flow Simulations of Gasoline-Like Fuels under Diesel Operating Conditions". In: *29th Annual Conference on Liquid Atomization and Spray Systems* May (2017).

[92] Saha, K. et al. "Modeling of Flash Boiling Phenomenon in Internal and Near-Nozzle Flow of Fuel Injectors". In: *Energy, Environment, and Sustainability* (2018), pp. 167–181. DOI: 10.1007/978-981-10-7449-3_7.

[93] Guo, H. et al. "Numerical study on spray collapse process of ECN spray G injector under flash boiling conditions". In: *Fuel* 290.December 2020 (2021), p. 119961. DOI: 10.1016/j.fuel.2020.119961.

[94] Jia, H. et al. "The effect of the divergent-convergent GDI injector on inner flow and spray characteristics at high injection pressure". In: *Energy Sources, Part A: Recovery, Utilization and Environmental Effects* 00.00 (2021), pp. 1–16. DOI: 10.1080/15567036.2021.1929574.

[95] Salvador, F. J. et al. "Numerical analysis of flow characteristics in diesel injector nozzles with convergent-divergent orifices". In: *Proceedings of the Institution of Mechanical Engineers, Part D: Journal of Automobile Engineering* 231.14 (2017), pp. 1935–1944. DOI: 10.1177/0954407017692220.

[96] Giussani, F. et al. "VOF Simulation of The Cavitating Flow in High Pressure GDI Injectors". In: September (2017). DOI: 10.4995/ilass2017.2017.4989.

[97] Sauer, J. et al. "Unsteady cavitating flow - A new cavitation model based on a modified front capturing method and bubble dynamics". In: *American Society of Mechanical Engineers, Fluids Engineering Division (Publication) FED* 251.August (2000), pp. 1073–1079.

[98] Mouvanal, S. et al. "Numerical study of purging of a gasoline direct injection nozzle at the end of injection". In: *International Journal of Engine Research* 22.5 (2021), pp. 1670–1684. DOI: 10.1177/1468087420916658.

[99] Befrui, B. et al. "GDI multi-hole injector internal flow and spray analysis". In: *SAE 2011 World Congress and Exhibition* (2011). DOI: 10.4271/2011-01-1211.

[100] Befrui, B. et al. "Large Eddy Simulation of GDI Single-Hole Flow and Near-Field Spray". In: *SAE International Journal of Fuels and Lubricants* 5.2 (2012), pp. 620–636. DOI: 10.4271/2012-01-0392.

[101] Befrui, B. et al. "GDi skew-angled nozzle flow and near-field spray analysis using optical and X-Ray imaging and VOF-LES computational fluid dynamics". In: *SAE Technical Papers* 2 (2013). DOI: 10.4271/2013-01-0255.

[102] Befrui, B. et al. "Primary atomization of a GDi multi-hole plume using VOF-LES method". In: *SAE Technical Papers* 1 (2014). DOI: 10.4271/2014-01-1125.

[103] Gomaa, H. et al. "Numerical Comparison of 3D Jet Breakup Using a Compression Scheme and an Interface Reconstruction Based VOF-Code". In: *24th ILASS-Europe Conference, Portugal.* 2011.

[104] Shost, M. A. et al. "GDi nozzle parameter studies using les and spray imaging methods". In: *SAE Technical Papers* 1 (2014). DOI: 10.4271/2014-01-1434.

[105] Tu, P. W. et al. "Numerical Investigation of GDI Injector Nozzle Geometry on Spray Characteristics". In: *SAE Technical Papers* 2015-Septe.September (2015). DOI: 10.4271/2015-01-1906.

[106] Wang, B. et al. "Numerical Investigation of the Deposit Effect on GDI Injector Nozzle Flow". In: *Energy Procedia* 105 (2017), pp. 1671–1676. DOI: 10.1016/j.egypro.2017.03.545.

[107] Yue, Z. et al. "Spray characterization for engine combustion network Spray G injector using high-fidelity simulation with detailed injector geometry". In: *International Journal of Engine Research* 21.1 (2020), pp. 226–238. DOI: 10.1177/1468087419872398.

[108] Zhang, B. et al. "Modeling and detailed numerical simulation of the primary breakup of a gasoline surrogate jet under non-evaporative operating conditions". In: *International Journal of Multiphase Flow* 130 (2020). DOI: 10.1016/j.ijmultiphaseflow.2020.103362.

[109] Osher, S. et al. "Fronts propagating with curvature-dependent speed: Algorithms based on Hamilton-Jacobi formulations". In: *Journal of Computational Physics* 79.1 (1988), pp. 12–49. DOI: 10.1016/0021-9991(88)90002-2.

[110] Arienti, M. et al. "Coupled Level-Set/Volume-of-Fluid Method for Simulation of Injector Atomization". In: *Journal of Propulsion and Power* 29.1 (2013), pp. 147–157. DOI: 10.2514/1.B34198.

[111] Bode, M. et al. "Effects of Cavitation and Hydraulic Flip in 3-Hole GDI Injectors". In: *SAE International Journal of Fuels and Lubricants* 10.2 (2017). DOI: 10.4271/2017-01-0848.

[112] Chenadec, V. L. et al. "A 3D unsplit Forward/Backward Volume-of-Fluid approach and coupling to the level set method". In: *Journal of Computational Physics* 233.1 (2013), pp. 10–33. DOI: 10.1016/j.jcp.2012.07.019.

[113] Dukowicz, J. K. "A particle-fluid numerical model for liquid sprays". In: *Journal of Computational Physics* 35.2 (1980), pp. 229–253. DOI: 10.1016/0021-9991(80)90087-X.

[114] Johansen, A. M. "Monte carlo methods". In: *International Encyclopedia of Education* (2010), pp. 296–303. DOI: 10.1016/B978-0-08-044894-7.01543-8.

[115] Abraham, J. "What is adequate resolution in the numerical computations of transient jets?" In: *SAE Technical Papers* 412 (1997). DOI: 10.4271/970051.

[116] Vallet, A. et al. "Development of a Eulerian model for the "Atomization" of a liquid jet". In: *Atomization and Sprays* 11.6 (2001), pp. 619–642. DOI: 10.1615/atomizspr.v11.i6.20.

[117] Khuong-Anh, D. "The Eulerian-Lagrangian Spray Atomization (ELSA) Model of the Jet Atomization in CFD Simulations: Evaluation and Validation". PhD thesis. 2012.

[118] Leung, T. F. et al. "Evaluation of an eulerian-lagrangian spray atomization (ELSA) model for nozzle flow: Modeling of coupling between dense and disperse regions". In: *47th AIAA Thermophysics Conference, 2017* June (2017), pp. 1–14. DOI: 10.2514/6.2017-4352.

[119] Malaguti, S. et al. "Numerical characterization of a new high-pressure multi-hole GDI injector". In: *ILASS - Europe 2010, 23rd Annual Conference on Liquid Atomization and Spray Systems* September (2010), pp. 1–10.

[120] Nishad, K. et al. "LES based modeling and simulation of spray dynamics including gasoline direct injection (GDI) processes using KIVA-4 code". In: *SAE Technical Papers* April (2012). DOI: 10.4271/2012-01-1257.

[121] Banerjee, R. et al. "Numerical investigation of stratified air/fuel preparation in a GDI engine". In: *Applied Thermal Engineering* 104 (2016), pp. 414–428. DOI: 10.1016/j.applthermaleng.2016.05.050.

[122] Sphicas, P. et al. "A Comparison of Experimental and Modeled Velocity in Gasoline Direct-Injection Sprays with Plume Interaction and Collapse". In: *SAE Int. J. Fuels Lubr.* 10 (2017), pp. 184–201. DOI: 10.4271/2017-01-0837.

[123] Khan, M. M. et al. "Experimental and numerical study of flash boiling in gasoline direct injection sprays". In: *Applied Thermal Engineering* 123 (2017), pp. 377–389. DOI: 10.1016/j.applthermaleng.2017.05.102.

[124] Postrioti, L. et al. "Experimental and Numerical Analysis of Spray Evolution, Hydraulics and Atomization for a 60 MPa Injection Pressure GDI System". In: *SAE Technical Papers* 2018-April (2018), pp. 1–17. DOI: 10.4271/2018-01-0271.

[125] Di Ilio, G. et al. "Evaluation of a scale-resolving methodology for the multidimensional simulation of GDI sprays". In: *Energies* 12.14 (2019), pp. 1–13. DOI: 10.3390/en12142699.

[126] Sparacino, S. et al. "Impact of different droplets size distribution on the morphology of GDI sprays: Application to multi-hole injectors". In: *AIP Conference Proceedings* 2191.December 2019 (2019). DOI: 10.1063/1.5138872.

[127] Sparacino, S. et al. "Impact of the primary break-up strategy on the morphology of GDI sprays in 3D-CFD simulations of multi-hole injectors". In: *Energies* 12.15 (2019). DOI: 10.3390/en12152890.

[128] Sparacino, S. et al. "3D-CFD Simulation of a GDI Injector under Standard and Flashing Conditions". In: *E3S Web of Conferences* 197 (2020), pp. 1–13. DOI: 10.1051/e3sconf/202019706002.

[129] Payri, R. et al. "Numerical Analysis of GDI Flash Boiling Sprays Using Different Fuels". In: *Energies* (2021), pp. 1–23.

[130] Duronio, F. et al. "ECN Spray G injector: Numerical modelling of flash-boiling breakup and spray collapse". In: *International Journal of Multiphase Flow* 145.September (2021). DOI: 10.1016/j.ijmultiphaseflow.2021.103817.

[131] Sciortino, D. D. et al. "A systematic approach to calibrate spray and break-up models for the simulation of high-pressure fuel injections". In: *International Journal of Engine Research* (2021), p. 146808742110507. DOI: 10.1177/14680874211050787.

[132] Berni, F. et al. "A zonal secondary break-up model for 3D-CFD simulations of GDI sprays". In: *Fuel* 309.October 2021 (2022), p. 122064. DOI: 10.1016/j.fuel.2021.122064.

[133] Befrui, B. et al. "ECN GDi Spray G : Coupled LES Jet Primary Breakup - Lagrangian Spray Simulation and Comparison with Data". In: *ILASS Americas 28th* June (2016).

[134] Saha, K. et al. "Coupled Eulerian Internal Nozzle Flow and Lagrangian Spray Simulations for GDI Systems". In: *SAE Technical Papers* 2017-March.March (2017). DOI: 10.4271/2017-01-0834.

[135] Quan, S. et al. "A one-way coupled volume of fluid and eulerian-lagrangian method for simulating sprays". In: (2017), pp. 1–9. DOI: 10.1115/ICEF2016-9390.

[136] Nocivelli, L. et al. "Analysis of the Spray Numerical Injection Modeling for Gasoline Applications". In: *SAE Technical Papers* 2020-April.April (2020), pp. 1–13. DOI: 10.4271/2020-01-0330.

[137] Mohan, B. et al. "Coupled in-nozzle flow and spray simulation of Engine Combustion Network Spray-G injector". In: *International Journal of Engine Research* 22.9 (2021), pp. 2982–2996. DOI: 10.1177/1468087420960612.

[138] Pandal, A. et al. "A consistent, scalable model for Eulerian spray modeling". In: *International Journal of Multiphase Flow* 83.April (2016), pp. 162–171. DOI: 10.1016/j.ijmultiphaseflow.2016.04.003.

[139] Wang, Y. et al. "Application of Interface Area Density Modeling to Define Spray Plume Boundary Department of Mechanical and Industrial Engineering University of Massachusetts-Amherst General Motors Global R & D". In: May (2015).

[140] Saha, K. et al. "Modeling the Dynamic Coupling of Internal Nozzle Flow and Spray Formation for Gasoline Direct Injection Applications". In: *SAE Technical Paper* (2018), pp. 1–13. DOI: 10.4271/2018-01-0314.Abstract.

[141] Navarro-martinez, S. et al. "An investigation on the impact of small-scale models in gasoline direct injection sprays (ECN Spray G)". In: *International Journal of Engine Research* (2019), pp. 1–9. DOI: 10.1177/1468087419889449.

[142] Schmidt, D. P. et al. "The Eulerian Lagrangian Mixing-Oriented (ELMO) Model". In: (2021). DOI: 10.48550/arXiv.2107.03508.

Chapter 5

Computational Methodology

"Life is and will ever remain an equation incapable of solution but it contains certain known factors."
—Nikola Tesla

5.1 Introduction

As introduced in Chapter 1, the present research reports the development of a predictive methodology capable of hydraulically characterizing a GDI injector regardless of the features or the employed software and analyze the behavior of the fluid downstream of the injector (external flow) once this methodology has been validated. This methodology will be applied and validated on two GDI injectors with different characteristics. The first one is the ECN well-known injector named Spray G, which is selected as a reference due to the extensive database available in the literature. The second one, an industrial injector used in real applications by a car manufacturer called Product Injector Unit (PIU).

In addition to what is mentioned in the previous sections, it is common to separate the study of the injection process into two distinct but dependent parts depending on the area of interest and the composition of the fluid. The internal nozzle flow is mainly focused on determining the influence of the injector geometry on the flow pattern, on studying phenomena such as cavitation and flash boiling, the effect of needle lift and wobble on the flow path as well as the influence of possible manufacturing defects. On the contrary,

the study of external flow includes processes related to spray behavior such as fuel breakup, atomization, air-fuel mixture, evaporation and combustion processes.

It is well known and also already discussed in the document that coupling both parts of the problem and treating it as a single problem either from experiments or from simulations results in a better representation of reality. However, this process has associated challenges which have to be addressed as far as possible. For instace, to implement the coupling, a mapping process is required to spatially distribute the parcels with their corresponding physical quantities resulting from the primary atomization model inside the nozzle. In addition, the coupling would also require an interpolation since the computational time-steps used in both fields are quite different (on the order of 10^{-8} for the internal nozzle flow calculations and 10^{-6} for the spray analysis) [1].

The current Thesis includes the separate study of the different fields that make up the GDI injection process and also takes into account the coupling of these domains. For this purpose, the problem is approached by solving the complete trajectory of the flow from the first moment it is injected until it leaves the injector and develops as a spray through two different CFD codes involving two contrasting meshing strategies: an automatic mesh generation with Adaptive Mesh Refinement (AMR) algorithm through CONVERGE™ and a static meshing technique which allows the selection of different types of cell shape in StarCCM+. The methodology used for the investigation and optimization of these fields of research, both internal and external flow, and independently of the employed software, is based on the classical conservation equations of Navier Stokes, which describe the behavior of fluid dynamics. The multi-phase internal nozzle flow study is performed in an Eulerian framework using a single-fluid approach and the interface-capturing Volume-of-Fluid method is considered to simulate the two-phase (liquid and gas) flow inside the nozzle. In order to consider the phase change existing in the in- and near-nozzle field, the well-known Homogeneous Relaxation Model is selected, in which attention must be paid to the variables that define it and influence the behavior of the fluid. On the other hand, the study of the external flow is carried out in an Eulerian-Lagrangian or Droplet Discrete Model approach for its simplicity and accuracy in the results. The associated models concerning atomization and breakup, collision and coalescence, evaporation as well as turbulence (RANS and LES) will be presented in this chapter, having to be properly calibrated when employed in GDI cases. Finally, the coupling between research fields is performed under a one-way coupling strategy; first the internal flow is simulated in an Eulerian framework and then the obtained

results are transferred as input for the study of the external flow from a DDM approach.

However, it is necessary to mention that these codes are relatively new as is the case of CONVERGE™ . StarCCM+ is the result of the evolution of a primitive simulation software called StarCD, which was initially more focused on diesel calculations. Just as experimental strategies used for diesel injection were adapted in the GDI study, the sub-models employed in these software have been mostly validated for diesel applications, so their accuracy may vary or even require further calibration. Nevertheless, developers and the research community, including the present Thesis, are making an effort to solve these problems and improve the calculations.

5.2 Computational Fluid Dynamics Modeling

Computational Fluid Dynamics (CFD) is considered the science that produces quantitative predictions of fluid-flow phenomena such as heat transfer and chemical reactions by means of computer-based numerical simulations [2]. This technique is held in high regard and is considered powerful in that it can alleviate many of the limitations of experimental analysis. It has the ability to minimize research and study time while complementing the experimental findings. For these reasons, among many others, the aerospace engineering industry incorporated CFD tools into the design, research and development and manufacture stages of aircraft and jet engines since the 1960s. In recent years, CFD methods have been applied to other branches of knowledge and especially to the design of internal combustion engines (ICEs) and injection systems, becoming an essential tool in the design process due to its potential for optimizing key performance parameters through quick and cost-effective analysis.

It is worth mentioning that in the context of injection systems, the computational study becomes a challenge since the injection process is associated with a turbulent flow originating inside the nozzle and continuing downstream of the nozzle. During this dynamic motion, numerous fluctuations are generated over a wide range of length scales. The turbulent Reynolds number associated with the flow inside a real injector can be in the range of 2000 to 30000 or even higher nowadays [3] with an integral scale of the order of tens of centimeters, while the Kolmogorov scale is of the order of microns, the scale on which the diameters of the droplets are found [4]. This scale separation and their sizes makes it computationally very complex to solve all of them in an unsteady multi-phase flow. Therefore, there is a tendency to model some

or most of the terms of the equations governing the statistical properties in order to minimize the complexity and computational expense [5]. This section presents the modeling strategy followed throughout this thesis to deal with the difficulties mentioned above. First of all, the fundamentals in the form of the classical equations of computational fluid dynamics of Navier-Stokes are outlined. It also discusses in detail the approaches available in the literature for the study and resolution of turbulence. Subsequently, the sub-models involved in the study of internal and external flow such as phase change, breakup and atomization models, those that take into account the collision and coalescence of droplets or the evaporation of droplets. Finally, the numerical algorithms and discretization schemes used in the software are presented.

5.2.1 Navier-Stokes equations

The dynamics of the multi-phase fluid during the injection process is governed by the classical Navier-Stokes conservation equations of mass, momentum and energy. For numerical resolution, the equations are adapted to the problem to be studied, and the equations can be simplified by disregarding some terms. The turbulent compressible transport equations for mass and momentum can be expressed according to Equation 5.1 and Equation 5.2, respectively.

$$\frac{\partial \rho}{\partial t} + \frac{\partial (\rho u_i)}{\partial x_i} = S \tag{5.1}$$

$$\frac{\partial (\rho u_i)}{\partial t} + \frac{\partial (\rho u_i u_j)}{\partial x_j} = -\frac{\partial P}{\partial x_i} + \\ + \frac{\partial}{\partial x_j}\left[\mu\left(\frac{\partial u_i}{\partial x_j} + \frac{\partial u_j}{\partial x_i}\right) - \frac{2}{3}\mu\frac{\partial u_k}{\partial x_k}\delta_{ij}\right] + \frac{\partial \tau_{ij}}{\partial x_i} + S_i \tag{5.2}$$

In the above equations, u represents the velocity of the fluid, ρ corresponds to the density, S is a source term (e.g., evaporation for the mass conservation equation, and spray coupling or mass sources for the momentum equation), P is the pressure, μ reflects the viscosity, δ_{ij} is the Kronecker delta and τ_{ij} denotes the Reynolds stresses of the system ($\tau_{ij} = \rho\, u_i' u_j'$) which need to be modeled to provide mathematical closure and to account for turbulence effects (discussed in Section 5.2.2).

Coupled with this, the compressible energy transport expression in terms of internal energy for multi-phase flows is defined from Equation 5.3.

$$\frac{\partial \rho e}{\partial t} + \frac{\partial (\rho u_j e)}{\partial x_j} = -P\frac{\partial (\rho u_j)}{\partial x_j} + \\ + \sigma_{ij}\frac{\partial (\rho u_i)}{\partial x_j} + \frac{\partial}{\partial x_j}\left(K\frac{\partial T}{\partial x_j}\right) + \frac{\partial}{\partial x_j}\left(\rho D_{diff}\sum_m h_m \frac{\partial Y_m}{\partial x_j}\right) + S \quad (5.3)$$

where Y_m corresponds to the mass fraction of each species defined as Equation 5.4, D_{diff} is denoted as the mass diffusion coefficient, e is the specific internal energy, K represents the conductivity, h_m defines the species enthalpy, σ_{ij} is the stress tensor, and T is temperature.

$$Y_m = \frac{M_m}{M_{tot}} = \frac{\rho_m}{\rho_{tot}} \quad (5.4)$$

being M_m the mass of species in the cell, M_{tot} the total mass in the cell, ρ_m the density of each species, and ρ_{tot} the density of the cell.

In some studies involving more than one species, as is the case in the present research, it is necessary to add another transport equation, in this case the so-called species transport equation, defined from Equation 5.5. The species equations can be solved alone or together with any of the other transport equations.

$$\frac{\partial \rho_m}{\partial t} + \frac{\partial (\rho_m u_j)}{\partial x_j} = \frac{\partial}{\partial x_j}\left(\rho D_{diff}\frac{\partial Y_m}{\partial x_j}\right) + S_m \quad (5.5)$$

It should be mentioned that for turbulent cases, the molecular mass diffusion coefficient is denoted as $D_t = \nu_t / Sc_t$ and the conductivity coefficient is defined as $K_t = C_p \mu_t / Pr_t$. Both parameters are defined from the turbulent viscosity and turbulent Schmidt-Prandtl numbers, respectively.

5.2.2 Turbulence modeling

One of the major problems in fluid mechanics is the treatment of turbulence. In most of the case studies the regime is turbulent, so adequate turbulence models are necessary to approximate the results to reality. It should be noted that turbulence is a property of the flow and not of the fluid. Turbulent flow can be defined as: three-dimensional, time dependent, dissipative and conditioned by boundary conditions. Thus, an enormous amount of information

is required to completely describe a turbulent flow. Turbulence, through a convective process, enhances considerably the momentum, energy and species rate of the mixture resulting in a production of unsteady 3D rotational eddies with a great range of spatial and temporal scales that interact with the flow in a dynamically complex motion [6].

The complexity of deeply characterizing turbulent flow analytically and even experimentally, makes CFD simulations a fundamental tool to capture and understand the chaotic effects due to turbulence. The turbulent flow has a series of fluctuations in the fields of velocity, pressure or density, which can be of small scale and high frequency being very expensive and complex to simulate computationally. Therefore, the equations governing the process are manipulated to eliminate the small scales and thus obtain a set of equations that are simpler to solve. However, these modified equations contain a number of additional variables as well as turbulence models needed to determine the velocity field and other variables.

The turbulence models are framed in the context of computational fluid mechanics, therefore the stability of the solution and the simulation time are very important parameters, without forgetting that the results must represent reality. The three most important methods that currently exist to deal with turbulence are presented in Figure 5.1 and described in the following lines.

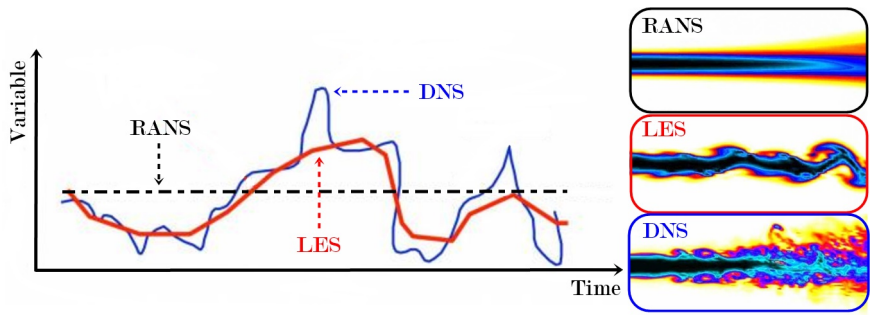

Figure 5.1: Typical time evolution of a specific local parameter predicted by RANS, LES and DNS turbulence approaches.

- **Reynolds-Averaged Navier-Stokes (RANS)**. RANS methods are characterized by employing the average value of the flow variables, thus modeling the full range of turbulent scales. They are based on a statistical treatment of the fluctuations about a stationary or a slowly varying flow [7]. Accordingly, the model predictions at a given spatial time

is a uniform average quantity, as depicted in Figure 5.1. The instantaneous dependent variables are decomposed into two parts: a mean, time- or ensemble-averaged part of the flow and a fluctuating component representing deviations from this mean. This operating method results in additional unclosed higher-order terms in the transport equations due to interactions between turbulent fluctuations. These terms need to be modeled by introducing turbulence closure models, which add additional transport equations to the classical conservation expressions. There are numerous ways of dealing with the unclosed non-linear term of the Navier-Stokes equation depending on the technique used for modeling. These different strategies, which will be described in detail below, comprise either modeling the turbulent viscosity or modeling the Reynolds stress tensor by adding the corresponding transport equations. The employment of these techniques greatly reduces the computational power required and thus the associated computational cost, making them the mainstay of flow calculations for engineering applications over the last decades.

- **Large Eddy Simulation (LES)**. This method seeks to directly represent three-dimensional, non-stationary turbulent motions, while the effects of small scales are modeled. In other words, it filters the Navier-Stokes equations spatially to separate the large and small scale turbulent structures. The large-scale turbulence is solved by the discretized equations, while the small-scale turbulence is modeled through the subgrid-scale models (SGS) (see Figure 5.2). This is due to the fact that large scales are more effective in the transport of properties, while small scales are weaker and have lower transport capacity. The spatial filter is typically associated to the mesh size and must be small enough to allow a meaningful quantity of energy associated with the largest eddies to be resolved. Despite the simplicity of the models, the dependence on meshing strategy in addition to solving the transient flow equations makes the required computational resources so challenging that they are only feasible for research-scale applications. It is well true that thanks to enormous computational progress and the increasingly possibility of using parallel architectures, LES applications are much more affordable for widespread industrial use where large-scale time-dependent flow characteristics have an important role to play.
- **Direct Numerical Simulation (DNS)**. This approach consists in solving the scales of motion, with initial and boundary conditions appropriate to the problem at hand, which means that the complete in-

stantaneous Navier-Stokes equations (mean flow and all turbulent fluctuations) are calculated without any model. Thus, the non-stationary Navier-Stokes equations are solved explicitly on sufficiently fine meshes that allow capturing all the temporal and spatial scales of the turbulence (see Figure 5.1). The resolution of the mesh has to be chosen so that even the smallest scales (Kolmogorov scales) are solved, this being the limitation of the method. Currently, this type of schemes are reserved for low to moderate Reynolds number problems since the resolution of the grid is proportional to the Reynolds number. The main advantage of the method is the procurement of accurate results in exchange for long simulation times and thus high computational costs. This scheme is still used to study turbulence, and its validity is comparable to that of experiments [7].

Figure 5.2 summarizes the different turbulent approaches described in the energy spectrum. As illustrated, the RANS model encompasses the modeling of all spatial frequencies corresponding to eddies of all sizes. The opposite case is the DNS where all the turbulent scales present are resolved without the need to use any turbulent model. In between these two approaches, the LES scheme resolves the large turbulent scales above the spatial filter (Δ_e) and models the smaller energy eddies by using SGS models. In the present thesis, the RANS and LES approaches have been employed for the analysis and will be described in detail in the following sectiosn. More detailed information and description of the models can be found in the literature [2, 7].

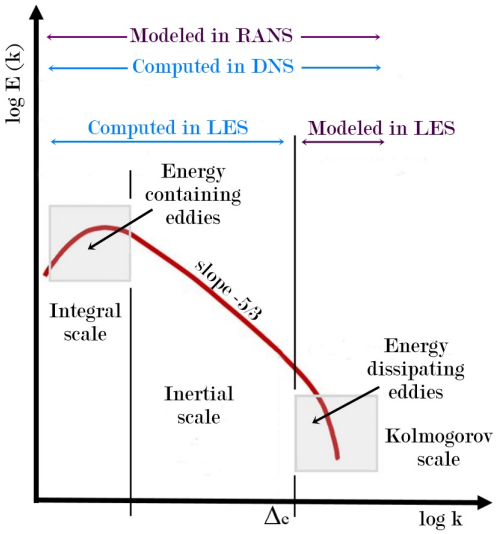

Figure 5.2: Sketch of Kolmogorov energy spectrum as function of the wave numbers for all turbulent flows: RANS, LES and DNS turbulent schemes.

5.2.2.1 Reynolds-Averaged Navier-Stokes (RANS)

The operating principle of the RANS models introduces an additional unclosed term that accounts for the effects of turbulence in the classical conservation

equations, known as Reynolds stresses or τ_{ij} in Equation 5.4. The treatment of this new term depends on the model used for it, and are categorized according to the number of additional transport equations needed to be solved together with the governing Navier-Stokes equations (Equations 5.1 and 5.2). Two-equation turbulent models are the most commonly used in the study of the GDI injection process. In RANS, flow variables, such as the velocity, decomposed into an ensemble mean and a fluctuating term as follows:

$$u_i = \bar{u}_i + u_i^{'} \tag{5.6}$$

where u_i is the instantaneous velocity, $\bar{u}_i$ the ensemble mean term and $u_i^{'}$ the fluctuating term.

Among the two-equation models, most used and generally accepted fall into k-ε and k-ω models. These along with their diverse variants are explained below as they have been applied in the present research work.

- **k-ε models**

  Conventionally, RANS models employ an effective turbulent viscosity to model the Reynolds stress term (Boussinesq hypothesis). Therefore, additional turbulent diffusion (i.e., diffusive mixing) models the turbulent convective mixing.

  The turbulence length scale le suitable for all two-equations k-ε models is described as,

  $$le = C_{\mu}^{3/4} \frac{k^{3/2}}{\varepsilon} \tag{5.7}$$

  being C_{μ} a model constant which can be tuned as function of a particular flow, k the turbulent kinetic energy and ε the turbulent kinetic energy dissipation rate.

  Standard and RNG k-ε models

  The Standard k-ε model is the most commonly selected based on the eddy viscosity concept. Despite being the most popular model and having numerous advantages, there are certain weaknesses, such as the incapability of capturing the subtler relationships between the turbulent energy production and the turbulent stresses caused by anisotropy of the normal stresses. In addition, the performance of the k-ε model is considered poor in some significant cases, like: (1) some unconfined flows; (2) flows with large extra strains (e.g., curved boundary layers, swirling

flows); (3) rotating flows; and (4) flows driven by anisotropy of normal Reynolds stresses [8].

It is important to mention that both models, Standard and RNG (Renormalization Group), are similar although the RNG model has certain improvements that increase its accuracy and also make it applicable to a wider number of flows:

- Includes an additional term in the equation that improves the accuracy in high vorticity flows.
- The swirl effect is incorporated to improve swirling flows.
- Provides an analytical formula for turbulent Prandtl numbers.
- Offers an analytical differential equation for the effective viscosity that takes into account the effects of low Reynolds numbers.

The modeled Reynolds stress for the Standard [6] and RNG k-ε [9] models is represented proportional to mean rates of deformation as proposed by Boussinesq [10]. This expression is defined as,

$$\tau_{ij} = \bar{\rho}\widetilde{u_i' u_j'} = 2\mu_t S_{ij} - \frac{2}{3}\delta_{ij}\left(\rho k + \mu_t \frac{\partial \tilde{u}_i}{\partial x_i}\right) \tag{5.8}$$

where the over-bar denotes the ensemble mean and the tilde means the Favre average.

The turbulent kinetic energy (k) is defined as half of the trace of the stress tensor (Equation 5.9), the turbulent viscosity (μ_t) is expressed as Equation 5.10 and, finally, the mean strain rate tensor S_{ij} is described according Equation 5.11.

$$k = \frac{1}{2}\widetilde{u_i' u_i'} \tag{5.9}$$

$$\mu_t = C_\mu \rho \frac{k^2}{\varepsilon} \tag{5.10}$$

$$S_{ij} = \frac{1}{2}\left(\frac{\partial \widetilde{u_i}}{\partial x_j} + \frac{\partial \widetilde{u_j}}{\partial x_i}\right) \tag{5.11}$$

Although these terms were already added in the classical conservation equations (Equation 5.3), it is interesting to repeat that the models use turbulent diffusion ($D_t = \nu_t / Sc_t$) and turbulent conductivity

($K_t = C_p\mu_t/Pr_t$) terms to account for the presence of turbulence in mass transport and energy transport.

Both studied models (Standard and RNG k-ε models) require additional transport equations to determine the turbulent viscosity (Equation 5.10). One of the equations is referred to the turbulent kinetic energy (k) and the other one to the turbulent kinetic energy dissipation rate (ε). Both of them are described in Equation 5.12 and Equation 5.13, respectively.

$$\frac{\partial \rho k}{\partial t} + \frac{\partial (\rho u_i k)}{\partial x_i} = \tau_{ij}\frac{\partial u_i}{\partial x_j} + \frac{\partial}{\partial x_j}\left(\frac{\mu + \mu_t}{Pr_k}\frac{\partial k}{\partial x_j}\right) - \rho\varepsilon + \frac{C_s}{1.5}S_s \quad (5.12)$$

$$\frac{\partial \rho \varepsilon}{\partial t} + \frac{\partial (\rho u_i \varepsilon)}{\partial x_i} = \frac{\partial}{\partial x_j}\left(\frac{\mu + \mu_t}{Pr_\varepsilon}\frac{\partial \varepsilon}{\partial x_j}\right) + C_{\varepsilon 3}\rho\varepsilon\frac{\partial u_i}{\partial x_i} + \\ + \left(C_{\varepsilon 1}\frac{\partial u_i}{\partial x_j}\tau_{ij} - C_{\varepsilon 2}\rho\varepsilon + C_s S_s\right)\frac{\varepsilon}{k} + S - \rho R \quad (5.13)$$

where S represents the user-defined source term and S_s expresses the source term that accounts for interactions with the discrete phase in cases where is needed. The $C_{\varepsilon i}$ terms are model constants that consider compression and expansion. Equation 5.13 includes at the end of the expression the term R which has a null value ($R = 0$) for the Standard k-ε model but for the RNG approach it is defined from the following structure,

$$R = \frac{C_\mu \eta^3 (1 - \eta/\eta_0)}{(1 + \beta\eta^3)}\frac{\varepsilon^3}{k} \quad (5.14)$$

being the expression for η,

$$\eta = \frac{k}{\varepsilon}|S_{ij}| = \frac{k}{\varepsilon}\sqrt{2S_{ij}S_{ij}} \quad (5.15)$$

To summarize, the model constants involved in the above equations are depicted in Table 5.1.

	Standard k-ε	***RNG k-ε***	***Realizable k-ε***
C_μ	0.09	0.0845	0.09
$C_{\varepsilon 1}$	1.44	1.42	1.44
$C_{\varepsilon 2}$	1.92	1.68	1.9
$C_{\varepsilon 3}$	-1.00	-1.00	-1.00
σ_k	1.00	1.39	1.00
σ_ε	0.7692	1.39	0.833
β	-	0.012	-
η_0	-	4.38	-

Table 5.1: Default values of constants of the k-ε turbulence models.

Realizable k-ε model

In certain scenarios such as when the mean strain rate is high, Standard k-ε model can produce negative values for turbulent kinetic energy. This type of result is considered non-realizable because it is not physically possible. From this need, the Realizable model arises which imposes certain constraints to ensure that there are no negative values of the turbulent normal stresses and at the same time do not violate Schwarz's inequality [11]. Thus, the value of the calculated turbulent kinetic energy is always a real physical value. The Realizable k-ε model works well for rotational flows.

The main and most important difference between the Realizable k-ε and the Standard k-ε is that while the expressions for turbulent viscosity are the same (Equation 5.10), the model constant C_μ for the Realizable k-ε varies as function of k, ε and u^* (friction velocity). Equation 5.16 defines the constant for the Realizable k-ε:

$$C_\mu = \frac{1}{A_0 + A_s \dfrac{k u^*}{\varepsilon}} \tag{5.16}$$

being A_0 and A_s model constants, and u^* can be expressed as function of the strain rate S_{ij} and the rotation rate Ω_{ij} as follows,

$$u^* = \sqrt{S_{ij} S_{ij} + \bar{\Omega}_{ij} \bar{\Omega}_{ij}} \tag{5.17}$$

The turbulent kinetic energy transport equation for this model is the same one as for the Standard and RNG k-ε models (Equation 5.9). However, the turbulent dissipation is denoted as,

$$\frac{\partial \rho\varepsilon}{\partial t} + \frac{\partial(\rho u_i \varepsilon)}{\partial x_i} = \frac{\partial}{\partial x_j}\left[\left(\mu + \frac{\mu_t}{\sigma_\varepsilon}\right)\frac{\partial \varepsilon}{\partial x_j}\right] + C_1\rho\varepsilon S - \\ - C_2\rho\frac{\varepsilon^2}{k+\sqrt{\nu\varepsilon}} + C_{1\varepsilon}\frac{\varepsilon}{k}C_{3k}P_b + S_\varepsilon \quad (5.18)$$

where C_2 and $C_{3\varepsilon}$ are additional model constants and P_b the production term.

To summarize, the model constants involved in the above equations are similar to the ones of the Standard k-ε model and depicted in Table 5.1.

It should be mentioned the main limitation of the Realizable k-ε model which is the production of non-physical turbulent viscosities in situations when the computational domain contains both rotating and stationary fluid zones. This happens due to the introduction of the effects of mean rotation in the definition of the turbulent viscosity.

- **k-ω models**

  Another of the most common ways to deal with turbulence is from the k-ω turbulent models. This approach also adds two additional transport equations and typically two different variations of this model are known which will be described below as they will be used in the studies to follow. The variations mentioned are the Standard k-ω and the Shear Stress Transport (SST) models. Both models use similar transport equations for k and ω but the SST model differs from the Standard model in the following aspects:

  - There is a gradual change from the standard k-ω model in the inner region of the boundary layer to the k-ε model in the outer part of the boundary layer.
  - The SST model incorporates a modified turbulent viscosity equation in order to account for the transport effects of the principal turbulent shear stresses (Equation 5.19).

$$\tau_{ij} = \mu_t\left(2S_{ij} - \frac{2}{3}\delta_{ij}\frac{\partial \widetilde{u_k}}{\partial x_k}\right) - \frac{2}{3}\rho k\delta_{ij} \quad (5.19)$$

  Each k-ω model uses a different formulation of the effective turbulent viscosity (μ_t). Whereas, all the two-equation k-ω models take as a ref-

erence the turbulence length scale le expressed as,

$$le = \frac{k^{1/2}}{C_\mu^{3/4}\omega} \tag{5.20}$$

Standard k-ω (1998) model

The transport equation for the turbulent kinetic energy (k) is defined by Equation 5.23 whereas the transport equation for the dissipation rate (ω) is expressed as Equation 5.22.

$$\frac{\partial \rho k}{\partial t} + \frac{\partial \rho u_j k}{\partial x_j} = P - \beta^* \rho \omega k + \frac{\partial}{\partial x_j}\left[(\mu + \sigma_k \mu_t)\frac{\partial k}{\partial x_j}\right] \tag{5.21}$$

$$\frac{\partial \rho \omega}{\partial t} + \frac{\partial \rho u_j \omega}{\partial x_j} = \frac{\alpha \omega}{k} P - \beta \rho \omega^2 + \frac{\partial}{\partial x_j}\left[(\mu + \sigma_\omega \mu_t)\frac{\partial \omega}{\partial x_j}\right] \tag{5.22}$$

For both expression, the turbulent viscosity is described as,

$$\mu_t = \frac{\rho k}{\omega} \tag{5.23}$$

The mean strain tensor rate (S_{ij}) and the production term (P) are defined for this model through Equation 5.24 and Equation 5.25, respectively.

$$S_{ij} = \frac{1}{2}\left(\frac{\partial \widetilde{u_i}}{\partial x_j} + \frac{\partial \widetilde{u_j}}{\partial x_i}\right) \tag{5.24}$$

$$P = \tau_{ij}\frac{\partial \widetilde{u_i}}{\partial x_j} \tag{5.25}$$

The model constants involved in the above equations take the values presented in Table 5.2.

SST k-ω model

The SST k-ω model stands out for combining the advantages of the Standard k-ω model and the Standard k-ε model. In general, it can be said that the SST k-ω model works very effectively when it comes to analyzing external flows but it is not so recommended for simulations that include the combustion process [12].

Standard k-ω (1998)					
Variable	**Value**	**Variable**	**Value**	**Variable**	**Value**
σ_k	0.5	σ_ω	0.5	α	13/25
f_β	$\frac{1+70\chi_\omega}{1+80\chi_\omega}$	β_0^*	0.09	β_0	9/125
β^*	$\beta_0^* f_\beta$	β	$\beta_0 f_\beta$	χ_ω	$\left\lvert\frac{\Omega_{ij}\Omega_{ij}\hat{S}_{ki}}{(\beta_0^*\omega)^3}\right\rvert$
Ω_{ij}	$\frac{1}{2}\left(\frac{\partial u_i}{\partial x_j}-\frac{\partial u_j}{\partial x_j}\right)$	f_{β^*}	$\begin{cases}1 & (\chi_k \leq 0)\\ \frac{1+680\chi_\omega^2}{1+400\chi_\omega^2} & (\chi_k > 0)\end{cases}$	χ_k	$\frac{1}{\omega^3}\frac{\partial k}{\partial x_j}\frac{\partial \omega}{\partial x_j}$

Table 5.2: Default values of constants of the Standard k-ω (1998) turbulence model.

The present model expresses the turbulent viscosity as,

$$\mu_t = \frac{\rho a_1 k}{max[a_1\omega, SF_2]} \tag{5.26}$$

being a_1 a model constant, F_2 defined as Equation 5.32 and S expressed as,

$$S = \sqrt{2S_{ij}S_{ij}} \tag{5.27}$$

Same as the model described above, the transport equation for the turbulent kinetic energy (k) is defined through Equation 5.21. Whereas, the transport equation expression for the dissipation rate (ω) is expressed by

$$\frac{\partial \rho\omega}{\partial t} + \frac{\partial \rho u_j \omega}{\partial x_j} = \frac{\alpha}{\nu_t}P - \beta\rho\omega^2 + \\ + \frac{\partial}{\partial x_j}\left[(\mu + \sigma_\omega \mu_t)\frac{\partial \omega}{\partial x_j}\right] + 2(1-F_1)\frac{\rho\sigma_{\omega 2}}{\omega}\frac{\partial k}{\partial x_j}\frac{\partial \omega}{\partial x_j} \tag{5.28}$$

The strain tensor (S_{ij}) follows the same expression as Equation 5.24 while the production term (P) differs from the classic models and takes the form of Equation 5.29.

$$P = min\left[\tau_{ij}\frac{\partial u_i}{\partial x_j}, 10\beta^*\rho\omega k\right] \tag{5.29}$$

Each constant in the turbulent kinetic energy and dissipation rate transport equations (such as σ_k) is a blend of inner (subscript 1) and outer (subscript 2) constants. For some constant ϕ, Equation 5.30 below defines the blending function:

$$\phi = F_1\phi_1 + (1 - F_1)\phi_2 \tag{5.30}$$

The expressions for F_1 and F_2 are like,

$$F_1 = tanh\left(min\left[max\left[\frac{\sqrt{k}}{\beta^*\omega d}, \frac{500\nu}{d^2\omega}\right], \frac{4\rho\sigma_{\omega 2}k}{CD_{k\omega}d^2}\right]^4\right) \tag{5.31}$$

$$F_2 = tanh\left(max\left[2\frac{\sqrt{k}}{\beta^*\omega d}, \frac{500\nu}{d^2\omega}\right]^2\right) \tag{5.32}$$

where

$$CD_{k\omega} = max\left[2\rho\sigma_{\omega 2}\frac{1}{\omega}\frac{\partial k}{\partial x_j}\frac{\partial \omega}{\partial x_j}, 10^{-10}\right] \tag{5.33}$$

To summarize, the model constants and auxiliary functions involved in the above equations are shown in Table 5.3.

SST k-ω					
Variable	**Value**	**Variable**	**Value**	**Variable**	**Value**
α_1	5/9	σ_{k1}	0.85	β_1	0.075
α_2	0.44	σ_{k2}	1.00	β_2	0.0828
κ	0.41	$\sigma_{\omega 1}$	0.500	β^*	0.09
a_1	0.31	$\sigma_{\omega 2}$	0.856		

Table 5.3: Default values of constants of the SST k-ω turbulence model.

5.2.2.2 Large Eddy Simulations (LES)

The main difference that distinguishes the RANS from the LES approach is how the fields involved in the analysis are decomposed for modeling. As discussed in Section 5.2.2.1, RANS models decompose the field into an ensemble mean and a fluctuating component. In contrast, in the LES cases the field is decomposed into a resolved field and a sub-grid field [13] as follows,

$$u_i = \overline{u}_i + u_i^{'} \tag{5.34}$$

where the over-bar indicates the resolved field and the prime denotes the sub-grid field. The resolved velocity field is described as a spatial average of the actual velocity field, which contrasts from the RANS approach, where the mean velocity field is an ensemble average of the mean velocity field. The difference in field decomposition means that, unlike RANS, LES filter have properties like those reflected in Equations 5.35 and 5.36.

$$\overline{\overline{u_i}} \neq \overline{u_i} \tag{5.35}$$

$$\overline{u_i'} \neq 0 \tag{5.36}$$

If the LES decomposition is included to the classical conservation equation of momentum (Equation 5.2), the following expression is obtained,

$$\frac{\partial\left(\bar{\rho}\tilde{u}_i\right)}{\partial t} + \frac{\partial\left(\bar{\rho}\tilde{u}_i\tilde{u}_j\right)}{\partial x_j} = -\frac{\partial \bar{P}}{\partial x_i} + \frac{\partial \bar{\sigma}_{ij}}{\partial x_j} - \frac{\partial \tau_{ij}}{\partial x_j} \tag{5.37}$$

where,

$$\widetilde{u_i} \equiv \frac{\overline{\rho u_i}}{\bar{\rho}} \tag{5.38}$$

Terms with '$-$' and '$\sim$' are the filtered quantities obtained through the Reynolds filtering and Favre-filtering, respectively. Density (ρ) and pressure (p) are Reynolds filtered, whereas velocity (u_i) and other thermodynamics variables are Favre-filtered to consider the compressibility of the fluid [7]. σ_{ij} is the stress tensor expressed by,

$$\bar{\sigma}_{ij} \cong \widetilde{\sigma}_{ij} = \mu\left(\frac{\partial \widetilde{u}_i}{\partial x_j} + \frac{\partial \widetilde{u}_j}{\partial x_i}\right) - \frac{2}{3}\mu\frac{\partial \widetilde{u}_k}{\partial x_i}\delta_{ij} \tag{5.39}$$

τ_{ij} is the stress flux tensor, computed as $\tau_{ij} = \overline{\rho}(\widetilde{u_i u_j} - \widetilde{u_i}\,\widetilde{u_j})$ at the sub-grid scale and needs to be closed by an additional sub-grid model. The great majority of LES models have as their principle of operation the modeling of the sub-grid stress tensor (τ_{ij}). However, there is also the possibility of using the upwinding (i.e. numerical viscosity) as LES model.

In the frame of the present investigation the most popular One-Equation Viscosity model and the Dynamic Structure sub-grid LES approaches have been considered and are described in the following lines. Both models are characterized by the addition of an extra transport equation (Equation 5.40)

for the kinetic energy sub-grid as formulated by Yoshizawa and Horiuti [14] and Menon et al. [15].

$$\frac{\partial k}{\partial t} + \bar{u}_i \frac{\partial k}{\partial x_i} = -\tau_{ij} \frac{\partial \bar{u}_i}{\partial x_j} - \epsilon + \frac{\partial}{\partial x_i}(\frac{\nu_t}{\sigma_k} \frac{\partial k}{\partial x_i}) \tag{5.40}$$

One-Equation Viscosity model

The One-Equation Viscosity model is characterized for using the sub-grid kinetic energy in modeling the turbulent viscosity. This approach represents the sub-grid kinetic energy as,

$$k = \frac{1}{2}(\overline{u_i u_i} - \bar{u}_i \bar{u}_i) \tag{5.41}$$

The model for the sub-grid stress tensor is given by Equation 5.42 where the turbulent viscosity, ν_t, is given as Equation 5.43.

$$\tau_{ij} = -2\nu_t \bar{S}_{ij} + \frac{2}{3} k \delta_{ij} \tag{5.42}$$

$$\nu_t = C_k k^{1/2} \Delta \tag{5.43}$$

being C_k a constant that can be adjusted by the user, defined as 0.05 for the present study [15]. In this framework, Δ is defined as the grid filter and its size and shape are fixed by the computational cell, therefore the filter type is a box for this analysis ($\Delta = \sqrt[3]{V_c}$). The sub-grid dissipation is defined as,

$$\varepsilon = \frac{C_\varepsilon k^{3/2}}{\Delta} \tag{5.44}$$

In the same way as the turbulent viscosity, the sub-grid dissipation can be tuned by adjusting the constant C_ε in the previous equation. For the current research, the value is set equal to 1 following the recommendations of Yoshizawa and Horiuti [14].

Dynamic Structure model

Unlike the previous model, the Dynamic Structure does not use turbulent viscosity to model the sub-grid stress tensor [16]. To enforce a budget on the energy flow between the resolved and the sub-grid scales, this model also adds the additional transport equation for the sub-grid kinetic energy presented in Equation 5.40. To that end, the sub-grid stress tensor (τ_{ij}) models must be a function of the sub-grid turbulent kinetic energy (k), resulting in a set of

six Fredholm integral equations of the second kind that can be solved via an iterative method. The modeled stress tensors are given by,

$$\tau_{ij} = c_{ij} k \tag{5.45}$$

$$T_{ij} = c_{ij} K \tag{5.46}$$

where the *test* level kinetic energy is defined by,

$$K = \frac{1}{2}\left(\widehat{\overline{u_i u_i}} - \widehat{\overline{u}}_i \widehat{\overline{u}}_i\right) \tag{5.47}$$

The trace of the Leonard term relates the *test* and *grid* level kinetic energies so that an additional transport equation for K is not required. That is,

$$K = \widehat{k} + \frac{1}{2} L_{ii} \tag{5.48}$$

Substituting these models for the two stress tensors into the Germano identity yields the following,

$$L_{ij} = K c_{ij} - \widehat{k c_{ij}} \tag{5.49}$$

Alternatively, in an algebraic model, it is removed the tensor coefficient from the integral and then solved for τ_{ij}. Thus the model for the sub-grid tensor becomes,

$$\tau_{ij} = 2k \left(\frac{L_{ij}}{L_{ii}}\right) \tag{5.50}$$

The constants adopted for both LES models are shown in Table 5.4.

	Dynamic Structure	***One-Equation Viscosity***
Variable	**Value**	**Value**
C_{les}	2.0	2.0
C_k	0.5	0.05
C_ϵ	1.0	1.0
C_{ps}	0.03	0.03
$1/Pr_k$	1.0	1.0

Table 5.4: Default values employed for the constants of the LES turbulence models.

5.2.3 Internal nozzle flow

As it has been mentioned several times throughout this document, the direct gasoline injection process involves numerous associated phenomena. To capture those specifically related to internal flow, it is necessary to implement a series of models to understand physical processes such as phase change by cavitation or flash boiling, which, despite extensive theoretical and experimental research, are not yet fully understood.

In recent years, there have been many advances in experimental techniques for visualization of internal flow as well as in computational models developed for modeling the flow inside the nozzle coupled with the increased availability of computational power. This has allowed to carry out more in depth analyses, understanding the behavior of the flow inside the nozzle with the associated phase changes, recirculation movements, possible formation of tip wetting or the presence of dribble phenomena [17]. One of the main challenges is to correctly model and simulate the multi-phase systems due to the tightly coupled coexisting phenomena such as turbulence, phase change and mass transfer between phases. On the other hand, another challenge to consider is to achieve a balance between computational efficiency and maintaining an accurate description of the relevant processes.

In this context, in order to simulate the two-phase (liquid and gas) flow inside and near the nozzle the Volume-of-Fluid (VOF) is selected. Meanwhile, the phase change that takes place in the injection process either by phenomena such as cavitation or the widespread in the field of gasoline flash boiling have been modeled from the well-known Homogeneous Relaxation Model (HRM). Both sub-models will be discussed in the present section.

5.2.3.1 Volume-of-Fluid (VOF)

The VOF approach works under the assumption that both fluids share jointly a momentum and energy equation (Equations 5.2 and 5.3) and are coupled through the interface. It has the ability to be applied to both compressible and incompressible fluids. In low pressure applications, liquids can be considered as incompressible and gases as compressible. However, it should be noted that certain high pressure applications require the applicability of compressibility because of the importance it can have in the solution. The principle of operation of the VOF method is based on the tracking of the volume of fluid in each of the cells. The volume of fluid is typically represented by the void fraction α, which reflects the fraction of gas that occupies the cell volume, in other words the volume of the cell that is not occupied by liquid.

The problems addressed in this thesis typically consist of three-component two-phase mixture: a liquid phase (subindex 1), a vapor phase (subindex 2) and the ambient non-condensable gas (N_2 or air) (subindex 3). The mixture density is computed as the weighted average of each component densities and it is expressed through the following equation:

$$\rho = \alpha_1\rho_1 + \alpha_2\rho_2 + \alpha_3\rho_3 = \alpha_g\rho_g + (1-\alpha_g)\rho_l \tag{5.51}$$

being α_i the volume fraction of each component and the subindex g the sum of vapor and non-condensable gas.

Volume fractions α_i and mass fractions Y_i are related through,

$$\rho_i\alpha_i = Y_i\rho \tag{5.52}$$

Finally, the global void fraction α_g takes the form,

$$\alpha_g = \frac{Y_g/\rho_g}{\sum Y_i/\rho_i} \tag{5.53}$$

For this application, the void fraction is not solved with an explicit transport equation which means that it is not transported directly. Individual species are solved first through the species mass fraction transport equation (Equation 5.5), and then the void fraction is calculated. In this way, the sum of Equation 5.5 for all components simplifies to the continuity Equation 5.1. Continuity is resolved to provide the density of the mixture, and simultaneously all the species transport equations are solved for the species mass fractions. A specific reconciliation procedure is carried out at the end of every cycle to ensure that any discrepancies due to rounding error are adjusted by renormalizing the mass fractions of the species to meet global continuity.

The gas-phase densities are obtained according to the equation of state for an ideal gas, being R_i the gas constant and T the temperature,

$$\rho_i = \frac{p}{R_iT} \tag{5.54}$$

In order to compute the void fraction of each cell, the VOF method interprets function α_g as the following meanings:

$\alpha_g = 0$, if the computational cell is filled with pure liquid.

$0 < \alpha_g < 1$, if the computational cell is filled with both liquid and gas.

$\alpha_g = 1$, if the computational cell is filled with pure gas.

It is important to mention that the present studies where the VOF approach is used to address the multi-phase fluid does not expect sharp or nearly sharp interface between liquid and vapor phases and therefore do not implement the interface-capturing function. For this reason, available models such as HRIC or PLIC will not be described. More information about the mentioned models can be found in [18, 19].

5.2.3.2 Homogeneous Relaxation Model (HRM)

Phase change is an important phenomenon to take into account especially in GDI injection because of the tendency of the fuel to produce instantaneous phase changes (flash boiling) when operating conditions are suitable. Mass transfer resulting from phase change may arise at the liquid-gas interface. Generally, in a multi-component mixture, it may take place between the liquid fuel and its vapor, or it may arise when the gas is liberated or absorbed into the liquid solution. In both cases, various species and different mechanisms are implicated.

The phase change phenomena involved in the present Thesis, cavitation and flash boiling, have a similar behavior with a specific thermodynamic difference and under different time scales (Section 3.4.4 and 3.4.5). Cavitation process represents the vapor formed from a pressure drop in the liquid flow at constant low temperatures while flash boiling effect takes place at slightly higher temperatures and lower pressure drop. Another important difference between phenomena is that cavitation implies a very small amount of superheating to evaporate the liquid, and as a result the process is extremely rapid whereas flash boiling requires a higher degree of superheating, and the process involves a significantly longer time. As it is already mentioned, the model for mass exchange between liquid and vapor is based on the HRM model as proposed by Bilicki and Kestin [20]. This model determines the ratio at which the instantaneous vapor quality x (the mass fraction of vapor in a two-phase mixture) tends to its equilibrium value $\bar{x}$ over a given time-scale θ and proposes the following simple linearized Equation 5.55 to determine such rate.

$$\frac{Dx}{Dt} = \frac{\bar{x} - x}{\theta} \tag{5.55}$$

The instantaneous non-equilibrium vapor quality x (or dryness) is defined as,

$$x = \frac{Y_{vap}}{Y_{vap} + Y_{liq}} = \frac{m_{vap}}{m_{vap} + m_{liq}} \tag{5.56}$$

It should be noted that the ratio excludes the local air fraction. The equilibrium vapor quality $\bar{x}$ is function of the thermodynamic properties at the local pressure and can be expressed by the following equation with bounds at zero and unity,

$$\bar{x} = \frac{h - h_{l,sat}}{h_{v,sat} - h_{l,sat}} \tag{5.57}$$

where h corresponds to the actual enthalpy of liquid and vapor, excluding air content, and subscripts l, sat and v, sat refer to saturated liquid and vapor, respectively.

The time scale θ of Equation 5.55 is evaluated using an empirical fit proposed by Downar-Zapolski et al. [21]. For vaporization, the time scale θ_E can be represented as follows:

$$\theta_E = \theta_0 \alpha_g^{-0.54} \varphi^{-1.76} \tag{5.58}$$

For condensation, the time scale θ_C can be defined as:

$$\theta_C = F\theta_0 \alpha_g^{-0.54} \varphi^{-1.76} \tag{5.59}$$

where α_g corresponds to the global gas phase volume fraction, F is the time scale factor by which the evaporation time scale is factored. A typical value for F is 5000, meaning condensation occurs 5000 times slower than evaporation under similar conditions. The value of the coefficient θ_0 is $3.84e-7s$ and the non-dimensional pressure ratio (φ) is given by

$$\varphi = \left| \frac{P_{sat} - P}{P_{crit} - P_{sat}} \right| \tag{5.60}$$

being the subscripts *sat* and *crit* the saturation and critical pressure of the fluid, respectively.

It is important to note that the default values of the correlations shown in Equation 5.58 and 5.59 have been experimentally determined in flashing flows in water pipes with upstream pressures in excess of 10 bar. In the absence of data for other fluids, normally for GDI applications the existing values tends to be used, although this should be validated.

The species transport equation (Equation 5.5) has a source term S_m, that it is calculated by considering the time-resolved evolution of x, obtained through the integration of Equation 5.55 from the current state $x^{(0)}$ at the time t_0, to the new state $x^{(1)}$ at the time $t_0 + \Delta t$, which is expressed as,

$$x^{(1)} = \bar{x} - \left(\bar{x} - x^{(0)}\right) e^{\Delta t/\theta} \tag{5.61}$$

The initial value $x^{(0)}$ stands for the most current state and is determined by Equation 5.56 as $x^{(0)} = Y_{vap}^{(0)}/(Y_{vap}^{(0)} + Y_{liq}^{(0)})$. Therefore, designating the cell volume with V, the source term S_m in Equation 5.5 associated with vapor production is defined by:

$$S_{vap} = \frac{(x^{(1)} - x^{(0)}) + (m_{vap} + m_{liq})}{V\Delta t} = \frac{(x^{(1)} - x^{(0)})\rho^{(0)} + (Y_{vap}^{(0)} + Y_{liq}^{(0)})}{\Delta t} \tag{5.62}$$

Accordingly, the source term related to the liquid transport equation is $S_{liq} = -S_{vap}$.

It is important to note that Equations from 5.55 to 5.60 are applicable for single chemical component flows and, for the most part, the presence of a non-condensable gas modifies the phase behavior of a system [22]. The effect that the presence of a third component, such as air, may have on the system and especially on the mixture deserves further discussion. The use of this phase change model implicitly assumes that the air content, being very small, does not alter the vapor-liquid equilibrium. Therefore, the enthalpy of air is excluded from the calculation of $\bar{x}$ in Equation 5.57 resulting in the evaporation capacity of the liquid fuel also in the presence of non-condensable gas. Finally, the correlation provided by Equations 5.58 and 5.60 uses the overall void fraction and the overall pressure to calculate the time scale of mass transfer, as in the original model [21], but this does not affect the equilibrium value at which the mixture will relax [23].

Characteristic parameters of the HRM model

The characteristic parameters of this model are presented in Table 5.5. These will be modified throughout the study to observe how they influence the solution, being always the reference configuration the one presented in the aforementioned table.

Homogeneous Relaxation Model (HRM)	
Variable	**Value or Expression**
Time scale coefficient	3.84 e-07 s
Condensation time scale factor	5000
Power index of void fraction	-0.54
Power index of pressure ratio	-1.74

Table 5.5: Configuration of the HRM phase change model.

5.2.4 Spray modeling

During the injection process in GDI engines, the liquid is injected into the combustion chamber using a fuel injection system where the nozzle plays an important role (Section 2.4). As it has been discussed several times throughout the document (i.e. Section 3.5), the injection process involves numerous associated sub-processes (atomization, mixing, evaporation, among others). The great influence that the atomization and mixing processes have on the overall combustion efficiency, engine performance and thus on pollutant emissions, makes a correct understanding and detailed modeling of the associated sub-processes indispensable.

As with internal flow, the increasing improvement in experimental diagnostic techniques, the huge advances in computational modeling as well as the enormous improvement in computing power has encouraged the development of more in-depth spray analysis to understand in detail the phenomena that take place during the injection process. In this context, numerous spray breakup models have been developed to characterize fuel injection using CFD techniques. Thus, the atomization process is modeled in two different phases: primary and secondary atomization. Primary atomization considers the rupture of liquid jet due to increasing instabilities of the liquid/gas interface or a combination of turbulent perturbations and instability theories [24]. It is often studied by VOF or EE methods. Meanwhile, the rupture of the fuel ligaments is usually modeled by a Discrete Phase Model (DPM) using a Lagrangian approach. However, this approach only operates accurately in regions where droplets are dispersed in the absence of liquid ligament.

This section describes the physics behind the numerical spray sub-models used to perform the modeling of the sub-processes associated with gasoline direct injection.

5.2.4.1 Discrete Phase Modeling (DPM)

The Eulerian-Lagrangian (EL) or also known as the Discrete Droplet Model (DDM) approach is, as already seen in Section 4.3.2, the most common formulation for the study of spray behavior and performance. This method is based on, through a Lagrangian approach, capturing the dynamics of liquid droplets, spray breakup, heat transfer, evaporation and collision. However, the ambient gas and vapor phase (carrier phase) are resolved using an Eulerian approach. One thing that has been highlighted is the main assumption made in the EL approach which is to consider the liquid droplets as a particle point implying that the flow inside and around the particles does not need

to be resolved. Because of this, drop effects are reflected through empirical correlations and the inter-phase interactions through exchange terms [25].

Both software used in the present Thesis, CONVERGE™ and STAR-CCM+, have implemented the DPM approach to model the behavior of the multi-phase flow. As mentioned above, the gas phase (considered as a continuum) is solved from an Eulerian approach through the Navier-Stokes equations presented in Section 5.2.1. On the other hand, the liquid phase (considered as a discrete phase) is defined in a Lagrangian framework based on the equation presented below (Equation 3.38).

The trajectories of the discrete particles are determined individually during the computation of the continuous phase, based on the equation of motion of the droplets (Equation 3.38) defined from Newton's second law which consists of modeling the drag force experienced by the droplets.

In this study of spray development, the drop parcel approach is considered, which is based on introducing into the computational domain a certain number of parcels at a given rate from the user-defined position of the injector. A parcel is defined as a set of droplets of similar sizes, positions and physical properties (velocity, temperature, among others) that are grouped in a way that allows solving Lagrangian equations for averaged properties of each parcel thus making the computational cost of the model much lower and thus more affordable.

Parcels can be injected into the computational domain from different size distributions [26]. The most common, and therefore used in this study, is known as the **blob injection model** in which the injected drop sizes are equal to the nozzle diameter or effective diameter of the injector.

5.2.4.2 Drop drag and liquid/gas coupling

One of the main terms of the equation of motion of drops (Equation 3.38) is defined as the drag term which is made up of several parts, highlighting the drag coefficient. The drag coefficient (C_D) can be assumed, under Schiller-Naumann correlation [27], to be equal to that of a spherical droplet [28], in which case it is given by the O'Rourke expression [29] presented in Table 3.3. However, as a droplet moves through a gas it can undergo deformation (in the most extreme case taking the shape of a disk) and affect the drag coefficient, which has a strong dependence on the shape of the droplet. Therefore, one option is to use a dynamic drag coefficient that varies linearly between the drag coefficient of a sphere and that of a disk [28], and which expression corresponds to Equation 3.40.

Equation 3.40 considers the droplet distortion y. For the calculation of y in this study, the TAB (Taylor Analogy Breakup) model of O'Rourke and Amsden [29] is adopted, which is on the basis of the Taylor analogy between an oscillating deformed drop and a spring-mass system. Equation 5.63 shows the equation of a damped, forced harmonic oscillator.

$$F - k_s x - d_s \dot{x} = m\ddot{x} \tag{5.63}$$

where in this case x is the displacement of the droplet equation from its spherical undisturbed position, F represents the external aerodynamic (drag) forces, k_s is the spring constant representing the surface tension and d_s the damping parameter analogous to the viscous forces.

Taylor's analogy is based on relating the external force to the aerodynamic force, the restoring force to that exerted by the surface tension of the liquid and the damping force to the viscosity of the liquid as follows:

$$\frac{F}{m} = C_F \frac{\rho_g |\boldsymbol{U}|^2}{\rho_l r_0} \tag{5.64a}$$

$$\frac{k_s}{m} = C_{k,s} \frac{\sigma}{\rho_l r_0^3} \tag{5.64b}$$

$$\frac{d_s}{m} = C_{d,s} \frac{\mu_l}{\rho_l r_0^2} \tag{5.64c}$$

where ρ_l and ρ_g are the discrete (liquid) phase and continuous (gas) phase densities, $\boldsymbol{U}$ represents the relative velocity between the droplet and the surrounding ambient gas, r_0 denotes the undisturbed droplet radius, σ is the drop surface tension, μ_l corresponds to the drop viscosity, and $C_F = 1.3$, $C_{k,s} = 8$, $C_{d,s} = 5$ and $C_b = 0.5$ (defined below) are dimensionless constants determined by O'Rourke and Amsden [29] by means of experimental tests.

5.2.4.3 Atomization and drop breakup modeling

During the injection process, at the moment the fluid is injected into the discharge chamber, it undergoes different processes such as atomization. This section focuses on the techniques that allow modeling this process of a continuous liquid into droplets.

There are two subsets of spray modeling: primary atomization and secondary atomization. The primary atomization model makes assumptions about the physics inside the nozzle and thus provides initial and boundary

conditions for liquid fuel injection at the nozzle outlet and in the near-nozzle region (spray droplet size and distribution, droplet velocities, temperature, among others). On the other hand, in the secondary atomization models, the droplets penetrate the domain where they become hydrodynamically unstable and break into smaller droplets. In addition, droplets can interact with each other directly through collision (phenomenon and model described below), creating larger or smaller droplets and changing the dynamics of the spray plume.

Determining the appropriate atomization and breakup models (and the associated determination of model constants) for a specific spray simulation is complex. In particular, a trial-and-error procedure known as calibration is usually necessary.

Primary Atomization

- **Huh atomization model**

  Huh's model is founded on the premise that the two most important mechanisms in spray atomization are the inertia of the gas and the internal turbulent stresses developed in the nozzle. Atomization according to the present model is considered to be divided into two phases:

  - The turbulence present inside the nozzle produces initial perturbations on the jet surface as it leaves the nozzle orifice.
  - Once the disturbances achieve a certain level, they grow exponentially due to pressure forces. These forces are driven by the interaction with the surrounding fluid (surface wave growth), until these perturbations are detached from the jet surface in the form of droplets.

  The model calculates the initial perturbations from an analysis of the flow through the hole and then uses standard wave-growth theory, along with other assumptions, to account for the atomization process.

  Nozzle Turbulence

  The average turbulence kinetic energy (k_a) and its dissipation rate (ε_a) at the hole exit are calculated from the following relations, which are derived from force and energy balances:

$$k_a = \frac{U_{inf}^2}{8\left(\frac{L}{D}\right)} \left\{ \frac{1}{C_d^2} - K_c - 1 \right\} \tag{5.65}$$

$$\varepsilon_0 = K_\varepsilon \frac{U_{inf}^3}{2L} \left\{ \frac{1}{C_d^2} - K_c - 1 \right\} \tag{5.66}$$

being U the average injection velocity over the time period of injection, L corresponds to the nozzle length, D represents the nozzle diameter and K_ε is an empirical coefficient, value of 0.5, proportional to the initial dissipation rate of turbulent kinetic energy at the nozzle exit. Furthermore, K_c is the form loss coefficient, normally equal to 0.45. It is a proportionality constant for the pressure loss (Δp_f) associated with the sharpness of the nozzle entrance corner and can be calculated as $K_c = 2\Delta p_f / \rho U^2$. C_d is defined as the nozzle discharge coefficient.

Surface Wave Growth

The interaction between the liquid jet and the surrounding gas field defines the second stage of the primary atomization process. This interaction causes the perturbation amplitude to increase with the growth velocity of the $Re[\omega]$ wave until these perturbations detach from the jet surface. These detached parts create the so-called "secondary droplets". The amplitude of the perturbation follows the dispersion equation, which is derived by Taylor [30] as

$$(\omega + 2\nu\kappa^2)^2 + \frac{\sigma\kappa^3}{\rho_d} - 4\nu^2\kappa^3(\kappa^2 + \frac{\omega}{\nu})^{1/2} + (\omega + iU\kappa)^2 \frac{\rho}{\rho_d} = 0 \tag{5.67}$$

where ω is the wave celerity and σ is the coefficient of surface tension, ν represents the liquid kinematic viscosity, i is the imaginary number and $\kappa = 2\pi/L_w$ is the wavenumber with $L_w = L_A/C_2$ the wavelength of surface perturbation ($C_2 = 0.5$) and $L_A = C_1 L_t$ the atomization length scale ($C_1 = 2.0$).

The time scale of atomization τ_A is taken to be a linear combination of the turbulent time scale τ_t and the wave growth time scale τ_W:

$$\tau_A = C_3\tau_t + C_4\tau_W = \tau_{spn} + \tau_{exp} \tag{5.68}$$

being $\tau_{spn} = C_3\tau_t$ the spontaneous time scale ($C_3 = 1.0$) and $\tau_{exp} = C_4\tau_W$ the exponential time scale ($C_4 = 1.5$).

Droplet Size Distribution

The Huh approach assumes that droplets exit the nozzle with diameter D_d then breakup into secondary droplets. The breakup rate for droplets can be defined as:

$$\frac{dD_d}{dt} = -\frac{2L_A}{\tau_A K_A} \tag{5.69}$$

where D_d is defined as the diameter of the parent droplet and K_A a model constant to control the break-up rate ($K_A = 0.1$).

This initial breakdown process tends to stop when the spontaneous time scale is greater than the exponential scale.

The probability density function depicted in Equation 5.70 estimates the diameter of the secondary droplets that form from the rupture of the mother droplet.

$$f(x) = C\frac{\Phi(x)}{\tau_A(x)} \tag{5.70}$$

being x the droplet size, C a normalization constant and $\Phi(x)$ can be described as a dimensionless turbulence energy spectrum (assuming isotropic turbulence), estimated with the following expression:

$$\Phi(x) = \frac{(\kappa(x)/\kappa_e)^2}{(1 + (\kappa(x)/\kappa_e)^2)^{11/6}} \tag{5.71}$$

defined $\kappa_e = 2\pi/L_e$ and $L_e = L_t/0.75$ with L_t being the turbulence length scale.

The distribution function for droplet diameters, $F(x)$, is then;

$$F(x) = \int_{x_{min}}^{x} f(x)dx \tag{5.72}$$

where x_{min} is the minimum droplet size expressed following the Kelvin-Helmholtz instability theory as:

$$x_{min} = 2\pi\frac{\sigma_d(\rho_d + \rho)}{U^2\rho_d\rho} \tag{5.73}$$

Droplet Velocity Distribution

The initial velocity for each droplet is defined by the polar angle (θ_d) and the azimuthal angle (α_d). The polar angle is assumed to be equal

probability of velocity direction between the user-specified inner cone angle θ_i and outer cone angle θ_0.

$$\theta_d = \theta_i + X_r(\theta_0 - \theta_i) \tag{5.74}$$

where X_r is defined as a random number between 0 and 1. Assuming that the azimuthal angle is defined as the user-specified swirl angle and the magnitude of the droplet velocity at nozzle exit is the liquid film velocity V_f, the components of droplet velocity are calculated as: $u_{d,x} = V_f sin(\theta_d) sin(\alpha_d)$, $u_{d,y} = V_f sin(\theta_d) cos(\alpha_d)$ and $u_{d,z} = V_f cos(\theta_d)$.

- **Kelvin-Helmholtz (KH) atomization model**

  The Kelvin-Helmholtz (KH) model is based on the analysis of the stability of a cylindrical viscous jet subjected to an infinitesimal perturbation [31]. For this purpose, it introduces an infinitesimal perturbation and solves the conservation equations of continuity and momentum, obtaining oscillating velocity and pressure profiles. The main purpose of the calculation is to obtain a dispersion relation (relation between the wavelength, $\omega_{KH} = \omega_{KH}(k_{KH})$, and the growth rate of the perturbation, $\lambda_{KH} = 2\pi/k_{KH}$.

  This model assumes that the rupture is produced by the most unstable wave, i.e., the one with the maximum growth rate. It relates growth rate and wavelength by special functions and highly correlated expressions, making analytical resolution impossible. Therefore Reitz and Bracco [32] solved the equation numerically by curve fitting; obtaining for the maximum growth rate, Ω_{KH}, and its corresponding wavelength, Λ_{KH} , the following expressions respectively:

$$\Omega_{KH}\left[\frac{\rho_l r_p^3}{\sigma}\right]^{0.5} = \frac{(0.34 + 0.38We_g^{1.5})}{(1+Oh)(1+1.4T^{0.6})} \tag{5.75}$$

$$\frac{\Lambda_{KH}}{r_p} = 9.02\frac{(1+0.45Z_l^{0.5})(1+0.4T^{0.7})}{(1+0.87We_g^{1.67})} \tag{5.76}$$

being $We_g = \rho_g U^2 r_0/\sigma$ and $We_l = \rho_l U^2 r_0/\sigma$ the gas a liquid Weber numbers, respectively. $Re_l = U r_p/\nu_l$ is the Reynolds number, $Oh = \sqrt{We_l}/Re_l$ corresponds to the Ohnesorge number and $T = Oh\sqrt{We_g}$ represents the Taylor number. Note that $U = |u_i - v_i|$ where u_i is the fluid-phase velocity and v_i is the drop velocity.

In the KH model, the initial diameters of the parcels are set to be equal to the nozzle orifice diameter d_0 and the atomization process of the large injected bubbles is characterized using the stability analysis for liquid jets as described above. The breakup of the parcels and the resultant droplets is obtained by presuming that the droplet breakup radius r_c is proportional to the wavelength of the fastest growing unstable surface wave given by Equation 5.76. In another words,

$$r_c = B_0 \Lambda_{KH} \tag{5.77}$$

where B_0 is a model constant typically set to 0.61 but it is one of the constants that enters into the calibration process so that smaller values of B_0 result in smaller droplet sizes while larger values mean bigger droplets.

The rate of change of drop radius in a parent parcel is given by

$$\frac{dr_p}{dt} = -\frac{(r_p - r_c)}{\tau_{KH}}, \qquad (r_c \leq r_p) \tag{5.78}$$

being the breakup time τ_{KH} expressed as,

$$\tau_{KH} = \frac{3.726 B_1 r_p}{\Lambda_{KH} \Omega_{KH}} \tag{5.79}$$

The breakup time constant B_1, ranging from 5 to 100, is related to the initial disturbance level on the liquid jet and has been found to vary from one injector to another. Once breakup takes place and it is established that child droplets should be incorporated into the calculation, they are attributed a velocity component normal to the trajectory of the parent droplet. This normal velocity is computed by,

$$v_n = C_1 \Lambda_{KH} \Omega_{KH} \tag{5.80}$$

where C_1, typically set to 0.188, is the last constant that makes up the calibration set of the KH model.

- **Kelvin-Helmholtz-ACT (KH-ACT) atomization model**

  The KH-ACT model is a modified version of the KH scheme in which aerodynamic effects, cavitation and turbulence are included during the primary atomization process. In fact, for the calculation of instantaneous length and time scales, the assumptions presented above are used:

$$L_{KH} = r - r_{KH} \tag{5.81}$$

$$\tau_{KH} = \frac{3.726 B_1 r_p}{\Lambda_{KH} \Omega_{KH}} \tag{5.82}$$

The rate of decrease in droplet radius (Equation 5.78) is proportional to the ratio of length to time scale (L_A/τ_A). Thus the largest ratio determines the dominant breakup process.

$$\frac{L_A}{\tau_A} = max \left\{ \frac{L_{KH}(t)}{\tau_{KH}(t)}; \frac{L_{CAV}}{\tau_{CAV}}; \frac{L_T(t)}{\tau_T(t)} \right\} \tag{5.83}$$

Aerodynamic-Induced Breakup

If the aerodynamically induced breakup process is prevailing, then the KH model, as expressed by Equation 5.81, is selected for primary atomization. However, if cavitation or turbulence processes dominate, the following breakup principle is employed:

$$\frac{dr}{dt} = -C_{T,CAV} \frac{L_A}{\tau_A} \tag{5.84}$$

being $C_{T,CAV}$ the model constant which ranges from 0.1 to 1.

Cavitation-Induced Breakup

The cavitation generated inside the injector can reach the outside of the nozzle, which causes the radius of the injected parcels to be affected, thus decreasing their value, and enhancing jet atomization. The subsequent premise is that cavitation features are conducted to the jet periphery by the turbulence velocity within the fluid, and either burst at the periphery or collapse before reaching it. Therefore, the characteristic cavitation time-scale is defined as [33],

$$\tau_{CAV} = min(\tau_{collpase} : \tau_{burst}) \tag{5.85}$$

All cavitation bubbles generated inside the orifice that reach the orifice outlet are gathered into a single artificial bubble that occupies the accumulated area of the smaller bubbles:

$$R_{CAV} = r_{hole} \sqrt{(1 - C_a)} \tag{5.86}$$

where R_{CAV} represents the effective radius of an equivalent bubble from the nozzle and is defined as length scale for the cavitation-induced

breakup ($L_{CAV} = R_{CAV}$). The area reduction coefficient (C_a) is calculated from flow simulations inside the injector and r_{hole} is the exit radius of the nozzle orifice.

Bubble collapse depends on the bubble size and its time is determined following Rayleigh Plesset [34] theory as,

$$\tau_{collapse} = 0.9145 R_{CAV} \sqrt{\frac{\rho_l}{\rho_v}} \tag{5.87}$$

Cavitation bubbles are distributed throughout the walls of the hole; nevertheless, the effective bubble is located at the center of the liquid spray when it is injected. The average time necessary for a cavitation bubble to achieve the jet periphery can be derived as follows,

$$\tau_{burst} = \frac{r_{hole} - R_{CAV}}{u'_{turb}} \tag{5.88}$$

where u'_{turb} is usually obtained from inner nozzle flow simulations.

Turbulence-Induced Breakup

This model is according to Huh Gosman's premise that turbulent fluctuations in the liquid jet are responsible for the initial perturbations on the jet surface. These waves grow according to KH instabilities until they breakup from the surface. The relevant length and time scales ($L_T(t)$ and $\tau_T(t)$, respectively) for turbulence-induced breakup are calculated as follows:

$$L_T(t) = \frac{C_\mu K(t)^{1.5}}{\varepsilon(t)} \tag{5.89}$$

$$\tau_T(t) = \frac{C_\mu K(t)}{\varepsilon(t)} \tag{5.90}$$

where C_μ and C_ε are the turbulent constants of the model and $K(t)$ and $\varepsilon(t)$ the instantaneous turbulent kinetic energy and dissipation rate, respectively. The initial turbulent kinetic energy and turbulent dissipation rate can be readily estimated from the below equations as follows:

$$K_0 = \frac{U_{inf}^2}{8\left(\frac{L}{D}\right)} \left\{ \frac{1}{C_d^2} - K_c - (1 - s^2) \right\} \tag{5.91}$$

$$\varepsilon_0 = K_\varepsilon \frac{U_{inf}^3}{2L} \left\{ \frac{1}{C_d^2} - K_c - (1 - s^2) \right\} \tag{5.92}$$

taking the model constants to be the following: $K_c = 0.45$, $K_\varepsilon = 0.27$ and $s = 0.01$. C_d is defined as the nozzle discharge coefficient.

Secondary Atomization

- **KH-RT Breakup model**

  The KH-RT breakup model is based on the combination of two sub-models such as the Kelvin-Helmholtz (KH) and the Rayleigh-Taylor (RT). Both models consider the growth of instabilities in a droplet but each has its own physics.

  In the Kelvin-Helmholtz (KH) approach instabilities are due to the slip velocity of the droplet, which eventually shears small child droplets off the parent, and are categorized within the stripping regime. On the other hand, instabilities associated with the Rayleigh-Taylor (RT) model are due to the slip velocity of the droplet, which eventually shears small child droplets off the parent one, within the catastrophic regime. These two models work in competition with each other, the instabilities grow simultaneously and it is first checked if the RT mechanism is able to break the droplet, which means that the instabilities have grown sufficiently. If not, it is the KH model that takes over the droplet breaking.

  Some software, such as CONVERGE™ , allows to activate what is known as KH-RT breakup length, which allows to have an intact core zone (L_b) defined by Equation 5.93 where only the KH model operates. Once this length is reached, the KH-RT mechanism comes into action, as shown in Figure 5.3.

$$L_b = C_{bl}\sqrt{\frac{\rho_l}{\rho_g}}d_0 \tag{5.93}$$

  Assuming high gas Weber numbers, C_{bl} must be equal to $B_1/2$ and d_0 takes the initial value of the droplet.

  The KH-RT model was developed as an alternative to the TAB model and preferably used for high Reynolds numbers. The only difficulty with this model is the problem of correctly adjusting the coefficients involved in the rupture mechanism.

  The atomization breakup associated to the KH model is based on the expressions proposed by Reitz [35] (Equations 5.75 and 5.76). The wavelength and growth-rate in turn are used to formulate a characteristic

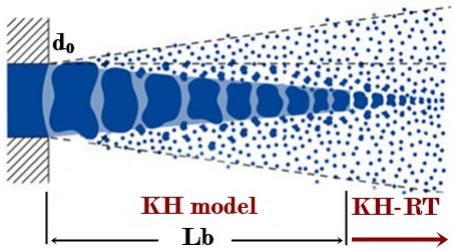

Figure 5.3: Schematic of the KH-RT spray breakup model. Adapted from [34].

time-scale (Equation 5.79) and length-scale for breakup (Equation 5.96) caused by these instabilities.

$$R_{KH} = B_0 \Lambda_{KH} \tag{5.94}$$

If the condition that $R_p > R_{KH}$ is met, the correct conditions are satisfied for the breakup to occur due to instabilities associated to the KH model, in which case the parent droplet radius decreases according to Equation 5.78. The droplets radius (R_p) in the parent parcel remains unchanged; whereas it is the number of droplets that is calculated to conserve mass. The child parcels are assigned a velocity that is normal to the original velocity of the parent parcel (Equation 5.80).

Rayleigh-Taylor instabilities are claimed to be the reason for the catastrophic mechanism of rupture. Following Senecal et al. [36], the relationship between the wavenumber and growth-rate as a function of the droplet acceleration a, where it is also incorporated the effect of viscosity on these instabilities, can be expressed as:

$$\omega_{RT} = -k_{RT}^2 \left(\frac{\mu_l + \mu_g}{\rho_l + \rho_g} \right) + \\ + \sqrt{K_{RT} \left(\frac{\rho_l - \rho_g}{\rho_l + \rho_g} \right) a - \frac{k_{RT}^3 \sigma}{\rho_l + \rho_g} + k_{RT}^4 \left(\frac{\mu_l + \mu_g}{\rho_l + \rho_g} \right)^2} \tag{5.95}$$

The wavelength and growth-rate in turn are employed to provide a characteristic time-scale and length-scale for the RT breakup that is caused by these instabilities:

$$R_{RT} = \frac{1}{2} C_3 \Lambda_{RT} \tag{5.96}$$

$$\tau_{RT} = \frac{C_\tau}{\Omega_{RT}} \tag{5.97}$$

being C_τ a model coefficient which takes the value of 1 and C_3 which ranges between 0.1 to 5.33 as reported in the literature. Equation 5.95 is solved numerically to give the wavelength Λ_{RT} corresponding to the maximum growth-rate Ω_{RT}. This is assumed to be the critical mode.

If the condition that $R_p > R_{RT}$ is met, it is assumed that the instabilities associated to the RT model are growing on the droplet. The instability should have a duration of τ_{RT} for a breakup event occurs and produce child droplets with new diameter R_{RT}.

- **Modified KH-RT Breakup Model**

  This model makes it possible to use the two breakup mechanisms without having to define an *ad hoc* breakup length (L_b). The primary atomization is left to the aerodynamic instabilities (KH waves) and is therefore responsible for the breakup of the parent parcels. Once the child droplets are created the secondary breakup is modeled with the competing effects of the KH and RT mechanisms.

5.2.4.4 Drop turbulent dispersion modeling

The effects of the turbulent flow on the dispersion of spray drops (parcels) are predicted by inserting an instantaneous fluctuating velocity $\boldsymbol{u}_i^{'}$ into the gas velocity $\boldsymbol{u}_i$ through a stochastic tracking method. Both RANS and LES turbulence models include source terms to account for the reduction of turbulent kinetic energy as a result of the work performed by turbulent eddies to dissipate the liquid spray droplets.

The source term S_s contain the fluctuating component of the fluid-phase velocity $\boldsymbol{u}_i^{'}$:

$$S_s = -\frac{\sum\limits_p N_p \left(F_{D,i}^{'} |\boldsymbol{u}_i^{'}|\right)_p}{V} \tag{5.98}$$

where the summation is over all the parcels in the cell, N_p is the number of droplets in a parcel, V is the cell volume and

$$F_{D,i}^{'} = -\frac{F_{D,i}}{|\boldsymbol{u}_i^{'}| + |\boldsymbol{u}_i| - |\boldsymbol{u}_p^{'}|} |\boldsymbol{u}_i^{'}| \tag{5.99}$$

with $\mathbf{u}_i$ the cell gas velocity, $\mathbf{u}_i^{'}$ the turbulent velocity of the cell gas, $\mathbf{u}_p^{'}$ the droplet velocity and most important $F_{D,i}$ the drag force on a drop.

O'Rourke Dispersion Model

The O'Rourke turbulent dispersion model implies that every discretized gaseous turbulent eddy is represented by a Gaussian distribution for the random velocity fluctuation and a time scale. Thus, the fluctuating velocity components of $u_i^{'}$ follows a Gaussian probability distribution defined as the following expression,

$$G(u_i^{'}) = \frac{1}{\sqrt{2\pi\sigma^2}} \exp\left(\frac{-(u_i^{'})^2}{2\sigma^2}\right) \tag{5.100}$$

being the variance σ^2 proportional to the turbulent kinetic energy (k) by a factor of 2/3 [26].

The new values of the trajectory ($u_i^{'}$) are calculated once every turbulence correlation time (t_d), parameter that is defined as the lesser of the eddy breakup time and the time for a droplet to traverse an eddy [37]. This drop-eddy interaction time takes the form presented in Equation 5.101.

$$t_{int} = \min\left(\frac{k}{\varepsilon}, c_{ps}\frac{k^{3/2}}{\varepsilon}\frac{1}{|\boldsymbol{u}_i^{'} + \boldsymbol{u}_i - \boldsymbol{v}^{'}|}\right) \tag{5.101}$$

where c_{ps} is an empirical constant and ε is the dissipation of turbulent kinetic energy.

Gosman and Ioannides Dispersion Model

The model proposed by Gosman and Ioannides [38] assumes that the particles undergo a sequence of turbulent eddies as it traverses a turbulent flow field. Here, an eddy is a local disturbance to the Reynolds-averaged velocity field. The particle remains in the eddy until either the eddy time-scale τ_e is exceeded, or the separation between the particle and the eddy exceeds the length scale of the eddy, l_e. In practice, an eddy transit time, τ_c serves in place of the latter. For this purpose and as in the O'Rourke model, the turbulence is assumed to be isotropic and to possess a Gaussian probability distribution in the fluctuating velocity. The main difference between the two methods is the way in which the time interval t_{int} over which the droplet interacts with the randomly sampled velocity field is determined. For this particular model, it takes the form of:

$$t_{int} = min(\frac{C_\mu^{1/2}k^{3/2}}{\varepsilon|\boldsymbol{u}^{'}|}, -\tau ln[1 - \frac{C_\mu^{1/2}k^{3/2}}{\varepsilon\tau|\boldsymbol{u} - \boldsymbol{v}|}]) \tag{5.102}$$

being τ the droplet "relaxation" time, defined as

$$\tau = \frac{4}{3}\frac{\rho_d D}{\rho C_D |\boldsymbol{u} - \boldsymbol{v}|} \tag{5.103}$$

It should be mentioned that in circumstances where $C_\mu^{1/2} k^{3/2}/\varepsilon\tau|\boldsymbol{u}-\boldsymbol{v}| > 1$ Equation 5.102 has no solution. This can be interpreted as implying that the droplet has been "captured" by the eddy, in which case $t_{int} = C_\mu^{1/2} k^{3/2}/\varepsilon|\boldsymbol{u}'|$.

5.2.4.5 Drop collision and coalescence modeling

The fundamental theoretical principles of the collision and coalescence models were described in Chapter 3.5. To deal with the collision and coalescence phenomena existing during the injection process without overly penalizing the computational cost of the studies, efficient collision and coalescence models based on the parcel concept described in a previous section are developed to estimate the number of droplet collisions (parcels) and their outcomes in a relatively efficient way. There are two models commonly used computationally for the treatment of collision and coalescence: O'Rourke model [39] and No Time Counter (NTC) [40] method.

Despite the widespread use of the O'Rourke model in many applications, the NTC collision method has been chosen for the present Thesis, which, even though it has a linear dependence on the number of parcels, has proven to be faster and more accurate than the traditional method on numerous occasions [41]. The NTC method is derived from techniques used in gas dynamics for Direct Simulation Monte Carlo (DSMC) calculations and involves stochastic (randomly determined) sub-sampling of the parcels within each cell. The way it operates makes collision calculations faster and, unlike the O'Rourke model which experiences an additional computational cost as it increases with the square of the number of parcels, the NTC collision model has a linear cost as mentioned above. In addition to this important difference, it should also be noted that O'Rourke's method assumes that multiple collisions can occur between parcels, this process being governed by the Poisson distribution. However, the Poisson distribution is not entirely correct unless the collisions have no effect on the properties of the parcels. The collision process directly affects the physical properties of the parcels (velocity, size and number) and this is why the method of repeated sampling used by the NTC method generates more accurate answers.

The NTC method is implicitly proposed from the basic probability model for stochastic collision. The standard probability model assumes that the

cell size is small enough so that spatial variations of the spray quantities can be disregarded. These assumptions are a subset of those needed to derive the O'Rourke collision model. This section gives a simple description of the implemented model, for more details see the work of [40].

The operating principle of the NTC method first categorizes the parcels into groups occupying the same cell, requiring only $2N$ operations, where N is the number of droplets in a cell. Subsequently, the NTC method chooses a stochastic subsample of all possible pairs in a cell. The number of pairs selected does not influence the final mean response, as long as the number satisfies the restrictions imposed by Schmidt and Rutland [40]. The probabilities of the pairs in the subsample are multiplied by the reciprocal of this fraction, increasing the probability of collision. Sampling is performed with substitution so that multiple collisions of a pair can be computed consistently.

The expected number of collisions in the cell during a time interval of Δt, considering that a single cell contains N droplets with a collision cross section given by σ_i, is given by the sum of the probability of all possible collisions:

$$M_{coll} = \sum_{i=1}^{\sqrt{M_{cand}}} q_i \sum_{j=1}^{\sqrt{M_{cand}}} \frac{q_j V_{i,j} \sigma_{i,j}}{(qV\sigma)_{max}} \tag{5.104}$$

where q is the number of droplets in a parcel, the value of $(qV\sigma)_{max}$ is used to scale the probability of selection of a collision and M_{cand} is defined as the number of pairs of possible collision candidates.

Equation 5.104 is considered the final expression of the NTC method for application to parcels representing varying numbers of drops. The overall cost will be proportional to the product of the limits of the summation, namely M_{cand} which is proportional to N_p by having q a dependency on $1/N_p$. Pairs of possible collision candidates are selected with replacement, so that multiple collisions can occur between the parcels, which is useful for accurate description when using large time intervals in dense jets.

Once a pair of parcels is sorted, a random number (r) between 0 and 1 is generated to determine whether the collision occurs or not, taking place when the following condition is met:

$$r < \frac{q_g V_{i,j} \sigma_{i,j}}{(qV\sigma)_{max}} \tag{5.105}$$

being q_g the greater number of droplets between q_i and q_j.

5.2.4.6 Drop evaporation modeling

In addition to the atomization models explained above, an evaporation model is also required. The standard approach to describe the evaporation process is to consider a one-component fuel model and assume phase equilibrium due to its simplicity and low consumption of computational resources [**Ayoub1995**].

Frössling Correlation Evaporation Model

Among the evaporative models, the Frössling evaporation model is one of the most widely used in the literature. This model is based on expressing the rate of change in the drop radius ($\dot{R}$) due to vaporization according to the Frössling correlation [26] as follows:

$$\dot{R} = \frac{dr}{dt} = -\frac{\rho_g D}{2\rho_l r_0} B_d Sh_d \tag{5.106}$$

where D is the mass diffusivity of liquid vapor in the gaseous phase of density ρ_g and B represents the mass transfer number, which can be related to the fuel mass fraction as:

$$B_d = \frac{Y_1^* - Y_1}{1 - Y_1^*} \tag{5.107}$$

where Y_1^* denotes the vapor fuel mass fraction at the droplet surface, Y_1 refers to the vapor fuel mass fraction, and Sh is the Sherwood number [26], which can be expressed as,

$$Sh_d = \left(2 + 0.6 Re_d^{1/2} Sc^{1/3}\right) \frac{\ln(1 + B_d)}{B_d} \tag{5.108}$$

where Re_d is the drop Reynolds number (Equation 3.3), Sc is the Schmidt number of the gas-phase, defined as $Sc = \mu_g/\rho_g D$, and $\ln(1 + B_d)/B_d$ is the Spalding function to consider the heat transfer modification in turbulent boundary layers.

The physical properties for the calculation of Reynolds and Schmidt numbers are calculated at a temperature function of the temperature of the droplets and the temperature of the surrounding gas, given by:

$$\widehat{T} = \frac{T_g + 2T_d}{3} \tag{5.109}$$

Within the Schmidt equation, the variation of the diffusivity with temperature is represented as,

$$\rho_g D = 1.293 D_0 (\widehat{T}/273)^{n_0 - 1} \tag{5.110}$$

being D_0 and n_0 experimentally-determined model constants. On the other hand, assuming that the partial pressure of fuel vapor to be equal to the equilibrium vapor pressure, the calculation of the saturated mass fraction Y_1^*, is performed by the following formula:

$$Y_1^* = \frac{M_{liquid}}{M_{liquid} + M_{mix}\left(\frac{p_g}{p_v} - 1\right)} \tag{5.111}$$

where M_{liquid} and M_{mix} refer to the molecular weights of the evaporating fuel and mixture (without including the vapor form the liquid species), respectively, p_g and p_v are the gas pressure and vapor fuel pressure, respectively.

5.2.4.7 Configuration of the spray model

This section contains the values taken as a reference from the spray models for the external flow simulation. It is important to mention that this configuration as well as the values will be varied throughout the study to analyze the influence of both the values and the models on the development and characteristics of the spray. The models used, presented in Table 5.6, differ from one software to another either due to availability in the software or due to the requirements of the contracting company to which the study injector belongs, so Table 5.7 depicts the variables and their values corresponding to the CONVERGE™ software, while Table 5.8 shows the data corresponding to StarCCM+.

	CONVERGE	**StarCCM+**
Injection method	Blob method	Blob method
Drag model	Dynamic drop drag	Schiller-Naumann
Atomization model		
RANS simulations	KH-ACT + KH-RT	Huh model + KH-RT
LES simulations	KH-RT + Breakup Length	-
Drop turbulent dispersion model	O'Rourke	Gosman and Ioannides
Drop collision model	NTC collision	NTC collision
Drop evaporation model	Frössling	Quasi-Steady evaporation

Table 5.6: Different models and sub-models implemented depending on the employed software.

5.2.5 VOF-spray one-way coupling. Mapping

The part dedicated to the coupling between internal and external flow through the mapping strategy has been carried out under the CONVERGE ™ software,

Atomization model for CONVERGE™ software			
Kelvin-Helmholtz ACT			
KC constant	0.45	*KE constant*	0.27
S constant	0.01	C_{TCAV}	1.0
LES simulation	OFF	*RANS simulation*	ON
Kelvin-Helmholtz		**Rayleigh-Taylor**	
Fraction of injected mass/parcel	0.05	*Model breakup time constant,* C_I	1.0
Shed mass constant, s	0.1-0.25	*Model size constant,* C_{RT}	0.1
Model size constant, B_0	0.61	*Breakup Length Model,* C_{bl}	
Model velocity constant, C_1	0.188	*LES simulation*	3.5
Model breakup time constant, B_1	7	*RANS simulation*	OFF

Table 5.7: Configuration of the primary and secondary atomization models for CONVERGE™ software.

Atomization model for StarCCM+ software			
Huh atomization			
Length scale coefficient, C_1	2.0	*Turbulence time scale coefficient,* C_{A1}	0.92
Wave length scale coefficient, C_2	0.5	*Turbulence length scale coefficient,* C_{A2}	0.4565
Spontaneous time scale coefficient, C_3	1.0	*Droplet breakup rate coefficient, KA*	0.1
Exponential time scale coefficient, C_4	1.5	*Minimum We number for breakup*	6.0
Kelvin-Helmholtz		**Rayleigh-Taylor**	
Maximum shed mass constant, s	0.3	*Model breakup time constant,* C_I	1.0
Model size constant, B_0	0.61	*Model size constant,* C_{RT}	0.1
Model velocity constant, C_1	0.188		
Model breakup time constant, B_1	5		

Table 5.8: Configuration of the primary and secondary atomization models for StarCCM+ software.

so the explanation described below is the one corresponding to the operation of this tool when under the mentioned coupling conditions.

The mapping methodology allows the combination between internal flow and external flow or, in other words, between VOF and Lagrangian spray modeling. This means that the initialization of the jet simulations is carried out with parcel data coming from the VOF simulations. This model has the great advantage of allowing the combination of high fidelity simulations of a fuel injector and nozzle system with computational inexpensive parcel-based spray simulations.

The one-way coupling through mapping process first performs a VOF simulation, which detects and identifies the injectors and nozzles involved in

the study based on the defined regions. From this simulation, maps corresponding to the defined sections are extracted, containing parcel position, velocity, turbulence, temperature, and cell size information from the VOF simulation. Once the necessary internal flow data have been extracted, the Lagrangian simulation (DDM) is performed with the corresponding models discussed above (Section 5.2.4). The parcels are initialized with the position, velocity, turbulence, and temperature data extracted from the VOF simulation. It is necessary to specify for each injector the maximum mass that is assigned to each liquid parcel and the volume fraction threshold. If a cell has a liquid volume fraction below the threshold, the model does not inject liquid parcels or vapor fuel. The software adjusts the number of parcels injected to match the total injected mass defined, so the liquid mass injected at a given time-step in the Lagrangian simulation is equal to the liquid mass at the corresponding time in the VOF simulation. The injection schemes is as follows:

1. At a given time-step, determine the total mass to inject.
2. For each defined data point, sum the liquid volume fraction of data points for which the liquid volume fraction exceeds the threshold.
3. Divide the total mass (determined in step 1) by the sum of the acceptable liquid volume fractions (determined in step 2). The result is the mass per unit volume fraction.
4. For each data point with a liquid volume fraction above the threshold, multiply the mass per unit volume fraction by the liquid volume fraction of the cell. The result is the mass to inject per cell.
5. Divide the mass to inject per cell by the maximum parcel mass and add 1 (Equation 5.112 below). This process ensures that each cell has at least one parcel.

$$\text{parcels per cell} = \frac{\text{mass to inject per cell}}{\text{maximum parcel mass}} + 1 \tag{5.112}$$

In those cells where multiple parcels are injected, all of them share the same radius defined according to the Equation 5.113.

$$R_p = \sqrt{C_a} \cdot 0.5 \cdot d_0 \tag{5.113}$$

5.2.6 Numerical methods

The computational studies carried out in the present Thesis have been conducted by means of two commercial software such as CONVERGE™ and StarCCM+. Both codes stand out for being based on the finite volume method to solve numerically the classical conservation equations in their integral form.

Usually, the steps followed by the CFD codes to perform the numerical resolution are as follows:

1. The governing transport equations of fluid flow are integrated over all the control volumes of the domain.
2. The obtained integral equations are discretized into a system of algebraic equations.
3. The solution of the algebraic equations is achieved by applying an iterative numerical algorithm.

Referring to the first step mentioned above, the classical governing transport equations presented above (Section 5.2.1) can be transformed from their differential form to an integral form as follows:

$$\frac{\partial \phi}{\partial t} + \frac{\partial (u\phi)}{\partial x} = 0 \Rightarrow \frac{d}{dt}\int_{V_c} \phi \, dV + \int_S u \cdot n\phi \, dS = 0 \tag{5.114}$$

being S the surface area, n the surface normal and V_c the cell volume. The integration of the resulting control volume represents the conservation of a global flow variable ϕ for each individual discrete cell in the domain. Therefore, the integral form of the equation is satisfied by adding all the fluxes on the faces of the cells. However, this does not occur in the software employed in the present study (CONVERGE™ and StarCCM+) where all values are placed and stored at the center of the cell as shown in Figure 5.4. Thus and to solve the integral form of the equation, the velocity and ϕ must be interpolated to the surface of the cell (step 2).

There are different methods in the literature to relocate the position of the values and obtain them on the cell surface (step 2). One of the most commonly used options is to upwind the surface value for ϕ, resulting in an accurate first-order spatial scheme:

$$\phi_{i+1/2} = \phi_i \tag{5.115a}$$

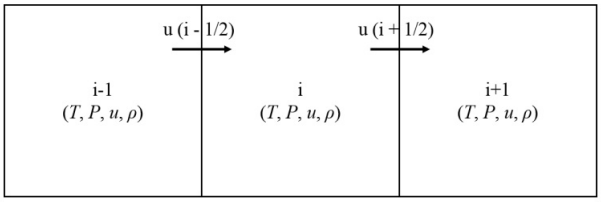

Figure 5.4: Scheme representing the central position of the values of the different variables in a one-dimensional spatial domain. Adapted from [42].

$$\phi_{i-1/2} = \phi_{i-1} \tag{5.115b}$$

Another widespread method is the result of a second-order accurate spatial scheme, in which the two values of adjacent cells are averaged and the resulting value is placed on the surface. Thus, the resultant value of ϕ at the surface can be expressed as,

$$\phi_{i+1/2} = \frac{1}{2}\phi_i + \frac{1}{2}\phi_{i+1} \tag{5.116a}$$

$$\phi_{i-1/2} = \frac{1}{2}\phi_i + \frac{1}{2}\phi_{i-1} \tag{5.116b}$$

To determine the convection flux term of the transport equation in its integral form there are different discretization schemes not only differentiated between first-order and second-order as mentioned in the previous lines but also depending on the method used in the calculation. Although there are several others in the literature, the most common ones are listed below and have therefore been used in this research. For more details about the available discretization schemes the reader is referred to the work of Versteeg and Malalasekera [2].

- **1st-Order**: *First-order upwind scheme.* This scheme scales the transported quantity by the upstream or downstream mass flowrate depending on flow direction. Only use when a higher-order scheme fails to give convergence, or in order to obtain an initial solution before switching to a higher-order scheme.
- **2nd-Order**: *Second-order upwind scheme.* This scheme introduces linear interpolation of cell values on either side of the upstream or downstream face. Using this scheme can lead to poorer convergence properties, but gives accuracy as good as, or better, than the first-order scheme.

- **Central**: *Central-differencing scheme.* This scheme is second-order accurate but is prone to dispersive error and stability problems. However, central-differencing is useful in large eddy simulation (LES) where upwind schemes accelerate the rate at which turbulent kinetic energy decays.

Depending on the type of study (internal flow or external flow) and based on the calculation software (CONVERGE™ and StarCCM+) the discretization scheme employed is different. Table 5.9 summarizes the discretization schemes implemented according to the different types of studies and software.

Software	Type of study	Scheme
CONVERGE	Internal Flow	1st-Order Upwind *(density, energy, passives, species and turbulence)* 2nd-Order Central *(momentum)* 1st-Order Upwind *(turbulence)*
	External Flow	2nd-Order Central *(density, energy, passives, species and momentum)*
StarCCM+	Internal Flow	1st-Order Upwind *(density, energy, momentum, species and turbulence)*
	External Flow	2nd-Order Upwind *(density, energy, momentum, species and turbulence)*

Table 5.9: Different discretization schemes to solve for the convective term in the transport equations according to the different types of studies and software.

In most discretization schemes, so-called flux limiters are used to ensure physically realistic results with the high-resolution schemes. A flux limiter is a function that constrains fluxes to significant values near discontinuities in the domain. Near these discontinuities, a flux limiter shifts to a first-order spatial discretization to prevent spurious oscillations in the solution. In the remaining part of the domain, though, the flux limiter adopts a higher-order spatial discretization to enhance the accuracy of the solution.

In the case of unsteady simulations, the transport equations not only use discretization schemes for the convective term but also need to be discretized

in time. The expression for the time evolution of the scalar of a general flow variable ϕ is given by:

$$\frac{\partial \phi}{\partial t} = F(\phi) \tag{5.117}$$

being F a function which includes any spatial discretization. If the time derivative term is discretized using the backward differences method, the corresponding first and second-order accurate temporal discretization schemes can be expressed respectively as:

$$F(\phi) = \frac{\phi^n + 1 - \phi^n}{\Delta t} \tag{5.118a}$$

$$F(\phi) = \frac{3\phi^n + 1 - 4\phi^n + \phi^{n-1}}{2\Delta t} \tag{5.118b}$$

where n, $n+1$ and $n-1$ represent the values at discrete times t, $t+\Delta t$ and $t-\Delta t$ respectively.

Finally, and corresponding to step 3, an iterative numerical algorithm is adopted to obtain solutions to the algebraic system of equations. The iterative algorithm takes as starting point in each time-step the values of the previous time-step (t-1), which are stored for all transported quantities. Subsequently, the explicit sources are computed for each submodel enabled at that particular moment. The pressure-velocity coupling is determined from an iterative method depending on the studied case and again on the software selected. In the present work, both the Semi-Implicit Method for Pressure-Linked Equations (SIMPLE) and the Pressure Implicit with Splitting of Operators (PISO) have been used [43]. Finally, the turbulence equations are usually resolved outside of the iterative loop for efficiency reasons. The order for resolving the transport equations is presented in Figure 5.5.

SIMPLE algorithm

The Semi-Implicit Method for Pressure-Linked Equations (SIMPLE) was originally put forward by Patankar and Spalding [44] and is essentially a guess-and-correct procedure for the calculation of pressure. It is an iterative method for calculating pressure and velocities, and when others scalars are coupled to the momentum equations, the calculations needs to be done sequentially [2].

PISO algorithm

The PISO algorithm, which stands for Pressure Implicit with Splitting of Operators, is suited for transient cases where the convective CFL number is small. It was developed originally for non-iterative computation of unsteady compressible flows. Recently, it has been adapted successfully for the iterative solution of steady state problems [45]. PISO algorithm includes one predictor step and two corrector steps, which means similar to SIMPLE algorithm with a further corrector step.

Comparing the PISO algorithm against the SIMPLE method:

- PISO is faster than SIMPLE at short time-steps, though both algorithms have the same level of temporal accuracy [45].
- PISO becomes unstable at long time-steps, when the combined CFL rises much above 10, while SIMPLE remains stable.
- As time-step size increases, SIMPLE loses temporal accuracy of transient solutions. However SIMPLE can still obtain accurate steady state solutions, if they exist, by using large time-step size.

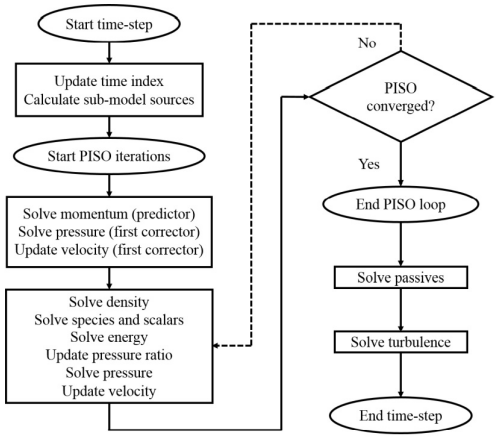

Figure 5.5: Scheme representing the solution order of the transport equations using the PISO algorithm [46].

Therefore, SIMPLE for situations where large time step sizes can be used, such as in achieving steady state, but use PISO when the problem requires the use of a small time step size and higher temporal precision.

In the present Thesis, in the case of CONVERGE™ , the transport equations are solved sequentially using PISO. On the other hand, for StarCCM+ cases, transport equations are treated sequentially with a Segregated Flow Solver and using an Implicit Unsteady Solver loop which corresponds to a SIMPLE method.

5.2.6.1 Rhie-Chow algorithm

As previously mentioned, all transported quantities are located at the center of the cell. This phenomenon can lead to a decoupling of the pressure and velocity which can produce fluctuations in the pressure and velocity solution. To counteract this effect, the Rhie-Chow interpolation scheme was developed which can be used to maintain the variables and eliminate undesirable checkerboarding [47].

The Rhie-Chow scheme operates by approaching the beneficial effects of the staggered grid scheme but keeping the variables placed. It includes a pressure gradient term to cancel the placed pressure update and a pressure term. This additional pressure term is equivalent to the staggered pressure update. This definition process results in

$$u^*_{i+1/2} = \frac{u^*_i + u^*_{i+1}}{2} - \frac{dt}{\rho}\left(\frac{P_{i+1} - P_i}{dx}\right) + \frac{dt}{2\rho}\left(\frac{P_{i+1} - P_{i-1}}{2dx} + \frac{P_{i+2} - P_i}{2dx}\right) \tag{5.119}$$

The Rhie-Chow scheme minimizes the checkerboarding effect in the pressure and velocity, but it also introduces a small error to the solution, similar to the error presented in staggered approach. Although it adds a small error, it is suggested that most simulations be run with the Rhie-Chow scheme activated [47].

5.2.6.2 Iterative linear solvers

Not only an iterative algorithm is necessary to solve the algebraic system of equations, but also a linear solver is needed for each of the governing conservation equations. Once the governing equations have been discretized, each of the equations can be expressed as a linear system of the form,

$$Ax = b \tag{5.120}$$

Solvers are usually iterative so they start with an assumed value of the variable x_0 and finds subsequent values that increasingly approach the given value of x. The process can be described as the limit given by

$$\lim_{n\to\infty}(x_n) = x \tag{5.121}$$

In each iteration, it is checked that,

$$\frac{\parallel r_n - r_0 \parallel}{\parallel r_0 \parallel} < \frac{1}{\text{tol scale}} \tag{5.122}$$

where r_n

$$r_n = \frac{\| Ax_n - b \|_2}{\| b \|_2} \tag{5.123}$$

The iteration loop stops if the criterion of Equation 5.122 is satisfied or a defined maximum iterations are reached.

The iterative solver chosen for the cases developed with CONVERGE™ software is the one called point-wise successive over-relaxation (SOR) while for the cases with StarCCM+ the scheme is called algebraic multigrid (AMG) Linear Solver with a relaxation scheme of Gauss-Seidel.

5.2.6.3 Courant-Friedrichs-Lewy (CFL) numbers

The Courant-Friedrichs-Lewy (CFL) is a necessary condition for convergence while solving certain partial differential equations numerically. It estimates the number of cells through which the related quantity will move in a single time step. In other words, it expresses that the distance that any information travels during the time-step length within the mesh must be lower than the distance between mesh elements. Therefore, a higher CFL number generally produces a less computationally expensive simulation. Different CFL numbers are defined: the convective CFL number (Equation 5.124a), the speed of sound CFL number (Equation 5.124b), and the diffusive CFL number (Equation 5.124c).

$$CFL_u = u\frac{\Delta t}{\Delta x} \tag{5.124a}$$

$$CFL_{mach} = c\frac{\Delta t}{\Delta x} \tag{5.124b}$$

$$CFL_v = \nu\frac{\Delta t}{\Delta x^2} \tag{5.124c}$$

where Δt is the time-step, Δx is the grid spacing, u is the cell velocity, c is the speed of sound, and ν is the viscosity.

5.2.6.4 Configuration of the solver

This section includes the values defined to configure the solver for the study of both internal and external flow in both software. Table 5.10 shows the variables and their values corresponding to the CONVERGE™ software, while Table 5.11 shows the data corresponding to StarCCM+.

Solver setup for CONVERGE software			
PISO parameters			
Internal Flow		*External Flow*	
PISO convergence criterion multiplier	20.0	*PISO convergence criterion multiplier*	20.0
Minimum number of PISO iterations	10.0	*Minimum number of PISO iterations*	2
Maximum number of PISO iterations	50.0	*Maximum number of PISO iterations*	9
PISO tolerance	1e-03	*PISO tolerance*	1e-03
Simulation time parameters			
Internal Flow		*External Flow*	
Initial time step	1e-10 s	*Initial time step*	5e-09 s
Minimum time step	1e-10 s	*Minimum time step*	1e-09 s
Maximum time step	5e-07 s	*Maximum time step*	2.5e-05 s
Maximum convention CFL limit	0.5	*Maximum convention CFL limit*	1.0
Maximum diffusion CFL limit	2.5	*Maximum diffusion CFL limit*	2.0
Maximum Mach CFL limit	10	*Maximum Mach CFL limit*	50.0
Simulated time	0.0008 s	*Simulated time*	0.001 s

Table 5.10: Configuration of the solver parameters for CONVERGE™ software.

Solver setup for StarCCM+ software			
Internal Flow. Segregated Flow Solver parameters		*External Flow. PISO Solver parameters*	
Velocity. AMG Linear Solver		Velocity. AMG Linear Solver	
Under-relaxation factor	0.5	*Under-relaxation factor*	1
Max. Cycles	30	*Max. Cycles*	30
Convergence tolerance	0.1	*Convergence tolerance*	0.1
Cycle type	Flex cycle	*Cycle type*	Flex cycle
Pressure. AMG Linear Solver		Pressure. AMG Linear Solver	
Under-relaxation factor	0.2	*Under-relaxation factor*	1
Max. Cycles	100	*Max. Cycles*	100
Convergence tolerance	0.1	*Convergence tolerance*	0.1
Cycle type	V cycle	*Cycle type*	V cycle
		PISO AMG convergence tolerance	1e-03
		PISO AMG max. cycles	100
Simulation time parameters			
Internal Flow		*External Flow*	
Initial time step	5e-07 s	*Initial time step*	2e-06 s
Minimum time step	1e-10 s	*Minimum time step*	1e-06 s
Maximum time step change factor	2	*Maximum time step*	2
Target mean CFL for time step	0.5	*Target mean CFL for time step*	0.5
Target max. CFL for time step	5	*Target max. CFL for time step*	1
Simulated time	0.0008-0.0015 s	*Simulated time*	0.0015 s

Table 5.11: Configuration of the solver parameters for StarCCM+ software.

5.3 Pre-processing

This section presents the pre-processing stage involving the complete case setup for both internal nozzle and external flow cases in both CONVERGE™ and StarCCM+ codes. First, the geometry definition in Section 5.3.1 followed by the fluid properties and different types of fuels in Section 5.3.3. The computational domain and the appropriate boundary and initial conditions are shown in Section 5.3.4 succeeded by the computational grid and the different meshing strategies considered, presented in Section 5.3.5. The numerical algorithms, discretisation schemes and solution strategy are already reported in Section 5.3.6.

5.3.1 Geometry

This section includes the description of the two injectors with different characteristics analyzed in this research to demonstrate the validity of the predictive methodology developed. On the one hand, the Delphi multi-hole solenoid injector, part of the well-known ECN network and referred to as Spray G, has been used as the basis for the analysis. On the other hand, and with the main objective of validating the mentioned methodology, an industrial injector of commercial applicability (another solenoid injector), has also been studied, in this case belonging to the Denso brand, which will hereinafter be designated as the Production Injector Unit (PIU).

5.3.1.1 ECN Spray G injector

The injection system used in this work and adopted as a reference belongs to the Delphi brand designated with the AV67-026 series and were donated to the ECN network with the aim of enhancing and broadening the knowledge in this field. A total of twelve injectors were donated together with six pairs of drivers. The idea was to distribute these injectors among the different institutions that make up the ECN network. For this purpose, and with the objective of ensuring homogeneity in the results, the six injectors that presented similar injection quantities and behavior profiles were selected. Throughout this work the computational results will be validated with experimental data, as far as possible data obtained from the CMT-Motores Térmicos will be used, but in the case that no specific operating conditions are available, the database provided by ECN will be used.

The Spray G injector is defined as spray-guided suited for direct injection spark ignition (DISI) operation and considered as solenoid driven with a VCO

nozzle. It is 8-hole injector with counter-bore shape in its orifices. In addition, a remarkable feature of this injector is that it has 5 needle guides on the nozzle wall which reduce the mass flow passage. Despite this, the injector can be considered symmetrical in the plane that includes holes numbered as 1 and 5 (see Figure 5.7a). The main characteristics of the internal geometry of the Spray G injector are presented in Table 5.13 in the same way as they can be visualized in a sketch showing a cut-plane of the nominal internal geometry of the injector represented in Figure 5.6. The sketch displays the tip of the needle with a spherical shape, the needle seat, and the geometry of one of the holes being all of them identical. In this illustration it is possible to visualize perfectly the typical stepped shape of the orifices. The orifice diameter hereon is always referred to the inner section of the hole, whereas the outer section will be referred to as counter-bore.

5.3.1.2 Production Injector Unit (PIU) injector

The PIU injector is an industrial application injector currently commercialized and belongs to the Denso trademark. It forms part of a private project with a renowned international automotive company which provided three different injectors to be studied (7YHC-029/030/031). Before choosing the injector to work with, tests were carried out to calculate the injection quantity of each of them to ensure the consistency of all of them. Finally, the reference injector from which the geometry design for the simulations was obtained is the 7YHC-029.

The PIU injector, unlike the Spray G injector which was designed as a centrally mounted injector, is configured to be positioned on the lateral side of the cylinder, side mounted. For this reason, the orifices have a clear deviation (angle of inclination) from the injector axis in order to avoid undesired phenomena such as wall wetting when the injected fuel impinges on the opening valves. This injector is also considered solenoid driven with a VCO nozzle and has 6 orifices with divergent shape. These orifices have the same size between them but the inclination from each other. Table 5.12 shows the different inclinations of the orifices axes where it can be discerned the existence of a symmetry. In fact, this injector can be considered symmetrical in the plane including holes 1 and 4 (see Figure 5.12). The main characteristics of the internal geometry of the PIU injector are also reported in Table 5.13 in the same way as they can be visualized in a sketch showing a cut-plane of the nominal internal geometry of the injector depicted in Figure 5.6.

Holes	1	2	3	4	5	6
Drill angle [°]	7.5	36	53.5	44.5	53.5	36

Table 5.12: Orifice drill angle for the PIU nozzle relative to nozzle axis.

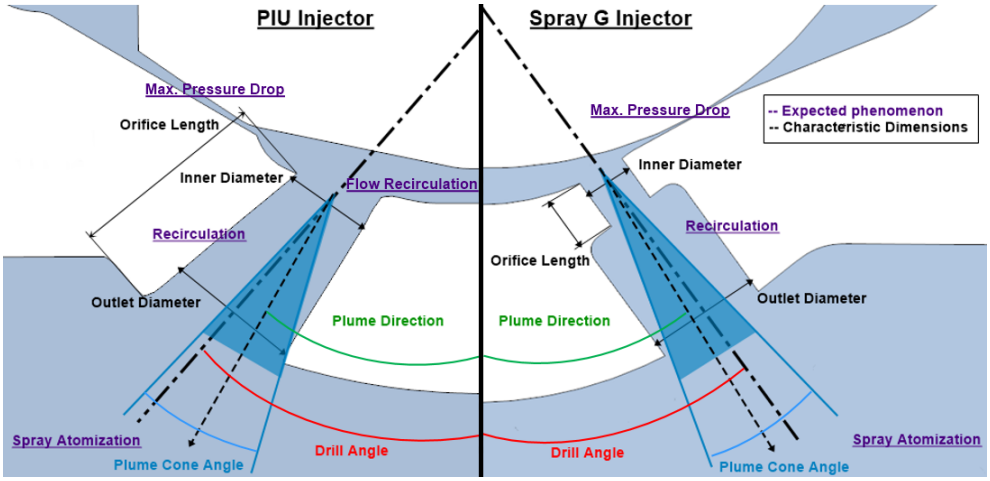

Figure 5.6: Sketch of the geometrical characteristics of the studied injectors.

Parameter	Spray G	PIU
Bend angle	0°	$\sim 26°$
Number of holes	8	6
Orifice shape	circular	circular
Hole shape	straight	diverging
Nozzle shape	step hole	conical hole
L/D ratio	1.4	2.4
Orifice diameter	165 µm	195 µm
Orifice length	$160 - 180$ µm	465 µm
Step/Outlet diameter	388 µm	360 µm
Orifice drill angle	37°	variable *

** see Table 5.12*

Table 5.13: Main geometrical characteristics of the studied injectors.

5.3.2 Operating conditions

This section contains the "real" engine operating conditions that have been used in this study and which depend to a large extent on the injectors analyzed. This is mainly due to the fact that the objectives set by the different

institutions indirectly involved (ECN and the international automotive company), despite being along the same guidelines, differ from each other.

5.3.2.1 Spray G injector

For the specific case of the ECN injector, this same network defines a fairly large test matrix which has different conditions that occur regularly in a real engine. The standard reference condition, known by the same name as the injector, is called Spray G (SG). It is taken as a baseline because it is the typical operating condition of GDI engines. The SG condition is supposed to be non-flashing due to the back pressure is higher than the saturation pressure of the fuel. However, evaporation of the liquid is expected because of the chamber temperature is higher than the fuel evaporation temperature and convective heating occurs. The other defined operating conditions are based on parametric variations of the reference condition (SG) in order to study phenomena unique to GDI engines. The most outstanding ones are known as SG2 or flash boiling and SG3 or early injection. In case of G2 as the pressure in the chamber is below the saturation pressure of iso-octane, flashing phenomenon is expected. The operating condition SG3 is the same as SG2 except the ambient pressure. It corresponds to an early injection. These last two conditions, SG2 and SG3, the fuel is injected into a cold atmosphere and therefore evaporation is not expected. These conditions can also be defined according to the parameter R_p (Equation 3.30) which indicates the tendency to flash boiling. If the ratio is greater than unity, flashing conditions are present, while if, on the contrary, the ratio is less than unity, there is no indication of flash boiling. The SG condition, taking isooctane as a reference, has an $R_p = 0.12$, the SG2 condition shows an $R_p = 1.41$ and the SG3 condition exhibits an $R_p = 0.70$. Once again, this affirms that, of the three mentioned conditions, the only one that induces flash boiling is the SG2 condition. Table 5.14 summarizes the main characteristics of the above-mentioned operating conditions.

Later on, additional operating conditions were included that were of interest because they caused specific phenomena such as spray collapse or because they were attracting attention among industry or research groups. Among these new operating conditions are SG4 ($7\,kg/m^3$) defined as double density, SG6 ($3.5\,kg/m^3$, 800 K) where the ambient gas temperature is increased and SG7 ($9\,kg/m^3$, 800 K) condition that meets the necessary characteristics to generate a strong spray collapse. Another recently added operating condition worth paying attention to is the multiple injection condition, SGM-1 (680 µs - 1000 µs dwell - 185 µs). This is identical to the SG condition in terms of pres-

Parameter	SG standard	SG2 flash boiling	SG3 early injection
Inj. Pressure	20 MPa	20 MPa	20 MPa
Inj. Temperature	363 K	363 K	363 K
Ambient Pressure	0.6 MPa	0.05 MPa	0.1 MPa
Ambient Temperature	573 K	333 K	333 K
Ambient Density	3.5 kg/m^3	0.5 kg/m^3	1.12 kg/m^3
Ambient Gas	Nitrogen	Nitrogen	Nitrogen
Electronic Injection	0.680-0.780 ms	0.680-0.780 ms	0.680-0.780 ms
Injected mass	10 mg	10 mg	10 mg

Table 5.14: Operating conditions standardized by ECN.

sures and temperatures but differs in the energizing time. It has a main pulse identical to that of the SG condition (680 µs) and after 1000 µs of dwell time injects a small post pulse of 185 µs. This condition will also be analyzed in the present work as well as the influence of the variation of the times between injections.

5.3.2.2 PIU injector

The test matrix corresponding to the PIU injector was imposed by the contracting company but follows the same guidelines in order to look for the phenomena of interest that occur in a GDI engine. This test matrix for the PIU injector is presented in Table 5.15.

Parameter	PIU injector
Inj. Pressure	10/20/28 MPa
Inj. Temperature	363 K
Ambient Pressure	0.05/0.3/0.6/1.0 MPa
Ambient Temperature	303 K
Ambient Density	0.56/3.33/6.67/11.12 kg/m^3
Ambient Gas	Nitrogen
Electronic Injection	1.5 ms

Table 5.15: Test matrix of injection conditions for both experiments and simulations for PIU injector.

5.3.3 Fuel properties

This section gathers the necessary information concerning the fuels used in the analyzed GDI injection system. Surrogate fuels have been chosen over

the years to study the behavior of gasoline in a simplified way. These fuels contain a limited number of pure components blended together to achieve the particular combustion and emission characteristics. Initially, this study was planned to be carried out with a surrogate liquid fuel such as iso-octane (2,2,4 trimethylpentane) which aimed to simulate the octane number or, in other words, to control the degree of autoignition of gasoline. Due to the growing interest of the scientific community to know more about the behavior of the flow with other alternative fuels, added to the fact that iso-octane, despite being a good substitute for combustion, does not accurately represent the volatility conditions of gasoline, the study was extended to other surrogate fuels such as hexane, pentane, heptane and ethanol. Among the surrogates, mono-component fuels are the simplest to replicate, and in this particular scenario, they are carefully chosen to have a distillation curve similar to the distillation curve of a commercial gasoline in order to simulate its volatility. However, going one step further, this work also includes a multi-component named by the ECN network as E00 which is composed of three mono-components in different percentages: 46% iso-octane, 36 % pentane and 18% undecane. The most relevant characteristics of each of the analyzed fuels are presented in Table 5.16.

Fuel properties (@363K)	μ [Ns/m^2]	ρ [kg/m^3]	ν [m^2/s]	σ [N/m]	P_v [Pa]
Ethanol (C2H5OH)	3.973e-04	725.00	5.480e-07	0.0156	139884.8
Iso-octane (C8H18)	2.551e-04	636.15	4.010e-07	0.0129	70439.8
E00 (*)	2.465e-04	615.98	4.001e-07	0.0115	227857.6
Heptane (C7H16)	2.243e-04	626.02	3.583e-07	0.0137	71003.8
Hexane (C6H14)	1.758e-04	596.02	2.950e-07	0.0115	170777.6
Pentane(C5H12)	1.560e-04	552.65	2.820e-07	0.0090	439149

** (46 % Iso-octane (C8H18) + 36 % Pentane (C5H12) + 18 % Undecane (C11H24))*

Table 5.16: National Institute of Standards and Technology (NIST) fuel properties sorted from highest to lowest density and viscosity. [48].

In Table 5.16, μ and ν represent the dynamic and kinematic viscosity, respectively, ρ defines the density, σ the surface tension and P_v the vapor pressure.

The properties of the multi-component fuel have been calculated from the properties of each of the component species following the procedure below, where X refers to the volume fraction and Y is the mole fraction.

Density. Given the density and volume fraction of each species, the density of the mixture can be calculated from the following relation,

$$\rho = \sum_{i=1}^{n} \rho_i X_i \tag{5.125}$$

Kinematic viscosity. For the calculation of the kinematic viscosity, use is made of the correlation of Kendall and Monroe correlation of the American Petroleum Institute (API), which is valid for mixtures of components with similar nature [49].

$$\nu = \left(\sum_{i=1}^{n} X_i \nu^{1/3} \right)^3 \tag{5.126}$$

Dynamic viscosity. The dynamic viscosity of the mixture can be calculated by means of Equation 5.127, knowing the value of the kinematic viscosity.

$$\mu = \rho\nu \tag{5.127}$$

Vapor pressure. Using Raoult's Law [50], the vapor pressure of a mixture of different liquids can be estimated from the following expression,

$$P_v = \sum_{i=1}^{n} X_i P_{vi} Y_i \tag{5.128}$$

Surface tension. For the calculation of the surface tension of multi-component fuels, the method of Winterfeld, Scriven and Davis is applied (Equation 5.129), which is applicable for mixtures of non-aqueous liquid fluids [51].

$$\sigma = \sum_{i=1}^{n} \sum_{j=1}^{n} \xi_i \xi_j (\sigma_i \sigma_j)^{1/2} \tag{5.129}$$

being $\xi_i = Y_i X_i / X_m$ and $X_m = \sum_{j=1}^{n} Y_i X_i$.

5.3.3.1 CONVERGE™ cases

In CONVERGE™ cases, liquids have been treated as compressible fluids whose compressible liquid density correlation is described by Equation 5.130 which includes a reference pressure ($P_{ref} = 101325$), reference density (ρ_{ref}) and bulk modulus ($bulkmodulus = 1.9E09$) obtained from the study of Dymond et al. [52]. The viscosity of the liquid is defined from Sutherland's Law.

Other liquid and gaseous species have been specified as compressible and the material properties used were obtained from the software's own database [42] which follows NIST correlations. Regarding the gaseous phases, both are treated on the basis of the equation-of-state of ideal and perfect gases.

$$\rho_{liq} = \rho_{ref} e^{\left(\frac{P_{inj}-P_{ref}}{bulkmodulus}\right)} \tag{5.130}$$

It is important to mention that the reference densities and critical temperature involved in the compressible liquid density correlation differ from one fuel to another, so Table 5.17 includes the values corresponding to each of the studied liquids. To define the multi-component fluid in CONVERGE™ , the mass fractions of each of its components are specified. For this reason, Table 5.17 only shows the values corresponding to the individual components.

	Ref. Density[kg/m^3]	**Bulk Modulus (Pa)**	**Critical Temp. (K)**
Ethanol (C2H5OH)	785.58	1.9E09	516.25
Iso-octane (C8H18)	688.5	1.9E09	543.8
Heptane (C7H16)	680.02	1.9E09	540.26
Hexane (C6H14)	654.63	1.9E09	507.43
Pentane(C5H12)	614.22	1.9E09	460.4
Undecane (C11H24)	735.72	1.9E09	638.76

Table 5.17: Fuel properties involved for the compressible liquid density correlation.

5.3.3.2 StarCCM+ cases

In the case of StarCCM+, the liquid is assumed to be incompressible Newtonian fluid with a density value of 636 kg/m^3 , constant dynamic viscosity of $4.806{\cdot}10^{-4}$Pa·s, and also constant specific heat capacity of 2027.59 J/(K·kg). The selection of constant properties can influence the results obtained. However, Giannadakis et al. [53] shown a 3% difference in the discharge coefficient between the use of constant properties and variable properties. Furthermore, in previous studies of this group [54], simulations with constant and temperature-dependent properties were compared by observing similar approximations of mass flow rate and similar spray angles. Regarding the gaseous phases, both are treated on the basis of constant density.

5.3.4 Computational domain. Boundary and Initial conditions

This section contains the description of the computational domain as well as the defined initial and boundary conditions. It should be noted that these definitions are dependent on both the software used in the study and the analysis objective, in other words, whether it is desired to study the internal flow or external flow.

5.3.4.1 CONVERGE™ domain. Boundary and Initial conditions

The studies carried out with the CONVERGE™ software are based exclusively on analyzing the behavior of the fluid during the injection process using the injector corresponding to the ECN network.

Internal Nozzle Flow

Computational Domain

The computational domain, displayed in Figure 5.7a, used for the simulations is extracted using x-ray tomography techniques. No time resolution is required to obtain the geometry and the experiments are run using the white-beam mode at sector 7-BM [55]. The determination of this geometry was carried out by Argonne National Laboratory [56] obtaining eight ECN Spray G nozzles with a pixel resolution of 1.17 µm per pixel, from five images per rotational angle of the nozzle with a total of 1800 angles (every 0.1° from 0° to 180°).

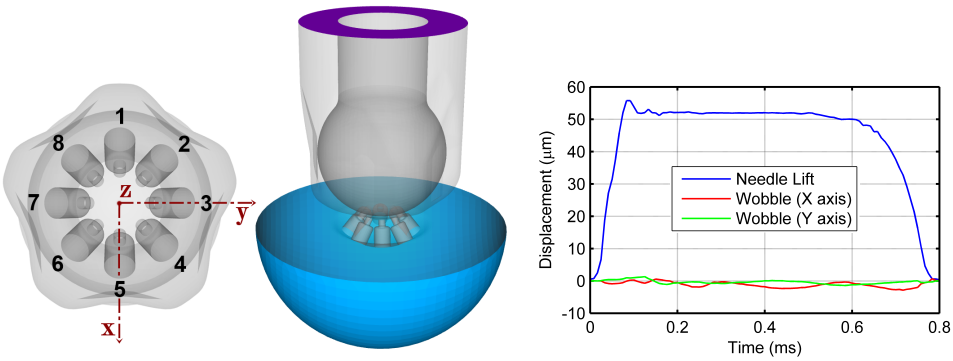

(a) Spray G geometry (b) Needle displacement

Figure 5.7: Sketch of the Spray G nozzle geometry with the numbered holes besides the computational domain used for the CFD simulation and averaged needle lift and wobble profile provided by Argonne National Laboratory [56].

The computational domain that is extracted directly from the x-ray techniques has rough surfaces and some manufacturing defects (see Figure 5.8) so the ECN network created different geometry models. In the first place and being the most used SG domain to date is the generation 1 (Gen 1) which stands out for being a geometry considered ideal where the surfaces have been treated and smoothed and the manufacturing defects have been eliminated. In addition, it should be noted that all the holes have the same dimensions whose value (see Table 5.13) is the average of the measured values. Later, the use of generation 2 (Gen 2) geometry, which advocated enlarging the size of the exit holes, was proposed and did not find much success in the scientific community. In order to go one step further and bring the results closer to the experimental ones, the generation 3 (Gen 3) was released, which takes into account the existing differences in orifice size between the different nozzles that make up the SG injector and is intended to match most of the experimental parameters measured and reported [57]. The new characteristics of this domain are summarized in Table 5.18. Finally, the trend that will be followed in the coming years is to use the so-called generation 3.2 (Gen 3.2) which describes in detail the study injector, none of the existing manufacturing defects have been eliminated and it has only been adapted in terms of file size to make it computationally manageable. The present study includes the use of Gen 1 and Gen 3 geometries.

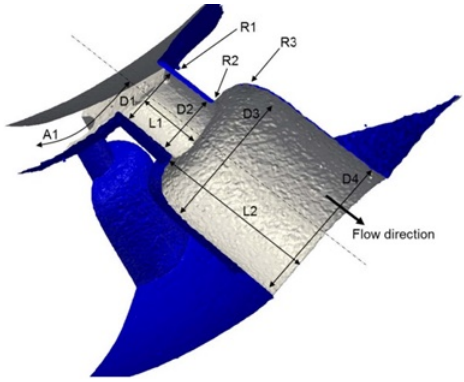

ID	Feature µm
D1	Hole inlet diameter
D2	Hole outlet diameter
R1	Hole inlet corner radius
R2	Hole outlet corner radius
L1	Hole length
A1	Drill angle
D3	Counter-bore upstream diameter
D4	Counter-bore downstream diameter
R3	Counter-bore fillet
L2	Counter-bore length

Figure 5.8: Measured dimensions of Spray G from x-ray nozzle tomography. Adapted from [58].

Figure 5.7a represents the computational domain used for the study of the internal nozzle flow. This geometry reflects generation 1 but is applied in the same way to generation 3 because the differences in dimensions are not visible to the naked eye. The upper part colored in purple corresponds to the

Features	Hole 1	Hole 2	Hole 3	Hole 4	Hole 5	Hole 6	Hole 7	Hole 8	Ideal
D1 [µm]	177	172	168	172	172	172	166	170	165
D2 [µm]	177	172	172	175	175	172	170	172	165
R1 [µm]	17	19	10	15	19	7	6	7	0
R2 [µm]	11	6	17	11	7	6	7	11	0
L1 [µm]	159	161	168	172	159	162	162	162	170
A1 [°]	37	37	37	37	37	37	37	37	37
D3 [µm]	388	388	388	388	388	388	388	388	388
D4 [µm]	388	388	388	388	388	388	388	388	388
R3 [µm]	57	55	55	55	49	65	66	63	40
L2 [µm]	474	461	465	472	490	494	494	494	470

Table 5.18: Computational dimensions of the Spray G Gen 3 injector geometry compared to the ideal Gen 1.

injector inlet while the area colored in blue and with dimensions of 6 mm in diameter refers to the outlet. This dimension, as will be seen in Section 6.2 corresponding to the results of the investigation, is sufficient to study the in- and near-nozzle flow. It can be observed again, as mentioned in Section 5.3.1, how this injector has 8 radially distributed orifices and 5 bumps, and can be considered symmetrical in the 1-5 plane. It is important to take into account the numbering of the orifices since the peculiar configuration of the injector may cause the flow to differ from one orifice to another.

Boundary Conditions

It is necessary to define boundary conditions to be able to carry out the required studies. These are specified according to the operating condition. In order to correctly assign the different boundary conditions, the geometry is divided into several parts occupying the Inlet, Outlet and Walls groups. Within each boundary condition different types can be distinguished:

- *Dirichlet*: this boundary condition is also known as a no-slip condition and assigns a constant value to the variable along the entire contour.
- *Neumann*: assigns a value to the first derivative of the variable. It is usually zero (*Zero Gradient Neumann*).
- *Law-of-the-wall*: only applicable in the *wall* option. This condition models the flow behavior in the vicinity of the wall, resembling more closely the wall conditions the closer it is to the wall and resembles free-flow conditions as it moves away.

In the following lines, the boundary conditions are described in detail according to the different parts of the injector.

- ***Inlet:*** upper part of the injector colored purple in Figure 5.7a, defined as an *inflow* condition. Details of the defining characteristics are given in Table 5.19.

Inflow		
Boundary	**Condition**	**Value**
Pressure Boundary Condition [MPa]	Dirichlet	20
Velocity Boundary Condition [m/s]	Neumann	-
Temperature Boundary Condition [K]	Dirichlet	363
Species Boundary Condition (Y_{IC8H18})	Dirichlet	1
Species Boundary Condition (Y_{N2})	Dirichlet	0
TKE Boundary Condition (*intensity*)	Dirichlet	0.01
EPS Boundary Condition (*length scale*) [m]	Dirichlet	0.0001

Table 5.19: Values of the boundary condition in the Inlet boundary for internal nozzle flow study under CONVERGE™ software.

- ***Outlet:*** semi-spherical part of the injector colored blue in Figure 5.7a, defined as an *outflow* condition. Details of the defining characteristics are given in Table 5.20.

Outflow		
Boundary	**Condition**	**Value**
Pressure Boundary Condition [MPa]	Dirichlet	0.6
Velocity Boundary Condition [m/s]	Neumann	-
Temperature Boundary Condition [K]	Dirichlet	573
Species Boundary Condition (Y_{IC8H18})	Dirichlet	0
Species Boundary Condition (Y_{N2})	Dirichlet	1
TKE Boundary Condition (*intensity*)	Dirichlet	0.01
EPS Boundary Condition (*length scale*) [m]	Dirichlet	0.0001

Table 5.20: Values of the boundary condition in the Outlet boundary for internal nozzle flow study under CONVERGE™ software.

- ***Wall:*** include all parts of the injector colored grey in Figure 5.7a, defined as a *wall* condition. Details of the defining characteristics are given in Table 5.21.

  With respect to these wall conditions, it is important to emphasize that they are all defined as stationary, in other words, they have no movement at all for those steady cases where the needle is fully lifted (45 µm). However, for the transient cases, the lower part of the needle (needle

Wall		
Boundary	**Wall Treatment**	**Value**
Velocity Boundary Condition [m/s]	Law-of-wall	-
Temperature Boundary Condition [K]	Dirichlet	573
TKE Boundary Condition (*intensity*)	Neumann	-
EPS Boundary Condition (*length scale*) [m]	Wall model	-
Law-of-wall roughness parameters		
Absolute roughness [m]		0.0
Roughness constant		0.5

Table 5.21: Values of the boundary condition in the Wall boundary for internal nozzle flow study under CONVERGE™ software.

ball) takes the roll of movement boundary and a time-dependent lift and lateral movement (wobble) of the needle, if any, is introduced. In order to simulate this motion, the surface of the needle follows the averaged needle lift and wobble profile provided by Argonne National Laboratory [56] (see Figure 5.7b). Since there is no sealing algorithm, a minimum space is required between the needle and its seat. A value of 2 µm is used for the "closed" position of the needle at the start and the end of the injection.

The boundary conditions for LES approaches are identical except that the one-equation models used allow only the turbulent kinetic energy to be defined.

In summary, the inlet boundary has been modeled applying a fixed value pressure boundary condition and zero gradient for velocity. Temperature has been defined as a stipulated value corresponding to the fuel operating condition. Walls have been designated as law-of-the-wall condition and their corresponding boundary layers modeled using a standard wall function in RANS cases and the Werner and Wengle wall function for LES approaches. A zero normal gradient condition for velocity is defined for the outlet boundary. In this boundary, pressure and temperature have a fixed value according to the operation conditions. Regarding the turbulence boundary conditions, the use of LES models, One Equation in this particular case, allows to initialize only the turbulent kinetic energy defined through the turbulent intensity with a value of 0.01 whereas RANS models require to initialize not only the turbulent intensity (0.01) but also the turbulent dissipation through a length scale of 0.0001 m.

Initial Conditions

For the purpose of initializing the simulation, the nozzle as well as orifices are filled with liquid fuel at the injection temperature. The nozzle is defined at a constant pressure equal to the injection pressure but the orifices are at a pressure comparable to that of the discharge chamber. On the other hand, the outlet plenum is filled with non-condensable gas (nitrogen) at constant discharge pressure and temperature. For the RANS approach, the turbulence has been initialized from the turbulent kinetic energy with a value of $1\,m^2/s^2$ and the turbulent dissipation which takes the value of $100\,m^2/s^3$. On the other hand, for approaches LES only the turbulent kinetic energy is initialized and takes the value of $1\,m^2/s^2$. Figure 5.9 displays the initialization employed for the variables considered to be of interest.

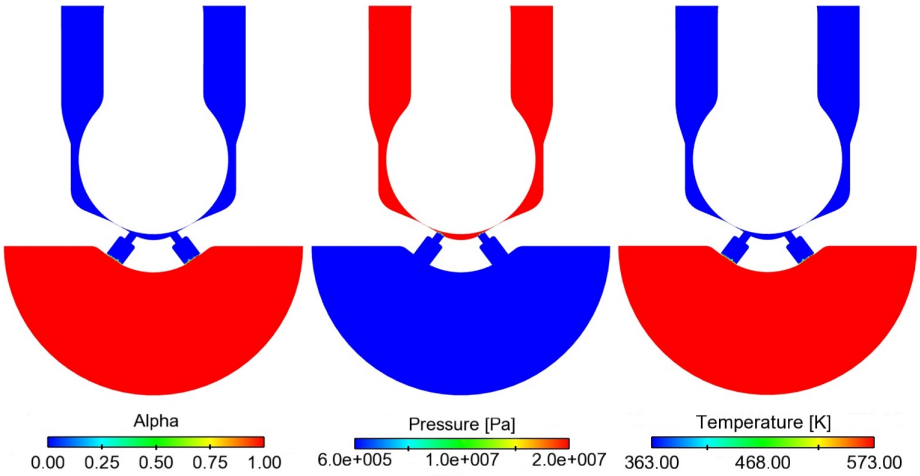

Figure 5.9: Initialization of the variables alpha, temperature and pressure for the Spray G injector under the SG reference condition.

External Flow

Computational domain

Figure 5.10 represents the computational domain used to simulate the external flow which attempts to resemble a test bench combustion chamber of a GDI engine where the fuel would ideally be injected. The cylinder style domain as well as its dimensions were determined from a study which will be presented in the Section 7.2. It has a height of 125 mm, a radius of 100 mm and an indentation of 25 mm deep and 27 mm radius. This last part, the indentation, was designed so that the computational domain resembles the

experimental facilities with which the studies from which the computational results are validated are carried out.

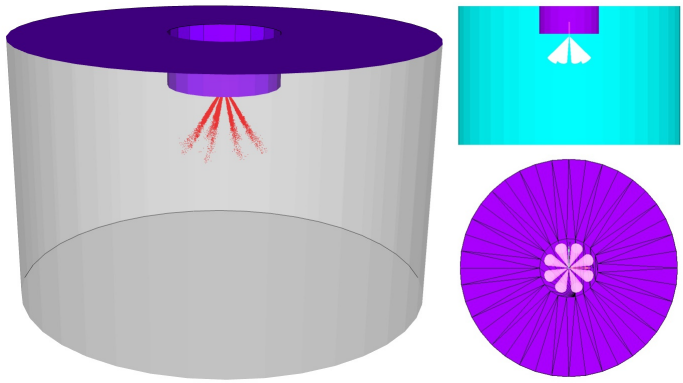

Figure 5.10: Computational domain used to study the external flow of the Spray G injector from different perspectives for a better understanding.

A noteworthy feature of this computational domain is that it does not have any geometrical features that include the injector. This is due to the fact that, in order to reduce computational cost mainly, the software used, CONVERGE™ in this particular case, has models that allow defining the injector together with its different nozzles in a fictitious way. For this purpose, it is only necessary to define the injector with its own characteristics, which for the Spray G injector are reflected in Figure 5.11.

Two injector positions were considered for visualization and computational purposes, a primary orientation recommended for visualization in SAE J2715 [59] but which is not as computationally favorable as will be noted in Section 7.2 and a secondary orientation defined with a 22.5° angle from the primary. The primary and secondary orientations are shown in the upper right part of Figure 5.11. In the primary orientation, three spray grouping zones can be noted, allowing the penetration of each spray to be calculated separately. In this position, the electrical connector and a small mark on the tip of the nozzle known as the "dimple" point towards the chamber. The secondary position is at a 22.5° clockwise angle to the primary and provides four separate spray zones with two plumes each. Knowledge of the orientation of the injector and its orifices is important due to the asymmetry of the injector which can cause the fluid behavior to differ from one nozzle to another.

Boundary Conditions

In the same way that occurs in the internal flow, it is necessary to define some boundary conditions which, in the case of external flow, are simpler. This

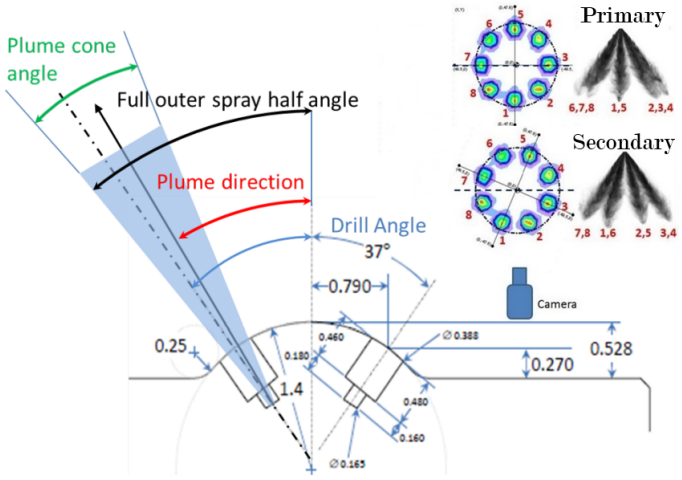

Figure 5.11: Spray G injector characteristics for the external flow study and the different injector orientations.

computational domain has been divided into two main zones, the upper part colored in purple in Figure 5.10 which has been designated as *Wall* condition and the lower part of the cylinder colored in gray or blue in Figure 5.10 which has been designated as *Outflow* condition. The following lines contain in detail the definition of the above mentioned boundary conditions.

- ***Wall:*** include all parts of the injector colored purple in Figure 5.10, defined as a *wall* condition. Details of the defining characteristics are given in Table 5.22.

Wall		
Boundary	**Wall Treatment**	**Value**
Velocity Boundary Condition [m/s]	Law-of-wall	-
Temperature Boundary Condition [K]	Dirichlet	363 or 573 *
TKE Boundary Condition (*intensity*)	Neumann	-
EPS Boundary Condition (*length scale*) [m]	Wall model	-
Law-of-wall roughness parameters		
Absolute roughness [m]		0.0
Roughness constant		0.5

** depends on the operating conditions to be simulated*

Table 5.22: Values of the boundary condition in the Wall boundary for external flow study under CONVERGE™ software.

- ***Outlet:*** cylindrical part of the injector colored blue in Figure 5.10, defined as an *outflow* condition. Details of the defining characteristics are given in Table 5.23.

Outflow		
Boundary	**Condition**	**Value**
Pressure Boundary Condition [MPa]	Dirichlet	0.6
Velocity Boundary Condition [m/s]	Neumann	-
Temperature Boundary Condition [K]	Dirichlet	573
Species Boundary Condition (Y_{IC8H18})	Dirichlet	0
Species Boundary Condition (Y_{N2})	Dirichlet	1
TKE Boundary Condition (*intensity*)	Dirichlet	0.02
EPS Boundary Condition (*length scale*) [m]	Dirichlet	0.003

Table 5.23: Values of the boundary condition in the Outlet boundary for external flow study under CONVERGE™ software.

As for internal flow, studies have been carried out with different turbulence models, RANS and LES, and the initialization of these variables differs from one model to another. The boundary conditions are identical except that in the LES only the turbulent kinetic energy is defined.

In summary, the defined wall has been designated as law-of-the-wall condition and their corresponding boundary layers modeled using a standard wall function in RANS cases and the Werner and Wengle wall function for LES approaches. A zero normal gradient condition for velocity is defined for the outlet boundary. In this boundary, pressure and temperature have a fixed value according to the operation conditions. Regarding the turbulence boundary conditions, for RANS cases, the turbulent kinetic energy has been defined through the turbulent intensity with a value of 0.02 and the turbulent dissipation through a length scale of 0.003 m, whereas for the LES approaches only the turbulent kinetic energy has been defined through the same intensity value, 0.02.

Initial Conditions

The initialization of this type of simulations is much simpler than in the internal flow cases. Only one region is defined in the whole computational domain filled with non-condensable gas (nitrogen) at constant discharge pressure and temperature, as function of the desire combustion chamber condition. For the RANS approach, the turbulence has been initialized from the turbulent kinetic energy with a value of $1\,\mathrm{m}^2/\mathrm{s}^2$ and the turbulent dissipation which

takes the value of $100\,m^2/s^3$. On the other hand, for approaches LES only the turbulent kinetic energy is initialized and takes the value of $1\,m^2/s^2$.

5.3.4.2 StarCCM+ domain. Boundary and Initial conditions

Internal Nozzle Flow

Computational Domain

In the case of the StarCCM+ software and specifically for the study of internal nozzle flow, the two injectors targeted by this Thesis have been analyzed: the Spray G injector (Figure 5.7a) and the PIU injector (Figure 5.12). The computational domain concerning the Spray G injector corresponds to generation 1 and has the same characteristics as the one used in the previous software (see Section 5.3.4.1) except that the semi-spherical surface that defines the outlet of the geometry, which has a diameter of 9 mm instead of 6 mm as previously defined. The enlargement of the domain is mainly due to the needs of the software, for the case of CONVERGE™ 6 mm are necessary to avoid that the boundary conditions influence the solution while in the case of StarCCM+ it was observed that this dimension was insufficient and needed to be extended.

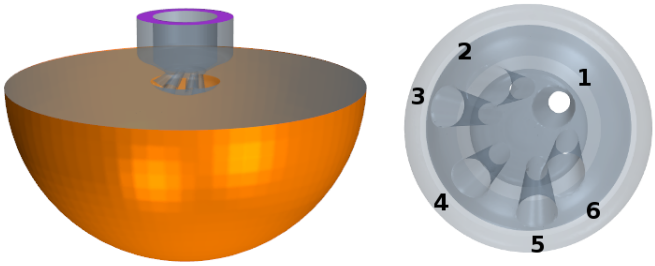

Figure 5.12: Sketch of the PIU nozzle geometry obtained by x-ray beside the computational domain used for the CFD simulation.

Regarding the computational domain concerning the PIU injector, the geometry used for the simulations as well as the needle lift and wobble profiles have been obtained from x-ray techniques [56]. Unlike the Spray G injector, for which the research community itself has provided the computational domain ready to be introduced into the calculation software, the PIU injector has numerous manufacturing defects and the high resolution of the x-ray technique (1.17 µm per pixel) makes the geometry complex to handle due to the large number of elements that make it up. Therefore, a surface smoothing process

as described in Figure 5.13 was carried out, eliminating the most relevant manufacturing defects that could compromise the convergence of the case or generate unrealistic meshes. In addition, the number of elements constituting the geometry was significantly reduced without sacrificing the accuracy of the computational domain.

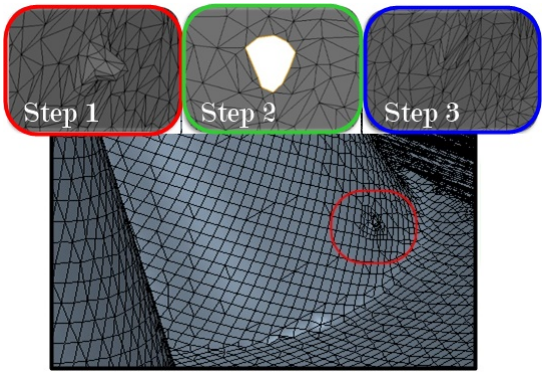

Figure 5.13: Surface smoothing process to eliminate the existing manufacturing defects in the computational domain obtained by the x-ray technique.

Figure 5.12 represents the computational domain employed for the study of the PIU internal nozzle flow. The Spray G one has been previously described (Section 5.3.4.1). Thus, regarding the PIU domain, the upper part colored in purple corresponds to the injector inlet while the area colored in orange and with dimensions of 9 mm in diameter refers to the outlet surface. This injector may be considered symmetrical in the plane intersecting holes 1-4 although it is necessary to mention that, due to a manufacturing defect, there is an observed deviation in the x-ray tomography images of 4 µm which will minimally affect the results in case the geometry is considered symmetrical in its research. Again, it is important to take into account the numbering of the orifices which will henceforth be referred to as shown in Figure 5.12.

Boundary Conditions

The way StarCCM+ expresses the boundary conditions is different from the CONVERGE™ software but they are under the same framework. Nomenclature of each software is maintained in the present Thesis. The following lines provide a detailed description of the boundary conditions according to the different parts of the injector. In this case, the surfaces also fall into three conditions: *Inlet*, *Outlet* and *Wall*. For those studies in which, in order to reduce computational cost, only half of the geometry is taken into account, a

new condition known as *Symmetry* is included which does not need to specify any extra value to the boundary condition.

- ***Inlet:*** upper part of the injector colored purple in Figure 5.12, defined as a *stagnation inlet* condition. Details of the defining characteristics are given in Table 5.24.

Stagnation Inlet	
Physics Conditions	**Specification**
Flow Direction Specification	Boundary-normal
Stagnation Inlet Option	None
Turbulence Specification	Intensity + Length scale
Physics Values	**Value**
Total Pressure [MPa]	20
Total Temperature [K]	363
Turbulent Intensity	0.01
Turbulent Length Scale [m]	0.0001
Volume Fraction [IC8H18, C8H18, N2]	[1, 0, 0]

Table 5.24: Values of the boundary condition in the Stagnation Inlet boundary for internal nozzle flow study under StarCCM+ software.

- ***Outlet:*** semi-spherical part of the injector colored orange in Figure 5.12, defined as a *pressure outlet* condition. Details of the defining characteristics are given in Table 5.25.
- ***Wall:*** include all parts of the injector colored grey in Figure 5.12, defined as a *wall* condition. Details of the defining characteristics are given in Table 5.26.

  For steady cases, the surfaces defined as wall condition have no movement and the needle is at its maximum position defined at 45 µm for the Spray G injector and 50 µm for the PIU injector. On the other hand, in transient cases, the needle is divided into two sections defining the lower part of them as a time-dependent moving surface that follows a lifting profile and lateral movement (wobble), if any. In the case of Spray G injector, the lift and wobble profiles are as previously defined in Figure 5.7b while in the case of the PIU injector they vary according to the injection pressure as illustrated in Figure 5.14. Since there is no sealing algorithm as before, a minimum space is required between the needle and its seat. A value of 2 µm is used for the "closed" position of the needle and the start and end of the injection for both injectors.

Pressure Outlet	
Physics Conditions	**Specification**
Backflow Specification	Direction: Extrapolated Pressure: Environmental
Pressure Outlet Option	Averaged Pressure
Turbulence Specification	Intensity + Length scale
Physics Values	**Value**
Averaged Pressure [MPa]	0.6
Averaged Pressure Adjuster	0.5
Static Temperature [K]	303
Turbulent Intensity	0.01
Turbulent Length Scale [m]	0.0001
Volume Fraction [IC8H18, C8H18, N2]	[0, 0, 1]

Table 5.25: Values of the boundary condition in the Pressure Outlet boundary for internal nozzle flow study under StarCCM+ software.

Wall	
Physics Conditions	**Specification**
Reference Frame Specification	Region Reference Frame
Shear Stress Specification	No-Slip
Tangential Velocity Specification	Fixed
Thermal Specification	Temperature
User Wall Heat Flux Coefficient Specification	None
Wall Surface Specification	Smooth
Physics Values	**Value**
Blended Wall Function	E: 9 Kappa: 0.42
Static Temperature [K]	363 or 303 *

** depends on the operating conditions to be simulated*

Table 5.26: Values of the boundary condition in the Wall boundary for internal nozzle flow study under StarCCM+ software.

In this context, it is worthwhile to make a brief analysis based on Figure 5.14a about the behavior of the needle lift as a function of the injection pressure. It is observed that the lower the injection pressure, the steeper the opening ramp, in other words, the faster. However, the maximum lift achieved is similar in the three operating conditions, which suggests that a flow throttling occurs through the needle inside the nozzle.

To sum up, the inlet boundary has been modeled using a stagnation in-

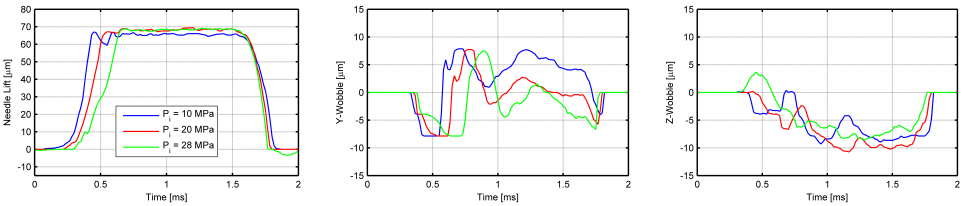

(a) Needle lift (b) Y-wobble (c) Z-wobble

Figure 5.14: Averaged needle lift and wobble profile comparison between different operating conditions for PIU injector.

let condition. A specified value stipulated for the temperature has been also defined. Walls have been modeled with isothermal and non-slip conditions. Reichardt's law is used to compute the near-wall velocity and Kader's law for temperature. The outlet condition has been defined as fixed outlet pressure with zero normal gradient condition for velocity, and as the inlet condition, the temperature has a defined value. Turbulence flow conditions are specified at the inlet (and for the reverse flow at the outlet) boundaries by the turbulence intensity value of 0.01 and turbulent length scale of 0.0001 m. It is interesting to note that the employed values are identical to those selected for the CONVERGE™ software.

Initial Conditions

The initialization for the internal flow in the cases carried out with StarCCM+ follows the same strategy as presented in Section 5.3.4.1. In this particular, the explanation is based on one of the operating conditions (see Table 5.15) defined specifically for the PIU injector. The nozzle as well as orifices are filled with liquid fuel (iso-octane) at the injection temperature. The nozzle is defined at a constant pressure equal to the injection pressure but the orifices are at a pressure comparable to that of the discharge chamber. On the other hand, the outlet plenum is filled with non-condensable gas (nitrogen) at constant discharge pressure and temperature. In this case, only RANS turbulence models are considered, so that the turbulence has been initialized from the turbulence intensity with a value of 0.01, the turbulent length scale of 0.0001 m and the turbulent velocity scale of 1 m/s.

External Flow

Computational Domain

In the case of the external flow study using StarCCM+ software for the computations, it only includes analyses carried out for the PIU injector. The

computational domain used, however, is identical to the one represented in Figure 5.10, same dimensions and geometry. Likewise, as the previous software, the injector is defined in a fictitious way from a set of characteristics including the dimensions of the injector and the existing losses in it.

Boundary Conditions

Once again, the computational domain for the study of the external flow is divided into two parts, the one colored in purple in Figure 5.10 which is designated as *Wall* condition and the one colored in gray or blue defined as a *Pressure Outlet* condition. The following lines provide a detailed description of the boundary conditions according to the different parts of the computational domain.

- ***Wall:*** include all parts of the injector colored purple in Figure 5.10, defined as a *wall* condition. Details of the defining characteristics are given in Table 5.27.

Wall	
Physics Conditions	**Specification**
Lagrangian Specification	Use Phase Default
Reference Frame Specification	Region Reference Frame
Shear Stress Specification	No-Slip
Tangential Velocity Specification	Fixed
Thermal Specification	Adiabatic
User Wall Heat Flux Coefficient Specification	None
Wall species Option	Impermeable
Wall Surface Specification	Smooth
Physics Values	**Value**
Blended Wall Function	E: 9 Kappa: 0.42

Table 5.27: Values of the boundary condition in the Wall boundary for external flow study under StarCCM+ software.

- ***Outlet:*** cylindrical part of the injector colored blue in Figure 5.10, defined as a *pressure outlet* condition. Details of the defining characteristics are given in Table 5.28.

In summary, the defined wall has been modeled with isothermal and non-slip conditions. Reichardt's law is used to compute the near-wall velocity and Kader's law for temperature. The outlet condition (colored in grey or blue in Figure 5.10) has been defined as fixed outlet pressure with zero normal

Pressure Outlet	
Physics Conditions	**Specification**
Backflow Specification	Direction: Boundary-Normal Pressure: Environmental
Pressure Outlet Option	Averaged Pressure
Species Specification	Mass Fraction
Turbulence Specification	K+Omega
Physics Values	**Value**
Averaged Pressure [MPa]	0.6
Averaged Pressure Adjuster	0.5
Static Temperature [K]	303
Turbulent Kinetic Energy [m^2/s^2]	10
Specific Dissipation Rate [1/s]	0.0001
Species Mass Fraction [C8H18, Air]	[0, 1]

Table 5.28: Values of the boundary condition in the Pressure Outlet boundary for external flow study under StarCCM+ software.

gradient condition for velocity, and a specific value for temperature based on the operating conditions. Regarding the turbulence boundary conditions, they have been specified through the turbulent kinetic energy with a value of $1\,m^2/s^2$ and the specific dissipation rate with a value of $0.0001\,1/s$.

Initial Conditions

The computational domain for external flow is very simple and only one initialization region is defined. In order to make the studies as similar as possible to the experiments, in this case the study domain is filled with air at constant discharge pressure and temperature. In this case, only RANS turbulence models are considered, so that the turbulence has been initialized from the turbulent kinetic energy with a value of $1\,m^2/s^2$ and the specific dissipation rate with a value of $0.0001\,1/s$.

5.3.5 Computational grid

The research problem is approached through two different CFD codes (CONVERGE™ and StarCCM+) involving two different meshing strategies: an automatic mesh generation and adaptive refinement algorithms through CONVERGE™ and meshing technique in StarCCM+.

5.3.5.1 CONVERGE™ mesh strategy

CONVERGE™ code is equipped with a set of robust and innovative grid-related capabilities based on a cut-cell Cartesian method. It automatically creates the mesh at runtime, dynamically adapts the mesh throughout the simulation, and invokes Adaptive Mesh Refinement (AMR) to maximize both accuracy and computational efficiency. It therefore obviates the requirement for the computational mesh to be customized with the geometry of concern [36] and eliminates the time-consuming manual mesh generation or specific templates or scripts for automated meshing features. This software automatically renders a simple orthogonal grid on the basis of a few user-defined grid control parameters. This automated grid generation method eliminates all user meshing time. CONVERGE™ can easily simulate the most complex moving geometries and will automatically adjust the grid as needed at each time-step to appropriately resolve the flow. To carry out this meshing process, an automatic domain decomposition technique is required to efficiently balance the load over the computation.

CONVERGE™ provides multiple tools to manage the mesh size before and during the simulation (see Figure 5.15). Among them, the *grid scaling* technique which coarsens or refines the base grid size, the *fixed embedding* which refines the grid at specified locations and times and the *Adaptive Mesh Refinement (AMR)* which automatically changes the grid based on fluctuating and moving conditions.

- **Base Size:** reference parameter that defines the side length of the hexahedral cells and from which the other parameters that act as mesh control tools are set.
- **Fixed Embedding:** refines the mesh according to user specifications at particular locations in the domain where finer resolution is essential for the accuracy of the solution. For each fixed embedding, the user must specify a positive embedding scale to refine the grid in the desired location according to,

$$dx_{embed} = dx_{base}/2^n \tag{5.131}$$

  where dx is the corresponding mesh size.
- **Adaptive Mesh Refinement (AMR):** automatically adjusts the grid according to fluctuating and moving conditions, such as temperature, velocity or species, among others. The AMR is in charge of refining

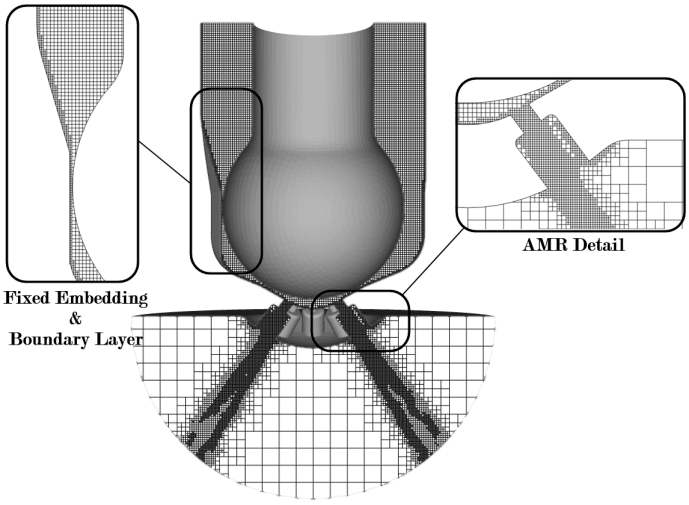

Figure 5.15: Spray G computational mesh illustrating the strategy considered in CONVERGE™ consisting in 2 levels of fixed embedding, 3 levels of AMR, and 1 layer with 3 levels of wall refinement (Gen 1).

the mesh (adding embedding) in those areas where there are gradients of the selected variable, in other words, where the flow field is most under-resolved or where the sub-grid field is the largest. The method is therefore based on estimating the magnitude of the sub-grid fields (Equation 5.132) to determine where to add embedding.

$$\phi' = \phi - \bar{\phi} \tag{5.132}$$

being ϕ the actual scalar field, $\bar{\phi}$ the resolved scalar field, and ϕ' the sub-grid scalar field. Expressing the sub-grid for any scalar as an infinite series and taking only the second-order term, the scale of the sub-grid can be approximated as,

$$\phi' = -\frac{dx_k^2}{24}\frac{\partial^2 \bar{\phi}}{\partial x_k \partial x_k} \tag{5.133}$$

Following this theorem, a cell reduces its size under this method if the sub-grid scalar defined by Equation 5.133 is above the value specified by the user. Conversely, a cell increases its value, in other words, it undoes the embedding if the absolute value of the sub-grid is below 1/5 of the user-specified value [42].

Internal Nozzle Flow

Within the study of internal nozzle flow with CONVERGE™ two main types of simulations can be distinguished, those carried out with RANS turbulence models and those in which LES approaches have been used. The way of treating turbulence leads to quite dissimilar necessary resolution.

- **RANS mesh**

  In this type of simulations and with the objective of reducing the computational cost without affecting the accuracy of the results, AMR is used as a refinement method, in addition to fixed embedding and boundary layer techniques. A distinction will also be made under this category between generations of computational domains. This is mainly because generation 3 (Gen 3) has a higher level of detail including, among other things, fillet radii at the boundary connections as described in Section 5.3.4.1. This requires smaller cell size to capture such details in order to ensure case convergence. It is important to mention that these cell sizes as well as the meshing strategy have been determined as optimal after performing the corresponding mesh independence study that will be presented in Section 6.2.2.

  Generation 1 has a base size of 140 µm with 2 levels of fixed embedding (35 µm) defined on the nozzle and orifices, a boundary layer with 3 levels of embedding (17.5 µm) defined only on the nozzle walls side and an AMR of 3 levels of refinement (17.5 µm) defined to act on the orifices and on the discharge volume when the sub-grid criterion associated with the velocity exceeds 1 m/s. The definition of this mesh can be observed in Figure 5.16 where the mesh is represented in its initial state (Figure 5.16a) in which the AMR is not yet in place due to the absence of velocity gradients and the mesh in a time corresponding to mid-injection (Figure 5.16b) where the mesh has been refined in the orifices and in the discharge volume due to the action of the AMR.

  The meshing scheme adopted in Generation 3 does not differ greatly from that of the lower generation: a base size of 140 µm with 2 levels of fixed embedding (35 µm) defined on the nozzle and 3 levels (17.5 µm) on the orifices, one boundary layer with 3 levels of embedding (17.5 µm) defined only on the nozzle region and an AMR of 3 levels of refinement (17.5 µm) for the discharge volume and 4 levels of refinement (8.75 µm) applied inside the orifices which follows the velocity sub-grid criterion of 1 m/s.

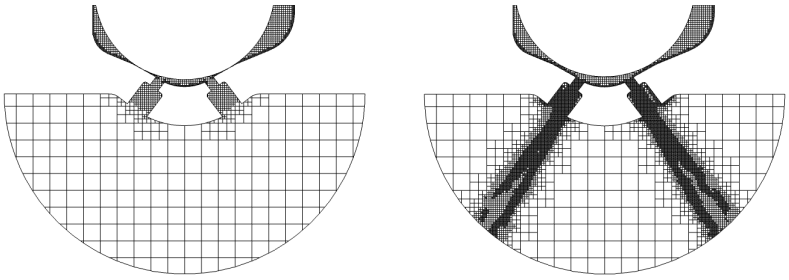

(a) t = 0.0 ms aSOI (b) t = 0.7 ms aSOI

Figure 5.16: Vertical cross section of the mesh evolution in time due to the AMR technique.

- **LES mesh**

  The use of LES models implies a high dependency on cell size in turbulent kinetic energy modeling. Several studies such as the ones performed by Keskinen et al. [60] indicate that the use of a moving mesh (AMR technique) in LES can influence the statistics in a manner that is not directly related to the mesh resolution. One of the variables that is most affected and hence most sensitive to changes in the mesh is the RMS (Root Mean Square) of the fluctuating velocity, especially in the tangential and radial components. Therefore, it has been adopted a fixed mesh for the study. The choice of the mesh sizes and refinements are based on compliance with the quality criteria explained in the following Section 6.6.5. Figure 5.17 shows the final configuration. The selected base size is 135 µm which has been refined through fixed embedding to 8.44 µm. The minimum cell size takes place in the needle seat where the main pressure drop occurs and has a value of 4.22 µm. The resulting mesh has a total of 22.4 million of cells which represents only half of the domain due to the symmetric condition which has been implemented in this particular type of simulations because of the enormous computational cost involved.

Table 6.1 summarizes the main parameters that define the meshes employed for the internal nozzle flow investigation in CONVERGE™ code.

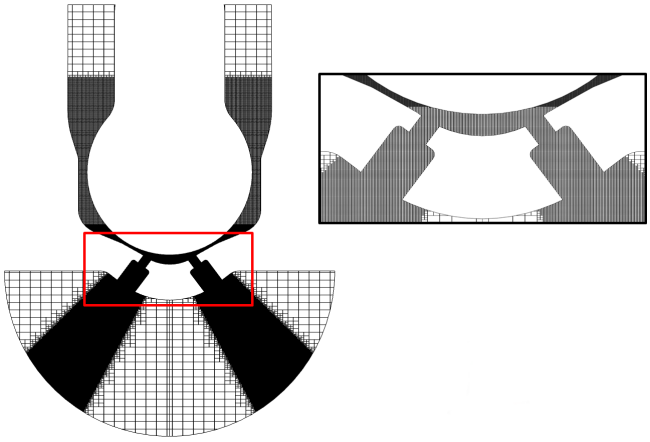

Figure 5.17: Vertical cross section of the hexahedral mesh with 6 mm outlet domain and cone-shaped refinement strategy for LES approach.

Case	Gen 1. RANS	Gen 3. RANS	Gen 1. LES
Element Type	Hexahedral	Hexahedral	Hexahedral
Discharge volume radius	6 mm	6 mm	6 mm
Minimum cell size (nozzle)	17.5 µm	8.75 µm	4.22 µm
Minimum cell size (plenum)	17.5 µm	17.5 µm	8.44 µm
Maximum cell size	140 µm	140 µm	135 µm
Cell count	1.1 million	1.6 million	22.4 million
Peak cell count	1.5 million	2.0 million	22.4 million

Table 5.29: Mesh information for each of the internal nozzle flow simulations corresponding to CONVERGE™ software.

External Flow

For the external flow framework and considering CONVERGE™ as the computational code, a differentiation is also made between the meshing technique used studies with RANS models and investigations with LES approaches.

- **RANS mesh**

  The computational domain concerning the external flow (Figure 5.10) is simple and therefore it is only necessary to define a base cell size in this particular case of 8 mm and an AMR meshing technique with 5 levels of refinement down to a cell of 0.25 mm that decreases the cell size as

the spray penetrates the chamber. The resulting mesh has a maximum peak number of 112000 cells. Those optimal sizes for the study of the external flow of the Spray G injector have again been extracted from a mesh independence study that will be presented in Section 6.2.2.

- **LES mesh**

  For the LES studies, the same computational domain as in the previous case is used but the mesh size has to be much smaller in order to capture the turbulent structures typical of these studies. In this particular, the cell sizes and meshing strategy are determined by the compliance with the mesh quality criteria defined for this research (see Section 6.6.5.1). The base cell size is then defined with a value of 1 mm and an AMR meshing strategy with an embedding level of 4 down to 0.0625 mm is applied (see Figure 5.18). The resulting mesh has a total of 15 million of cells. The main difference with RANS meshing strategy, in addition to the cell sizes, is the existence of fixed 10 mm refinement cones that allow to ensure accuracy in the first millimeters of the jet since the particle velocity is so high that at certain moments the AMR does not act in time and can lead to inaccuracy or even divergence of the solution. It is important to mention that due to the computational cost of these simulations it is not possible to assume a fixed mesh as in the previous case of internal nozzle flow and the idea of simulating only half of the geometry is not considered. Therefore, the aforementioned AMR meshing strategy is adopted and the possible variations in the statistics are assumed.

  Figure 5.18 represents the different meshing strategies implemented in the external flow LES simulations. It also depicts two different injection times, initial injection time on the left (t = 0 ms aSOI) and near final injection time on the right (t = 0.7 ms aSOI), in order to appreciate the evolution of the mesh sizes as the AMR intervenes.

5.3.5.2 StarCCM+ mesh strategy

The computational domain in StarCCM+ simulations has the option of spatial discretization using a static, structured mesh composed of hexahedral cells or a static, unstructured mesh composed of polyhedral cells generated by the software itself. A structured mesh would support higher order discretization schemes with no numerical divergence, leading to less numerical diffusion and relatively higher accuracy. Nevertheless, this would result in some cells in regions of high geometric complexity presenting large aspect ratios or significant skewness, which would lead to discretization errors. It should be pointed

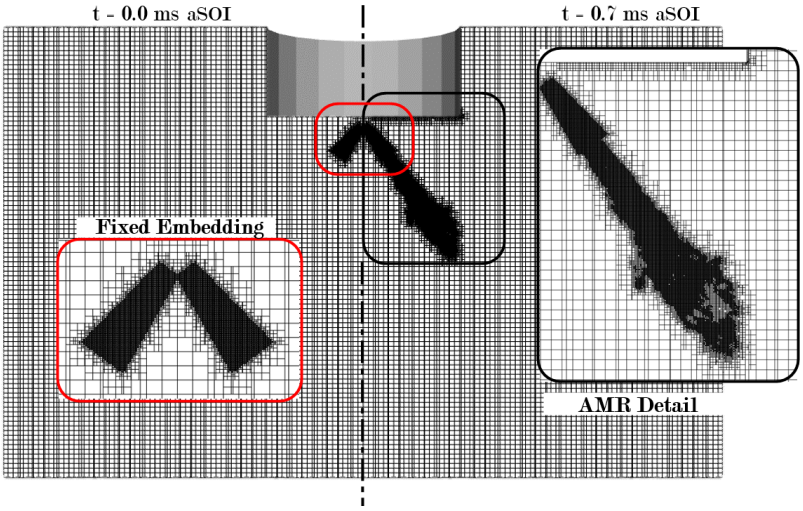

Figure 5.18: Spray G computational mesh applied for external flow LES simulation illustrating the strategy considered in CONVERGE™ consisting in 4 levels of fixed embedding and 5 levels of AMR.

out that CONVERGE™ , even employing structural meshes, does not experience these issues due to the previously mentioned automatic cut-cell Cartesian method. Due to the mesh independence study carried out and presented in Section 6.3.1, it was observed that the polyhedral unstructured mesh presented the same accuracy in results as the hexahedral one with less than half the number of cells and hence computational cost [61].

The studies performed with the StarCCM+ code are carried out using RANS turbulence models. On the other hand, the analysis of the flow behavior in the internal and near field of the injector was conducted for different geometries, Spray G and PIU injectors while the study of the external spray behavior is performed only for the PIU injector. It is important to mention that in StarCCM+ v12.04, used throughout this Thesis, the automatic meshing option is not available, so the meshing strategies implemented in these studies are focused on obtaining high precision results while optimizing the calculations.

Internal Nozzle Flow

- **Spray G injector mesh**

  In this particular internal flow study, two different meshing strategies have been employed, taking advantage of the different capabilities offered

by the calculation code: hexahedral and polyhedral mesh strategies. It is noteworthy that the computational domain used corresponds to the aforementioned generation 1 (Gen 1).

The hexahedral meshing strategy employed is shown in Figure 5.19a. As already mentioned, this code does not have an adaptive meshing in this version, so the cell size has to be reduced in those areas where gradients are expected to be noticeable or where a higher precision in the mesh is needed to adequately capture the flow behavior. For this, first a base cell size of 140 µm is defined. Three prism layers with a total thickness of 8.625 µm are attached to the walls obtaining a wall y + of ∼5 as maximum value. This software includes surface control algorithms which, apart from the boundary layers, allows to control the mesh in the areas close to walls. It enables to define a smaller cell size in the areas close to the walls and to increase it as it moves away from them. This refinement has been applied in the nozzle zone defining the minimum cell size with a value of 17.5 µm and a surface growth rate of 1.05. In addition, this geometry has a fixed refinement (volumetric control) in the orifices and the needle seat area where higher pressure gradients are expected. The behavior of this tool is identical to the fixed embedding of CONVERGE™ , so it defines a fixed cell size of 8.75 µm in this case. Finally, two cones of two different sizes, 17.5 µm and 35 µm, respectively, have been defined for each spray in order to adequately capture the behavior of the jet in the near-field. This meshing strategy results in a total of 11.4 million of cells.

It is important to emphasize that the sizes and distribution of the meshing strategy come from applying the aforementioned predictive methodology on which this Thesis is based. This means that first the studies were carried out with the Spray G geometry and the CONVERGE™ software, where indeed the optimal sizes and meshing distribution were selected. Subsequently, this strategy and sizes were transferred to this software, adapting the different ways of meshing between codes and thus verifying the validity of this methodology.

On the other hand, a completely different meshing strategy was used based on a polyhedral unstructured mesh which, according to the literature [61], allows to achieve high precision in the results and at the same time reducing the number of cells used and thus the computational cost of the solution. Figure 5.19b displays the final mesh result achieved after applying this type of strategy.

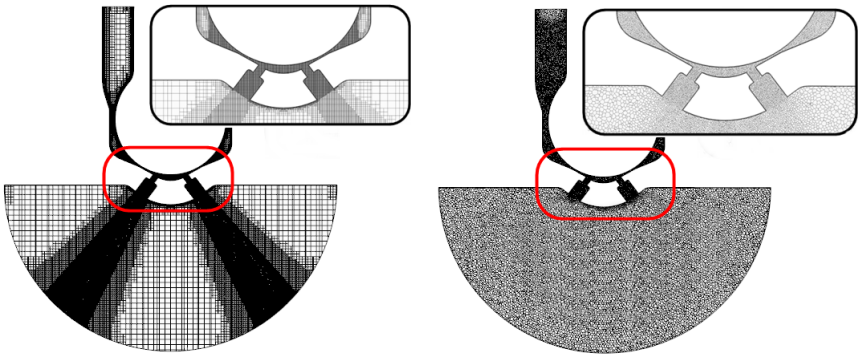

(a) Hexahedral mesh (b) Polyhedral mesh

Figure 5.19: Spray G computational mesh applied for internal nozzle flow simulation illustrating both strategies considered in StarCCM+.

For this kind of mesh, a similar strategy to the previous one has been used. However, the defined cell sizes have been obtained from a mesh sensitivity study that will be presented in Section 6.3.1. The base cell size is 60 µm and, in the same way as in the hexahedral case, three prism layers with a total thickness of 8.625 µm are defined. A surface control with a minimum near-wall size of 18 µm and a surface growth rate of 1.05 is applied. In addition, a control volume is also available to refine in detail, down to 18 µm, the areas corresponding to the holes and the needle seat. This meshing strategy results in a total of 5.1 million of cells reducing the total number of cells by 44% with respect to the hexahedral strategy.

Table 6.10 summarizes the main characteristics of the different meshes used in the two software programs.

- **PIU injector mesh**

  Once the previous strategies have been validated by comparing the results obtained with experimental data and implementing the bases of the predictive methodology (applying the strategies used, meshing in this case, to all types of injectors), the injector PIU is then studied. For this purpose, the two previous strategies have been adopted and a third one has been added with the idea of better capturing the behavior of the sprays due to the particular orientation of the orifices and the interaction between them. The different meshing strategies are shown in Figure 5.20.

Code	**CONVERGE**	**StarCCM+**	**StarCCM+**
Element Type	Hexahedral	Hexahedral	Polyhedral
Discharge volume radius	6 mm	9 mm	9 mm
Minimum cell size (nozzle)	17.5 µm	8.75 µm	18 µm
Minimum cell size (plenum)	17.5 µm	17.5 µm	18 µm
Maximum cell size	140 µm	140 µm	60 µm
Cell count	1.1 million	11.4 million	5.1 million
Peak cell count	1.5 million	11.4 million	5.1 million

Table 5.30: Mesh information for each of the simulations corresponding to StarCCM+ software compared to CONVERGE™ Spray G case.

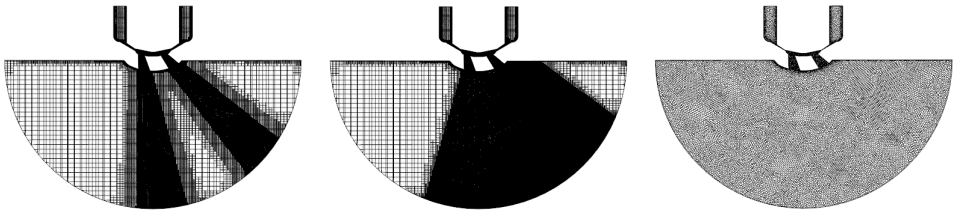

(a) Strategy 1 (b) Strategy 2 (c) Strategy 3

Figure 5.20: Different meshing strategies used in the study of the internal nozzle flow for the PIU injector.

The first strategy refers to the hexahedral mesh seen above and shown for the PIU injector in Figure 5.20a. This mesh is characterized by refining each of the sprays individually. It has a base cell size of 140 µm, and three prism layers are defined with a total thickness of 8.625 µm. A surface control refinement has been applied in the nozzle zone defining the minimum cell size with a value of 17.5 µm and a surface growth rate of 1.05. In addition, a control volume with a cell size of 8.75 µm is defined in the area of the orifices and the needle sac and seat. Finally, two cones of two different sizes, 17.5 µm and 35 µm, respectively, have been defined for each spray in order to adequately capture the behavior of the jet at the outlet of the injector. This meshing strategy results in a total of 7.18 million of cells.

Continuing with the hexahedral meshing strategy, and assuming the same base size (140 µm), in addition to the surface control and volume control, a cone is used that encompasses the six sprays to capture the jets together and improve the prediction of jet-to-jet interaction by avoiding

unrefined areas in between them. This cone has a cell size of 17.5 µm and generates a total of 15.24 million of cells. This meshing strategy is illustrated in Figure 5.20b.

Finally, the last meshing strategy chosen for the study of the PIU injector with the StarCCM+ software is the polyhedrical mesh, illustrated in Figure 5.20c. The main reasons for this choice is the accuracy of the results together with the reduction in computational cost compared to hexahedral meshing. The strategy developed for the Spray G injector has also been adapted for this mesh. The base cell size is 60 µm with three prism layers with a total thickness of 8.625 µm. A surface control with a minimum near-wall size of 18 µm and a surface growth rate of 1.05 is defined. In addition, a control volume is also available to refine in detail down to 18 µm the areas corresponding to the holes and the needle seat. This meshing strategy results in a total of 1.5 million of cells.

Since this is the meshing strategy selected for the main studies of this injector, an expanded cut in the area of the holes is shown in Figure 5.21 in order to appreciate in detail the structure of the mesh. The prism layers are observed as well as the existing refinement inside the holes and the growth of the mesh outside these zones.

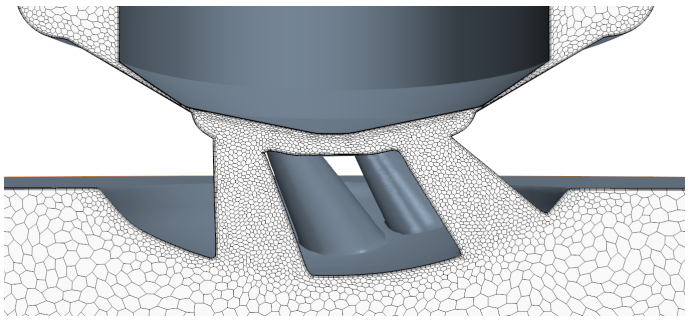

Figure 5.21: Details of the most optimal mesh used as the main strategy in the PIU injector investigation.

External Flow

- **PIU injector mesh**

  Consistent with the internal flow studies, after having observed the accuracy of the results and with the main objective of reducing the computational cost, a polyhedral mesh type is used to analyze the behavior

of the external flow. The meshing strategy adopted in this particular case (see Figure 5.10) is to define a base size of 8 mm for the whole computational domain and, due to the orientation of the holes all of them towards the same direction, to refine the mesh using a fixed 2 mm cone-shaped mesh that encompasses the sprays of all of them. An important parameter to define in this code is the growth of the mesh in order to adapt from the more refined zones to the zones with the base cell size. For the present study a surface growth rate of 20 has been determined. Figure 5.22 illustrates the meshing strategy described in the previous lines which has a maximum number of 123500 cells. It is necessary to mention that the zebra-lines appearing in the image (in the refined zone) are not due to the refinement but to the visualization due to the type of element and meshing strategy.

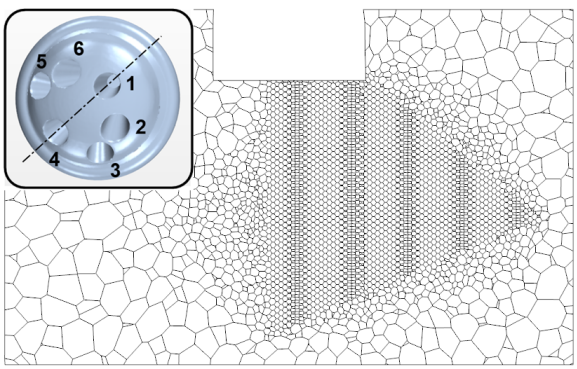

Figure 5.22: PIU computational mesh applied for external flow simulation illustrating the strategy considered in StarCCM+ consisting in a base size of 8 mm and a fixed cone-shaped refinement of 2 mm.

5.3.6 Summary of numerical algorithms and discretisation schemes

Throughout the previous Section 5.2 the numerical algorithms, discretization schemes, models and submodels that have been employed to carry out the present investigation have been explained. This section summarizes the selected configurations in order to facilitate the reader's understanding.

5.3.6.1 Numerical setup in CONVERGE™

Internal Flow

As it was mentioned before, employed solvers, places all calculated values in the center of the calculation cell, where the conservation equations are solved by means of the finite volume method. CONVERGE™ solver transport equations are solved sequentially using a pressure-velocity coupling iteration method known as PISO (Section 5.2.6). Transported quantities are located at the center of the cell which can result in a decoupling pressure-velocity. Rhie-Chow algorithm is used to prevent the mentioned effect. The discretization scheme used for computing the convection flux in density, energy, species, turbulence and passives transport equations is first-order upwind scheme whereas the second-order central difference discretization scheme is used for the momentum. Better numerical stability is obtained using a SOR algorithm. The time-step is controlled by the CFL. Values for velocity-based CFL are below 0.5, for viscosity-based CFL below 2.5 and for speed-of-sound-based CFL below 10 which results in time-steps between $5 \cdot 10^{-7}$ and 10^{-10} s. The multiphase system, carried out in Eulerian framework, is modeled using a single-fluid approach governed by conservation equations for mass, momentum, and energy. Turbulence has been treated in different ways, on the one hand by RANS approaches and on the other hand from LES approaches. For the RANS case, it is necessary to define a turbulence closure model and therefore, in the present research, approaches framed in the k-ε (Standard k-ε, RNG k-ε, Rapid distonsion k-ε and Realizable k-ε) and k-ω (Standard k-ω (1998), k-ω (2006) and SST k-ω) groups have been used. On the contrary, for the cases in which turbulence is treated from LES approaches, two different sub-grid models have been adopted: Dynamic Structure and One-Equation Viscous model. In addition to these turbulence models, a standard law-of-the-wall profile is used to determine the tangential components of the wall stress tensor in the U-RANS simulations, while the Werner and Wengle wall model [62] is considered in LES. The Werner and Wengle wall model is suitable for dealing with cells located at both the viscous ($y^+ \leq 5$) and buffer ($5 < y^+ < 30$) sub-layers.

In the mentioned multi-phase system, three different species are considered for the analysis: a liquid phase, a vapor phase and the ambient non-condensable gas (N_2). The inteface-capturing method known as VOF is selected to simulate the two-phase (liquid and gas) flow. In addition, in this type of studies there is a mass transfer due to the phase change that takes place between the liquid phase and its vapor. The model of heat and mass exchange between the liquid and vapor phases of the same species is based on the HRM.

External Flow

The external flow study has a numerical setup similar to the one described above, in other words, the transport equations are solved by a PISO scheme and the Rhie-Chow algorithm is adopted to prevent the decoupling between pressure and velocity due to the position of the transported quantities. The discretization scheme used for computing the convection flux in density, energy, momentum, species and passives transport equations is second-order upwind scheme whereas the first-order central difference discretization scheme is used for the turbulence. In addition, the SOR algorithm is also used to improve the stability of the solution. The time-step is controlled by the CFL. Values for velocity-based CFL are below 1, for viscosity-based CFL below 2 and for speed-of-sound-based CFL below 50 which results in a time-step between 10^{-9} and $2.5 \cdot 10^{-5}$ s.

The computational code solves the governing equations of mass, momentum, species, energy and turbulence in addition to sub-models used to define the physics of fuel spray in DDM. This means that, using a Lagrangian approach, liquid droplet dynamics, spray breakup, heat transfer, evaporation and collision are captured. However, the ambient gas as well as vapor phase are solved using Eulerian approach. Turbulence, as in the case of internal flow, has been treated from RANS (Standard k-ε, RNG k-ε, Rapid distonsion k-ε, Realizable k-ε and Standard k-ω (1998), k-ω (2006) and SST k-ω) and LES (Dynamic Structure and One-Equation Viscous model) approaches.

For external flow, the injection sub-model known as blob method is employed, which consists of injecting into the computational domain an initial droplet with a characteristic size of the effective nozzle diameter (165 µm) and a velocity function of the injected mass flow rate profile (Figure 5.7b). The nominal direction of the nozzle (37°) is employed and the selected cone angle is dependent on the operating condition under study. For the SG reference condition, the cone angle takes a value of 20°, the SG2 flash boiling condition has a cone angle greater of 25° and finally, the SG3 condition defines the initial cone angle of each jet to be 20°. The selected values are in accordance with the literature [63] and the studies that will be shown later (Section 6.6.2.1). With respect to the atomization sub-models that make up the external flow case studies, depending on whether the turbulence is treated with RANS or LES models, are different. In RANS approaches, a primary atomization model called KH-ACT is used while the secondary atomization is carried out by the well known KH-RT model. On the contrary, in the LES approach a breakup length is defined which determines the distance at which the KH model acts as the primary atomization model and from this distance the breakup is carried

out on the basis of the KH-RT standards. In addition to these sub-models for both RANS and LES approaches, an evaporation model based on Frossling correlation is also taken into account. A dynamic drop drag force is used to calculate the force on a particle in the dispersed Lagrangian phase due to its velocity relative to the continuous phase. The faster collision method which is the NTC is activated for detecting collisions in any particular cell and turbulent dispersion is considered thanks to the O'Rourke model.

5.3.6.2 Numerical setup in StarCCM+

Internal Flow

An Eulerian framework is employed for simulating the multi-phase fluid inside the nozzle and the near-nozzle spray. The classical conservation equations for mass, momentum and energy are solved used a single fluid approach. Those transport equations are solved sequentially with a Segregated Flow Solver and using an Implicit Unsteady Solver loop. An AMG linear solver is used with a relaxation scheme of Gauss-Seidel. The discretization scheme used for computing the convection flux in momentum, energy and species transport equations is first-order upwind whereas the discretization in time is defined as first-order backward Euler scheme. The time-steps depends on the CFL number being the target mean CFL number selected to 0.5 and the maximum to 5 which results in a time-step between $5 \cdot 10^{-7}$ and 10^{-10} s.

A VOF interface-capturing method is used to simulate the two-phase (liquid and gas) flow inside the nozzle. The model for mass exchange between the liquid and vapor phases of the same species is based on the HRM. Regarding the turbulence, RANS approach is selected due to its low computational cost. Therefore, a closure model is required. The SST k- ω is employed. In addition, a k-ω all-y+ wall treatment model is adopted.

External Flow

The external flow study has a numerical setup similar to the one described above with the difference that the transport equations are solved from the PISO solver. An AMG linear solver is used with a relaxation scheme of Gauss-Seidel. The discretization scheme used for computing the convection flux in momentum, energy and species transport equations is second-order upwind whereas the discretization in time is defined as first-order backward Euler scheme. The time-steps depends on the CFL number being the target mean CFL number selected to 0.5 and the maximum to 1 which results in a time-step between $2 \cdot 10^{-6}$ and 10^{-9} s.

As in the previous software, a DDM model known also as blob method is used to simulate the behavior of the spray once it leaves the injector. The computational code solves the governing equations of mass, momentum, species, energy and model turbulence by RANS approaches. Standard k-ϵ and SST k-ω closure models are used. Regarding the atomization sub-models, Huh Atomization is used as the primary breakup model whereas Kelvin-Helmholtz (KH) and Rayleigh-Taylor (RT) breakup mechanisms are jointly responsible for secondary atomization. In addition to these sub-models, the evaporation phenomenon is according to the quasi-steady evaporation model based on Frossling scheme. A drop drag force based on the Schiller-Naumann correlation is employed. The faster collision method which is the NTC is activated for detecting collisions in any particular cell and turbulent dispersion is considered thanks to the Gosman and Ioannides model.

5.4 Post-processing

This section summarizes the codes or strategies implemented to calculate the parameters referred to as the results of each of the simulations, whether they are internal or external flow studies.

5.4.1 Internal nozzle flow

5.4.1.1 ROI and ROM calculation

The main parameters driving the internal flow study are the rate of injection (ROI) and the rate of momentum (ROM). These are typically calculated from the density and velocity variables at the outlet of the orifices either from the inner orifice or the counter-bore as shown in Figure 5.23. The values are extracted in planes perpendicular to the outflow of the orifices by applying Equations 5.134 and 5.135, respectively.

$$\dot{m}_i = \int\int \rho(\vec{n_i} \cdot \vec{v}) dA_i \tag{5.134}$$

$$\dot{M}_i = \int\int \rho(\vec{n_i} \cdot \vec{v})^2 dA_i \tag{5.135}$$

being ρ the density, $\vec{n}$ the normal vector to the plane, $\vec{v}$ the velocity vector and A_i the area corresponding to the surface of each plane.

There are several ways to experimentally measure the flux momentum, frontal and lateral [64]. On the one hand, the frontal position consists of

placing the piezoelectric target perpendicular to the injector and capturing all the sprays together so that it is essential to know their angle of impact. In addition, this configuration does not allow to know the air entraiment in case there is one, which can lead to incorrect measurements. On the other hand, the target can be placed laterally to capture the momentum of each spray individually. This configuration also has some uncertainties such as that the sprays are too close together and there may be interaction between plumes and to avoid this phenomenon the target has to be far enough away from the tip of the injector so that it can lose part of the measurement if the spray does not impact completely on it. There are numerous uncertainties with respect to momentum flux measurements that have not been resolved to date. Therefore, it is also not possible to associate a specific cause to the differences between strategies, either because of an incorrect setting angle or because the lateral configuration does not accurately capture the total momentum of the spray. For this study, the frontal configuration has been selected because it is the most widespread, but it must be taken into account that this configuration may imply differences of 12% with the lateral configuration. With the aim of making the computational and experimental measurement strategies as similar as possible, this work includes the calculation of momentum in a plane at a certain distance from the tip of the injector (Figure 5.23).

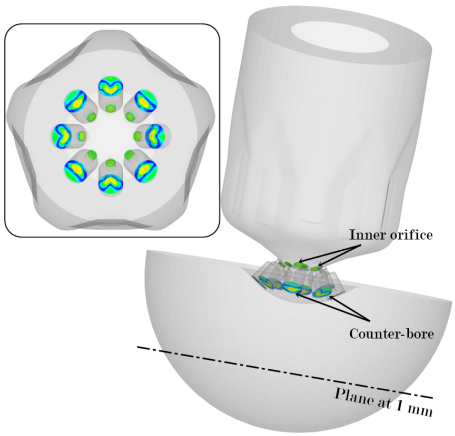

Figure 5.23: Sketch of one of the study geometries (Spray G) to explain the areas where to calculate the desired results.

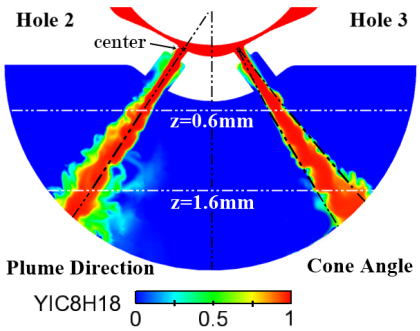

Figure 5.24: Definition of the spray angle and the plume direction through the liquid mass fraction.

5.4.1.2 Spray angle and plume direction calculation

The calculation of the angles is often performed from a variable that defines the spray itself, either the velocity, the liquid volume fraction or, as in this case, the liquid mass fraction. When the liquid leaves the injector nozzle and comes into contact with the environment, it begins to mix with the non-condensable gas. This means that the contours of the spray are not perfectly defined, but there is a mixture of liquid and gas. For this reason, it is necessary to choose a threshold that determines the limits of the intact spray core being, in this case, a mass fraction greater than 0.25 considering that below this value the liquid-gas mixture is high. An upper limit (z = 0.6 mm) and a lower limit (z = 1.6 mm) have been chosen to define the sample space, avoiding the influence of the outlet (Figure 5.24). Once the boundaries are determined, the planes that cut the holes through the center of each hole are defined. Then, the domain is vertically discretized with 20 µm samples to obtain the limits of the spray. For each of these limits, the slope is calculated taking as a reference point the center of the inner hole as defined in the ECN angle specification. Now that all the slopes have been estimated, they are averaged to acquire the spray angle as final value. The spray direction is computed in the same way by the bisector of the spray angle in each point, and averaging them at the end.

5.4.2 External flow. Macroscopic parameters

5.4.2.1 Liquid and vapor penetration calculation

Two of the most relevant parameters to characterize the spray in the external flow study are liquid and vapor penetration. Typically the commercial codes, in particular those used in this research, have their own algorithm to calculate the penetration. For liquid penetration, this algorithm is mainly based on the cumulative mass theory, which means that at each instant of time it calculates the total mass injected. The user or the code itself defines a threshold which can be typically 99%, 97% or 95% and it is automatically applied to detect the distance at which the selected criterion is met, e.g. 95% of the total mass injected. In addition, this algorithm tends to calculate the penetrations individually in each jet taking as a reference the geometric axis of a singe spray, which does not consider the possible deviations of the spray from this axis as can be the case of flash boiling. This methodology is not incorrect or inaccurate, but it does not match that used experimentally and therefore could lead to significant differences between results if the objective is to validate the computational model. In recent studies, Saha et al. [65] demonstrated that

the mentioned method based on the specific mass underestimated the spray penetration by up to 20 mm. For this reason, a new methodology is developed to allow an accurate comparison with the experimental results. This consists in projecting the data corresponding to the Liquid Volume Fraction (LVF) (variable that best reflects the amount of liquid in each cell in DDM) on a two-dimensional plane with an identical orientation to the one used experimentally to take the images from which the penetration values are calculated. Once the study variable (LVF) is placed in the desired plane, a threshold is applied to it, being the same for both experimental and computational studies. For Spray G injector, the explained method has been recently implemented by the ECN network to unify the calculations of all participating institutions and therefore two different thresholds have been set: 2e-04 mm^3/mm^2 (high threshold) and 2e-03 mm^3/mm^2 (low threshold). In the case of the PIU injector, no threshold has been selected so that the liquid penetration is calculated taking into account all the LVF existing in the domain. Equations 5.136, 5.137 and 5.138 explain the relationship of the liquid volume fraction to the optical thickness of the liquid along the light path of the experimental technique.

$$I/I_0 = e^{-\tau} \tag{5.136}$$

$$\tau \frac{\pi d^3/6}{C_{ext}} = \int_{-y_\infty}^{y_\infty} LVF dy \rightarrow \tau \frac{\pi d^3/6}{C_{ext}} = PLV \tag{5.137}$$

$$PLV = \sum_{i=y_{min}}^{y_{max}} LVF_i \Delta y \tag{5.138}$$

where, for the ECN case, d is the droplet diameter taken as 7 µm according to Phase Doppler Interferometer (PDI) measurements provided by General Motors (GM) to the ECN and C_{ext} is the extinction cross-section acquired from MIE theory. It was assumed that the droplet diameter and extinction coefficient are constant along the light path. C_{ext} can be calculated, being function of the droplet diameter, light wavelength, and the collection angle of the optical setup. It was calculated to be $44.6 \cdot$ 10e-06 mm^2 for Spray G with iso-octane [66].

For vapor penetration, the procedure used is similar. In this case, the variable corresponding to the vapor mass fraction is projected on the above mentioned plane and the penetration is defined as the distance from the position of the injector tip to where the 0.1% of the mixture fraction is located.

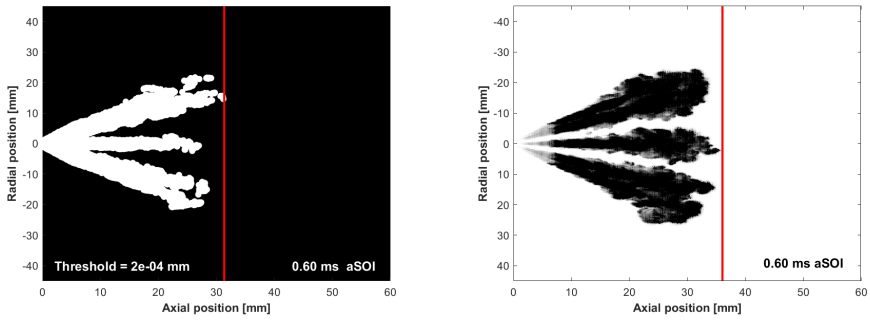

(a) LVF projection (b) Vapor projection

Figure 5.25: Example of the projection of LVF and vapor variables for liquid and vapor penetration calculation.

Figure 5.25 shows an example of the results obtained after applying the aforementioned penetration strategy.

Finally, to validate the results obtained computationally from the available experimental data, the cumulative error is used, which is determined by Equation 5.139.

$$\text{error} = \sum_{i=0}^{n} \frac{\sqrt{(S_{exp,i} - S_{CFD,i})^2}}{S_{exp,i}} \tag{5.139}$$

5.4.2.2 Spray angle calculation

Another parameter used to characterize the jet is the spray angle. As one of the objectives is to validate the results with experimental data, the criteria explained below for the calculation of this parameter are based on the experimentally employ strategies.

There are a number of ways to determine the spray angle once the contour is identified. The different methods reported in the literature can lead to significant changes in the resulting spray spreading angle, so it is essential to justify the selection of one method over the others [67]. In this work, the four definitions most commonly used by the scientific community have been considered and are graphically illustrated in Figure 5.26,

- **Triangle Criterion**. The concept is on the basis of the angle of an isosceles triangle. The isosceles triangle is calculated by considering the

height as half of the spray penetration (0.5 S) and an area equivalent to the spray region from the nozzle exit to half of the penetration. This definition of the angle was described by Naber and Siebers [68].

- **Trapezoidal Criterion**. This scenario is analogous to the previous one defined by Naber and Siebers, but modified for situations where the spray contour is not available close to the nozzle tip. In this particular case, the angle is that of an isosceles trapezoid with the same surface as the jet. The base of the trapezoid matches the spray contour closest to the nozzle. The trapezoid method demands that the two lines forming the angle intersect at the geometric origin of the spray (exit hole).
- **Fitted angle between intervals**. Adjusted angle between intervals. In this case, two lines are adjusted to the spray contour, starting at 12% of the penetration and ending at 60%. The lines may not cross at the nozzle orifice, which means that the jet origin is not taken into account. The distances between lines can be varied. It is typical, in the experimental results, that the computational data is calculated in three different intervals: S1(5-30 %), S2 (12-50 %) and S3 (12-60 %).
- **Fixed Origin**. The origin is set and then two lines are fitted using a weighted average of each point of the contour defined in polar coordinates. In the same way as in the previous case (fitted angle), different intervals can be considered for the calculation of the spray angle, being typical the use of the ranges already mentioned.

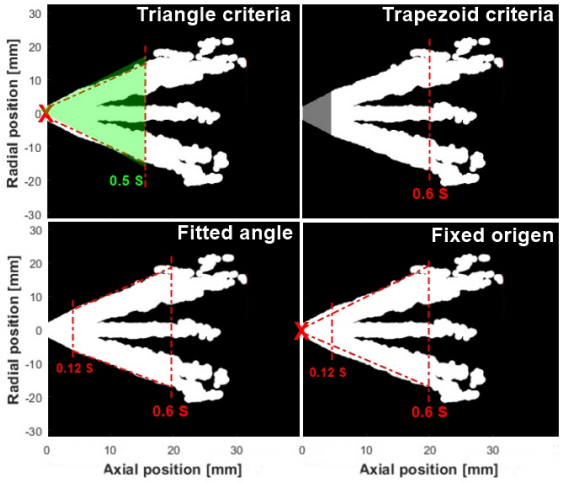

Figure 5.26: Different spray spreading angle definitions found in the literature.

References

[1] Battistoni, M. et al. "Coupled simulation of nozzle flow and spray formation using diesel and biodiesel for CI engine applications". In: *SAE Technical Papers* (2012). DOI: 10.4271/2012-01-1267.

[2] Versteeg, H. K. et al. "An introduction to computational fluid dynamics". In: *Longman scientific and Technical* (1995).

[3] Bornschlegel, S. et al. "Multi-hole gasoline direct injection:In-nozzle flow and primary breakup investigated in transparent nozzlesand with X-ray". In: *International Journal of Engine Research* 19.1 (2018), pp. 67–77. DOI: 10.1177/1468087417746860.

[4] Zhuang, H. et al. "Impact of Fuel Sprays on In-Cylinder Flow Length Scales in a Spark-Ignition Direct-Injection Engine". In: *SAE International Journal of Engines* 10.3 (2017). DOI: 10.4271/2017-01-0618.

[5] Sirignano, W. A. *Fluid Dynamics and Transport of Droplets and Sprays*. Cambridge University Press, 1999. DOI: 10 . 1017 / CBO9780511529566.

[6] Launder, B. E. et al. "The numerical computation of turbulent flows". In: *Computer methods in applied mechanics and engineering* (1974), pp. 269–289. DOI: 10.1007/JHEP10(2012)057.

[7] Pope, S. B. "An explanation of the turbulent round-jet/plane-jet anomaly". In: *AIAA Journal* 16.3 (2008), pp. 279–281. DOI: 10.2514/3.7521.

[8] Shaheed, R. et al. "A comparison of standard kâepsilon and realizable kâepsilon turbulence models in curved and confluent channels". In: *Environmental Fluid Mechanics* 19.2 (2019), pp. 543–568. DOI: 10.1007/s10652-018-9637-1.

[9] Yakhot, V. et al. "Development of turbulence models for shear flows by a double expansion technique". In: *Physics of Fluids A* 4.7 (1992), pp. 1510–1520. DOI: 10.1063/1.858424.

[10] Wilcox, D. C. *Turbulence Modelling for CFD 3rd Edftion*. 2006, p. 536.

[11] Shih, T. H. et al. "A new k-epsilon eddy viscosity model for high Reynolds number turbulent flows". In: *Computer Fluids* 24.3 (1995), pp. 227–238. DOI: 10.1007/978-3-319-27386-0_7.

[12] Povilaitis, M. et al. "Simulation of hydrogen-air-diluents mixture combustion in an acceleration tube with flamefoam solver". In: *Energies* 14.17 (2021). DOI: 10.3390/en14175504.

[13] Sagaut, P. *Large eddy simulation for incompressible flows: an introduction*. Springer Science & Business Media, 2006.

[14] Yoshizawa, A. et al. "A Statistically-Derived Subgrid-Scale Kinetic Energy Model for the Large-Eddy Simulation of Turbulent Flows". In: *Journal of the Physical Society of Japan* 54.8 (1985), pp. 2834–2839. DOI: 10.1143/JPSJ.54.2834.

[15] Menon, S. et al. "Effect of subgrid models on the computed interscale energy transfer in isotropic turbulence". In: *Computers and Fluids* 25.2 (1996), pp. 165–180. DOI: 10.1016/0045-7930(95)00036-4.

[16] Pomraning, E. "Development of Large Eddy Simulation Turbulence Models". PhD thesis. University of Wisconsin, 2000.

[17] Medina, M. et al. "Mechanisms of fuel injector tip wetting and tip drying based on experimental measurements of engine-out particulate emissions from gasoline direct-injection engines". In: *International Journal of Engine Research* 22.6 (2021), pp. 2035–2053. DOI: 10.1177/1468087420916052.

[18] Muzaferija, S. et al. "Computation of free-surface ows using interface-tracking and interface-capturing methods Flows of two (or more) immiscible uids are often encountered in". In: November (1999).

[19] Youngs, D. L. "Time-dependent multi-material flow with large fluid distortion." In: January 1982 (1982).

[20] Bilicki, Z. et al. "Physical Aspects of the Relaxation Model in Two-Phase Flow". In: *Proceedings of the Royal Society A: Mathematical, Physical and Engineering Sciences* (1990). DOI: 10.1098/rspa.1990.0040.

[21] Downar-Zapolski, P. et al. "The non-equilibrium relaxation model for one-dimensional flashing liquid flow". In: *International Journal of Multiphase Flow* 22.3 (1996), pp. 473–483. DOI: 10.1016/0301-9322(95)00078-X.

[22] Matsoukas, T. *Fundamentals of Chemical Engineering Thermodynamics*. Prentice Hall, 2012.

[23] Battistoni, M. et al. "Effects of noncondensable gas on cavitating nozzles". In: *Atomization and Sprays* 25.6 (2015), pp. 453–483. DOI: 10.1615/AtomizSpr.2015011076.

[24] Ashgriz, N. *Handbook of atomization and sprays: theory and applications*. Springer Science & Business Media, 2011.

[25] Faeth, G. M. "Mixing, transport and combustion in sprays". In: *Progress in Energy and Combustion Science* 13.4 (1987), pp. 293–345. DOI: 10.1016/0360-1285(87)90002-5.

[26] Amsden, A. et al. "KIVA-II: A computer program for chemically reactive flows with sprays, Los Alamos - National Laboratory, report LA-11560-MS". In: *Los Alamos National Lab. (LANL)* May (1989), LA–11560–MS.

[27] Schiller, L. et al. "A drag coefficient correlation". In: 77 (1935), pp. 51–86.

[28] Lippert, A. M. et al. "Mesh independence and adaptive mesh refinement for advanced engine spray simulations". In: *SAE Technical Papers* 2005.724 (2005). DOI: 10.4271/2005-01-0207.

[29] O'Rourke, P. J. et al. "The Tab Method for Numerical Calculation of Spray Droplet Breakup". In: *1987 SAE International Fall Fuels and Lubricants Meeting and Exhibition*. 1987. DOI: 10.4271/872089.

[30] Taylor, G. I. "Generation of ripples by wind blowing over a viscous fluid". In: *The Scientific Papers of G.I. Taylor, vol. 3*. Ed. by G. K. Batchelor. Cambridge: Cambridge University Press, 1963. Chap. 25, pp. 244–254.

[31] Reitz, R. D. "Atomisation and other breakup regimes of a liquid jet". PhD thesis. Ph.D. Thesis, Princeton University, 1978.

[32] Reitz, R. D. et al. "Mechanisms of breakup of round liquid jets". In: *Encyclopedia of Fluid Mechanics* August (1986), pp. 233–249.

[33] Arcoumanis, C. et al. "Analysis of the flow in the nozzle of a vertical multi-hole Diesel engine injector". In: *SAE Paper 980811* (1998).

[34] Brennen, C. E. *Cavitation and bubble dynamics*. 2013, pp. 1–249. DOI: 10.1017/CBO9781107338760.

[35] Reitz, R. D. "Mechanisms of Atomization Processes in High-Pressure Vaporizing Sprays". In: *Atomization and Spray Technology* 3 (1987), pp. 309–337.

[36] Senecal, P. K. et al. "A new parallel cut-cell cartesian CFD code for rapid grid generation applied to in-cylinder diesel engine simulations". In: *SAE Technical Papers* 2007.724 (2007), pp. 776–790. DOI: 10.4271/2007-01-0159.

[37] Crowe, C. T. et al. "Particle mixing in free shear flows". In: *Progress in Energy and Combustion Science* 14.3 (1988), pp. 171–194. DOI: 10.1016/0360-1285(88)90008-1.

[38] Gosman, A. D. et al. "Aspects of Computer Simulation of Liquid-Fuelled Combustors." In: *AIAA Paper* 7.6 (1981), pp. 482–490. DOI: 10.2514/6.1981-323.

[39] O'Rourke, P. J. "Collective Drop Effects on Vaporizing Liquid Sprays". PhD thesis. Princeton University, 1981.

[40] Schmidt, D. P. et al. "A New Droplet Collision Algorithm". In: *Journal of Computational Physics* 164.1 (2000), pp. 62–80. DOI: 10.1006/jcph.2000.6568.

[41] Schmidt, D. P. et al. "A New Droplet Collision Algorithm". In: *Journal of Computational Physics* 164.1 (2000), pp. 62–80. DOI: 10.1006/jcph.2000.6568.

[42] Richards, K. J. et al. "Convergent Science v2.4 Documentation". In: *Convergent Science Inc.* (2018), p. 1207.

[43] Barton, I. E. "Comparison of simple- and piso-type algorithms for transient flows". In: *International Journal for Numerical Methods in Fluids* 26.4 (1998), pp. 459–483. DOI: 10.1002/(SICI)1097-0363(19980228)26:4<459::AID-FLD645<3.0.CO;2-U.

[44] Patankar, S. V. et al. "A calculation procedure for heat, mass and momentum transfer in three-dimensional parabolic flows". In: *International Journal of Heat and Mass Transfer* 15.10 (1972), pp. 1787–1806. DOI: 10.1016/0017-9310(72)90054-3.

[45] Issa, R. I. et al. "The computation of compressible and incompressible recirculating flows by a non-iterative implicit scheme". In: *Journal of Computational Physics* 62.1 (1986), pp. 66–82. DOI: 10.1016/0021-9991(86)90100-2.

[46] Belmar Gil, M. "Computational study on the non-reacting flow in Lean Direct Injection gas turbine combustors through Eulerian-Lagrangian Large-Eddy Simulations". PhD thesis. Valencia (Spain): Universitat Politècnica de València, 2020. DOI: 10.4995/Thesis/10251/159882.

[47] Rhie, C. M. et al. "Numerical study of the turbulent flow past an airfoil with trailing edge separation". In: *AIAA Journal* 21.11 (1983), pp. 1525–1532. DOI: 10.2514/3.8284.

[48] Lemmon, E. W. et al. "Thermophysical Properties of Fluid Systems". In: *NIST Chemistry WebBook, NIST Standard Reference Database Number 69*. Ed. by P. J. Linstrom et al. 2011.

[49] Kendall, J. et al. "American Chemical Society". In: *Analytical Chemistry* 41.7 (1969), 92A–93A. DOI: 10.1021/ac60276a790.

[50] Schmitz, K. S. *Thermodynamics of the Liquid State*. 2017, pp. 203–260. DOI: 10.1016/b978-0-12-800514-9.00005-5.

[51] Escobedo, J. et al. "Surface-tension prediction for liquid mixtures". In: *AIChE Journal* 44.10 (1998), pp. 2324–2332. DOI: 10.1002/aic.690441021.

[52] Dymond, J. H. et al. "Transport properties of nonelectrolyte liquid mixtures-VII. Viscosity coefficients for isooctane and for equimolar mixtures of isooctane + n-octane and isooctane + n-dodecane from 25 to 100??C at pressures up to 500 MPa or to the freezing pressure". In: *International Journal of Thermophysics* (1985). DOI: 10.1007/BF00522146.

[53] Giannadakis, E. et al. "The influence of variable fuel properties in high-pressure diesel injectors". In: *SAE Technical Papers* January (2009). DOI: 10.4271/2009-01-0832.

[54] Payri, R. et al. "Nozzle Flow Simulation of GDi for Measuring Near-Field Spray Angle and Plume Direction". In: *SAE Technical Paper 2019-01-0280* (2019), pp. 1–11. DOI: 10.4271/2019-01-0280.Abstract.

[55] Kastengren, A. et al. "The 7BM beamline at the APS: A facility for time-resolved fluid dynamics measurements". In: *Journal of Synchrotron Radiation* 19.4 (2012), pp. 654–657. DOI: 10.1107/S0909049512016883.

[56] Duke, D. J. et al. "Internal and near nozzle measurements of Engine Combustion Network "Spray G" gasoline direct injectors". In: *Experimental Thermal and Fluid Science* 88 (2017), pp. 608–621. DOI: 10.1016/j.expthermflusci.2017.07.015.

[57] Strek, P. et al. "X-Ray Radiography and CFD Studies of the Spray G Injector". In: *SAE Technical Paper 2016-01-0858* (2016). DOI: 10.4271/2016-01-0858.

[58] Vaquerizo, D. "Study on Advanced Spray-Guided Gasoline Direct Injection Systems". PhD thesis. Universitat Politècnica de València, 2017. DOI: 10.4995/Thesis/10251/99568.

[59] Hung, D. L. et al. "Gasoline fuel injector spray measurement and characterization - A new SAE J2715 recommended practice". In: *SAE International Journal of Fuels and Lubricants* 1.1 (2009), pp. 534–548. DOI: 10.4271/2008-01-1068.

[60] Keskinen, J. P. et al. “Influence of mesh deformation on the quality of large eddy simulations”. In: *International Journal for Numerical Methods in Fluids* (2016). DOI: 10.1002/fld.4215.

[61] Wang, W. et al. “Comparison of hexahedral, tetrahedral and polyhedral cells for reproducing the wind field around an isolated building by LES”. In: *Building and Environment* 195.October 2020 (2021), p. 107717. DOI: 10.1016/j.buildenv.2021.107717.

[62] Wengle, H. et al. “Large-eddy Simulation of Turbulent Flow Over Sharp-edged Obstacles in a Plate Channel”. In: 1993, pp. 192–199. DOI: 10.1007/978-3-663-13986-7_26.

[63] Saha, K. et al. “Coupled Eulerian Internal Nozzle Flow and Lagrangian Spray Simulations for GDI Systems”. In: *SAE Technical Papers* 2017-March.March (2017). DOI: 10.4271/2017-01-0834.

[64] Payri, R. et al. “Momentum Flux Measurements on an ECN GDi Injector”. In: *SAE Technical Paper 2015-01-1893*. 2015. DOI: 10.4271/2015-01-1893.

[65] Saha, K. et al. “Modeling the Dynamic Coupling of Internal Nozzle Flow and Spray Formation for Gasoline Direct Injection Applications”. In: *SAE Technical Paper* (2018), pp. 1–13. DOI: 10.4271/2018-01-0314.Abstract.

[66] Payri, R. et al. “Numerical Analysis of GDI Flash Boiling Sprays Using Different Fuels”. In: *Energies* 14.18 (2021), p. 5925. DOI: 10.3390/en14185925.

[67] Payri, R. et al. “Study of liquid and vapor phase behavior on Diesel sprays for heavy duty engine nozzles”. In: *Applied Thermal Engineering* 107 (2016), pp. 365–378. DOI: 10.1016/j.applthermaleng.2016.06.159.

[68] Naber, J. D. et al. “Effects of Gas Density and Vaporization on Penetration and Dispersion of Diesel Sprays”. In: *SAE Paper 960034*. Vol. 105. 412. Society of Automotive Engineers, Inc., Warrendale, Pennsylvania, USA, 1996, pp. 82–111. DOI: 10.4271/960034.

Chapter 6

Internal and Near Nozzle Flow Characterization

"There are no secrets to success.
It is the result of preparation, hard work and learning from failure."
— Colin Powell

6.1 Introduction to the Steady State Analysis

This Chapter covers the code verification and model validation processes which determines how detailed the computational methodology developed is in describing reliably and accurately the behavior of the fluid in the in- and near-nozzle region and some of the phenomena that take place during the injection process. Verification is the process of determining that an implemented or selected model accurately represents the conceptual description of the phenomena to be studied and the model solution. Therefore, verification does not deal with whether the model itself is a proper description of the physics of the problem at hand; it is not a physical issue but a mathematical or computational matter. Validation, on the other hand, involves determining the level to which a model is an appropriate representation of the real problem from the perspective of the expected applications of the model. The methodology validation entails the identification and quantification of the numerical error in the computational solution, the estimation of experimental uncertainty and, finally, the comparison between the computational results and the experimental data [1].

Throughout this section and with the objective of accurately characterizing different GDI injectors, a predictive methodology is presented that allows to establish an optimal meshing strategy, the selection of the turbulence model as well as to observe the influence of the parameters involved in the phase change models by solving the case of the Spray G injector taken as a reference. Subsequently, this methodology will be validated by using it in the study of in- and near- nozzle flow in the PIU industrial injector.

6.2 Spray G Injector. CONVERGE™ software. Steady State Analysis

This section gathers the different stages carried out to develop the above mentioned predictive methodology in terms of meshing strategy, discharge volume size and turbulent models, among others. The results obtained allow the characterization of the Spray G injector belonging to the ECN network during the steady state.

6.2.1 Determination of the steady state condition

In general, the injection process is defined as a completely transient process due to the opening and closing movement of the needle. However, there will come a time when the mass flow rate through the injector will remain constant over time, because the needle is kept open with a lift equal to 45 µm (max. of Spray G). This is what is called steady state, determined by the moment in which this mass flow stays unchanged. The computational domain presented in Figure 5.7a is used to define the steady state, except that the discharge volume has dimensions of 3 mm in diameter. It is important to note that this study is carried out under the standard operating condition of the ECN, Spray G (see Table 5.14).

Figure 6.1 represents the mass flow as a function of injection time measured at the outlet of the orifices [2]. It can be seen how, after a transient period when high mass flow values due to the pressure difference between the pressure at which the fuel is injected and the pressure at which the discharge chamber is located, the values of this variable tend to stabilize. To determine the stationary moment and the time from which it can be considered, it is established the criterion that the variation of the variable of study, the mass flow in this case, must not exceed ± 1% of the average value. It may be observed in the upper right part of this same Figure 6.1 how the stipulated criterion is fulfilled after 0.12 ms. Therefore, it can be said that the steady

state is reached in this simulation time. Even so, to give a margin of error and avoid the uncertainty to affect the results, in the following studies, when needed, it will be considered that the steady state begins at 0.15 ms.

Not only has it been proven that this variable of interest reaches the steady state, but together with ROI, the rest of flow variables such as velocity or pressure, among others, also reach steady state conditions at 0.15 ms.

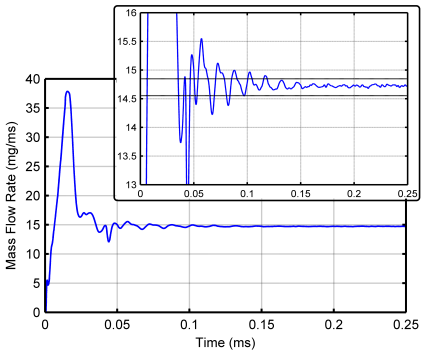

Figure 6.1: Steady state determination from the evolution of the ROI as a function of time at SG ECN conditions.

6.2.2 Mesh sensitivity and validation

In general, the finer the mesh, the more accurately the contours of a geometry can be captured and the more "data points" there are in the geometry to generate accurate response. However, the greater the computational cost is. Thus, a mesh study is something an analyst can perform to determine the dependence of results on mesh density. One of the most widely adopted forms is following the approach described below:

- *Refine the mesh in the area(s) of interest.* Some best practices listed below should be used when refining the mesh:
  - Only modify the mesh size. Do not alter any other mesh settings, such as the type or order of the elements. This will ensure a fair comparison between cases.
  - Make sure that the increase in mesh size between different runs is “significant”. By significant means a minimum of 5-10%. This percentage is a guide based on experience and analytical judgment.
  - Obtain at least three different meshes. Two meshes may be sufficient to demonstrate mesh independence. But in the case of relatively coarse initial meshes, it will usually take three or more runs to establish mesh independence.

Based on the aforementioned premises, in order to find an optimal cell base size that provides good results in the study of the internal nozzle flow with an adequate level of accuracy and a minimum computational cost, a sensitivity study has been carried out taking into account three different cell sizes with the same discretization levels (first order for all equations) and other three changing the discretization level to second order for the momentum equation. The meshing strategy followed is the one presented in Section 5.3.5.1, and only the base cell size is changed. The computational domain corresponds to the Spray G injector with a discharge volume of 3 mm (see Figure 5.7a).

Case	**ROI [mg/ms]**	**Difference [%]**	**N° Cells**	**CPU-h**
200 µm	14.95	1.6	421836	55.80
140 µm	14.72	0.96	1017429	246.75
100 µm	14.58	-	2393021	589.39
140 *µm	14.81	0.27	1017429	234.54
130 *µm	14.85	0.47	1224669	285.98
120 *µm	14.92	-	1503600	510.06
Experimental ROI [mg/ms] = 14.71				

** 2nd Discretization Order in Momentum Equation*

Table 6.1: Obtained results from the mesh independence analysis carried out for the Spray G geometry under SG reference condition with CONVERGE™

Table 6.1 shows all the results for the different meshes studied including the mass flow rate, the number of cells and the computational cost of each case. This table also presents the difference between meshes where the value has been calculated taking as a reference a mesh with one degree higher refinement order, that is, the difference referring to the mesh with base size of 200 µm of base size is calculated taking as a reference the mesh of 140 µm. The mesh independence analysis is divided into two different sections, the first one includes the meshes in which first-order discretization schemes have been used for all the equations. On the other hand, the most optimal mesh of that study (140 µm) is compared with meshes of different sizes of the base cell but where a second-order discretization is used for the moment equation.

These results exhibit small differences in ROI between meshes of different base sizes, so it could be said that all of them are valid for carrying out subsequent studies. From the first block of studied cases (first order of discretization) the most optimal mesh can be considered the 140 µm one. It is within 1% difference with respect to the most refined mesh, considered the

most accurate. Thus, it offers similar results with a computational cost 2.4 times lower. Comparing this result with those obtained from meshes with second-order discretization for the momentum equation, it is observed that the differences are again very small. Therefore, 140 µm is chosen as the base cell size and second-order discretization since, theoretically, it provides a high accuracy with lower computational cost. As occurred with ROI, no significant differences (1%) were observed in other parameters of interest.

Finally, it can be noticed that the base cell sizes chosen by researchers with the same objective are around the selected value of 140 µm with minimum cell sizes of 17.5 µm in the most sensitive areas of orifices and needle seat [3, 4].

6.2.3 Comparison between submerged and non-submerged conditions

Once the most suitable mesh for the present study has been determined, it is of interest to analyze the influence of downstream conditions on the behavior of the fluid. In this case, submerged conditions are taken into account, which means that the discharge volume is filled with liquid (IC_8H_{18}), thus resembling the study conditions to those experimentally available where ROI is measured with the Bosch method on a commercial EVI (EinspritzVerlaufsIndikator) rate meter [5]. On the other hand, it is also analyzed the results of studying the injection in non-submerged conditions which defines the discharge volume with a non-condensable gas such as N_2.

For this comparison, it has been used characteristic parameters of the internal flow such as mass flow rate, momentum flux and dimensionless coefficients that characterize the injector such as discharge, momentum, area and velocity coefficients (Section 3.4.3). In addition, the three most important operating conditions of the ECN have been included in this comparison: SG, SG2 and SG3.

Table 6.2 presents the obtained results from the aforementioned comparison. This study clearly concludes that the behavior of the fluid in terms of macroscopic variables is similar in both cases and that, of course, a study in non-submerged conditions can be compared with experimental data obtained in submerged tests. The differences obtained are less than 3% in all cases.

Once it has been verified that the macroscopic variables that characterize the flow through the injector are not altered by the conditions existing in the discharge volume, it is interesting to observe if visually the near-field spray behavior is the same. For this purpose, a vertical section of the injector colored by the volume fraction represents the amount of vapor and liquid in the cells

Submerged	**ROI [mg/ms]**	**ROM [N]**	$\mathbf{C_d}$	$\mathbf{C_m}$	$\mathbf{C_a}$	$\mathbf{C_v}$
Spray G	14.22	2.27	0.53	0.34	0.82	0.65
Spray G2	13.97	2.35	0.51	0.34	0.76	0.68
Spray G3	13.94	2.33	0.51	0.34	0.76	0.67
Non-Submerged	**ROI [mg/ms]**	**ROM [N]**	$\mathbf{C_d}$	$\mathbf{C_m}$	$\mathbf{C_a}$	$\mathbf{C_v}$
Spray G	14.72	2.29	0.53	0.34	0.82	0.65
Spray G2	13.92	2.31	0.51	0.34	0.77	0.66
Spray G3	13.85	2.29	0.51	0.34	0.77	0.66

Table 6.2: Comparison between submerged and non-submerged conditions for different operating points and the Spray G injector.

both in submerged conditions (Figure 6.2) and in non-submerged conditions (Figure 6.3) is presented. It is important to mention that the purpose of this section is to observe the differences between submerged and non-submerged conditions and not to make a comparison between operating conditions (SG, SG2 and SG3) or to quantify the differences between them (explained later in this section).

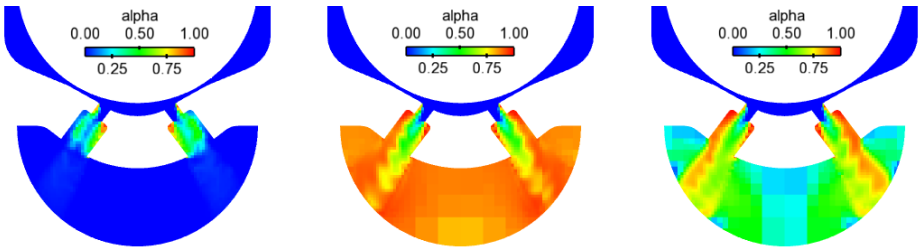

(a) Spray G (b) Spray G2 (c) Spray G3

Figure 6.2: Vertical cut-plane representing the α variable for the Spray G injector under different submerged operating engine points.

Visually, some differences can be noticed between the same operating points in submerged and non-submerged conditions. Firstly, referring to the SG condition, the submerged condition (Figure 6.2a) allows to appreciate where vapor is generated, specifically in the interior of the orifices, corresponding to the phase change of the fuel due to the conditions existing in the chamber. On the other hand, in non-submerged conditions (Figure 6.3a), a more realistic condition because it is the scenario typically found in a real engine, it is possible to observe how the liquid, once injected into the discharge

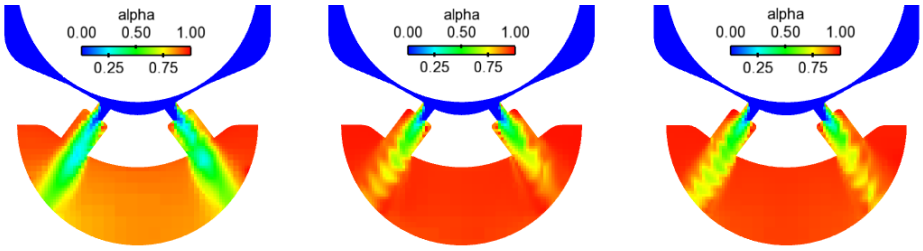

(a) Spray G (b) Spray G2 (c) Spray G3

Figure 6.3: Vertical cut-plane representing the α variable for the Spray G injector under different non-submerged operating engine points.

chamber, in addition to phase change, mixes with the surrounding gas. Referring to the SG2 condition where the operating conditions are favorable to the appearance of flash boiling, in the submerged scenario (Figure 6.2b) it can be observed how the discharge volume which is initially filled with liquid, a large part has been occupied by the vapor generated from the instantaneous boiling corresponding to the flash boiling phenomenon. This effect, although occurring similarly in the non-submerged condition (Figure 6.3b), cannot be observed since the variable represented does not distinguish between gaseous species. Finally, the SG3 condition shows a behavior identical to that observed in SG2, highlighting a lower vapor generation (see Figure 6.2c) since the discharge pressure is higher in the case of SG3. In both conditions, SG2 and SG3, it can be seen that the spray does not develop in a continuous way but presents certain discontinuities due to the rapid boiling of the liquid.

Once the results have been analyzed, in which no differences in the internal flow characterization values have been appreciated, but variations in the spray behavior have been observed, and taking into account that one of the objectives is to study spray pattern, the non-submerged case, which is closer to the real engine operation, will be the one selected for further studies.

6.2.4 Discharge volume sensitivity

This Section includes the study of the independence of the nozzle flow results on the discharge volume by studying three discharge chambers with different sizes, 3 mm, 6 mm and 9 mm, and comparing them with each other from the parameters that characterize the injector as well as the calculation of the plume cone angle and plume direction. For this purpose, the optimum mesh chosen from the mesh independence study (Section 6.2.2) and operating conditions

corresponding to the standard Spray G have been selected. This study arises from the need to analyze whether the 3 mm diameter domain is sufficient to prevent the boundary conditions applied in the outlet from affecting the solution, or as it seems to be observed, a larger diameter chamber is necessary.

Table 6.3 shows the data corresponding to ROI and ROM variables together with the dimensionless coefficients that characterize the injector and compares them with the data from experimental results.

Submerged	**ROI [mg/ms]**	**ROM [N]**	$\mathbf{C_d}$	$\mathbf{C_m}$	$\mathbf{C_a}$	$\mathbf{C_v}$
3 mm	14.72	2.29	0.53	0.34	0.82	0.65
6 mm	14.21	2.26	0.52	0.33	0.82	0.64
9 mm	14.36	2.31	0.53	0.34	0.82	0.64
Experimental	14.71	2.63*	0.55	0.40	0.75	0.73

** from frontal configuration*

Table 6.3: Results of the parameters characterizing the Spray G injector internal flow for different discharge volumes under SG reference condition.

It is not possible to determine whether a larger discharge volume than the one used so far is necessary only considering the values shown in Table 6.3. The values are similar between the different cases and so the comparison with the experimental data is almost identical. For this reason and being the objective of this study to analyze the behavior of the near-field spray, the plume cone angle (Table 6.4) and plume direction (Table 6.5) are calculated to determine the the near-field spray patterns. Not only that, but in order to understand the behavior of the fluid as the discharge volume varies, a vertical cut-plane colored by the velocity variable for each of the cases studied is presented in Figure 6.4. It is important to mention that the angles have been calculated from the velocity variable considering that it is the one that can best capture the spray behavior.

Table 6.4 reports the results obtained for the plume cone angle which is defined as the jet opening measured from nozzle tip to some distance downstream of the flow (see Figure 5.24). There are no experimental data to compare these results with because it is a very complicated parameter to measure experimentally. However, their values are necessary to carry out computational studies of external flow (DDM) where it is mandatory to specify the angle at which the spray is injected. There is a clear trend that the opening angle of the spray becomes greater as it develops and the fuel oil mixes with the ambient gas. The results go from having an average spray opening angle of 9.76° for

the 3 mm discharge volume, to 12.41° for 6 mm and 18.44° for 9 mm. This trend can also be observed in Figure 6.4. Not only that, but in this image, in the case of 6 mm outlet plenum a small recirculation velocity can me observed in the center of the jets, expected as a response of the gas to the presence of the surrounding sprays. However, this velocity becomes quite noticeable in the case of 9 mm outlet plenum volume and may be the consequence of the sprays having this tendency to deflect inward, behavior which has not been appreciated experimentally.

Cone Angle [°]	**1**	**2**	**3**	**4**	**5**	**6**	**7**	**8**
3 mm	7.00	9.14	11.56	10.58	12.08	7.30	12.25	8.19
6 mm	11.75	14.16	12.40	12.36	10.31	14.46	10.93	12.92
9 mm	16.43	20.20	14.79	21.17	15.74	20.30	17.98	20.91

Table 6.4: Plume cone angle results in each of the orifices that make up the Spray G injector for different discharge volumes under SG reference condition.

Referring to the plume direction, Table 6.5, defined as the angle between the vertical injector axis and the spray axis (see Figure 5.24). This table shows the results of the spray direction for the different cases of study, which reflects a deviation with respect to the geometric axis (37°) of each spray. In addition, the experimental results are presented for the different orifices and therefore, the differences between computational and experimental data are calculated.

Cone Angle [°]	**1**	**2**	**3**	**4**	**5**	**6**	**7**	**8**
3 mm	29.13	31.54	29.18	31.00	26.89	29.29	26.54	29.81
6 mm	32.62	31.55	32.15	31.56	31.23	29.88	31.02	29.88
9 mm	29.34	29.73	29.58	30.14	28.03	27.43	27.09	29.34
Experimental	32.00	32.69	34.49	34.76	35.23	34.92	33.54	32.21

Error [%]	**1**	**2**	**3**	**4**	**5**	**6**	**7**	**8**
3 mm	8.96	3.49	15.41	10.80	23.67	16.11	20.85	7.44
6 mm	1.95	3.48	6.80	9.21	11.35	14.41	7.51	7.22
9 mm	8.30	9.05	14.24	13.29	20.46	21.43	19.21	8.90

Table 6.5: Plume direction results in each of the Spray G injector orifices and differences compared to the experimental data for different discharge volumes under SG reference condition.

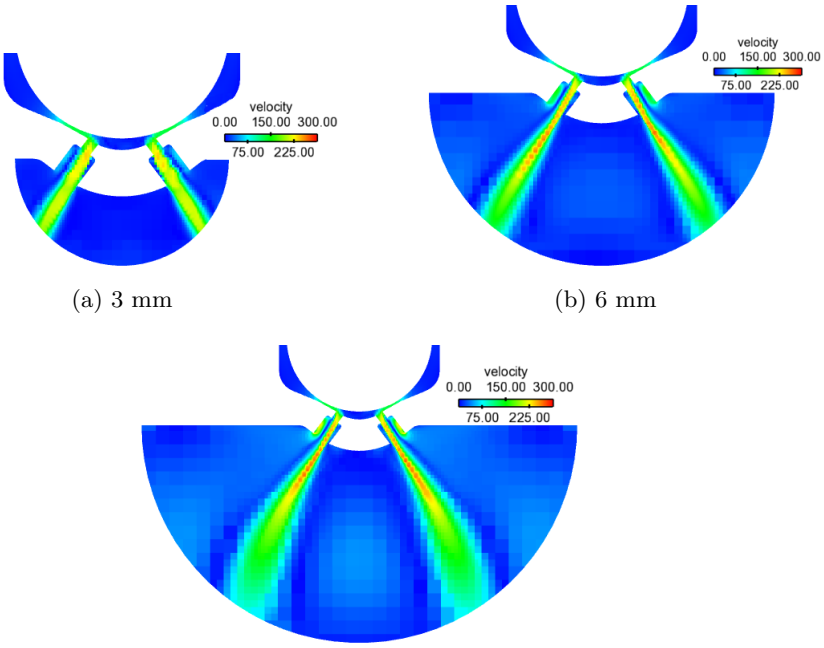

(a) 3 mm

(b) 6 mm

(c) 9 mm

Figure 6.4: Vertical cut-plane of the Spray G injector representing the velocity variable for different discharge volumes under SG reference condition.

These results show how the 3 mm discharge volume has larger deviations from the geometrical axis defined at 37°. The spray does not have enough space to develop because only the first few millimeters are taken into account, which are not enough to adequately capture the trend. On the other hand, the results corresponding to the 9 mm discharge volume reveal the aforementioned tendency for the sprays to move towards the center of the volume as they develop. Thus, the spray deflection moves away from that calculated experimentally. That said, it is the 6 mm discharge volume that best fits the experimental results.

The same internal flow characterization and the absence of experimental results to validate the spray cone angle make that, based on the plume direction spray data, allow to conclude that the optimum discharge volume to carry out the following internal flow studies is 6 mm.

6.2.5 RANS turbulence model selection

Once the optimal meshing strategy for this particular study and the size of the discharge volume needed to avoid the influence, if any, of the boundary conditions on the solution are determined, the next step is to analyze which turbulence model best captures the injection process or is more suitable for the study of these specific cases.

Five different turbulence sub-models have been selected based on the main k-ε and k-ω approaches: Standard k-ε, Realizable k-ε, RNG k-ε, Standard k-ω (1998) and SST k-ω. The internal flow of the Spray G injector has been characterized for each of the turbulence models employed and the results are presented in Table 6.6 along with the experimental values for the standard ECN SG condition.

As it can be observed, the existing differences between the results obtained either by comparing models or by taking experimental values as a reference, are minimal or negligible which means that all the tested turbulence models are able to reproduce the structures occurring inside the nozzle with the flow being mainly dominated by cavitation or flash boiling phenomena. The data closest to the experimental data are found in the RNG k-ε and Standard k-ε models with differences in mass flow of the order of 3%. The model that differs the most is the Realizable k-ε) with 4% in mass flow. If the momentum flux results are compared with the experimental data obtained from the frontal configuration, the differences vary from 12% to 15%.

Submerged	**ROI [mg/ms]**	**ROM [N]**	$\mathbf{C_d}$	$\mathbf{C_m}$	$\mathbf{C_a}$	$\mathbf{C_v}$
Standard k-ε	14.21	2.26	0.52	0.33	0.82	0.64
Realizable k-ε	14.15	2.25	0.53	0.34	0.82	0.64
RNG k-ε	14.37	2.30	0.54	0.35	0.83	0.65
Standard k-ω (1998)	14.27	2.23	0.53	0.34	0.84	0.63
SST k-ω	14.38	2.27	0.54	0.34	0.84	0.64
Experimental	14.71	2.63	0.55	0.40	0.75	0.73

Table 6.6: Results of the parameters characterizing the Spray G injector internal nozzle flow under SG reference condition for different turbulence models.

Although these data provide a lot of information about the injector, they do not allow to determine which turbulence model is the most suitable for this type of study. Therefore, only three turbulence models are selected to analyze, as in the previous study, the plume cone angle and plume direction and see if they provide any data to determine whether a turbulence model

stands out over another. The selection of the models is based on the idea of the development of the predictive methodology, so the four models chosen are those that are commonly found in most commercial software or that are easy to implement in in-house codes due to the extensive information published in the literature. Therefore, the turbulence models selected are: Standard k-ε, RNG k-ε, and SST k-ε.

Plume Direction [°]	**1**	**2**	**3**	**4**	**5**	**6**	**7**	**8**	**Mean**
Standard k-ε	32.62	31.55	32.15	31.56	31.23	29.88	31.02	29.88	31.24
RNG k-ε	33.49	34.09	32.69	34.29	32.64	33.16	32.18	34.49	33.38
SST k-ω	32.73	32.96	32.89	32.75	31.82	31.96	31.82	31.76	32.33
Experimental	32.00	32.69	34.49	34.76	35.23	34.92	33.54	32.21	33.73

Error [%]	**1**	**2**	**3**	**4**	**5**	**6**	**7**	**8**	**Mean**
Standard k-ε	1.95	3.48	6.80	9.21	11.35	14.41	7.51	7.22	7.38
RNG k-ε	4.66	4.31	5.21	1.34	7.35	5.02	4.04	7.09	1.04
SST k-ω	2.29	0.84	4.65	5.78	9.68	8.48	5.12	1.38	4.15

Table 6.7: Results of the plume direction calculation in each of the orifices and differences compared to the experimental data that make up the Spray G injector under SG reference condition for different turbulence models.

Table 6.7 collects the results corresponding to the plume direction of each of the orifices and compares them with the experimental results. In addition, the values of the computational and experimental differences are also presented. These data show variability in the results depending on the orifice analyzed, which may be mainly due to the geometrical characteristics of the injector (8 radially distributed orifices and 5 bumps). No clear trend of behavior is shown. Therefore, the mean plume direction of all the holes has been calculated and compared it with the experimental data, also presented in Table 6.7. Based on this result it could be said that RNG k-ε model is the closest to the experimental data and therefore suggested as the turbulence model to deal with this type of studies. Another factor to take into account for the choice of this model as the appropriate one for the study of internal flow in GDI injectors is based on the study carried out by Saha et al. [6] where they tested the Standard k-ε and RNG k-ε turbulence models on the same injector but with a larger discharge volume (9 mm). They found that for the Standard k-ε model the results had some influence of the pressure outlet boundary condition which was reduced by increasing the discharge volume as done in this work. However, the RNG k-ε model significantly reduced this influence and even led to its elimination. They determined, thanks to turbulent

viscosity distributions, dominant with respect to molecular viscosity and numerical viscosity in reasonably refined grids, that the differences were notable between models. The Standard k-ε model implied more turbulence-induced mixing, which can contribute to higher vapor dispersion while the RNG k-ε accounted for low, medium and high strain rates in the flow. Although the problem created by the Standard k-ε model can be eliminated by enlarging the download volume [7], this implies a larger number of cells and therefore higher computational cost, so the use of the RNG k-ε is advocated as a reasonable choice for these problems with in-nozzle and near-nozzle analyses.

Although the turbulence model for the following studies has already been established, it is interesting to present the results obtained from the plume cone angle to observe how the spray behaves with the different turbulence models. Due to the lack of experimental data, these results cannot be used as validation parameters.

Cone Angle [°]	**1**	**2**	**3**	**4**	**5**	**6**	**7**	**8**
Standard k-ε	11.75	14.16	12.40	12.36	10.31	14.46	10.93	12.92
RNG k-ε	5.24	13.95	6.14	11.54	7.83	10.07	8.20	14.72
SST k-ω	13.52	11.07	12.92	11.38	13,05	11.23	12.93	11.45

Table 6.8: Plume cone angle in each of the orifices that make up the Spray G injector under the SG reference condition for different turbulence model.

Table 6.8 summarizes the aforementioned data and shows a clear trend in the cone angle results (see orifice numbers in Figure 5.7a). Similar outcomes are seen for odd orifices but differ from those for even orifices. This may be mainly due, as mentioned above, to the specific distribution of the orifices in the Spray G injector nozzle or to the influence of the mesh orientation on the spray development [3]. Another noteworthy fact is how the RNG model obtains lower angles than the other turbulence models considered [6].

6.2.6 Influence of the phase change model parameters

Once the meshing strategy and the fundamental configuration of the models employed for the study of the in- and near- nozzle flow have been determined, it is important to dedicate a section to study the influence of the parameters of the phase change model on the behavior of the fluid during the injection process. As it is previously explained in Section 5.3.2, the main operating conditions set by the ECN and that will be studied in this Thesis involve phase change phenomena. This is mainly due to the fact that in the reference

condition, the so-called SG, which is considered non-flashing, evaporation is expected by definition of the chamber temperature. On the other hand, another important condition to be highlighted is the one known as SG2 or flash boiling condition where a sudden phase change is expected. For these reasons, it is of particular interest to consider the influence of the phase change model on the results.

The phase change model implemented is known as the HRM (see Section 5.2.3.2) whose constants have typically been optimized for cases where water flowing through a nozzle is under flashing conditions [8]. The present work includes fluids and operating conditions different from those used in the work of Downar-Zapolski et al. [8] where the aforementioned model constants were determined. Therefore, it is essential to analyze the sensitivity of the model in cases such as the present one where the fluid is not water and the phase change model plays an important role. This section presents a sensitivity analysis of the exponents of α and φ in Equation 5.58 under SG and SG2 operating conditions. The uncertainty ranges of these model constants are not documented in the literature, to the best of the author's knowledge. It is true that the calculation software sets the ranges between -5 and 0 for both indexes since positive values would not be correct. The HRM is a phenomenological model and changing the sign of the exponent would change the physical dependence of θ with respect to the two variables. In the case of the time constant (θ_0), no study has been carried out since the changes proposed in the literature are in the same order of magnitude ($\sim 10^{-7}$) and the differences in the results are not significant.

The exponent associated with the variable α, which means gas phase volume fraction, has been varied by $\pm$ 50%, being the default value -0.54, the maximum value -0.27 and the minimum value -0.81. The effect of varying this parameter is reflected in Figure 6.5 for SG and SG2 operating condition. As it can be observed in both figures, where the mass fraction of the fuel vapor species is presented, there is hardly any difference in the results shown when the exponent of α is varied. This is mainly because α is a variable that approaches a constant value as it travels through the nozzle. Along the fluid path the influence of α over the time-scale will be reduced so it will not be a dominant factor in the study. The value obtained by Downar-Zapolski et al. [8] will be maintained for the following analysis.

On the other hand, the exponent corresponding to the variable φ, which represents the non-dimensional pressure ratio, has been varied following the previous criterion of $\pm$ 50% of the reference value being the baseline value -1.74, the maximum value -0.88 and the minimum value -2.64. The φ param-

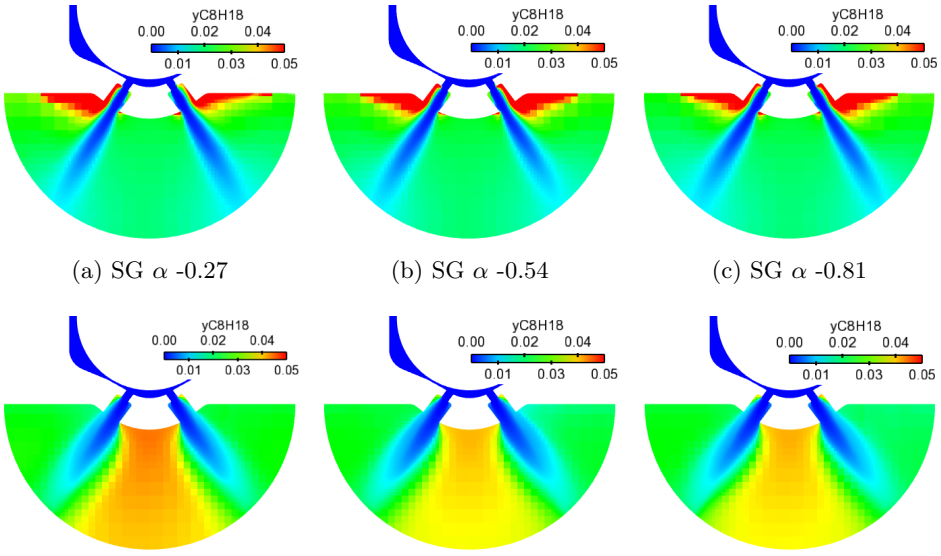

(a) SG α -0.27 (b) SG α -0.54 (c) SG α -0.81

(d) SG2 α -0.27 (e) SG2 α -0.54 (f) SG2 α -0.81

Figure 6.5: Vertical cut-planes of the Spray G injector that represent the fuel vapor mass fraction and reflect the variation of the variable as a function of the exponent associated with α under SG and SG2 condition.

eter is complex to describe physically since it is responsible for incorporating the effect of the physical properties of the fuel in the time-scale estimation. The increase in temperature for any fuel is associated with a corresponding rise in saturation pressure while the local pressure remains constant, resulting in an increase in the value of φ. As in the previous case, Figure 6.6 reports the results of the variation of the exponent associated to the variable φ for both SG and SG2 conditions. While in the SG condition the variation of the exponent has a certain impact on the results, it significantly affects the vapor formation in the SG2 condition and can even change the order of magnitude depending on the local pressure values. Consequently, in areas prone to evaporation, φ has high values and a considerable influence on vapor formation. This study is accompanied with data on the parameters that characterize the internal nozzle flow presented in Table 6.9. They have only been extracted for the SG condition but the conclusions can be extrapolated to SG2. The obtained values are similar among the cases studied, with differences up to 3%. Therefore, it could be said that the integral variables are not notably affected by the variation in the phase change model parameters. It is worth mentioning that the obtained results throughout this study are in agreement

with the literature referring to Saha et al. [6] who carried out a similar study corroborating the same statements presented in previous lines. To choose the appropriate exponent, -1.74 reference value is the closest to the experimental results. Furthermore, basing the choice on the flash boiling condition, as it is defined as mild-flash boiling and of the three tested exponents the -1.74 is the one showing moderate vapor generation, it seems to be the optimal choice for further studies.

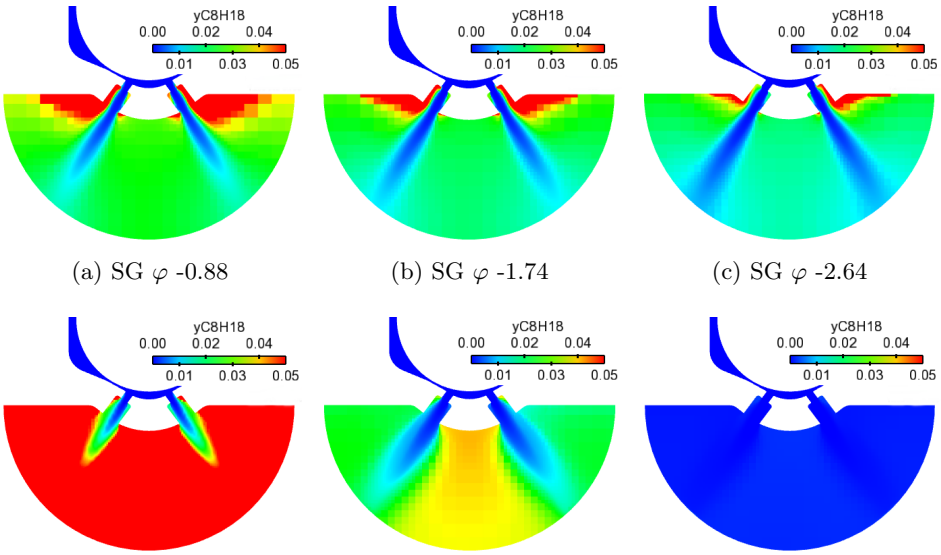

(a) SG φ -0.88 (b) SG φ -1.74 (c) SG φ -2.64

(d) SG2 φ -0.88 (e) SG2 φ -1.74 (f) SG2 φ -2.64

Figure 6.6: Vertical cut-planes of the Spray G injector that represent the fuel vapor mass fraction and reflect the variation of the variable as a function of the exponent associated with φ under SG and SG2 conditions.

Submerged	**ROI [mg/ms]**	**ROM [N]**	$\mathbf{C_d}$	$\mathbf{C_m}$	$\mathbf{C_a}$	$\mathbf{C_v}$
SG, $\varphi - 0.88$	14.21	2.29	0.53	0.35	0.81	0.66
SG, $\varphi - 1.74$	14.37	2.30	0.54	0.35	0.83	0.65
SG, $\varphi - 2.64$	13.91	2.28	0.52	0.35	0.78	0.67
Experimental	14.71	2.63	0.55	0.40	0.75	0.73

Table 6.9: Characterization of the Spray G injector internal nozzle flow under SG reference condition for different exponents associated with φ parameter.

6.3 Spray G Injector. StarCCM+ software. Steady State Analysis

The predictive methodology to be developed in this work is based on carrying out the entire study process from the identification of the optimal meshing strategy and the appropriate discharge volume to the methods and codes to process the results for a reference injector such as the ECN and then apply it to industrial application injectors as the PIU injector selected for this work.

Section 6.2 above details the studies of mesh independence, domain independence, turbulence model and an analysis of the influence of the phase change model constants on the behavior of the fluid during the injection process, all during the steady state, in other words, with the needle lifted to a fixed position. According to the aforementioned predictive methodology, the results obtained in the previous studies would lay the groundwork for reproducing similar studies in injectors with different characteristics or even different calculation software.

This section presents the validity of the predictive methodology when applied to the same injector (ECN Spray G) but using a different software such as StarCCM+.

6.3.1 Mesh sensitivity and validation

6.3.1.1 Hexahedral mesh

It is worth mentioning once again that the main difference between the software chosen for this study is that CONVERGE™ dynamically adapts the mesh throughout the simulation maximizing accuracy and computational efficiency while StarCCM+ v12.04 does not have this type of meshing strategies and discretizes the domain using a static mesh composed of hexahedral cells. Therefore, due to the existing differences between meshing strategies from one software to another, to transfer the optimal mesh from the previous case carried out with CONVERGE™ to the present study with StarCCM+ special attention has been paid once the spray is developed to the areas where the adaptive mesh reduced the cell size. Therefore, accepting a base cell size of 140 µm as the optimal cell size, and in order to accurately capture the velocity gradients in these regions, a refinement cone is defined for each spray of the same cell size as the reference strategy, 17.5 µm, and to ensure that all the fluid motion is captured for each spray, a larger cone with a cell size of 35 µm is defined to catch the flow gradients surrounding the jet.

Although the objective is to transfer the data from the studies already performed to those yet to be conducted, this section also presents a sensitivity analysis of the base cell size using the same values studied in Section 6.2.2 as reference. The meshing strategy is presented in Section 5.3.5.2 and as the base cell size varies, the associated refinements vary proportionally, i.e., for the 200 µm mesh the minimum size will be 25 µm while for the 100 µm base cell size the minimum size will be 12.5 µm. The results obtained from this mesh study are summarized in Table 6.10.

Case	**ROI [mg/ms]**	**Difference [%]**	**N° Cells**	**Exp. Difference [%]**
200 µm	17.38	0.99	2.8 million	18.15
140 µm	17.21	0.47	7.8 million	16.99
100 µm	17.13	-	18.5 million	16.45

Experimental ROI [mg/ms] = 14.71

Table 6.10: Obtained results from the mesh sensitivity study carried out for the Spray G geometry with StarCCM+ code under SG reference condition.

It is observed, similar to the previous study, that there is no variation between the results of mass flow rate, so any cell sizes tested can be valid for the next studies. It is true that, visually, the mesh with 200 µm of base cell had a greater amplitude of the spray cone angle, and it is the mesh of 140 µm of base size with values close to 11.5° of cone angle that most resembled the results previously discussed (Section 6.2). Therefore, based on prior experience, it is still affirmed that the most optimal mesh is the one with a base cell size of 140 µm.

On the other hand, comparing the mass flow rate results obtained with these grids with the experimental data, it is observed that the discrepancies between both are high, around 17% for the reference case. This gives an idea that the mesh is not fine enough to adequately capture the flow behavior inside the spray. Therefore, the next stage is to decrease the size in the area corresponding to the orifices and the needle seat where the velocity gradients are more pronounced in addition to adding a prism layer to treat the near wall areas more precisely as it was done in the case of CONVERGE™ . Before that, another important fact that was observed in these studies carried out with a discharge volume of 6 mm that initially seemed adequate. Once the jet was developed and the simulation progressed in time, the influence of the outlet boundary condition on the solution was greater and even caused the case to diverge. For this reason, it was determined that since the conditions applied to the outlet were not defined in the same way between codes, in this particular

case it was necessary to extend the discharge volume up to 9 mm [7], thus avoiding the aforementioned influence.

Reducing the minimum size in the orifice and needle seat zones to 8.75 µm and adding a prism layer to treat the wall increased the number of cells in the study to 10.15 million and reduced the mass flow rate value to 16.30 mg/ms, which means 5.6% of reduction. Even so, the difference with the experimental result is still high, around 11%. Therefore, observing the behavior of the spray inside the nozzle, it is proposed to carry out an independence of the number of prism layers in order to see how they influence the solution.

Case	**ROI [mg/ms]**	**Difference [%]**	**N° Cells**	**Exp. Difference [%]**
1 Prism Layer	16.30	5.81	10.15 million	10.8
2 Prism Layer	15.41	3.4	10.8 million	4.76
3 Prism Layer	14.89	-0.39	11.44 million	1.22
5 Prism Layer	14.94	-	12.73 million	1.56

Experimental ROI [mg/ms] = 14.71

Table 6.11: Obtained results from the prism layer sensitivity study carried out for the Spray G geometry with StarCCM+ code under SG reference condition.

The results obtained from the prism layer sensitivity study are presented in Table 6.11. It is observed that independence is achieved by setting up the mesh with at least 3 prism layers and the use of this strategy reduces the differences between computational and experimental results from ∼11% to ∼1.3%. The obtained results are within the considered experimental uncertainty and therefore, it can be said that the optimal meshing strategy to be used in the StarCCM+ code has been found. It is important to mention that although the mesh size inside the nozzle had to be reduced and extra prism layer added, it does not mean that the descriptive methodology fails, just that the change of software makes the needs to be somewhat different. Mainly the way that each code has to generate the mesh is very different so it was expected the need to make some changes in the strategy.

6.3.1.2 Polyhedral mesh

Taking advantage of one of the capabilities of StarCCM+ code, which is to generate polyhedral static meshes and knowing the benefits of the same (high accuracy with lower computational cost), this work includes the implementation of this meshing strategy to study the behavior of the flow during the injection process. In this case, as no previous studies based on this type of mesh are available, a new strategy suitable for this mesh model had to be

developed. To the best of the author's knowledge, there are not many papers published in the literature that base their meshing strategy to study the GDI process on polyhedral meshes. The study by Moulai et al. [9] has been one of the few using strategy. In the analysis, they used a mesh with minimum nozzle sizes between 20 to 30 µm, which, based on the experience of previous studies, may seem too large to obtain accurate results. This research does not have a validation of the model from experimental data so the accuracy of the results cannot be relied upon. However, it does give an idea of the sizes around which the appropriate mesh should be defined. That is why for the present case a base cell size of 60 µm was chosen, arriving at minimum cell sizes of 18 µm, similar to the hexahedral cases, inside the holes and at the needle seat.

As in previous cases, to find the optimum cell size for analyzing the internal nozzle flow, it is necessary to carry out a mesh sensitivity/independence study where, starting from the reference case mentioned, the base size has been reduced from 60 to 50 and 40 µm, generating cells with a minimum size of 15 and 12 µm, respectively. It is worth mentioning that given the need to apply prism layers to treat the walls more precisely, this strategy also includes 3 prism layers (see previous Section 6.3.1.1).

The results of this mesh independence are presented in Table 6.12, which shows no difference in the calculated mass flow rate between simulations and the error between the different meshes is below 1%, so it can be said that there is mesh independence. In this scenario, the most efficient meshing strategy is the one that has lower computational cost or, in other words, lower number of cells, since these two concepts are related to each other. This is the case of the polyhedral mesh with a base size of 60 µm which has a computational cost of 1232.92 CPU-h with respect to 5315.93 CPU-h corresponding to the mesh with a base cell size of 40 µm.

Case	**ROI [mg/ms]**	**Difference [%]**	**N° Cells**	**Exp. Difference [%]**
60 µm	15.04	0.57	5.8 million	2.24
50 µm	15.13	0.13	8.3 million	2.86
40 µm	15.15	-	14.43 million	2.99

Experimental ROI [mg/ms] = 14.71

Table 6.12: Obtained results from the polyhedral mesh sensitivity study for the Spray G geometry with StarCCM+ code under SG reference condition.

The final meshing strategy obtained from the presented analyses is illustrated in Figure 5.19b.

6.4 Spray G Injector. Steady State Validation

Once the studies presented in the previous Sections 6.2 and 6.3 have been carried out, where mainly the optimal meshing strategy for each software and type of mesh element have been established, as well as the necessary discharge volume in each code so that the stipulated boundary conditions do not affect the solution, the desired analyses can be performed.

This section includes the results obtained from studying the flow behavior in the in- and near- nozzle flow of the Spray G injector during the steady state operation of the injection process under different operating conditions, namely SG, SG2 and SG3. The objective is to validate the results obtained with experimental data from previous research performed in the same research institution [5, 10]. This work has been carried out under the two software employed in the current Thesis, CONVERGE™ and StarCCM+. Part of the results presented in this section are based on previously published papers that are part of this work [2].

6.4.1 Results and discussion

An important variable in characterizing the internal nozzle flow of an injector is the rate of injection (ROI) or injection rate. The Spray G injector has been extensively characterized by numerous institutions [10, 11]. Although the experimental data used to validate the computational results obtained from these studies are those presented in [12]. Vaquerizo, D. [12] carried out an extensive study of the Spray G injector in order to characterize it under different operating conditions. This research included the effects of injection pressure, ambient pressure, energizing time, fuel temperature, and even injection frequency. Not only that, but he also conducted near-field spray radiography experiments whose data provides the "area density" of the spray, therefore integrating along the radial and axial coordinates can provide the total mass in the domain. The value experimentally obtained for the standard Spray G condition from the classical steady state injection rate measurement technique is 14.71 g/s while the integrated mass result obtained by radiography is 14.95 g/s which implies a difference of only 1% and thus validates the experimental obtained results. It is important to clarify that this experimental data will be used to validate the computational results in the three operating conditions studied (SG, SG2 and SG3). This is due to the fact that it has been demonstrated that the variation of the discharge pressure does not influence the rate of injection results [5].

Figure 6.7a summarizes the results of mass flow rate (ROI) obtained from the three operating conditions and the different typologies of meshes previously studied: hexahedral with AMR from CONVERGE™ code, hexahedral steady mesh from StarCCM+ code and polyhedral steady mesh from StarCCM+ code. The analysis of these results will be divided into two parts, on the one hand the comparison between operating conditions and on the other hand the outcomes obtained between the different meshes and codes.

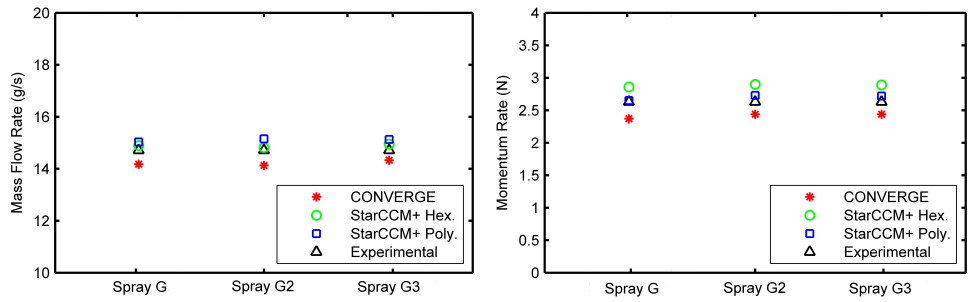

(a) ROI (b) ROM

Figure 6.7: Steady state result for mass flow rate and momentum flux for Spray G injector under three operation conditions and for three different typologies of mesh compared to experimental results.

Firstly, the analysis of the results between different operating conditions reveals that the mass flow rate obtained results are very similar with very small differences between them not exceeding 1% in any case. This again affirms the experimental theory explained above that the ROI is not affected by changes in discharge pressure. Taking as reference one of the two used codes in the analysis, CONVERGE™ , some vertical cut-planes have been presented in Figure 6.8 to show the difference in the behavior of the three conditions in order to understand, in a visual way, the concept of each one and to observe how they behave. It may be evidenced in the case of Spray G (Figure 6.8a) how the fuel evaporates mainly in the orifices due to the high temperature of the discharge chamber. There is also vapor fuel throughout the domain although in smaller quantity. As regards the SG2 condition, it can be observed that vapor fuel is also generated, although in smaller quantity, but creating a different distribution in the discharge volume where the largest amount of vapor fuel is located in the center of the chamber surrounded by the sprays. The reason for this is that the vapor generated is caused by the flash boiling phenomenon, an instantaneous evaporation which takes place

when the vapor saturation pressure is above the ambient pressure, which in the SG2 condition is quite low, below atmospheric pressure. Finally, the SG3 condition corresponds to an early injection where the discharge pressure is close to the atmospheric pressure and therefore does not meet the necessary requirements for vapor generation as the previous ones, in other words it does not have a high discharge temperature and vapor pressure, for iso-octane fuel, is below atmospheric pressure (so below discharge pressure).

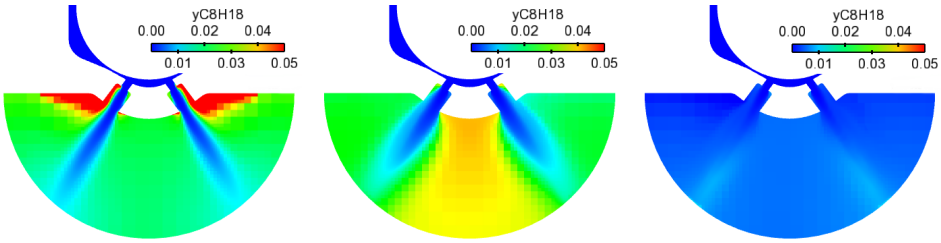

(a) SG (b) SG2 (c) SG3

Figure 6.8: Comparison of the vapor mass fraction generated as a function of the studied operating conditions for Spray G injector in CONVERGE™ .

On the other hand, referring to the results obtained for the different meshing strategies employed, it is observed that the CONVERGE™ adaptive mesh underpredicts the experimental results for the three operating conditions while the two meshing strategies performed with StarCCM+ remain above the experimental value. Taking only the SG condition as a reference and knowing that the conclusions provided can be extrapolated to the other two operating conditions studied, it is noted that for the CONVERGE™ software the relative difference with the experimental values is 3.33%, while for the hexahedral mesh designed with StarCCM+ it is slightly lower, 1.22%, and the polyhedral mesh obtained with the latter code presents a 2.18% discrepancy. It is important to mention that, only considering this variable, it cannot be affirmed that any mesh or code predicts better the behavior of the internal flow since all the values are within the experimental uncertainty. However, it can be stated that taking into account the number of cells of each of the meshes tested, the adaptive mesh generated with CONVERGE™ is the most optimal as it has a lower computational cost, followed by the polyhedral mesh and in last place the hexahedral mesh of StarCCM+. This study confirms one of the statements mentioned in previous lines that, under the use of the same computational code, the polyhedral mesh has a high accuracy using less than half the number of cells than the hexahedral mesh.

In addition to the rate of injection, the rate of momentum (ROM) is a valuable measure to further characterize the injector nozzle. ROM data is commonly coupled with ROI to provide even better insight into the fuel flow at the nozzle outlet. Unlike the injection rate (ROI) which has been studied by numerous institutions as mentioned above, the difficulty and uncertainty in the results surrounding momentum flux measurements has meant that, to the best of the author's knowledge, only CMT-Motores Térmicos, the institution under which this Thesis is being conducted, has carried out this type of measurement for GDI. The test rig used to perform the rate of momentum measurements on was designed and thoroughly described by Gimeno, J. [13] and the results obtained are published [10, 12].

Figure 6.7b presents the results of the rate of momentum (ROM) obtained from the different types of meshes under the three operating conditions studied. In addition, this same graph includes the experimental results obtained after using the frontal configuration and temporally averaging the steady state data of the injection. According to Payri et al. [14], the rate of momentum (ROM) of a fluid may be expressed by the injection rate multiplied by the fluid velocity. That being said, it makes sense that the momentum flux results follow the same trend as those obtained in the injection rate measurements. Hence, CONVERGE™ software provides lower momentum flux values in all conditions, while StarCCM+ is always above the experimental results. Taking again as reference the standard Spray G condition and extrapolating the results and trends to the other two operating conditions (SG2 and SG3), the difference between the CONVERGE™ result and the experimental data is 9.5% while the hexahedral mesh of StarCCM+ has a discrepancy of 8.5% and the polyhedral mesh fits perfectly to the experimental value with a difference of less than 1%. Once again, it can be stated that the polyhedral mesh approximates its results with a similar accuracy to the hexahedral mesh but with a smaller number of cells and, therefore, with a lower computational cost. The estimations computationally obtained fit quite well, taking into account the existing and already mentioned uncertainty, to those acquired experimentally. Therefore, both ROI and ROM results can be validated, being very useful to understand the behavior of the internal flow.

Table 6.13 reports the results in value form for ROI and ROM obtained from the different meshing strategies under the standard non-flashing Spray G condition. From these data, dimensionless flow coefficients (Section 3.4.3) are calculated to characterize the flow capacity and hydraulic behavior of the nozzle. The differences with the experimental data obtained in the measurement of the ROI and ROM variables are transmitted to the dimensionless coefficients of C_d and C_m since they are directly related and therefore, the area and

velocity coefficients will also be altered. In this case, and knowing the small discrepancies with the experimental data, the interesting point is to analyze the behavior of the flow through the GDI injectors from these coefficients. It may be stated that this type of nozzle, characteristic of GDI injectors, has low discharge coefficients. This phenomenon is the result of the fact that the liquid fuel does not fill the orifices, so that most of the cross section of the orifices is occupied by gas. The gas is not vapor fuel, but an ambient gas (N_2 in this case) that is drawn inward, creating strong recirculation zones inside the holes. Another fact to note is the values of the velocity and area coefficients. A high effective area leads to a reduction of the effective velocity. This theoretically means that the hexahedral mesh strategy from StarCCM+ is suitable to predict flow detachment occurring in the orifice.

Cases	**ROI [mg/ms]**	**ROM [N]**	**Cd**	**Cm**	**Ca**	**Cv**
CONVERGE™	14.22	2.37	0.53	0.36	0.78	0.67
Star CCM+ Hexa.	14.89	2.86	0.57	0.43	0.71	0.78
Star CCM+ Poly.	15.03	2.64	0.56	0.40	0.79	0.71
Experimental	14.71	2.63	0.55	0.40	0.75	0.73

Table 6.13: Comparison between experimental and computational Spray G nozzle flow coefficients in the steady state period for non-flashing SG condition.

Once the obtained results have been validated and the hydraulic behavior of the injector has been characterized from the dimensionless coefficients, it is interesting to observe the structure of the flow and the formation of the spray when it leaves the injector in the different meshing strategies employed. Therefore, Figure 6.9 provides the liquid volume fraction and velocity profile contours at the outlet of the small orifices of the injector as well as at the outlet of the counter-bore for the studied standard SG condition. The liquid volume fraction profile indicates that the inner orifices are completely filled with liquid, while the orifice outlets are partially filled with vapor and ambient gas. These images reveal the existence of a possible backflow of ambient gas (N_2) from the chamber into the counter-bore, a statement that is consistent with the explanation for the low discharge coefficient values. On the other hand, the velocity profile indicates that the gas in the StarCCM+ case is highly accelerated compared to the liquid while CONVERGE™ shows a lower gas velocity. There are several reasons which may explain the effect, highlighting the phenomenon of compressibility between phases, taking into account that in the case of StarCCM+ the species have been defined as incompressible,

and on the other hand the possible existence of differences in liquid to vapor formation in the counter-bore as well as the possible expansion of the gas. The image also proves the existence of hole-to-hole variations, as demonstrated by previous studies [3]. Although the mass flow rate and momentum flow rate are similar, with not overly significant deviations, in the three meshes show a clear difference in the shape of the spray. In the current studied geometry, reminding that it belongs to generation 1, the hole dimensions are the same for all eight holes and the minimum cell size is enough in each mesh to not be concerned about numerical diffusion. Therefore, the mesh type and its definition, the differences in the minimum cell size and the turbulence model are presumably one of the main reasons for this variation in spray shape.

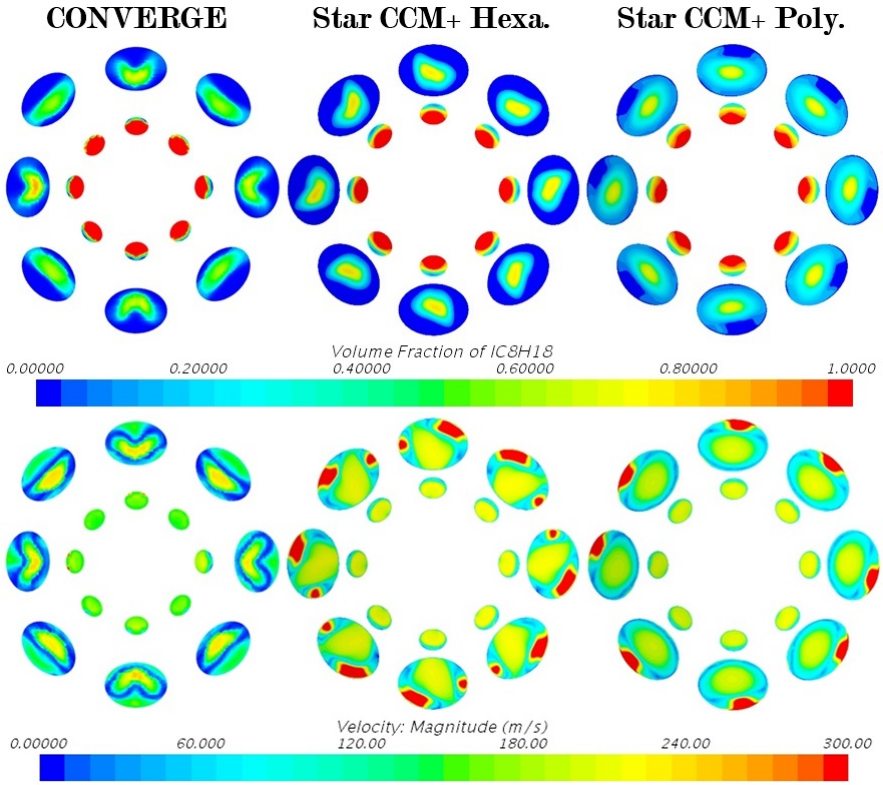

Figure 6.9: Cut-plane through hole and counter-bole exit of Spray G injector showing liquid volume fraction and velocity magnitude for SG condition at steady state for the different meshing strategies

It has been pointed out in previous lines, how important is, not only the characterization of the internal nozzle flow in terms of mass flow rate, mo-

mentum flux or even the hydraulic characterization from the dimensionless coefficients, but also the determination of the spray defining angles such as the spray plume cone angle or the plume direction. The analysis of these variables is increasingly important due to the shortage of results published in the literature because of the great difficulty involved in obtaining these values experimentally. This lack of experimental data has meant that much of the research known to date has been performed starting from an *ad hoc* value of spray angle and calibrating it until the results chosen for validation matched the experimental validation data [15]. This is an imprecise way of performing these analyses resulting in incorrect approximations since the spray angle has a strong influence in the penetration results. A wider angle usually implies lower liquid plume penetrations and narrower angle should lead to higher penetrations. In addition, another factor to be taken into account, as previously observed and Baldwin et al. [16] demonstrated in their work, the geometry influences the development of the jet. For this reason, it is important that the angle calculation technique accurately estimates the corresponding angles for each spray in order to observe differences in behavior, if any.

The calculation of the angles has been carried out according to the methodology explained in Section 5.4.1.2 for the three different meshing strategies. However, it should be mentioned that after analyzing experimental contours and visualizing results corresponding to the spray, it was determined that the velocity variable, although it adequately predicted the spray deviation with respect to the geometric axis of the orifice, underpredicted the spray cone angle values. For this reason, in addition to the need to unify the variables used for the calculation of spray characteristic data, the mass fraction of liquid is adopted instead. Figure 6.10 reports the results obtained corresponding to the calculation of the spray cone angle and plume direction for the reference condition Spray G. In the case of the plume direction, the results have been displayed together with the experimental data which were presented in the ECN 5 workshop by Matusik, K. but not reported in any subsequent article.

Concerning the calculation of the spray cone angle, Figure 6.10a, there is a clear difference between codes. The values obtained with the CONVERGE™ code are lower in all holes than the values calculated for the StarCCM+ meshes. The average value of spray cone angle for CONVERGE™ simulations is approximately 20° whereas for the hexahedral and polyhedral meshes in StarCCM+ is around 23°. Factors that could influence the disparity of the results are the mesh structure and the turbulence model that generates greater dispersion in the StarCCM+ cases. These data again confirm that the polyhedral mesh provides similar results in terms of accuracy to those obtained with the hexahedral mesh of the same code but at a much lower

computational cost. Although these results cannot be validated with experimental data due to a lack of such data as a consequence of the difficulties and the high uncertainty in the measurements, Saha et al. [17] gave an estimation of the overall cone angle from an Eulerian simulation. In this particular case, and unlike the present work, the authors measured the angle of the cone in two different directions to capture the ellipsoidal shape of the jets. The results obtained were 21° in the vertical cut-plane and 29° perpendicular to this vertical cut-plane. Based on these estimations, the overall cone angle was assumed to be 25°. The measurements performed in this analysis correspond to those made in the vertical cut-plane, so it may be stated that the two approaches are similar and the technique applied in the calculation as well as the selected variable are suitable for this type of analysis.

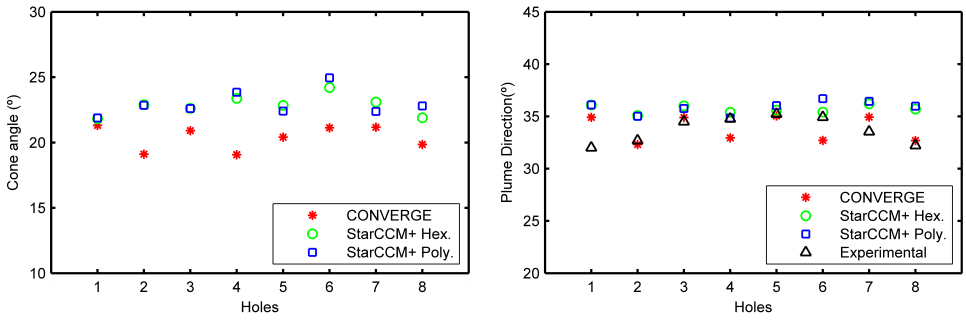

(a) Cone Angle (b) Plume Direction

Figure 6.10: Spray cone angle and plume direction approximation with liquid mass fraction for Spray G injector under the reference SG condition for three different types of meshes.

On the other hand, concerning the study of the spray plume direction, some experimental data are available, although in a very limited way. Manin et al. [18] made efforts to perform measurements to characterize the liquid phase in Spray G including the calculation of the spray direction. For this estimation, the authors calculated the complete spray cone which was estimated by defining the outer edge of the liquid spray boundary, and obtained as the mean value of the full liquid spray cone angle 68°. Therefore, this being the total value of the spray opening, half of it would correspond to the individual direction of each spray, 34°. On the other hand, as mentioned above, Matusik, K. individually calculated the time evolution of the direction of each jet for three different Spray G injectors (AV67-012, AV67-016 and AV67-021). For comparison, the measurements made for the AV67-021 injector have been

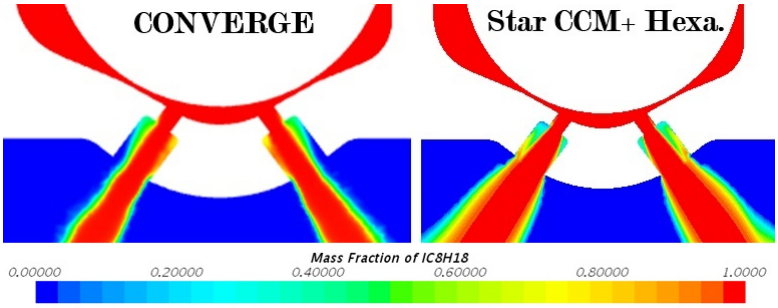

Figure 6.11: Vertical cut-plane representing the liquid mass fraction in two different software to observe the difference between the spray cone angle and the plume direction for Spray G injector under SG reference condition.

chosen, and as the data are time-dependent, the values corresponding to the injection time of 0.6 ms, which represents a steady state of the injection process, have been selected. The experimental data together with those obtained computationally are reflected in Figure 6.10b. It is observed that the values do not follow any marked trend either experimentally or computationally. For the case of CONVERGE™ , it is true that a certain pattern could be defined that even orifices tend to predict a larger spray deflection and therefore have a smaller angle value, which means that they deviate inwards. This is not to say that this will occur as a stipulated pattern for all conditions, but rather is related to the differences in spray shape shown in Figure 6.9. The computational results obtained with CONVERGE™ seem to be closer to the experimental one with an average value of approximately 34° and have a lower value than the results obtained with StarCCM+ with an average value of 36° in the polyhedral mesh and 35.5° in the hexahedral mesh. The difference between codes is mainly due to the phase change that takes place in each orifice. Figure 6.11 illustrates the vertical cut-planes corresponding to CONVERGE™ software on the left and StarCCM+ on the right. From them, it is possible to extract the justification for this difference in the deviation of the jets. The orifices referred to the CONVERGE™ simulation have part of the counter-bore filled with gas, which is not vapor fuel but ambient gas (N_2 in these cases) that is drawn into the interior, creating strong recirculation zones inside the orifices. This phenomenon causes the spray to deviate inwards from the geometrical axis resulting in narrower plume direction angles. On the other hand, this effect does not occur in the case of the StarCCM+ code orifices, where practically the entire counter-bore is filled with liquid phase, so there is not so pronounced deviation of the plume direction of the jet from the geometrical

drill angle. It is worthwhile to reference that the predicted trends from both software, despite the existing differences, estimate the liquid plume direction close to the experimental values and contribute to the GDI spray behavior understanding.

As part of this framework, another study of interest and of great added value to the scientific community is the analysis of how the spray cone angle behaves when the operating conditions change from non-flashing (SG) to flashing (SG2). Taking into account that there are almost negligible differences between spray cone angle and plume direction results in both software, CONVERGE™ will be used for the following analysis as it was done in the operating conditions comparison simply for consistency and illustrative purposes. Figure 6.12 depicts the results obtained by processing the images of the liquid mass fraction in the SG and SG2 conditions. In most of the holes, the spray cone angle calculated for the SG2 condition is slightly higher than for the SG condition. This is a consequence of the decreased ambient density and low ambient pressure, which causes the spray to transform with a significantly larger spray plume width and reduced penetration of both liquid and vapor components [19]. In addition, another reason why the spray cone angle of the flashing condition is higher is due to the fact that the fuel vapor generated by the downstream conditions cause the injector orifices including the counter-bore to be filled with this species as opposed to the non-flashing condition where the counter-bore is partially occupied by the non-condensable gas and the recirculation phenomenon associated to this effect causes the spray angle to be narrower as mentioned above.

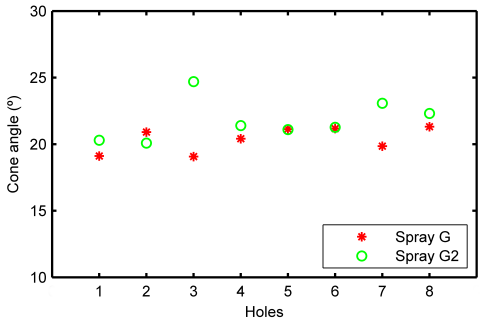

Figure 6.12: Comparison between spray cone angle approximation employing liquid mass fraction under flashing and non-flashing conditions for Spray G injector.

6.5 PIU Injector. Steady State Analysis and Validation

This section includes the studies corresponding to the PIU injector for industrial application under steady state operating conditions which implies that

the needle is in a fixed lifted position of 50 µm. This particular represents the accuracy and validation of the developed predictive methodology in terms of meshing strategy. This means that for the study of this singular injector, which differs geometrically from the reference injector of the ECN, the same meshing strategy has been employed including the base size, minimum cell sizes and specific mesh structure used that was developed for the study of the previous injector. In addition, this transfer of information is checked in terms of performance.

After determining the accuracy and validity of the above mentioned predictive methodology in terms of meshing strategy, this section also includes other studies of interest such as the influence of the needle position on the parameters characterizing the internal flow behavior (ROI and ROM) or the justification of using only half geometry to save computational resources in those cases where the injector has symmetrical geometric characteristics as in the PIU injector scenario. In addition, a scalability and efficiency study has been carried out to determine the most efficient use of these computational resources. And finally, an analysis of the flow behavior in the in- and near-nozzle region is presented for different operating conditions where both the injection pressure and the discharge pressures downstream of the injector are varied.

It is important to mention and make clear that unlike the reference injector Spray G which has been analyzed using two different software as CONVERGE™ and StarCCM+, for the case of the PIU industrial production injector only StarCCM+ has been used. The main reason is that this injector is associated to a private project with an international automotive company and the requirements of this project were to study it under the mentioned computational code. This fact is of no great importance, as both commercial codes have been demonstrated to be valid and produce similar results.

6.5.1 Mesh strategy and validation

The process of determining the optimal meshing strategy for the PIU injector is much more compact than the previous works presented thanks to the use of the developed predictive methodology. In terms of meshing approach, it encompasses the possibility of using the same meshing strategies (Section 6.3.1.1 and 6.3.1.2), including not only the mesh structure but also the base and minimum cell sizes, in injectors of different geometrical features. This section verifies the success achieved.

The study of the PIU injector is not only based on the application of the most optimal meshing strategy as considered the polyhedral mesh, but also

includes results obtained by applying the strategy followed for the mesh with hexahedral elements. Therefore, it can be said that the methodology related to the meshing strategy is valid regardless of the mesh element type used. A third mesh structure has been added to the study (see Figure 5.20), which aims to encompass all the sprays so that nothing of them is left uncaptured. The new strategy has been specifically designed for this nozzle due to the arrangement of the sprays. The injector is designed to be placed on the side of the combustion chamber, so the jets do not hit the valves or the cylinder wall. Thus, the orifices are all arranged in the same orientation, which can lead to certain significant interactions between jets. This arrangement makes it easier to capture them all together from an overall refining cone.

This section includes the validation of the predictive methodology in terms of meshing strategy by applying the two optimal meshes (polyhedral (Figure 5.20c) and hexahedral (Figure 5.20a)) presented above for the Spray G injector, in the study of the flow behavior during the injection process for the PIU injector. In addition, due to the geometrical characteristics of this specific injector, a third meshing strategy has been added to the study (Figure 5.20b). For more information about the grids, please refer to Section 5.3.5.2.

Cases	**Base & Min. Cell Size [µm]**	**N° Cells**	**ROI [mg/ms]**	**Exp. Difference [%]**
Hexahedral	140 & 8.75	7.18 mill.	17.03	1.67
Hexa. Global Cone	140 & 8.75	15.21 mill.	17.05	1.79
Polyhedral	60 & 18	4.74 mill.	16.99	1.43

Experimental ROI [mg/ms] = 16.75 ± 0.2

Table 6.14: Comparison between meshing strategies implemented for the study of internal flow behavior in the PIU injector.

Table 6.14 gathers the ROI results obtained for the three different typologies of meshes considered in this study. It is observed how all of them obtain ROI data very close to each other and to the experimental data. These results affirm the feasibility of transferring meshing strategies between injectors with different geometrical characteristics thus reducing the computational cost that implies to carry out a mesh and domain independence. Regarding the latter, the discharge volume used in all cases is 9 mm, taken as a reference also from the preliminary study carried out for the ECN injector. Therefore, the basis of the predictive methodology in relation to the meshing strategy is established.

Although all three strategies give results very close to the experimental data, the computational cost of the simulations must be taken into account. Once again, the polyhedral mesh is shown to be of high accuracy and quality with a much lower computational cost compared to the other meshing strate-

gies. While the polyhedral mesh has a computational cost of 1089.25 CPU-h, the hexahedral mesh with global cone refinement offers a computational cost of 5800.72 CPU-h, in other words, the latter strategy is almost 6 times more expensive computationally speaking than the polyhedral mesh. For this reason essentially, the polyhedral mesh will be chosen for the following studies.

6.5.2 Scalability study

This section includes a scalability study carried out mainly with the objective of determining the most efficient use of the computational resources since the detailed analysis of the PIU injector encompasses a large test matrix necessary to conduct the coupling study (Section 8.3) as well as all the tests that had to be carried out to obtain the correct results. The scaling study was performed for the PIU injector with an 9 mm outlet plenum under a specific test point defined by $P_{inj} = 20MPa$, $P_{back} = 0.6MPa$, $T_{inj} = 363K$ and $T_{back} = 303K$. The polyhedral mesh strategy is selected for this study with a base size of 60 µm and a 18 µm minimum grid size at 50 µm of peak needle lift. This study has been carried out taking into account the complete geometry so it has 1.83 million cells. The cluster used for this study is built with Intel Xeon E5-2630 v3 CPU, with 8 cores/CPU, 2 CPU/node and 2 GB of RAM/CPU. Cases were run until the simulation reached a stabilized value (1.5 ms) representing the steady state on 1, 2, 4, 8, 16, 32 and 64 processors. The speedup of the code ($S(n) = T_s(n = 1)/T(n)$) with the increase in the number of processors has been presented along with the ideal speedup (Figure 6.13a). An ideal speedup means that the speedup is equal to the number of times the processors have been increased, relative to the baseline case. It should be noted that in practical applications, it is not possible to achieve an ideal speedup. The ratio of speedup to the number of times processors have been incremented is called "scaling efficiency" defined as $E(n) = S(n)/n$ (Figure 6.13b). In the high performance computing (HPC) community, a scaling efficiency above 70% is usually considered an indication of good code scalability.

Figure 6.13 presents the results obtained from the aforementioned study showing both scalability (Figure 6.13a) and efficiency (Figure 6.13b). This work demonstrates that for the present investigation and the resources used, increasing the number of CPUs used for the simulation rapidly decreases the simulation efficiency to values slightly above 50%. However, the total simulation time is reduced. These numbers are below what experts consider to be good scalability but still not too far from optimal. The obtained results have allowed to optimize the computational resources in the simulations of the whole text matrix.

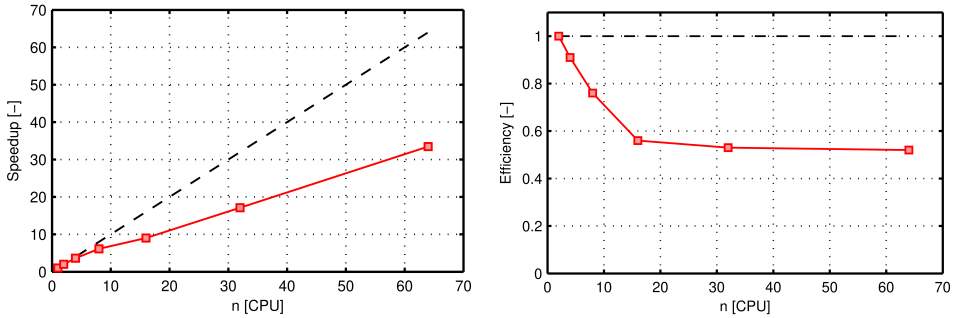

(a) Speedup (b) Efficiency

Figure 6.13: Results of the scalability study performed with the PIU at steady state conditions for a specific test point of P_{inj} = 20 MPa, P_{back} = 0.6 MPa, T_{fuel} = 363 K and T_{back} = 303 K.

6.5.3 Symmetry simulation assessment

After analyzing the meshing strategies in depth in Section 6.5.1, it was observed that the polyhedral mesh generated many more cells than expected (always comparing with the reference cases carried out for the ECN injector) at the exit of the holes. The definition of the mesh in the StarCCM+ software is associated with parameters such as surface growth rate, among others, which define a more accurate mesh (higher number of cells) depending on the complexity of the geometry. A thorough investigation led to determine that the high precision computational domain obtained from x-ray techniques had been extended to areas outside the injector which do not need that high level of detail and only provided an additional computational cost to the case by adding extra cells (see Figure 6.14a). For this reason, a smoothing process was carried out on the area that was called external nozzle and corresponds to the surface that directly connects with the holes at the exit of the nozzle (see Figure 6.14b). This procedure led to reduce the number of mesh elements from 4.74 million to 1.83 million, thus decreasing its computational cost by three times. A third meshing strategy (see Figure 6.14c) was incorporated into this study that included a near-field refinement of the orifice exit to ensure that the smooth procedure was sufficiently accurate and captured the flow behavior at the outlet of the injector accordingly.

Before moving on to the Table 6.15 showing the results obtained from this study, it is important to mention the employed technique to measure the rate of momentum.

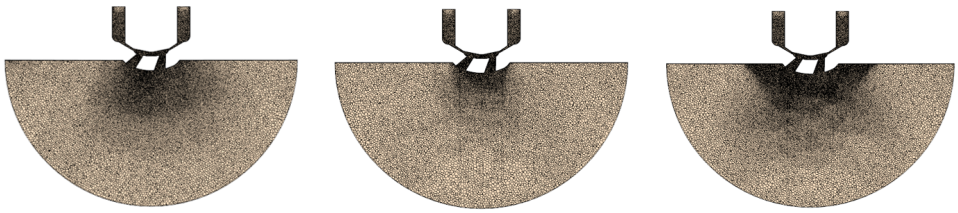

(a) Polyhedral (b) Poly. + Smooth (c) Poly. + Refinement

Figure 6.14: Vertical cut-planes representing the different polyhedral meshing strategy tested for the PIU injector in StarCCM+ code.

Following the data acquisition strategy presented in Section 5.4.1.1, the momentum flux will be measured by placing a plane at a given distance from the tip of the injector with an inclination equal to that used in the experimental measurements. This inclination needs to be placed perpendicular to the injector bend angle of 26° which is determined in such a way that the individual impingement angles of each spray plume are minimized. It is important to mention that due to the limitation of the discharge volume the computational target is located 3 mm away from the tip injector while experimentally it is located at 4.5 mm. Figure 6.15 accompanying the text explains this new measurement concept graphically and helps to understand it.

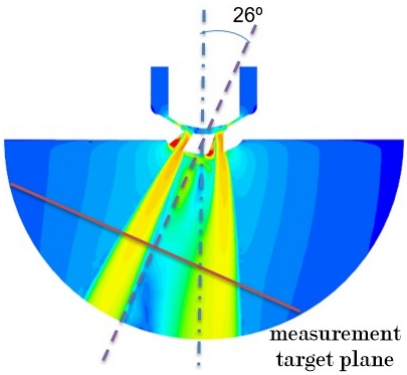

Figure 6.15: Strategy for measuring momentum flux for the PIU injector.

Table 6.15 provides the characterization of the internal flow from the three meshing strategies mentioned above. All of them give mass flow rate results very close to the experimental data and offer momentum flux values with differences of approximately 6 to 7.5%. Taking into account the experimental uncertainty behind the momentum flux measurements, the discrepancies associated with these values can be considered to be in the optimal range. Again, since the characterization of the internal nozzle flow is so similar in all three cases, the computational cost associated with each strategy comes into play in determining the most optimal mesh. The method of smoothing and generating simpler surfaces with fewer elements reduces the number of mesh elements by 2.5 times and thus the computational cost by the same factor. For these

reasons, it is the candidate meshing strategy to be chosen as optimal and used in the following studies.

Cases	ROI [mg/ms]	Exp. Difference [%]	ROM [N]	Exp. Difference [%]	CPU-h
Polyhedral	16.99	1.43	2.68	7.2	2551.9
Poly. + Smooth	16.91	0.96	2.65	6.0	845.34
Poly. + Refinement	16.88	0.78	2.69	7.6	1634.8
Experimental	16.75 ± 0.2	–	2.5 ± 0.1	–	

Table 6.15: Comparison between different meshing strategies having as main reference the polyhedral base mesh for the PIU injector at reference operating condition.

One of the final objectives of all these studies is to obtain a configuration of both computational domain and meshing strategy as optimal as possible in terms of accuracy and computational cost that allows to characterize the in- and near-nozzle region of the injector under different operating conditions both with needle in a fixed position or including the transient behavior of the injection from the vertical and lateral movement of the needle. Therefore, in parallel to the determination of the most optimal meshing strategy for this particular case, it is proposed to optimize the computational domain by taking advantage of the symmetry of the PIU injector. Figure 5.12 illustrates the mentioned symmetry existing in the plane that cuts the orifices 1 and 4. It is important to take into account that there is a small deviation detected from the x-ray technique of 4 µm with respect to the geometrical center of the injector which can infer in the obtained results. If so, it is necessary to analyze if the deviation that this causes is acceptable or, on the contrary, it is necessary to consider the geometry in its totality. For this purpose, the geometry has been divided in two using the symmetry plane as a reference and these two new computational domains generated separately have been analyzed. The obtained results have been compared with the acquired data using the complete computational domain. The meshing strategy adopted for this test, since it has been carried out in parallel to the previous study, corresponds to the initial one shown in Figure 6.14a. The obtained results are presented in Table 6.16.

The use of a symmetry condition does not modify the flow behavior during the injection process since the characterization of the internal flow offers very close values between the different computational domains tested. It is true that one of the two halves studied, in this case the so-called “right half geometry”, shows somewhat higher values than the complementary half. Quantifying these differences, they are approximately around 1% in the case of mass flow

Cases	ROI [mg/ms]	Exp. Difference [%]	ROM [N]	Exp. Difference [%]	CPU-h
Complete Geom.	16.99	1.43	2.68	6.0	1528.8
Left Half Geom.	17.16	2.45	2.64	5.6	779.4
Right Half Geom.	17.27	3.10	2.72	8.8	840.6
Experimental	16.75 ± 0.2	–	2.5 ± 0.1	–	

Table 6.16: Validation at reference operating conditions of the application of one half of the geometry due to the PIU injector symmetry characteristic.

rate and 3% in the case of momentum rate. This is mainly due to those 4 µm of deviation with respect to the geometrical axis of the injector mentioned above.

Not only is the flow characterization during the injection process important to determine the feasibility of a strategy, but observing how the flow behaves downstream of the injector. Validating the use of the symmetry condition or in other words using only half of the computational domain to study the injection process is something that requires precision in the outcomes. Therefore, the judgment is not only based on the parameters that characterize the nozzle flow but also the contours generated along the whole computational domain have been observed to compare them between the different cases. Figure 6.16 represents the streamlines for both cases and cut-planes at the exit of the orifices colored by the velocity variable. It is possible to observe how both the contours and the streamlines show a similar behavior in either case. To highlight a small difference, mainly due to the symmetrical condition, orifice 1 has a non-condensable air entrance that is not centered but has a tendency to deviate towards one side, a phenomenon that when applying the symmetry condition is not captured and generates a small increase in the gas velocity in that area, which may also explain the higher mass flow rate shown in Table 6.16. These results together with the flow characterization discussed in the previous paragraphs determine that the implementation of the symmetry condition is more than acceptable in terms of accuracy with a recognized decrease in the computational cost of the simulation. For the following studies and since both analyzed halves present similar results, the so-called “left half geometry” one will be selected.

As it has been previously mentioned, in order to combine efforts and since the differences between cases are not significant and always within the margin established as experimental uncertainty, the two studies presented above were carried out simultaneously. Thus, the union of both optimizations, in other words, of the meshing strategy including the smooth process of the external surface to the injector in addition to the feasibility of adopting the symmetry

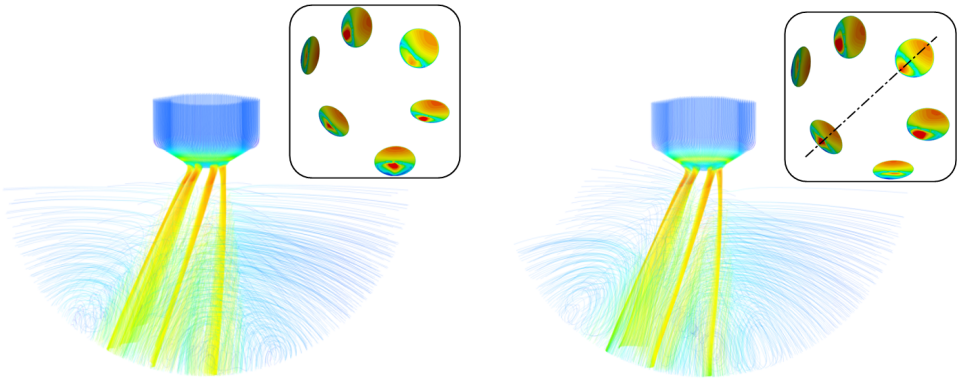

(a) Full Geometry (b) Half Geometry

Figure 6.16: Velocity streamlines and orifices cut-planes colored by velocity variable to compare the flow behavior downstream of the PIU injector between the full computational domain and half of it.

condition to save computational cost, give rise to the results presented in Table 6.17 where the characterization of the injector is reflected not only in terms of mass flow and momentum rate but also hydraulically from its dimensionless coefficients. The obtained results from the above optimizations yield a difference of barely 1% in the rate of injection and a discrepancy of 4% in the momentum flux. The dimensionless flow coefficients, being related to these two variables, behave in accordance with them, presenting minimal differences between computational and experimental results.

Cases	**ROI [mg/ms]**	**ROM [N]**	$\mathbf{C_d}$	$\mathbf{C_m}$	$\mathbf{C_a}$	$\mathbf{C_v}$
PIU Injector	16.92	2.65	0.60	0.38	0.95	0.63
Experimental	16.75 $\pm$ 0.2	2.5 $\pm$ 0.1	0.60	0.36	0.98	0.60

Table 6.17: Comparison between experimental and computational nozzle flow coefficients for PIU injector under reference operating conditions.

The results presented in this section not only signify a correct modeling of the in- and near-nozzle flow behavior but also, and perhaps more importantly, the effectiveness and validity of the predictive methodology in terms of meshing strategy and computational domain. Although certain modifications have been made in both cases, these are proper to the peculiarity of this in-

jector and to improve the efficiency of the study of the same, but without the mentioned improvements, the developed model is just as accurate.

6.5.4 Needle lift dependence

The injection process begins when the needle inside the injector nozzle starts to rise, which means that the movement of the needle plays an important role in terms of internal flow characteristics and spray breakup near the nozzle. However, the needle is surrounded by a stainless steel nozzle and operates under highly transient and fuel pressure conditions. Thus, conventional optical techniques are unable to capture the needle motion and therefore make it difficult to study the influence of the needle lift. As a result, the effect of needle movement on in- and near- nozzle flow as well as on spray dynamics has not yet been well revealed.

During the fuel injection process, the flow is mainly limited by the smallest flow area inside the injector. There are two possible options for this restriction: at the orifices and at the needle seat (also called valve area). In the initial and final stages, since the needle is only slightly raised, the valve area is the restrictive zone. In the fully open stage, although the needle seat area still constrains the flow path to some extent, it is less of a determining factor than in the initial stages. Ideally, one would like to have an injector where the flow rate is only affected by the nozzle size and not by the needle lift. However, it is not always possible to increase the elevation to ensure that there is no throttling at the seat without causing other problems. As the needle lift increases so does the opening time and closing time, which can affect the minimum operating voltages required for dynamic flow. All these factors must be balanced in the design of an injector [20]. The objective of this study is to provide a better understanding of how the flow behaves with different needle lifts, the trends and influence of lift on ROI and ROM.

The study encompasses six different needle lifts which are in the range of 40-90 µm selected so as to study needle lifts above and below those required by the PIU injector in its operating range. For all cases the mass flow rate and momentum flux have been obtained and compared in the experimental results taking into account that these are at a fixed lift. Results obtained from this analysis are presented as values in Table 6.18. The flow rate increases sharply when the needle starts to open the valve. The metering process is primarily controlled by the valve area at this stage. Thus, when the needle lift takes the value of 40 µm, the mass flow obtained is not noticeably different from the reference case of 50 µm or from the experiments. As the needle takes higher values of lift, the flow path is greater and with it the mass flow rate

values as well as the momentum flux increase. This growth trend as the needle opening is larger becomes asymptotic, at certain lifts the flow rate will remain constant. In this particular injector the beginning of this asymptotic tendency is observed, but the mass flow rate values have not stabilized with the maximum needle lift studied. This means that throughout the range, the position of the needle is decisive for the ROI, which can have serious implications for engine operation.

Cases (N.L.)	**ROI [mg/ms]**	**Exp. Difference [%]**	**ROM [N]**	**Exp. Difference [%]**	**CPU-h**
40 µm	16.22	−3.2	2.44	−2.8	797.3
50 µm	16.99	1.4	2.68	6.8	842.1
60 µm	17.4	3.9	2.83	12.7	883.6
70 µm	17.72	5.8	2.9	15.5	810.8
80 µm	18.03	7.6	2.97	18.3	830.5
90 µm	18.19	8.6	3.2	20.3	862.9
Experimental	16.75 ± 0.2	–	2.5 ± 0.1	–	

Table 6.18: Study of the influence of the needle lift on the internal flow characterization parameters of the PIU injector at reference operating conditions.

Together with this explanation, it is interesting to observe the behavior of the pressure inside the nozzle in the different cases studied, a variable that is presented in Figure 6.17. The picture illustrates how the pressure gradients at the needle seat are much larger as the lower the needle lift is. At a high needle lift of around 70 or 80 µm, the lift is large enough to produce a negligible influence on the flow field. The injector with higher needle elevation produces higher flow velocity due to lower flow resistance and higher discharge coefficient. This also explains the increase in mass flow rate values. In this particular case, the discharge coefficient is increased by up to 12% when comparing the 40 µm case with the 90 µm case which may explain another reason why the discharge coefficient of this type of injectors has such a low value.

6.5.5 Steady state results for PIU injector

Based on the optimal configuration achieved through the studies presented in the previous sections for the PIU injector, the following lines present the characterization of the internal nozzle flow not only in terms of mass flow rate and momentum flux but also the hydraulic characteristics obtained from the dimensionless coefficients of discharge, area and velocity , for a wide range of operating conditions including different injection pressures and various discharge pressures. The results obtained computationally for all the operating conditions analyzed have been compared and validated with experimental data

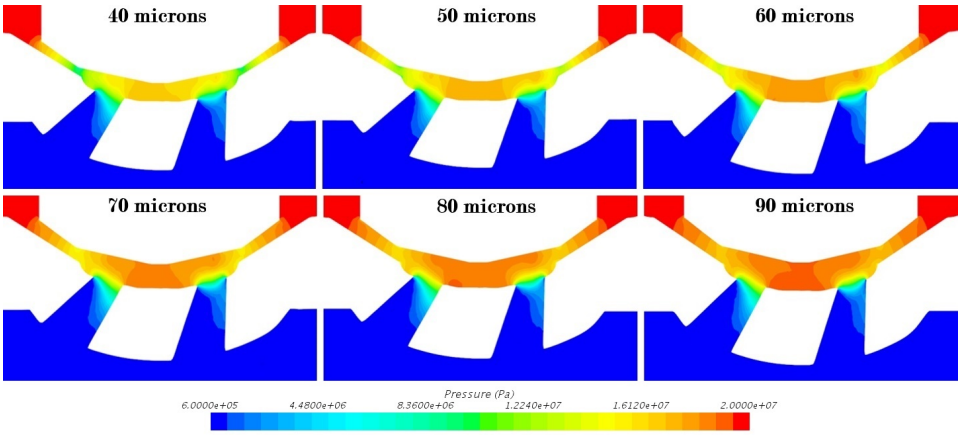

Figure 6.17: Vertical cut-planes of PIU injector showing pressure values for different needle lift positions reference operating conditions.

provided by the same department where the present Thesis is being carried out [21]. Regarding these experimental data, it is important to mention that the data have been evaluated after 50 repetitions for the same operating condition. For this reason, associated with each ROI or ROM value is specified a standard deviation value corresponding to the existing shot-to-shot variability. Another important point to note is the absence of ROI measurements for operating conditions where the discharge pressure is below atmospheric. This is due to the impossibility of reaching vacuum conditions in the test bench used to determine the experimental ROI. On the other hand, ROM results have been provided for these conditions with subatmospheric ambient pressure since the employed experimental technique allows reaching these more extreme conditions.

Table 6.19 summarizes the values of rate of injection and rate of momentum for the different operating conditions analyzed, representing the value obtained for the steady state. In addition, the discrepancies between experimental and computational data, if any, are reported. Regarding the mass flow rate measurements, the obtained results from the optimum configuration differ by a maximum of 3.5% from the experimental data. These differences have been calculated taking into account the mean value in both studies, but if the experimental standard deviation is considered, all conditions accurately determine the injection rate values. On the other hand, with reference to the rate of momentum, again, the observed differences during the validation are minimal, obtaining a maximum discrepancy of 6.5% corresponding to one of the most critical conditions where the injector reaches its injection pressure

limit and the liquid is injected into a vacuum scenario. Even obtaining experimental data under these conditions is rather challenging, the values can be said to be within the existing experimental uncertainty. Given the high precision of the results obtained, these studies corroborate the validity of the model and its applicability regardless of the operating condition being analyzed.

Cases		ROI [mg/ms]		Exp. Difference [%]	ROM [N]		Exp. Difference [%]
P_{inj}	P_{back}	CFD	Exp.		CFD	Exp.	
10 MPa	1 MPa	11.39	11.8 ± 0.2	- 3.47	1.16	1.1 ± 0.1	5.45
10 MPa	0.6 MPa	11.63	11.8 ± 0.2	- 1.44	1.21	1.2 ± 0.1	0.83
10 MPa	0.3 MPa	11.82	11.9 ± 0.2	- 0.67	1.25	1.2 ± 0.1	4.17
10 MPa	0.05 MPa	11.96	–	–	1.29	1.3 ± 0.1	-0.77
20 MPa	1 MPa	16.55	16.5 ± 0.2	0.30	2.47	2.4 ± 0.1	2.91
20 MPa	0.6 MPa	16.71	16.7 ± 0.2	0	2.53	2.5 ± 0.1	1.2
20 MPa	0.3 MPa	16.82	16.7 ± 0.2	0.72	2.57	2.6 ± 0.1	- 0.15
20 MPa	0.05 MPa	16.91	–	–	2.61	2.7 ± 0.1	-3.3
28 MPa	1 MPa	19.72	19.7 ± 0.2	0.10	3.51	3.4 ± 0.1	3.23
28 MPa	0.3 MPa	19.93	19.6 ± 0.2	1.68	3.62	3.7 ± 0.1	-2.16
28 MPa	0.05 MPa	20.01	–	–	3.65	3.9 ± 0.1	-6.4

Table 6.19: Characterization of the internal nozzle flow for a wide range of operating conditions including different injection pressures and various discharge pressures for the PIU injector.

The main purpose of Figure 6.18 is to visually reflect the computational results of both rate of injection and rate of momentum represented in Table 6.19 and thus improve the understanding of them while showing the trends of each variable. In this case the experimental values have not been represented since their proximity to the computational values makes the graph less legible and thus worsens the comprehension of the concepts. In addition, this picture allows to explain the effect of the injection pressure and the ambient density on the internal flow.

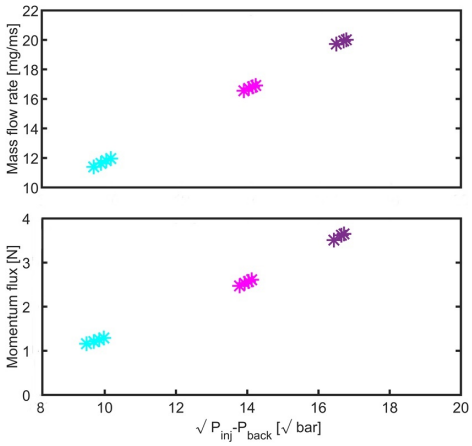

Figure 6.18: Averaged steady ROI and ROM as function of the square root of the pressure difference across the nozzle PIU injector.

For several years, many studies have been carried out for diesel injectors with the aim of showing the

influence of injection pressure on injection rate [13]. However, although no disparate trends are expected, GDI injectors have been less investigated in this scope. Figure 6.18 clearly demonstrates how a higher injection pressure directly implies an increase in the injection rate, suggesting a linear dependency, due mainly to an acceleration of the flow. The proportional relationship between the increase in injection pressure and the rate of injection can be defined from Equation 6.1 where P_{inj} and P_{back} are the injection pressure and the ambient pressure, respectively.

$$\dot{m} \propto \sqrt{P_{inj} - P_{back}} = \sqrt{\Delta P} \tag{6.1}$$

In addition, Figure 6.18 also captures the effect of ambient density, or in other words discharge pressure, on injection rate. The computational trend followed in this case by both the rate of injection and the rate of momentum is that as the discharge pressure is reduced and with it the ambient density, a small increase in the values of mass flow and momentum is experienced. This trend has been widely observed in the literature although, in this particular case, it is not reflected in the experimental results. That said, the experimental data could be within the uncertainty of the measurements.

It has also been considered interesting to graphically represent the result of the hydraulic characterization of the PIU injector from the dimensionless discharge, area and velocity coefficients as well as to add the values of effective velocity obtained in the different operating conditions treated. These results are presented in Figure 6.19. First of all, referring to the obtained results for the discharge coefficient, a slight downward trend can be intuited when the pressure drop is higher, but it can be said that the discharge coefficient is practically constant for the whole range of studied pressure drops (which covers almost all or even more than the nominal operating range of the injector). Subsequently, using the injection rate and momentum measurements, it is feasible to estimate the area coefficient and the velocity coefficient together with the effective flow velocity at the outlet orifices of the nozzle. In this particular case, it is observed how the velocity coefficient increases with the difference of pressures, in other words, when the discharge pressure is lower. In the same way, for a given injection pressure, the area coefficient is reduced as the pressure difference increases. The effect of these two behaviors causes the discharge coefficient to remain almost constant. Finally, the effective velocity is represented, which shows a clear trend of linear growth up until the highest values of pressure drop. Gimeno, J. [13] stated in his research that non-cavitating diesel injectors result in a velocity coefficient with asymptotic

correlation to the square root of the pressure drop, thus the effective velocity is linearly dependent on that same magnitude.

Low values of the velocity coefficient and discharge coefficient are obtained, in addition to the, albeit visible, unmarked trends with the square root of the pressure drop or Reynold's number. This is significantly different from traditional diesel injectors, where the trends are obvious and the values are substantially greater, even with cavitating nozzles [13]. The characteristic geometric design of GDI injectors is what makes these differences in behavior to be significant, greatly affecting the internal flow features of these injectors. Modern GDI injectors are designed with larger orifices, stepped counter-bore or divergent geometries as in this case, and operate at much lower pressure compared to diesel conditions. In addition, the needle lift profile reaches much lower values than the internal diameters of the orifices. These design peculiarities are mainly aimed at increasing turbulence and mixing, increasing spray breakup and promoting plume-to-plume interaction that enhances flame propagation. As demonstrated in Section 6.5.4 above, the low elevation of the needle causes the flow to constrict resulting in low values of the hydraulic coefficients. Another peculiar feature of the design of these injectors is flow detachment and recirculation zones due to the sharp angles between the needle seat and the orifices, and the low value of L/D at the nozzle orifices [7, 22]. All of these above mentioned peculiarities make the resulting behavior for the internal and external flow of this type of GDI injectors much more challenging. The complex phenomena characteristic of GDI injectors as well as the extensive variables that directly or indirectly influence the flow behavior, and the complexity involved in analyzing each of them separately, present a great effort to be carried out if the objective is to create fully predictive

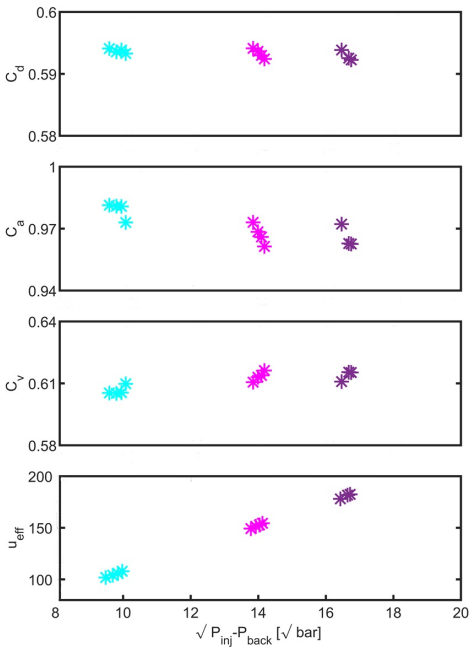

Figure 6.19: Effect of rail pressure on the different hydraulic coefficients characterizing the internal flow behavior. Note that different colors denote injection pressures of PIU injector.

injection and combustion models as is the case of the present Thesis. Despite the complexity mentioned above, the results presented in this section show a high accuracy in the results, faithfully reproducing the behavior and trends of the variables involved in the study of the in- and near- nozzle flow. Therefore, it can be stated that the predictive methodology developed to study the behavior of the internal flow during the steady state has been validated.

6.6 Spray G Injector. Transient State Analysis and Validation

The previous sections have been used to lay the groundwork. This means determining the optimal meshing strategy including base and minimum cell sizes, selecting the best performing turbulence models for the specific study, choosing the appropriate domain size so that the boundary conditions do not affect the solution of the problem and understanding how the constants of the HRM phase change model affect the behavior of the internal flow. In addition, the results obtained during the steady state of the injection, meaning that the needle is in a fixed position, have been validated. Once all the above-mentioned research has been accomplished, the study proceeds to approximate the real operating conditions, which means introducing the fast transient behavior that characterizes the injection process. The present Section gathers the study and characterization of the internal nozzle flow for the Spray G injector belonging to the ECN, under different operating conditions and various surrogate fuels employing different software under transient conditions, in other words, considering the vertical and lateral movement of the needle.

The main motivation of this study is to extend the predictive methodology developed in the previous sections so that, regardless of the characteristics of the injector and the software employed, an accurate hydraulic characterization of the injector under transient operating conditions may be performed. For this purpose and in order to demonstrate the validity of the predictive methodology, the results obtained have been compared with experimental data obtained from previous studies carried out in this same department, CMT-Motores Térmicos. After validation, the results of this predictive methodology will be used to analyze the behavior of the fluid downstream of the injector (external flow). Thus, following the footsteps of the research community in replacing experimental practice as far as possible.

6.6.1 Transient analysis under different software

As mentioned several times throughout the document, the injection process is characterized by its transient behavior. The injection begins when the needle starts to open, remains opened for a few microseconds and then closes, completing the injection process. This transient behavior is reflected computationally by an up and down movement of the needle. In addition, it is possible to add the consideration of the lateral movement or wobble that characterizes the needle. In the context of the Spray G injector, the transient behavior is defined from the average needle lift and wobble profile provided by Argonne National Laboratory [11] and obtained from x-ray measurements depicted in Figure 5.7b. For this initial study under transient conditions, two completely different meshing strategies have been selected, the adaptive mesh generated by CONVERGE™ with hexahedral elements and, on the other hand, the mesh with polyhedral elements developed in StarCCM+ (Section 6.4). Both software base the needle movement on the aforementioned lift and lateral movement profile. The initial needle position is defined at 2 µm of uplift due to the absence of a sealing treatment. It is important to note that the handling of the mesh with moving surfaces is different depending on the software involved. CONVERGE™ dynamically adapts the mesh throughout the simulation, adding cells in areas with complex phenomena and removing cells that are not essential to yield accurate results. StarCCM+ generates an interpolation field that allows moving the mesh vertices to their new position causing the cells to deform.

Figure 6.20 illustrates the results of rate of injection and rate of momentum under the SG reference condition obtained from the two different meshing strategies. It aims to evaluate the accuracy of the computational simulations when the needle is in motion and to analyze the internal flow behavior from two different software under identical transient conditions. For comparison and validation, the latest experiments performed by the CMT group [12] were considered. In general, the obtained results for both methodologies offer a good agreement between computational and experimental profiles.

Analyzing in detail the results, concerning the rate of injection, it is observed that in the first moments of injection both software reflect a much faster needle opening than experimentally experienced. However, in the last injection instants where the needle is closing, the closure slope follows a similar trend for all computational and experimental cases. This effect was also observed by other researchers such as Baldwin et al. [16] and was solved by initializing the internal pressure field with a hyperbolic tangent in order to decrease the pressure in the saddle region. In this case the initialization is

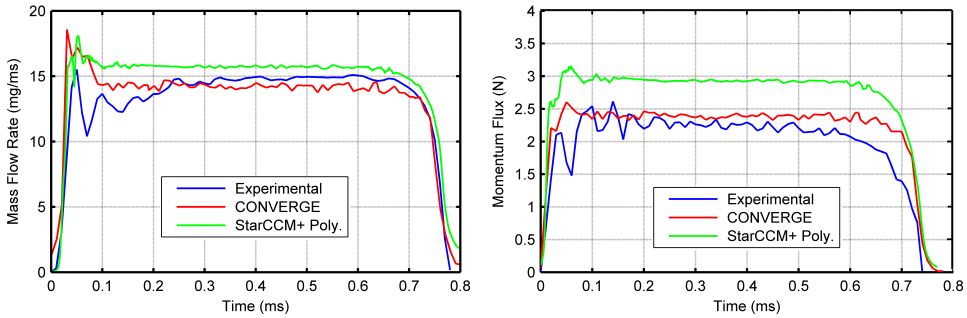

(a) ROI (b) ROM

Figure 6.20: Validation of mass flow rate and momentum flux predictions for transient simulation carried out with different software compared with experimental measurements for the Spray G injector under SG reference condition.

at constant pressure (Figure 5.9), which means that from the moment the injection begins the flow is injected with a pressure equal to the selected value. Another effect to highlight is the existence of non-zero value of ROI at initial and final stages of injection (t=0 ms and t=0.78 ms aSOI), The reason for this phenomenon is the initialization of the needle lift which is fixed at 2 µm of elevation in the first instant. This effect could be mitigated by employing a sealing algorithm as Mohapatra et al. [23] did in one of their papers. Finally, an experimental overshoot is also observed in the first instants of the injection which occurs when the needle elevation reaches its maximum. This phenomenon is well reproduced by the computational results. While the mentioned effect can experimentally be attributed to the presence of pressure waves upstream of the injector at both opening and closing being coupled with the position of the needle, computationally it cannot be ascribed to this reason. Simulations do not take into account the possible upstream pressure variation since a constant pressure is imposed as initial condition. This results in the stagnated fuel inside the orifices being pushed outwards, and temporarily increases the flow through the measuring section, thus producing the aforementioned overshoot. This effect can be computationally attenuated by employing alternative initialization strategies (see Section 6.7).

Once the needle reaches its maximum position, it remains in this stationary condition for a short period of time. During such time certain oscillations are observed in both the computational and experimental profiles. In the experimental case, these variations are a consequence of the way of measuring the mass flow rate or due to small pressure waves generated inside the rail

and transferred downstream of the injector. On the other hand, computational variations are due to the presence of vapor in the nozzle holes which leads to restrict the exit area of the counter-bore [9]. This effect may also be experimentally visible but is minimized by the effect of the variation in pressure inside the rail. The origins of both fluctuations are different so they cannot be physically comparable with each other in terms of frequency and amplitude.

After explaining the phenomena that appear in the rate of injection and rate of momentum profiles, a comparison is performed with the available experimental data in order to validate the employed methodology. The same observed trends in the study of these variables during the steady state (Section 6.4) are also evident in the transient state. The computational mass flow rate obtained from the CONVERGE™ code simulations falls below the experimental values while the StarCCM+ data overpredicts the experimental estimations (see Figure 6.20a). Meanwhile, the predictions obtained for momentum flux change the trends defined above (Figure 6.20b). During the transient simulations, the averaged values reached in the steady phase of the injection are in agreement with those presented in Section 6.4.1, even though both simulation profiles are above the experimental estimations. The discrepancy in trends is mainly due to experimental behavior. Observing the tendency of the momentum rate profile published by Payri et al. [10], it becomes apparent that during the first moments of the injection, the values of this variable have a downward trend until after a few milliseconds, the momentum values suffer an increase and tend to stabilize. This effect can be attributed to the electrical signal, or to an initial pressure drop inside the rail that stabilizes with time. What is certain and remarkable is that using an energizing time (ET) of 680 µs as stipulated by the ECN in its conditions, a stable value of momentum is not reached as it is in the case of mass flow rate. On the contrary, the use of a signal with 1200 µs ET allows to observe correctly the stabilization of the momentum at an average value of 2.63 N, value suggested by experimentalists for comparatives. This uncertainty in the results is added to the already existing concerning the momentum measurement methodology. Numerous efforts are needed by experimentalists to understand the phenomena occurring during the injection process in terms of momentum flux and thus give clarity to the results, improving comparisons and validations.

Concerning the StarCCM+ scenario, which exhibits a larger discrepancy with respect to the experimental result presented in Figure 6.20b, it may be stated that the trend followed by the profile is adequately captured. However, comparing the momentum value averaged between times 0.4 and 0.6 ms with

the experimentally defined one, a relative difference of 10% is observed, while in the stationary case it was only 1% for the polyhedral mesh. In this context, there are several factors to be taken into account that could explain the differences. Firstly, the particular treatment of the mesh by the software in scenarios with moving parts causes the cells to deform, thereby changing their shape with respect to the steady simulations. This can affect the flow diffusivity, thus modifying the obtained results.Secondly, the steady simulation has been performed with a fixed needle lift of 45 µs while the peak elevation in the transient simulation is 56 µs and the stabilization value corresponds to approximately 52 µs. As discussed in Section 6.5.4, the needle lift influences the steady mass flux and thus the momentum flux. Therefore, in order to understand the influence of the needle position on this particular injector a simulation with a fixed needle elevation of 55 µs was performed, observing a variation of 3% in the result and which could account the perceived difference.

The SG condition, as mentioned above, is assumed to be evaporative but non-flashing because the back pressure is higher than the fuel saturation pressure. Therefore, the liquid fuel jet is expected to remain intact up to the first few millimeters downstream of the injector outlet, similar to the behavior of high-pressure diesel injections. Therefore, an Eulerian approach may be able to significantly predict spray penetration in the early stages of injection. This analysis is considered interesting because it provides a better understanding of the spray behavior in the near field of the injector both during the steady state, with fixed needle, and in the transient state of the injection, with moving needle, and has therefore been conducted. The obtained results have been compared with experimental measurements of liquid spray penetration carried out by the CMT in previous works [24]. It is important to mention that for this study and the consequent calculation of the penetrations, the stationary and transient simulations corresponding to the CONVERGE™ code have been considered. The choice is based on the purpose of simplifying the analysis since both codes offer good estimations. However, CONVERGE™ has a more realistic scenario since all the species are considered compressible and also exhibits smaller differences in macroscopic flow parameters.

The obtained results of this interesting study are reported in Figure 6.21 where the computational penetrations for the stationary and transient cases are presented together with the experimental data for the first 3 mm downstream of the injector. The image clearly indicates that the penetration obtained under stationary conditions, with the needle in a fixed position, is much faster than that obtained under transient conditions where realistic needle movement is included. The slow behavior of the transient simulation can be attributed to the initialization strategy implemented. The orifices start filled

with liquid, fluid that, after starting the needle lift, moves with quite low velocity, thus underpredicting the penetration data. Based on these results, it can be stated that the Eulerian approaches have the ability to adequately predict the penetration of the liquid in the first millimeters of the injector outlet. Saha et al. [7], in a similar study, compared the Eulerian results with a Lagrangian LES approach concluding that the Eulerian predictions provided a better estimation compared to the Lagrangian results in the early stages of injection; however, in the later phases it started to deviate considerably from the measured data and the Lagrangian approach performed relatively better. This observed effect may be a consequence of several phenomena such as the initialization of the operating conditions [16] or the lifting needle position and the initialization of the needle, among others.

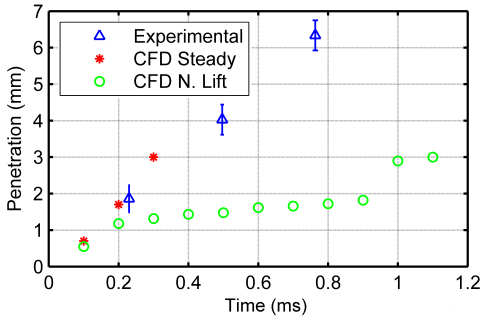

Figure 6.21: Liquid penetrations measured with an Eulerian approach for both steady case with needle in a fixed position and transient case taking into account needle movement, compared with experimental data for the Spray G injector under reference conditions.

Figure 6.22 represents two vertical cut-planes where the velocity variable is displayed at a simulation time corresponding to 0.03 ms. This image seeks to explain and understand why the simulations, in which the transient behavior of the injection process is taken into account, underestimate the penetration of liquid in the near field of the injector. The images show how, for this particular time, the spray in the simulation with fixed needle lift has developed reaching the first 3 mm downstream of the injector while in the transient simulation, the needle is still in a minimum position thus preventing the flow passage and making the spray unable to develop at the expected velocity. According to the needle lift profile (Figure 5.7b) and the obtained mass flow rate patterns, in the transient cases the needle reaches its maximum position comparable to the steady state in 0.1 ms, which is 3 times longer than the time analyzed. Therefore, even if the flow moves through the injector during this time, it is not until 0.1 ms that the nozzle flow can be considered fully developed.

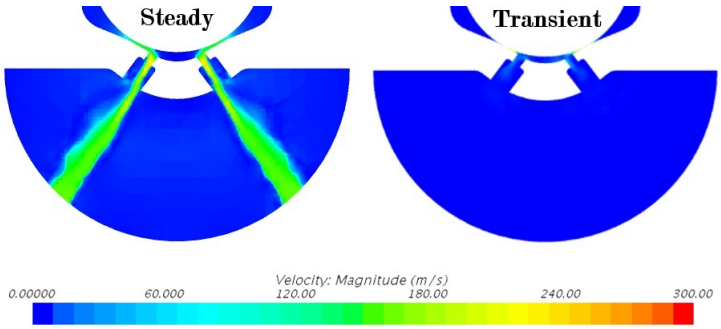

Figure 6.22: Vertical cut-planes representing the velocity field for both stationary and transient simulations at a time of 0.03 ms for the Spray G injector under reference conditions.

6.6.2 Influence of different surrogate fuels on the transient injection performance

The previous study encompasses the validation of the aforementioned predictive methodology so that both software are valid to continue the study of the injection process. However, for this study as for the subsequent ones, the CONVERGE™ software has been chosen for the same reasons mentioned above.

This section gathers the results obtained from analyzing the in- and near-nozzle flow behavior during the transient process of the GDI injection under the most typical engine operating conditions defined by the ECN: SG, SG2 and SG3. Mainly, the research carried out in this Thesis is intended to be carried out with a surrogate fuel such as iso-octane (2,2,4 trimethylpentane), which seeks to emulate the octane number of gasoline, or in other words, to control the degree of self-ignition. Even though, it does not adequately reproduce the volatility properties of gasoline. One of the main parts of this section will be focused only on the study of the injection process under the use of iso-octane as reference fuel. However, in recent years, there has been a growing interest among the scientific community to learn more about the behavior of injection under alternative fuels. Therefore, this study has been extended to mono-component fuels such as hexane (C_6H_{14}), pentane (C_5H_{12}), heptane (C_7H_{16}) and ethanol (C_2H_5OH). Furthermore, going one step further, the ECN has recently shown a special interest in multi-component fuels which bring their behavior a little closer to that of gasoline but also make the modeling process more complex. This work has wanted to go hand in hand and in accordance with the new implementations of the ECN and therefore the new

multi-component fuel named by this group as E00, which is composed of three mono-components in different percentages (46% iso-octane, 36% pentane and 18% undecane), is also included in this section.

6.6.2.1 Iso-Octane validation and discussion

This preliminary section contains the validation and discussion of the results obtained after analyzing the internal flow behavior by means of the Spray G injector belonging to the ECN under different realistic engine operating conditions and employing the reference surrogate fuel, iso-octane. In the present context, the three main operating conditions defined by the ECN (SG, SG2 and SG3) have been studied and the results have been presented in terms of total injection rate, momentum flux, non-condensable gas phase (NCG) injection rate and vapor fuel injection rate in Figure 6.23. The overall values of mass flow and momentum have been reported and thus compared with the existing experimental data for SG condition. On the other hand, the purpose of providing the NCG data is to analyze the presence of the recirculation phenomenon inside the orifices typical of this type of GDI geometries.

Figure 6.23a provides the injection rate results obtained in perpendicular planes at the exit of the counter-bore. As in Section 6.6.1 above, it is evident that both the opening and closing transient phases are captured properly and accurately. The period corresponding to the steady state of the injection is a little below the experimental prediction in the three studied conditions but the difference of about 3.5% can be considered to be within the so-called experimental uncertainty. A remarkable fact, as observed in the steady state analysis (Section 6.4), is that the values obtained for these three operating conditions are very similar in spite of the differences involved in their definition. It is well known in the literature how the variation of the discharge pressure, in the ranges that are being treated in this research, minimally affects the macroscopic variables of the flow [25]. Furthermore, the difference in the ambient gas densities present in the discharge chamber is also small enough to not cause large variations in the results. This behavior is replicated by the global momentum flux variable presented in Figure 6.23b. The comparison of these data with the experimental results allows validating the correct behavior of the model and methodology implemented and, therefore, may be considered as a basis for further studies with other types of combustibles.

Once the model has been validated, the injection rate of vapor fuel phase has been acquired and it is presented in Figure 6.23c. These could not be compared with experimental data due to the difficulty of measuring this variable by experimental techniques. The image clearly represents the definition of

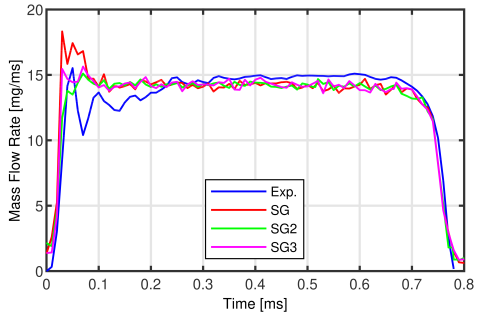

(a) Total Injection Rate

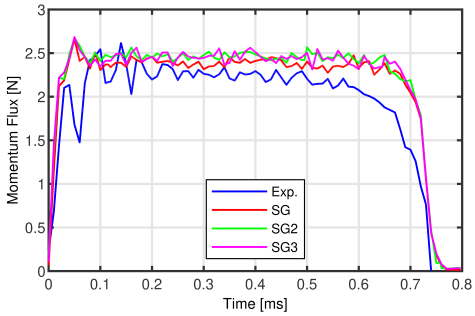

(b) Momentum Flux

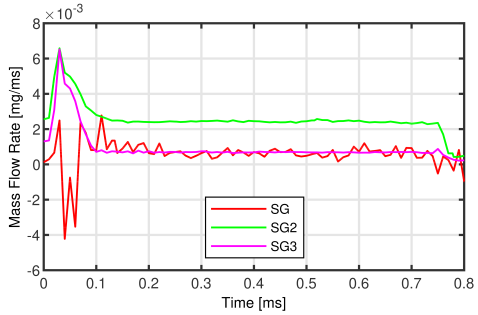

(c) Vapor Fuel Injection Rate

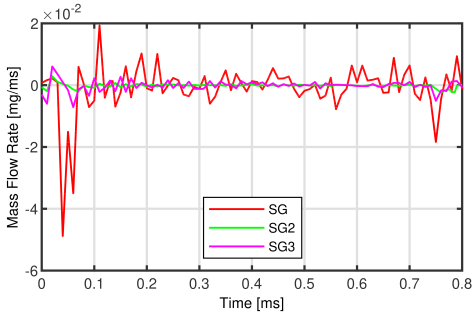

(d) NCG Injection Rate

Figure 6.23: Obtained results in terms of total injection rate, momentum flux, non-condensable injection rate and vapor fuel injection rate for the Spray G injector under different operating conditions (SG, SG2 and SG3) employing the reference surrogate fuel, iso-octane.

each of the studied operating conditions. The SG condition is an evaporative condition which, as noted, upon contact of the fuel with the hot conditions in the discharge chamber, it begins to evaporate, turning a small amount of fuel into vapor. The evaporation rate stabilizes once the needle is fully opened and the conditions in the chamber stabilize. On the other hand, the SG2 condition, with low ambient pressure, is the operating condition defined as mild flash boiling. In this case, the phase change is due to the fact that the pressure in the chamber is below the saturation pressure of the iso-octane giving rise to the occurrence of the flash boiling phenomenon. Finally, the case of SG3 is typical of a homogeneous GDI engine operating point which given the low ambient temperature and the lack of tendency to generate flashing conditions, is expected to be the less evaporating. However, it is noted that the data does report a vapor presence (similar to SG) at the orifice outlet but

it must be kept in mind that the quantities being discussed and so cavitation phenomenon are very small. These values may be the result of a pressure drop at the inlet of the inner hole, during the start of the injection when the needle begins to open since the phase change model is applied for both cavitation and flash boiling.

In addition to the aforementioned, the quantity of non-condensable gas passing through the counter-bore outlet has also been measured and reported in Figure 6.23d. This variable indicates the existence of recirculation inside the orifices, a phenomenon that is typical in this type of GDI injectors and that was intuited in Figure 6.9. As it is observed, there is only fluctuation of the non-condensable gas quantity in the SG condition. The flow under the SG condition deviates once it is flowing through the orifices, not occupying the entire volume of the counter-bore and thus allowing the entry of air inwards. This air entrance is more abrupt at the beginning of the injection when the needle begins to rise. Throughout the injection, a continuous inflow and outflow of non-condensable gas can be sensed, thus producing a recirculation inside the counter-bore and helping the air-fuel mixture. In the other two conditions, SG2 and SG3, the downstream characteristics of the nozzle make the liquid tend to expand at the outlet of the nozzle and so occupy a larger part of the volume in the counter-bore preventing the entry of ambient gas. Although during most of the injection the average values of the NCG mass flow are null, it is possible to appreciate a small recirculation of NCG inside the orifices during the initial and final stages of the injection period, when the liquid does not occupy a large part of the orifice. This explanation can be further supported by Figure 6.24 where the mass fraction of liquid fuel for the three operating conditions is displayed.

The images in the upper part of Figure 6.24, where the mass fraction of liquid is reflected at the outlet of the orifices and the counter-bores, support the statement mentioned in the previous lines. In the case of SG it is observed how the liquid tends to deflect towards the injector axis in a way that allows the entry of air from the discharge chamber, generating a recirculation phenomenon and thus improving the mixing. In the particular scenario of SG2, the low pressure in the discharge chamber leads to the occurrence of flash boiling, which generates an enlargement of the spray opening, thus increasing its spray cone angle. The images demonstrate how the flow behavior differs from that of the SG from inside the nozzle where the flow tends to occupy a larger part of the counter-bore and thus allows less non-condensable air to recirculate. Finally, the SG3 condition lies between the two behaviors mentioned above. The low ambient density allows the fluid to escape from the

nozzle more easily, thus occupying a large part of the counter-bore as it passes through, and allowing a minimal entry of non-condensable air into the nozzle.

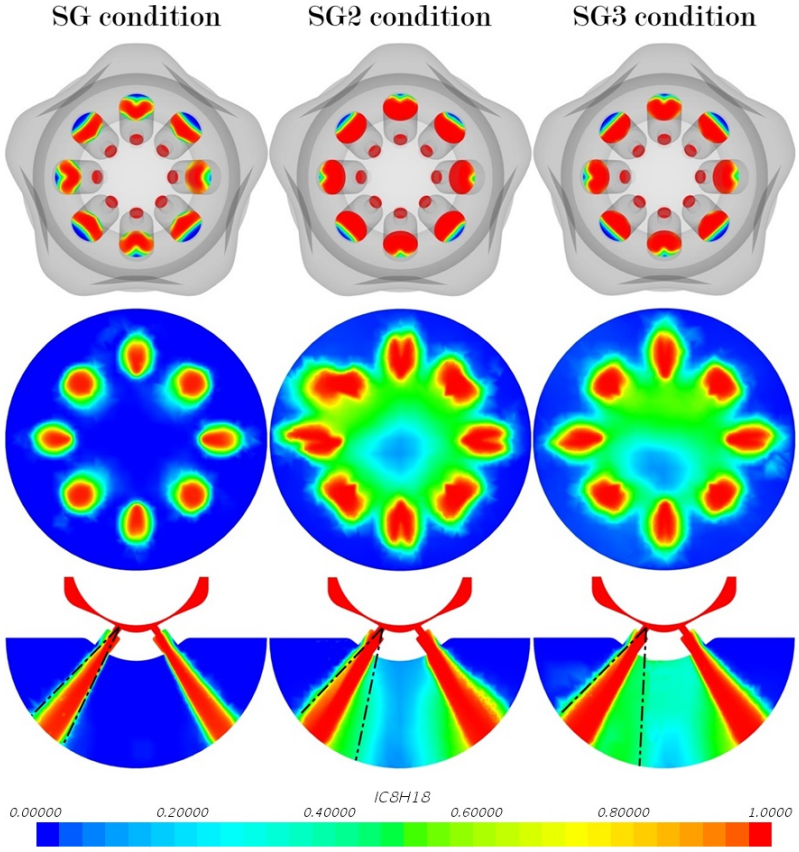

Figure 6.24: Cut-planes at the exit of the small orifice and counter-bore as well as at 1 mm downstream of the injector tip representing the liquid mass fraction field averaged between the steady phase of the injection (0.4 to 0.6 ms) for the Spray G injector under three studied operating conditions.

Focusing now on the images in the second row of Figure 6.24 where the mass fraction of liquid at 1 mm downstream of the injector tip is reflected, it is observed how the disparity in the behavior upstream, in the nozzle, is transferred to the spray when it begins to develop in the first millimeters. The SG condition has a defined jet boundary with no apparent interaction between the sprays, thus avoiding phenomena such as spray collapse. The shape of the sprays varies from one to another, an effect that can be attributed to the geometrical arrangement of the injector which has 8 orifices and 5 bumps that

makes the flow distribution uneven between orifices or, on the other hand, it can also be generated by the influence of the mesh in the spray distribution [7]. It is possible, according to the theory, that any misalignment of the flow with the grid results in a stair-stepping pattern that generates numerical viscosity and distorts the solution. With respect to the SG2 condition, the disparity between jets is also observed, but the increase in the amplitude of the jets is clearly noticeable, an effect that is due to the presence of the flash boiling phenomenon. A higher spray cone angle together with the proximity of the orifices to each other, causes a jet-to-jet interaction technically called spray collapse, an effect that must be taken into account in the analysis since it changes the typical behavior of the spray. Referring finally to the SG3 condition, it is observed that the spray core is wider than in SG and narrower than in the case of SG2. However, although the ambient pressure is above the fuel saturation pressure, it is observed that there is an interaction between jets. Looking in detail at the evolution of the contours throughout the injection process, it has been observed how initially, due to the lower ambient pressure, the flow encounters a lower resistance to its progression, opening the spray to a large extent in the first moments at the exit of the orifice. This fact means that there is an interaction between jets from the first instant. Moreover, a local stationary vortex appears, which remains in time and causes a greater mixing process between the liquid and the ambient gas, thus occupying the central part of the sprays as can be visualized in Figure 6.25. It is important to mention that this behavior is locally observed in the first millimeters downstream of the injector, which does not exempt that if a larger discharge volume is taken into account, it could be observed that as the spray develops, the effect of the stationary vortex may be reduced until it disappears. This condition of SG3 has been little studied by researchers and is currently beginning to gain importance. For this reason there is limited data available in the literature on the behavior of the spray under this condition. In order to determine if what is being captured is accurate, which is applicable to all three conditions studied, it would be necessary to have experimental contours of variables such as density or volume fraction of liquid in cut-off planes 1 mm downstream of the injector tip. This analysis allows to give a glimpse of the behavior of the fluid in the first millimeters downstream of the injector under three different operating conditions, leaving the discussion open awaiting further experimental documentation.

It has been mentioned several times throughout this analysis how the operating condition, or in other words the changes in pressure, temperature and density in the discharge chamber affect the behavior of the spray. Therefore, it is considered of great interest to dedicate a few lines to discuss the evolution

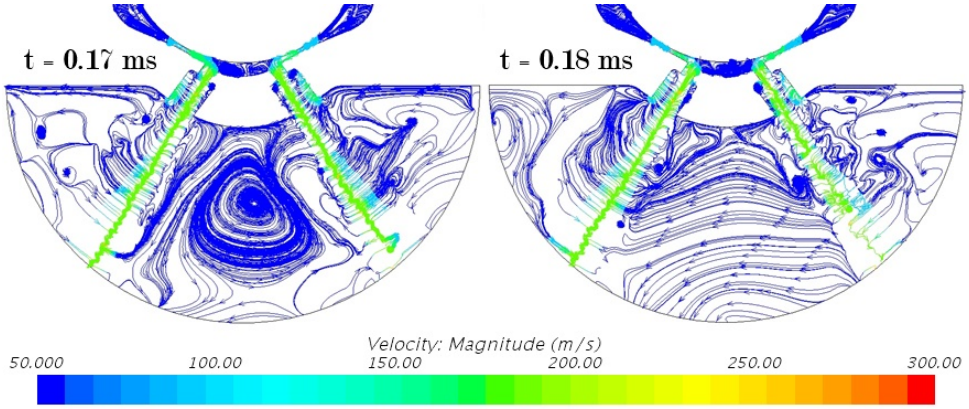

Figure 6.25: Representation of vorticity through iso-lines and colored by the velocity variable at two different times during the transient phase of needle opening for the Spray G injector under the SG3 operating condition.

of the near-field spray in terms of both spray cone angle and spray plume direction throughout the injection process under the different target operating conditions. For this purpose, the calculation methodology described in Section 5.4.1.2 has been adopted and the results are presented in Figure 6.26. Getting the evolution of the angles as a function of time, thus collecting the behavior of the spray along the whole injection can improve the accuracy of the external flow studies, since the angle distribution that faithfully reproduces the spray pattern would be introduced as an input parameter.

To a large extent, the results for the spray cone angle and the spray plume direction encompass the previous explanations. Figure 6.26 reflects the obtained results for both parameters in the three conditions of study. In the upper part of both images (Figure 6.26a and 6.26b) the SG condition is represented, where it is shown how the jets are deflected inward as the plume direction differs from the 37° of inclination of the geometrical axis of the orifices. On the other hand, it reveals a very similar behavior in all the orifices in spite of the differences in the shape of the sprays, which means that in the cutting planes considered for the calculation, the spray has the same opening. Furthermore, due to this calculation, it is possible to understand how in the initial moments of the injection the spray tends to open and then stabilize once the injection process reaches the stationary state. Regarding the SG2 condition, depicted in the center of Figures 6.26a and 6.26b, a similar behavior is observed, the jets are still deflected inward. It is in the spray cone angle results where the differences between operating conditions can be

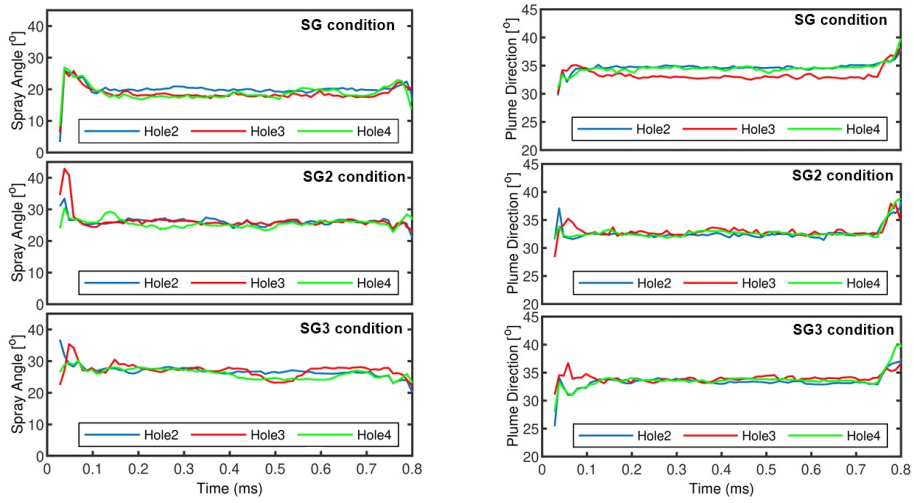

(a) Spray Angle (b) Plume Direction

Figure 6.26: Spray cone angle and spray plume direction evolution of the whole injection process for the Spray G injector under three operating conditions: SG, SG2 and SG3.

perceived. Clearly the SG2 condition has a higher cone angle, attributed to the aforementioned flash boiling effect. Finally, addressing the SG3 condition displayed in the bottom part of Figures 6.26a and 6.26b, once again the deflection of the sprays can be noted, which leads to the conclusion that regardless of the conditions downstream of the injector, this type of counter-bore geometry causes a deflection of the spray towards the center of the domain of the same magnitude regardless the conditions. In this case, and focusing on the upper image of Figure 6.26a, the large opening of the spray in the initial moments of the injection when the needle begins to rise is clearly noticeable. Subsequently, the spray opening stabilizes at a high value to be a condition considered non-evaporative and not to meet the requirements to generate flash boiling. Although it has been seen in Figure 6.24 that the intact spray core in the SG3 condition is in terms of width between the SG and SG2 conditions, the selected criteria for the spray angle includes also part of the mixing zone in the discharge volume. For this reason, the spray cone angle prediction is higher than in the other two studied conditions and thus differs from the values recommended by the ECN to be introduced as input parameter for the external flow investigation. However, this recommendation is to consider the same value that is used in the SG reference condition which is around 20° and

based on what has been observed, the value should be defined between the SG angle and the SG2 angle.

Tables 6.20 and 6.21 collect the time-averaged between 0.4 and 0.6 ms aSOI and standard deviation for both spray cone angle and spray plume direction measurements in order to quantitatively compare between operating conditions. To the best of the author's knowledge, only angle data for the SG condition exist in the literature [18], so the other operating conditions cannot be validated. Concerning the obtained results for the spray cone angle (Table 6.20), the aforementioned trends are once again confirmed. The SG condition has smaller opening angles. In SG2 the flash boiling phenomenon causes the jets to open, reaching mean values of around 25°. Finally, the SG3 condition predicts a spray opening similar to SG2 due to the high mixing ratio in the center of the domain.

Spray Angle [°]	SG	SG2	SG3
Hole 2	19.98 ± 0.41	25.58 ± 0.71	26.55 ± 0.30
Hole 3	18.16 ± 0.45	25.74 ± 0.55	25.76 ± 1.72
Hole 4	17.78 ± 0.51	24.94 ± 0.79	24.50 ± 0.49

Table 6.20: Time-averaged measurements and standard deviation for the spray cone angle for the three studied operating conditions for the Spray G injector.

On the other hand, Table 6.21 reports the deviation of the spray with respect to the geometrical axis of the orifices, 37°. All the operating conditions studied exhibit this known deviation, mainly attributed to the peculiar counter-bored shape, and are close to the experimentally calculated values at 34° [18]. It is true, however, that the SG2 condition shows a larger spray deviation which is due to the fact that the expansion of the spray due to flash boiling takes place largely towards the interior of the domain affecting the calculated spray direction.

6.6.2.2 Iso-Octane and E00 comparison

Once it is validated the flow behavior in the in- and near- nozzle region considering the iso-octane reference fuel under the three different ECN operating conditions, a comparison of the presented results with those obtained from the same study but considering the E00 multi-component surrogate fuel recently defined by the ECN has been carried out. It should be remembered once again that the purpose of introducing this fuel is to bring the overall behavior closer

Plume Direction [°]	SG	SG2	SG3
Hole 2	34.73 ± 0.14	32.30 ± 0.24	33.27 ± 0.16
Hole 3	32.97 ± 0.24	32.86 ± 0.42	34.03 ± 0.29
Hole 4	34.46 ± 0.28	32.66 ± 0.22	33.78 ± 0.16

Table 6.21: Time-averaged measurements and standard deviation for the spray plume direction for the three studied operating conditions for the Spray G injector.

to that of gasoline and to improve volatility, a property that iso-octane does not reproduce correctly.

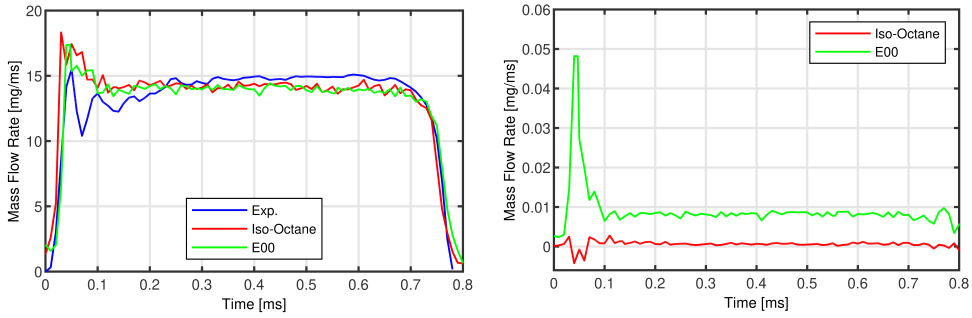

(a) Total Injection Rate

(b) Vapor Fuel Injection Rate

Figure 6.27: Comparison in terms of total injection rate and vapor fuel injection rate for the Spray G injector under the SG operating condition for the two main gasoline surrogate components, iso-octane and E00.

This comparison includes mainly the study of the flow behavior from the macroscopic variables that define it such as the total injection rate and, in this particular case, the vapor fuel injection rate has also been included. The results under SG condition are presented in Figure 6.27. In the case of the total injection rate, the outcomes are compared with the experimental data of iso-octane as study fuel, since for the moment there are no experimental data available to validate the behavior of E00. The obtained behavior in terms of total injetion rate (Figure 6.27a) is very similar in both cases and it is possible to claim that both fuels predict similar values. The opening and closing ramps are almost identical and the steady state does not show any disparity in the results. Nevertheless, focusing on the vapor fuel injection rate, a difference of an order of magnitude in the amount of vapor generated is observed. Although

no experimental data is available for comparison, it is understood that iso-octane generates less vapor due to its low volatility and for this reason it could be said that the E00 multi-component has a closer to standard gasoline behavior. The main reason why the E00 surrogate has a higher amount of fuel vapor is because it has a high percentage of pentane in its composition. Pentane is a fuel whose saturation pressure is much higher than iso-octane for the same temperature conditions, as shown in Figure 6.29 and Table 5.16. Thus, it is considered a much more volatile fuel. It is important to mention that although the SG reference condition is defined as an evaporative but non-flashing condition, being SG2 condition the flash boiling state, this definitions are only applicable to iso-octane. Each fuel has its own properties and the specification may differ. This is what happens in the case of E00, as pentane has a saturation pressure up to 6 times higher than that corresponding to iso-octane under the same conditions, this species has a much greater tendency to phase change under similar circumstances.

This phenomenon, in which a part of the pentane changes phase, could generate a modification in the spray pattern and in the flow behavior in general. Therefore, and with the aim of observing if there is any difference in the flow characteristics between fuels, the mass fraction of nitrogen for both iso-octane and E00 under two operating conditions SG and SG2 are displayed in Figure 6.28. In this case, in addition to SG, the SG2 condition is taken into account, since it is the one defined by default for iso-octane as flash boiling.

Considering only the case of SG, it can be noted how the spray nucleus (zone without N_2 content) itself is similar in both fuels. In the case of iso-octane it is observed that there is a small amount of vapor generated by the evaporative conditions in the innermost zone of the sprays. However, in the case of E00, the phase change that takes place is greater and therefore clearly shows the presence of fuel vapor and the mixture with the non-condensable gas, which implies an opening of the spray towards the interior of the domain. In both cases, the tendency is to generate this phase change towards the interior of the domain. Meanwhile in the case of SG, as mentioned above, it is not possible to consider the existence of a noticeable interaction between jets, in the case of E00, a slight jet-to-jet interaction is observed that obviously cannot be compared with a case under flashing conditions, as will be seen below.

On the other hand, referring to the SG2 condition, the behavior is completely different between fuels. Remember again that the mass fraction of non-condensable gas is being reflected, in other words, all species that form the fuel are being considered in this analysis. The iso-octane contour is the

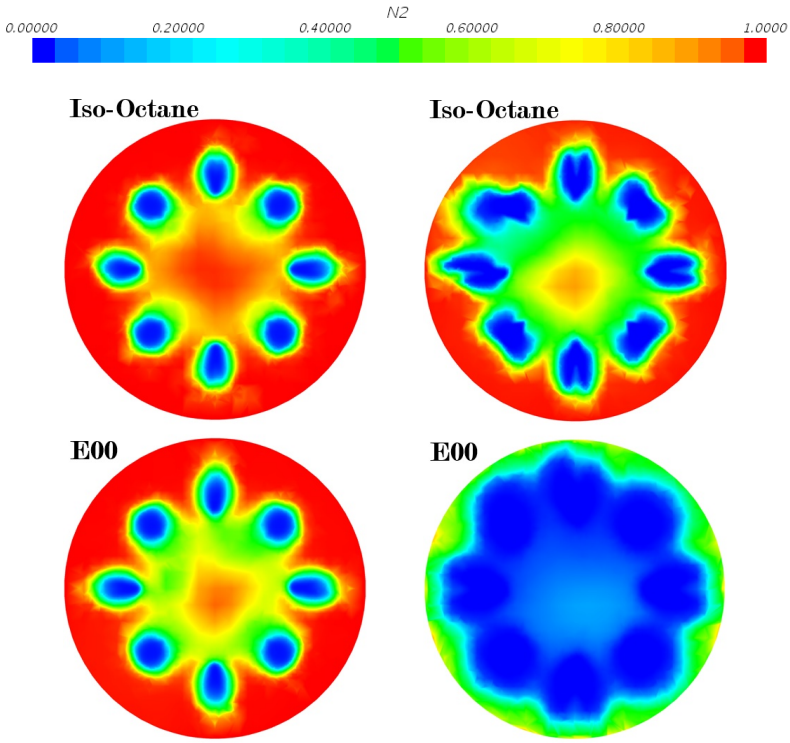

(a) Spray G condition (b) Spray G2 condition

Figure 6.28: Slice planes at 1 mm downstream of the injector tip representing the mass fraction of non-condesable gas for the Spray G injector under the different studied fuels, iso-octane and E00.

same as that observed in Figure 6.24 and the explanation can be adapted to this case. the phase change produced by the flashing conditions generates that the sprays have a larger aperture and interact with each other giving rise to the famous spray collapse. Focusing more attention on the E00 fuel, it is a clear example that the definition of conditions by the ECN is only applicable to iso-octane. As a result of the E00 higher volatility, it is clearly seen how in the spray zone and in the interior of the domain the non-condensable gas is negligible and all of this area is occupied by the fuel in both liquid and vapor phases. A different definition is observed in the shape of the sprays being in the case of E00 more uniform and with a greater amplitude. This behavior is more in line with what is expected based on the latest guidelines proposed by the ECN network. However, experimental data would be necessary to define which fuel is closer to the standard gasoline expected behavior. Continuing

with the analysis of the E00, the amplitude in the spray opening leads to a higher interaction between jets and therefore to a higher spray collapse, a phenomenon that has to be taken into account due to its disadvantages in the engine performance.

As it has been demonstrated throughout this section, the behavior of the two fuels is very different, not in macroscopic terms but in the shape and behavior of the sprays. Once again, to determine whether E00 better reproduces the behavior associated with gasoline, experimental data would be needed to determine the shape and distribution of jets in the near field. As this is not available to date, and basing the opinion on the good behavior of iso-octane but its lack of volatility, the author considers that the E00 surrogate fuel may be a fuel to contemplate for further studies related to GDI investigations.

6.6.2.3 Surrogate fuels comparison

Gasolines are made up of several types of hydrocarbons and their distinction is based on the various elements that contribute to their formation. Because of this, it is difficult to replicate accurately the same composition of gasoline in the research environment, so substitutes that emulate its behavior are sought. It is usually common to find in the literature that gasoline has been replicated by surrogate fuels such as iso-octane or even n-heptane but as stated and even demonstrated (Section 6.6.2.2) the volatility is not adequately captured. This property is essential when flash boiling is studied, where large amount of fuel is generated, current simulations tend not to replicate the behavior. Therefore, this section is based on the comparison of internal flow behavior under different surrogate fuels not only with the objective of mimicking the behavior of commercial gasoline but also to look for more extreme conditions such as taking mild flash boiling one step further and turning it into strong flash boiling. The lack of experimental data for alternative fuels makes it impossible to compare the obtained outcomes. However, the validation of the model under the reference fuel makes it possible to study the injection process and the behavior of the in- and near-nozzle flow under different surrogate fuels by applying the well-known predictive methodology that has been developed throughout the document. It is important to mention that in order to reproduce the internal flow behavior under different fuels, the needle lift profile associated to the iso-octane study has been adopted, so if there would be any change in it associated to the type of fuel [26], it is being obviated in the present research.

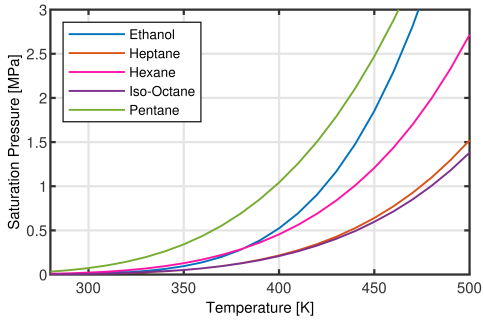

Figure 6.29: Saturation pressure of the studied surrogate fuels.

The study has been carried out for the three main ECN reference conditions. Figure 6.29 displays the saturation pressure curves as a function of fuel temperature for the different fuels analyzed. It is clearly seen how iso-octane and heptane have similar behaviors and therefore are used indifferently to replicate the gasoline performance. Hexane has higher saturation pressures and will therefore have a greater tendency to phase change under the same discharge conditions. As a noteworthy fact, after numerous studies, Huang et al. [27] and Kar et al. [28] determined that the saturation pressure curve corresponding to hexane is the closest to the curve of commercial gasoline, so it is proposed as a surrogate fuel to replicate the behavior of the real engine. Finally, ethanol has a similar tendency to that of hexane initially, but from a certain temperature the slope of the curve is much steeper, giving rise to a greater predisposition to phase change under such conditions. Of all the fuels analyzed, pentane stands out, as mentioned above, for its high volatility and the difference with the other studied fuels accentuates, as the temperature increases.

Once explained in some detail the characteristics of each fuel as a function of the saturation pressure of each one, it is easier to understand the behavior they present in the analysis. Figure 6.33 reports the evolution of the internal flow characteristics along the injection in terms of mass flow and momentum rate for the studied surrogate fuels under the reference operating condition of SG. First of all, Figure 6.30a and Figure 6.30b, where the total injection rate is shown but in an augmented form to better appreciate the differences between fuels, shows how the behavior of all the fuels is very similar among them, reflecting minimal differences in the mass flow rate values. These differences are mainly due and attributed to the densities of each one (see Table 5.16). The density of ethanol, the fuel with the highest mass flow rate, is 14% greater in relative value than iso-octane. The other fuels have very similar values of densities and therefore give rise to ROI results very close to each other. The fuel that stands out for having a lower injection rate is pentane because it has a density 13% lower than iso-octane. Similar behavior is also observed in the momentum flux measurements, Figure 6.30c, where the differences between fuels, although already small, are even reduced. This is due to the fact that

for the momentum calculation it is the velocity that takes importance in the equation and therefore the effect of density is attenuated (Equation 5.135).

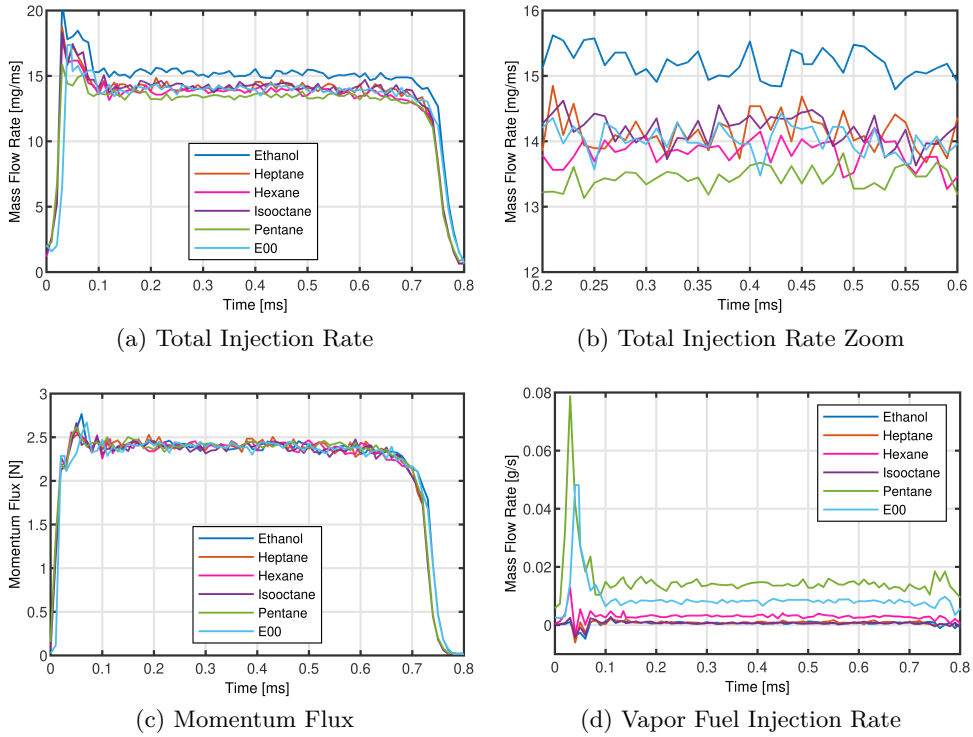

(a) Total Injection Rate

(b) Total Injection Rate Zoom

(c) Momentum Flux

(d) Vapor Fuel Injection Rate

Figure 6.30: Obtained results in terms of total injection rate, momentum flux and vapor fuel injection rate after analyzing the internal flow behavior for the Spray G injector under SG condition for all the studied surrogate fuels.

Another variable that has been analyzed and therefore considered of interest is the vapor fuel injection rate. This variable gives an idea of the tendency of each fuel to generate vapor, in this case, under evaporative conditions such as those of SG. The results obtained are related to the previous explanation of fuel saturation pressure. Fuels such as heptane and iso-octane, commonly used as substitutes for gasoline for both experimental and computational studies, produce little vapor since their boiling point is one of the highest of all the fuels studied, in both cases approaching 100 °C, and for this reason it is said that they do not adequately capture the volatility behavior of gasoline. Ethanol does not present a large amount of vapor at the exit of the orifices either, although its boiling point is somewhat lower than in the case of iso-octane. However, hexane, a fuel noted for its proximity in properties to commercial

gasoline, reports the presence of vapor at the exit of the orifices. Finally, pentane is the most volatile of all the fuels analyzed, with a boiling point of 36 °C, so, as expected, it is the one that generates the most vapor in the evaporative working conditions. This fuel is followed in behavior by E00 due to its high amount of pentane in its composition. As it was discussed in Section 6.6.2.2 above, the behavior of E00 did not differ much from iso-octane under the SG condition, but on the other hand, under flash boiling conditions, its behavior is closer to what is expected, but it is not known if it can even overpredict the expected vapor generation. Looking at the vapor fuel injection rate results, the vapor generated by hexane is somewhere in between iso-octane and E00. This, coupled with the proximity of the fuel properties to those of gasoline, makes hexane pose and gain strength as a surrogate fuel that could predict in detail the actual behavior of the GDI injection. It is important to mention that this study is only intended to give an idea of the performance of the different surrogate fluids since the lack of experimental data prevents validation of the results. This makes it unknown whether the amounts of predicted vapor are adequate since, as it will be demonstrated below (Section 6.6.3), the phase change model employed as well as the variables that comprise it, have a great influence on the results.

	SG		SG2		SG3	
Surrogate fuels	ROI [g/s]	ROM [N]	ROI [g/s]	ROM [N]	ROI [g/s]	ROM [N]
Ethanol (C_2H_5OH)	15.16	2.39	15.15	2.47	15.15	2.48
Iso-Octane (C_8H_{18})	14.17	2.38	14.22	2.46	14.28	2.45
Heptane (C_7H_{16})	14.16	2.40	14.20	2.49	14.05	2.46
E00	13.99	2.39	13.78	2.40	13.93	2.44
Hexane (C_6H_{14})	13.87	2.40	13.79	2.48	13.75	2.46
Pentane (C_5H12)	13.51	2.41	13.29	2.45	13.33	2.44
Experimental*	ROI [g/s] = 14.71			ROM [N] = 2.63		

**Results obtained for iso-octane under SG condition but applicable to SG2 and SG3*

Table 6.22: Time-averaged between 0.4 and 0.6 ms injection rate and momentum flux for all the studied surrogate fuels at the three most popular operating conditions employing Spray G injector.

Table 6.22 summarizes the results time-averaged between the times of 0.4 and 0.6 ms for all the surrogate fuels studied and the three operating conditions described, SG, SG2 and SG3. They are also accompanied by the average experimental results obtained for iso-octane under SG conditions. The data have been ordered from highest to lowest mass flow rate which, for the reasons explained, can also be said to be ordered from highest to lowest density (see

Table 5.16). As in previous studies, the variation of the operating conditions does not affect notably the characterization of the internal flow in macroscopic terms. It is also clear that the mass flow does show a small variation between fuels while this tendency disappears in the momentum flux values due to the influence of density is diminished.

In addition to all the above, it has been considered of interest to reflect visually by means of a bar graph presented in Figure 6.31 the behavior of all the fuels analyzed in terms of vapor fuel generated for the three operating conditions under study. This allows again to highlight the effect of the properties of each of the surrogates involved. Since the SG condition has already been addressed in previous lines, greater attention will be paid to the SG2 and SG3 conditions. In the first three fuels shown on the left side of Figure 6.31, ethanol, iso-octane and heptane, the amount of vapor released is very small despite the fact that in the flashing condition the fuel saturation pressure is above the discharge pressure. For the flash boiling phenomenon to take place, this is one of the premises to be fulfilled, however, fuels have other types of properties that influence the phase change. Taking as an example the case of ethanol, it is strange that having almost twice saturation pressure than iso-octane for working conditions of 363 K, it generates negligible amounts of vapor. In this particular case, other fuel properties must be taken into account, such as the latent heat of evaporation, which is defined as the amount of energy that must be added to a liquid substance to transform a quantity of that substance into a gas. In the case of ethanol, the value of this property is up to 6 times greater than iso-octane for the same operating conditions, so this high number tends to reduce the evaporation rate significantly [29]. Proceeding with the study, the other three remaining fuels have a high tendency to generate vapor not only in the condition defined as flash boiling (SG2) but also in the SG3 condition. This is the clear example that the SG3 condition is defined as non-flashing based on the properties of iso-octane, however, hexane, E00 and pentane have a saturation pressure above 1 bar which is the discharge pressure at the men-

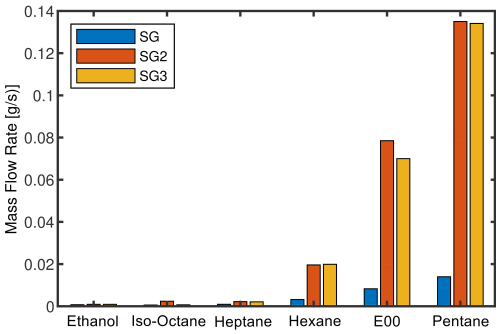

Figure 6.31: Representation of the amount of vapor fuel generated in steady state operation of the Spray G injector for all the surrogate fuels considered under the three different ECN reference operating conditions.

tioned working point. This means that for these three fuels in particular the SG3 condition is also considered flashing. In addition to the predisposition to generate flash boiling conditions, both hexane and pentane, and therefore E00, have a lower latent heat than iso-octane and therefore have a greater tendency to phase change, explaining the obtained results.

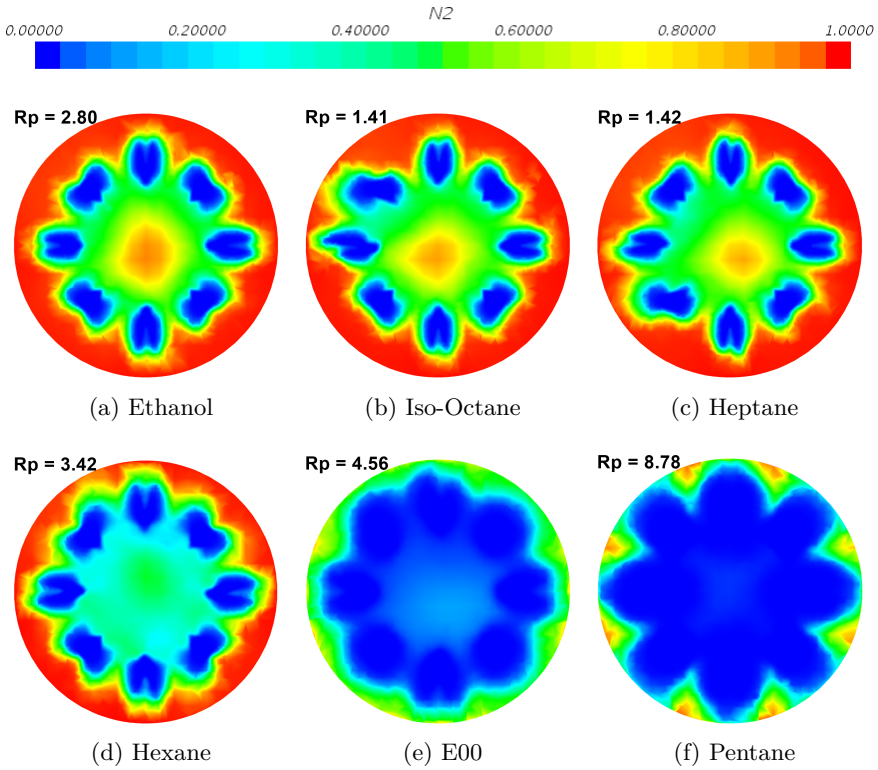

(a) Ethanol (b) Iso-Octane (c) Heptane

(d) Hexane (e) E00 (f) Pentane

Figure 6.32: Slice planes at 1 mm downstream of the Spray G injector tip representing the mass fraction of non-condesable gas under the SG2 condition for all the studied surrogate fuels.

To conclude this section, it is considered of interest to emphasize the behavior of the in- and near-nozzle flow under flash boiling conditions, since recently it is the topic where researchers are putting their efforts to understand in depth the behavior of the fluid under these conditions [1, 30]. For this purpose, the mass fraction of nitrogen in a cut plane at 1 mm downstream of the injector has been reflected in Figure 6.32, where the behavior of the fluid when the fuel properties are altered is clearly shown. Each image is documented with the corresponding ratio of pressures (R_p) that determines the

intensity of the flash boiling (Equation 3.30). As a complementary material, the radial distribution of liquid and vapor mass fraction in a line contained in the same plane at 1 mm from the tip of the injector is presented in Figure 6.33. The flash boiling conditions tend to change the behavioral patterns of the sprays among them as the spray aperture increases (see Figure 6.24). The greater the intensity of the flash boiling, the larger the spray aperture. In this case something similar is observed, in the first three fuels ethanol (Figure 6.32a), iso-octane (Figure 6.32b) and heptane (Figure 6.32c) the sprays have broadened compared to the SG condition, and therefore, a small interaction between sprays is seen (Figure 6.33a). Referring to the case of hexane (Figure 6.32d), it is observed that its higher saturation pressure and therefore, higher R_p as well as the properties associated with this fuel such as its latent heat of vaporization make the generated flash boiling intensify, giving rise to a greater phase change, Figure 6.33b, and to a greater interaction between jets so that the central part of the domain is largely occupied by liquid and fuel vapor. Nevertheless, in this case the spray core opening is similar to that obtained in the iso-octane base case. Finally, dealing with the fuels that have a greater tendency to phase change either because of their high saturation pressure (high R_p) or high volatility, E00 and pentane, it is observed that the sprays tend to open more than all the fuels previously analyzed. It could therefore be defined that the flash boiling in this case goes from mild flashing defined for iso-octane ($R_p = 1.41$) to strong flashing ($R_p = 8.78$). The amount of vapor generated in both cases is high. It is also observed that the central part of the domain is completely occupied by fuel in both phases, liquid and vapor. The formation of spray collapse depends on several factors being a combination of the characteristics of the injector geometry, the thermodynamic properties of the fuel and the ambient pressure. In these two last cases of E00 and pentane, although hexane could be included, it is observed that the interaction between sprays is high and therefore it could be said that the spray collapse phenomenon is present and should be considered by the possible adverse effects that it entails. However, in the other cases, iso-octane, heptane and ethanol, there is this spray interaction that will obviously change the expected behavior of the spray but, not being so strong, this interaction will not remain many millimeters downstream of the injector thus obtaining the two regions of collapse and non-collapse that were defined in Figure 3.20.

6.6.3 Influence of the geometry on the transient injection performance

The ECN, as mentioned throughout the document, aims to create a benchmark for both experimental and computational validations for diesel and gasoline

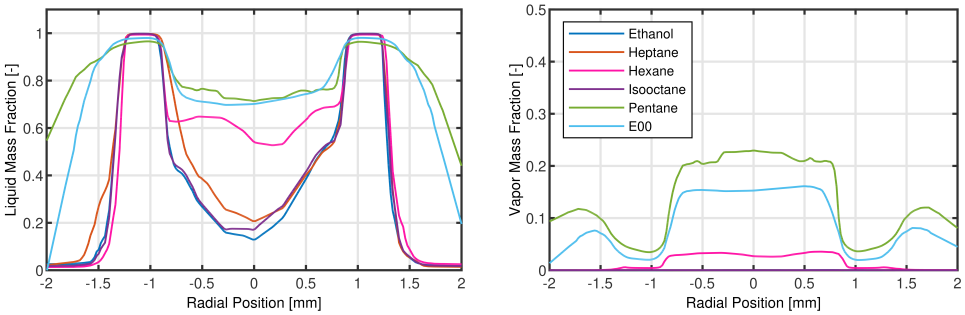

(a) Liquid Mass Fraction (b) Vapor Mass Fraction

Figure 6.33: Radial distribution of liquid and vapor mass fraction in a line contained in a plane at 1 mm from the tip of the Spray G injector under the SG2 condition for all the studied surrogate fuels.

applications. Research in the gasoline branch is much more recent and started for computational researchers from an ideal geometry generated by x-ray data [11]. This initial geometry has been and is still known to be the first generation (generation 1) used to study the flow behavior during the GDI injection process. Generation 1 stands out for being a geometry which has been treated and smoothed as well as manufacturing defects have been eliminated in order to minimize meshing and convergence problems. It is the most studied geometry to date and although it adequately captures the real behavior of the injection process, its simplification makes that some effects and/or phenomena that take place during this event are minimized or even neglected. For this reason, and with the main objective of making the studies more and more similar to reality, a new generation of geometry (generation 3) has been recently developed, which faithfully reproduces both the dimensions and the shape of the nozzle, although it is true that it has a small treatment to make it more manageable for researchers (Section 5.3.4.1).

This research project started shortly after laying the computational and experimental groundwork in ECN for the GDI study, so most of it is focused on studying the injection process from the use of generation 1 injector. However, and due to the evolution and the path that this research network is following, it has been considered of interest for the scientific community to introduce the implementation of this new generation 3 comparing the flow behavior with the corresponding generation 1 and giving a small idea of the similarities and differences between both. For these reasons, the present section gathers the mentioned studies where mainly both generations of geometries are compared

in terms of macroscopic parameters such as injection rate and also the spray behavior in the in- and near- nozzle in accordance with shape and direction [31].

Figure 6.34 presents this comparative and the conclusions drawn from it can be extrapolated to another macroscopic variable that also defines the behavior of the flow such as the momentum flux. This image reports the results obtained in both geometries for the three main operating conditions set by the ECN: SG, SG2 and SG3. For all of them, the same behavior is observed, the opening and closing ramps are perfectly predicted in both generations, however, the values during the stationary period of the injection are in the case of geometry 3, 1 g/s above the values obtained for generation 1. If comparison of these values is made with the experimental data of 14.71 g/s obtained for the same stationary time interval between 0.4 and 0.6 ms, it is noted an overestimation of 3.6% in the case of the geometry of generation 3 and an underestimation of 3.3% for generation 1. The main reason that justifies this discrepancy is the existing difference in the size of the orifices as well as in the inlet and outlet corner radius that completely modifies the behavior of the flow allowing a greater amount of liquid to pass, causing it to deviate more from the geometric axis of the injector, as it will be explained later, and thus achieving higher fluid velocities. Taking as reference the SG condition, Table 6.23 reflects the results concerning the macroscopic parameters and dimensionless coefficients defining the internal flow characteristics for both geometries. In addition to give consistency to the previous statement, it is observed that in spite of the difference in the macroscopic results, the dimensionless coefficients are identical between the geometries. Comparing the values of the dimensionless coefficients with the experiments, it can be stated that globally both geometries correctly approximate the experimental behavior. However, a debate arises. In addition to the uncertainty in the momentum measurements, there is the further concern about the orifice dimension employed for the calculation of the dimensionless flow coefficients (Equation 3.16 and 3.24). Until now, values corresponding to the ideal geometry (165 µm) have been employed, nevertheless, the latest x-

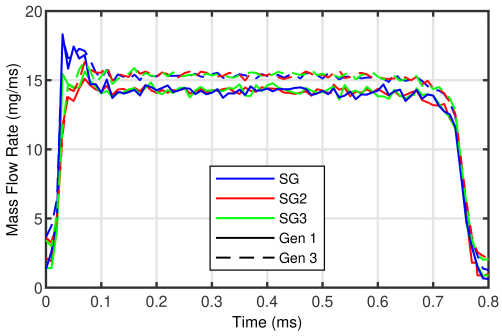

Figure 6.34: Mass flow rate comparison for three different operating conditions under two different studied generations of Spray G geometry.

ray measurements have shown that the orifices have sizes up to 10 µm larger in some of them (Table 5.18). This brings the inner hole diameter to an average value of 172 µm, which implies a variation in the calculation of the dimensionless coefficients of up to 8%, which is the maximum difference seen in the data presented in the mentioned table. Although the presented computational and experimental values give a very close idea of the hydraulic characteristics of the injector, there is a need to reach an agreement in the scientific community so that the same methodologies are implemented in order to allow more accurate comparatives.

	ROI [mg/ms]	**ROM [N]**	$\mathbf{C_d}$	$\mathbf{C_m}$	$\mathbf{C_a}$	$\mathbf{C_v}$
Generation 1	14.25	2.41	0.53	0.36	0.77	0.69
Generation 3	15.27	2.66	0.53	0.37	0.76	0.70
Experimental	14.71	2.63*	0.55	0.40	0.75	0.73

** from frontal configuration*

Table 6.23: Results of the parameters characterizing the internal nozzle flow for both Spray G geometry generations, gen 1 and gen 3, under SG reference condition.

Once the differences between geometries have been analyzed in quantitative terms, it is considered of great interest to study in detail the physical behavior of the flow inside the nozzle and of the spray once it leaves the nozzle. Therefore, the mass fraction of liquid at the outlet of the orifices of both the small orifice and the counter-bore for each studied geometry is reflected in Figure 6.35. From this information, it is possible to explain the behavior of the spray in the first few millimeters of injection so that the reader can get a realistic idea of the jet pattern. The most remarkable phenomenon that can be clearly seen in both images is how generation 3 has a larger counter-bore space occupied by non-condensable gas and even in the interior of the small orifices small amounts of that gas are also visible, an effect that is not seen in generation 1. This tends to mean that the recirculation event inside the orifices is also greater and thus the sprays are deviated from their geometrical axis even more. The difference in value of this deviation between both generations is between 1.5 and 2.5 degrees depending on the orifice, since not all have the same size and inlet and outlet orifice radii (Table 6.24). The deviation of the spray pattern means that, once developed, the sprays are also closer together, which may not be a problem for the SG condition, but under flash boiling conditions such as SG2 this proximity between jets could result

in a much more severe spray collapse. Despite this difference in spray direction, the spray amplitude has a similar behavior, being around 20 degrees of cone angle. Table 6.24 provides the estimations of both parameters as well as the differences with respect to generation 1 (Tables 6.20 and 6.21). As it will be discussed further below (Section 6.6.4.2), according to Pratama et al. [32] the Spray G injector is categorized within the cavitation range belonging to hydraulic flip formation during its entire operating range. However, in neither of the two geometries this effect is observed. The flow detachment, as this effect is defined, should be present from the orifice inlet, but only a large air entrainment is evident in the counter-bore zone. The occurrence of this phenomenon also depends to a large extent on the orientation of the orifices, a characteristic that is not taken into account in the calculation of the value that categorizes the injector into one range or another and that seems to be of great importance. The reference case for the aforementioned study has no inclination at all, while the Spray G geometry has its orifices tilted at 37° degrees to the geometrical axis of the injector. However, despite the non-existence of the hydraulic flip, in the hypothetical case of its occurrence, it would be attenuated accepting that generation 3 is more accurate. The larger the entrance radius to the orifice due to the smaller incoming flow angle results in a higher contraction coefficient, a higher discharge coefficient, and a more much higher velocity distribution in the nozzle side where the hydraulic flip occurs [32].

	Spray Angle [°]	Diff. w/ Gen 1 [°]	Plume Direction [°]	Diff. w/ Gen 1 [°]
Hole 2	19.18 ± 0.67	-0.8	32.31 ± 0.43	-2.42
Hole 3	18.65 ± 0.80	+0.49	31.26 ± 0.32	-1.71
Hole 4	19.29 ± 0.75	+1.51	31.92 ± 0.31	-2.54

Table 6.24: Time-averaged measurements and standard deviation for the spray cone angle and plume direction for the Spray G generation 3 geometry under SG reference condition.

6.6.3.1 Phase change model parameters influence under generation 3 geometry

As it has already been mentioned and also hinted at, the trend in the studies associated with injection and GDI combustion processes within the ECN framework is to use more realistic geometries that are closer to the original, leaving aside idealizations and therefore putting more effort, care and detail in the study. Generation 1 has served for a long period of time to give a

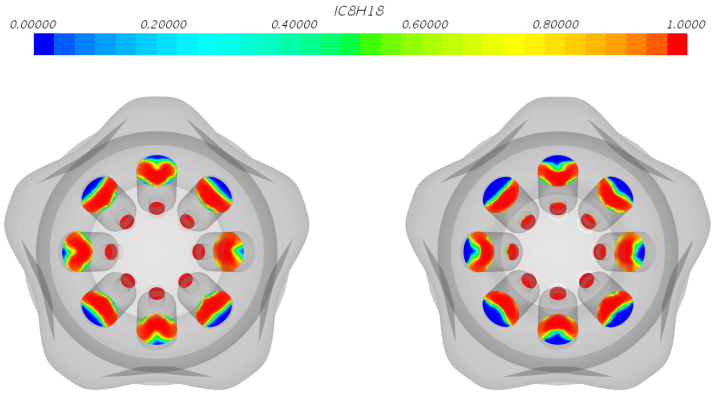

(a) Generation 1 (b) Generation 3

Figure 6.35: Orifice cross-sectional liquid mass fraction contours at steady state phase of the injection process (t = 0.5 ms) of both studied Spray G geometries under SG condition.

general idea of the internal flow and spray development behavior under typical operating conditions of a GDI engine. However, and having observed in previous lines the existing differences between generations not only in terms of geometry, which has quite an impact on the spray, but also in the values corresponding to the macroscopic variables that define the internal flow and the distribution of the liquid as it passes through the nozzle and the orifices, it is considered necessary to start implementing this new generation of geometry in the computational studies. Therefore, the ECN has recently included in its guidelines for future studies the recommendation to use exclusively the new generation of geometries for the relevant investigations. In addition, computational researchers have become concerned about the effect of varying the exponents that affect the variables defining the phase change model (Equation5.58). This topic was already of great importance and was studied in detail by Saha et al. [6]. This work has also reflected in Section 6.2.6 the studies that were carried out in stationary conditions under this benchmark. However, all these analyses and the conclusions obtained were related to the generation 1 geometry and it has been shown that the variation in the flow behavior under different values of the exponents that are part of the definition of the phase change equation is more significant when generation 3 is used. All the above mentioned has led the author of the present Thesis to perform a brief study of the influence of the exponents of the variables α and ϕ as well as the time constant θ_0 on the flow behavior in the in and near nozzle

region adopting the new generation of injector as the computational domain of study.

Before discussing the studies carried out and the results obtained, it is important to mention that the present investigation has been conducted taking into account the transient behavior of the injection, in other words, considering the movement of the needle as opposed to the previous study shown in Section 6.2.6 where the needle was raised in a fixed position. Another aspect to highlight is that the following study only focuses on the flow structure since, as shown in Table 6.6, variations in the parameters of the phase change model do not significantly influence the macroscopic parameters such as ROI and ROM. The following lines include the evolution of the flow behavior when the exponent associated with ϕ (non-dimensional pressure ratio) and the time constant θ_0 are modified (Equation 5.58). The influence of α has been discarded from the investigation since, as observed in Section 6.2.6, it was minimal under both flashing and non-flashing conditions. Moving on to the outcomes, the first row of images of Figure 6.36 presents the results in the orifice cross-sectional planes obtained by varying the exponent corresponding to the ϕ variable under SG condition. The images reflect the evolution of the vapor fuel mass fraction both at the outlet of the small orifice and at the counter-bore. In line with what has already been observed, the variation in the amount of vapor generated by changing the exponents of the pressure ratio is minimal. The exponent value of -0.88 would be the one that generates a greater amount of fuel vapor, a difference that is almost imperceptible in the images. On the contrary, and as shown in Figure 6.36, the variation of this exponent has a great influence on the flash boiling condition of SG2 where it goes from not generating any fuel vapor at all in the case of -2.84 to having almost half of the counter-bore occupied with a small amount of fuel vapor. The change in the pattern of internal flow behavior coupled with the presence of vapor inside the orifices causes the spray development to be altered as well, effect that can be clearly seen in the second row of images of Figure 6.36. In this image, where the density is visualized, it echoes what actually happens when changing the mentioned exponent, not only is a greater phase change generated inside the orifices as the ϕ exponent increases but once the spray starts to develop, in the first millimeters downstream of the injector, also the jets experience a greater phase change thus being their spray cone angle greater. Finally, another fact to point out, although not visually represented, is that generation 3 allows (due to the geometrical characteristics of the orifices) the phase change that occurs inside the orifices to extend downstream, occupying a larger space. To determine which value is appropriate, experimental contours obtained by x-ray techniques would be required to rep-

resent the variables to be compared. At the moment, only density data in planes 2 mm downstream of the injector are available in the ECN database, a measurement that cannot be taken in this computational domain because the discharge volume is too small to yield comparable data at that distance.

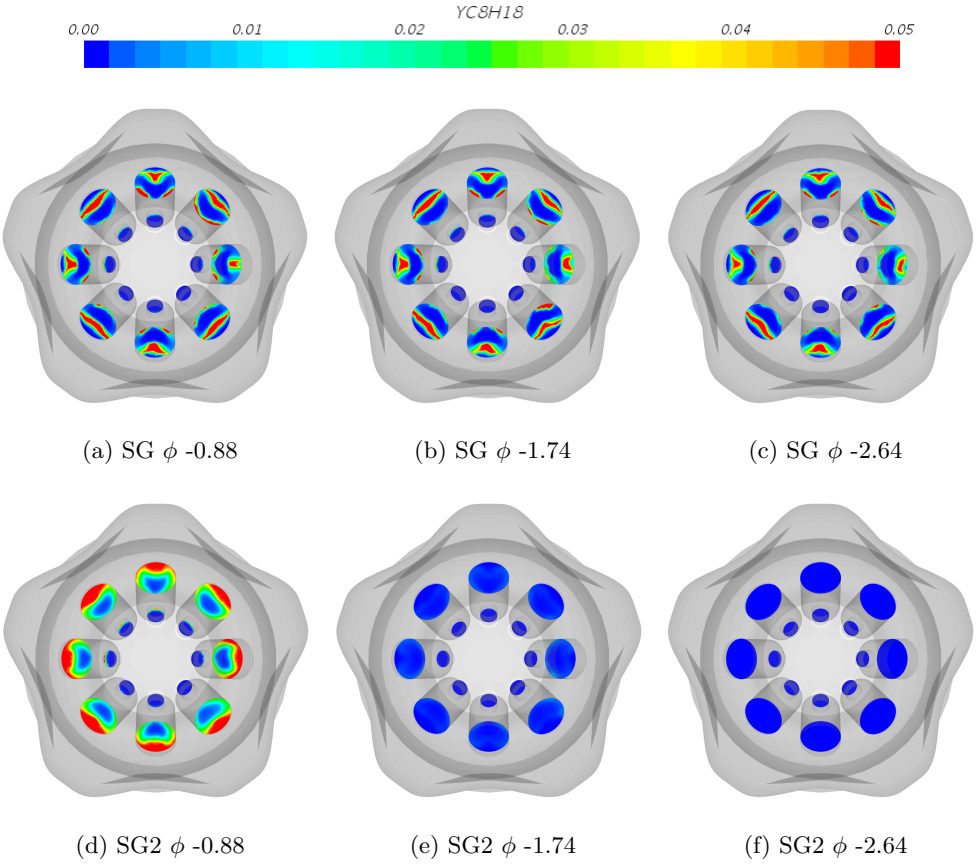

(a) SG ϕ -0.88 (b) SG ϕ -1.74 (c) SG ϕ -2.64

(d) SG2 ϕ -0.88 (e) SG2 ϕ -1.74 (f) SG2 ϕ -2.64

Figure 6.36: Orifice cross-sectional vapor mass fraction contours (t = 0.5 ms) reflecting the flow behavior as function of the exponent associated with ϕ for the Spray G injector under SG and SG2 conditions.

The behavior presented so far does not differ greatly from that observed in the similar study conducted for stationary conditions and generation 1 (Section 6.2.6). Except for the fact that the effects observed are more pronounced in the case of generation 3. However, if attention is focused on the time scale constant (θ_0), which was not studied in the previous section because the recommended ranges of variation were in the same orders of magnitude as the

reference value and did not involve large effects on the flow features, it is observed that the proposed new generation completely changes the flow patterns both inside the nozzle and downstream of it. The mentioned effect is clearly seen in Figure 6.38 where a horizontal cross-sectional cut perpendicular to the geometrical axis of the injector is reflected. The changes carried out start from the reference value of 3.84e-07 s and the orders of magnitude are decreased, 2 for one of the cases and 6 for the other. It should be noted that the presented results are obtained under flash boiling conditions, SG2. The images clearly illustrate that the change in the time constant is one of the variables that most affects the behavior of the phase change. Starting from the reference value (Figure 6.38a), there is hardly any abrupt phase change in spite of being in flash boiling conditions, since the core of the spray remains intact (high density values corresponding to the fuel). Once the order of magnitude is reduced, as in the case of Figure 6.38b, a major phase change can be perceived. Around the spray core a cloud of vapor fuel appears, generated by this phase change. Finally, in the most extreme case corresponding to Figure 6.38c, the spray nucleus practically disappears and it all transforms into a cloud of vapor fuel coming from this extreme phase change that has taken place. The observed effect is in agreement with the physical behavior marked by the equations defining the phase change. A lower value of θ_0 seems to enhance the effect of flash boiling, which is to be anticipated as θ_0 significantly decreases the equilibrium time scale, leading to a meaningful increase in the phase change rate equilibrium condition ($\frac{Dx}{Dt}$) over the running time.

The effects observed are interesting and add value to the results already available in the literature. However, it is not possible to determine which values are the most suitable to simulate the behavior of internal and external flow since, as already stated, the available experimental data are limited in this particular area of study. It is recognized that, qualitatively, computational studies tend to underpredict the spray cone angle and thus decrease the existing jet-to-jet interaction effect and that the real geometry (generation 3) features improve the representation of the initial jet expansion. It is worth repeating that more experimental studies are needed to correctly determine the proper constants for an accurate analysis of spray behavior and spray shape.

6.6.4 Multiple Injections Analysis

The studies that have been carried out so far contemplate a single main injection. However, the growing interest that has been expressed in recent years in multiple injection strategies and the advantages they can provide (see Section 2.4.4) has led to the study of their influence on the behavior of the in- and

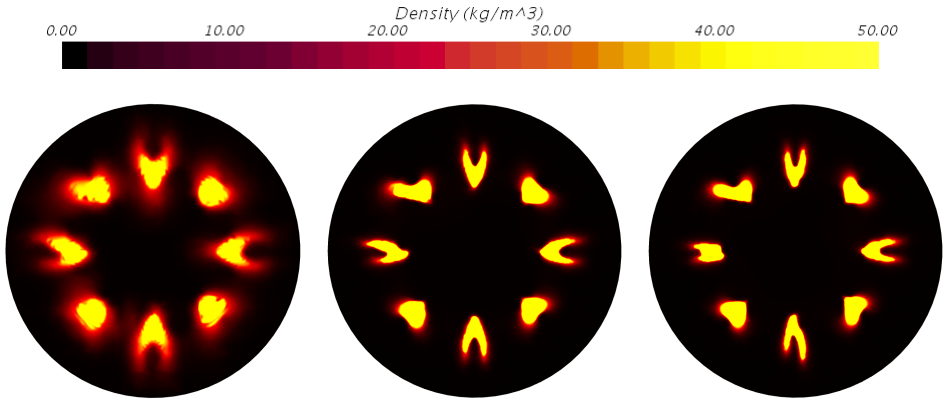

(a) ϕ -0.88 (b) ϕ -1.74 (c) ϕ -2.64

Figure 6.37: Horizontal cross-sectional density contours at 1 mm downstream of the Spray G injector during the steady state phase of the injection process (t = 0.5 ms) reflecting the flow behavior as function of the exponent associated with ϕ under SG2 condition.

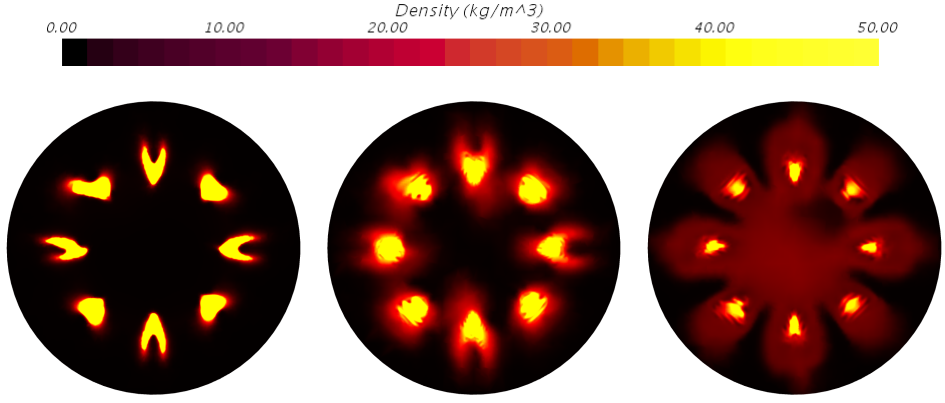

(a) θ_0 3.84e-07 (b) θ_0 3.84e-09 (c) θ_0 3.84e-13

Figure 6.38: Horizontal cross-sectional density contours at 1 mm downstream of the Spray G injector during the steady state phase of the injection process (t = 0.5 ms) reflecting the flow behavior as function of the exponent associated with θ_0 under SG2 condition.

near-nozzle region. This type of strategy is more common in Diesel engines, where it has been commonly employed in recent years. However, the concept is relatively new for GDI engines and therefore its study is not as widespread. The objective of this research is to understand more in depth the concept of

multiple injection and to provide the scientific community with a basis for further work in this field. The vast opportunities afforded by the use of multiple injection strategies have led the ECN itself to define among its standards a specific operating condition to study the effect of multiple injection.

This section presents the methodology developed and implemented for the particular study of multiple injections as well as the validation of the same with experimental data available in the literature. In addition, once the model has been validated, the study focuses on analyzing the behavior of the in- and near-nozzle flow under the operation of both pilot and post-injections. For this purpose, and as in the previous cases, CONVERGE™ software has been used. The injector of study is the already known Spray G and the reference condition used is the one called SG-M1 by the ECN, which is based on the standards of the SG reference condition but varying the energization during the injection. This operating condition is included in the post-injection group and has a main injection of 680 µs, 1000 µs dwell time, and 186 µs for post-injection (Figure 6.39). It is important to note that both the injection and ambient pressures and temperatures are identical to the SG condition.

6.6.4.1 Specific methodology for multiple injection strategy

In order to study multiple injection strategies, it is more than necessary to take into account the transient behavior of the injection and thus impose the corresponding lifting profile on the needle. Under this framework, there are numerous doubts and discrepancies about the different needle elevation profiles for multi-injection conditions available in the literature. Vaquerizo, D. [12] presents in his work a profile that lacks the initial overshoot characteristic of the Spray G reference condition. The only difference between the SG-M1 operating condition and the SG reference condition is the extra post-injection added, so that the main injection should have very similar characteristics in terms of needle lift and injection rate in both cases. On the other hand, Chinmoy et al. [23] presented in their work another uplift profile for the same injector completely different from the one

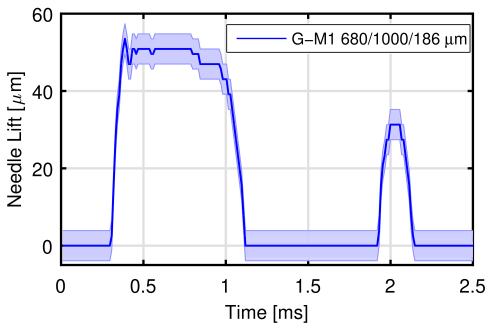

Figure 6.39: Needle lift profile for the Spray G injector under multiple injection condition (SG-M1). Adapted from [12].

mentioned above. In this case, the profile had a similar shape to the one presented in Figure 5.7b and corresponding to the single injection, however, the needle lift in the steady state is 10 µm below the reference condition of 53 µm. For the present study, it has been imposed a lifting law identical to the one presented in Figure 6.39, which has been obtained from experimental x-ray techniques at the Argonne National Laboratory facilities [12]. This profile meets the above characteristics, the shape is similar to the reference condition lift profile and the needle lift in the steady stage, although it is 3 µm below, it is also close to the reference condition, within the existing variability in the measurements. It is important to mention that for the multiple injection analysis, the lateral movement of the needle (wobble) has not been considered, which does not imply any limitation as it has been demonstrated in other works [11] and in later sections (Section 6.7) to have minimal influence on the solution and flow behavior.

As mentioned in Section 6.6.1, for unsteady GDI simulations, the needle is initially raised at 2 µm to avoid geometrical overlapping problems. This initial elevation causes that once the injection begins the flow passes quickly through the orifices generating in the initial instants mass flow values corresponding to this elevation (Figure 6.20a). For single injection studies this is not a major problem, as proved earlier, but in the case of multiple injections it is something that needs to be addressed. There is a dwell time between the main injection and the post-injection where the needle remains completely closed, in the case that computationally this closing position corresponds to a needle elevation of 2 µm, this would cause the flow to continue passing during all this time. Not only that, but also the start-of-injection (SOI) and end-of-injection (EOI) are two crucial phases of the transient movement of the needle that generate pressure waves and flow turbulence. The cavitation phenomenon, a critical problem for needle seat, is often experienced in both starting and closing events. In addition, phenomena such as liquid fuel dribble, which is a major contributor to unburned hydrocarbon emissions, can occur in the EOI phase. Hot gas ingestion takes place in the counter-bore and nozzle regions during the dwell time between injections. This gas ingestion can negatively impact the SOI of the next cycle by delaying liquid injection and leading to increased vaporization of the liquid [33]. For these reasons, among others, and with the objective of correctly capturing the influence of the use of multiple injections on injection behavior it is necessary to find a strategy that will adequately fully model the opening and closing of the needle.

For this purpose, a sealing algorithm based on opening and closing events is proposed to control the flow passage between regions. CONVERGE™ offers the possibility of employing boundary sealing features, preventing flow

between different parts of the same region. The tool allows to define the temporal instants in which it is desired to disconnect regions from each other, thus avoiding the flow passage. This type of approaches are typically used in engine modeling to prevent flow between the piston and the cylinder, however, in this case it has been used to prevent the flow from passing once the injection is complete. The most suitable and by definition the most correct area to apply this restriction in the flow path is at the needle seat. In order to do so, the geometry has to be modified so that the nozzle is divided into two different surfaces, one from the needle seat upstream of the injector and the other encompassing the nozzle bag, as presented in Figure 6.40.

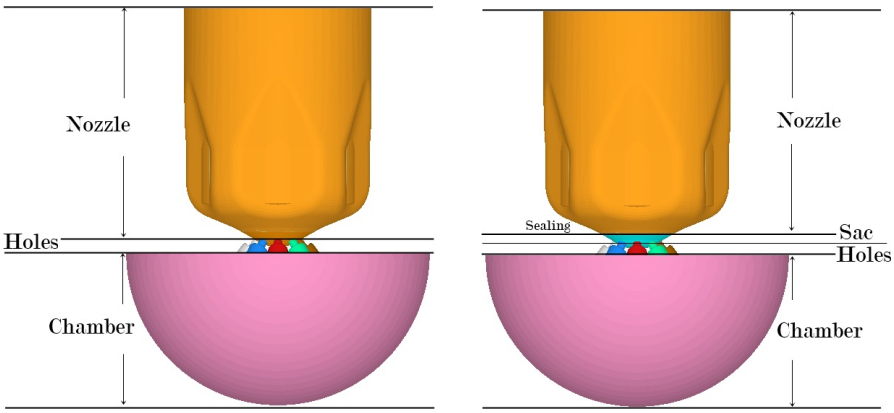

(a) Original domain (b) Modified domain

Figure 6.40: Process of modifying the Spray G computational domain in order to use the sealing algorithm.

6.6.4.2 Multiple injection model validation

Once the new methodology to be used for the analysis of multiple injections has been defined, validation of the developed model is carried out by comparison with experimental data. For this purpose the data available in CMT-Motores Térmicos and presented in the work of Vaquerizo, D. [12] have been considered. The results of the comparison in terms of rate of injection are reported in Figure 6.41 below.

The obtained results are unexpected, especially when they are based on a correctly validated methodology (Section 6.6.1). However, there is an explanation for that. First of all, one of the most remarkable facts is the correct

performance of the sealing algorithm that allows to completely restrict the flow passage, thus obtaining a zero injection rate when the needle is completely closed, or in other words, during the dwell time. It can also be noticed that at the first injection times there is no initial value of injection rate as in the case of single injection (Figure 6.20a).

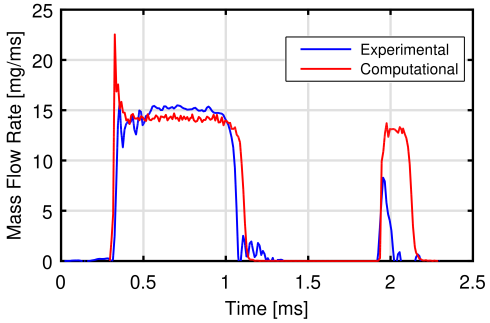

Figure 6.41: Injection rate validation for multiple injection strategy for the Spray G injector under SG-M1 ECN operating conditions.

On the other hand, focusing attention only on the main injection reveals that the opening slope perfectly captures the trend and produces a more pronounced overshoot than the single injection case. This latter phenomenon is due to the fact that the needle lift of the multiple injection case has a more pronounced initial overshoot, which is also transferred to the injection rate profile. Another noteworthy fact is the discrepancy in the duration of the injection, which makes the computational closure later than the experimental one. First of all, the lift profile adopted for the simulations does not correspond to the one presented in [12], on which the corresponding results are supposed to be based and taken to conduct the computational comparison and validation. Experimentally, shown in the work of Vaquerizo, D. [12], there are the three possible current outputs of the ECU which produce different outcome profiles. The main changes are found in the intensity used to carry out the opening of the injector, while the ET remains the same. In the experimental work, three different boosters are used: high, medium and low, observing how all of them produce the same needle opening, but differ in the needle closure. Comparison of Figure 6.41 indicates is that the booster adopted for the measurement of the needle lift profile and the one used to obtain the injection rate profiles are different. This clearly makes the needle closure differ between experimental and computational scenarios. Leaving this aside, the results obtained are similar to those present in the single injection.

Finally, and perhaps the most interesting part of this study, is the modeling corresponding to the post-injection. The first remarkable detail is that, under the multi-injection strategy, the needle lift associated to the post-injection of 186 µs takes the value of 31 µm of lift, which is much higher than the needle opening generated by a single injection with the same ET which lifts only 4 µm. This value is even greater than the lift associated with a single injection

of 200 µs of ET (maximum lift of 13 µm) or 220 µs (25 µm of maximum opening) [12]. This behavior may be due to the needle moving differently in the dynamic response than in the static response due to the close time between the main event and post-injection. It is also probably related to the fuel pressure wave just after the main injection event. The pressure may fluctuate significantly after the injection event and may be substantially lower at the time of the post-injection event which may change the lift induced by the command [12]. On the other side, another noticeable fact is the large difference in both the shape and values of the injection rate for post-injection. It is intriguing that the main injection generates such close results between simulations and experiments and that, under the same methodologies in both cases, the post-injection behavior is not adequately captured. The computational results are governed by the definition of the lifting profile leaving aside effects that may occur on the rail or interior ducts of the injector, for example. This means that the simulations faithfully reproduce the expected behavior based on a specific needle movement. The dwell time between injections is large enough to avoid influences of one injection on the next. In order to ensure that the approach is computationally adequate and the mass flow rate associated with the defined needle lift is predicted, a stationary simulation is carried out with the needle positioned at 31 µm. The mass flow rate obtained is 12.59 g/s while the one reached at a specific point of the stationary part of the post-injection is around 13 g/s with a minimum difference of 3%. Furthermore, based on the only result published in the literature, to the best of the author's knowledge, Figure 6.42b, the computational result shown in the present Thesis accurately reproduces the post-injection duration as well as the value reached in the stationary part. It is true that these other experiments also present an overshoot in the injection rate profile of the post-injection that is not reproduced by the simulations, a fact that may be attributed to a discrepancy in the electrical signal. Accordingly, it could be stated that the computational data and both the methodology and the model employed faithfully reproduce the flow behavior in the in- and near- region during the injection process under multiple injection conditions.

Nevertheless, none of the above explanations justify the behavior observed experimentally and which generates the large discrepancy with computational results (Figure 6.41). Therefore, in order to find a justification, the image in Figure 6.42a corresponding to the study of the behavior of post-injections with different ET in the post-injection carried out and presented by Vaquerizo, D. [12] has been analyzed. It is observed how the injection rate is modified, lengthened and increased, as the post-injection ET is higher. However, there is a large difference between the ET of 186 µs with the ET of 240 µs that is not

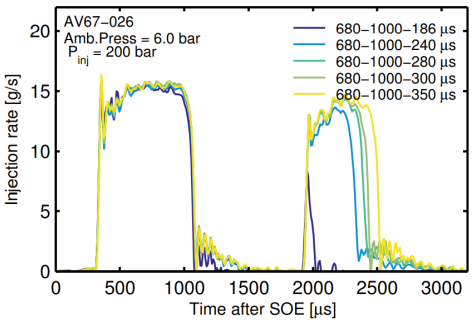

(a) Exp. results [12]

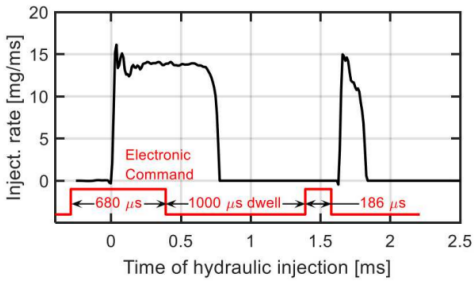

(b) Exp. results [34]

Figure 6.42: Experimental results of ECN's multi-injection G-M1 operating condition provided by various experimental sources [12, 34].

perceived in the other cases even when the variation in the ET is of the same order. The justifications given throughout the document [12] are related to the pressure wave dynamics affecting the second injection. In addition, the author attributes the difference in the needle lift and injection rate between single and multiple injection to the behavior related to the injector solenoid retaining charge after the first injection, which would make the energization at the second command considerably faster and therefore the needle takes less time to open. However, for low energizing times the solenoid does not appear to retain enough energy to adequately capture the expected behavior. It is clear that this behavior cannot be attributed to a specific fact alone, but that several factors may be influencing the result. Nonetheless, it is obvious that the behavior at low ET has a high uncertainty and, therefore, it is recommended that the experimental community invests effort in studying what is influencing the data obtained.

To summarize, the computational results have been successfully validated based on previous experience gained during the single injection studies. Furthermore, the observed post-injection behavior, although differing from the experimental data available in the department, is in good agreement with that published in the work of Sphicas et al. [34]. This divergence between experimental results leads to believe that the department's experimental techniques, due to the high difficulty and uncertainty involved, are not adequately capturing the behavior of internal flow in multiple injections under low ET, therefore, further research in this field is suggested.

Once the model developed to study the behavior of the internal flow under multiple injection conditions has been validated, it is interesting to observe

the phenomena that take place in the critical phases of needle opening and closing. Moreover, this is the perfect scenario to carry out this study because of the application of the sealing in the initial and final instants of the injection in order to replicate as realistically as possible the needle closure. GDI injectors have a tendency to generate cavitation in the needle seat during the low lift periods of the needle's transient motion. The prolonged duration of this effect has adverse effects being a major contributor to injector failures, such as abrasion and degradation, in the needle-seat region [35]. Figure 6.43 reflects the volumetric fraction of vapor fuel instants after the beginning of the injection and instants before the closing in both injections, main and pilot. It can be clearly seen how the cavitation phenomenon is generated in the needle seat, which seems to be larger in the main injection because, perhaps, the velocity gradients and the existing pressure difference is greater due to the lack of a previous injection that influences the performance. The cavitation generated in the sac disappears as the needle rises and so the pressure drop decreases.

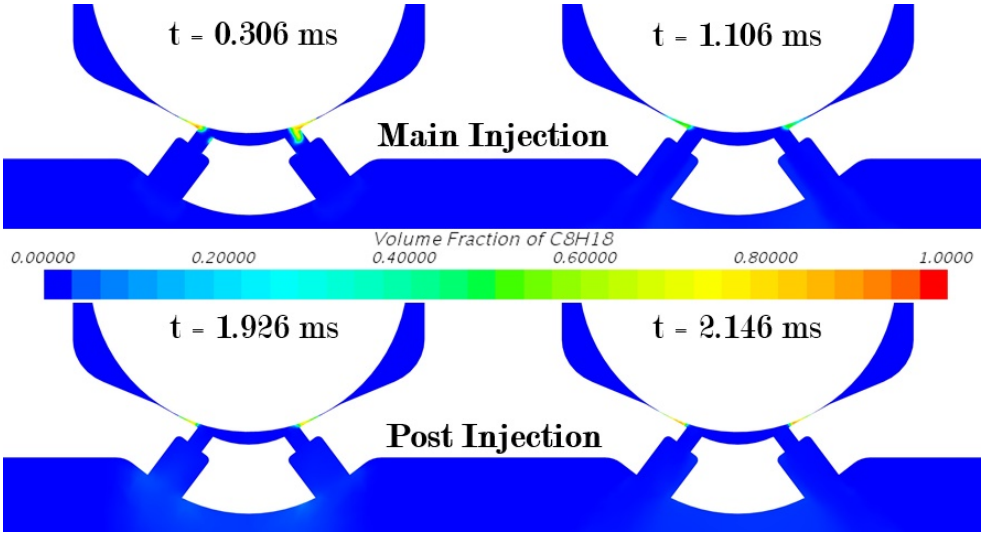

Figure 6.43: Fuel vapor volume fraction in the first ms at the start of main and post injection as well as last ms at the end of the injection in both cases, main and post, for the Spray G injector under G-M1 operating condition.

It is also interesting to explain that in this type of GDI injectors the flow tends to detach from the wall with no possibility of subsequent reattached and giving rise to an entry of air from the discharge chamber inside the orifices. This effect is known by the name of hydraulic flip. The phenomenon

is typically analyzed along with cavitation, however, this particular injector does not have a tendency to cavitate under the defined operating range. This statement can be demonstrated from the calculation of the cavitation number defined by Equation 6.2, explained more in detail in [36].

$$\sigma_c = C_a^2 \left[\frac{P_{amb} - P_v}{P_{inj}} + \frac{\lambda L}{D} + 1 \right] \tag{6.2}$$

being C_a the contraction/area coefficient, P_{amb} the ambient pressure, P_v the vapor saturation pressure of the fuel, P_{inj} the injection pressure, λ the friction coefficient, L the nozzle hole length, and D the nozzle hole diameter. The calculation yields a value of 0.6 which, according to Pratama et al. [32], is in the range corresponding to the occurrence of hydraulic flip. The cavitation range is defined between 0.72 and 1 (above 1 would be the non-cavitating condition). The increase or decrease in injection pressure and needle lift hardly changes the cavitation number and, therefore, hydraulic flip should appear during all the operation range. However, the occurrence of this phenomenon also depends to a large extent on the internal features of the orifices, their inlet and outlet radii and their inclination, characteristics that are not all taken into account when calculating the cavitation number. It should also be noted that the cavitation number used for this statement was initially developed for a model nozzle but its accuracy in commercial ones was validated [32]. In addition, it is important to mention that other definitions of the cavitation number are available but most of them do not take into account the effect of the nozzle geometry, which makes it difficult to determine the cavitation regime.

6.6.4.3 Pilot injections analysis

In literature [37], it is indicated that, when the fuel injection is too early, the possibilities of wall impingement of fuel spray and wetted wall are increased, but when the injection timing is too late, the fuel-air mixing time is shortened. Meanwhile, a study by Yang and Anderson [38] demonstrated that fuel injection timing during the intake stroke improves volumetric efficiency, however, a retarded injection timing during the compression stroke reduces knock tendency. As a result, double injection is proposed as a compromise for the two competing requirements, and can increase the full load torque output of the engine.

Multiple injection or split injections can be divided into two groups, pilot injections which take place before the main injection and post injections, the

ones analyzed earlier, which operate after the main injection. Pilot injections are the focus of this section. In the case of direct gasoline injection, a pilot injection allows to generate very favorable conditions of pressure and temperature in the cylinder so that the combustion of the main injection is as stable and uniform as possible. In addition, this increase in the temperature in the combustion chamber occurs uniformly so that it avoids the formation of hot spots leading to knocking and thereby reducing engine noise. However, operating with pilot injections requires a precise optimization of them for each engine speed, since a poor performance of the pilot injections can lead to an increase in CO and HC emissions as well as soot and particulates [39]. Similar to the behavior of the main injection, on the one hand, a very early pilot injection increases the interaction of the jet and the walls, thus increasing emissions due to flame irregularities near the wall. On the other hand, an injection too close to the main injection does not enable proper jet atomization and mixing, resulting in incomplete combustion, increasing emissions accordingly. It must be taken into account that a too high mass injected in the pilot injection is associated with a further increase in emissions.

For this study, it is assumed that the methodology and the model used for the multiple injection research (Section 6.6.4.1) have been properly validated. The research has two main objectives: on the one hand to analyze the behavior of in- and near- nozzle flow under multiple injection strategies focusing on pilot injections, and on the other hand, as part of the development and validation process of the already known predictive methodology, to acquire the necessary results to use them as input parameters following the one-way coupling strategy and thus explore the behavior of the external flow under multiple injection conditions without the need of experimental data (Section 8.2.2).

In order to carry out the pilot injection study, a new strategy had to be developed to define the needle lift profiles. The reason for this is the lack of experimental data, as the ECN has only one multiple injection operating condition (G-M1). The complexity of the measurements, the time required for the experiments and the associated cost have meant that no lift profiles are available for other operating conditions where multiple injections are included. However, what is available and has been published in the work of Vaquerizo, D. [12] is the single injection lifting profiles for different ET. due to the lack of prior influence that can modify the patterns, the strategy followed in this section is to use the known lift profiles with different ET (180, 240 and 300 µs) together with the needle lift corresponding to the main injection of 680 µs (see Figure 6.44a). To define these injections, a constant time of 400 µs has been maintained between the beginning of the pilot injection and the beginning

of the main injection. According to the experimental definition, this would mean that in addition to varying the ET of the pilot injection, the dwell time between injections would also be varying between 220, 160 and 100 µs.

Figure 6.44b illustrates the injection rate results obtained from the developed strategy for the study of multiple injections. First of all, experimental mass flow rate data are not available for the same conditions, but the obtained data for similar operating conditions are presented in Figure 6.45. Focusing attention only on the computational data, highlight the absence of the characteristic overshoot that was present in Figure 6.41 corresponding to the main injection without previous influence. This is mainly due to the fact that the single injection starts with imposed initial conditions in which the existing gradients are more abrupt while the pilot makes the mixture present in the discharge chamber more homogeneous leading to a smoother behavior of the second injection. In fact, for the case in which the ET is small (180 µs) which has less influence on the chamber conditions due to its short duration, a small flow increase can still be visualized in the first instants of the main injection. Another feature to note is that no influence of the pilot injections on the main is observed. This is due to the imposed lifting profiles. The movement of the needle faithfully reproduces the imposed lifting law and if it does not have the influence of the pilot on the main, it will not be reproduced in the results either. The lack of needle lift profiles obtained from x-rays makes this phenomenon impossible to reproduce computationally.

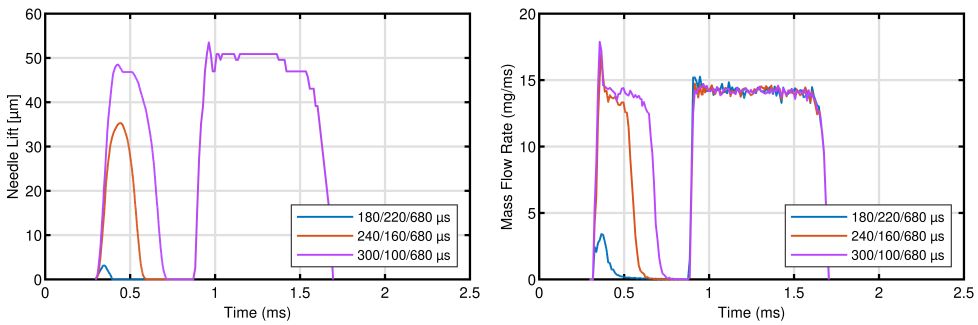

(a) Needle Lift (b) Injection rate

Figure 6.44: Computational strategy regarding the needle lift ROI profiles adopted for the study of pilot multiple injections together with the results obtained from the application of this model for Spray G injector.

Concentrating now the attention, on the pilot injections and comparing the computational results with the experimental data shown in Figure 6.45a,

it can be seen that the behavior of the longest duration pilot injection (300 µs) presents similar overshoot, ROI and duration to the experimental one. However, the other two pilot injections of lower ET are not correctly captured. As mentioned above, the experimental data at low ET have a high uncertainty and are highly dependent on boundary conditions. Another observation is that computationally the needle dynamic after needle closure, or in other words, the possible bounces that the needle provides, is ignored. This is due to the processing of the data obtained from the x-ray that does not allow to take into account such rebounds although from an inspection with the magnified images it is assured that the needle rebounds when it hits the seat, moving slowly up and down at a certain frequency [12].

Some other experimental effects shown in Figure 6.45a that are not captured by the computational results due to the definition of the lifting profiles. The main point to note is the influence of pilot injections on the main injection. First of all, a mismatch in the injection rate profile between different conditions is observed. The operating condition with a higher ET (300 µs) has a greater influence on the main injection, generating a longer injection rate profile and thus a higher total injected mass. If one compares the results of the main injection in terms of total injected mass, the condition with a pilot injection of 180 µs has 11.4 mg, those of 240 µs generate a total of 11.72 mg and finally the one corresponding to 300 µs obtains 12.53 mg. Therefore, in this particular case, the pilot injections influence the behavior of the main injection by increasing its total injected mass by about 10%. This influence is also noticed, as demonstrated in Figure 6.45b, when the ET of the pilot injection is kept fixed and the dwell time between injections is varied. To better reflect the effect of the pilot on the main, the onset of the main injection has been phased so that they can be compared with each other. In fact, the pilot injection remains unchanged and only the distance between injections changes. In this particular case, reducing the dwell time from 800 µs to 400 µs generates an increase in the total injected mass of 10% [12].

6.6.4.4 Post injections analysis

Under the same framework of multiple injections, this work also deals with the study of post-injections to understand their behavior but also to obtain the necessary data to study the performance of the external flow for the one-way coupling strategy without the need of experimental input parameters. Post-injections are characterized by the fact that they take place after injection in order to reduce exhaust emissions [40]. An injection at the final stage of the main combustion on the one hand, introduces an impulse which helps

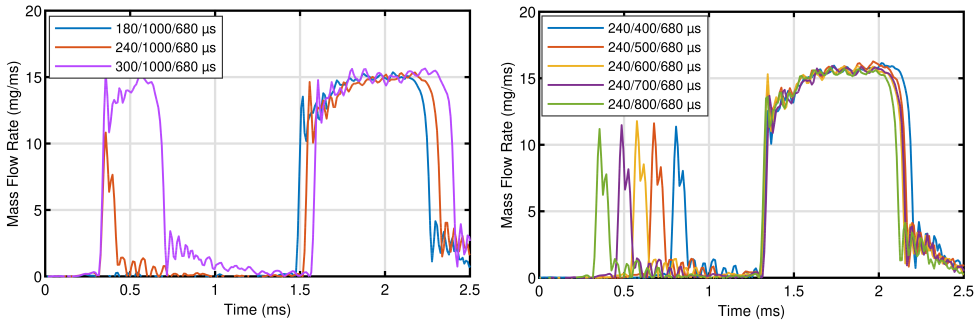

(a) Pilot ET variation

(b) Dwell time variation

Figure 6.45: Experimental results obtained from the variation of ET in the pilot injection as well as the influence of the variation in the dwell time between injections for Spray G injector.

to homogenize the mixture, bringing fresh oxygen to the soot from the main injection, causing the overall soot oxidation to improve [41]. It also provides an additional heat release that will favor the oxidation of soot and unburned hydrocarbons. These post-injections are necessary in the case of high EGR rates that reduce the oxygen concentration in the chamber, and disfavor soot oxidation [42].

To carry out this study, a strategy similar to the one explained in previous Section 6.6.4.3 has been used. Again, the lack of experimental data means that the lifting profiles have to be generated. In this case, it would not be entirely correct to define the post-injections with lifts according to a single injection because, as shown in Figure 6.39, the main injection influences the post-injection making the needle lift go from just a few microns to almost 30 µm. Therefore, what has been done is to use the same post injection lift profile and to vary the dwell time between the main injection and the post injection: 400 µs, 700 µs and 1000 µs. The needle lift profiles considered in the simulations are presented in Figure 6.46a. It is true that given the influence of the main on the post-injection when the dwell time is 1000 µs, it is to be expected that the effect when reducing the distance between injections is greater. This phenomenon is therefore being avoided since the main effect between injections is reflected in the needle lift profile, which due to the employed strategy is not taking into account these possible variations. However, since the objective is also to analyze the spray pattern under these conditions, this definition should be more than valid for that purpose. In addition, the study also shows the validity of the model to accurately simulate the in-

and near-nozzle flow behavior which could give more than realistic results by applying the correct lift profiles, experimentally observed.

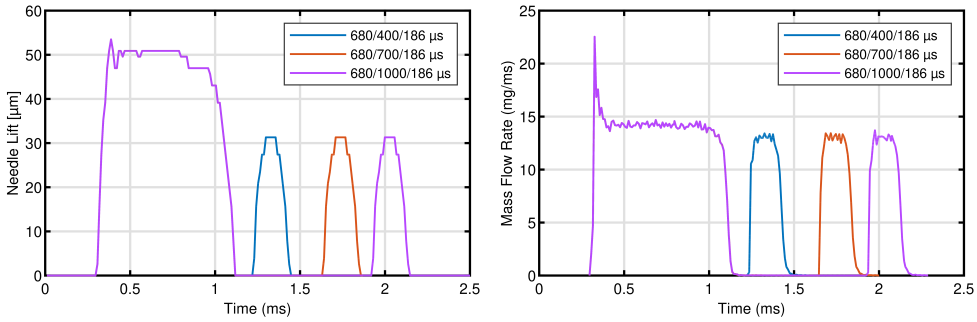

(a) Needle Lift (b) Injection rate

Figure 6.46: Computational strategy regarding the needle lift profiles adopted for the study of post multiple injections together with the results obtained from the application of this model for Spray G injector under SG like conditions.

The results obtained are shown in Figure 6.46b, where the same behavior is mainly observed in the three post-injections, differing only in the distance to the main injection. As already mentioned, no influence was expected to be noted between injections since the flow behavior depends mainly on the movement of the needle. Since in this case the behavior of the flow in terms of injection rate is not realistically observed, reference is made to the work of Vaquerizo, D. [12] who studied the influence of the main injection on the flow when the dwell time was varied. It was observed that the lower the dwell time, the greater influence of the post was, thus increasing notably the duration of the injection rate. However, the trend of the influence was observed to be nonlinear and the author himself defined the behavior as chaotic. Explanations for the observed behavior were sought by attributing it to effects on the rail pressure, the energizing signal, and the needle movement. However, further research is required in this area to understand in depth the behavior of the flow under both pilot and post multiple injection conditions.

6.6.5 High fidelity simulations. LES approach

After developing all the previous studies treating turbulence with RANS approach, it is time to go a step further in accuracy of the results and use LES approaches for turbulence treatment. For the purpose of creating and extending the computational benchmark, this study is again based on ECN's

multi-hole direct fuel injector, Spray G. Throughout these last years and as it has been seen in the previous sections of the document, as near nozzle region is concerned, most of the research has been devoted to quasi-steady main injection phase using a long pulse duration to avoid the dependency on the transient conditions and to get convergence statistics. The jet throughout the injection process is influenced by flow oscillations, large turbulent and vortex structures, shear stresses and cavitation resulting in fast spray atomization [43]. Since this phase plays an important role in understanding how flow evolves during needle closure, it remains an important topic of research. However, and although some hints have been presented in Section 6.6.4.2, little information is available on the transient opening phase in which the flow begins to open, in which the needle begins to develop, or the closing phase, which is affected by the phenomena that take place during injection. The first part of this study includes the study and comparison of two different LES sub-grid models in addition to the assessment of mesh quality to ensure the accuracy of the results, since studies with LES models do not follow standard patterns of mesh independence. Once the model that best captures the behavior of the injection is determined, the injector will be characterized in terms of mass flow rate and momentum flux. The results will be compared with experimental data available in the literature and with values obtained in previous work from RANS simulations (Section 6.6.2). The second part of this study will evaluate the deviation in the plume direction versus geometric angle (drill angle) and spray angle using a new in-house post-processing methodology described in Section 5.4.1.2.

The present study is carried out under the consideration of the Spray G geometry of generation 1 and the reference operating condition SG. Due to the high computational cost involved in this type of simulations, advantage has been taken of the symmetrical feature of this injector in the plane intersecting orifices 1-5 (see Figure 5.7a), and only half of the geometry has been considered for simulation. The research includes both the study of the transient process of injection, opening and closing of the needle, and the stationary part of it where the variation of the lift and wobble profile is at most 3 µm. The needle movement and wobble (only in one direction for being symmetrical) during this stage of the injector operation have been introduced from the complete lift profile (Figure 5.7b). The modeling of turbulence from LES approximations is highly dependent on cell size. For this reason, the present study uses a fixed mesh whose sizes have been based on the mesh quality criteria explained in the next Section 6.6.5.1. The mesh selected for this approach, as illustrated in Figure 5.17, is a cartesian grid with hexahedral elements. The use of fixed

embedding allows a minimum size of 4.22 µm to be defined in the seat from a base of 135 µm.

6.6.5.1 LES quality assessment

The grid resolution and the modeling of the small scales affect the turbulent resolution in scale-resolved large eddy simulations (LES). This type of models are characterized by modeling part of the turbulence flow energy which means that the local grid size and the numerical method employed have a clear influence on the degree of contribution of the model. The grid resolution is an important factor to consider because it not only affects the numerical discretization error but also the subgrid scale model contribution as mentioned above. The application of these models requires a quality assessment to ensure enough resolution of the turbulent flow energy and precise LES results [44]. In order to quantify the reliability of the LES model implemented, several authors defined indexes of quality in terms of both numerical and model accuracy [45, 46]. According to [47] a reliable LES requires that the modeled turbulent kinetic energy (k_{sgs}) be less than 20 of the total turbulent energy ($k_{sgs} + k_{res}$), in other words $\frac{k_{sgs}}{k_{sgs}+k_{res}} < 0.2$. Nevertheless, as mentioned in [48] and [49] the knowledge of k_{res} for this work in the case of a moving needle injection can only be obtained by repeating the simulation several times, which cannot be computationally afforded. Although these are indicative point measurements that are not particularly accurate for anisotropic turbulence, another option is to use metrics based on the turbulence resolution length scale such as the LSR metric; see for example [50] and its application by Battistoni et al. [48] to a moving needle injection. For the current work, and with the objective of working consistently on both transient and stationary parts, the criterion selected to determine the quality of the model will be one of the most widespread on the basis of viscosity defined by [51].

- *Index based on the viscosity (IQ_υ)*: this criterion evaluates the contribution relative to the laminar viscosity (υ), the sub-grid viscosity (υ_{sgs}) and the numerical viscosity (υ_{num}) according to Equation 6.3. Celik et al. [51] suggested that IQ_υ values between 0.75 and 0.85 are acceptable, which means at least 75% of the turbulent kinetic energy is resolved, because that can ensure appropriate LES quality for High-Reynolds-number flows.

$$IQ_\upsilon = \frac{1}{1 + \alpha_\upsilon (\frac{s^*}{(1-s^*)})^n} \tag{6.3}$$

where s^*, always lower than 1, can be defined by Equation 6.4.

$$s^* = \frac{\langle \upsilon_t \rangle + \langle \upsilon_{num} \rangle}{\langle \upsilon_t \rangle + \langle \upsilon_{num} \rangle + \langle \upsilon \rangle} \tag{6.4}$$

The two constants which appear in Equation 6.3 have been calibrated at $\alpha_\upsilon = 0.05$ and $n = 0.53$ based on DNS outcomes [52].

For the comparison between sub-models, only the steady part of the injection has been studied, in other words, time ranges from 0.15 to 0.51 ms aSOI (360 µm). In the analysis, duration of 19 residence times with an acquisition frequency of 10^6Hz have been employed. Figure 6.47 presents the results obtained from the mesh quality analysis for the two sub-grid models by averaging the variables during the studied time. It can be observed how the Dynamic Structure model has a much lower mesh quality, being well below the ranges established as optimal (75% of the energy resolved). On the contrary and mentioning its capacity of favoring the analysis of coarser meshes, the sub-grid Viscous One-Equation model meets the quality criteria stipulated by Celik et al. [51]. Apart from the quality index, the difference between models in the response with respect to the computational cost was analyzed. Although both models resolve an additional equation to compute the sub-grid kinetic energy, the Viscous One-Equation model, that uses the turbulent viscosity to model the sub-grid tensor, has 20% higher CPU cost than the Dynamic Structure approach, 48141 CPU-h compared to 39917 CPU-h.

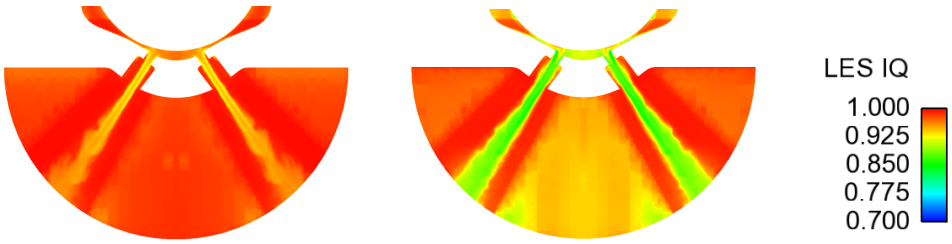

(a) Viscous One-Equation (b) Dynamic Structure

Figure 6.47: LES quality assessment based on the viscosity evaluated for two different sub-grid LES models for Spray G injector.

Once the turbulence model that best suits the study of the injection process has been chosen, results that will be justified in Section 6.6.5.3, the study and validation of the mesh as well as its associated quality is extended to

the transient phases. The present case has been divided into three different parts when simulating: opening phase from 0 to 0.15 ms, steady phase from 0.15 to 0.51 ms and closing phase from 0.51 to 0.8 ms. The quality index for the steady part of the simulation (from 0.15 to 0.51 ms) has been analyzed from time-averaged variables. By contrast, the opening and closing phases cannot be averaged over time. For this reason, the quality index has been extracted at each time-step for the transient phases of the simulation, opening and closing. In the current study, several simulations have been carried out with the aim of comparing the results with those obtained by RANS approaches. Therefore, the accuracy of the previous assumption could also be verified. Results obtained from the computed IQ_v criterion affirm that the index requirement is globally satisfied inside the injector and the discharge chamber. Figure 6.48 graphically shows the results achieved and prove the conclusion extracted, providing acceptable critical index values that evidence the reliability and quality of the simulation. In this particular case and unlike the previous study, the label has been adapted to the range 0.7 to 1 to observe more clearly the fulfillment of the quality premise in the whole computational domain.

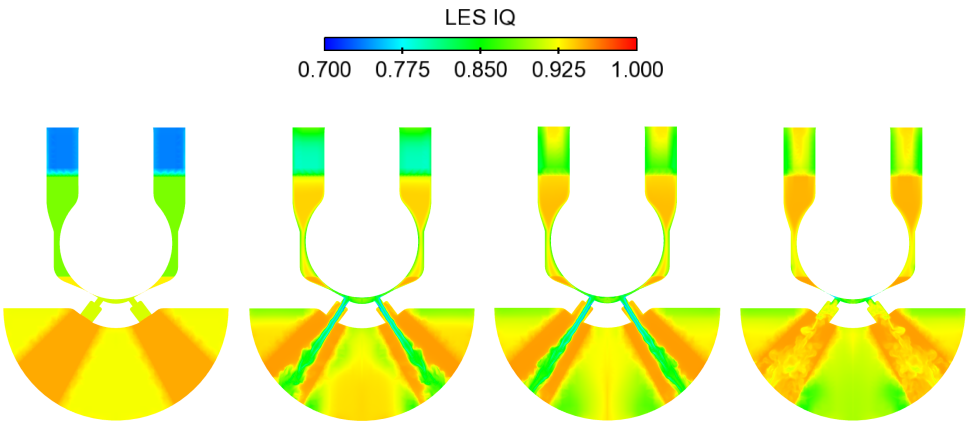

(a) t = 0 ms (b) t = 0.15 ms (c) t = 0.51 ms (d) t = 0.80 ms

Figure 6.48: LES quality assessment using an index based on the viscosity evaluated in several time-steps for Spray G injector under SG reference condition.

6.6.5.2 LES sub-grid model comparison

This section summarizes the results obtained from the comparison between sub-grid LES models during steady state injection and validate them with ex-

perimental data from previous studies carried out at CMT-Motores Térmicos. Regarding to the mass flow results, in the stationary part of the injection, the changes in the values are minor and mainly due to the presence of vortices inside the counter-bore. Although the quality of the mesh of both approached was different and even the Dynamic Structure model was far below the selected criterion, Figure 6.49 displays similar trends. If zoomed in as shown in the image, a slight difference between models is visible at certain instants of the stationary, leading to a 2% variance (Table 6.25). Quality compliance makes the Vicous One-Equation model more reliable. Nevertheless, these results tend to overpredict the experimental results by around 9%. In order to explain this effect, the time-averaged mass flow rate of each orifice has been calculated and presented in Table 6.25. The experimental stationary ROI value is 14.71 g/s, assuming 1.84 g/s for each hole. Comparing this result with that presented in the table, it is observed minimal differences between experimental and computational in orifices 2, 3 and 4, with the greatest discrepancy in orifices 1 and 5. These are the holes where symmetry has been applied which means that the flow condition is not correctly capturing the behavior of the fluid, resulting in a higher mass flow rate and therefore an overestimation of the results.

With reference to momentum flux, displayed in Table 6.25, an overestimation of about 6% is also found. Due to the computational discharge volume is 6 mm in diameter, the momentum measurements have been made in a plane at 1 mm while the experimental data are collected at 3 mm. Although momentum rate is supposed to be conserved, previous work by this group [10] has shown how the data acquisition distance affected the results. This fact coupled with the symmetry condition may be the main reasons for the, though small, disparity in results.

The root-mean-square (RMS) velocity is one of the leading indicators of the resolved energy and is expressed by the use of the resolved instantaneous velocity vector $\tilde{u}$ and its time-averaged value noted $< \tilde{u} >$: $\tilde{u}'_{rms} = \sqrt{< \tilde{u}\tilde{u} > - < \tilde{u} >^2}$. Figure 6.50 represents the $\tilde{u}'_{rms}$ comparison between subgrid models. The central part of the spray near the nozzle does not indicate the presence of $\tilde{u}'_{rms}$ and refers to the area where the liquid remains intact. As the flux moves away from the orifice outlet, the liquid mixes with the ambient gas due to turbulent phenomena which in turn increase the mixing and atomization of the spray. In the Dynamic Structure approach, the spray begins to interact with the environment a few millimeters after the orifice exit, whereas for the Viscous One-Equation model this intact part extends further downstream to near the outlet. The $\tilde{u}'_{rms}$ shows higher levels of spatially located velocity fluctuations in areas which are characterized by higher levels

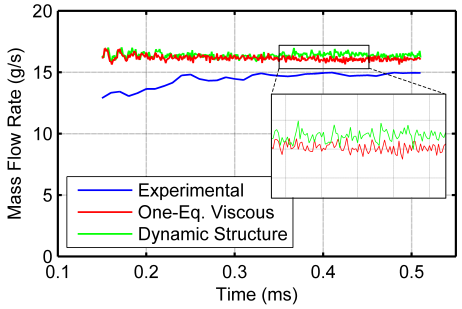

Figure 6.49: Mass flow rate predictions for transient simulation compared experimental measurements for Spray G injector under SG reference condition.

	ROI (g/s)	ROM (N)
Viscous One-Eq.	16.07 ± 0.14	2.80 ± 0.061
Dynamic Struc.	16.40 ± 0.19	2.87 ± 0.093
Experimental	14.78 ± 0.16	2.63 ± 0.078

ROI (g/s)	Dynamic Struc.	Viscous One-Eq.
Hole 1	2.14 ± 0.076	2.27 ± 0.056
Hole 2	2.04 ± 0.045	1.96 ± 0.048
Hole 3	2.00 ± 0.068	1.92 ± 0.065
Hole 4	2.04 ± 0.040	1.95 ± 0.041
Hole 5	2.10 ± 0.062	2.14 ± 0.057

Table 6.25: Time-averaged measurements and standard deviation. ROI and ROM results in both LES apporaches compared to experimental data for Spray G injector under SG reference condition.

of small-scale turbulence and where the liquid-vapor mixture is noticeable. The Viscous One-Equation has larger oscillations compared to the Dynamic Structure generating more mixing and resolving a larger amount of energy in the inner part of the spray.

Figure 6.51 provides the results obtained from the calculation of the cone angle and plume direction for both sub-grid models. Both approaches, Viscous One-Equation and Dynamic Structure, show a slight variability of the values for hole 3 while the other two, holes 2 and 4, have more differences. On the one hand, the orientation of the mesh, since hole 3 is oriented with the cartesian mesh, could influence the results as seen in other works [7]. On the other hand, the studied geometry has 5 bumps and 8 orifices, so the flow distribution is not the same in all of them. Therefore, the turbulence generated upstream of the injector may affect some directions more than others. The difference between orifices can also be seen in the direction of the spray. Thus, orifice 3 is deflected inwards, deviating from the geometrical axis of the orifice, while the other orifices show a

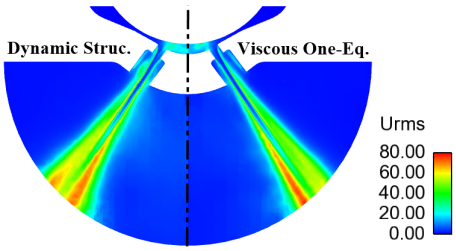

Figure 6.50: $\tilde{u}'_{rms}$ comparison between sub-grid models in a vertical cut-plane along holes 3-7 for Spray G injector under SG reference condition.

minimal deviation. This deflection effect is displayed in Figure 5.24, where the counter-bore of orifice 2 (on the left) is practically full of liquid while orifice 3 (on the right) is largely occupied by non-condensable gas. This recirculation of air is the main reason of the deflection of the spray, causing it to deviate from the geometric axis of the orifice.

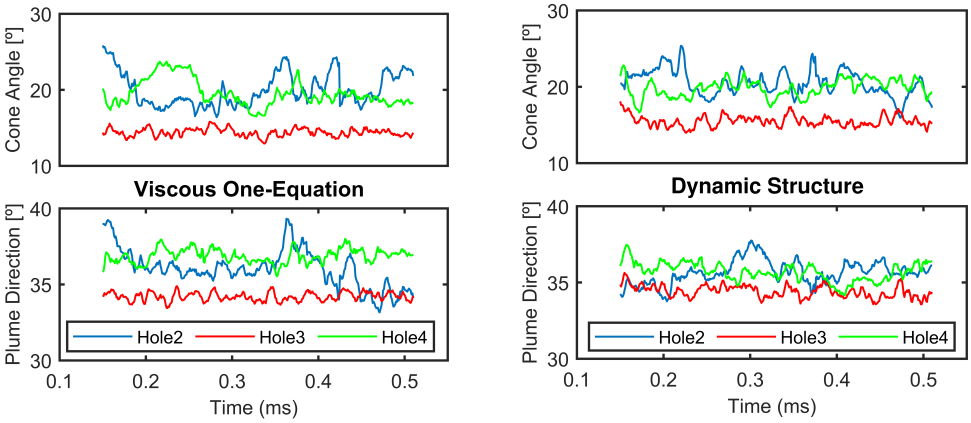

Figure 6.51: Cone angle and plume direction calculation for both sub-grid models for Spray G injector under SG reference condition.

The time-averaged and standard deviation cone angle and plume direction for both sub-grid models studied are plotted in Table 6.26. The results in both models are quite similar. A narrower spray is seen in hole 3 while holes 2 and 4 are around 20° of cone. With respect to the plume direction, a small deviation of approximately 1-1.5° is observed in holes 2 and 4 while hole 3, in both approaches, has more significant deviation. Predicted trends from both approaches estimate the liquid plume direction and cone angle close to literature values.

	Viscous One-Eq.		Dynamic Struc.	
	Cone Angle (°)	Plume Direction (°)	Cone Angle (°)	Plume Direction (°)
Hole 2	20.03 ± 2.21	36.04 ± 1.23	20.53 ± 1.69	35.66 ± 0.67
Hole 3	14.41 ± 0.52	34.21 ± 0.28	15.50 ± 0.73	34.42 ± 0.34
Hole 4	19.56 ± 1.73	36.88 ± 0.46	19.83 ± 1.16	35.70 ± 0.53
Literature results [2, 18]	Cone angle (°) ≈ 20		Plume Direction (°) ≈ 34	

Table 6.26: Time-averaged measurements and standard deviation for the cone angle and plume direction for Spray G injector under SG reference condition.

As a summary of the above analysis, it can be said that both models, Dynamic Structure and Viscous One-Equation, add a transport equation for the sub-grid kinetic energy but the calculation of the sub-grid stress tensor is different. While the Viscous One-Equation model uses the turbulent viscosity to model the sub-grid stress tensor, the Dynamic Structure approach models the sub-grid stress tensor as a function of the sub-grid turbulent kinetic energy. As far as macroscopic parameters are concerned, it can be said that similar results were observed for rate of injection (ROI) and rate of momentum (ROM) variables in both approaches, although the Dynamic Structure tends to provide slightly higher results than the Viscous One-Equation model, namely 2%. Looking at mixing and atomization, both models addressed similar values, so neither stands out from the other. Finally, analyzing the quality of the mesh, the Dynamic Structure model, although not far away, falls below the limits established to ensure the accuracy of the results, suggesting the need for further refinement. Therefore, for a specific meshing strategy and based on the obtained results, the One-Equation Viscosity sub-grid model is preferred as it minimizes the computational cost under the same accuracy in the results and, consequently, it has been the model chosen for this study.

6.6.5.3 Transient nozzle flow analysis using LES

Once the preliminary analysis of the comparative studies of sub-grid LES models has been carried out and the most suitable one for this particular application has been chosen, it is proceeded to analyze the behavior of the in- and near-nozzle flow, focusing now mainly on the transient phases of the injection, opening and closing. The results obtained will be compared and validated with experimental data carried out in CMT-Motores Térmicos and already published in the literature [12] as well as with data obtained from this study treating turbulence with RANS approaches.

As it is previously mentioned, this analysis has been conducted in three different phases: opening, stationary and closing (see Figure 5.7b). Both the opening and closing transients of the needle are considered to be rapid and time dependent. Since the approach used to cope with turbulence is LES, a sample size study has been carried out to determine how many simulations would be needed to get statistically significant data so results can be compared to those obtained from RANS approaches. The sample size is base in the following equation: $n = \left(\frac{Z\sigma}{e}\right)^2$ where Z is the statistical confidence level, σ the standard deviation and e the assumed error. For this analysis a statistical confidence level of 95% has been considered while the error used for

the calculation is limited to 5% of the average variable analyzed. The present study has been carried out for two macroscopic variables such as ROI and ROM. The obtained conclusions are the same for both variables, so only the mass flow rate is reported.

Figure 6.52 shows the results obtained from the sample size and relates them to the rate of injection for the times involved during the needle opening process. Until 0.2 ms aSOI, it can be seen that there is an area where the sample size shows its maximum. This is due to the low values of mass flow rate and the similarity between simulations, which results in small standard deviation and, above all, low assumed error. After that, when ROI is not close to zero, the sample size is reduced having a maximum value of 3. This means that the sample size required to obtain accurate results for ROI does not exceed 3 simulations. It is also worth mentioning that the existing standard deviation in the ROI and ROM variables between simulations has been calculated. The difference is so small that it can be assumed that a single simulation is sufficient if the study is focused on macroscopic variables.

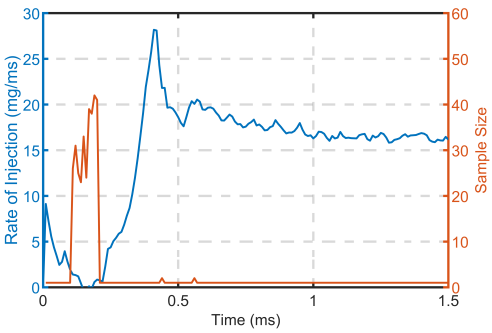

Figure 6.52: Sample size related to the injection rate during the needle opening process for Spray G injector under SG reference condition.

In order for this statement to take strength, the fluctuations of the fluid were analyzed using the root mean square velocity variable ($\tilde{u}'_{rms}$). The study has been carried out in the opening phase and the results obtained for a time close to half of the needle opening, t = 0.075 ms. The computation of the studied parameter has been performed using 2, 3 and 4 simulations. Figure 6.53 depicts the values of the variable $\tilde{u}'_{rms}$ for the three mentioned cases in a vertical plane over orifice 3 ans in a horizontal plane at 1 mm from the tip of the injector. It can be immediately noticed that the difference between the results obtained with 2 and 3 simulations is significant, both in the shape of the variable and in the values of the same. However, if the results obtained with 3 and 4 simulations are compared, the difference is minimal.

In addition, to make the study more precise, a quantitative comparison of the $\tilde{u}'_{rms}$ obtained in the plane at 1 mm from the tip of the injector has been carried out for the three cases considered. To this end, the variable has been

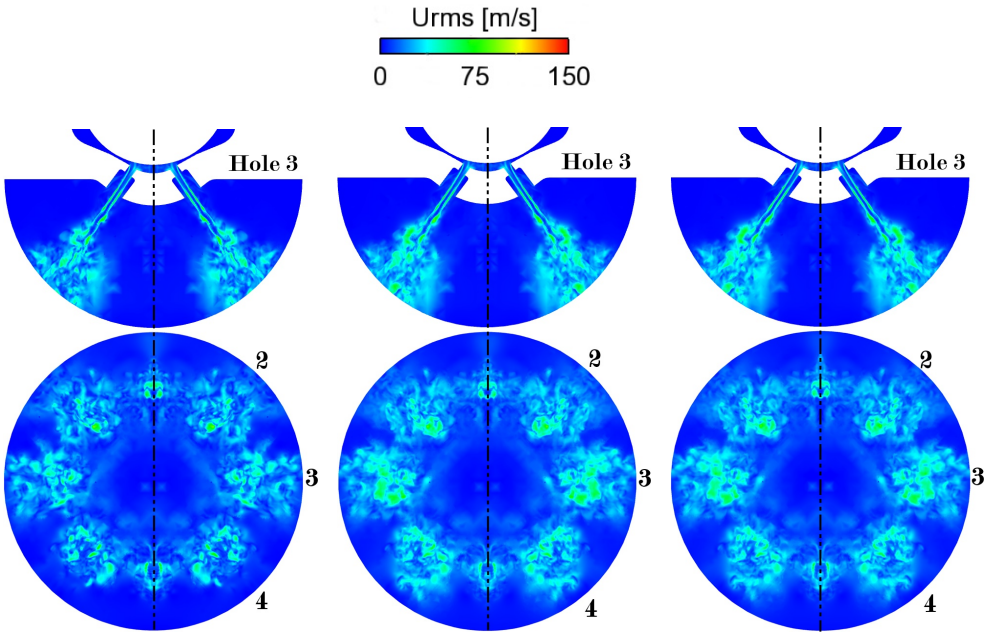

(a) 2 simulations (b) 3 simulations (c) 4 simulations

Figure 6.53: Averaged $\tilde{u}'_{rms}$ representation in a vertical cut plane through orifice 3 and in a plane at 1 mm from the tip of the injector at t = 0.075 ms for Spray G injector under SG reference condition.

extracted in lines starting at the center of the plane and crossing the jets in the middle, or, in other words, in the lines resulting from intersecting the vertical planes that cut each of the orifices with the horizontal plane at 1 mm. This research has been conducted for all orifices so the conclusions drawn can be considered similar for all of them. Figure 6.54 summarizes the data obtained from this analysis. As previously observed, the fluctuations captured with 2 simulations differ greatly from those obtained with 3 simulations. However, comparing the root mean square velocity obtained from 3 simulations with that of 4 simulations, it is noticed that the trends are the same, perfectly capturing the fluctuations of the variable for the three different sprays. It is true that in some specific points, the value of the variable differs from one case to another, but in no case is it greater than 8%. This statement again corroborates the obtained results from the sample size study, 3 simulations are enough to provide accurate and comparable results with data available in the literature if a opening/closing transient phase study is to be carried out beyond macroscopic variables.

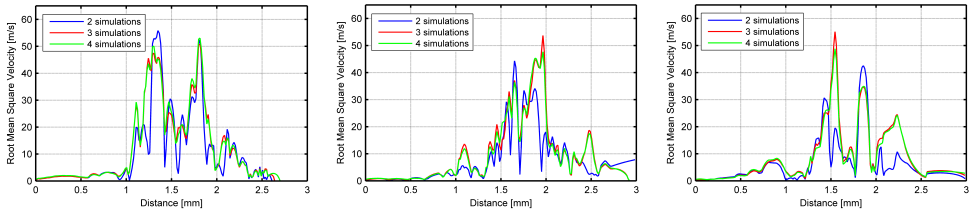

(a) Hole 2 (b) Hole 3 (c) Hole 4

Figure 6.54: $\tilde{u}'_{rms}$ comparison between different sample sizes using 2, 3 and 4 simulations at t = 0.075 ms for Spray G injector under SG reference condition.

Once the sample size required for the comparison has been analyzed, the results are validated with those obtained by means of RANS approximations and from experimental measurements [5, 10] in order to prove the accuracy of the computational simulations when the needle is in motion. Figure 6.55 displays the obtained results from this comparison for both rate of injection and rate of momentum. It is important to mention that the shaded area in the experimental data corresponds to the equivalent of the standard deviation (STD) obtained from carrying out 50 repetitions of the same measurement. In the early time of injection, Figure 6.55a illustrates that the computational results represent a faster opening for both approaches while the closing seems to be similar even in the LES results where a higher mass flow is obtained. It is observed that in both approaches, RANS and LES, the quasi-steady state is reached at 0.1 ms aSOI of injection. This quasi-steady condition is achieved before the needle lift reaches its maximum. It is proven in Section 6.5.4 of the steady state analysis that the higher the needle lift, the higher the mass flow rate. However, for the transient cases with a moving needle, it is observed that the mass flow reaches its maximum before the needle opens completely. This could be explained by an effect of the chocking of the flow which takes time to attenuate mainly due to the very low needle lift values. This phenomenon has also been observed by other researchers and reflected in articles such as the one published by Yue et al. [49].

As commented in Section 5.3.4, the injection pressure was set as a constant value and the minimum needle lift was settled at 2 µm. This justifies the effect that can be seen at the beginning of the simulation on the mass flow rate. At the opening phase, an expansion wave travels upstream of the injector nozzle which temporarily reduces the injection pressure. The duration and intensity of this wave depends not only on the fluid but also on the geometry of the injector. As in other studies [49], the effect is appreciable in this particular

injector for refined meshes and not for thicker ones. This outcome can be mitigated by the use of pressure ramps that evolve from ambient pressure to injection pressure as demonstrated in previous research of this group [53]. On the other hand, the experimental overshoot, which arises when the needle lift reaches it maximum, is well reproduced by both computational results being more pronounced in the case of the LES model.

During the period of time in which the needle lift remains in the steady lift, no significant variations are observed in the ROI results obtained with LES approaches due to the presence of vortices inside the counter-bore. Regarding the comparison between the ROI profiles, the estimation offered by the RANS model adjusts quite well to the experimental curve while the LES values overpredicts the results. In order to explain it, the time-averaged mass flow has been calculated in each of the holes following the present numbering in the Figure 5.7a. Table 6.27 includes the results for the five compared holes. Small differences are observed in holes 2, 3 and 4 between both approaches but the main differences are found in holes 1 and 5 for the reasons explained in Section 6.6.5.2 above. It is worth noting that, despite observing this behavior, the effect of the symmetry boundary condition on holes 2, 3 and 4 analyzed in the paper is expected to be small [49]. Table 6.27 also reflects the experimental measured mass flow rate at standard Spray G conditions per orifice at steady state, which can be used to validate the present results. This value has been obtained by splitting the total mass flow rate result presented in Table 6.28 between the 8 existing orifices, which eliminates the possible and existing variation between orifices due to the asymmetry of the geometry upstream of the injector [16]. For the reasons mentioned above, only orifices 2, 3 and 4 will be taken into consideration. In the case of RANS simulations, the individual mass flow rate differences range between 2-4% while in the LES approach these discrepancies are between 4-6%. Both results obtained with RANS and LES approaches are considered reasonably good prediction taking into account the possible added experimental uncertainty.

After discussing the outcomes of the mass flow rate, Figure 6.55b shows the results for the momentum flux. As earlier mentioned, the computational results have been measured in the same way as the experimental data with the aim of being consistent. However, an overestimation of the momentum can be seen. For computational cases, the maximum distance is 1 mm since the discharge volume chosen for these analyses is 6 mm in diameter. For the experimental case, there is no limitation in the volume of discharge so that the momentum can be measured at various distances from the tip, taking as a reference the results at 2 mm for the comparison of this analysis. Theoretically, the momentum rate should be preserved, but some differences have been

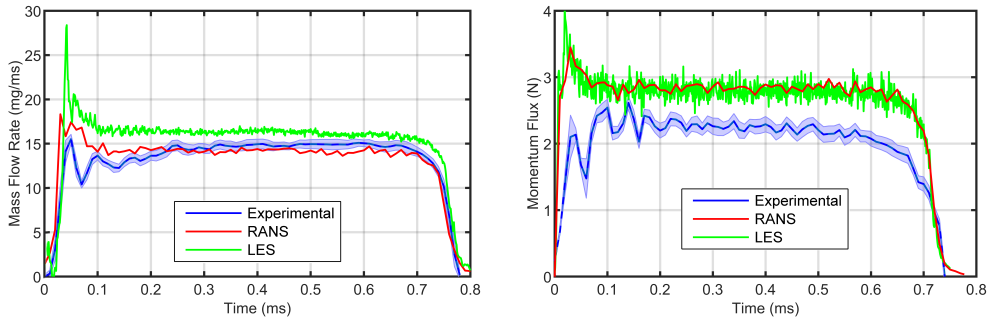

(a) ROI (b) ROM

Figure 6.55: Mass flow rate and momentum flux predictions for transient simulation compared with RANS solution and experimental measurements for Spray G injector under SG reference condition.

	RANS		LES	
	Time-Averaged [g/s]	STD [-]	Time-Averaged [g/s]	STD [-]
Hole 1	1.76	0.074	2.27	0.056
Hole 2	1.80	0.097	1.96	0.048
Hole 3	1.79	0.052	1.92	0.065
Hole 4	1.76	0.098	1.95	0.041
Hole 5	1.80	0.062	2.14	0.057
Experimental	1.84 ± 0.078 [g/s]			

Table 6.27: Holes mass flow rate comparison between RANS and LES approaches. Time-averaged measurements and standard deviation.

observed when this value is requested at different distances from the injector [10]. The variation in the data acquisition distance may be one of the reasons for the existing difference in the momentum flux values.

On the other hand, there are several uncertainties in the experimental momentum flux measurement. The first of these is related to the angle of impact of the sprays on the target, which must be known in order to make a correction of the measurements. Although some studies have been based on the characterization of the Spray G liquid spray and the calculation of the spray angle [18], there are still some discrepancies in the literature. The other uncertainty is related to the air entrainment. The value in this configuration is unknown and unlikely to be perpendicular to the spray direction. This

effect would cause the value measured to be different than what it should be. The air could take away momentum in the injector axis to provide it in the perpendicular axis where it is not measured.

	ROI [g/s]	ROM [N]	C_d	C_m	C_v	C_a
Experimental	14.71	2.63	0.55	0.40	0.73	0.75
RANS	14.25	2.84	0.53	0.43	0.81	0.65
LES	16.15	2.80	0.60	0.42	0.70	0.86

Table 6.28: Comparison between experimental and computational nozzle flow coefficients in the steady state period for non-flashing condition.

The time average values of the rate of injection and the rate of momentum when the needle is completely open are used to compute the dimensionless nozzle flow coefficients described by [5]: the momentum coefficient (C_m), the discharge coefficient (C_d), the velocity coefficient (C_v) and the area coefficient (C_a). Table 6.28 summarizes the obtained results together with the steady state mass flow and momentum rates in order to evaluate the activity of the injectors in a steady state and to further validate the simulations.

The mass and momentum flow profiles (Figure 6.55) displayed differences compared to the experimental results. These same effects are noticed in Table 6.28. The existing overestimation in the LES models is transferred to the dimensionless coefficients, giving a higher discharge, momentum and area coefficients, then underestimating the velocity coefficient. High effective area leads to a reduction in effective velocity. This means that the flow detachment occurring in the orifice is underpredicted by the LES approach while the RANS model overestimates this phenomenon.

Once the macroscopic variables of mass flow and momentum flux as well as the non-dimensional coefficients which define the hydraulic behavior of the injector have been analyzed, the study of contours with different variables and vortex structures that make up the spray is carried out. Figure 6.56 displays in detail the area near the injector exit as well as the structures and behavior of the spray in the near-nozzle field. In Figure 6.56a, the variable α is represented by an isosurface where the dark part reflects the higher concentration of liquid. In the same figure, the liquid mass fraction and the lines corresponding to the magnitude of the velocity are shown as contours. These visible contours correspond to two planes that are perpendicular to each other and pass through the middle of the spray. The core of the spray remains intact at the exit of the counter-bore and, as the flow develops, it begins to

mix with the ambient gas. The most remarkable effect of this image is the existing interaction between sprays that can be seen in the upper part of the image. The plume-to-plume interaction in gasoline direct injectors has been and is currently widely studied due to the ability this effect has to change the shape of the spray as well as its characteristics and the atomization process [54]. In this specific simulation, the effect is noticeable when the needle is in its opening phase, in particular this image corresponds to 100 µm aSOI, and it is minimized when the needle opening evolves to a stationary state. Although the aim of this analysis is not to focus on the spray atomization process, it can be stated that adjacent sprays are necessary when the atomization phenomena that occur in this type of injectors are to be studied more in detail.

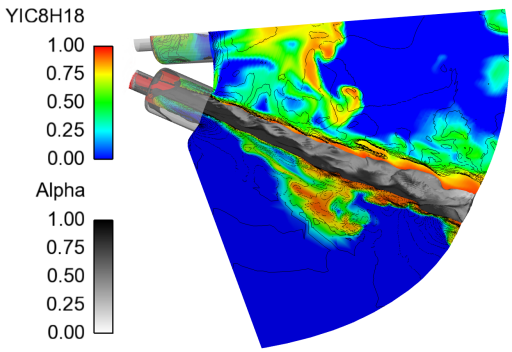

(a) Iso-surface of α joined to liquid mass fraction contours and velocity lines.

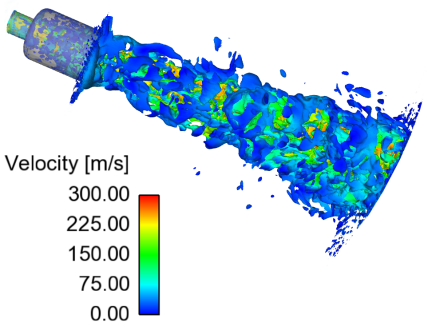

(b) Spray and vortex structures shown by the iso-surface of Q-criterion = -1E11 s^{-2} colored by velocity variable.

Figure 6.56: Close look at the near-nozzle region of the spray and vortex structures. Time = 100 µs aSOI for Spray G injector under SG reference condition.

Figure 6.56b present a closer look at the near-nozzle region of the spray and vortex structures shown by the Q-criterion iso-surface where the velocity has been plotted. The geometry used for this study is known as "nominal geometry" which has significantly different features from the real geometry. This geometry does not take into account the surface finish and defects so it has a prescribed smooth wall. Furthermore, the geometric characteristics of the hole, that is the diameter of the hole and the counter-bore as well as the length of the hole slightly differ from the real ones (Table 5.18). This may affect the atomization of the spray.

In the case of this nominal geometry, the first 3 millimeters downstream of the nozzle exit show that the core of the spray remains intact until the area closest to the outlet boundary where it seems to start breaking-up, corresponding to the so-called primary atomization. This indicates that due to the effect of the shape of the counter-bore geometry, the instabilities grow more slowly. The representation of the velocity together with the isosurfaces of the Q-criterion reflects how the drop in velocity coincides with the zones that are further away from the spray's core, which means the mixture of the liquid with the ambient gas and the beginning of the formation of structures that lead to the atomization of the spray. Vortices start to be generated at the entrance of the holes due to the deviation of the flow. These remain and continue to develop in the internal region, probably causing the formation of unstable structures and ligaments that later result in a primary atomization. This correlation effect between vortex structures and primary rupture was observed by [55] and [49], who report evidence of a vortex-driven primary breakup mechanism in diesel and gasoline injectors, respectively.

As part of the analysis of the stationary phase of the simulation, which corresponds to the moment when the needle is at its maximum opening, the liquid mass fraction has been averaged and compared with the root-mean-square (RMS) velocity ($\tilde{u}'_{rms}$). As mentioned above, one of the main characteristics of LES models is the ability to solve large turbulent scales. The root-mean-square velocity is directly related with the turbulence intensity and is the greatest indicator of the resolved energy in the domain. The resolved part of the energy is commonly represented from the turbulent kinetic energy (TKE) and may be deduced from the filtered velocity fluctuations as $k_{res} = \frac{1}{2}\tilde{u}'_{rms}\tilde{u}'_{rms}$. Figure 6.57 represents the time-averaged liquid mass fraction and the iso-surfaces corresponding to the $\tilde{u}'_{rms}$ in a cut-plane along holes 3-7. The central part of the spray near the nozzle outlet remains intact and therefore there are no signs of $\tilde{u}'_{rms}$. As the fluid moves away from the injector outlet, it is observed how the liquid mixes with the ambient gas producing turbulent phenomena which in turn increase the mixing and atomization of the spray. It is therefore affirmed and corroborated that root-mean-square velocity ($\tilde{u}'_{rms}$) fluctuation has higher levels of spatially located fluctuations in areas where the liquid-vapor mixture is noticeable.

Figure 6.58 depicts the modeled turbulent kinetic energy for the same orifice (hole 3) in both approaches, RANS on the left and LES on the right. As mentioned above, LES models stand out for resolving much of the turbulent energy and modeling the small scales motion. In contrast, RANS models all turbulent scales. Therefore, the picture demonstrates that RANS approach

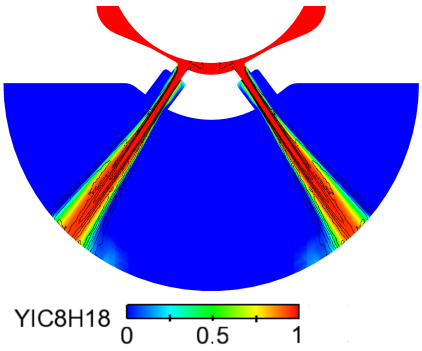

Figure 6.57: Vertical cut-plane representing the liquid mass fraction and the iso-surfaces corresponding to the $\tilde{u}'_{rms}$ in the LES approach for holes 3 and 7 of the Spray G injector.

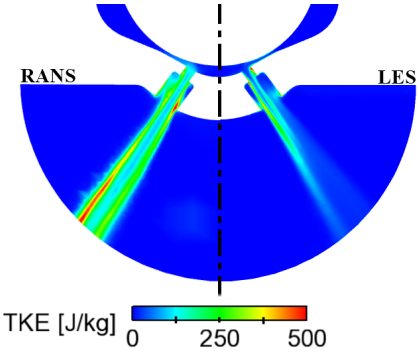

Figure 6.58: Modeled TKE comparison, RANS on the left part and LES on the right part for holes 3 and 7 for Spray G injector under SG reference condition.

has a higher modeled turbulent kinetic energy compared to LES, but when evaluating the total energy (modeled + resolved in case of LES and only modeled in RANS), it is the LES model that exhibits the highest turbulence. The quality criteria used in the previous sections (Section 6.6.5.1) proved how the mesh was sufficient for this study to provide accurate results.

Focusing on the image on the right where the TKE belonging to the LES approximation is reflected, it can be noticed how the modeled energy corresponds to the area where the spray core remains intact, without mixing with the environment. For this reason, the $\tilde{u}'_{rms}$ is very small as shown in Figure 6.57. As described above, the $\tilde{u}'_{rms}$ is directly related to the resolved TKE, so if the $\tilde{u}'_{rms}$ is very small, it means that in those areas the energy is not being resolved but modeled. This statement is supported by Figure 6.58 where it is verified that in those areas where the $\tilde{u}'_{rms}$ is low, which means that the turbulence scales are very small, the modeled TKE becomes more important.

As in Section 6.6.5.2 above, the spray plume angle and spray direction have also been calculated for both turbulence treatment models. The methodology explained in Section 5.4.1.2 has been adopted for the computation of these variables.

Figure 6.59 provides the obtained results from the calculation of the spray angle and plume direction for both approaches, RANS (Figure 6.59a) and LES (Figure 6.59b). Both studies show the same trend in the spray angle and plume direction evolution. Figure 6.60 represents from velocity iso-surfaces colored

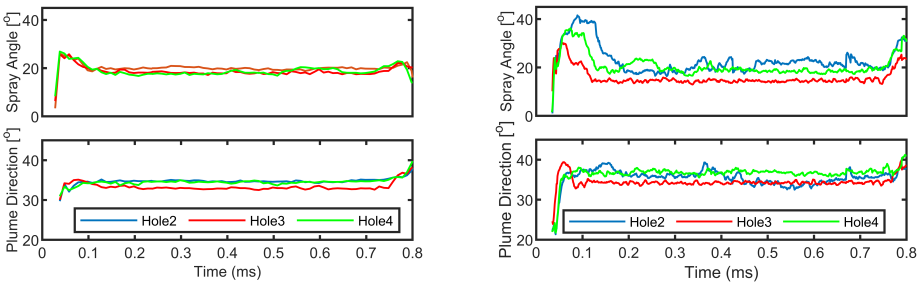

(a) RANS (b) LES

Figure 6.59: Spray angle and plume direction comparison between RANS and LES simulations for Spray G injector under SG reference condition.

by the mass fraction variable, the evolution of the spray at certain injection times for the LES scenario. There is no data in the first millisecond due to the distance taken for the angle calculation, for those first times, the jet has not developed enough to enter the acquisition window. With respect to the spray angle in both approaches, it is observed that in the first instants when the needle starts to rise and the jet begins to develop, the angle of the spray is much greater (Figure 6.60a). Subsequently, it stabilizes corresponding to the time when the needle is at its maximum (Figures 6.60b and 6.60c). Finally, at the closing stage, it is observed how the angle tends to open again (Figure 6.60d). This phenomenon is predominantly because of the environment where the fuel is being injected is quiescent prior to injection, putting up resistance to the incoming fluid and therefore increasing the spray angle. In addition, in the first instants of the injection, the liquid tends to occupy the entire volume of the orifice and the counter-bore which can also cause the spray angle to be initially larger. This effect is mitigated as the needle rises and the injection develops by the existing recirculation of the non-condensable gas into the counter-bore. It is important to mention that this effect of increasing the spray opening angle at the beginning of the injection and at the end of the injection is common and widely reported in the literature [24].

The RANS results indicate a steady behavior of the angle without oscillations in time and with similar results between sprays. On the contrary, in LES, both spray angle and plume direction have higher variability which is reflected in the standard deviation reported in Table 6.29 and that can be caused by the generation of vortices along the jet. In addition, the LES results reveal that for orifices 2 and 4 the spray angle is similar while the results for hole

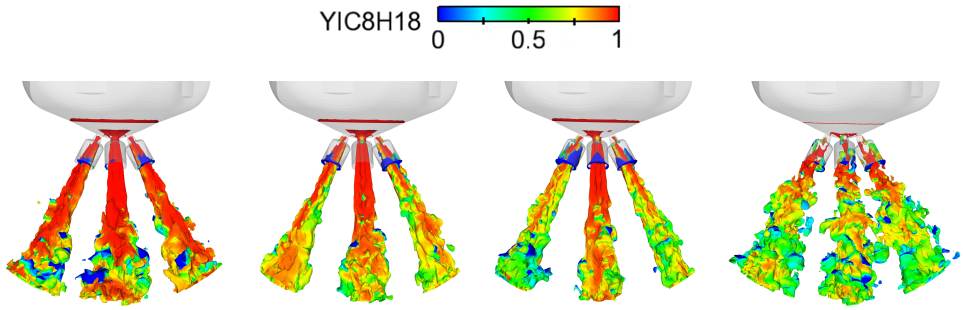

(a) t = 0.075 ms (b) t = 0.125 ms (c) t = 0.675 ms (d) t = 0.775 ms

Figure 6.60: Iso-surface of velocity variable colored by liquid mass fraction for different time steps corresponding to two opening times and two closing times for Spray G injector under SG condition.

3 are lower mainly due to the two reasons explained above (Section 6.6.5.2). To support this statement and explain the observed differences, the velocity streamlines have been presented in Figure 6.61, which have as their origin the plane that cuts the inner holes. It can be noticed how the streamlines are not equally distributed along the three holes, which has consequences at the exit of the orifice and thus the angle of the jet is affected. Furthermore, the velocity of the streamlines at the nozzle exit is also different between the three holes, which changes the diffusion of the momentum with the surrounding ambient air and can make these differences even greater. In addition to this, the difference between orifices can also be seen in the direction of the spray. Thus, orifice 3 is deflected inwards, deviating from the geometrical axis of the orifice, while the other orifices show a minimal deviation. This deflection effect has the same origin and therefore shares the explanation presented in previous lines (Section 6.6.5.2).

	LES		RANS	
	Spray Angle [°]	Plume Direction [°]	Spray Angle [°]	Plume Direction [°]
Hole 2	20.03 ± 2.21	36.04 ± 1.23	19.98 ± 0.41	34.73 ± 0.14
Hole 3	14.41 ± 0.52	34.21 ± 0.28	18.16 ± 0.45	32.97 ± 0.24
Hole 4	19.56 ± 1.73	36.88 ± 0.46	17.78 ± 0.51	34.46 ± 0.28
Lit. results	Spray angle [°] ≈ 20 [2]		Plume Direction [°] ≈ 34 [18]	

Table 6.29: Time-averaged measurements and standard deviation for the spray angle and plume direction in RANS and LES simulations.

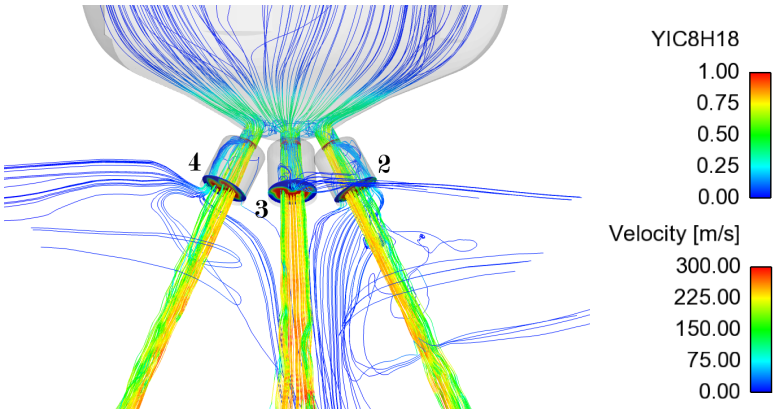

Figure 6.61: Velocity streamlines starting at the small orifice planes which are colored with the mass fraction of liquid for Spray G injector under SG reference condition. Time = 150 µs aSOI.

The time-averaged and standard deviation spray angle and plume direction for both approaches studied are displayed in Table 6.29 and compared with the literature results [2, 18]. The LES results state a narrower spray in hole 3 while holes 2 and 4 are around 20°. With respect to the plume direction, a small deviation of approximately 1-1.5° is observed in holes 2 and 4 while hole 3, in both approaches, has more significant deviation. The reasons for these results have been explained above. In the case of LES, if the spray amplitude is related to the $\tilde{u}'_{rms}$ as shown in Figure 6.62, it can be seen that those orifices with a larger spray angle are also those with a higher $\tilde{u}'_{rms}$ at the top of the jet and along the length of the jet. In these areas of higher $\tilde{u}'_{rms}$, the liquid-vapor mixing is greater, which lead to a larger spray opening. In the case of RANS, the spray angle and plume direction resemble results previously published in the literature. The deviation of the spray angle from the geometric axis of the orifice can be highlighted. The plume direction is smaller compared to the LES model, a result that could be intuited from the

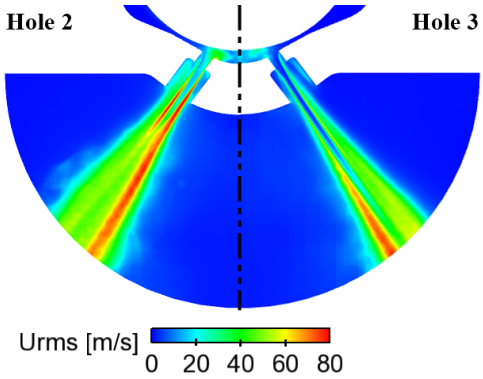

Figure 6.62: $\tilde{u}'_{rms}$ comparison in a vertical cut-plane along hole 2 (left) and hole 3 (right) for Spray G injector under SG condition.

calculated area C_a in Table 6.28. The area coefficient in the case of RANS was lower than the experimental one and than the one obtained with LES, thus suggesting the presence of a greater gas recirculation inside the orifices, generating the deflection of the jet. In conclusion, predicted trends from both approaches estimate the liquid plume direction and spray angle close to literature values and contribute to the GDI spray behavior understanding.

6.7 PIU Injector. Transient State Analysis and Validation

After having studied more in depth the behavior of the in- and near- nozzle under various operating conditions but considering only the injector belonging to the ECN, this Section aims to continue with the development of the predictive methodology by means of commercially available CFD models for accurate reproduction of hydraulic characteristics of a GDI injector under transient operation modes. For this study the CFD software employed is StarCCM+ 12.04. The developed methodology was applied and tested on on the PIU injector in order to validate its applicability in injectors of different characteristics under transient conditions.

The currently reported available models are capable of replicating the experimental trends and hydraulic characteristic parameters of GDI injectors with errors lower than 5% in the discharge coefficient [56] as discussed at the 6th meeting of the Engine Combustion Network in Valencia, Spain in September of 2018. Nevertheless, new research revealed significantly different behaviors in the needle opening. The needle lift profile is much slower in the first opening instants, making this behavior not well captured by CFD [57]. To the best of the author's knowledge, a fully predictive model and methodology that takes into account this type of behavior has not been developed yet. The current research moves into that direction and focuses on predicting first instants of the rate of injection as well as the spray momentum. The ambition is to develop a methodology that provides accurate results to be used as input boundary conditions for spray simulations replacing experimental data [58]. The purpose of this approach is to follow-up in the footsteps of the research community to supplant experimental measurement as far as possible, as it has been implemented over the last few years.

6.7.1 Nozzle analysis and comparison

Throughout this document, the characteristics of both injectors have been mentioned and explained in depth (Section 5.3.1) and although the reader

can get an idea of the differences and similarities, at no time has a comparison been made between the two. This Section, apart from being based on the development of the mentioned predictive methodology, also includes a small comparison between both injectors with similar technology, under similar operating conditions. While the Spray G injector has been extensively analyzed by numerous institutions both experimentally and computationally, the PIU injector is the first time that has been characterized. Although the technology employed in both injectors is similar, solenoid driven with a valve covered orifice (VCO) nozzle, the nozzles present numerous differences such as that the Spray G has been designed to be installed on the top of the cylinder while the PIU injector operates mounted on the side of the cylinder. This fact makes the characteristics of the nozzle in terms of orifice geometry and orifice distribution to be completely different. Not only that, but another noticeable difference is that the maximum injection pressure for the SprayG is 23 MPa whilst for the PIU is 28 MPa.

Among disparities between injectors, the needle lift profiles used in each case are one to be highlighted and which influences the studies to be carried out. Figure 6.63 provides the comparative needle lift profile of both injectors for similar injection conditions, which are 20 MPa injection pressure, 363 K injection temperature, 0.6 MPa ambient pressure for Spray G and 0.3 MPa ambient pressure for PIU and 303 K ambient temperature. Despite the differences in operating conditions, it is known that the discharge pressure does not significantly affect the flow characteristics to any great extent, so that both cases are directly comparable (Seccion 6.5.5). In order to better visualize the differences, lift profiles have been normalized by dividing by their corresponding maximum value, 55 µm for Spray G and about 70 µm for PIU. The first difference that stands out is the energizing time (ET) in both injectors. For the Spray G, typically an ET of 680 µs is used while the PIU injector injector has an ET of 1500 µs for the study.

Proceeding under the framework of the needle movement, and once the needle lift has been analyzed and compared, the study focuses on the lateral movement or also known as wobble. The simulations with moving needle in which the transient behavior of the injection is taken into account have a much higher computational cost than steady state simulations and therefore it is necessary to consider it. In this work and since the test matrix devised encompasses several operating conditions, the option of taking advantage of the geometrical characteristic of symmetry that both geometries have and reducing both the number of elements and the associated computational cost is proposed. However, before applying the symmetry condition, it must be taken into account that the lateral movement of the needle is not symmetrical (see

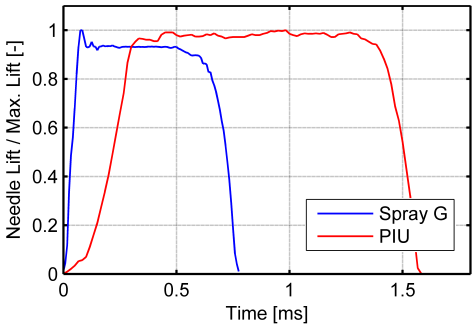

Figure 6.63: Needle lift profile obtained from x-ray of both injectors for similar injection conditions: P_{inj} = 20 MPa, T_{fuel} = 363 K, T_{back} = 303 K and P_{back} = 0.6 MPa for Spray G and 0.3 MPa for PIU injector.

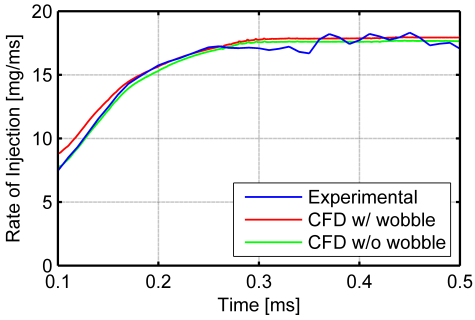

Figure 6.64: Analysis of the influence of the needle wobble on the PIU injector nozzle flow behavior under reference condition: P_{inj} = 20 MPa, T_{fuel} = 363 K, T_{back} = 303 K and 0.3 MPa.

Figure 5.7b and 5.14a) and therefore it is necessary to analyze its implication in the outcome.

Duke et al. [11] demonstrated how wobble movement does not cause any appreciable change in the flow area into the sac for Spray G. This being known, it can be stated that the Spray G injector can be treated as symmetric by neglecting the lateral movement of the needle. On the other hand, the analysis of the wobble effect on the PIU injector is carried out to observe if the behavior is the same or, on the contrary, the lateral movement of the needle changes the flow pattern. Figure 5.14a represents in the y-direction the lateral motion from orifice 1 to 4 while in the z-direction the motion just perpendicular to it is defined. To study this effect, the complete geometry has been considered, Figure 5.12, imposing the 3D movement of the needle. The obtained results have been displayed in Figure 6.64 where the data for the complete geometry taking into account the vertical and lateral movement of the needle together with the mass flow rate profile obtained only considering the upward and downward movement of the needle are reported. Furthermore, these results have been compared with the experimental injection rate profile. It is represented a zoom at the end of the needle opening transient to better visualize the results. The first thing that can be noticed in the image is a small constant offset (less than 2% in the stabilized region) which will be explained later. Another important fact is the impossibility to capture the experimentally observed oscillations, even by imposing the needle elevation movements [16, 59]. In spite of this, it may be stated that both profiles reflect

similar results and good agreement with the experimental data. Even when the y-displacement of the needle is maximum (at about 0.4 ms), the mass flow rate barely changes. These statements would corroborate the effect already observed by Duke et al. [11] and justify the use of half geometry without the wobble movement for further studies. Thus, resulting in mesh sizes of a total of 2,296,585 cells for Spray G and 794,444 cells for PIU injector (Section 5.3.5.2).

Notwithstanding, in order to better understand the wobble effect and its importance as well as to support the previous statement, the averaged steady state hole to hole variation is provided in Table 6.30, where the results of simulations of a case with needle lift and wobble are compared against the results of a case with only needle lift (performed with half of the domain). Except for orifice 1, the difference between the two simulations is relatively small. In fact, the uneven distribution of mass and momentum between the holes is well reproduced by the simulation without imposing needle wobble. The differences in orifice 1, as well as the differences in total injection rate and momentum flux (which are larger for momentum than for mass flow) are mainly attributed to the simplification of the geometry (half of the nozzle), applying symmetry boundary condition, already discussed and explained. The nozzle is not exactly symmetrical by about 4 µm, as stated several times before and observed in x-ray tomography images (see Figure 5.12). As reported in the literature, for steady state operation, the effect of needle wobble on the nozzle flow pattern and nozzle characteristics can be neglected [16]. It would only be significant for partial values of needle lift [60], and perhaps if a time-resolved approach to turbulence (i.e., large eddy simulations) is applied.

Back to the distinctions between injectors, another aspect to highlight of both injectors is the existing disparity in the shape and number of the orifices. In order to carry out a correct comparison between injectors, it is necessary to reflect the characteristics of both in terms of size and number of orifices. As presented in Table 6.31, from these two mentioned parameters, the total exit area is calculated, observing that the PIU injector has 4.5% more exit surface. This aspect together with the fact that the needle lift, which as already known plays an important role in restricting the flow path, is greater in the PIU injector, means that the stabilized mass flow for the same condition is expected to be greater in the PIU injector.

6.7.2 Simulation strategy

These simulations have a series of problems behind them for which this work intends to provide a solution. The first problem is related to the computational

	w / wobble		w / o wobble		Difference	
	ROI [g/s]	ROM [N]	ROI [g/s]	ROM [N]	ROI [%]	ROM [%]
Experimental	16.7 ± 0.2	2.5 ± 0.1				
CFD Total	17.9	2.95	17.6	2.59	1.50	12.38
Hole 1	3.10	0.602	2.64	0.507	14.8	15.8
Hole 2	3.23	0.636	3.25	0.550	0.67	13.5
Hole 3	2.83	0.539	2.84	0.532	0.18	1.44
Hole 4	2.68	0.512	2.78	0.527	3.87	2.77
Hole 5	2.84	0.563	2.84	0.532	0.11	5.50
Hole 6	3.19	0.557	3.25	0.550	1.96	1.16

Table 6.30: Steady state values of rate of injection (ROI) and spray rate of momentum (ROM) compared between a complete nozzle domain with needle wobble and half of the domain without needle wobble. The geometry corresponds to the PIU injector, and the injection conditions are P_{inj} = 20 MPa and P_{back} = 0.3 MPa.

	Spray G	**PIU**
Orifice diameter [µm]	165	195
Orifice area [µm^2]	21382.46	29864.77
Number of orifices [µm]	8	6
Total area [µm^2]	171059.72	179188.6
Difference [%]	4.53	

Table 6.31: Comparison in terms of nozzle area between both studied injectors.

cost of studying the transient behavior of the injection. For example, for the case of the PIU injector, the computational time step is about 10 ns, and to complete the 1.5 ms injection duration, more than 25000 CPU/h are required. The tendency of the mass flow rate when the needle reaches its maximum opening and thus achieves steady state (around 0.3 ms), is to remain without significant changes in the injection rate values or in the flow pattern and structures, as it can be observed in Figure 6.64. Therefore, what is proposed is to shorten the simulation by eliminating part of the steady state, especially for the PIU injector, since the corresponding ET is more than twice that of Spray G. Thus, most of the RANS simulation steady state, a total time of 0.8 ms, is removed in order to save computational cost. Figure 6.65a shows a visual example of the strategy proposed for the shortened needle lift employed in the reduced computational cost calculations. During post-processing, and

for comparison purposes, the steady state of the simulation is lengthened by the same amount of time that it was removed, as reflected in the injection rate illustrated in Figure 6.65b. Under the same context and also with the aim of making the calculation more efficient, the number of processors used for these studies are based on the scalability analysis carried out for the steady state injection (Section 6.5.2).

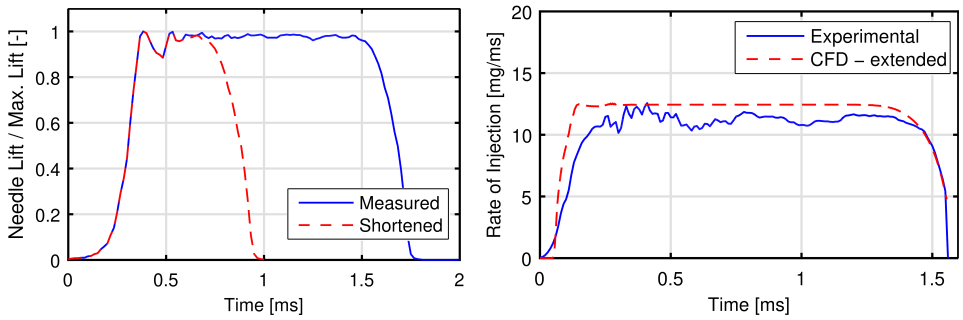

(a) Needle lift (b) Rate of injetion

Figure 6.65: Needle lift and rate of injection results of shortening the injection duration strategy for PIU injector under the test point of $P_{inj} = 10$ MPa and $P_{back} = 0.3$ MPa.

The second issue detected is related to the initialization procedure corresponding to the inlet boundary conditions. As defined in Section 5.3.4.2, the most common method to set the boundary conditions related to the inlet is defining a constant pressure equal to the rail injection pressure. On the other hand, it should be noted that the initial conditions of the simulation include a minimum needle lift of 2 µm which causes the flow to pass rapidly through the orifices generating a mass flow rate value corresponding to that needle position. These effects do not accurately capture the evolution of the variables that characterize the flow, so it is necessary to find a strategy to improve this behavior. Some authors successfully proposed in their work [16, 59] to modify the inlet pressure time evolution. During needle opening an expansion wave travels upstream of the injector nozzle, which temporarily reduces the injection pressure. The duration and intensity of this wave depend not only on the fluid, but also on the geometry of the injector. Based on this premise, it is proposed for this particular case to define the inlet pressure from a linear or parabolic growth from the discharge pressure to the injection pressure with a duration equal to the needle opening. This time is equal to the time it takes for the needle to reach its maximum position. For fast needle openings such

as diesel injections, a linear surge provides accurate results [59], however a parabolic or sinusoidal surge is more similar to one-dimensional simulations of injector performance [61]. Figure 6.66 reports, for a particular test point, both the definition of this strategy and the results obtained from it employing linear and parabolic pressure ramps as well as comparing them with experimental data for the same operating condition and with the results obtained from the classical constant pressure strategy. The injection rate results obtained are depicted in Figure 6.66b where the unrealistic mass flow rate at the orifices outlet is clearly visible when a constant inlet pressure is adopted due to the remarkable effect of the initial needle lift. However, this effect is reduced with the proposed strategies by minimizing it to a large extent with the linear increase of the pressure and eliminating it almost completely when applying a parabolic rise.

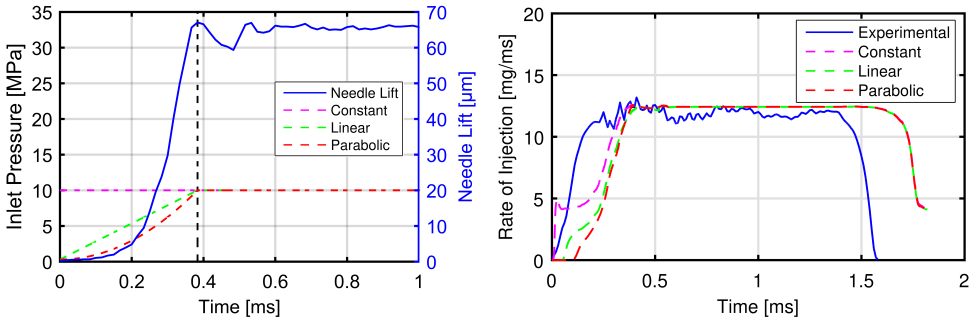

(a) Inlet pressure time evolution

(b) Rate of injetion

Figure 6.66: Effect of changing the inlet pressure time evolution in the simulations considering the effect of pressure drop at the needle opening. Example for the test point corresponding to P_{inj} = 10 MPa and P_{back} = 0.3 MPa for the PIU injector.

The third of the concerns can be clearly visualized in Figure 6.66b. There is a noticeable delay between the experimental and computational rate of injection attributed mainly to the initial evolution of the needle lift as illustrated in Figure 6.65a and Figure 6.66a. The needle opens very slowly in the first moments of injection (first 0.2 ms), a phenomenon that is even more accentuated at low injection pressures. However, this is not observed in the mass flow rate experimental measurements where the rising slope of the signal is the same from the start of injection. In addition, the uncertainty in the x-ray measurements is of the order of 1-2 µm, which is equal to the initial value of the needle lift during this time. Therefore, this initial part can be modified,

assuming a constant opening velocity for the entire transient, but also for the closing transient. This new lift profile has been termed "educated needle lift" and is depicted in Figure 6.67a.

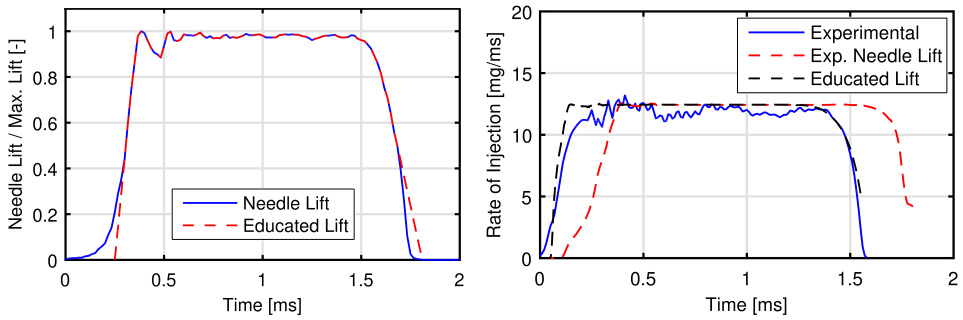

(a) Needle lift from x-ray data

(b) Rate of injetion

Figure 6.67: Effect of changing the needle lift profile to remove the slow initial rising. Example for the test point corresponding to $P_{inj} = 10$ MPa and $P_{back} = 0.3$ MPa for the PIU injector.

It has been noted that due to this strategy the onset of injection is delayed and thus the duration of injection is slightly modified. Figure 6.67b collects the results obtained from the initial case using a parabolic initialization of the pressure in the inlet boundary as well as the results obtained from educating the needle lift profile and compares them with the experimental data for a specific operating point. The differences between the experimental and computational profile are greatly reduced by the use of the explained methodology. The opening and closing stages are adequately captured and the only weakness of the model is the inability to capture the oscillations of the rate of injection during steady state operation. Nevertheless, these oscillations are mainly attributed to the pressure variations inside the injector [59] It is important to mention that although this methodology has been explained for the PIU injector, it can be applied to any injector such as the Spray G included in this study, and of course for any operating condition. Concerning Spray G injector, only two of the three mentioned strategies are applied, the possibility of studying only half computational domain due to its symmetric characteristic and the initialization of the injection pressure from a parabolic growth. However, the needle lift profile associated with this injector is already treated and therefore educated by the ECN itself to make its study as simple as possible without neglecting the necessary precision (see Figure 6.63).

6.7.3 Results and validation

6.7.3.1 Validation

In order to validate the methodology created by comparing the results obtained with existing experimental data, the nominal conditions of each injector are considered. This corresponds to an injection pressure of 20 MPa for both geometries but a discharge pressure of 0.6 MPa for the Spray G injector and 0.3 MPa for the PIU injector. In these cases and in order to approximate the measurement methodology to the one used experimentally, the mass flow rate data is obtained at the exit section of the orifices, whilst the spray momentum is captured as the momentum through a plane perpendicular to the injector bend angle and located 1.5 mm far from the nozzle tip for Spray G and 3 mm for PIU. The difference in target position is mainly due to the arrangement of the holes. For the Spray G injector, the opening of the jets is larger so that to capture the momentum of all of them, the target has to be positioned closer to the injector. However, the PIU injector has an arrangement of sprays closer together which allows to capture the momentum at a greater distance.

Figure 6.68 summarizes the validation of the methodology implemented for both geometries by reflecting the injection rate as well as the corresponding experimental profiles. The accuracy of the proposed models in both cases is highlighted. The opening and closing slopes are captured with precision especially for the Spray G case whose needle movement is faster as it can be verified in Figure 6.63. Not only the opening and closing of the injector is accurately predicted but also the stationary state is well captured although this will be analyzed in more detail in the following lines by means of nozzle coefficients. As mentioned above, the experimental oscillations in the mass flow rate profiles are not adequately reproduced computationally since they are mainly attributable to variations in the upstream pressure of the nozzle and not to the movement of the needle itself. Furthermore, the strategy of shortening the needle lift profile means that they are not included in the simulated model (see Section 6.7.2). Regarding the Spray G injector, these oscillations seem to be significant during the first 300 µs of the injection, so that the rate of injection is reduced and remains well below the steady state value. Comparing the needle lift profiles (Figure 6.63), it is observed that the one corresponding to the Spray G injector has an initial overshoot while this effect is not seen in the PIU injector. This phenomenon, as indicated in Figure 6.68a, is also transmitted to the simulations where they correctly capture the overshoot in the injection rate profile. This emphasizes the sensitivity of this type of injector to needle position. Since the needle elevation values are generally small compared to other types of injectors, small variations in the

elevation value can create a strong restriction, limiting the flow capacity of the nozzle.

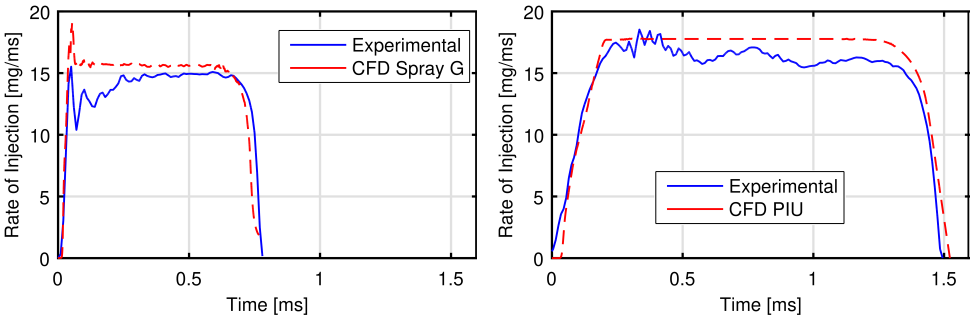

(a) Spray G (b) PIU

Figure 6.68: Computational and experimental rate of injection of both injectors at similar injection conditions: $P_{inj} = 20$ MPa, $T_{fuel} = 363$ K, $T_{back} = 303$ K for both injections, and $P_{back} = 0.6$ MPa for Spray G and 0.3 MPa for PIU.

In addition to the injection rate, the momentum flux obtained for both injectors, reported in Figure 6.69, has also been analyzed. As in the previous study, a very good approximation to the experimental behavior can be observed in both cases, except for the already explained oscillations present during the stationary state of operation of the injector. In these cases in particular, the main differences are observed at the end of the transient opening phase of injection where simulations predict an overshoot in the signal for both geometries which is not experimentally observed. This phenomenon could be accounted for by two different reasons:

- The computationally observed overshoot might result from the initialization characteristics inside the nozzle (Section 5.3.4.2) which is presumably not necessarily the exact same situation as in the experiments. Indeed, the exact initial conditions are unknown and may vary from one injection to another. The observed effect may be due to remaining fuel inside the orifices being pushed outward and temporarily increasing the momentum flow through the metering section.
- The experimental technique includes a plate (for the sensor to measure the force of the entire jet) that may alter the transient behavior of the jet. For example, the assumption that the flow is reflected parallel to

the surface may not be entirely true for the first drops arriving at the sensor; these may be projected in a perpendicular direction. In addition, it should be noted that the distance at which measurements are taken differs experimentally and computationally due to the limited computational discharge volume. Although the momentum flux should be conserved, it was proven in [10] how the variation of the data acquisition distance influenced the obtained measurements.

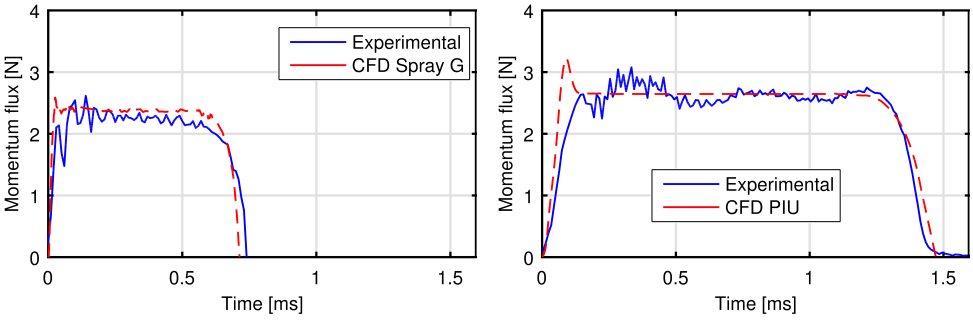

(a) Spray G (b) PIU

Figure 6.69: Computational and experimental rate of momentum of both injectors at similar injection conditions: $P_{inj} = 20$ MPa, $T_{fuel} = 363$ K, $T_{back} = 303$ K for both injections, and $P_{back} = 0.6$ MPa for Spray G and 0.3 MPa for PIU.

Once the methodology adopted has been validated and the accuracy of the results obtained has been demonstrated, in addition to explaining the phenomena that take place during the opening and closing ramps of the injection, the next step is to study the steady state of the injection process. The objective of this is to further validate the model by representing averaged values of rate of injection and rate of momentum when the needle is fully open and closed. These values have been used for the calculation of the dimensionless coefficient that define the injector flow capacity and characterize the hydraulic nozzle behavior [5]: the discharge coefficient (C_d), the velocity coefficient (C_v) and the area coefficient (C_a). The results obtained from this study are reported in Table 6.32 together with the total injected mass calculated both from the experimental data and for the two injectors. In addition, Table 6.33 consecutively lists the existing differences expressed in percentage between the computational and experimental data for both studied injectors. The data clearly show a systematic overestimation of the total injected mass

of about 5-6% which is mainly attributed to the lack of computational prediction of the existing oscillations in the injection rate. These random variations cause the total injected mass to be reduced in both injectors as can be noted in Figure 6.68. On the other hand and as expected, the PIU has a higher injected mass than the Spray G injector. This fact cannot be seen directly from the total injected mass measurement as the ET of both injectors are very different. However, referring to the discharge coefficient, a difference of 6.8% is observed between both injectors, being higher in the case of the PIU injector. This effect is due to, as mentioned above, the difference in the total areas of both injectors of about 4.5% (Table 6.31), the discrepancy in the maximum needle lift of 15 µm and the difference in the type and characteristics of the orifice.

Consequently, the computational studies also overestimate the nozzle coefficient with a maximum difference of 0.04 which corresponds to approximately the 5% mentioned. The fact that the PIU has a modestly greater discharge coefficient is captured by the simulations. However, the expected trend in the velocity coefficient is not replicated. This may be attributed to the overprediction in the area coefficient given by the simulations, which is higher for the PIU. A larger effective area leads to a decrease in the effective velocity. This implies that the flow detachment arising in the orifice (see Figure 6.70b) is better captured by the simulations for the counter-bored geometries than for diverging orifices. However, the discrepancies are minor and within the range of uncertainty.

	Inj. quantity [mg]		$C_d[-]$		$C_a[-]$		$C_v[-]$	
Case	Exp.	CFD	Exp.	CFD	Exp.	CFD	Exp.	CFD
Spray G	10.39	11.04	0.55	0.58	0.94	0.96	0.59	0.61
PIU	22.62	23.90	0.59	0.60	0.93	0.97	0.62	0.60

Table 6.32: Injected quantity and nozzle flow coefficients of both nozzles for nominal conditions of each of them.

In order to visually support the previous explanations, Figure 6.70 illustrates the flow patterns inside the orifices from the representation of the liquid volume fraction contours plane of both nozzles (orifices 1 and 5 of Spray G, and 1 and 4 of PIU) together with the velocity vectors. In both cases, the position of the needle is raised to its stationary state. The orifices are not completely filled with liquid but that most of the cross-sectional area of the orifices is filled with gas. This visually explains the low discharge coefficient

Case	Inj. quantity variation	C_d variation	C_a variation	C_v variation
Spray G	6.26 %	5.45 %	3.39 %	2.13 %
PIU	5.66 %	1.69 %	3.23 %	4.30 %

Table 6.33: Existing differences between experimental and computational injected quantity and nozzle flow coefficients of both nozzles for nominal conditions of each of them.

values that characterize this type of injectors. The gas filling the orifices is not vapor fuel but ambient gas which is draged inwards, creating strong recirculation areas inside the orifices. The amount of ambient gas that enters the orifices depends on many factors including the orifice drill angle and their relative position (Figure 6.70b) in addition to the characteristics of the upstream injector geometry (there is a significant difference between the two studied injectors, Figure 6.70).

The geometry of the orifices as well as the recirculation phenomenon inside the orifices directly affect the behavior of the spray pattern [32]. One of the main effects this has on the spray is the deviation of the spray from its corresponding geometrical axis. The greater the recirculation phenomenon, the larger the deviation of the spray, as can be seen in Figure 6.70. On the other hand, GDI injectors are designed with this type of geometry to help increase the air-fuel mixing. As again noted in Figure 6.70, this is achieved in both cases since none of the injectors have their orifices filled with only liquid (liquid volume fraction equal to one). In these recirculation zones, the velocity is relatively higher than in the surrounding areas where only fuel is available. Figure 6.71 reflects this phenomenon through velocity contours plotted at two different axial position of all the orifices. In the case of the PIU injector, these planes visualized in the image are located at the entrance and exit of the orifices while in the Spray G injector, due to its counter-bored shape, they are positioned at the exit of the small orifice and the counter-bore. This flow velocity causes the momentum transfer between phases to increase and thus, as mentioned above, the air-fuel mixture is enhanced. In both cases, the areas of maximum recirculation are visible on the outside of the orifices. Figure 6.71 further demonstrates the difference in flow between holes, which is more accentuated in the PIU injector than in the Spray G due to the distribution and inclination of the orifices.

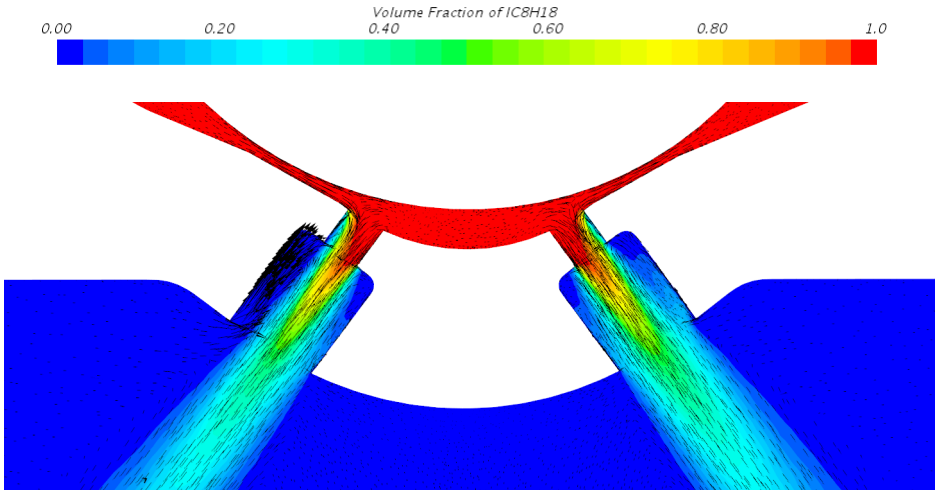

(a) Spray G

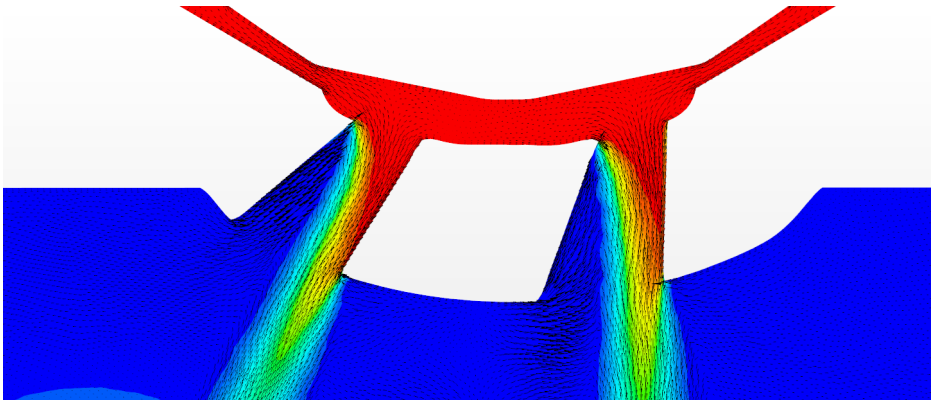

(b) PIU

Figure 6.70: Symmetry plane liquid volume fraction contours at steady state condition of both studied geometries. Injection conditions are: $P_{inj} = 20$ MPa, $T_{fuel} = 363$ K, $T_{back} = 303$ K and $P_{back} = 0.6$ MPa for Spray G and 0.3 MPa for PIU.

6.7.3.2 Parametric variation: effect of injection pressure (PIU)

In order to go one step further, this section presents the results obtained and the corresponding discussion on the basis of the injection pressure variation. For this purpose, the PIU injector has been selected but the conclusions drawn in this study may also be extrapolated to the ECN injector, Spray G. Among the results analyzed, the rate of injection and the rate of momentum are shown

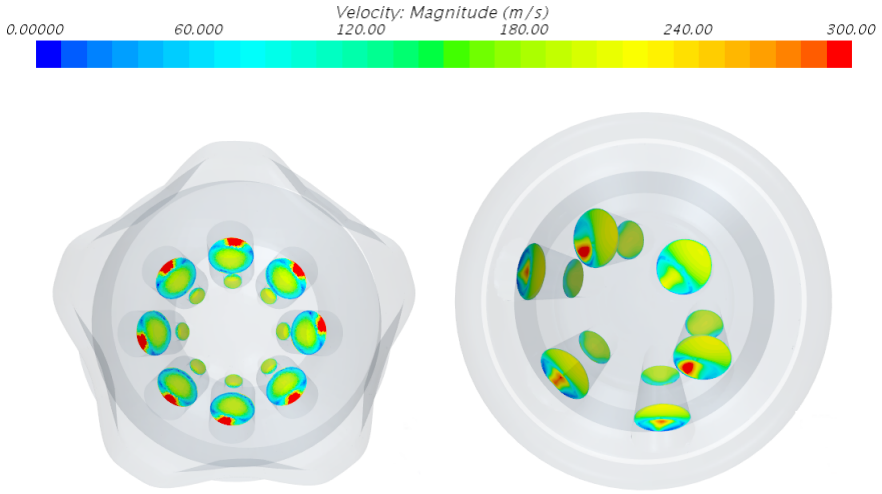

(a) Spray G (b) PIU

Figure 6.71: Orifice cross-sectional velocity contours at steady state conditions of both studied geometries. Injection conditions are: P_{inj} = 20 MPa, T_{fuel} = 363 K, T_{back} = 303 K and P_{back} = 0.6 MPa for Spray G and 0.3 MPa for PIU.

in Figure 6.72 for the three injection pressures studied, 10, 20 and 28 MPa, which reflect the complete range of operation of the injector, and the same discharge pressure equal to 0.3 MPa. As in the other previous cases, the experimental data with which the results obtained have been compared are shown in blue, regardless of the injection pressure tested, while the computational results are displayed in different colors, one for each condition. The first observation to be drawn from these images is that the behavior exhibited by the experimental results as the injection pressure varies is perfectly reproduced computationally:

- The injection rate as well as the momentum flux increase, with a trend proportional to the square root of the pressure drop, as the injection pressure increases. The methodology created and employed is able to accurately predict this trend and behavior both quantitatively and qualitatively.
- As the pressure difference is greater, the injection duration is slightly shortened. This effect is again accurately reproduced by the simulations.

As in the validation scenarios, Table 6.34 gathers the steady state injection data by adding information about the total injected mass as well as the

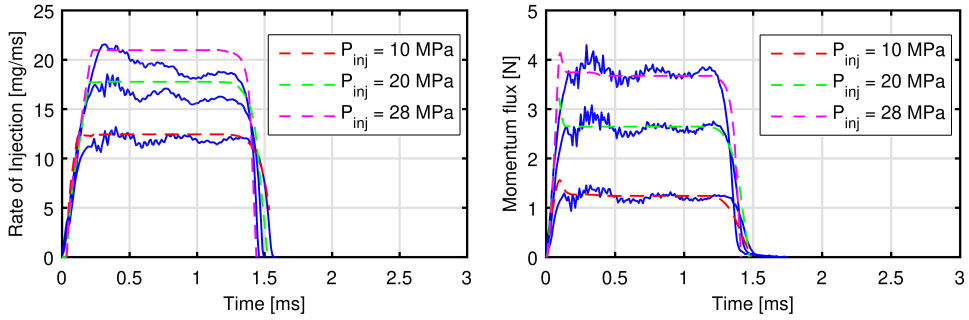

(a) Rate of injection (b) Momentum flux

Figure 6.72: Experimental and computational rate of injection and momentum flux of the PIU nozzle for different injection pressure values and a discharge ambient pressure of 0.3 MPa

dimensionless hydraulic coefficients. In addition, the subsequent Table 6.35 reports the differences between these outcomes and the experimental data for each operating condition. Once again, as mentioned above, the lack of accurate prediction of the oscillations in the injection rate profiles causes the total mass injected as well as the discharge coefficient (C_d) to be overpredicted. Nonetheless, the nozzle flow coefficients evolution when injection pressure changes is accurately reproduced by the model: velocity coefficient C_v increases and area coefficient C_a decreases as the injection pressure becomes higher. These two effects allow the discharge coefficient to remain almost constant.

	Inj. quantity [mg]		$C_d[-]$		$C_a[-]$		$C_v[-]$	
P_{inj} [MPa]	Exp.	CFD	Exp.	CFD	Exp.	CFD	Exp.	CFD
10	16.86	17.79	0.60	0.60	1.02	1.03	0.58	0.59
20	22.62	23.90	0.59	0.60	0.93	0.97	0.62	0.60
28	25.77	27.59	0.58	0.60	0.90	0.95	0.63	0.60

Table 6.34: Injected quantity and nozzle flow coefficients of the PIU nozzle for different injection pressure values and a discharge ambient pressure of 0.3 MPa.

P_{inj} [MPa]	Inj. quantity variation	C_d variation	C_a variation	C_v variation
10	5.52 %	0.00 %	1.72 %	0.10 %
20	5.66 %	1.69 %	3.23 %	4.30 %
28	7.06 %	3.25 %	4.76 %	5.53 %

Table 6.35: Existing differences between experimental and computational injected quantity and nozzle flow coefficients of the PIU nozzle for different injection pressure values and a discharge ambient pressure of 0.3 MPa.

6.8 Summary and Conclusions

This section summarizes the main outcomes experienced throughout this Chapter. These will be grouped according to the different categories of analysis done throughout the paper. On the one hand, the main results and the associated discussion of the steady state study of the injection under the two different injectors will be discussed, and then the results obtained in the analysis of the transient behavior of the injection, again using both injectors, will be reported.

6.8.1 Spray G injector steady state conclusions

This section gathers the different stages carried out to develop the desired predictive methodology in terms of meshing strategy, discharge volume size and turbulent models, among others. It also determines the validation of the predictive methodology by applying it to the same injector but under different calculation software. The results obtained correctly validate the applicability of the developed methodology to different calculation software obtaining in both codes, StarCCM+ and CONVERGE™ , results of injection rate and momentum close to the experiments with differences of less than 5% for ROI and 10% for ROM. This work also shows how under the same computational code, the polyhedral mesh has good accuracy using less than half the number of cells than the hexahedral mesh.

The injector is described, under both calculation codes, from the dimensionless flow coefficients which characterize the flow capacity and hydraulic behavior of the nozzle. The conclusions obtained from this study are that the geometrical characteristics of this type of GDI injectors make them have low discharge coefficients. This phenomenon is the result of the liquid fuel not filling the orifices, so that most of the cross section of the orifices is occupied by gas. The gas is not vapor fuel, but an ambient gas (N2 in this case) that is

drawn inward, creating strong recirculation zones inside the holes. Thus, the values of the velocity coefficient are also substantially low. Another fact to note is that a high effective area leads to a reduction of the effective velocity. This theoretically means that the hexahedral mesh strategy from StarCCM+ is more prone to predict flow detachment occurring in the orifice.

This investigation is completed with the calculation of the spray angles in the first millimeters downstream of the injector, in the near field for both study software. CONVERGE™ software predicts a larger spray deflection because the recirculation inside the orifices is larger but it can be said that both codes capture to a greater or lesser extent the spray deflection towards the injector axis. With respect to the spray cone angle, the results obtained for the SG non-flashing condition are close to those reported in the literature and have a lower value than those obtained for the flash boiling condition under which, as it is known, the sprays tend to open.

A study of the influence of downstream conditions on the behavior of the fluid was carried out considering submerged (liquid-filled discharge chamber) and non-submerged (non-condensable gas-filled discharge chamber) discharge conditions, obtaining differences in the macroscopic flow parameters of less than 3%. This together with the contours of the fluid behavior along the injector determined that despite the similarity in the results the non-submerged case is closer to reality since it is the caustics that a real engine has during its operation. The statement supports the use of Bosh method for masuring ROI as always done in CMT.

In addition, the influence of the exponents present in the HRM phase change model equation on the internal nozzle flow behavior was also determined. The variation of the exponent associated with the liquid volume fraction does not have a significant influence on the flow in either of the two operating conditions studied, the reference SG and the SG2 flashing condition. It was observed that the variation of the exponent associated with the pressure ratio barely influenced under the standard SG condition while for SG2 it changed the vapor behavior pattern completely. The time constant was not treated in this study since the literature reported minimal variations under generation geometry 1 of Spray G nozzle.

6.8.2 PIU injector steady state conclusions

This section gathers the studies carried out for the PIU injector under stationary conditions, with the needle raised to a fixed position, in order to determine the accuracy and validity of the predictive methodology developed in terms

of meshing strategy. In addition, the influence of the needle position on the flow behavior inside the nozzle, the justification of the use of the symmetric condition taking advantage of the injector characteristics to reduce computational cost and, finally, a parametric study to see the behavior of the injector under different operating conditions.

As regards meshing strategy, the results clearly showed that the polyhedral type cell configuration gave results with high accuracy and really close to the experiments with a computational cost up to 6 times lower than the classical hexahedral element strategies also studied. These results validated, therefore, the predictive methodology developed.

On the other hand, it was demonstrated how the use of a symmetry condition did not incur in significant differences in the internal flow characterization parameters nor in the behavior of the spray downstream of the injector, if global performance is taken into account. However, a small discrepancy was locally observed in one of the holes affected by this symmetry assumption, mainly attributed to the small deviation detected from the x-ray technique of 4 µm with respect to the geometrical center of the injector. The study of the influence of the needle lift showed how this part of the injector is the one that mainly restricts the flow passage. In addition, it was observed that the lower the needle lift, the higher the pressure gradients at the needle seat, as expected.

Finally, with respect to the characterization of the internal nozzle flow under different operating conditions, it was observed that the injection pressure has a high influence on the obtained results while the ambient density or in other words the discharge pressure produces minimal variations in the macroscopic parameters of the internal flow. In relation to the dimensionless hydraulic flow coefficients, it was observed to a slight downward trend when the pressure drop is higher, but it can be said that the discharge coefficient is practically constant for the whole range of pressures. On the other hand, the velocity coefficient increases with the injection pressure while the area coefficient decreases with the injection pressure. The effect of these two behaviors causes the discharge coefficient to remain almost constant. Finally, the effective velocity trend of linear growth up until the highest values of pressure drop has been clearly obtained.

6.8.3 Spray G injector transient state conclusions

6.8.3.1 Transient analysis conclusions

The studies carried out in this subsection seek to extend the applicability of the predictive methodology developed in stationary cases to studies that take into account the transient behavior of the injection process. This is validated under different software codes, CONVERGE™ and StarCCM+, from experimental data obtained in previous works of this research group. Regarding the macroscopic results describing the internal flow, the injection rate and momentum flux profiles are adequately captured by both codes. A faster ramp opening is presented in the computational case, an effect that can be attenuated with a more realistic imposition of the injection pressure, in other words, using as input condition a parabolic pressure ramp. Another important phenomenon is the presence of liquid in the first moments of injection, which is due to the fact that the needle is initially raised a few microns to avoid surface overlapping. This effect can be corrected by using a sealing algorithm.

Concerning the values obtained in the stationary phases of the injection, in the case of the mass flow rate, the behavior is similar to that observed in the steady state studies, the ROI profile obtained by CONVERGE™ under predicts the value by approximately 3% while the StarCCM+ remains above the experimental value by approximately 5%, both values within the experimental uncertainty. It is important to mention that, although the behavior has been shown to be adequate, the use of incompressible conditions for all species, as is the case for StarCCM+, may induce a small deviation in the results. However, for the momentum flux case the predictions obtained in the steady state scenario are modified. While the CONVERGE™ case reports a moment profile similar to the experimental one and with a trend according to that observed in the stationary cases, the StarCCM+ case shows an over-prediction of 10%. In this case there are several factors that influence this behavior. On the one hand, the determination of the experimental mean momentum value is carried out with ET signals almost twice as long as the simulated signal, which allows the pressure in the rail to stabilize and report constant values in time higher than the experimental profile presented. On the other hand, the geometry generation adopted in the study is the primitive one where the existing differences between orifices are not taken into account. Finally, the needle lift values used in the stationary case are lower than the actual needle lift in its steady-state operation. This effect may result in a 3% difference in the results obtained.

On the other hand, the penetration study assesses that Eulerian approximations adequately predicts the liquid penetration in the first millimeters of

the injector exit and shows that the simulation with a fixed needle lift has a faster answer than the transient simulations, which can be attributed to different factors including the initialization and the boundary conditions. In order to understand this behavior, more studies in this area need to be done.

6.8.3.2 Surrogate fuels conclusions

This section includes the validation of the in and near nozzle flow behavior during the transient process of GDI injection using the surrogate fuel par excellence, iso-octane, under the most typical engine operating conditions defined by the ECN: SG, SG2 and SG3. Once the model is validated, the influence of fuel properties on the internal nozzle flow behavior is studied using different single-component surrogate fuels. In addition, the study is taken a step further by including the multi-component fuel recently added by the ECN to replicate the characteristics of gasoline. The results obtained in terms of mass flow and momentum are close to the experiments with differences lower than 5%. A remarkable fact is that despite the differences between the operating conditions studied, the injection rate and momentum results are similar for all cases. This justifies the fact that the variation in discharge pressure minimally influences the macroscopic parameters of internal flow and the variation in ambient density is small enough to have meaningful influence on the results.

The calculation of the amount of non-condensable gas at the outlet of the orifices together with the liquid mass fraction contours in the planes perpendicular to the orifices and the calculation of the spray cone angle, determine that the SG condition has a non-condensable gas recirculation phenomenon inside the orifices that deflects the spray towards the injector axis. On the contrary the SG2 condition due to its tendency to flash boiling, and the SG3 condition due to its low discharge pressure, have a larger spray aperture, thus occupying more space inside the orifices and resulting in less ambient gas entrance. The three studied conditions present a disparity in the spray contours between orifices which may be due to the upstream distribution of the injector geometry (5 bumps and 8 holes) which causes the flow not to be distributed uniformly or to the influence of the mesh orientation. The SG2 condition, given its tendency to generate flash boiling, has wider sprays than the SG reference condition and jet-to-jet interaction is also observed, giving rise to the well-known flash boiling phenomenon consequences. On the other hand, the SG3 condition presents a larger spray amplitude than the SG condition, which is strange because this condition is not considered evaporative or flashing for iso-octane fuel. The explanation is due to the fact that the low ambient pressure allows the flow to exit more easily, opening in the first moments of

the injection and generating a stationary vortex in the center of the domain that increases notably the mixing process.

After validating the model using the iso-octane reference fuel, its behavior was compared with the proposed multi-component fuel to approximate the behavior of gasoline by improving the volatility properties that iso-octane lacks. The results obtained in terms of total injection rate were very similar between fuels and close to the experiments, however, focusing on the vapor fuel injection rate, a difference of an order of magnitude in the amount of vapor generated is observed. The absence of experimental results prevents the determination of which behavior is closer to reality but, keeping in mind that iso-octane does not capture the volatility of gasoline, it could be said that E00 is closer to the real expected performance. Analyzing the shape of the sprays downstream of the nozzle, no significant differences in the spray core are observed under the SG condition. On the contrary, under the SG2 flashing condition the behavior of the sprays is very different, being the E00 opening much larger and appreciating a greater interaction between sprays, in other words, a greater spray collapse.

Subsequent to this study, a comparison was made between different surrogates including ethanol, heptane, iso-octane, hexane, E00 and pentane. The differences in injection rate presented were small and mainly due to the dissimilar densities of each fuel. This variation in results was attenuated in the momentum flux profiles because the effect of density is theoretically null. These conclusions are applicable to all studied conditions, SG, SG2 and SG3. Under the SG condition, different phase change ratios were observed, being higher in those fuels with higher volatility. This behavior was also replicated under the SG2 condition where not only the fuel volatility but also the saturation pressure is taken into account. Ethanol presented an exception to this behavior because despite having a higher saturation pressure than iso-octane and therefore being under flash boiling conditions, it hardly generated any vapor. This was due to the fact that the latent heat of evaporation is 6 times higher than that of iso-octane. Under this flashing condition, it was also observed that those fuels with a greater tendency to phase change, hexane, E00 and pentane produced a strong flash boiling resulting in higher interaction between sprays, spray collapse, which has to be taken into account because of its adverse effects on engine performance.

6.8.3.3 Geometry influence conclusions

In this particular case, the study is based on the comparison between the different generations of geometries provided by the ECN for the study of the GDI

reference injector. Generation 1, which is considered the ideal one because any manufacturing defects have been eliminated and the dimensions of the bores and inlet and outlet orifice radii have been modified, has currently been compared with generation 3, which is not the most recent geometry but faithfully and realistically reproduces the peculiarities of the injector, taking into account the differences in terms of bore dimensions and considering the existing curvatures in the inlet and outlet orifice radii. This study has brought to light certain differences in the macroscopic flow parameters both injection rate and momentum flux mainly due to the difference in the size of the orifices. On the other hand, another important difference that has been observed is how generation 3 has a larger counter-bore space occupied by non-condensable gas and even in the interior of the small orifices some amount of gas is also visible, an effect that is not seen in generation 1. This phenomenon produces a greater spray deflection towards the injector axis resulting in a difference in drill angle between generations of between 1 and 2 degrees depending on the orifice observed. Despite this difference in spray direction, the spray amplitude has a similar behavior, being around 20 degrees of cone angle.

It has also been shown how the geometry used also affects the amount of vapor generated both inside the nozzle and downstream of it, being greater in the case of generation 3. For this reason, this new generation has been involved in the study of the influence of the variables that make up the HRM phase change model during the transient process of injection, discarding the influence of the exponents associated with liquid volume fraction because it has been shown in previous sections that the change in the behavior patterns of the flow is minimal. The variation of the exponent associated with the non-dimensional pressure ratio produces little change in flow behavior under the SG reference condition. However, under the SG2 flashing condition the model goes from not generating any vapor under high absolute values of the exponents to finding the orifice partially filled with vapor at small absolute value of the exponents. This phenomenon changes not only the flow behavior but also the spray pattern downstream of the injector, a phenomenon that has been demonstrated thanks to the density profiles obtained 1 mm downstream of the injector tip. In addition to this, the influence of the time scale constant under the SG2 condition has also been analyzed since the influence of the time scale constant in the SG reference condition is much lower. This study has allowed to observe how low values of the time scale constant enhance the effect of flash boiling thus generating a greater phase change since it significantly decreases the equilibrium time scale and thus increases the phase change rate over the running time.

The effects observed are interesting and add value to the results already available in the literature. However, it is not possible to determine which values are the most suitable to simulate the behavior of internal and external flow since the available experimental data are limited in this particular area of study and the author does not have experimental profiles reflecting the studied variables, either densities or liquid or vapor mass/volume fraction, at 1 mm downstream of the injector tip. Therefore, this study leaves the question open for future experimental studies that will provide the necessary data to determine the correct constants associated with the phase change model and thus adequately capture the behavior of the GDI spray in the simulations.

6.8.3.4 Multiple injections conclusions

This sub-section deals with the study of an injection strategy quite common in diesel engines but relatively new in GDI applications, the multiple injection. The recent interest in this technique has led the ECN to create a specific operating condition for the study. One of the main problems encountered computationally in carrying out this type of study is that the needle cannot be completely closed to avoid overlap between surfaces. This results in an initial mass flow rate according to the stipulated initial lift and also impairs the correct reproduction of phenomena such as cavitation at the seat that take place in the initial and final stages of injection and that influence the flow behavior. For this reason, a sealing strategy based on opening and closing events to control the flow passage between regions is successfully implemented.

Concerning the obtained results, certain discrepancies have been observed between the experimental data available in the department and the simulations performed so, to validate the behavior of the multi-injections, it has been resorted also to the only experimental result available in the literature, to the best of the author's knowledge, which does fit the computational result obtained. In addition to validating the computational results, the study has also focused on finding an explanation for the behavior experimentally observed under low ET, reaching the conclusion that the problem cannot be attributed to a single factor but that there are several external agents that may be influencing the needle opening. Among these factors are the influence of the pressure wave dynamics in the second injection, the retaining charge by the solenoid after the first injection that may be altering the natural behavior of the needle or even a limitation in the experimental techniques for low ET.

This subsection also includes the study of different pilot injections where the ET of the pilot injection is varied maintaining the DT between injections and also keeping the characteristics of the main injection. Similarly, it has also

been carried out a study of different post injections where the ET of the main and post injections are preserved and the DT between injections are changed. The handicap of this study is that no needle lift profiles are available for these conditions, so it was necessary to resort to a strategy to create them. In the case of pilot injections, the individual lift profiles for different ET are available in the department and, as these are not influenced by a predecessor injection, they are used together with the lift profile of the main. For the post-injections, as the uplift profile corresponding to ECN condition G-M1 is available, what it is done is to vary the DT between injections keeping the uplift profiles intact. This study determines that the computational results faithfully reproduce the imposed uplift profiles so that if there were any influence of the pilot on the main or of the main on the post, as these uplift profiles do not consider them, they are not reproduced in the results either. However, due to the lack of experimental data, they are a suitable starting point to be used as input parameters in the study of the external flow where it is expected to see influences on the flow behavior and spray patterns.

6.8.3.5 LES approach conclusions

This subsection presents the numerical study of the internal and near-nozzle flow for the ECN multi-hole GDI injector where the accuracy of the calculations is improved by employing LES approaches in the treatment of the turbulence of the transient and stationary phases of the injection event. The results obtained have been validated and compared both with experimental data provided by the CMT-Motores Térmicos research group and available in the literature and with results also presented in this document where turbulence has been addressed by RANS models. The main findings of this particular research are summarized below.

As the results were compared with RANS data, a sample study is necessary to determine how many simulations are required to eliminate the variable component between simulations and ensure precision in the comparison. The analysis reveals that 3 simulations are sufficient to accurately carry out the above-mentioned comparison. It is noteworthy to highlight that if the study is only focused on macroscopic variables such as ROI or ROM, a single simulation is adequate for the analysis as the standard deviation between simulations is negligible.

Concerning the mass flow rate and momentum flux results, the quasi-steady condition is achieved before the needle lift reaches its maximum. Comparison of the results obtained with the LES model with the experimental data reveals differences of 9% in the ROI results and 6% in the ROM values. This is

mainly due to the fact that the applied symmetry condition does not correctly capture the fluid behavior in the cut orifices. In combination to this effect, the data acquisition distance can influence the momentum flux results. The calculation of dimensionless nozzle flow coefficients reflects the same conclusions as the ROI and ROM profiles. The discharge coefficient of this type of injectors is low due to the existence of the recirculation phenomenon which reduces the presence of liquid inside the counter-bore. The mentioned differences in ROI and ROM lead to higher discharge, momentum and area coefficient compared to the experimental results. LES models underestimate the flow detachment occurring inside the orifice while the RANS approach has an inverse behavior, overestimating this effect.

The use of LES approaches has allowed a more accurate study of spray behavior, improving the modeling of primary atomization by aerodynamic interaction. During the needle opening phase there is a strong interaction between jets, so it is necessary to have the adjacent jets available for the study of the atomization process. In the steady part of the simulation, high $\tilde{u}'_{rms}$ fluctuation values have been observed in areas where the liquid-vapor mixture is noteworthy. These same areas where $\tilde{u}'_{rms}$ is high have very low values of modeled TKE. Therefore, the modeled TKE becomes important in areas where the spray remains intact without interaction with the environment.

Referring to the spray angle and plume direction, results have been shown as a function of time, something that, to the author's best knowledge, has not been previously presented to date. The results obtained from RANS model do not present variation between sprays and are steady over time, without oscillations. On the contrary, LES approach displays higher variability with time and between orifices. This is caused by the asymmetric effect of upstream turbulence due to the distribution of bumps and holes in the geometry, which is amplified in LES models. Predicted trends from both turbulence approaches estimate values of spray angle and liquid plume direction close to the literature.

6.8.4 PIU injector transient state conclusions

This subsection gathers the main results obtained in the study of the in- and near- nozzle behavior under transient conditions, with moving needle, and different operating conditions by employing mainly the PIU injector and comparing its behavior in terms of needle lift profiles and nozzle flow hydraulic coefficients with the reference GDI injector Spray G belonging to the ECN. In addition, this subsection provides answers to three main issues that are commonly encountered when dealing with and analyzing real injectors installed in GDI engines:

- *Computational cost*: in RANS approaches, since the needle lift oscillations are small and have a negligible effect on the flow solution, most of the steady-state operation is not simulated. This shortens the injection duration and simulation time. The part that is not simulated is then included during post-processing of the simulation.
- *Pressure inlet boundary condition*: a realistic evolution of the inlet value is required as input to reproduce the experimental shapes of injection rate and momentum, especially during the opening transient phase. A parabolic increase of the discharge pressure to the injection pressure during the opening transient is successfully implemented.
- *Needle lift profile*: the x-ray technique provides an elevation curve with very low elevation values during the first few microseconds of the injection duration. This low elevation restricts the flow and causes the results of the simulations to differ from the experimental ones. By eliminating this small elevation of the needle, the accuracy of the simulations significantly improves.

Simulations have shown that GDI injectors are sensitive to the needle position, accurately knowing its value evolution in time allows predictive simulations in terms of rate of injection and momentum. Similarly, the upstream pressure (inlet pressure) plays a major role in the transient behavior of both signals, during the transients but also for the oscillations in steady state operation.

Low discharge coefficients of GDI nozzles, due either to the counter-bore or the conical shape, propitiate the ambient gas to flow inside the orifices and generate recirculation zones that enhance the air-fuel mixing. Expected spray cone angles of these type of nozzles are wider than typical straight or converging orifices. A secondary effect of this recirculation is the deviation of the spray axis from the orifice drill angle.

When compared to experiments, the presented simulations report a maximum difference of $\sim$5% in total injected quantity and hydraulic nozzle coefficients for two different nozzles and several injection conditions. The deviation in results could be reduced by bringing the simulation a little closer to the real model, for instance, by using temperature-dependent fluid properties. Finally, it should be noted that this is the expected error when the described methodology is applied to a different injection condition or nozzle, even though additional tests would be needed to confirm this general applicability.

References

[1] Guo, H. et al. “Numerical study on spray collapse process of ECN spray G injector under flash boiling conditions”. In: *Fuel* 290.December 2020 (2021), p. 119961. DOI: 10.1016/j.fuel.2020.119961.

[2] Payri, R. et al. “Nozzle Flow Simulation of GDi for Measuring Near-Field Spray Angle and Plume Direction”. In: *SAE Technical Paper 2019-01-0280* (2019), pp. 1–11. DOI: 10.4271/2019-01-0280.Abstract.

[3] Saha, K. et al. “Modeling of Internal and Near-Nozzle Flow for a Gasoline Direct Injection Fuel Injector”. In: *Journal of Energy Resources Technology* 138.5 (2016), p. 052208. DOI: 10.1115/1.4032979.

[4] Guo, H. et al. “Numerical investigation on flashing jet behaviors of single-hole GDI injector”. In: *International Journal of Heat and Mass Transfer* 130 (2019), pp. 50–59. DOI: 10.1016/j.ijheatmasstransfer.2018.10.088.

[5] Payri, R. et al. “Internal flow characterization on an ECN GDi injector”. In: *Atomization and Sprays* 26.9 (2016), pp. 889–919. DOI: 10.1615/AtomizSpr.2015013930.

[6] Saha, K. et al. “Investigation of Homogeneous Relaxation Model Parameters and Their Implications for Gasoline Injectors”. In: *Atomization and Sprays* 27.4 (2017), pp. 345–365. DOI: 10.1615/AtomizSpr.2017016338.

[7] Saha, K. et al. “Numerical Investigation of Two-Phase Flow Evolution of In- and Near-Nozzle Regions of a Gasoline Direct Injection Engine During Needle Transients”. In: *SAE International Journal of Engines* 9.2 (2016), pp. 1230–1240. DOI: 10.4271/2016-01-0870.

[8] Downar-Zapolski, P. et al. “The non-equilibrium relaxation model for one-dimensional flashing liquid flow”. In: *International Journal of Multiphase Flow* 22.3 (1996), pp. 473–483. DOI: 10.1016/0301-9322(95)00078-X.

[9] Moulai, M. et al. “Internal and Near-Nozzle Flow in a Multi-Hole Gasoline Injector Under Flashing and Non-Flashing Conditions”. In: *SAE Technical Paper 2015-01-0944* 2015-01-0944 (2015). DOI: 10.4271/2015-01-0944.Copyright.

[10] Payri, R. et al. “Momentum Flux Measurements on an ECN GDi Injector”. In: *SAE Technical Paper 2015-01-1893*. 2015. DOI: 10.4271/2015-01-1893.

[11] Duke, D. J. et al. "Internal and near nozzle measurements of Engine Combustion Network "Spray G" gasoline direct injectors". In: *Experimental Thermal and Fluid Science* 88 (2017), pp. 608–621. DOI: 10.1016/j.expthermflusci.2017.07.015.

[12] Vaquerizo, D. "Study on Advanced Spray-Guided Gasoline Direct Injection Systems". PhD thesis. Universitat Politècnica de València, 2017. DOI: 10.4995/Thesis/10251/99568.

[13] Gimeno, J. "Desarrollo y aplicación de la medida de flujo de cantidad de movimiento de un chorro Diesel". PhD thesis. E.T.S. Ingenieros Industriales, Universtitat Politècnica de València, 2008. DOI: 10.4995/Thesis/10251/8306.

[14] Payri, R. et al. "Experimental and computational study of the influence of partial needle lift on nozzle flowin diesel fuel injectors". In: *Atomization and Sprays* 22.8 (2012), pp. 687–714. DOI: 10.1615/AtomizSpr.2012005810.

[15] Sphicas, P. et al. "A Comparison of Experimental and Modeled Velocity in Gasoline Direct-Injection Sprays with Plume Interaction and Collapse". In: *SAE Int. J. Fuels Lubr.* 10 (2017), pp. 184–201. DOI: 10.4271/2017-01-0837.

[16] Baldwin, E. et al. "String flash-boiling in gasoline direct injection simulations with transient needle motion". In: *International Journal of Multiphase Flow* 87 (2016), pp. 90–101. DOI: 10.1016/j.ijmultiphaseflow.2016.09.004.

[17] Saha, K. et al. "Coupled Eulerian Internal Nozzle Flow and Lagrangian Spray Simulations for GDI Systems". In: *SAE technical paper 2017-01-0834*. 2017. DOI: 10.4271/2017-01-0834.

[18] Manin, J. et al. "Experimental Characterization of DI Gasoline Injection Processes". In: *SAE Technical Paper 2015-01-1894* (2015). DOI: 10.4271/2015-01-1894.

[19] Xu, M. et al. "Flash Boiling: Easy and Better Way to Generate Ideal Sprays than the High Injection Pressure". In: *SAE International Journal of Fuels and Lubricants* 6.1 (2013), pp. 137–148. DOI: 10.4271/2013-01-1614.

[20] Chen, J. L. et al. "Influence of needle lift on gasoline injector static flows". In: *SAE Technical Papers* 412 (1996). DOI: 10.4271/961121.

[21] Shahangian, N. et al. "Spray Orientation Assessment and Correction Method for GDI Momentum Flux Measurements". In: October (2019), pp. 231–241.

[22] Moon, S. et al. "Ultrafast X-ray study of multi-hole GDI injector sprays: Effects of nozzle hole length and number on initial spray formation". In: *Experimental Thermal and Fluid Science* 68 (2015), pp. 68–81. DOI: 10.1016/j.expthermflusci.2015.03.027.

[23] Mohapatra, C. et al. "Modeling sealing in transient injector simulations". In: *American Society of Mechanical Engineers, Fluids Engineering Division (Publication) FEDSM* 1A-2017 (2017), pp. 1–10. DOI: 10.1115/FEDSM2017-69309.

[24] Payri, R. et al. "ECN Spray G external spray visualization and spray collapse description through penetration and morphology analysis". In: *Applied Thermal Engineering* 112 (2017), pp. 304–316. DOI: 10.1016/j.applthermaleng.2016.10.023.

[25] Bautista Rodriguez, A. "Study of the Gasoline direct injection process under novel operating conditions". PhD thesis. Universitat Politècnica de València, 2021.

[26] Salvador, F. J. et al. "Using one-dimensional modeling to analyze the influence of the use of biodiesels on the dynamic behavior of solenoid-operated injectors in common rail systems: Results of the simulations and discussion". In: *Energy Conversion and Management* 54.1 (2012), pp. 122–132. DOI: 10.1016/j.enconman.2011.10.007.

[27] Huang, Y. et al. "Numerical investigation to the dual-fuel spray combustion process in an ethanol direct injection plus gasoline port injection (EDI + GPI) engine". In: *Energy Conversion and Management* 92 (2015), pp. 275–286. DOI: 10.1016/j.enconman.2014.12.064.

[28] Kar, K. et al. "Measurement of vapor pressures and enthalpies of vaporization of gasoline and ethanol blends and their effects on mixture preparation in an SI engine". In: *SAE International Journal of Fuels and Lubricants* 1.1 (2009), pp. 132–144. DOI: 10.4271/2008-01-0317.

[29] Kale, R. et al. "Experimental investigation on GDI spray behavior of isooctane and alcohols at elevated pressure and temperature conditions". In: *Fuel* 236.April 2018 (2019), pp. 1–12. DOI: 10.1016/j.fuel.2018.08.153.

[30] Payri, R. et al. "Numerical Analysis of GDI Flash Boiling Sprays Using Different Fuels". In: *Energies* 14.18 (2021), p. 5925. DOI: 10.3390/en14185925.

[31] Medina, M. et al. "High-Speed Imaging Study on the Effects of Internal Geometry on High-Pressure Gasoline Sprays". In: *SAE Technical Papers* 2020 (2020), pp. 1–14. DOI: 10.4271/2020-01-2111.

[32] Pratama, R. H. et al. "Hydraulic flip in a gasoline direct injection injector and its effect on injected spray". In: *Fuel* 310.PB (2022), p. 122303. DOI: 10.1016/j.fuel.2021.122303.

[33] Pickett, L. M. et al. "Transient rate of injection effects on spray development". In: *SAE Technical Papers* 6 (2013), pp. 15–16. DOI: 10.4271/2013-24-0001.

[34] Sphicas, P. et al. "Interplume velocity and extinction imaging measurements to understand spray collapse when varying injection duration or number of injections". In: *Atomization and Sprays* 28.9 (2018), pp. 837–856. DOI: 10.1615/AtomizSpr.2018025956.

[35] Gomez Santos, E. "Simulation and numerical modelling of three-phase flow in automotive high-pressure fuel injectors." In: (2020), pp. 1–124.

[36] Sou, A. et al. "Effects of Asymmetric Inflow on Cavitation in Fuel Injector and Discharged Liquid Jet". In: *Atomization and Sprays* 26.9 (2016), pp. 939–959. DOI: 10.1615/AtomizSpr.2015013501.

[37] Pei, Y. Q. et al. "Experimental study on the particulate matter emission characteristics for a direct-injection gasoline engine". In: *Proceedings of the Institution of Mechanical Engineers, Part D: Journal of Automobile Engineering* 228.6 (2014), pp. 604–616. DOI: 10.1177/0954407013493899.

[38] Yang, J. et al. "Fuel injection strategies to increase full-load torque output of a direct-injection SI engine". In: *SAE Technical Papers* 724 (1998). DOI: 10.4271/980495.

[39] Seo, J. et al. "Numerical investigation of the combustion characteristics and wall impingement with dependence on split-injection strategies from a gasoline direct-injection spark ignition engine". In: *Proceedings of the Institution of Mechanical Engineers, Part D: Journal of Automobile Engineering* 227.11 (2013), pp. 1518–1535. DOI: 10.1177/0954407013491216.

[40] O'Connor, J. et al. "Post injections for soot reduction in diesel engines: A review of current understanding". In: *SAE International Journal of Engines* 6.1 (2013), pp. 400–421. DOI: 10.4271/2013-01-0917.

[41] Vanegas, A. et al. "Experimental investigation of the effect of multiple injections on pollutant formation in a common-rail di diesel engine". In: *SAE Technical Papers* 2008.724 (2008). DOI: 10.4271/2008-01-1191.

[42] Kavuri, C. et al. "Post-injection strategies for gasoline compression ignition combustion under high load conditions: Understanding the role of premixed, main, and post-injections in soot mitigation and load extension". In: *Fuel* 233.June (2018), pp. 834–850. DOI: 10.1016/j.fuel.2018.06.137.

[43] Torregrosa, A. J. et al. "Study of turbulence in atomizing liquid jets". In: *International Journal of Multiphase Flow* 129 (2020), p. 103328. DOI: 10.1016/j.ijmultiphaseflow.2020.103328.

[44] Zamani, H. et al. "Large eddy simulation of GDI single-hole and multihole injector sprays with comparison of numerical break-up models and coefficients". In: *Journal of Applied Fluid Mechanics* 9.2 (2016), pp. 1013–1022. DOI: 10.18869/acadpub.jafm.68.225.22889.

[45] Meyers, J. et al. "Database analysis of errors in large-eddy simulation". In: *Physics of Fluids* 15.9 (2003), pp. 2740–2755. DOI: 10.1063/1.1597683.

[46] Geurts, B. J. et al. "A framework for predicting accuracy limitations in large-eddy simulation". In: *Physics of Fluids* 14.6 (2002). DOI: 10.1063/1.1480830.

[47] Pope, S. *Turbulent Flows*. sixth. Cambridge University Press, 2009.

[48] Battistoni, M. et al. "Large-Eddy Simulation (LES) of Spray Transients: Start and End of Injection Phenomena". In: *Oil & Gas Science and Technology - Revue d'IFP Energies nouvelles* 71.4 (2016), p. 4. DOI: http://dx.doi.org/10.2516/ogst/2015024.

[49] Yue, Z. et al. "Spray characterization for engine combustion network Spray G injector using high-fidelity simulation with detailed injector geometry". In: *International Journal of Engine Research* 21.1 (2020), pp. 226–238. DOI: 10.1177/1468087419872398.

[50] Brusiani, F. et al. "LES simulation of ICE non-reactive flows in fixed grids". In: *SAE Technical Papers* 2008.724 (2008), pp. 776–790. DOI: 10.4271/2008-01-0959.

[51] Celik, I. B. et al. "Index of resolution quality for large eddy simulations". In: *Journal of Fluids Engineering, Transactions of the ASME* 127.5 (2005), pp. 949–958. DOI: 10.1115/1.1990201.

[52] Celik, I. et al. "Assessment measures for engineering LES applications". In: *Journal of Fluids Engineering, Transactions of the ASME* 131.3 (2009), pp. 0311021–03110210. DOI: 10.1115/1.3059703.

[53] Shahangian, N. et al. "Transient nozzle flow simulations of gasoline direct fuel injectors". In: *Applied Thermal Engineering* (2020), p. 115356. DOI: 10.1016/j.applthermaleng.2020.115356.

[54] Cheng, Q. et al. "Investigation on the spray characteristics of standard gasoline, n-pentane, iso-octane and ethnaol with a novel heated tip SIDI injector". In: *Applied Thermal Engineering* 110 (2017), pp. 539–552. DOI: 10.1016/j.applthermaleng.2016.07.201.

[55] Shi, J. et al. "Evidence of vortex driven primary breakup in high pressure fuel injection". In: September (2017), pp. 6–8. DOI: 10.4995/ilass2017.2017.5707.

[56] Grover, R. O. et al. "String Flash-Boiling in Flashing and Non-Flashing Gasoline Direction Injection Simulations with Transient Needle Motion University of Massachusetts Amherst General Motors Research and Development Energy Systems Division , Argonne National Laboratory , Lem". In: *ILASS Americas 28th Annual Conference on Liquid Atomization and Spray Systems* May (2016).

[57] Battistoni, M. et al. "Highly resolved Eulerian simulations of fuel spray transients in single and multi-hole injectors: Nozzle flow and near-exit dynamics". In: *Fuel* 251 (2019), pp. 709–729. DOI: 10.1016/j.fuel.2019.04.076.

[58] Shahangian, N. et al. "Nozzle Flow and Spray Development One-Way Coupling Methodology for a Multi-Hole GDi Injector". In: *SAE Technical Paper Series* (2019). DOI: 10.4271/2019-24-0031.Abstract.

[59] Marti-Aldaravi, P. et al. "Numerical Simulation of a Direct-Acting Piezoelectric Prototype Injector Nozzle Flow for Partial Needle Lifts". In: *SAE Technical Papers* 2017-24-01 (2017). DOI: 10.4271/2017-24-0101.

[60] Battistoni, M. et al. "Effect of Off-Axis Needle Motion on Internal Nozzle and Near Exit Flow in a Multi-Hole Diesel Injector". In: *SAE International Journal of Fuels and Lubricants* 7.1 (2014), pp. 2014–01–1426. DOI: 10.4271/2014-01-1426.

[61] Payri, R. et al. "Using one-dimensional modeling to analyze the influence of the use of biodiesels on the dynamic behavior of solenoid-operated injectors in common rail systems: Detailed injection system model". In: *Energy Conversion and Management* 54.1 (2012), pp. 90–99. DOI: 10.1016/j.enconman.2011.10.007.

Chapter 7

External Flow Analysis

"Everything is theoretically impossible, until it is done."
—Robert A. Heinlein

7.1 Introduction

This section is mainly dedicated to the study of the external flow individually, following the trend in the literature that considers the analysis of internal and external flow separately, despite the great dependence between them. Section 6 includes the study of the internal flow under diverse operating conditions and using different injection strategies. It includes the validation of one of the main objectives pursued throughout this document as the predictive methodology, determining a high accuracy of the same with high applicability regardless of the characteristics of the injector or the simulation code adopted. Looking for a continuity to this study and, above all, seeking to extend the applicability of the predictive methodology also to the study of the spray pattern, the following lines collect the validation and corresponding discussion focused on the mentioned objectives.

In order to carry out the above mentioned analysis and meet the proposed objectives, the most common approach in the study of external flow has been chosen, the Droplet Discrete Model (DDM), where the input parameters to be imposed, such as the flow injection velocity, and the geometrical and hydraulic parameters that characterize the injector are directly obtained from

the experiments. As in the case of internal flow, the development of the predictive methodology for spray characterization will be carried out with the reference injector of the ECN network, Spray G, and using the software code CONVERGE™ . The determination of the validity as well as the accuracy of the developed predictive methodology will be carried out on the basis of experimental data present in the literature with special consideration of the macroscopic parameters defining the spray behavior such as liquid and vapor penetrations, spray angle, and axial velocity of the ambient gas. In addition, attention will also be paid to the spray shape by comparing it with data from the liquid phase of the spray obtained by experimental DBI techniques and images corresponding to the vapor phase where Schliren techniques were employed.

7.2 Sensitivity Analyses

As mentioned above, this section is based on the use of the Droplet Discrete Model or blob-model for the study of the external flow. In this type of approaches a detailed geometry of the injector is not used but a virtual injector is defined from the geometrical and hydraulic parameters of the real injector, presented in Section 5.3.4.1. In CONVERGE™ it is only necessary to define the sizes of the orifices both diameter and length, the position of the orifices and the direction of the spray. The fields that define the injection characteristics and that are obtained from the experiments are the injection rate (presented in Figure 6.20a) and the discharge coefficient defined at a value of 0.55 (see Table 6.28). In addition, it is also necessary to give other input information such as the particle temperature that is defined based on the operating conditions (in this study is set to 363K, equal to the injection temperature).

7.2.1 Domain independence

This subsection presents the results of analyzing the influence of the geometry on the spray characteristics using the SG reference condition as operating point. It is important to determine a domain size so that, as in the internal flow, the boundary and initial conditions do not influence the spray behavior. The computational domain chosen for the study is cylindrical, therefore this study includes the variation of the two main measures that make it up, height and radius. Tables 7.1 and 7.2 include the results of both studies. The chosen sizes, the computational cost of the simulation and the accumulated differences in the liquid and vapor penetration variable chosen for the validation of the model are presented. The differences are calculated with respect to the

size immediately smaller, taking as reference the larger sizes since they are the ones considered without influence. The differences between study cases are minimal and in all cases less than 5%, the threshold determined as experimental uncertainty, so it could be said that for both height and radius, any size of those chosen for the study would be valid. Based on previous studies in this department and the expected values of spray penetrations, 100 mm height and 100 mm radius have been chosen [1, 2].

Height	CPU-h	Differences [%]	
		Liquid	Vapor
60 mm	0.92	2.95	2.10
80 mm	2.20	2.10	0.99
100 mm	2.30	1.92	1.54
120 mm	2.49	-	-

Table 7.1: Sensitivity analysis and influence of domain height on macroscopic penetration parameters.

Radius	CPU-h	Differences [%]	
		Liquid	Vapor
80 mm	2.3	3.41	0.45
100 mm	2.37	2.55	0.93
120 mm	2.41	2.04	1.43
140 mm	2.47	-	-

Table 7.2: Sensitivity analysis and influence of domain radius on macroscopic penetration parameters.

7.2.2 Mesh independence

Once the computational domain to work with has been chosen, it is common to carry out a study that collects the influence of the cell size on the spray pattern. In this case, the study is proposed taking as reference two different base sizes, 4 mm based on studies present in the literature [3] and 8 mm in order to reduce the computational cost. Making use of the valuable AMR tool present in CONVERGE™ , both studies were made to work in parallel reaching similar minimum cell sizes as seen in Table 7.3. This table presents two different outcomes, firstly a comparison between the similar cases with different base sizes (8 mm and 4 mm) displayed in the lower part, and on the other hand, the influence on the spray behavior according to the variation of the minimum cell size, a study that is complemented with the evolution of the penetration as a function of time depicted in Figure 7.1. The differences were minimal and less than 4% in all the cases tested, as indicated at the bottom of the Table 7.3 where the reported values are the cumulative differences between cases with the same minimum cell size. For this reason, and always taking into account computational savings, the appropriate size for these studies was 8 mm base cell.

The next step is to study the optimal minimum cell size. This analysis is presented in the upper part of the Table 7.3 where the accumulated differences

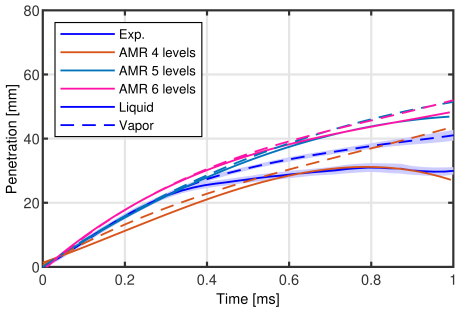

Figure 7.1: Mesh influence on the spray macroscopic penetration variables for the Spray G injector under SG reference condition.

Case (Independence)	CPU-h	Differences [%] Liquid	Vapor
8_4 (Min. 0.5 mm)	0.71	25.20	17.21
8_5 (Min. 0.25 mm)	2.20	5.55	4.18
8_6 (Min. 0.125 mm)	3.86	-	-
Case (8 mm vs. 4 mm)	CPU-h	Differences [%] Liquid	Vapor
4_3 (Min. 0.5 mm)	1.89	1.96	1.85
4_4 (Min. 0.25 mm)	5.02	1.78	1.34
4_5 (Min. 0.125 mm)	27.07	4.06	3.18

Table 7.3: Sensitivity analysis and influence of mesh size on the macroscopic penetration parameters for the Spray G injector under SG reference condition.

reflected correspond to the comparison of each case with the immediately superior more refined. This study is complemented by Figure 7.1 which displays the evolution of the liquid and vapor penetrations for the different cases of study under a base cell size of 8 mm and compares them with the experimental results. Each case includes in its name the number of refinement levels it has, which means that the 8_5 case has a base cell size of 8 mm with 5 AMR refinement levels. Starting with the 8 mm case and 4 refinement levels (0.5 mm minimum cell size), and despite being one of the minimum sizes used in the literature [4, 5], for this particular case one can observe large cumulative differences with respect to a cell size immediately below. Comparing the penetration behavior with the experimental trends, although at the end of the injection it seems to be more in line with the experimental values, in the initial instants it has a lower injection velocity. Simulations underpredicts the penetrations and does not capture the typical parabolic trend either. Comparing the next two refinement levels (0.25 and 0.125 mm minimum cell size respectively), cumulative differences between cases of approximately 5% are observed. Regarding the trends of the penetration curves, both cases capture well the initial injection behavior, deviating from the experiments in the final stages. It should be noted that, if necessary, it is possible to calibrate the constants of the breakup atomization models to adjust the curves to the experimental behavior. These constants are mostly part of the secondary rupture model. For this reason, together with a similar behavior between cases and the reference literature [3], the selected case setup for the subsequent studies is the 8 mm base cell and 5 refinement levels obtaining a minimum cell size of 0.25 mm, considered sufficient to capture the spray pattern.

7.2.3 Break-up model and turbulence influence

After determining the optimum domain and mesh size for the study of the GDI spray behavior, this section aims to show the influence of the atomization and turbulence models and their constants on the spray patterns (see Figure 7.2). One of the main features of the configuration used for the spray study is the use of a primary atomization model such as KH-ACT. This modifies the behavior of the classical Kelvin-Helmholtz (KH) model to include in-nozzle aerodynamic, cavitation and turbulence effects. Therefore, the objective was to observe the difference in spray behavior, if any, between the use or not of this model. The results obtained are illustrated in Figure 7.2a, in comparison with the experiments. The activation of the KH-ACT model causes the atomization to be higher, thus obtaining a smaller droplet size that opposes less resistance, drag force and, so penetrates more during practically all the injection time represented. Moreover, the smaller droplet size causes the evaporation to occur earlier, thus observing, under the present evaporative SG condition, how at the end of the injection time the vapor phase begins to gain distance respect to the liquid. On the contrary, the non-use of KH-ACT makes the droplet size bigger and so the penetration behavior tends to be more linear. Also, after some time, the penetration of this case would be higher due to the inertia of the larger droplets together with the delayed action of the evaporative process. The trends closer to the experiments are those of the KH-ACT model and therefore this configuration will be used from now on.

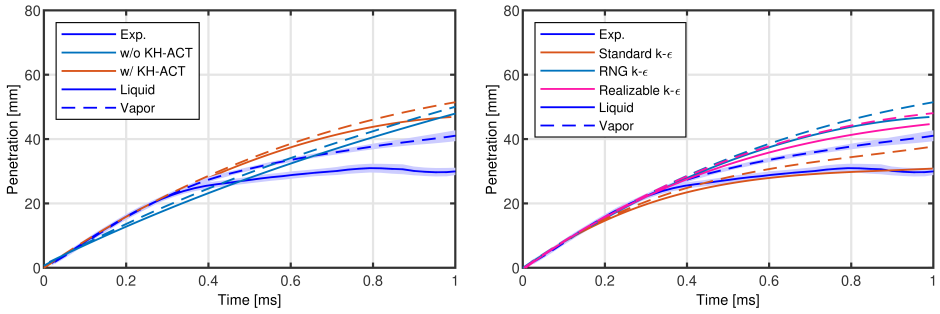

(a) Break-up model (b) Turbulence model

Figure 7.2: Break-up model and turbulence model influence for the Spray G injector under SG reference condition.

The next part of the study encompasses the effect of turbulence on spray behavior. For this purpose, three turbulence models (Standard k-ε, Realizable, k-ε and RNG k-ε) initially selected for their high capability of far from the

walls behavior have been analyzed. The first selected model was RNG k-ϵ for consistency with the one adopted in the internal flow research, however, as shown in Figure 7.2b, it does not correctly capture the behavior of the spray for this particular case even though it has been used in the literature in similar studies [6]. This is mainly due to the fact that the improvements that the RNG k-ε has over the classical Standard k-ε model (such as enhancing swirling flows or treatment of low Reynolds number flows) are not really applicable for this type of environment. The Realizable k-ε model also does not seem to accurately capture the spray pattern since it is not a rotational flow, where this model works accurately. In conclusion, it is the Standard k-ε model that faithfully captures the turbulent behavior of the spray. The existing over-prediction of the penetration values is mitigated, and the evaporation process is better captures under the SG reference condition. Therefore, from now on this Standard k-ε model will be the one used in the study.

7.2.4 Mesh orientation influence

Throughout the chapter on internal flow (Chapter 6) the possible influence of the mesh orientation on the flow behavior was mentioned several times and that is why this section deals with this problem. Saha et al. [7] demonstrated how the numerical diffusion was dependent on the alignment of the plumes with the cartesian mesh so they suggested rotating the entire geometry 22.5° in order to mitigate the effect. This research collects three different orientations, 0°, 22.5° and 30° (Figure 7.3b), in order to observe how they affect the behavior of the spray and the shape of the spray. On the one hand, Figure 7.3a shows the penetrations associated with each orientation where no differences between them can be notice, so it can be said that the mesh orientation does not influence the macroscopic results of the spray. On another side, Figure 7.3b presents, at the top, the parcel distribution as a function of the chosen orientation together with, and at the bottom, a slice 15 mm downstream of the injector tip reflecting the shape of each spray. These two images together show how at the 0° orientation, the sprays that are aligned to the cartesian grid appear to be split and their shape is different between odd and even sprays. Regarding the 30° orientation, although more uniform, an anomalous behavior between sprays is also observed. At certain temporal instants the spray appears to break, creating two clouds of particles, one at the head of the spray and the other behind it. Thus, this orientation is not recommended. Finally, focusing on the orientation corresponding to the one recommended in the literature [7], 22.5°, uniformity between sprays is observed taking into account that the geometry used belongs to generation 1 and the characteristics of each orifice have been defined on the basis of uniform measurements.

The behavior of the sprays is similar among them taking into account that the imposed boundary conditions and spray inputs are identical for all sprays, moreover, no influence of the mesh is observed. Therefore, this orientation is chosen for further studies.

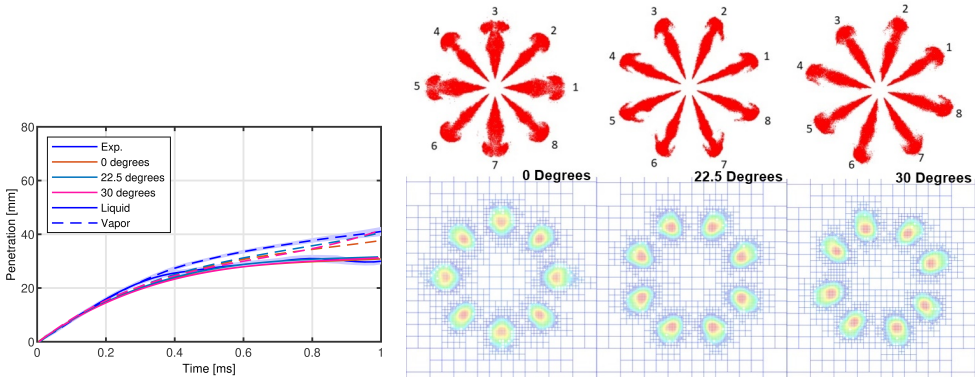

(a) Penetrations (b) Orientation influence

Figure 7.3: Mesh orientation influence for the Spray G injector under SG reference condition

7.3 Spray G Condition. Validation and Discussion

Once the sensitivity studies of both domain and mesh have been carried out and the influence of the turbulent model on the spray behavior as well as the effect of the atomization sub-models on the jet characteristics have been dealt with, this subsection includes the validation of the model presented for the study of the external flow. The operating condition used for the validation is the reference one, SG, and the experimental data adopted for the comparison come from previous studies carried out in the same department [1, 2] where the present Thesis has been performed.

Figure 7.4 presents the obtained results in comparison with experimental data. On the left part of the image, corresponding to Figure 7.4a, the computational liquid and vapor penetrations are presented. As it can be seen, in the case of the liquid penetration, it could not be said that there are differences between simulations and experiments because during the duration of the injection both curves overlap. A slight difference can be noticed at the end of the simulated time but the values are within the standard deviation of the experiments. Therefore, based on the aforementioned, it can be

assured that the model accurately captures more than the behavior of the spray in terms of liquid penetration. Regarding the vapor phase, in this case some differences are visible, being no greater than 5% in the cumulative calculation. This may be indicating that the evaporative model is not acting correctly since it underpredicts evaporation under this operating condition. On the other hand, in the central image corresponding to the calculation of the global spray angle, Figure 7.4b, it can be observed how computationally the jet opening is captured with high precision. It is true that in the initial instants, in the experimental case, a high spray angle is predicted, which could be due to an error in the processing or to the fact that the tendency of the jet in the first instants is to expand in amplitude and not in length due to the existing back pressure. It should also be noted that in the final instants of the injection, the experimental description of the spray tends to narrow faster than in the simulations. Despite these mentioned details, the accuracy of the model in predicting the overall spray angle can be strongly affirmed. Finally, with respect to the axial gas velocity measured at a distance of 15 mm as determined by the ECN and presented in Figure 7.4c, it can be observed that although the trend is captured to a large extent, the velocity values are underestimated. The reason for this effect may be attibuted to the direction of the sprays, which in classical DDM, is determined by the user, being in this case defined at 37° so the deflection of the jets towards the injector axis typically found in this type of injectors is not taken into account. A larger spray aperture may result in a lower induced velocity at the point of study. This effect has been observed in other works in the literature such as that of Nocivelli et al. [3] where, in contrast, the tendency was to overpredict the gas velocity. Blaming the problem on the poor accuracy of the AMR, in order to improve the behavior, they defined a fixed mesh refinement in the form of a cylinder that allowed to better capture the studied variable. Nevertheless, the improvement was not remarkable, being the trends the same and only reducing the overprediction value. In the present work, the same strategy was also tested, being the observed improvements minimal and not compensating in terms of computational cost, so it was discarded.

In addition to the macroscopic parameters that characterize the spray, a direct spray contour comparison with experiments is included. In order to provide a visualization as close as possible to the experiments, the values of the liquid volume fraction and the vapor fuel mass fraction have been projected on the experimental visualization plane. The obtained results have been reported in Figure 7.5. The images allow to corroborate the general conclusion already drawn: the developed model for the study of the spray behavior downstream of the injector accurately captures in detail the spray patterns. The shape

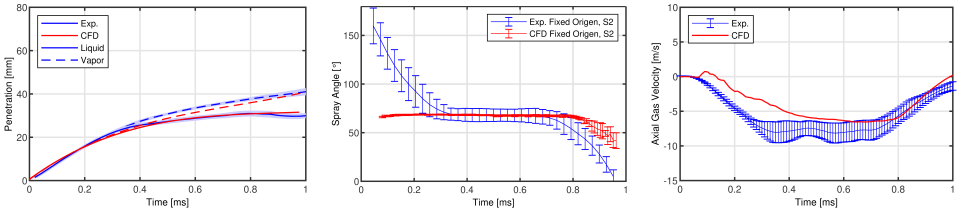

(a) Penetration (b) Spray Angle (c) Axial Gas Velocity

Figure 7.4: Validation of the DDM model employed to study of the external flow for the Spray G injector under SG reference condition.

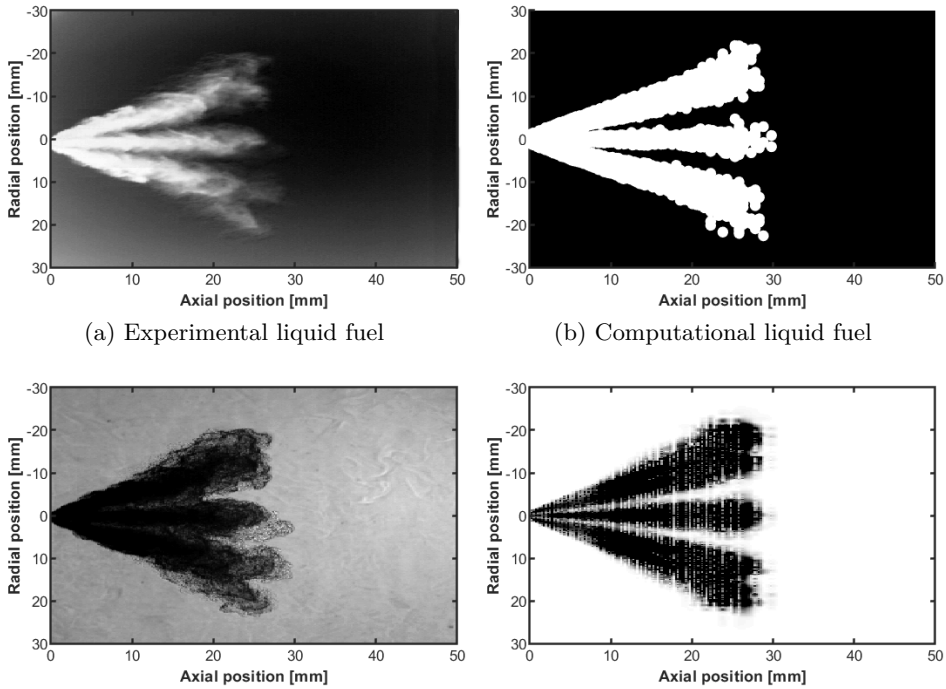

(a) Experimental liquid fuel (b) Computational liquid fuel

(c) Experimental vapor fuel (d) Computational vapor fuel

Figure 7.5: Spray morphology comparison for the Spray G injector under SG reference condition at t = 0.6 ms.

of the sprays is perfectly reproduced both in the liquid and vapor phases. However, what would justify the underprediction of the axial gas velocity is that, although the individual opening of each jet seems to adequately capture the experiments (the spray angle introduced is correct, demonstrating the

accuracy of the internal flow studies), the interaction that seems to exist in the experimental case is not so noticeable in the simulations. This may be because the initialization of the spray direction is defined according to the geometrical axis of each of the sprays. However, it has been observed throughout this work that the sprays tend to deviate towards the injector axis. A closer proximity between sprays would generate a greater interaction between them and therefore a higher induced gas velocity.

7.4 Influence of the Operating Condition on the Spray Patterns

Once the model to be used under the standard SG ECN condition is validated, this subsection determines the validity and applicability of the model under different operating conditions where the expected phenomena are very different, thus demonstrating the accuracy of the predictive methodology under development. The parameters from which the model will be evaluated are the same as those mentioned above, liquid and vapor penetrations, overall spray angle and axial gas velocity.

Before going into the outcomes, note that for SG and SG3 conditions the experimental data used in the validation belong to experimental studies carried out under the same experimental campaign at CMT. However, for the case of SG2 the come from the data openly shared repository in the ECN, belonging to the Sandia National Laboratories group [8]. This is due to the fact that in the first experimental campaign at CMT sub-atmospheric conditions were not taken into account due to limitations in the experimental techniques. However, later on, another similar experimental campaign was developed where conditions with ambient pressures below atmospheric values were included. This campaign took place in different experimental facilities. Therefore, there is a disparity between results that has yet to be resolved. Therefore, it was decided to use certified and shared experimental data by the ECN for the validation of the flash boiling condition.

The initial objective of the predictive methodology was to calibrate the model so that it would be valid for all the operating conditions tested. Some authors have achieved this, as in the case of Payri et al. [5], but they have had to sacrifice precision in some of the conditions in order to minimize the errors in the entire test matrix. This approach was too ambitious and even more so considering studies such as Jaramillo, D. [9] where it was clearly demonstrated that DDM models should be calibrated specifically for different operating conditions or those of Nocivelli et al. [3] who disregarded sub-models

such as the collision model to capture the characteristic shape of the spray under flashing conditions. Taking this into consideration, initially, for the study of the spray under the SG2 condition, the same model used for SG was considered. This led to results that were far off in terms of penetration, and the shape of the jets were dart-shaped and did not show the typical aperture achieved under flash boiling conditions. Subsequently, a calibration of the constants of the breakup models was attempted [9], but did not improve the performance. Finally, the proposed solution was to disregard the primary atomization model so that the breakup and atomization of the spray was left entirely in the hands of the KH-RT model. This allowed the spray to behave in a way in accordance with the literature, thus achieving a spray opening in line with the flashing condition and the associated air entrainment.

With respect to the results obtained depicted in Figure 7.6, it can be noticed a high precision in the penetrations obtained under the SG2 condition, although a small deviation is appreciated at the end of the injection, which incurs a cumulative difference of less than 7%. With respect to the SG3 condition, which uses exactly the same model as the SG case, it can be observed how the trend of the penetration curve is correctly captured incurring in a cumulative difference of less than 8% and mainly due to the experimental trend change, deviating from the parabolic trend in the middle of the injection, added to a small overprediction of the penetration in the final moments of the injection. Nevertheless, it can be stated that the predictive model is correctly applied to different operating conditions, thus obtaining high accuracy, properly capturing the expected spray pattern.

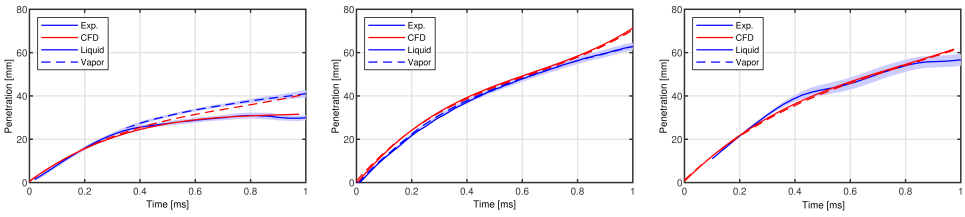

(a) SG condition (b) SG2 condition (c) SG3 condition

Figure 7.6: Validation of the applicability of the developed DDM model for the study of the Spray G injector external flow under different operating conditions.

The following two Figures 7.7 and 7.8 are going to be explained together as they are completely related to each other. Figure 7.7 reflects the global spray angles for the three studied conditions. It can be seen that the SG2

condition has a larger spray angle either because initially a 5° larger spray angle is defined for each individual spray or either because under flash boiling conditions the sprays tend to open due to the air encompassed inside them (see Figure 7.8). This generates an interaction between sprays, visible in the presented vapor projections, which increases the values of the induced velocity in the center of the domain at 15 mm downstream of the injector as depicted in Figure 7.7b. Regarding the SG3 condition, which is considered a non-evaporative and non-flashing condition for the iso-octane reference fuel, it has an individual spray opening similar to SG but overall the spray tends to open a few degrees more (see Figure 7.7a). This leads to the associated lower or, in this case, zero axial gas velocity induced in the center of the domain due to the large spray separation, as shown in Figure 7.7b.

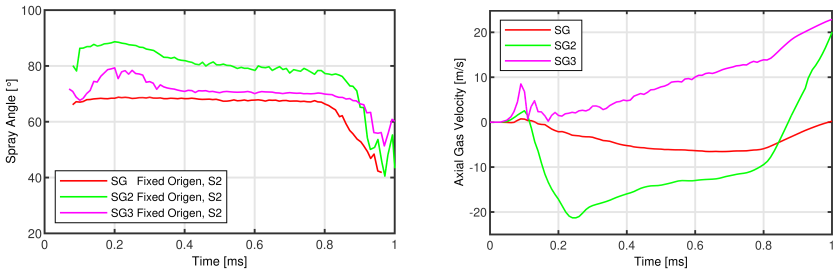

(a) Spray Angle (b) Axial Gas Velocity

Figure 7.7: Spray angle and axial gas velocity comparison between the different operating conditions tested for the Spray G injector.

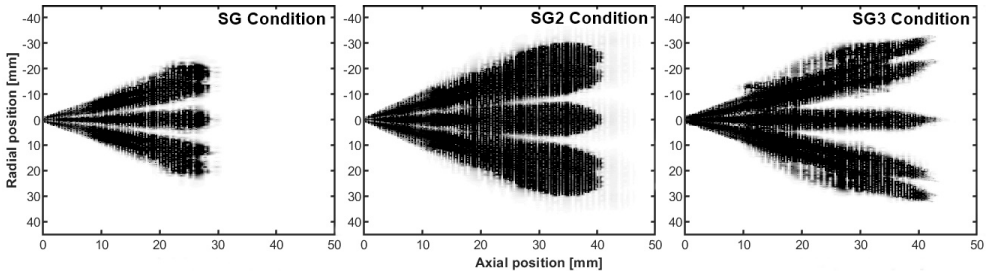

Figure 7.8: Vapor projection on the visualization plane for the different operating conditions at t = 0.6 ms for the Spray G injector.

The lack of experimental data of axial velocity and spray angle under SG2 and SG3 operating conditions makes impossible to validate the comparison computationally performed between conditions and observe trend. However,

the identified spray projection behaviors are similar to those reported in the literature by different researchers and institutions [3–5]. Therefore, the accuracy of the model and the validity of the predictive methodology employed can be affirmed.

7.5 Spray Patterns through Large Eddy Simulations

Following the same procedure that was carried out in the study of internal nozzle flow (Section 6.6.5), it is considered of interest to go one step further in the treatment of turbulence and analyze the behavior of the spray once it leaves the injector by considering the turbulent flow from a LES approach. There are not many works in the literature where LES models have been used to study the behavior of the GDI jet [10, 11]. Therefore, it is considered that this study may yield valuable conclusions for the scientific community. The methodology of this case is described in Sections 5.3.5.1 and 5.3.6.1 and differs from the one employed in previous RANS analysis. One thing to note is that unlike the internal nozzle flow, this case only considers to model the unclosed non-linear term from the one-equation Dynamic Structure sub-grid model, which is the most recommended for engine applications [12] although the Viscous One-Equation allows coarser meshes.

According to the procedure followed in studies involving scale-resolved large eddy simulations (LES), the first step is to determine whether the selected mesh meets the selected quality criteria, so that at least 75% of the energy is resolved. For the present study, the quality criterion of Celik at al. [13] governed by the Equation 6.3 has been relied upon. The study involved in the injection process has a transient nature so that the quality index cannot be calculated as time averaged. Another possible way to assess this quality would be to average the results from different realizations, but this is not possible in this context because only one simulation has been carried out since the objective is to study the macroscopic parameters of the spray which, as was the case in the internal flow (Section 6.6.5.3) do not vary significantly between simulations (Section 6.6.5.3). In order to ensure that the quality is globally guaranteed, different time instants have been individually evaluated. Figure 7.9 reflects the mesh quality obtained for the 0.6 ms time aSOI under two different scales. It can be clearly noticed that the turbulent scales of the spray, closest to the injector and around the jets, are above the established threshold; however further downstream, the center of the spray does not meet the stipulated quality criterion. For this work, a base cell size of 1 mm and a

minimum cell size of 0.0625 mm have been considered, values that are within what is stipulated as recommended in the literature [14]. Taking into account the accurate results of in the internal flow studies that did not meet but was close enough to the quality standards, for this particular research a compromise between computational cost and accuracy has been sought. Therefore, it has been considered that the adopted sizes are sufficient to focus the study on the macroscopic parameters of the jet.

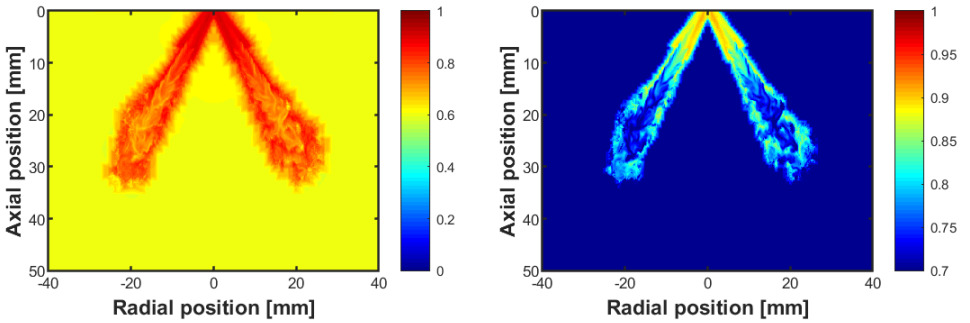

Figure 7.9: External flow LES quality assessment based on the viscosity evaluated for the Dynamic Structure sub-grid model for the Spray G injector under the SG reference condition.

The present study includes macroscopic results covering liquid and vapor penetrations, spray angle and axial gas velocity obtained from the consideration of LES approach to deal with the turbulent nature of the injection. These will be presented together with data obtained from previous studies employing RANS approach (Section 7.3) and corresponding experimental data. All these results are presented in Figure 7.10. Firstly, referring to the liquid and vapor penetrations reflected in Figure 7.10a, both RANS and LES models approximate the results and the spray behavior to the experimental trends. It is true that while the liquid penetrations trends are similar between RANS and LES with cumulative differences with respect to the experimental penetration of 5%, the vapor penetrations show a somewhat different behavior. The LES model seems to enhance the evaporation of the droplets, providing higher momentum for the fluid vapor phase thus generating a higher vapor penetration, a phenomenon that is also visible in Figure 7.11 where the vapor contours projected on the experimental visualization plane are reflected. The cumulative differences in the case of RANS for vapor penetrations are around 5% while for LES they are close to 7%, however both approaches are considered to capture experimental trends with high accuracy.

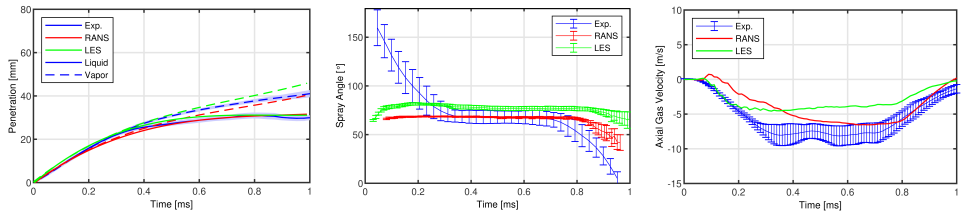

(a) Penetration (b) Spray Angle (c) Axial Gas Velocity

Figure 7.10: Comparison of spray pattern behavior in terms of macroscopic variables under different turbulence approaches for the Spray G injector under the SG reference condition.

Referring to the obtained results for the global spray opening taking into account the liquid phase (Figure 7.10b), it can be clearly appreciated that although the initial configuration of the DDM is the same for both approaches, RANS and LES, the direction of the sprays fixed at 37°, the case corresponding to the treatment of turbulence with LES models predicts a higher spray opening, over-predicting the estimated values by approximately 10°. This phenomenon is also observed in Figure 7.11, where the projected vapor contours exhibit a greater spacing between sprays. Despite this observed effect, it can still be said that the values obtained are within the limits of the experimental standard deviation, so the prediction is not far from the experimentally obtained values. The effect of over-prediction of the opening angle is attributed to the vortices calculated by the LES modeling which imply a larger opening. It is possible that, if the contours were averaged between different simulations in a way that approximates the RANS models, closer values would be observed.

Finally, Figure 7.10c captures the axial velocity of the gas at a distance of 15 mm from the tip of the injector in order to see the influence of the sprays on the surrounding gas. The effect shown in this image is a recirculation of gas in the opposite direction to the injector due to the induced velocity caused by the presence of the surrounding sprays. It is evident that the experimental trend is perfectly captured with high precision, however, the induced velocity is well below the experimental values. The main reason associated with this under-prediction of the axial gas velocity values is connected to the opening of the sprays. A larger spray aperture has been observed compared to the data obtained with RANS models. In addition, the user-defined spray direction does not take into account the inward deflection that the flow tends to suffer in this type of GDI injectors. This fact is not taken into account in either

RANS or LES, and thus is the main reason why these approaches differ from the experiments.

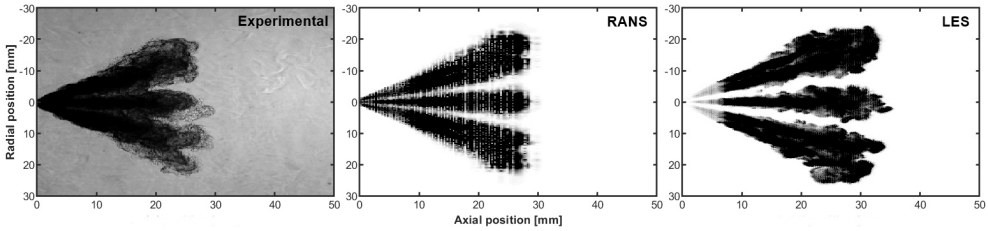

Figure 7.11: Vapor projection on the visualization plane for the different turbulence approaches using the Spray G injector under the SG reference condition at t = 0.6 ms.

Throughout the previous lines, reference has been made to Figure 7.11 where the vapor contours projected on the experimental visualization plane are reflected in order to qualitatively compare the behavior and shape of the sprays. The two approaches yield contours very close to the experimental ones showing again the validity of the implemented model and its accuracy. However, as already mentioned, the case where the turbulence treatment is based on LES approach tends to generate a higher evaporation of the spray droplets and thus a higher vapor penetration. In addition, a greater separation between sprays is observed which results in the under-prediction of the axial gas velocity values. As a general conclusion of the study it can be said that both approaches accurately capture the spray trends, thus validating again the implemented methodology independently of the turbulence treatment employed.

7.6 Summary and Conclusions

Throughout this Chapter numerous studies have been carried out, all of them based on the use of the classical DDM approach, also known as blob-model, where the parameters introduced all come from experimental data. This study includes the different steps to follow until the final model has been validated. It also includes the influence of certain sub-models on the behavior of the spray pattern. Once the model and methodology used have been validated, they have been used to study the spray behavior under different operating conditions. Finally, it has also been demonstrated how the treatment of turbulence slightly influences the macroscopic parameters of the jet using RANS

and LES models. For all this, the injector belonging to the ECN Spray G and the commercial software CONVERGE™ have been used.

Considering the domain (a cylinder) sensitivity study, it has been demonstrated that the sizes chosen for both height and radius, are large enough not to influence the spray behavior under the reference operating conditions, SG. In addition, these sizes have been considered with some margin to accommodate studies under different operating conditions where the expected spray penetrations may be larger.

On the other hand, within the study of the influence of the mesh, it was observed that under the use of the AMR tool for the refinement of the mesh as a function of the field gradients, it was the minimum cell size that really determined the spray behavior since the penetrations were not affected under a variation in the base cell size as long as the minimum cell size was kept the same.

This work has also captured the influence of taking into account or not the effects of turbulence, aerodynamics and cavitation on the primary atomization, or in other words, of activating or not the KH-ACT model. Taking these effects into account resulted in higher atomization leading to smaller droplet sizes and thus lower drag force resistance resulting in higher penetration velocities. In addition, smaller droplet sizes enabled the evaporation of the droplets to occur earlier. The non-activation of this model resulted in a more linear penetration behavior away from the widespread parabolic trend widely reported in the literature. Furthermore, a greater penetration after the end of the injection has been observed. It is typically associated with a greater inertia of the droplets because they have a larger size. In addition, in conjunction with this study, the influence of turbulence on spray behavior was determined by analyzing several RANS models, all of which were derived from the k-ε definition. The model that best captured the spray behavior in terms of the macroscopic penetration variable was the Standard k-ε model, since the advantages associated with the RNG k-ε or the Realizable k-ε as the treatment of rotational flows or enhancing swirling motions are not applicable to this type of flows.

Previous to the validation of the model the influence of the mesh orientation was also analyzed, observing how the numerical diffusion is dependent on the alignment of the mesh with respect to the sprays. If one wants to avoid it, the jets have to be rotated 22.5° with respect to the cartesian axes.

The validation of the model and methodology used was successful, obtaining cumulative differences in terms of vapor and liquid penetration with respect to the experimental data of at most 5%. In addition, this was coupled

with a correct capture of the overall spray aperture, obtaining values identical to the experimental data. However, the definition of the spray direction without taking into account the deflection of the sprays caused the axial gas velocity induced by the presence of the sprays to under-predict the experimental values. Once the model was validated and its accuracy demonstrated, following the objective of the predictive methodology, it was applied to the study of the external flow under different operating conditions, obtaining cumulative differences of 7% for SG2 and 8% for SG3. The precision of the macroscopic parameters obtained together with the spray vapor projections demonstrated the accuracy and validity of the adopted methodology. Nevertheless, it should be noted that the lack of a specific model in the present version of the software to deal with extreme conditions associated to flash boiling meant that the first atomization model KH-ACT had to be deactivated in the case of the SG2 condition because it did not adequately capture the behavior of the near-field spray.

Finally, this study reports the spray behavior in instances where the turbulence is treated from LES approach. The accuracy obtained in the macroscopic parameters is comparable to the RANS approach, although the quality criterion that ensures the accuracy and quality of the results is not fully satisfied. The minimum sizes obtained in the refining are within the ranges defined in the literature, but further reduction is needed to reach the stipulated quality of 75% of the resolved energy. In this case, a compromise between quality and computational cost has been sought without compromising model accuracy. The LES approach have been demonstrated to predict larger spray openings resulting in an under-prediction of the induced axial gas velocity even though the gas velocity trend is captured with greater detail and precision than the RANS approach.

All the aforementioned studies have determined the accuracy of the employed model and the validity and reliability of the predictive methodology developed throughout the document, which will continue to be tested in the final following chapter.

References

[1] Vaquerizo, D. “Study on Advanced Spray-Guided Gasoline Direct Injection Systems”. PhD thesis. Universitat Politècnica de València, 2017. DOI: 10.4995/Thesis/10251/99568.

[2] Bautista Rodriguez, A. "Study of the Gasoline direct injection process under novel operating conditions". PhD thesis. Universitat Politècnica de València, 2021.

[3] Nocivelli, L. et al. "Analysis of the Spray Numerical Injection Modeling for Gasoline Applications". In: *SAE Technical Papers* 2020-April.April (2020), pp. 1–13. DOI: 10.4271/2020-01-0330.

[4] Paredi, D. et al. "Validation of a comprehensive computational fluid dynamics methodology to predict the direct injection process of gasoline sprays using Spray G experimental data". In: *International Journal of Engine Research* 21.1 (2019), p. 146808741986802. DOI: 10.1177/1468087419868020.

[5] Payri, R. et al. "Numerical Analysis of GDI Flash Boiling Sprays Using Different Fuels". In: *Energies* 14.18 (2021), p. 5925. DOI: 10.3390/en14185925.

[6] Yue, Z. et al. "Application of an Equilibrium Phase (EP) Spray Model to Multi-component Gasoline Direct Injection". In: *Submitted to Fuel* (2018), pp. 1–8. DOI: 10.1016/S0140-6736(11)61351-2.

[7] Saha, K. et al. "Numerical Investigation of Two-Phase Flow Evolution of In- and Near-Nozzle Regions of a Gasoline Direct Injection Engine During Needle Transients". In: *SAE International Journal of Engines* 9.2 (2016), pp. 1230–1240. DOI: 10.4271/2016-01-0870.

[8] Hwang, J. et al. "Spatio-temporal identification of plume dynamics by 3D computed tomography using engine combustion network spray G injector and various fuels". In: *Fuel* 280.March (2020), p. 118359. DOI: 10.1016/j.fuel.2020.118359.

[9] Jaramillo Císcar, D. "Estudio experimental y computacional del proceso de inyección diésel mediante un código CFD con malla adaptativa". PhD thesis. Universitat politècnica de valència, 2017. DOI: 10.4995/Thesis/10251/92183.

[10] Befrui, B. et al. "Coupled LES Jet Primary Breakup - Lagrangian Spray Simulation of a GDi Multi-Hole Fuel Injector". In: *SAE International Journal of Fuels and Lubricants* 8.1 (2015), pp. 179–189. DOI: 10.4271/2015-01-0943.

[11] Lucchini, T. et al. "CFD Modeling of Gas Exchange, Fuel-Air Mixing and Combustion in Gasoline Direct-Injection Engines". In: *SAE Technical Papers* 2019-Septe.September (2019). DOI: 10.4271/2019-24-0095.

[12] Sphicas, P. et al. "A Comparison of Experimental and Modeled Velocity in Gasoline Direct-Injection Sprays with Plume Interaction and Collapse". In: *SAE Int. J. Fuels Lubr.* 10 (2017), pp. 184–201. DOI: 10.4271/2017-01-0837.

[13] Celik, I. B. et al. "Index of resolution quality for large eddy simulations". In: *Journal of Fluids Engineering, Transactions of the ASME* 127.5 (2005), pp. 949–958. DOI: 10.1115/1.1990201.

[14] Senecal, P. K. et al. "Large eddy simulation of vaporizing sprays considering multiinjection averaging and grid-convergent mesh resolution". In: *ASME 2013 Internal Combustion Engine Division Fall Technical Conference, ICEF 2013*. Vol. 2. 2013, pp. 1–16. DOI: 10.1115/ICEF2013-19082.

Chapter 8

External Flow Analysis. Coupling Strategy

"Research is to see what everybody else has seen, and to think what nobody else has thought."
—Albert Szent-Gyorgyi

8.1 Introduction

Throughout the different sections of the present Thesis document, the development and the corresponding validation with experimental data available in the literature of the predictive simulation strategy has been explained in detail. The described predictive methodology is capable of being applied to current and future generations of GDI injectors, regardless of the injector features and the software used, for the hydraulic characterization of the injector under steady and transient operating conditions. The ultimate purpose of employing this strategy is to follow in the footsteps of the research community and analyze the behavior of the fluid downstream of the injector (spray external flow) without the need for experimental data as input parameters.

The external flow is one of the broad and complex fields that make up the injection process along with the internal nozzle flow. The tendency that exists and is widely spread in the literature is to analyze both fields separately despite knowing the enormous influence of the internal flow characteristics as well as the geometry on the spray behavior. This strategy has been followed

throughout the previous chapters. However, this trend is increasingly changing tending to perform analyses of both processes jointly. The internal and external flow coupling strategy can complement previous analyses and provide a better understanding of the physics and even a better approximation of the actual injection behavior. The coupling is mainly supported by the temporal and spatial transfer of internal flow variables (velocity, turbulent kinetic energy, dissipation rate or void fraction) to a primary break-up model which uses them to initialize droplet properties like size and velocity. There are several methodologies of coupling between the study of internal and external flow, having been chosen for the present Thesis the ones known as one-way coupling and mapping.

For all the above mentioned, this chapter collects the final phase of the development of the already known predictive methodology which includes its applicability to the study of external flow behavior. This means that the obtained results of the internal flow study are incorporated as input parameters to analyze the behavior of the spray pattern. The accuracy of this methodology will be determined after being applied to the two injectors included in this study, Spray G and PIU, as well as its validity regardless of the software adopted, StarCCM+ or CONVERGE™ . As in the previous Chapter, the accuracy of the study will be mainly determined as a function of macroscopic jet variables such as liquid and vapor penetration, spray angle or gas velocity in addition to paying special attention to the spray pattern.

8.2 Spray G Injector. One-way Coupling

This section goes one step further and seeks to reflect the validity of the predictive methodology developed throughout the paper by coupling internal and external flow using the data obtained in the in- and near-nozzle flow study to determine the spray characteristics. Different strategies will be used, a DDM with computational input parameters and the coupling strategy known as mapping. For these purposes, the ECN reference injector, Spray G, has been used and the studies have been carried out under commercial software CONVERGE™ .

The validation of these strategies will be carried out on the basis of experimental data present in the literature in addition to comparing the results obtained with the classical methodology, presented in the previous Chapter 7, where the experimental data are taken into consideration as input parameters.

8.2.1 One-way coupling. Validation and discussion

This section presents the results obtained and their validation from the use of a one-way coupling strategy based on the DDM approach. For this purpose, a strategy similar to the previous study based on the blob injection method is adopted, which consists of injecting into the computational domain an initial droplet with a characteristic size of the effective nozzle diameter and a velocity function of the injected mass flow rate profile, which follows a user-defined direction (drill angle) and tends to generate an opening spray angle similar to that initially specified. These input parameters necessary for the study of the spray behavior are obtained from the internal flow simulations presented in Section 6.7. As mentioned above, the obtained data will be validated by experiments and compared with the reported results in Section 7 where the DDM input parameters were purely experimental.

Figure 8.1 presents the results of this study and the subsequent validation of the results. On the left side, corresponding to Figure 8.1a, the liquid and vapor penetrations obtained by using the DDM using experimental and computational input parameters are displayed, together with the experimental data. As it is observed, both computational approaches approximate the results accurately to the experimental data with differences of less than 7%. Focusing the attention on the obtained results with the DDM and computational input parameters, a higher penetration velocity and thus higher penetrations in the initial instants of the injection are observed. This effect is due to the mass flow rate profile introduced as input parameter. In Figure 6.20a it is clearly observed how in the instants right after the opening stage, the injection rate predicted by the simulations is higher, together with a higher overshoot than the experiments. Although the amount of total mass injected is similar in both cases, the distribution of the same over time is not, providing a greater amount in the initial instants in the computational case which causes the acceleration of the spray.

On the other hand, the right part corresponding to Figure 8.1b, reflects the spray opening angles calculated from the fixed origin method (Section 5.26) using the range called S2 which takes into account from 12 to 50% of the penetration in each time instant to carry out the calculation of the angle. The experimental data exhibits a very large angle value at the initial instants of injection which decreases as the liquid enters the discharge chamber. This may be due to the fact that the distribution of the liquid in the first instants picks up a larger amplitude thus tending to open in width and not so much in length but it can also be attributed to the processing of the data since the standard deviation, as observed, is quite large. This effect is not well captured

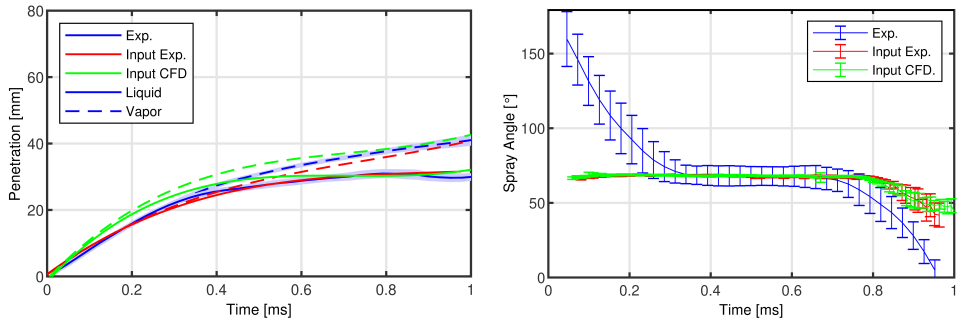

(a) Penetrations (b) Spray Angle

Figure 8.1: Validation of the DDM strategy with input parameters from previously performed internal flow simulations under the SG reference condition for the Spray G injector.

by the simulations, which have a fairly linear trend for this reference condition. However, it can be stated that during the instants when the injection is in the stationary part, the angle opening is accurately computationally captured.

The validity of the model defined for the study of the external flow, which provides results of high precision in terms of macroscopic parameters of the jet, can be re-affirmed. This again validates the proposed predictive methodology so future studies of spray pattern could be dispensed with the experiments because the computational models adequately capture the trends of the spray.

8.2.2 Multiple injection strategy. One-way coupling

This section includes the results of external flow when using multiple injection strategies. For this purpose, the one-way coupling strategy has been adopted, where as input parameters the computational injection rate profiles obtained in Sections 6.6.4.3 and 6.6.4.4 have been defined. Since the internal flow studies did not show any effect between injections because it was the needle lift profiles that determined the flow behavior, the objective was to employ the obtained data to evaluate the influence of one injection on the other, pilot in the main and main in the post, on the spray pattern.

This influence has been studied based on the macroscopic parameter spray liquid penetration compared to the obtained results under the same operating conditions (explained in detail in Sections 6.6.4.3 and 6.6.4.4). It is reported in Figure 8.2. On the one hand, Figure 8.2a displays the values of liquid penetrations for the different pilot injections tested compared to the penetration

obtained under the SG reference condition where only one main injection is involved. The results of the pilot injection are shown on the left side of the image while the penetration corresponding to the main injection is on the right side of the image. All multiple injections predict liquid penetrations greater than the reference condition. The distance between injections is small enough that the pilot injections generate an effect known in the literature as "slipstream" [1, 2], the steady gas is accelerated by the first injection and the following one loses less momentum causing it to penetrate further. Moreover, a higher momentum coupled with a higher turbulent kinetic energy means that successive injections benefit from these phenomena.

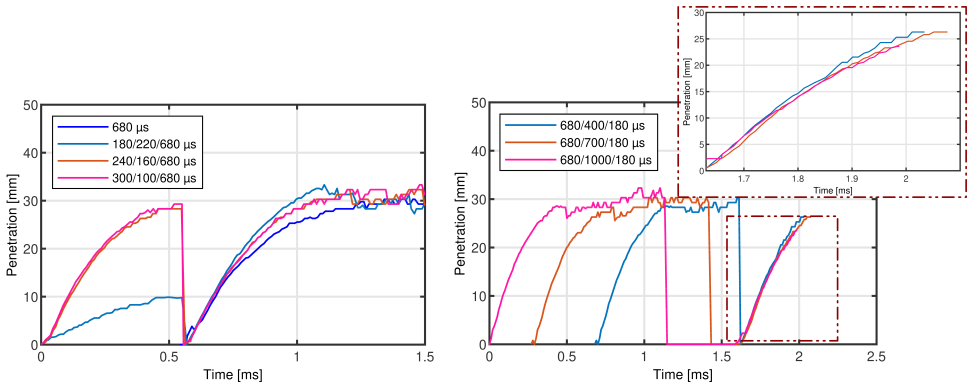

(a) Pilot injection influence

(b) Post injection influence

Figure 8.2: Influence of multiple injections, pilot and post, on spray pattern under SG like operating condition for the Spray G injector.

On the other hand, Figure 8.2b reflects the results obtained from post-injection strategies. The left side shows the the data corresponding to the main injection and the right side depicts the penetrations of the post-injections. As the dwell time between injections is different, what has been done is to phase the post-injections in such a way that the behavior of all of them can be observed together, since they are the objective of the study. The condition with a shorter dwell time between injections has a longer penetration, an effect associated to the already mentioned "slipstream" event. However, as the penetrations are separated from each other, this phenomenon ceases to have an influence, observing how the other two study conditions, DT 700 µs y DT 1000 µs, predict very similar liquid penetrations.

Although the internal flow study did not yield significant conclusions, the results of the external flow study provide clarity on the effect of one injection

on another in multiple injection strategies. As demonstrated, the distance between injections is an important parameter to be taken into account during injection process due to the existing influence between injections under short dwell times [2].

8.2.3 Influence of the surrogate fuels on the spray patterns

The previous validation of the model is an important part of this study, since the current lack of experimental data means that the obtained results with different fuels cannot be compared and validated. Therefore, starting from the mentioned validated model, which has demonstrated high accuracy, it is assumed that the model performance will be adequate for the different fuels used.

In this particular case, the same six surrogate fuels analyzed in Section 6.6.2 (ethanol, heptane, hexane, iso-octane, pentane and E00) are studied. The results have been focused on the same macroscopic jet variables as in the previous sections, penetration and spray angle, for the three reference study conditions SG, SG2 and SG3 (Figure 8.3). Starting the analysis with the SG reference condition (Figure 8.3a and 8.3d), a condition considered evaporative, the differences between fuels is noted. Those with similar boiling point and heat of vaporization such as heptane, hexane and iso-octane follow similar liquid and vapor penetration and spray angle trends. The multi-compound E00 shows a somewhat different behavior but under the same trends as the previous fuels. The two extreme cases are reflected in ethanol and pentane. Ethanol is the fuel with the highest injection rate and therefore a longer liquid penetration. On the other hand, this fuel also has low vapor latent heat so the tendency to evaporate is less than any other studied fuel in this work, which also justifies the higher liquid penetration. On the contrary, pentane is the most volatile fuel of all those presented and for this reason, together with the injection rate being about 6% lower than the iso-octane reference fuel, it has a shorther liquid penetration than the rest of the fuels analyzed. With respect to the spray angle, there is no clear trend between fuels under this concrete operating condition as they all seem to show a similar spray aperture, which is in agreement with what has been observed in the literature [3].

Referring to the SG2 condition (Figure 8.3b and 8.3e), there are hardly any differences between surrogate fuels in both penetration and spray angle. It was expected to see differences in the macroscopic variables depending on the degree of flash boiling of each fuel [3]. Clearly there is a limitation of the model since for the adopted software version, there is no flash boiling model applied to external flow cases, evaporation is considered by the common

models based on the Frösling correlation. Something similar occurs in the SG3 condition (Figures 8.3c and 8.3f), where a configuration identical to that used in the SG reference condition while for flash boiling conditions the KH-ACT primary atomization model was deactivated. Again, it is evident that under a non-evaporative condition, fuels with similar properties follow identical trends while ethanol, due to its higher injection rate and total mass injected, has a higher penetration of the spray. In addition, note the anomalous behavior of pentane, which under the conditions of SG3 would also be under the effects of flash boiling because its saturation pressure at working temperature is higher than the ambient pressure. Penetration is lower together with a lower cone angle mainly attributed to the collapse of the sprays.

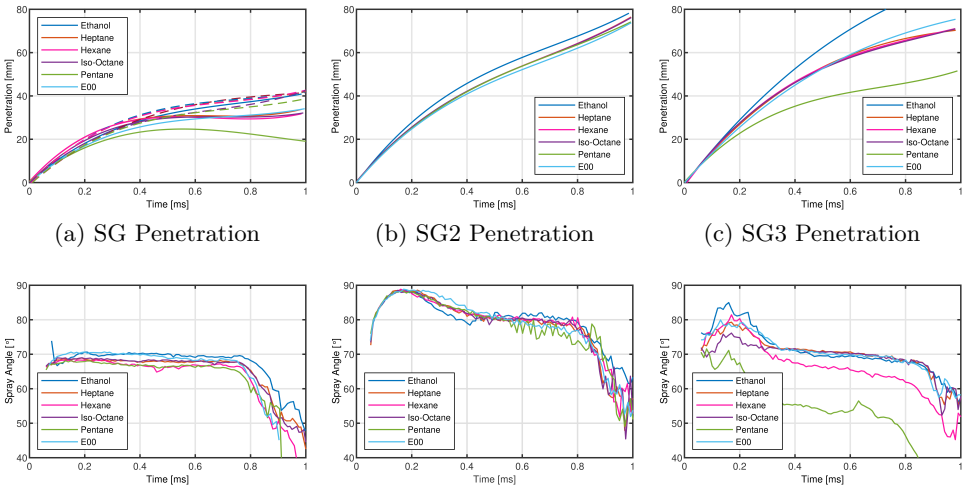

(a) SG Penetration (b) SG2 Penetration (c) SG3 Penetration

(d) SG Spray Angle (e) SG2 Spray Angle (f) SG3 Spray Angle

Figure 8.3: Study of the Spray G injector spray behavior in terms of macroscopic parameters of jet, penetration and spray angle for different surrogate fuels under three operating conditions.

Not only the macroscopic parameters have been referred to, Figure 8.4 reflects the projected vapor contours for all the surrogate fuel studied under the three different operating conditions. The images are accompanied by the pressure ratio (R_p) that defines the tendency to generate flash boiling (Equation 3.30). If the ratio is greater than one ($R_p > 1$), it indicates that it is operating under flashing conditions. The higher this value is, the greater the flash boiling phenomenon will be. As presented above, similarities under the same operating condition are visible. Under the SG condition, none of

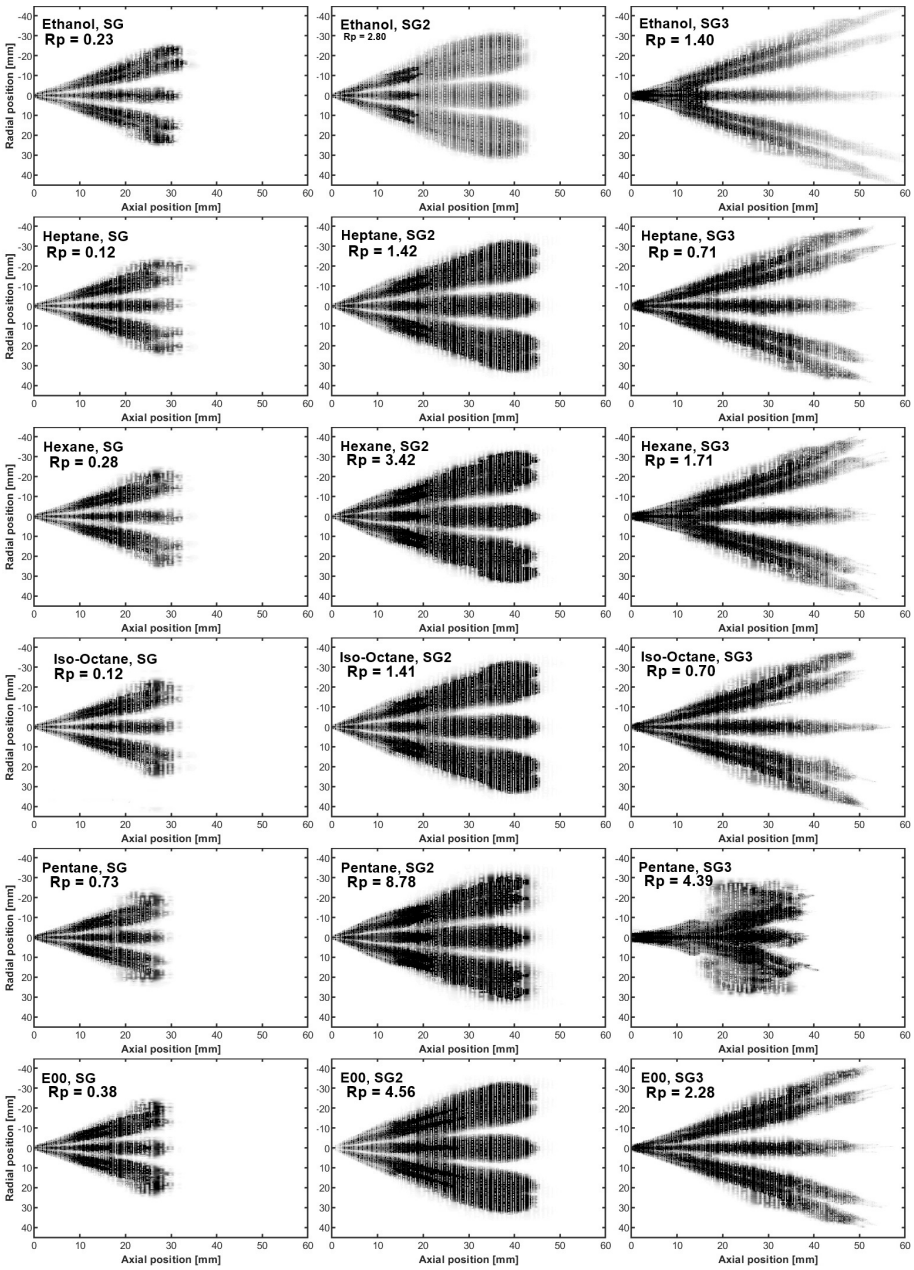

Figure 8.4: Vapor projection on the visualization plane of different surrogates for the Spray G injector under the three operating conditions at t = 0.6 ms.

the fuels have a pressure ratio (R_p) greater than unity so they are not under flash boiling conditions, as it was already known. For the SG2 operating condition defined as flashing condition, all the studied surrogate fuels have an R_p value above unity, being iso-octane and heptane those with a smaller value and E00 and pentane those with a higher value. Although there is a notable difference between the R_p values between fuels, the behaviour of the sprays is very similar to each other when the expected trend, based on the data presented in the literature [3], is to see a greater collapse of the sprays as the R_p is higher. This shows again the limitation of the sub-models applied since the flash boiling phenomenon is not correctly captured. To highlight another curiosity of the results in the SG2 operating condition, despite the fact that ethanol has a higher R_p value and therefore a higher flash boiling would be expected, it generates a lower amount of vapor than the rest of the fuels due to its low vapor latent heat. In the SG3 condition, the aforementioned limitation is also visible, since excluding iso-octane and heptane, the other fuels have an R_p greater than unity, which indicates that they are under flash boiling conditions. However, all of them behave similarly to each other and not at all close to the SG2 condition. In addition to this, it can be observed that pentane has an anomalous pattern of behavior compared to the other surrogate fuels. This is due to the fact that its R_p is much higher than the others and the sub-models do not adequately predict its behavior under the strong influence of flash boiling. Perhaps, the spray pattern would be better captured if the set-up chosen for the SG2 cases was used. However, and since no experimental data are available, it is not possible to check the results and validate them. Thus, the discussion is left open at the expense of experimental data that will provide clarity to the study.

8.2.4 Spray G injector. Mapping strategy

The present section collects the external flow results obtained from the coupling strategy called mapping. This consists of obtaining maps of internal flow variables such as velocity, turbulent kinetic energy, dissipation rate or void fraction, among others, and using them as boundary and initial conditions directly in the external flow (as explained in Section 5.2.5). Although this strategy has many advantages because it is one of the few that takes into account the influence of the upstream behavior of the injector on the spray pattern, it also has some drawbacks related to the uncoupled nature of the study. Among them, the most prominent is the limited temporal resolution of the transient nozzle flow phenomena, since usually the time-steps between internal and external flow simulations are very different (on the order of 10^{-8}

for nozzle flow and 10^{-6} for spray studies) and need an interpolation to be able to couple it. This means that the internal flow allows to work with the required precision, however, when interpolating the results to initialize the external flow there is a loss of resolution thus eliminating phenomena, such as oscillations, due to the difference between the frequencies of both approaches. On the other hand, another limitation of this type of strategies is the evidence of the feedback between regions such as the recirculation inside the orifices in this type of GDI injectors. Despite the above, it is still postulated as a good approach to study the external flow and this section seeks to reflect its validity. The consistency and accuracy of the mapping strategy would reflect the success of the predictive methodology developed throughout this Thesis, thus avoiding the need for the use of experimental data.

Figure 8.5 reports the macroscopic results that characterize the spray as penetration and spray angle for the three different operating conditions, SG, SG2 and SG3. In the case of SG, since it is an evaporative condition, both liquid and vapor penetrations are presented, while for SG2 and SG3, considered non-evaporative, only liquid penetrations are shown, (vapor phase gives identical results). Starting with the SG condition, it can be seen that both the vapor and liquid curves faithfully reproduce the experimental trend with cumulative differences of less than 8% in the liquid and 6% in the vapor. The liquid penetration in the final injection stage overpredicts the experimental value and the standard DDM curves with experimental input parameters, but still provides high accuracy results. With respect to the spray angle, the results obtained in the three cases, experimental, DDM with experimental inputs and mapping are very similar to each other. To highlight an observed trend in the three operating conditions, being more noticeable in the SG2 condition, the angle values from the mapping strategy are somewhat lower than the DDM with experimental inputs. This can be attributed to the fact that in the DDM case the direction of the spray is an input parameter defined in this case at 37°, while in the mapping case the values from the internal flow are taken where the tendency of the jet to deviate towards the injector axis is clearly observed reaching a direction of 34°. An overprediction in the penetration is observed in the three operating conditions, but in no case exceeds cumulative differences greater than 8%.

It has also been considered of interest to show the contours projected in this case for liquid phase in order to include the non-evaporative conditions. These results have been captured in Figure 8.6 where not only the differences between operating conditions but also between strategies can be discerned. All three conditions reflect an overprediction of the liquid values in the mapping case as well as showing clear differences in the shape of the sprays, a phenomenon

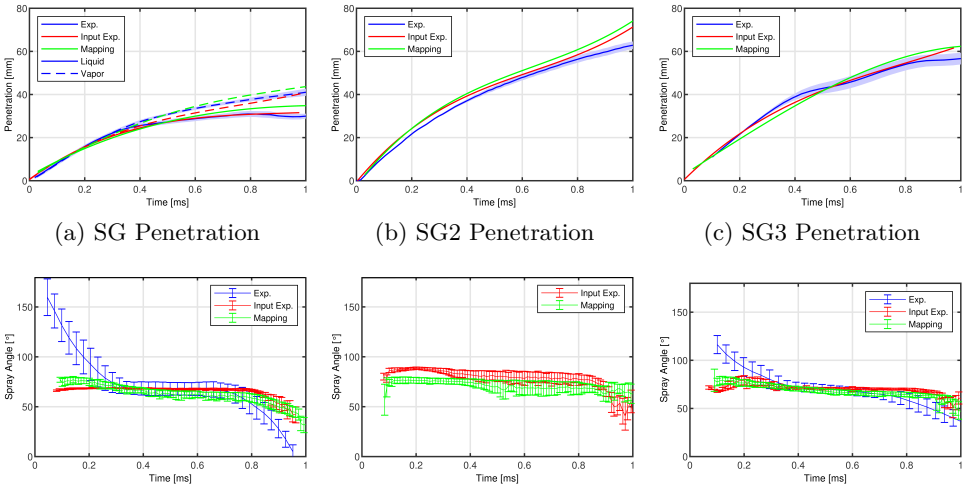

(a) SG Penetration (b) SG2 Penetration (c) SG3 Penetration

(d) SG Spray Angle (e) SG2 Spray Angle (f) SG3 Spray Angle

Figure 8.5: Validation of the mapping strategy in terms of penetration and spray angle for the three different studied operating conditions.

that together with the mentioned deviation of the spray direction has also been detected in the literature [4]. Concerning the noted differences in spray shape, it could be stated that for the three studied operating conditions, the projected liquid contours suggest a smaller overall spray aperture. In addition, specifically in the cases of SG and SG2, the individual sprays appear to have a smaller spray angle, which leads to a lower jet-to-jet interaction.

Despite these small differences in spray shape and spray direction, the accuracy of the penetration and angle values obtained together with the projected liquid contours allow to affirm the success of the predictive methodology developed, obtaining results with cumulative penetration differences between experiments and simulations of less than 8% and spray angles similar to the experiments that capture the tendency to deflect also observed experimentally. As final conclusion, it can be asserted that both approaches adequately and accurately capture the spray pattern. However, the mapping strategy avoids the need to perform experiments to define the input parameters, which significantly reduces the cost of the study.

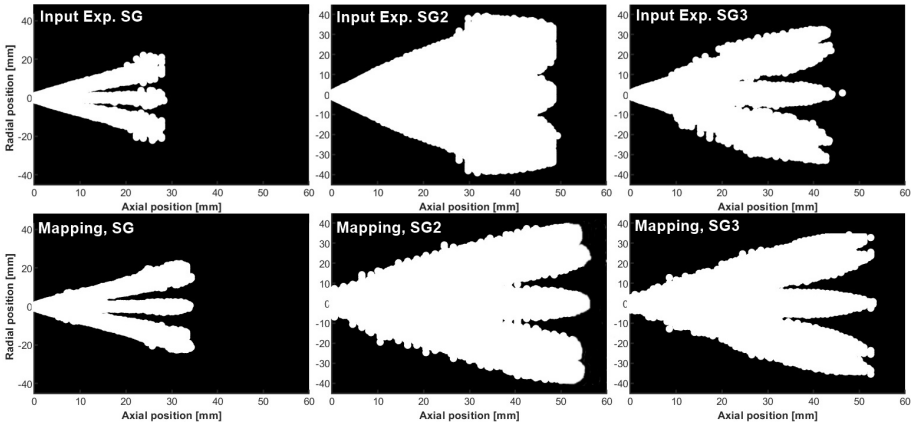

Figure 8.6: Liquid volume projection on the visualization plane of the different strategies for the Spray G injector external flow study under the three operating conditions analyzed at t = 0.6 ms.

8.3 PIU Injector. One-way Coupling

After analyzing the behavior of the external flow from the different coupling strategies for the reference injector Spray G, this section includes the same work applied to the industrial injector of real applicability known as PIU injector. As before, the DDM has been used as an approach to model the spray behavior taking into account liquid atomization and break-up phenomena, among others. The coupling between internal and external flow known as one-way coupling is employed, where the blob method is adopted as a submodel of injection. This approach has been chosen because of the proven high accuracy of the results and the associated low computational cost.

It is important to mention that this study, apart from being carried out with the software StarCCM+, is presented together with the results obtained from the same analysis but adopting the experimental data as input parameters. The objective is to compare the accuracy and differences between both approaches and to validate them with experimental spray results. In addition, and as considered of interest, the influence of the variables that make up the break-up models on the behavior of the spray is also included.

8.3.1 One-way coupling specific methodology

The proposed methodology in this specific work has been described throughout Chapter 5, however, it is considered necessary to mention some specific

details again as well as to discuss other aspects of interest. As already known, the StarCCM+ code allows the use of two different mesh types, hexahedral and polyhedral. In this case, the analysis has been carried out with a mesh with polyhedral elements to be in accordance with the internal flow study as well as to benefit from the advantages that this type of meshing has such as the reduction of the computational cost while maintaining the accuracy of the results. Following the developed predictive methodology the base cell sizes as well as the minimum cell size adopted, and the volume of the computational domain defined have been chosen on the basis of the studies carried out in the previous chapter (Chapter 7). The size of the computational domain corresponds therefore to 125 mm in height and 200 mm in diameter while the mesh has a base cell size of 8 mm and a minimum cell size in the spray direction where the fuel-air mixing takes place of 2 mm. Nevertheless, in order to check the validity of the grid, a mesh influence study was also carried out with a base size of 4 mm and a refined cone of 1 mm as minimum cell size. The obtained conclusion was that reducing the cell size both the reference and the minimum cell sizes provided a difference in penetrations of 3% being considered a minimum deviation. Therefore, with the previously computational cost savings in mind, the mesh used for the subsequent studies will be 8 mm base and 2 mm minimum size.

As mentioned earlier, the present one-way coupling strategy is based on the well-known DDM or blob-model procedure, where in-nozzle flow simulations are carried out to provide the 2D temporal distribution profiles of the variables of interest (velocity vector, liquid fuel volume fraction, temperature, turbulent kinetic energy or dissipation rate, among others) which are introduced as input and initialization variables for the study of the spray behavior. To carry this out, it is necessary to define the injector, with its characteristic dimensions and dimensionless coefficients, that will influence the size and behavior of the initial blob. In addition it is also necessary to give other input information such as the particle temperature, defined based on the operating conditions, that in this study is set to 363 K, equal to the injection temperature. Regarding the geometrical parameters, they depend on the nozzle hydraulic characteristics at the corresponding operating conditions: rate of injection, discharge coefficient (C_d), form loss coefficient and turbulence dissipation rate coefficient. The last two are typically determined from experimentally developed correlations, whereas the injection rate and discharge coefficient are obtained directly from experimental measurements. However, if a fully predictive CFD model is desired, experiments should not be used neither for defining boundary conditions nor inputs of the models. Therefore, validated nozzle flow simulations are employed to defined those data.

Among the several available types of injectors in StarCCM+, a nozzle type injector is selected so injected parcels can go through primary atomization. Unlike other methods, the nozzle type injector does not use spray cone angle as an input which consequently decreases solution dependency of this parameter. The diameter of the injector at the nozzle exit and the origin and axis of the injector orifices are the basic parameters that this sub-model requires as inputs. The center of each hole at nozzle outlet is used as point of reference to inject the parcels. The direction of geometrical axis of each hole is also used as the direction those parcels will follow. Table 8.1 lists the main parameters that characterize each of the orifices. Furthermore, each one should be defined by the following: axis and origin of each hole, mean injection velocity over the injection duration depending on effective area and fuel density as well as mass flow rate obtained from the experimental and/or computational internal nozzle flow studies depending on whether the study is carried out from the classical model (experimental dependence) or the one-way coupling where everything is computationally developed.

Parameter	Value
Nozzle Turbulence Dissipation Rate Coefficient	0.5
Nozzle Form Loss Coefficient	0.6
Nozzle Discharge Coefficient	0.6
Cone Randomization	1
Nozzle Diameter	195 µm
Nozzle Length	465 µm
Parcel Streams	10
Particle Temperature	363 K

Table 8.1: Necessary parameters for defining a nozzle injector type in a StarCCM+ Lagrangian DDM Model for the PIU injector.

This section gathers the obtained results, firstly, from the classical model where the experimental data are used as input parameters and, on the other hand, the one-way coupling model where the input parameters are obtained computationally. As mentioned, one of the input variables is the injection rate and the values adopted in these studies are those presented in Figure 6.72a. The approximation between the both, as quoted in the corresponding section, is very promising since the opening and closing ramps are perfectly captured. The only differences are the lack of oscillations in the signals of the computational results due to a constant value of the pressure inlet and an

overprediction by the computational model of at most 5% in the total injected quantity.

The discharge coefficient is directly related to the injection rate, so the differences between experiments and simulations are also reflected in this variable. Table 8.2 presents the values adopted in both approaches and the differences between them. Another parameter that is used as initialization of the injector is the nozzle form loss coefficient (K_c) which has been calculated from the simulations following Equation 8.1, where Δp_f is the pressure loss across the nozzle corner. Table 8.3 summarizes this value for all holes and different injection conditions. As it is observed, the obtained values are not far from the reference value recommended by the computer code and the variation in this coefficient is not expected to have a high impact on the behavior of the spray, so it has been kept at a constant value of 0.6 for all the orifices and conditions studied.

$$K_c = \frac{2\Delta p_f}{\rho U^2} \tag{8.1}$$

P_{inj} [MPa]	C_d experimental	C_d CFD
10	0.60	0.60
20	0.59	0.60
28	0.58	0.60

Table 8.2: Nozzle discharge coefficient comparison under three different values of injection pressure and 0.3 MPa of ambient pressure for the PIU injector.

	10 MPa	20 MPa	28 MPa
Hole 1	0.60	0.60	0.60
Hole 2	0.55	0.53	0.53
Hole 3	0.65	0.63	0.62
Hole 4	0.63	0.62	0.61
Hole 5	0.65	0.63	0.62
Hole 6	0.55	0.53	0.53

Table 8.3: Nozzle form loss coefficient for all holes under three different values of injection pressure and 0.3 MPa of ambient pressure for the PIU injector.

In a similar way, another coefficient that has to be defined to initialize the injector is the nozzle turbulence dissipation rate coefficient, which is defined by default at a value of 0.5. In order to determine the influence of this coefficient on the behavior of the spray, a study was carried out taking as values for the coefficient within a range between 0.3 and 0.7. The obtained results demonstrated how this variable has a limited influence on the spray penetration distance, obtaining differences in the values of at most 6%. Therefore, the decision was to maintain the default value of 0.5 as nozzle turbulence

dissipation rate coefficient. Finally, the number of injected parcels per time step is defined through the parcel stream parameter. It is important to note that this parameter does not influence the mass or volume flow rate, but has a great influence on the accuracy of the results characterizing the spray. In addition, it should also be known that it is directly proportional to the computational cost (CPU-h) so a compromise between accuracy and cost has to be reached. The sensitivity analysis preformed to achieve an optimal value of parcels resulted in the parcel number equal to 10, which corresponds to the value suggested by the software.

8.3.2 Turbulence model and constants analysis

In cases where turbulence is treated from RANS approaches, the k-ε model is the most widely used for spray simulations because of its accuracy in capturing the processes taking place in the injection process [5]. However, for GDI injection scenarios where recirculation is expected to be remarkable, the use of k-ω models could also be an interesting option. That is why in this study a comparison in terms of penetration of the behavior of both turbulent models has been collected. Figure 8.7a includes the obtained results for a specific operating point of all those considered in the study (20 MPa injection pressure and 0.6 MPa ambient pressure). It should be noted that for this analysis the experimental parameters have been used as input variables.

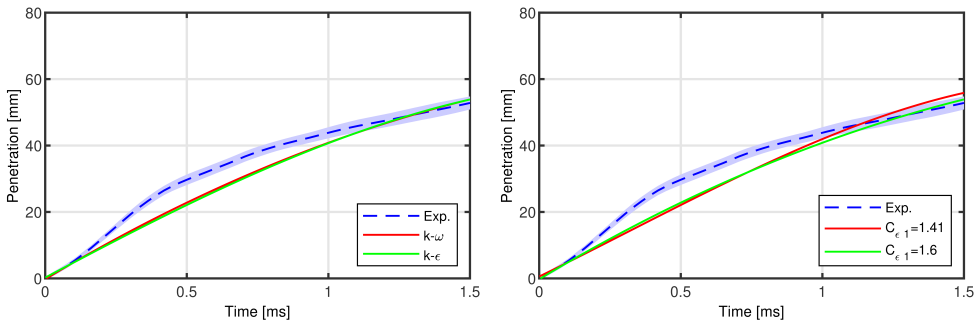

(a) Turbulence model (b) Round jet correction

Figure 8.7: For the PIU injector under 20 MPa of injection pressure and 0.6 MPa of ambient pressure: (On the left) Spray penetration for different turbulence models in comparison with the experimental. (On the right) Spray penetration for standard k-ε with and without the round jet correction in comparison with the experimental.

The computationally obtained curves do not show a difference between them, in fact, it can be said both overlap. So although the k-ω turbulence model theoretically could offer new insights and even improve the accuracy of the results, this is not the case. Therefore, the turbulence model selected for the following studies is the standard k-ε model because of its wide applicability.

Once the k-ε turbulence model has been selected, the so-called round jet correction, widely known and used in both diesel and GDI sprays, may improve the obtained results in a freestream jet when comparing to experiments [6]. The model includes the effect of reducing effective viscosity and spreading rate occurring in three-dimensional flows by modifying one of the constants of the dissipation rate equation. The values considered for this correction vary depending on the application and range from 1.41 to 1.6 [7]. In this case, the two cases corresponding to the limit values have been analyzed and compared to each other to determine if the spray behavior in this case is altered by this modification in the turbulence model. Figure 8.7b reports the results obtained in terms of penetration and clearly demonstrates, as expected, that the correction improves the accuracy of the model by slightly reducing the computational penetration value, especially for long distances from the nozzle tip where the spray is fully developed. Therefore, the value of 1.6 will be chosen to be used throughout the following analyses.

8.3.3 Spray atomization model calibration

As already explained (Section 5.2.4), DDM requires numerous submodels to consider droplet atomization and break-up, droplet evaporation and possible collision or coalescence, among other phenomena. These models, as seen in Section 5.2.4.3, have a series of constants in their definition, which in order for the models to properly work and provide data close to reality need to be calibrated. The GDI spray modeling in this particular scenario relies on the Huh Atomization Model to reproduce the primary atomization that takes place in the first instants when the liquid leaves the injector. Secondary atomization is handled by the Kelvin-Helmholtz (KH) and Rayleigh-Taylor (RT) breakup mechanisms. The constants corresponding to the primary atomization model have been kept as recommended in the literature [8] assuming that the first few millimeters of the injection are correctly captured, however, it has been considered necessary to analyze the effect of the main constants of the secondary atomization model [9]. Therefore, this section describes the calibration process of the constants B_1, which defines the break up time of the KH model, and C_3 related to the length scale for breakup of the RT. As before, experimental values have been used as input parameters in this analysis. In

addition, to validate the corresponding models and determine which constant best approximates the spray behavior, experimental data is used.

First of all, the effect of the constant corresponding to the length scale for the breakup of the RT, C_3, has been addressed. It ranges from a minimum of 0.1 up to a maximum of 1.0 in the consulted references [9], values taken as limiting for this study. In addition, to determine if there is a combined effect between the two studied constants, the maximum and minimum values of the constant C_3 for the four different values adopted in the study of B_1 will be analyzed. The study has been carried out for only one operating point of the large test matrix presented in Table 5.15 and the results are presented in Figure 8.8. Higher value of C_3 leads to larger droplet size and therefore longer penetration, regardless the value of B1. In fact, $C_3 = 1$ matches the experimental curve far from the nozzle except when B_1 is equal to 100. Thus, the use of its maximum value is recommended for following simulations.

Subsequently, the variable B_1 is treated, which typically varies from 5 to 100 according to the literature [10]. Within this specified range four different values have been considered, 5, 10, 30 and 100. For this analysis, the above constant C_3 has been taken equal to 1 since it is the value that best approximates the experiments results. The outcomes of this parametric study are presented in Figure 8.9. The effect of this constant on spray penetration is relatively small, except for the value of 100 which gives longer penetration, generally longer than experimental ones. For the other cases, the obtained results are almost identical to each other, with the curves overlapping between them. The reason of the mentioned behavior may be mainly due to the presence of a primary atomization model such as the Huh Model, which seems to dictate the droplet size and atomization. Based on the literature [11] and the values presented in the ECN workshops, the value of $B_1 = 30$ is taken for the following studies.

Both calibration constants have been varied within the recommended range, taking their maximum and minimum values for analysis. However, the spray penetration curve does not vary more than 10%. This indicates a low sensitivity of the studied injector to these modeling constants of the secondary atomization model. On one hand, the employed model is almost insensitive to tuning parameters so the error could not be minimized as much as desired. On the other hand, the model reproduces the experimental results with sufficient accuracy, which means that the selected approach is correct and accurate.

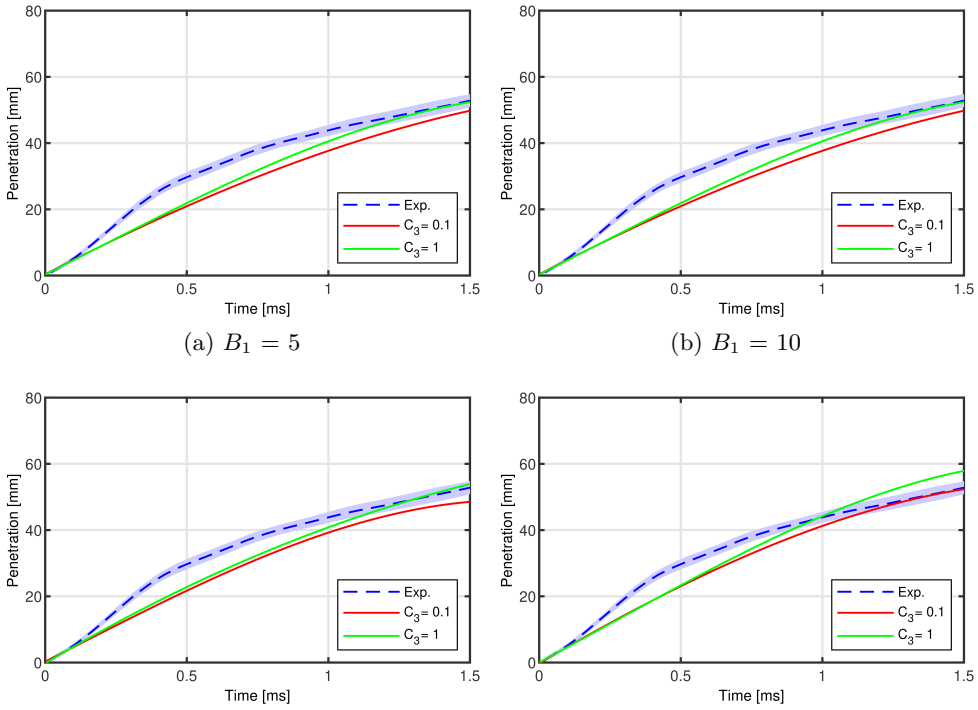

(a) $B_1 = 5$ (b) $B_1 = 10$

(c) $B_1 = 30$ (d) $B_1 = 100$

Figure 8.8: Calibration of the C_3 constant for PIU injector. Computational spray penetration comparison with experiments for an injection pressure 20 MPa, an ambient back pressure of 0.6 MPa and different values of B_1.

8.3.4 One-way coupling results

Once the sub-models that comprise the present study have been calibrated and validated, they can be used to fulfill the main objective of this research, which is to determine the accuracy of the spray simulations when using input parameters only from computational studies of internal flow. For this purpose, the results of the present work will be compared both with available experimental data for the same target injector as well as with results obtained from applying the same computational set-up but using as input parameters the data obtained directly from the experiments. Throughout the whole section the reader will find the experimental data presented in blue color, together with the spray simulations results with both type of inputs: the ones coming only from experimental data (in red) and the ones coming from the nozzle flow simulations with the proposed one-way coupling methodology (in green).

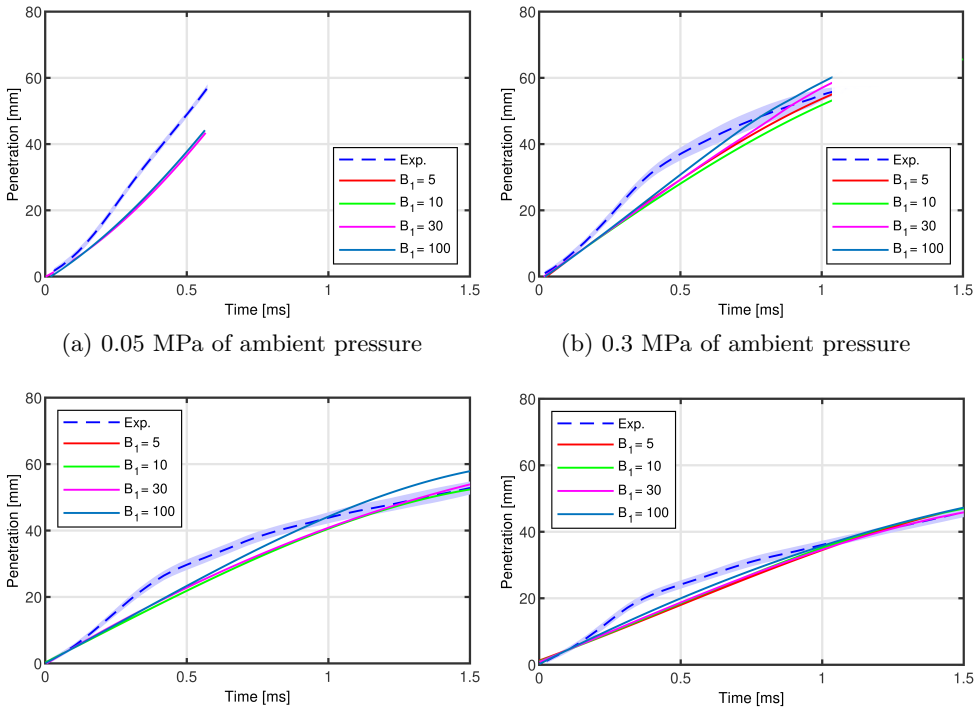

(a) 0.05 MPa of ambient pressure

(b) 0.3 MPa of ambient pressure

(c) 0.6 MPa of ambient pressure

(d) 1.0 MPa of ambient pressure

Figure 8.9: Calibration of the B_1 constant for PIU injector. Computational spray penetration comparison with experiments for an injection pressure 20 MPa and different values of ambient back pressure.

In order to demonstrate the validity of the predictive methodology employed, the whole map of injection conditions needs to be covered. Therefore, this section encompasses the results obtained for all the operating conditions presented in Table 5.15. The results obtained for the injection pressure of 10 MPa are presented in Figure 8.10, those for 20 MPa in Figure 8.11 and, finally, those for 28 MPa in Figure 8.12.

The behavior observed for all operating conditions analyzed with an ambient pressure equal or higher than 0.1 MPa is not the expected from the experimental data. The curves between 0.2 and 1.2 ms present a sort of bump that makes the curve differ from the parabolic trend commonly found [12]. The injection duration in which this phenomenon occurs, covers the major part of the injection. It can be attributed to a strong interaction of the different sprays occurring in nozzles where holes are close to each other

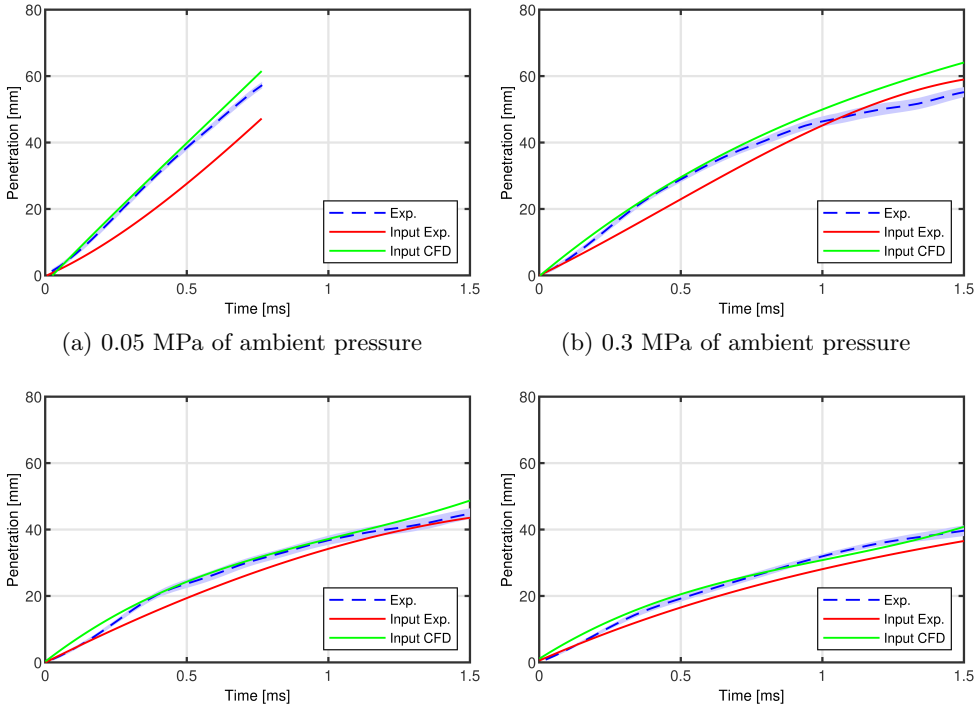

(a) 0.05 MPa of ambient pressure

(b) 0.3 MPa of ambient pressure

(c) 0.6 MPa of ambient pressure

(d) 1.0 MPa of ambient pressure

Figure 8.10: Spray penetration comparison between DDM approach with experimental data as input and one-way coupling methodology for the PIU injector under an injection pressure of 10 MPa.

and orifice drill angles are small. This phenomenon is not correctly captured by the computationally employed models and sub-models even though there is a specific collision model, which in this case is under-predicting the phenomenon. This explains that the computational curves do not adapt correctly to the experiments and thus generate a difference in the results larger than expected. In addition, in all the cases for all the injection pressures, it is observed how the one-way coupling approach predicts faster and higher penetrations with respect to the classical configuration with experimental input parameters. This is mainly due to the small over-prediction of the injection rate. Consequently, a higher discharge coefficient as well as a higher injection velocity due to a higher injection rate result in faster and higher penetrations. The approximations obtained by the classical model using experimental input parameters underpredict the experimental results. However, the effect of having a higher discharge coefficient and injection rate on penetration mitigates

the under-prediction of the penetration values, thus bringing the penetration values closer to the experimental data. Another important phenomenon observed is that at low back pressures, when the discharge pressure is below the fuel saturation pressure (0.05 MPa), the experimental penetration trend is not well captured by the CFD simulation. This is mainly because under these operating conditions the gasoline tends to change its behavior due to the presence of phenomena such as flash boiling and/or spray collapse and the models and sub-models employed are not adequate to capture this novel behavior. It is true, and as mentioned earlier, that newer versions of the codes used throughout this document are beginning to implement specific flash boiling models and improving the existing ones for predicting collapse in order to adapt to the characteristics of this fuel and improve the predictions of the external flow behavior under these operating conditions [13].

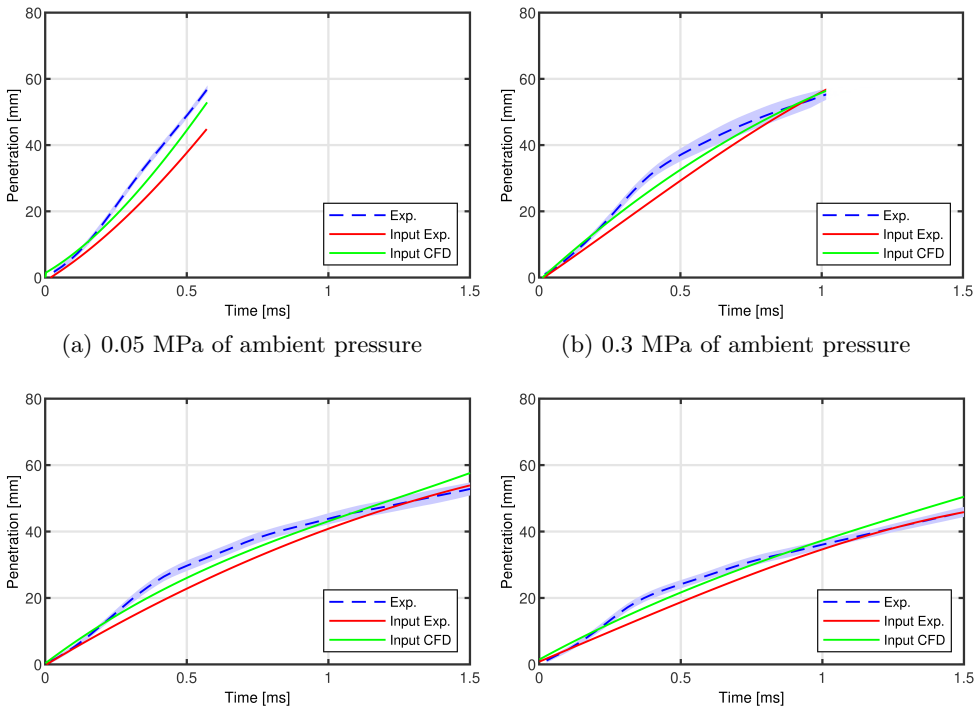

(a) 0.05 MPa of ambient pressure

(b) 0.3 MPa of ambient pressure

(c) 0.6 MPa of ambient pressure

(d) 1.0 MPa of ambient pressure

Figure 8.11: Spray penetration comparison between DDM approach with experimental data as input and one-way coupling methodology for the PIU injector under an injection pressure of 20 MPa.

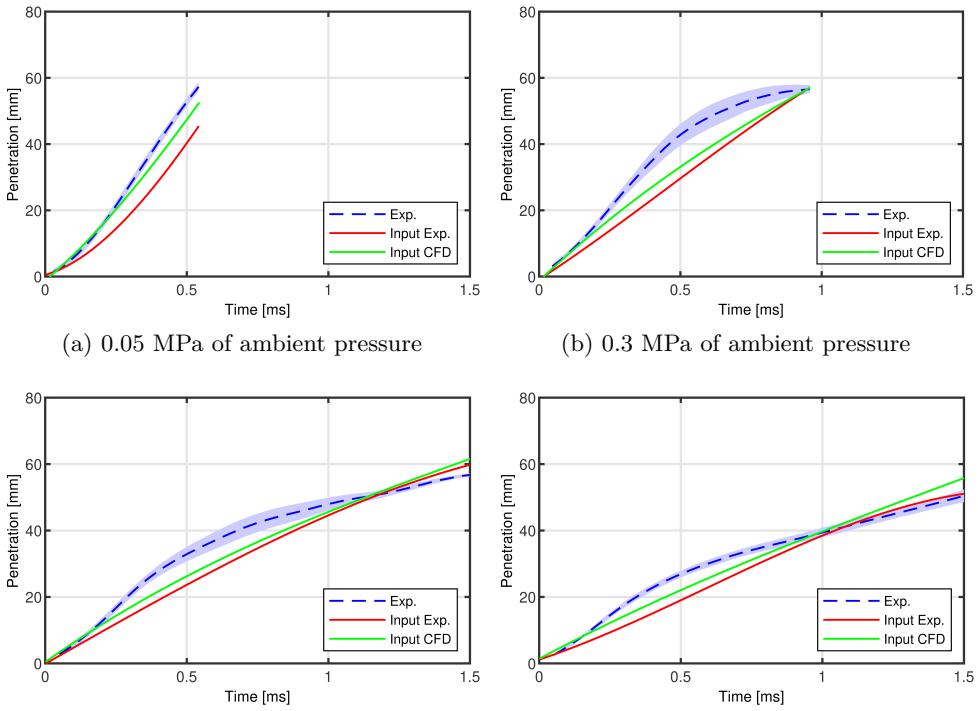

(a) 0.05 MPa of ambient pressure

(b) 0.3 MPa of ambient pressure

(c) 0.6 MPa of ambient pressure

(d) 1.0 MPa of ambient pressure

Figure 8.12: Spray penetration comparison between DDM approach with experimental data as input and one-way coupling methodology for the PIU injector under an injection pressure of 28 MPa.

As a summary, Table 8.4 includes the accumulated errors calculated from Equation 5.139 and obtained for three chosen reference conditions, the same back pressure of 0.6 MPa and the three different injection pressures studied, 10 MPa, 20 MPa and 28 MPa. The obtained deviations seem to have somewhat high values but they are mainly due to the bump apparently caused by the collapse of the sprays not being adequately captured, this generating a dispersion in the results at that particular point. Another detail that can be observed in this Table 8.4 is how the higher the injection pressure is, the larger the difference with experiments becomes for cases where the input parameters are experimental, while for the one-way coupling model the differences are maintained regardless of the injection pressure.

In addition to the aforementioned, and since there are no data on the microscopic parameters of the spray nor velocity distribution, it has been con-

P_{inj}	P_{back}	T_{inj}	T_{back}	Exp. Difference	CFD Difference
10 MPa	0.6 MPa	363 K	300 K	9.77 %	10.74 %
20 MPa	0.6 MPa	363 K	300 K	11.83 %	9.23 %
28 MPa	0.6 MPa	363 K	300 K	16.93 %	10.83 %

Table 8.4: Differences between the different computational approaches, with experimental and computational input parameters, and the experimental values considered for validation for the PIU injector under several reference operating conditions.

sidered of interest to present a temporal evolution of the spray shape and compare it with the images experimentally obtained. Figure 8.13 shows the liquid phase of the spray in the form of droplets colored by the particle velocity compared with the images obtained from the experimental DBI technique. These images have been acquired for one of the operating conditions studied, although the conclusions drawn from the analysis can be applied to the other conditions of interest. In both cases it is reflected how the spray jets, six for the present injector, are found together forming a single spray in a way that gives to understand the great jet-to-jet interaction that exists, justifying the behavior observed in the penetration curves. Computationally, this phenomenon is also seen, but the collision models do not adequately capture the level of interaction between particles. It can be concluded from this investigation that the model employed captures with certain limitations, especially in extreme operating conditions, the external flow behavior and provides results close to the experiments, always taking into account the mentioned limitation.

8.4 Summary and Conclusions

This section gathers the main findings found throughout the external flow studies conducted by means of coupling strategies such as one-way coupling and mapping. Since this Chapter encompasses the validity of the predictive methodology developed throughout the document by testing it on the different target injectors and independently of the software involved, the main outcomes will be presented in the different categories of analysis. On the one hand, the main results and the associated discussion will be presented for the coupling carried out for the Spray G injector of the ECN and, on the other hand, the conclusions obtained from the coupling carried out for the PIU injector will be presented.

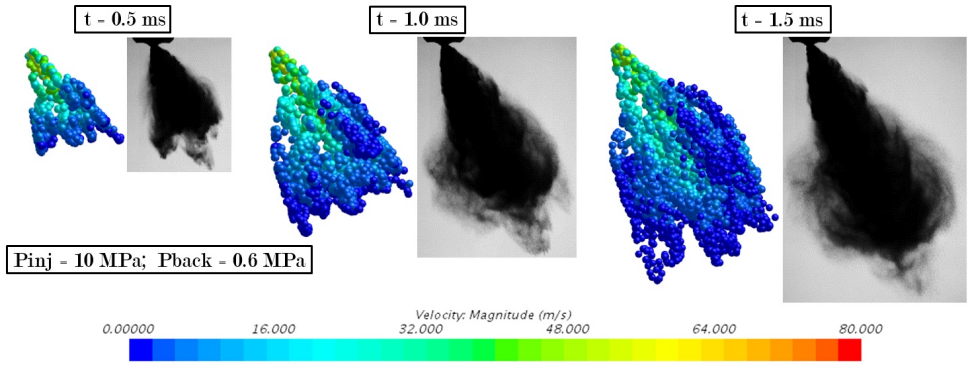

Figure 8.13: Spray shape evolution obtained from the one-way coupling approach and compared with experimental images obtained by DBI experimental technique for the PIU injector.

8.4.1 Spray G injector. Coupling discussion

Two different coupling strategies have been studied for the particular ECN, Spray G injector in order not to neglect the influence of the nozzle on the spray patterns and to validate the developed predictive methodology. On the one hand, the one-way coupling strategy has been employed where the input parameters for the DDM are obtained from internal nozzle flow simulations and, on the other hand, the well-known mapping approach has been used. Both strategies employ a fully predictive strategy where no experimental data is needed. The results have been validated with experimental data present in the literature and compared with the results obtained from the classical DDM with experimental input parameters. As a general conclusion of this study, before breaking down the findings according to the strategies adopted, it can be stated that the fully computational developed predictive methodology provides a high accuracy in the study of this field as far as macroscopic parameters and spray shape are concerned, allowing to leave aside the experimental data.

Regarding the obtained results from the one-way coupling, it has been observed that when introducing the computational injection rate profile, a higher initial penetration velocity is available due to a higher overshoot. However, trends of the penetration curves are similar to the experimental data. The spray angle is also accurately captured by this simulation strategy. Taking advantage of the precision of the one-way coupling approach, the spray behavior and spray characteristics have been analyzed using different surrogate fuels. The obtained behaviors are in accordance with the physical properties of each fuel. Pentane, which has a higher volatility, presents lower liquid penetrations

than the rest of the fuels, while ethanol, fuel with lower vapor latent heat which also presented a higher injection rate profile due to its higher density, has higher liquid penetrations. This study has also shown a limitation of the models involved which do not capture as expected the behavior of the sprays under the flash boiling phenomenon. This is mainly due to the fact that, in the present adopted version, no specific flash boiling model is available to deal with these conditions. Finally, and within this same research field, the influence between injections under multiple injection strategies has been analyzed, demonstrating that under short dwell times there is an influence of the first injection on the one that precedes it due to the well-known "slipstream" phenomenon. This is because the gas is accelerated by the first injection and the following one loses less momentum causing it to penetrate further.

On the other hand, concerning the mapping strategy, which together with the previous one is considered one of the final objectives of the predictive methodology developed, it offers really close approximations to the experimental behavior with cumulative differences of less than 8% in any of the cases studied. It is true that although the trends are captured, the mapping strategy tends to overpredict the spray penetration. An important fact is that the mapping takes into account the deviation of approximately 3°, as calculated in the internal flow, of the spray towards the injector axis, a phenomenon that is not considered in the classical DDM simulations since the direction of the spray is imposed by the user and is established in function of the geometrical values of the orifices.

8.4.2 PIU injector. One-way coupling discussion

A one-way coupling methodology is used for a particular GDI injector in order to study the external flow without neglecting the possible influence of the fluid behavior inside the nozzle. This study has therefore been based on the use of data obtained from the internal flow simulations as input parameters to analyze the spray patterns replacing the experimental input values used in the classical DDM approaches. For comparison purposes, experimental data and the computational results obtained from the classical approaches where experimental input parameters are used to study the spray behavior have been considered. In addition, the processing methods adopted for the calculation of the spray are similar between experiments and simulations looking for consistency. As a general conclusion before breaking down the different outcomes, it can be said that the accuracy of the methodology implemented is significant, obtaining results close to the experiments and thus taking a step forward towards fully predictive injection simulations.

Once the internal flow simulations have been validated, the injection rate and discharge coefficient data are employed to reproduce the spray behavior using a DDM approach and nozzle type injector in StarCCM+. The results carried out demonstrate that the turbulence model k-ω, although it can offer new insights or improve the accuracy of the results by capturing the possible recirculations existing in the GDI injection, finally obtains results very close to the k-ϵ model. For this reason, and given the large background of the latter model and its performance in the present research, it has been chosen to carry out the other studies. Regarding the necessary calibration of the sub-models that conform the DDM, a limited sensitivity of the spray patterns to the variation of the constants that conform the secondary break-up processes has been observed. This could be due to the presence of a primary atomization model such as the Huh model which seems to dictate the droplet size and the consequent atomization of the droplets allowing the influence of the secondary model to be minor.

Regarding the obtained results of the external flow studies carried out for all the operating points, it is observed that the behavior of the PIU injector does not follow the expected parabolic trends and has a bump in the middle instants of the injection, which can be attributed to a collapse of the jets due to the close arrangement of the orifices. This behavior is not computationally captured for two main reasons, some deficiencies of the model and a lack of sensitivity in the calibration constants which cause a deviation reflected in the accumulated errors between simulations and experiments. The computational results predict higher penetration compared to the experimental one also due to the overestimation of mass and momentum (about 5% given by the internal nozzle flow calculations). This effect is reflected in a reduction in the accumulated error. The computational results obtained, although considered of high quality, suggest more experimental and numerical investigation in order to understand the observed spray penetration behavior, and to develop or modify the models accordingly.

References

[1] Payri, R. et al. “Study of evaporative diesel spray interaction in multiple injections using optical diagnostics”. In: *Applied Thermal Engineering* 176.May (2020), p. 115402. DOI: 10.1016/j.applthermaleng.2020.115402.

[2] Martínez, M. et al. "Computational study of the Premixed Charge Compression Ignition combustion in a Rapid Compression Expansion Machine : Impact of multiple injection strategy on mixing , ignition and combustion processes". In: *Fuel* 318.January (2022), p. 123388. DOI: 10.1016/j.fuel.2022.123388.

[3] Bautista Rodriguez, A. "Study of the Gasoline direct injection process under novel operating conditions". PhD thesis. Universitat Politècnica de València, 2021.

[4] Nocivelli, L. et al. "Analysis of the Spray Numerical Injection Modeling for Gasoline Applications". In: *SAE Technical Papers* 2020-April.April (2020), pp. 1–13. DOI: 10.4271/2020-01-0330.

[5] Desantes, J. M. et al. "A Comparison of Diesel Sprays CFD Modeling Approaches: DDM versus Σ-Y Eulerian Atomization Model". In: *Atomization and Sprays* 26.7 (2016), pp. 713–737. DOI: 10.1615/AtomizSpr.2015013285.

[6] Pope, S. B. "An explanation of the turbulent round-jet/plane-jet anomaly". In: *AIAA Journal* 16.3 (2008), pp. 279–281. DOI: 10.2514/3.7521.

[7] Prieto, L. M. P. "CFD Modeling of Combustion and Soot Production in". PhD thesis. 2020. DOI: 10.4995/Thesis/10251/142189.

[8] Paredi, D. et al. "Validation of a comprehensive computational fluid dynamics methodology to predict the direct injection process of gasoline sprays using Spray G experimental data". In: *International Journal of Engine Research* 21.1 (2019), p. 146808741986802. DOI: 10.1177/1468087419868020.

[9] Jaramillo Císcar, D. "Estudio experimental y computacional del proceso de inyección diésel mediante un código CFD con malla adaptativa". PhD thesis. Universitat politècnica de valència, 2017. DOI: 10.4995/Thesis/10251/92183.

[10] Kong, S. C. et al. "The development and application of a diesel ignition and combustion model for multidimensional engine simulation". In: *SAE Technical Papers* 412 (1995). DOI: 10.4271/950278.

[11] Payri, R. et al. "Numerical Analysis of GDI Flash Boiling Sprays Using Different Fuels". In: *Energies* 14.18 (2021), p. 5925. DOI: 10.3390/en14185925.

[12] Desantes, J. M. et al. "Development and validation of a theoretical model for diesel spray penetration". In: *Fuel* 85.7-8 (2006), pp. 910–917.

[13] Duronio, F. et al. “ECN Spray G : Coupled Eulerian internal nozzle flow and Lagrangian spray simulation in flash boiling conditions”. In: (2022). DOI: 10.1177/14680874221090732.

Chapter 9

Conclusions and Future Work

"Success is not the triumph,
but everything you have striven to achieve."
—Rafael Nadal

Due to the natural tendency existing in the literature to study the GDI injection process separating the internal and external flow in the analysis, it has been considered convenient to divide the obtained conclusions of the different studies according to their objective. Therefore, each chapter of results has a final section where the main achievements of the corresponding research are summarized. Nevertheless, this section synthesizes the main outcomes from the present Thesis. In addition, it also includes future work that may be of scientific interest to improve the understanding and comprehension of GDI injection.

9.1 Conclusions

The growing interest in the field of gasoline direct injection (GDI) has led this Thesis to actively participate in providing a better understanding to the scientific community of the phenomena that take place during the injection process that directly affect combustion efficiency and thus the fuel consumption and generation of pollutants. With this premise in mind, the main objective of this research has been to develop a predictive methodology capable of being applied to current and future generations of GDI injectors, regardless of

the injector features and the software used, for the hydraulic characterization of the injector under steady and transient operating conditions. Once this predictive methodology has been successfully validated, the final goal is to study the behavior of the spray once it leaves the injector using the obtained results from the application of the aforementioned methodology. What has been sought throughout the research is to follow in the footsteps of the research and industry communities in replacing experimental practice as far as possible, as has been done in the past research projects.

The followed strategy in this research was to separate the stages to be studied so that each one can be investigated in greater depth. In this sense, the injection process was divided into two distinct parts, the in- and near-nozzle on the one hand and the development and structure of the spray on the other. The predictive methodology was mainly focused on the study of the internal flow and near-field in order to hydraulically characterize the injector. Firstly, the methodology was developed taking as reference the injector belonging to the ECN, Spray G, considering stationary conditions where the needle is raised in a fixed position. Validation was done under two different commercial software, StarCCM+ and CONVERGE™ . The successful applicability of the above methodology was demonstrated by obtaining results of injection rate and momentum close to the experiments with differences of less than 5% for injection rate and 10% for momentum flux. In addition, it was also possible to demonstrate how under the same computational code, the polyhedral mesh has a high accuracy using less than half the number of cells than the hexahedral mesh. Not only that, but the injector was characterized by means of the dimensionless flow coefficients, showing small values of discharge coefficient due to the presence of recirculation inside the orifices by the non-condensable ambient gas. This effect was corroborated with the calculation of the spray angles in the near field where a jet deviation of about 3° towards the injector axis caused by the peculiar geometry of the orifices and the presence of ambient gas in the interior of the orifices was observed. The next step was to validate the developed methodology by applying it to the characterization of an industrial injector of real applicability called PIU injector. The validation was carried out under different operating conditions including different injection pressures and various ambient densities. In all cases analyzed, differences with experimental data of less than 4% were obtained in both injection rate and momentum flux values. Therefore, given the high precision of the results obtained, these studies corroborate the validity of the model and its applicability regardless of the operating condition being analyzed, the software used and the geometrical characteristics of the injector being characterized.

The applicability of the predictive methodology was extended to cases where the transient nature of the injection process was taken into account by simulating the needle movement where the Spray G injector was used for this purpose. Regarding the macroscopic results describing the internal flow, the injection rate and momentum flux profiles were adequately captured by both considered codes with differences of less than 5% for the injection rate and 10% for the momentum flux. Even though, the difference in momentum is outside the experimental incertitude in GDI applications, there is a large uncertainty concerning the measurement momentum flux methodology that needs to be studied in depth in order to bring clarity to the comparison. A faster ramp opening was presented in the computational case, an effect that can be attenuated with a more realistic initialization of the injection pressure, in other words, using as input condition a parabolic pressure ramp. Another important phenomenon was the presence of liquid in the first moments of injection, which is due to the needle initially raised a few microns to avoid surface overlapping. This effect can be corrected by using a sealing algorithm.

After the transient behavior was validated using the reference fuel iso-octane, the model was applied to analyze the behavior of the in- an near- nozzle flow during the transient process of GDI injection using different surrogates fuels including ethanol, heptane, iso-octane, hexane, E00 and pentane under the most typical engine operating conditions defined by the ECN: SG, SG2 and SG3. The calculation of the spray angles in the near field showed that the flash boiling condition has a tendency to widen the sprays due to the rapid phase change and the presence of fuel vapor inside the sprays. Comparing the macroscopic parameters of injection rate and momentum flux under the different surrogates, the differences in injection rate presented were small and mainly due to the dissimilar densities of each fuel being ethanol the highest and pentane the lowest. This variation in results was attenuated in the momentum flux profiles because the effect of density is mitigated by velocity, as expected.

In addition, the complexity of the employed geometry corresponding to the ECN injector has been increasing so that it is more and more similar to the real one. This research has considered studying the differences between generation 1 and generation 3 in terms of macroscopic parameters. The study has brought to light certain differences in both injection rate and momentum flux mainly due to the difference in the size of the orifices. Another important difference that has been observed is how generation 3 has a larger counter-bore space occupied by non-condensable gas and, even in the interior of the small orifices, small amounts of gas are also visible, an effect that is not seen in generation 1. This phenomenon produces a greater spray deflection towards

the injector axis resulting in a difference in drill angle between generations of between 1 and 2 degrees depending on the orifice observed.

The study was extended by considering multiple injections for which, and because the needle cannot be completely closed to avoid overlap between surfaces, a sealing strategy based on opening and closing events to control the flow passage between regions was successfully implemented. However, the lack of experimental data for the study of multiple injection strategies together with the uncertainty in the existing data suggest that a greater effort by experimentalists in this field of study is needed.

Concluding the studies based on the ECN reference injector, Spray G, the aim was to improve the accuracy of the studies by employing LES approach in the treatment of the turbulence of the transient and stationary phases of the injection event. For this purpose and in order to save computational cost, only half of the geometry was used, which incurred a small error in the injection rate and momentum flux of 9% and 6% respectively. The use of LES approach has allowed a more accurate study of spray behavior, improving the modeling of primary atomization by aerodynamic interaction. Furthermore, time-dependent characterization of the injector in terms of spray angle and plume direction was included, which provide greater accuracy to external flow studies.

Following the applicability of the predictive methodology under transient operating conditions, a comparison between injectors, PIU and Spray G, in terms of needle lift profiles and nozzle flow hydraulic coefficients was carried out using StarCCM+ software. In addition, the study provides answers to three main issues that are commonly encountered when dealing with and analyzing real injectors installed in GDI engines:

- *Computational cost:* in RANS approach, since the needle lift oscillations are small and have a negligible effect on the flow solution, most of the steady-state operation is not simulated. This shortens the injection duration and simulation time. The part that is not simulated is then included during post-processing of the simulation.
- *Pressure input boundary condition:* a realistic evolution of the input value is required to reproduce the experimental shapes of injection rate and momentum, especially during the opening transient phase. A parabolic increase from the discharge pressure to the injection pressure during the opening transient is successfully implemented.
- *Needle lift profile:* the x-ray technique provides an elevation curve with very low elevation values during the first few microseconds of the in-

jection duration. This low elevation restricts the flow and causes the results of the simulations to differ from the experimental ones. By eliminating this small elevation by educating the needle lift, the accuracy of the simulations improves significantly.

This study, besides validating the predictive methodology used by reporting a maximum difference of 5% in the total injected amount and in the hydraulic coefficients of the nozzles for two different nozzles and various injection conditions, demonstrates again the characteristic low values of discharge coefficients, due to both the counter-bore and the conical shape, which cause the ambient gas to flow inside the orifices and generate recirculations that enhance the air-fuel mixture.

Once the predictive methodology for the study of the internal flow was created and validated by obtaining scientifically significant and accurate data, the study of the external flow was carried out. For this purpose, three different approaches were used; on the one hand, the well known DDM which starts from experimental data used as input parameters, on the other hand, a coupling strategy called one-way coupling was selected, also based on the DDM approach but, with the needed parameters to define the input parameters obtained only from the computational data extracted from the internal flow analysis, and finally, the mapping technique which employs 3D maps of internal flow variables such as velocity, turbulent kinetic energy, dissipation rate or void fraction, among others, and directly using them as boundary and initial conditions in the external flow. The objective in this case is to continue with the generated predictive methodology so that the studies tend to eliminate as much needed experimental data as possible.

First of all, a model was developed to be applied to all the mentioned cases based on the classical DDM approach with experimental inputs. The validation of the model and methodology was successful under the reference operating condition SG, obtaining cumulative differences in terms of vapor and liquid penetrations with respect to the experimental data of at most 5%. Once the model was validated and its accuracy demonstrated, following the objective of the predictive methodology, it was applied to the study of the external flow under different operating conditions, obtaining cumulative differences of 7% for SG2 and 8% for SG3. The precision of the macroscopic parameters obtained together with the spray vapor projections demonstrated the accuracy and validity of the adopted methodology. However, it is necessary to point out the limitation that exists under flash boiling conditions due to the lack of a specific model in the present version of the software to deal with extreme conditions.

This study was replicated using LES approach for the treatment of turbulence, obtaining high accuracy in prediction of the macroscopic parameters studied, although the quality criterion that ensures the accuracy and quality of the results was not fully satisfied. Due to the high computational cost, a compromise had to be found between quality and cost without compromising model accuracy. The LES approach has demonstrated to predict larger spray openings resulting in an under-prediction of the induced axial gas velocity even though the gas velocity trend is captured with greater detail and pressure than the RANS model.

The same employed model for the study of external flow was applied to the different coupling approaches mentioned above, one-way and mapping. Regarding the obtained results from the one-way coupling, when introducing the computational injection rate profile a higher initial penetration velocity is provided due to a higher overshoot presented in the injection rate profiles. However, the trends of the penetration curves are similar to the experimental measurements with cumulative differences at most 8%. Furthermore, the spray angle was also accurately captured by this simulation strategy. As done in the internal flow, this model was applied to study the behavior of the spray under different surrogate fuels. The obtained behaviors are in accordance with the physical properties of each fuel. Pentane, which has a higher volatility, presents lower liquid penetrations than the rest of the fuels, while ethanol, with lower vapor latent heat and higher injection rate due to its higher density, has higher liquid penetration. Again, this study showed the limitations of the sub-models in capturing the phase changes and associated behaviors related to flash boiling conditions. Finally, the influence between injections under multiple injection strategies was also analyzed, demonstrating that under short dwell times between injections there is an influence of the first injection on the one that precedes it due to the well-known "slipstream" phenomenon. This is because the gas is accelerated by the first injection and the following one loses less momentum causing it to penetrate further.

On the other hand, concerning the mapping strategy, which together with the previous one is considered one of the final objectives of the developed predictive methodology, it offers really close approximations to the experimental behavior with cumulative differences of less than 8% in any of the studied cases. Although the trends are captured, the mapping strategy tends to overpredict the spray penetration. Note that the mapping takes into account the deviation of approximately 3°, as calculated in the internal flow, of the spray towards the injector axis, a phenomenon that is not considered in the classical DDM simulations since the direction of the spray is imposed by the user and is established in function of the geometrical values of the orifices.

Finally, and as a last validation, the developed model for the study of the external flow was applied to a different software (StarCCM+) and to a distinct injector (PIU injector). Despite forced changes in the sub-models used because not all commercial codes have them, and being faithful to the methodology established, the results obtained from this one-way coupling were satisfactory for a long list of operating points. However, it was observed that the behavior of the PIU injector did not follow the expected parabolic trends in spray penetration and has a bump in the curve corresponding to the middle instants of the injection, which could be attributed to a collapse of the jets due to the close arrangement of the orifices. This behavior was not computationally captured for two main reasons, some deficiencies of the model and a lack of sensitivity in the calibration constants. So, there is a deviation reflected in the cumulative differences between simulations and experiments. The computational results associated with the one-way coupling strategy predict higher penetration compared to the classic DDM with experimental inputs mainly due to the overestimation of mass and momentum (about 5% given by the internal nozzle flow calculations). This effect was reflected in a reduction in the accumulated error. The obtained computational results, although considered of high quality, suggest more experimental and numerical investigation is needed in order to understand the observed spray penetration behavior and develop or modify the models accordingly.

As a final conclusion of this Thesis, it could be stated that the developed predictive methodology throughout the document has demonstrated to predict results of high quality and precision when compared with experimental data. The accuracy and reliability of these data, which allow to reproduce faithfully the behavior of the GDI injection regardless of the software used and the characteristics of the injector studied, enable to replace the need of considering experimental data in the research, thus reducing the cost associated to the analysis of the injection process.

9.2 Future work

The gasoline direct injection process is a complex event due to its transient nature and the numerous physical mechanisms involved. Throughout the present Thesis, several studies have been carried out that provide a great deal of knowledge in the field of GDI injection, thus contributing to a greater and broader vision of it. However, and since it is a recently expanding field of study many questions remain uncovered and should be further reviewed in order to reach a more reliable understanding of GDI technology.

- *Momentum flux measurements:* this parameter is surrounded by a great deal of uncertainty concerning the measurement methodology. This suggests that numerous efforts are needed by experimentalists to understand the phenomena occurring during the injection process in terms of momentum flux and thus give clarity to the results, improving comparisons and validations. In addition, the institutions that carry out this type of measurements are limited, so it would help the scientific community if researchers from different organizations were interested in the problem, thus providing different points of view.
- *Injection process characterization under different surrogate fuels:* the growing interest to know the performance of the injection process under alternative fuels together with a changing market in which e-fuels are more and more popular leads to propose a further study based on the characterization of the injection process under different surrogate fuels.
- *Multi-injection strategy:* during the last few years there has been a growing interest in multiple injection strategies and the advantages that these can offer, being therefore one of the objectives of study in this Thesis. However, on the one hand, it has been observed that the lack of experimental data either concerning needle lift profiles or characteristic data of the injection behavior (ROI, ROM, penetrations, among others) makes the computational validation very challenging. On the other hand, it has been observed that experimentally the behavior is not correctly understood. Further needle lift profile measurements could help to improve both the comprehension of the phenomena associated with multiple injections and the modeling. Experimental measurements of variables that define the spray pattern could help to understand the influence between injections.
- *Further internal nozzle flow experimental characterization:* new experimental techniques on the market such as high-resolution x-ray tomography techniques that allow investigation of the structure and dynamics of the flow in the nozzle together with techniques such as Phase Doppler Anemometry (PDA) that provide droplet velocity and size at the nozzle exit would greatly assist in understanding the flow and ultimately modeling it. In addition, the idea of supporting the x-ray measurements with Frontal Mie Scattering visualization using a planar illumination to improve the understanding of the measurements can also be considered.
- *Deeper analysis on phenomena affecting combustion performance:* there are several causes of soot formation including tip wetting and spray-wall impingement that are related to the injection process. Tip-wetting

is a phenomenon that cannot be mitigated by improving the injection strategy and is not fully understood to date. Therefore, it is proposed to improve the understanding and prediction of plume expansion under mostly flash-boiling conditions. On the other hand, also associated with mainly flash-boiling conditions, it is considered of interest to pay attention to the well-known wall shock effect in order to provide a better understanding of these spray-wall interactions and to identify the key factors to keep them under control.

- *Improved spray patterning under flash-boiling conditions:* throughout the document, some limitations have been observed in the models or sub-models adopted for the study of the GDI injection process, being the most outstanding one under flash boiling conditions. In the present version of the commercial software CONVERGE™ , and unlike the internal flow studies, there is no specific sub-model for the analysis of the spray that takes into account the phase change associated to the presence of flash boiling. Therefore, and knowing that the most recent versions of this same software have specific sub-models to deal with this phenomenon so interesting for the scientific community, it is proposed to use and validate them from experimental data as well as to provide a comparison with the approaches presented in this Thesis.
- *Eulerian-Lagrangian Spray Atomization (ELSA) model:* the present Thesis has collected the different approaches employed in the literature to study the behavior of the GDI injection process. However, it has not been possible to cover the complete study of the injection process taking into account the internal and external flow at the same time so as to consider the possible feedback between regions such as the recirculation inside the orifices in this type of GDI injectors. Therefore, it is proposed to use the ELSA model which allows to integrate the analysis of the two different fields of study (internal and external flow) so that not only the different phenomena taking place in both fields but also the different time and length scales of the problems are addressed.
- *Real engine application:* it is typical in the literature that, mainly due to the associated cost, when complete processes are studied, spray configuration is not paid too much attention even though the injection strategy is one of the critical elements that directly influences engine performance. Therefore, in order to improve the accuracy of the studies, it is proposed to use the predictive methodology developed in this Thesis in the global analysis of the engine cycle. This has been recently employed in the

study of PCCI strategies in a RCEM offering a high precision in the obtained results [1].

References

[1] Martínez, M. et al. "Computational study of the Premixed Charge Compression Ignition combustion in a Rapid Compression Expansion Machine : Impact of multiple injection strategy on mixing , ignition and combustion processes". In: *Fuel* 318.January (2022), p. 123388. DOI: 10.1016/j.fuel.2022.123388.

Global Bibliography

Abd, H. M. et al. “Effects of varying orifice diameter and Reynolds number on discharge coefficient and wall pressure”. In: *Flow Measurement and Instrumentation* 65.November 2018 (2019), pp. 219–226. DOI: 10.1016/j.flowmeasinst.2019.01.004 (cited on page 64).

Abraham, J. “What is adequate resolution in the numerical computations of transient jets?” In: *SAE Technical Papers* 412 (1997). DOI: 10.4271/970051 (cited on page 151).

Abramzon, B. et al. “Droplet vaporization model for spray combustion calculations”. In: 32.9 (1988), pp. 1605–1618. DOI: 10.2514/6.1988-636 (cited on page 90).

Agarwal, A. K. et al. “Evolution, challenges and path forward for low temperature combustion engines”. In: *Progress in Energy and Combustion Science* 61 (2017), pp. 1–56. DOI: 10.1016/j.pecs.2017.02.001 (cited on page 38).

Aleiferis, P. G. et al. “An analysis of spray development with iso-octane, n-pentane, gasoline, ethanol and n-butanol from a multi-hole injector under hot fuel conditions”. In: *Fuel* 105 (2013), pp. 143–168. DOI: 10.1016/j.fuel.2012.07.044 (cited on page 97).

Aliabadi, S. et al. “Stabilized-finite-element/interface-capturing technique for parallel computation of unsteady flows with interfaces”. In: *Computer Methods in Applied Mechanics and Engineering* 190.3-4 (2000), pp. 243–261. DOI: 10.1016/S0045-7825(00)00200-0 (cited on page 136).

Allocca, L. et al. “Schlieren visualization of a GDI spray impacting on a heated wall: Non-vaporizing and vaporizing evolutions”. In: *Energy* 108 (2016), pp. 93–98. DOI: 10.1016/j.energy.2015.09.107 (cited on page 125).

Allocca, L. et al. “Tomography of a GDI spray by PolyCO based x-ray technique”. In: *SAE Technical Papers* 6.April 2020 (2013). DOI: 10.4271/2013-24-0040 (cited on page 5).

Amsden, A. et al. “KIVA-II: A computer program for chemically reactive flows with sprays, Los Alamos - National Laboratory, report LA-11560-MS”. In: *Los Alamos National Lab. (LANL)* May (1989), LA–11560–MS (cited on pages 202, 214, 217).

An, Q. et al. “Volkswagen’s diesel emission scandal: Analysis of facebook engagement and financial outcomes”. In: *Lecture Notes in Computer Science (including subseries Lecture Notes in Artificial Intelligence and Lecture Notes in Bioinformatics)* 10968 LNCS (2018), pp. 260–276. DOI: 10.1007/978-3-319-94301-5_20 (cited on page 2).

Anderson, J. D. J. *Fundamentals of Aerodynamcis*. Fifth edit. Vol. 1. 2015 (cited on pages 60, 62).

Angarita-Jaimes, D. et al. “Three-component multi-phase velocimetry measurements on a GDI spray using optically efficient fluorescent tracers”. In: *Experiments in Fluids* 52.4 (2012), pp. 949–962. DOI: 10.1007/s00348-011-1174-3 (cited on page 96).

Antepara, O. et al. “A comparative study of interface capturing methods with AMR for incompressible two-phase flows”. In: *Proceedings of the 7th International Conference on Coupled Problems in Science and Engineering, COUPLED PROBLEMS 2017* 2017-Janua (2017), pp. 981–992 (cited on page 137).

Aori, G. et al. “Effect of Nozzle Configuration on Macroscopic Spray Characteristics of Multi-Hole Fuel Injectors Under Superheated Conditions”. In: *Atomization and Sprays* 26.5 (2016), pp. 439–462. DOI: 10.1615/AtomizSpr.2015011990 (cited on page 99).

Araneo, L. et al. “Analysis of PDA measurements in double injection GDI sprays”. In: *ILASS - Europe 2017, 28th Conference on Liquid Atomization and Spray Systems* September (2017), pp. 6–8. DOI: 10.4995/ilass2017.2017.5007 (cited on page 5).

Araneo, L. et al. “Flash boiling in a multihole G-DI injector - Effects of the fuel distillation curve”. In: *Fuel* 191 (2017), pp. 500–510. DOI: 10.1016/j.fuel.2016.11.104 (cited on page 99).

Archer, G. et al. “CO2 Emissions From Cars: The facts”. In: *Transport & Environment* August (2018), p. 53 (cited on page 1).

Arcoumanis, C. et al. "Effect of fuel injection processes on the structure of diesel sprays". In: *SAE Technical Papers* 41 2 (1997). DOI: 10.4271/970799 (cited on pages 64, 84).

Arcoumanis, C. et al. "Cavitation in real-size multi-hole diesel injector nozzles". In: *SAE Technical Papers* 724 (2000). DOI: 10.4271/2000-01-1249 (cited on pages 68, 69).

Arcoumanis, C. et al. "Analysis of the flow in the nozzle of a vertical multi-hole Diesel engine injector". In: *SAE Paper 980811* (1998) (cited on page 209).

Arienti, M. et al. "Coupled Level-Set/Volume-of-Fluid Method for Simulation of Injector Atomization". In: *Journal of Propulsion and Power* 29.1 (2013), pp. 147–157. DOI: 10.2514/1.B34198 (cited on page 147).

Ashgriz, N. et al. "Binary collision dynamics of fuel droplets". In: *International Journal of Heat and Fluid Flow* 8.3 (1987), pp. 205–210. DOI: 10.1016/0142-727X(87)90029-4 (cited on page 89).

Ashgriz, N. et al. "Coalescence and separation in binary collisions of liquid drops". In: *Journal of Fluid Mechanics* 221 (1990), pp. 183–204. DOI: 10.1017/S0022112090003536 (cited on page 89).

Ashgriz, N. *Handbook of atomization and sprays: theory and applications*. Springer Science & Business Media, 2011 (cited on pages 85, 201).

Baldwin, E. et al. "String flash-boiling in gasoline direct injection simulations with transient needle motion". In: *International Journal of Multiphase Flow* 87 (2016), pp. 90–101. DOI: 10.1016/j.ijmultiphaseflow.2016.09.004 (cited on pages 134, 307, 326, 330, 383, 394, 395, 397).

Banerjee, R. et al. "Numerical investigation of stratified air/fuel preparation in a GDI engine". In: *Applied Thermal Engineering* 104 (2016), pp. 414–428. DOI: 10.1016/j.applthermaleng.2016.05.050 (cited on page 153).

Bar-Kohany, T. et al. "State of the art review of flash-boiling atomization". In: *Atomization and Sprays* 26.12 (2016), pp. 1259–1305. DOI: 10.1615/AtomizSpr.2016015626 (cited on pages 71, 72).

Barton, I. E. "Comparison of simple- and piso-type algorithms for transient flows". In: *International Journal for Numerical Methods in Fluids* 26.4 (1998), pp. 459–483. DOI: 10.1002/(SICI)1097-0363(19980228)26:4<459::AID-FLD645>3.0.CO;2-U (cited on page 224).

Bataille, J. et al. *Continuum modeling of two-phase flows*. Tech. rep. 1981, p. 35 (cited on page 132).

Battistoni, M. et al. “Coupled simulation of nozzle flow and spray formation using diesel and biodiesel for CI engine applications”. In: *SAE Technical Papers* (2012). DOI: 10.4271/2012-01-1267 (cited on page 178).

Battistoni, M. et al. “Effect of Off-Axis Needle Motion on Internal Nozzle and Near Exit Flow in a Multi-Hole Diesel Injector”. In: *SAE International Journal of Fuels and Lubricants* 7.1 (2014), pp. 2014–01–1426. DOI: 10.4271/2014-01-1426 (cited on page 395).

Battistoni, M. et al. “Effects of noncondensable gas on cavitating nozzles”. In: *Atomization and Sprays* 25.6 (2015), pp. 453–483. DOI: 10.1615/AtomizSpr.2015011076 (cited on page 200).

Battistoni, M. et al. “Large-Eddy Simulation (LES) of Spray Transients: Start and End of Injection Phenomena”. In: *Oil & Gas Science and Technology - Revue d’IFP Energies nouvelles* 71.4 (2016), p. 4. DOI: http://dx.doi.org/10.2516/ogst/2015024 (cited on page 373).

Battistoni, M. et al. “Highly resolved Eulerian simulations of fuel spray transients in single and multi-hole injectors: Nozzle flow and near-exit dynamics”. In: *Fuel* 251 (2019), pp. 709–729. DOI: 10.1016/j.fuel.2019.04.076 (cited on page 392).

Baumgarten, C. “Mixture Formation in Internal Combustion Engine”. In: *Mixture Formation in Internal Combustion Engine* (2006). DOI: 10.1007/3-5403-0836-9 (cited on page 90).

Bautista Rodriguez, A. “Study of the Gasoline direct injection process under novel operating conditions”. PhD thesis. Universitat Politècnica de València, 2021 (cited on pages 7, 332, 427, 431, 450, 453).

Befrui, B. et al. “GDI multi-hole injector internal flow and spray analysis”. In: *SAE 2011 World Congress and Exhibition* (2011). DOI: 10.4271/2011-01-1211 (cited on pages 143, 144).

Befrui, B. et al. “Large Eddy Simulation of GDI Single-Hole Flow and Near-Field Spray”. In: *SAE International Journal of Fuels and Lubricants* 5.2 (2012), pp. 620–636. DOI: 10.4271/2012-01-0392 (cited on pages 143, 144).

Befrui, B. et al. “GDi skew-angled nozzle flow and near-field spray analysis using optical and X-Ray imaging and VOF-LES computational fluid dynamics”. In: *SAE Technical Papers* 2 (2013). DOI: 10.4271/2013-01-0255 (cited on pages 143, 144).

Befrui, B. et al. “Primary atomization of a GDi multi-hole plume using VOF-LES method”. In: *SAE Technical Papers* 1 (2014). DOI: 10.4271/2014-01-1125 (cited on pages 143, 144).

Befrui, B. et al. “Coupled LES Jet Primary Breakup - Lagrangian Spray Simulation of a GDi Multi-Hole Fuel Injector”. In: *SAE International Journal of Fuels and Lubricants* 8.1 (2015), pp. 179–189. DOI: 10.4271/2015-01-0943 (cited on page 437).

Befrui, B. et al. “ECN GDi Spray G : Coupled LES Jet Primary Breakup - Lagrangian Spray Simulation and Comparison with Data”. In: *ILASS Americas 28th* June (2016) (cited on page 157).

Belmar Gil, M. “Computational study on the non-reacting flow in Lean Direct Injection gas turbine combustors through Eulerian-Lagrangian Large-Eddy Simulations”. PhD thesis. Valencia (Spain): Universitat Politècnica de València, 2020. DOI: 10.4995/Thesis/10251/159882 (cited on page 225).

Benajes, J. et al. “Computational assessment towards understanding the energy conversion and combustion process of lean mixtures in passive pre-chamber ignited engines”. In: *Applied Thermal Engineering* 178.April (2020), p. 115501. DOI: 10.1016/j.applthermaleng.2020.115501 (cited on page 9).

Benra, F. K. et al. “A comparison of one-way and two-way coupling methods for numerical analysis of fluid-structure interactions”. In: *Journal of Applied Mathematics* 2011 (2011). DOI: 10.1155/2011/853560 (cited on page 9).

Bergwerk, W. “Flow Pattern in Diesel Nozzle Spray Holes”. In: *Proceedings of the Institution of Mechanical Engineers* 173.25 (1959). DOI: 10.1243/PIME (cited on pages 68, 69).

Berni, F. et al. “A zonal secondary break-up model for 3D-CFD simulations of GDI sprays”. In: *Fuel* 309.October 2021 (2022), p. 122064. DOI: 10.1016/j.fuel.2021.122064 (cited on page 156).

Berrocal, E. et al. “Two-photon fluorescence laser sheet imaging for high contrast visualization of atomizing sprays”. In: *OSA Continuum* 2.3 (2019), p. 983. DOI: 10.1364/osac.2.000983 (cited on page 78).

Bilicki, Z. et al. “Physical Aspects of the Relaxation Model in Two-Phase Flow”. In: *Proceedings of the Royal Society A: Mathematical, Physical and Engineering Sciences* (1990). DOI: 10.1098/rspa.1990.0040 (cited on page 198).

Birouk, M. et al. “Liquid jet breakup in quiescent atmosphere: a review”. In: 19.6 (2009), pp. 501–528 (cited on page 80).

Blander, M. et al. “Bubble nucleation in liquids”. In: *AIChE Journal* 21.5 (1975), pp. 833–848. DOI: 10.1002/aic.690210502 (cited on page 71).

Bode, J. et al. “Fuel spray in Diesel engines. Part I: Spray formation”. In: *ATA 92A065* (1992) (cited on pages 68, 69).

Bode, M. et al. “Effects of Cavitation and Hydraulic Flip in 3-Hole GDI Injectors”. In: *SAE International Journal of Fuels and Lubricants* 10.2 (2017). DOI: 10.4271/2017-01-0848 (cited on pages 148, 149).

Bormashenko, E. “Generalization of the Buckingham Pi- Theorem”. In: June (2016) (cited on pages 81, 82).

Bornschlegel, S. et al. “Flash boiling atomization in nozzles for GDI engines”. In: *28th Conference on Liquid Atomization and Spray Systems* September (2017), pp. 6–8. DOI: 10.4995/ilass2017.2017.4750 (cited on page 121).

Bornschlegel, S. et al. “Multi-hole gasoline direct injection:In-nozzle flow and primary breakup investigated in transparent nozzlesand with X-ray”. In: *International Journal of Engine Research* 19.1 (2018), pp. 67–77. DOI: 10.1177/1468087417746860 (cited on pages 117, 118, 179).

Bosch Extranet Service. “Sistemas de Inyección Electrónica”. In: (2018), p. 72 (cited on page 27).

Bosch, W. “The fuel rate indicator: A new measuring instrument for display of the characteristics of individual injection”. In: *SAE Technical Papers* (1966). DOI: 10.4271/660749 (cited on page 116).

Bosh. *Bosch Premium Fuel Injectors* (cited on page 51).

Bower, G. R. et al. “A Comparison of the Bosch and Zuech Rate of Injection Meters”. In: *SAE Technical Papers* (1991). DOI: https://doi.org/10.4271/910724 (cited on page 116).

Brennen, C. E. *Cavitation and bubble dynamics*. 2013, pp. 1–249. DOI: 10.1017/CBO9781107338760 (cited on pages 210, 212).

Brusiani, F. et al. “LES simulation of ICE non-reactive flows in fixed grids”. In: *SAE Technical Papers* 2008.724 (2008), pp. 776–790. DOI: 10.4271/2008-01-0959 (cited on page 373).

Caika, V. et al. “Integrated 1D/2D/3D Simulation of Fuel Injection and Nozzle Cavitation”. In: *SAE International Journal of Engines* 6.3 (2013), pp. 1544–1552. DOI: 10.4271/2013-24-0006 (cited on page 51).

Cando Comino, J. C. “Investigation of Knock Limits of Dual Fuel Engines”. PhD thesis. 2013 (cited on page 38).

Carreres, M. “Thermal Effects Influence on the Diesel Injector Perfomance through a Combined 1D Modelling and Experimental Approach”. PhD thesis. Universitat Politècnica de València, 2016. DOI: 10.4995/Thesis/10251/73066 (cited on page 6).

Cavicchi, A. et al. "Numerical and experimental analysis of the spray momentum flux measuring on a GDI injector". In: *Fuel* 206 (2017), pp. 614–627. DOI: 10.1016/j.fuel.2017.06.054 (cited on page 117).

Celik, I. B. et al. "Index of resolution quality for large eddy simulations". In: *Journal of Fluids Engineering, Transactions of the ASME* 127.5 (2005), pp. 949–958. DOI: 10.1115/1.1990201 (cited on pages 373, 374, 437).

Celik, I. et al. "Assessment measures for engineering LES applications". In: *Journal of Fluids Engineering, Transactions of the ASME* 131.3 (2009), pp. 0311021–03110210. DOI: 10.1115/1.3059703 (cited on page 374).

Chaves, H. et al. "Experimental study of cavitation in the nozzle hole of diesel injectors using transparent nozzles". In: *SAE Technical Papers* 412 (1995). DOI: 10.4271/950290 (cited on page 68).

Chaves, H. et al. "Binary cavitation in a transparent three hole GDI nozzle". In: September (2017). DOI: 10.4995/ilass2017.2017.5051 (cited on page 117).

Chen, J. L. et al. "Influence of needle lift on gasoline injector static flows". In: *SAE Technical Papers* 412 (1996). DOI: 10.4271/961121 (cited on page 319).

Chen, L. et al. "The influence of ethanol blends on particulate matter emissions from gasoline direct injection engines". In: *SAE Technical Papers* (2010), pp. 1–21. DOI: 10.4271/2010-01-0793 (cited on page 119).

Chenadec, V. L. et al. "A 3D unsplit Forward/Backward Volume-of-Fluid approach and coupling to the level set method". In: *Journal of Computational Physics* 233.1 (2013), pp. 10–33. DOI: 10.1016/j.jcp.2012.07.019 (cited on page 148).

Cheng, Q. et al. "Investigation on the spray characteristics of standard gasoline, n-pentane, iso-octane and ethnaol with a novel heated tip SIDI injector". In: *Applied Thermal Engineering* 110 (2017), pp. 539–552. DOI: 10.1016/j.applthermaleng.2016.07.201 (cited on page 386).

Chincholkar, S. P. et al. "Gasoline Direct Injection: An Efficient Technology". In: *Energy Procedia* 90.December 2015 (2016), pp. 666–672. DOI: 10.1016/j.egypro.2016.11.235 (cited on pages 3, 29).

Chryssakis, C. et al. "A unified fuel spray breakup model for internal combustion engine applications". In: *Atomization and Sprays* 18.5 (2008), pp. 375–426. DOI: 10.1615/atomizspr.v18.i5.10 (cited on page 85).

Cleary, V. et al. “Flashing liquid jets and two-phase droplet dispersion. I. Experiments for derivation of droplet atomisation correlations”. In: *Journal of Hazardous Materials* 142.3 (2007), pp. 786–796. DOI: 10.1016/j.jhazmat.2006.06.125 (cited on page 72).

Colebrook, C. F. “Turbulent Flow in Pipes, With Particular Reference To the Transition Region Between the Smooth and Rough Pipe Laws.” In: *Journal of the Institution of Civil Engineers* 12.8 (1939), pp. 393–422. DOI: 10.1680/ijoti.1939.14509 (cited on pages 54, 55).

Costa, M. et al. “Split injection in a homogeneous stratified gasoline direct injection engine for high combustion efficiency and low pollutants emission”. In: *Energy* 117.2016 (2016), pp. 405–415. DOI: 10.1016/j.energy.2016.03.065 (cited on pages 36–38).

Costa, M. et al. “Multiple Injection in a Mixed Mode GDI Boosted Engine”. In: *SAE Technical Paper* (2010), p. 15. DOI: https://doi.org/10.4271/2010-01-1496 (cited on page 116).

Crialesi-Esposito, M. “Analysis of primary atomization in sprays using Direct Numerical Simulation”. PhD thesis. Universtitat Politècnica de València, 2019. DOI: 10.4995/Thesis/10251/133975 (cited on page 6).

Crowe, C. T. et al. “Particle mixing in free shear flows”. In: *Progress in Energy and Combustion Science* 14.3 (1988), pp. 171–194. DOI: 10.1016/0360-1285(88)90008-1 (cited on pages 87, 88, 214).

Dahlander, P. et al. “High-speed photography and Phase Doppler Anemometry measurements of flash-boiling multi-hole injector sprays for spray-guided gasoline direct injection”. In: *10th International Conference on Liquid Atomization and Spray Systems, ICLASS 2006* (2006) (cited on page 77).

Dahlander, P. et al. “Measurements of Time-Resolved Mass Injection Rates for a Multi-Hole and an Outward Opening Piezo GDI Injector”. In: *SAE Technical Paper 2015-01-0929* (2015). DOI: 10.4271/2015-01-0929.Copyright (cited on page 51).

De la Garza, O. A. “Estudio de los efectos de la cavitación en toberas de inyección Diesel sobre el proceso de inyección y el de formación de hollín”. PhD thesis. Universtitat Politècnica de València, 2012. DOI: 10.4995/Thesis/10251/18153 (cited on page 6).

De la Morena, J. “Estudio de la influencia de las características del flujo interno en toberas sobre el proceso de inyección Diesel en campo próximo”. PhD thesis. Universtitat Politècnica de València, 2011. DOI: 10.4995/Thesis/10251/11098 (cited on pages 6, 68, 79).

Desantes, J. M. et al. "Development and validation of a theoretical model for diesel spray penetration". In: *Fuel* 85.7-8 (2006), pp. 910–917 (cited on page 464).

Desantes, J. M. et al. "A Comparison of Diesel Sprays CFD Modeling Approaches: DDM versus Σ-Y Eulerian Atomization Model". In: *Atomization and Sprays* 26.7 (2016), pp. 713–737. DOI: 10.1615/AtomizSpr.2015013285 (cited on page 460).

Di Ilio, G. et al. "Evaluation of a scale-resolving methodology for the multidimensional simulation of GDI sprays". In: *Energies* 12.14 (2019), pp. 1–13. DOI: 10.3390/en12142699 (cited on page 155).

Dou, Z. et al. "Effects of Reynolds number and Stokes number on particle-pair relative velocity in isotropic turbulence: A systematic experimental study". In: *Journal of Fluid Mechanics* 839.716 (2018), pp. 271–292. DOI: 10.1017/jfm.2017.813 (cited on page 87).

Downar-Zapolski, P. et al. "The non-equilibrium relaxation model for one-dimensional flashing liquid flow". In: *International Journal of Multiphase Flow* 22.3 (1996), pp. 473–483. DOI: 10.1016/0301-9322(95)00078-X (cited on pages 199, 200, 294).

Du, J. et al. "Study of spray collapse phenomenon at flash boiling conditions using simultaneous front and side view imaging". In: *International Journal of Heat and Mass Transfer* 147 (2020), p. 118824. DOI: 10.1016/j.ijheatmasstransfer.2019.118824 (cited on page 100).

Du, J. et al. "Study of spray structure under flash boiling conditions using 2phase-SLIPI". In: *Experiments in Fluids* 62.1 (2021), pp. 1–17. DOI: 10.1007/s00348-020-03123-1 (cited on page 123).

Duke, D. J. et al. "Time-resolved X-ray Tomography of Gasoline Direct Injection Sprays". In: *SAE International Journal of Engines* 9.1 (2015), pp. 143–153. DOI: 10.4271/2015-01-1873 (cited on page 5).

Duke, D. J. et al. "Internal and near nozzle measurements of Engine Combustion Network "Spray G" gasoline direct injectors". In: *Experimental Thermal and Fluid Science* 88 (2017), pp. 608–621. DOI: 10.1016/j.expthermflusci.2017.07.015 (cited on pages 57, 59, 79, 114, 115, 237, 241, 246, 301, 326, 350, 360, 394, 395).

Dukowicz, J. K. "A particle-fluid numerical model for liquid sprays". In: *Journal of Computational Physics* 35.2 (1980), pp. 229–253. DOI: 10.1016/0021-9991(80)90087-X (cited on page 150).

Duret, B. et al. “Improving primary atomization modeling through DNS of two-phase flows”. In: *International Journal of Multiphase Flow* 55 (2013), pp. 130–137. DOI: 10.1016/j.ijmultiphaseflow.2013.05.004 (cited on page 129).

Duronio, F. et al. “ECN Spray G injector: Numerical modelling of flash-boiling breakup and spray collapse”. In: *International Journal of Multiphase Flow* 145.September (2021). DOI: 10.1016/j.ijmultiphaseflow.2021.103817 (cited on page 156).

Duronio, F. et al. “ECN Spray G : Coupled Eulerian internal nozzle flow and Lagrangian spray simulation in flash boiling conditions”. In: (2022). DOI: 10.1177/14680874221090732 (cited on page 466).

Dymond, J. H. et al. “Transport properties of nonelectrolyte liquid mixtures-VII. Viscosity coefficients for isooctane and for equimolar mixtures of isooctane + n-octane and isooctane + n-dodecane from 25 to 100??C at pressures up to 500 MPa or to the freezing pressure”. In: *International Journal of Thermophysics* (1985). DOI: 10.1007/BF00522146 (cited on page 235).

Erjavec, J. *Automotive Technology : A systems approach.* 5th. Cenga. 2009, p. 1665 (cited on pages 31, 32).

Escobedo, J. et al. “Surface-tension prediction for liquid mixtures”. In: *AIChE Journal* 44.10 (1998), pp. 2324–2332. DOI: 10.1002/aic.690441021 (cited on page 235).

EuroVI. “Regulation (EC) No 715/2007 of the European Parliament and of the Council of 20 June 2007 on type approval of motor vehicles with respect to emissions from light passenger and commercial vehicles (Euro 5 and Euro 6) and on access to vehicle repair and mai”. In: *Official Journal of the European Union* (2007), pp. 1–15 (cited on page 2).

Faeth, G. M. “Mixing, transport and combustion in sprays”. In: *Progress in Energy and Combustion Science* 13.4 (1987), pp. 293–345. DOI: 10.1016/0360-1285(87)90002-5 (cited on page 202).

Fansler, T. D. et al. “Combustion instability in spray-guided stratified-charge engines: A review”. In: *International Journal of Engine Research* 16.3 (2015), pp. 260–305. DOI: 10.1177/1468087414565675 (cited on pages 32, 33).

Fathi, M. et al. "The influence of Exhaust Gas Recirculation (EGR) on combustion and emissions of n-heptane/natural gas fueled Homogeneous Charge Compression Ignition (HCCI) engines". In: *Applied Energy* 88.12 (2011), pp. 4719–4724. DOI: 10.1016/j.apenergy.2011.06.017 (cited on page 39).

Ferziger, J. H. et al. *Computational Methods for Fluid Dynamics*. 3rd. Berlin, 2002 (cited on pages 135, 137, 138).

Firat, M. "Investigation of multistage injection strategies in a DISI engine fueled with methane under stratified charge lean combustion conditions". In: *Environmental Progress and Sustainable Energy* 39.5 (2020), pp. 5–7. DOI: 10.1002/ep.13402 (cited on page 36).

Fischer, A. et al. "Methodology and Tools to Predict GDI Injector Tip Wetting as Predecessor of Tip Sooting". In: *SAE Technical Papers* 2018-April (2018), pp. 1–10. DOI: 10.4271/2018-01-0286 (cited on page 60).

Fontana, G. et al. "Experimental analysis of a spark-ignition engine using exhaust gas recycle at WOT operation". In: *Applied Energy* 87.7 (2010), pp. 2187–2193. DOI: 10.1016/j.apenergy.2009.11.022 (cited on page 39).

Franc, J.-P. "The Rayleigh-Plesset equation: a simple and powerful tool to understand various aspects of cavitation". In: *Fluid Dynamics of Cavitation and Cavitating Turbopumps*. Vol. 496. Vienna: Springer, 2007, pp. 1–41. DOI: 10.1007/978-3-211-76669-9_1 (cited on page 74).

Galindo, J. et al. "Assessment of the numerical and experimental methodology to predict EGR cylinder-to-cylinder dispersion and pollutant emissions". In: *International Journal of Engine Research* (2020). DOI: 10.1177/1468087420972544 (cited on page 9).

García-Oliver, J. et al. "Computational study of ECN Spray A and Spray D combustion at different ambient temperature conditions". In: *Transportation Engineering* 2.October (2020), p. 100027. DOI: 10.1016/j.treng.2020.100027 (cited on page 9).

Garcia-Oliver, J. M. "Aportaciones al estudio del proceso de combustión turbulenta de chorros en motores Diesel de inyección directa". PhD thesis. Valencia: E.T.S. Ingenieros Industriales. Universitat Politècnica de València, 2004. DOI: 10.4995/Thesis/10251/55164 (cited on page 6).

Gärtner, J. W. et al. "Numerical investigation of spray collapse in GDI with OpenFOAM". In: *Fluids* 6.3 (2021). DOI: 10.3390/fluids6030104 (cited on pages 134, 135).

Ge, H. et al. “A comparison of computational fluid dynamics predicted initial liquid penetration using rate of injection profiles generated using two different measurement techniques”. In: *International Journal of Engine Research* 20.2 (2019), pp. 226–235. DOI: 10.1177/1468087417746475 (cited on page 117).

Geurts, B. J. et al. “A framework for predicting accuracy limitations in large-eddy simulation”. In: *Physics of Fluids* 14.6 (2002). DOI: 10.1063/1.1480830 (cited on page 373).

Giannadakis, E. et al. “The influence of variable fuel properties in high-pressure diesel injectors”. In: *SAE Technical Papers* January (2009). DOI: 10.4271/2009-01-0832 (cited on page 236).

Gilles-Birth, I. et al. “A study of the in-nozzle flow characteristic of valve covered orifice nozzles for gasoline direct injection”. In: *SAE Technical Papers* 724 (2005). DOI: 10.4271/2005-01-3684 (cited on page 69).

Gimeno, J. “Desarrollo y aplicación de la medida de flujo de cantidad de movimiento de un chorro Diesel”. PhD thesis. E.T.S. Ingenieros Industriales, Universtitat Politècnica de València, 2008. DOI: 10.4995/Thesis/10251/8306 (cited on pages 6, 53, 62, 65, 66, 304, 323, 324).

Giussani, F. et al. “VOF Simulation of The Cavitating Flow in High Pressure GDI Injectors”. In: September (2017). DOI: 10.4995/ilass2017.2017.4989 (cited on pages 8, 142).

Goldberg, J. H. “Worldview of High-Risk Juvenile Delinquents”. In: *Criminal Justice and Behavior* 34.6 (2007), pp. 846–861. DOI: 10.1177/0093854807299413 (cited on page 116).

Gomaa, H. et al. “Numerical Comparison of 3D Jet Breakup Using a Compression Scheme and an Interface Reconstruction Based VOF-Code”. In: *24th ILASS-Europe Conference, Portugal*. 2011 (cited on page 143).

Gomez Santos, E. “Simulation and numerical modelling of three-phase flow in automotive high-pressure fuel injectors.” In: (2020), pp. 1–124 (cited on page 365).

Gong, C. et al. “Assessment of ultra-lean burn characteristics for a stratified-charge direct-injection spark-ignition methanol engine under different high compression ratios”. In: *Applied Energy* 261.December 2019 (2020), p. 114478. DOI: 10.1016/j.apenergy.2019.114478 (cited on page 37).

Gosman, A. D. et al. “Aspects of Computer Simulation of Liquid-Fuelled Combustors.” In: *AIAA Paper* 7.6 (1981), pp. 482–490. DOI: 10.2514/6.1981-323 (cited on page 214).

Gramlich, R. et al. “Air Entrainment and Momentum Distribution in the Near Field of Diesel Sprays from Group Hole Nozzles”. In: *ILASS Europe 2016, 27th Annual Conference on Liquid Atomization and Spray Systems* September (2016), pp. 4–7. DOI: 10.13140/RG.2.2.10584.90883 (cited on page 57).

Gravensen, P. et al. “Microfluidics - A review”. In: *Journal of Micromechanics and Microengineering* 3.4 (1993), pp. 168–182. DOI: 10.1088/0960-1317/3/4/002 (cited on page 62).

Greif, D. et al. “Numerical study of transient multi component fuel injection”. In: *SAE Technical Papers* 11.October (2013). DOI: 10.4271/2013-01-2550 (cited on page 131).

Grover, R. O. et al. “String Flash-Boiling in Flashing and Non-Flashing Gasoline Direction Injection Simulations with Transient Needle Motion University of Massachusetts Amherst General Motors Research and Development Energy Systems Division , Argonne National Laboratory , Lem”. In: *ILASS Americas 28th Annual Conference on Liquid Atomization and Spray Systems* May (2016) (cited on page 392).

Gueyffier, D. et al. “Volume-of-Fluid Interface Tracking with Smoothed Surface Stress Methods for Three-Dimensional Flows”. In: *Journal of Computational Physics* 152.2 (1999), pp. 423–456. DOI: 10.1006/jcph.1998.6168 (cited on page 136).

Guo, G. et al. “Optical Experiments Of String Cavitation In Diesel Injector Tapered Nozzles”. In: *Thermal Science* 24.1 Part A (2020), pp. 193–201. DOI: 10.2298/TSCI180405005G (cited on page 117).

Guo, H. et al. “Comparison of spray collapses at elevated ambient pressure and flash boiling conditions using multi-hole gasoline direct injector”. In: *Fuel* 199 (2017), pp. 125–134. DOI: 10.1016/j.fuel.2017.02.071 (cited on page 99).

Guo, H. et al. “Characterizing external flashing jet from single-hole GDI injector”. In: *International Journal of Heat and Mass Transfer* 121 (2018), pp. 924–932. DOI: 10.1016/j.ijheatmasstransfer.2018.01.042 (cited on pages 73, 99).

Guo, H. et al. “Numerical investigation on flashing jet behaviors of single-hole GDI injector”. In: *International Journal of Heat and Mass Transfer* 130 (2019), pp. 50–59. DOI: 10.1016/j.ijheatmasstransfer.2018.10.088 (cited on pages 134, 141, 285).

Guo, H. et al. “Numerical study on spray collapse process of ECN spray G injector under flash boiling conditions”. In: *Fuel* 290.December 2020 (2021), p. 119961. DOI: 10.1016/j.fuel.2020.119961 (cited on pages 141, 142, 281, 348).

Haider, A. et al. “Drag Coefficient and Terminal Velocity of Spherical and Nonspherical Particles”. In: *Powder Technology* 58 (1989), pp. 63–70. DOI: 10.1021/ie50688a011 (cited on page 86).

Harada, J. et al. “Development of direct injection gasoline engine”. In: *SAE Technical Papers* 412 (1997). DOI: 10.4271/970540 (cited on page 31).

Hasslberger, J. et al. “Flow topologies in primary atomization of liquid jets: A direct numerical simulation analysis”. In: *Journal of Fluid Mechanics* 859 (2019), pp. 819–838. DOI: 10.1017/jfm.2018.845 (cited on page 129).

Hay, N. et al. “Comparison of the various correlations for spray penetration”. In: *SAE Technical Papers* (1972). DOI: 10.4271/720776 (cited on page 92).

Hayashi, K. et al. “Interface tracking simulation of mass transfer from a dissolving bubble”. In: *ASME-JSME-KSME 2011 Joint Fluids Engineering Conference, AJK 2011*. Vol. 1. PARTS A, B, C, D. 2011, pp. 1593–1601. DOI: 10.1115/AJK2011-04007 (cited on page 136).

Hayashi, K. et al. “Effects of shape oscillation on mass transfer from a Taylor bubble”. In: *International Journal of Multiphase Flow* 58 (2014), pp. 236–245. DOI: 10.1016/j.ijmultiphaseflow.2013.09.009 (cited on page 136).

He, L. et al. “Numerical study on combustion and emission characteristics of a PFI gasoline engine with hydrogen direct-injection”. In: *Energy Procedia* 158 (2019), pp. 1449–1454. DOI: 10.1016/j.egypro.2019.01.348 (cited on page 29).

He, X. et al. “Characteristics of spray and wall wetting under flash-boiling and non-flashing conditions at varying ambient pressures”. In: *Fuel* 264 (2020). DOI: 10.1016/j.fuel.2019.116683 (cited on page 77).

Hentschel, W. et al. “Investigation of spray formation of di gasoline hollow-cone injectors inside a pressure chamber and a glass ring engine by multiple optical techniques”. In: *SAE Technical Papers* 724 (1999). DOI: 10.4271/1999-01-3660 (cited on page 48).

Hiroyasu, H. et al. “Structures of Fuel Sprays in Diesel Engines”. In: *SAE Technical Paper 900475*. 1990. DOI: 10.4271/900475 (cited on page 94).

Hiroyasu, H. et al. "Break-up length of a liquid jet and internal flow in a nozzle". In: *ICLASS-91, Gaithersburg, Maryland, July.* 1991 (cited on page 68).

Hobbs, J. M. et al. "The effect of orifice plate geometry upon discharge coefficient". In: *Flow Measurement and Instrumentation* 1.3 (1990), pp. 133–140. DOI: 10.1016/0955-5986(90)90002-D (cited on page 64).

Hoffmann, G. et al. "Fuel System Pressure Increase for Enhanced Performance of GDi Multi-Hole Injection Systems". In: *SAE Technical Paper 2014-01-1209* (2014). DOI: 10.4271/2014-01-1209 (cited on pages 48, 116, 124).

Huang, Y. et al. "Numerical investigation to the dual-fuel spray combustion process in an ethanol direct injection plus gasoline port injection (EDI + GPI) engine". In: *Energy Conversion and Management* 92 (2015), pp. 275–286. DOI: 10.1016/j.enconman.2014.12.064 (cited on page 344).

Hui, D. et al. "Comparation with different interface capturing schemes based on gradient smoothing method using unstructured meshes". In: () (cited on page 137).

Hung, D. L. et al. "Gasoline fuel injector spray measurement and characterization - A new SAE J2715 recommended practice". In: *SAE International Journal of Fuels and Lubricants* 1.1 (2009), pp. 534–548. DOI: 10.4271/2008-01-1068 (cited on page 243).

Husted, H. et al. "The effects of GDi fuel pressure on fuel economy". In: *SAE Technical Papers* 1 (2014). DOI: 10.4271/2014-01-1438 (cited on page 48).

Hwang, J. et al. "Spatio-temporal identification of plume dynamics by 3D computed tomography using engine combustion network spray G injector and various fuels". In: *Fuel* 280.March (2020), p. 118359. DOI: 10.1016/j.fuel.2020.118359 (cited on page 434).

Ibrahim, E. A. et al. "Modeling of spray droplets deformation and breakup". In: *Journal of Propulsion and Power* 9.4 (1993), pp. 651–654. DOI: 10.2514/3.23672 (cited on page 85).

Ishii, M. et al. *Thermo-Fluid Dynamics of Two-Phase Flow.* Vol. 51. 2. Heidelberg, Germany: Springer, 2013, pp. 535–535. DOI: 10.2514/1.j052026 (cited on pages 130, 132).

Issa, R. I. et al. "The computation of compressible and incompressible recirculating flows by a non-iterative implicit scheme". In: *Journal of Computational Physics* 62.1 (1986), pp. 66–82. DOI: 10.1016/0021-9991(86)90100-2 (cited on page 225).

Iwamoto, Y. et al. “Development of gasoline direct injection engine”. In: *SAE Technical Papers* 412 (1997). DOI: 10.4271/970541 (cited on page 31).

Jacobsohn, G. L. et al. “Comparison of turbulence modeling methods for evaluating GDI sprays with transient needle motion”. In: *SAE Technical Papers* 2019-April.April (2019), pp. 1–11. DOI: 10.4271/2019-01-0271 (cited on page 134).

Jaramillo Císcar, D. “Estudio experimental y computacional del proceso de inyección diésel mediante un código CFD con malla adaptativa”. PhD thesis. Universitat politècnica de valència, 2017. DOI: 10.4995/Thesis/10251/92183 (cited on pages 6, 434, 435, 461, 462).

Jia, H. et al. “The effect of the divergent-convergent GDI injector on inner flow and spray characteristics at high injection pressure”. In: *Energy Sources, Part A: Recovery, Utilization and Environmental Effects* 00.00 (2021), pp. 1–16. DOI: 10.1080/15567036.2021.1929574 (cited on pages 141, 158).

Jiang, C. et al. “Impact of gasoline direct injection fuel injector hole geometry on spray characteristics under flash boiling and ambient conditions”. In: *Fuel* 241.November 2018 (2019), pp. 71–82. DOI: 10.1016/j.fuel.2018.11.143 (cited on page 60).

Jiang, C. et al. “Impact of gasoline direct injection fuel injector hole geometry on spray characteristics under flash boiling and ambient conditions”. In: *Fuel* 241 (2019), pp. 71–82. DOI: 10.1016/j.fuel.2018.11.143 (cited on pages 59, 123).

Jin, J. D. et al. “A Model for Multicomponent Droplet Vaporization at High Ambient Pressures”. In: *SAE Technical Papers* (1985) (cited on page 91).

Johansen, A. M. “Monte carlo methods”. In: *International Encyclopedia of Education* (2010), pp. 296–303. DOI: 10.1016/B978-0-08-044894-7.01543-8 (cited on page 150).

Johansson, A. N. *Challenges and advantages of stratified combustion in gasoline direct-injected engines challenges and advantages of stratified combustion in gasoline direct-injected engines*. 2017 (cited on page 32).

Johansson, A. N. et al. “Reduction of Soot Formation in an Optical Single-Cylinder Gasoline Direct-Injected Engine Operated in Stratified Mode Using 350 Bar Fuel Injection Pressure, Dual-Coil and High-Frequency Ignition Systems”. In: *SAE International Journal of Engines* 10.3 (2017). DOI: 10.4271/2017-01-9278 (cited on page 48).

Johnson, T. et al. "Review of Vehicle Engine Efficiency and Emissions". In: *SAE Technical Papers* 2017-April.April (2017). DOI: 10.4271/2020-01-0352 (cited on page 30).

Kale, R. et al. "Experimental investigation on GDI spray behavior of isooctane and alcohols at elevated pressure and temperature conditions". In: *Fuel* 236.April 2018 (2019), pp. 1–12. DOI: 10.1016/j.fuel.2018.08.153 (cited on pages 99, 347).

Kalghatgi, G. "Is it really the end of internal combustion engines and petroleum in transport?" In: *Applied Energy* 225.February (2018), pp. 965–974. DOI: 10.1016/j.apenergy.2018.05.076 (cited on page 2).

Kalghatgi, G. et al. "Gasoline compression ignition approach to efficient, clean and affordable future engines". In: *Proceedings of the Institution of Mechanical Engineers, Part D: Journal of Automobile Engineering* 232.1 (2018), pp. 118–138. DOI: 10.1177/0954407017694275 (cited on page 38).

Kalwar, A. et al. *Overview, Advancements and Challenges in Gasoline Direct Injection Engine Technology*. April. 2020, pp. 111–147. DOI: 10.1007/978-981-15-0368-9_6 (cited on page 34).

Kanda, M. et al. "Application of a new combustion concept to direct injection gasoline engine". In: *SAE Technical Papers* 2000.724 (2000). DOI: 10.4271/2000-01-0531 (cited on page 49).

Kar, K. et al. "Measurement of vapor pressures and enthalpies of vaporization of gasoline and ethanol blends and their effects on mixture preparation in an SI engine". In: *SAE International Journal of Fuels and Lubricants* 1.1 (2009), pp. 132–144. DOI: 10.4271/2008-01-0317 (cited on page 344).

Kassa, M. et al. "Dual-Fuel Combustion". In: *The Future of Internal Combustion Engines*. 2018, pp. 1–17. DOI: 10.5772/intechopen.80570 (cited on page 37).

Kastengren, A. et al. "The 7BM beamline at the APS: A facility for time-resolved fluid dynamics measurements". In: *Journal of Synchrotron Radiation* 19.4 (2012), pp. 654–657. DOI: 10.1107/S0909049512016883 (cited on page 237).

Kavuri, C. et al. "Post-injection strategies for gasoline compression ignition combustion under high load conditions: Understanding the role of premixed, main, and post-injections in soot mitigation and load extension". In: *Fuel* 233.June (2018), pp. 834–850. DOI: 10.1016/j.fuel.2018.06.137 (cited on page 370).

Kawano, D. et al. “Numerical study on flash-boiling spray of multicomponent fuel”. In: *Heat Transfer - Asian Research* 35.5 (2006), pp. 369–385. DOI: 10.1002/htj.20117 (cited on page 75).

Kendall, J. et al. “American Chemical Society”. In: *Analytical Chemistry* 41.7 (1969), 92A–93A. DOI: 10.1021/ac60276a790 (cited on page 235).

Kent, J. C. et al. “Nozzle Exit Flow Characteristics for Square-edged and Rounded Inlet Geometries”. In: *Combustion Science and Technology* 30.1-6 (1983), pp. 121–132. DOI: 10.1080/00102208308923615 (cited on page 64).

Keskinen, J. P. et al. “Influence of mesh deformation on the quality of large eddy simulations”. In: *International Journal for Numerical Methods in Fluids* (2016). DOI: 10.1002/fld.4215 (cited on page 256).

Khan, A. R. et al. “The Resistance to Motion of a Solid Sphere in a Fluid”. In: *Chemical Engineering Communications* 62.1-6 (1987), pp. 135–150. DOI: 10.1080/00986448708912056 (cited on page 86).

Khan, M. M. et al. “Experimental and numerical study of flash boiling in gasoline direct injection sprays”. In: *Applied Thermal Engineering* 123 (2017), pp. 377–389. DOI: 10.1016/j.applthermaleng.2017.05.102 (cited on page 154).

Khuong-Anh, D. “The Eulerian-Lagrangian Spray Atomization (ELSA) Model of the Jet Atomization in CFD Simulations: Evaluation and Validation”. PhD thesis. 2012 (cited on page 152).

Kirkpatrick, A. T. et al. *Internal Combustion Engines: Applied Thermosciences*. John Wiley & Sons, 2015, pp. 1–635 (cited on pages 18, 28).

Kong, S. C. et al. “The development and application of a diesel ignition and combustion model for multidimensional engine simulation”. In: *SAE Technical Papers* 412 (1995). DOI: 10.4271/950278 (cited on page 462).

Krzeczkowski, S. A. “Measurement of liquid droplet disintegration mechanisms”. In: *International Journal of Multiphase Flow* 6.3 (1980), pp. 227–239. DOI: 10.1016/0301-9322(80)90013-0 (cited on pages 83, 84).

Kulkarni, V. et al. “Secondary atomization of newtonian liquids in the bag breakup regime: Comparison of model predictions to experimental data”. In: *ICLASS 2012 - 12th International Conference on Liquid Atomization and Spray Systems* (2012), pp. 1–8 (cited on page 85).

Lacey, J. et al. “Generalizing the behavior of flash-boiling, plume interaction and spray collapse for multi-hole, direct injection”. In: *Fuel* 200 (2017), pp. 345–356. DOI: 10.1016/j.fuel.2017.03.057 (cited on page 99).

Lafaurie, B. et al. *Modelling merging and fragmentation in multiphase flows with SURFER*. 1994. DOI: 10.1006/jcph.1994.1123 (cited on page 138).

Launder, B. E. et al. "The numerical computation of turbulent flows". In: *Computer methods in applied mechanics and engineering* (1974), pp. 269–289. DOI: 10.1007/JHEP10(2012)057 (cited on pages 182, 186).

Lazzaro, M. "Characterization of the liquid phase of vaporizing GDI sprays from Schlieren imaging". In: *Measurement Science and Technology* 30 (2019). DOI: 10.1088/1361-6501/AB228D (cited on page 5).

Lazzaro, M. "High-Speed Imaging of a Vaporizing GDI Spray: A Comparison between Schlieren, Shadowgraph, DBI and Scattering". In: *SAE Technical Papers* 2020-April.April (2020), pp. 1–15. DOI: 10.4271/2020-01-0326 (cited on page 5).

Lefebvre, A. H. et al. *Atomization and Sprays*. 2nd Ed. Boca Raton, FL: CRC Press, 2017 (cited on pages 80, 87).

Lehnert, B. et al. "GDI Sprays with up to 200 MPa Fuel Pressure and Comparison of Diesel-like and Gasoline-Like Injector Designs". In: *SAE Technical Papers* 2020 (2020), pp. 1–11. DOI: 10.4271/2020-01-2104 (cited on pages 47, 124).

Leick, P. et al. "Experimental characterization of tip wetting in gasoline DI injectors". In: *ICLASS 2018 - 14th International Conference on Liquid Atomization and Spray Systems* July (2018) (cited on page 119).

Lemmon, E. W. et al. "Thermophysical Properties of Fluid Systems". In: *NIST Chemistry WebBook, NIST Standard Reference Database Number 69*. Ed. by P. J. Linstrom et al. 2011 (cited on page 234).

Leung, T. F. et al. "Evaluation of an eulerian-lagrangian spray atomization (ELSA) model for nozzle flow: Modeling of coupling between dense and disperse regions". In: *47th AIAA Thermophysics Conference, 2017* June (2017), pp. 1–14. DOI: 10.2514/6.2017-4352 (cited on page 152).

Li, T. et al. "A comprehensive study on the factors affecting near-nozzle spray dynamics of multi-hole GDI injectors". In: *Fuel* 190 (2017), pp. 292–302. DOI: 10.1016/j.fuel.2016.11.009 (cited on page 99).

Li, X. et al. "Sensitivity analysis of fuel injection characteristics of GDI injector to injector nozzle diameter". In: *Energies* 12.3 (2019). DOI: 10.3390/en12030434 (cited on pages 58, 59, 67).

Lin, T. C. et al. “Effects of superheat on characteristics of flashing spray and snow particles produced by expanding liquid carbon dioxide”. In: *Journal of Aerosol Science* 61 (2013), pp. 27–35. DOI: 10.1016/j.jaerosci.2013.03.005 (cited on page 72).

Lindström, M. “Injector Nozzle Hole Parameters and their Influence on Real DI Diesel Performance”. In: (2009), pp. 1–45 (cited on page 57).

Ling, Y. et al. “A two-phase mixing layer between parallel gas and liquid streams: multiphase turbulence statistics and influence of interfacial instability”. In: *Journal of Fluid Mechanics* 859 (2019), pp. 268–307. DOI: 10.1017/jfm.2018.825 (cited on page 129).

Lippert, A. M. et al. “Mesh independence and adaptive mesh refinement for advanced engine spray simulations”. In: *SAE Technical Papers* 2005.724 (2005). DOI: 10.4271/2005-01-0207 (cited on page 202).

Liu, Y. et al. “Investigation of the liquid fuel film from GDI spray impingement on a heated surface with the laser induced fluorescence technique”. In: *Fuel* 250.February (2019), pp. 211–217. DOI: 10.1016/j.fuel.2019.03.120 (cited on page 125).

Lucchini, T. et al. “CFD Modeling of Gas Exchange, Fuel-Air Mixing and Combustion in Gasoline Direct-Injection Engines”. In: *SAE Technical Papers* 2019-Septe.September (2019). DOI: 10.4271/2019-24-0095 (cited on page 437).

Luo, F. et al. “The development of a data acquisition system for measuring the injection rate of a multihole diesel injector”. In: *Sensors and Actuators, A: Physical* 261 (2017), pp. 166–176. DOI: 10.1016/j.sna.2017.04.037 (cited on page 116).

Macian, V. et al. “New technique for determination of internal geometry of a Diesel nozzle with the use of silicone methodology”. In: *Experimental Techniques* 27.2 (2003), pp. 39–43. DOI: 10.1111/j.1747-1567.2003.tb00107.x (cited on page 59).

Malaguti, S. et al. “Numerical characterization of a new high-pressure multihole GDI injector”. In: *ILASS - Europe 2010, 23rd Annual Conference on Liquid Atomization and Spray Systems* September (2010), pp. 1–10 (cited on page 153).

Mamaikin, D. et al. “High Speed Shadowgraphy of Transparent Nozzles as an Evaluation Tool for In-Nozzle Cavitation Behavior of GDI Injectors”. In: *ILASS - Europe 2017, 28th Conference on Liquid Atomization and Spray Systems* September (2017). DOI: 10.4995/ilass2017.2017.4639 (cited on page 5).

Mamaikin, D. et al. "Experimental investigation of flow field and string cavitation inside a transparent real-size GDI nozzle". In: *Experiments in Fluids* 61.7 (2020), pp. 1–15. DOI: 10.1007/s00348-020-02982-y (cited on pages 5, 67, 118).

Mamaikin, D. et al. "The effect of transient needle lift on the internal flow and near-nozzle spray characteristics for modern GDI systems investigated by high-speed X-ray imaging". In: *International Journal of Engine Research* (2021). DOI: 10.1177/1468087420986751 (cited on pages 68, 79).

Manin, J. et al. "Transient cavitation in transparent diesel injectors". In: *ICLASS 2018 - 14th International Conference on Liquid Atomization and Spray Systems* (2020), pp. 1–9 (cited on page 117).

Manin, J. et al. "Experimental Characterization of DI Gasoline Injection Processes". In: *SAE Technical Paper 2015-01-1894* (2015). DOI: 10.4271/2015-01-1894 (cited on pages 98, 114, 115, 308, 339, 378, 384, 390, 391).

Marchitto, L. "Characterization of air/fuel mixture and combustion processes in a DISI engine through advanced optical and X-ray based diagnostics". PhD thesis. 2015 (cited on page 36).

Martí-Aldaraví, P. "Development of a computational model for a simultaneous simulation of internal flow and spray break-up of the Diesel injection process". PhD thesis. Valencia: Universitat Politècnica de València, 2014. DOI: 10.4995/Thesis/10251/43719 (cited on pages 7, 9, 50, 61, 130).

Marti-Aldaravi, P. et al. "Numerical Simulation of a Direct-Acting Piezoelectric Prototype Injector Nozzle Flow for Partial Needle Lifts". In: *SAE Technical Papers* 2017-24-01 (2017). DOI: 10.4271/2017-24-0101 (cited on pages 394, 397–399).

Martínez-López, J. "Estudio computacional de la influencia del levantamiento de aguja sobre el flujo interno y el fenómeno de la cavitación en toberas de inyección Diesel". PhD thesis. Valencia: Universitat Politecnica de Valencia, 2013. DOI: 10.4995/Thesis/10251/29291 (cited on page 7).

Martínez, M. et al. "Computational study of the Premixed Charge Compression Ignition combustion in a Rapid Compression Expansion Machine : Impact of multiple injection strategy on mixing , ignition and combustion processes". In: *Fuel* 318.January (2022), p. 123388. DOI: 10.1016/j.fuel.2022.123388 (cited on pages 449, 450, 484).

Matsoukas, T. *Fundamentals of Chemical Engineering Thermodynamics*. Prentice Hall, 2012 (cited on page 200).

Medina, M. et al. “Mechanisms of fuel injector tip wetting and tip drying based on experimental measurements of engine-out particulate emissions from gasoline direct-injection engines”. In: *International Journal of Engine Research* 22.6 (2021), pp. 2035–2053. DOI: 10.1177/1468087420916052 (cited on page 196).

Medina, M. et al. “The effects of injector geometry and operating conditions on spray mass, momentum and development using high-pressure gasoline”. In: *Fuel* 294.June (2021). DOI: 10.1016/j.fuel.2021.120468 (cited on page 115).

Medina, M. et al. “High-Speed Imaging Study on the Effects of Internal Geometry on High-Pressure Gasoline Sprays”. In: *SAE Technical Papers* 2020 (2020), pp. 1–14. DOI: 10.4271/2020-01-2111 (cited on pages 123, 351).

Medina, M. et al. “Mechanisms of fuel injector tip wetting and tip drying based on experimental measurements of engine-out particulate emissions from gasoline direct-injection engines”. In: *International Journal of Engine Research* (2020). DOI: 10.1177/1468087420916052 (cited on page 119).

Menon, S. et al. “Effect of subgrid models on the computed interscale energy transfer in isotropic turbulence”. In: *Computers and Fluids* 25.2 (1996), pp. 165–180. DOI: 10.1016/0045-7930(95)00036-4 (cited on page 194).

Meyers, J. et al. “Database analysis of errors in large-eddy simulation”. In: *Physics of Fluids* 15.9 (2003), pp. 2740–2755. DOI: 10.1063/1.1597683 (cited on page 373).

Miesse, C. C. “Correlation of Experimental Data on the Disintegration of Liquid Jets”. In: *Industrial & Engineering Chemistry* 47.9 (1955), pp. 1690–1701. DOI: 10.1021/ie50549a013 (cited on page 83).

Mishra, R. et al. “Three-component multi-fluid modeling of pseudo-cavitation phenomenon in diesel injector nozzles”. In: *International Journal of Engine Research* (2021). DOI: 10.1177/1468087421993348 (cited on page 131).

Mohan, B. et al. “Coupled in-nozzle flow and spray simulation of Engine Combustion Network Spray-G injector”. In: *International Journal of Engine Research* 22.9 (2021), pp. 2982–2996. DOI: 10.1177/1468087420960612 (cited on pages 9, 158).

Mohapatra, C. et al. “Modeling sealing in transient injector simulations”. In: *American Society of Mechanical Engineers, Fluids Engineering Division (Publication) FEDSM* 1A-2017 (2017), pp. 1–10. DOI: 10.1115/FEDSM2017-69309 (cited on pages 133, 327, 359).

Mojtabi, M. et al. "The effect of flash boiling on break up and atomization in GDI sprays". In: *22nd European Conference on Liquid Atomization and Spray Systems* (2008), pp. 8–10 (cited on page 75).

Montanaro, A. et al. "Wall impingement process of a multi-hole GDI spray: Experimental and numerical investigation". In: *SAE Technical Papers* (2012). DOI: 10.4271/2012-01-1266 (cited on pages 91, 125, 126).

Montanaro, A. et al. "Flash Boiling Evidences of a Multi-Hole GDI Spray under Engine Conditions by Mie-Scattering Measurements". In: *SAE Technical Papers* 2015-Septe.September (2015). DOI: 10.4271/2015-01-1945 (cited on page 5).

Montanaro, A. et al. "Experimental analysis of a GDI spray impacting on a heated wall". In: *DIPSI Workshop 2018 on Droplet Impact Phenomena & Spray Investigation* May (2018), pp. 29–32 (cited on page 125).

Moon, S. et al. "High-speed X-ray imaging of in-nozzle cavitation and emerging jet flow of multi-hole GDI injector under practical operating conditions". In: *ICLASS 2015 - 13th International Conference on Liquid Atomization and Spray Systems* December (2015) (cited on pages 67, 69).

Moon, S. et al. "Ultrafast X-ray study of multi-hole GDI injector sprays: Effects of nozzle hole length and number on initial spray formation". In: *Experimental Thermal and Fluid Science* 68 (2015), pp. 68–81. DOI: 10.1016/j.expthermflusci.2015.03.027 (cited on pages 59, 79, 324).

Morfeldt, J. et al. "Carbon footprint impacts of banning cars with internal combustion engines". In: *Transportation Research Part D: Transport and Environment* 95.May (2021), p. 102807. DOI: 10.1016/j.trd.2021.102807 (cited on page 2).

Motjabi, M. "Optical Analysis of Multi-Stream GDI Sprays under Various Engine Operating Conditions". In: (2011), pp. 1–331 (cited on page 49).

Moulai, M. et al. "Internal and Near-Nozzle Flow in a Multi-Hole Gasoline Injector Under Flashing and Non-Flashing Conditions". In: *SAE Technical Paper 2015-01-0944* 2015-01-0944 (2015). DOI: 10.4271/2015-01-0944.Copyright (cited on pages 133, 300, 328).

Mouvanal, S. et al. "Numerical study of purging of a gasoline direct injection nozzle at the end of injection". In: *International Journal of Engine Research* 22.5 (2021), pp. 1670–1684. DOI: 10.1177/1468087420916658 (cited on pages 57, 142).

Mugele, R. A.; Evans, H. D. "Droplet Size Distribution in Spray". In: *Industrial & Engineering Chemistry,* 43.6 (1951), pp. 1317–1324. DOI: 10.1252/kakoronbunshu1953.33.357 (cited on page 96).

Muzaferija, S. et al. “Computation of free-surface ows using interface- tracking and interface-capturing methods Flows of two (or more) immiscible uids are often encountered in”. In: November (1999) (cited on pages 137, 198).

Naber, J. D. et al. “Effects of gas density and vaporization on penetration and dispersion of diesel sprays”. In: *SAE Technical Papers* 412 (1996). DOI: 10.4271/960034 (cited on page 116).

Naber, J. D. et al. “Effects of Gas Density and Vaporization on Penetration and Dispersion of Diesel Sprays”. In: *SAE Paper 960034*. Vol. 105. 412. Society of Automotive Engineers, Inc., Warrendale, Pennsylvania, USA, 1996, pp. 82–111. DOI: 10.4271/960034 (cited on pages 66, 92, 116, 273).

Navarro-martinez, S. et al. “An investigation on the impact of small-scale models in gasoline direct injection sprays (ECN Spray G)”. In: *International Journal of Engine Research* (2019), pp. 1–9. DOI: 10.1177/1468087419889449 (cited on pages 9, 159).

Nishad, K. et al. “LES based modeling and simulation of spray dynamics including gasoline direct injection (GDI) processes using KIVA-4 code”. In: *SAE Technical Papers* April (2012). DOI: 10.4271/2012-01-1257 (cited on page 153).

Nocivelli, L. et al. “Analysis of the Spray Numerical Injection Modeling for Gasoline Applications”. In: *SAE Technical Papers* 2020-April.April (2020), pp. 1–13. DOI: 10.4271/2020-01-0330 (cited on pages 8, 9, 158, 427, 428, 432, 434, 437, 455).

Noh, W. et al. *SLIC (simple line interface calculation)*. Tech. rep. Livermore, CA: Lawrence Livermore National Laboratory (LLNL), 1976. DOI: 10.2172/7261651 (cited on page 137).

Nurick, W. H. “Orifice cavitation and its effects on spray mixing”. In: *Journal of Fluids Engineering* 98 (1976), pp. 681–687 (cited on page 70).

O’Connor, J. et al. “Post injections for soot reduction in diesel engines: A review of current understanding”. In: *SAE International Journal of Engines* 6.1 (2013), pp. 400–421. DOI: 10.4271/2013-01-0917 (cited on page 369).

O’Rourke, P. J. “Collective Drop Effects on Vaporizing Liquid Sprays”. PhD thesis. Princeton University, 1981 (cited on pages 86, 215).

O’Rourke, P. J. et al. “The Tab Method for Numerical Calculation of Spray Droplet Breakup”. In: *1987 SAE International Fall Fuels and Lubricants Meeting and Exhibition*. 1987. DOI: 10.4271/872089 (cited on pages 202, 203).

O'Rourke, P. J. et al. "The Tab Method for Numerical Calculation of Spray Droplet Breakup International Fuels and Lubricants Meeting and Exposition Toronto, Ontario". In: *SAE Technical Paper Series* 872089 (2018), pp. 2–10 (cited on pages 85, 86).

Osher, S. et al. "Fronts propagating with curvature-dependent speed: Algorithms based on Hamilton-Jacobi formulations". In: *Journal of Computational Physics* 79.1 (1988), pp. 12–49. DOI: 10.1016/0021-9991(88)90002-2 (cited on page 147).

Oza, R. D. "On the Mechanism of Flashing Injection of Initially Subcooled Fuels". In: *ASME* 1.March 1984 (2016) (cited on pages 70, 72).

Pandal, A. et al. "A consistent, scalable model for Eulerian spray modeling". In: *International Journal of Multiphase Flow* 83.April (2016), pp. 162–171. DOI: 10.1016/j.ijmultiphaseflow.2016.04.003 (cited on page 159).

Paredi, D. et al. "Validation of a comprehensive computational fluid dynamics methodology to predict the direct injection process of gasoline sprays using Spray G experimental data". In: *International Journal of Engine Research* 21.1 (2019), p. 146808741986802. DOI: 10.1177/1468087419868020 (cited on pages 428, 437, 461).

Park, J. et al. "Study on the Spray Dynamics and Sectional Spray Distribution using Spray Pattern Measurement of Multi-Hole GDI Injector". In: September (2019), pp. 2–4 (cited on page 120).

Parrish, S. E. "Evaluation of Liquid and Vapor Penetration of Sprays from a Multi-Hole Gasoline Fuel Injector Operating Under Engine-Like Conditions". In: *SAE Technical Paper 2014-04-01* 7.2 (2014), pp. 1017–1033. DOI: 10.4271/2014-01-1409 (cited on page 120).

Patankar, S. V. et al. "A calculation procedure for heat, mass and momentum transfer in three-dimensional parabolic flows". In: *International Journal of Heat and Mass Transfer* 15.10 (1972), pp. 1787–1806. DOI: 10.1016/0017-9310(72)90054-3 (cited on page 224).

Payri, F. et al. *Motores de combustion interna alternativos*. Editorial Universitat Politecnica de Valencia, 2011 (cited on pages 18, 21, 25).

Payri, R. et al. "Analysis of diesel spray atomization by means of a near-nozzle field visualization technique". In: *Atomization and Sprays* 21.9 (2011), pp. 753–774. DOI: 10.1615/AtomizSpr.2012004051 (cited on page 80).

Payri, R. et al. "Modeling gaseous non-reactive flow in a lean direct injection gas turbine combustor through an advanced mesh control strategy". In: *Proceedings of the Institution of Mechanical Engineers, Part G: Journal of Aerospace Engineering* 234.11 (2020), pp. 1788–1810. DOI: 10.1177/0954410020919619 (cited on page 9).

Payri, R. et al. "Using one-dimensional modelling codes to analyse the influence of diesel nozzle geometry on injection rate characteristics". In: *International Journal of Vehicle Design* 38.1 (2005), pp. 58–78. DOI: 10.1504/IJVD.2005.006605 (cited on page 116).

Payri, R. et al. "Using spray momentum flux measurements to understand the influence of diesel nozzle geometry on spray characteristics". In: *Fuel* 84.5 (2005), pp. 551–561. DOI: 10.1016/j.fuel.2004.10.009 (cited on page 70).

Payri, R. et al. "Experimental and computational study of the influence of partial needle lift on nozzle flowin diesel fuel injectors". In: *Atomization and Sprays* 22.8 (2012), pp. 687–714. DOI: 10.1615/AtomizSpr.2012005810 (cited on page 304).

Payri, R. et al. "Using one-dimensional modeling to analyze the influence of the use of biodiesels on the dynamic behavior of solenoid-operated injectors in common rail systems: Detailed injection system model". In: *Energy Conversion and Management* 54.1 (2012), pp. 90–99. DOI: 10.1016/j.enconman.2011.10.007 (cited on page 398).

Payri, R. et al. "Momentum Flux Measurements on an ECN GDi Injector". In: *SAE Technical Paper 2015-01-1893*. 2015. DOI: 10.4271/2015-01-1893 (cited on pages 5, 115, 117, 268, 301, 304, 328, 376, 382, 384, 402).

Payri, R. et al. "Internal flow characterization on an ECN GDi injector". In: *Atomization and Sprays* 26.9 (2016), pp. 889–919. DOI: 10.1615/AtomizSpr.2015013930 (cited on pages 5, 116, 139, 140, 285, 301, 382, 385, 402).

Payri, R. et al. "Study of liquid and vapor phase behavior on Diesel sprays for heavy duty engine nozzles". In: *Applied Thermal Engineering* 107 (2016), pp. 365–378. DOI: 10.1016/j.applthermaleng.2016.06.159 (cited on page 272).

Payri, R. et al. "ECN Spray G external spray visualization and spray collapse description through penetration and morphology analysis". In: *Applied Thermal Engineering* 112 (2017), pp. 304–316. DOI: 10.1016/j.applthermaleng.2016.10.023 (cited on pages 5, 79, 97, 122, 329, 389).

Payri, R. et al. "The effect of nozzle geometry over ignition delay and flame lift-off of reacting direct-injection sprays for three different fuels". In: *Fuel* 199 (2017), pp. 76–90. DOI: 10.1016/j.fuel.2017.02.075 (cited on page 23).

Payri, R. et al. "The effect of nozzle geometry over the evaporative spray formation for three different fuels". In: *Fuel* 188 (2017), pp. 645–660. DOI: 10.1016/j.fuel.2016.06.041 (cited on page 9).

Payri, R. et al. "Virtual injection modelling for ECN Spray G". In: *ICLASS 2018*. Chicago, 2018, pp. 1–8 (cited on page 56).

Payri, R. et al. "Nozzle Flow Simulation of GDi for Measuring Near-Field Spray Angle and Plume Direction". In: *SAE Technical Paper 2019-01-0280* (2019), pp. 1–11. DOI: 10.4271/2019-01-0280.Abstract (cited on pages 236, 282, 301, 378, 390, 391).

Payri, R. et al. "Spray Characterization of the Urea-Water Solution (UWS) Injected in a Hot Air Stream Analogous to SCR System Operating Conditions". In: *WCX SAE World Congress Experience*. 2019-01-0738. 2019, pp. 1–9. DOI: 10.4271/2019-01-0738 (cited on page 116).

Payri, R. et al. "Study of evaporative diesel spray interaction in multiple injections using optical diagnostics". In: *Applied Thermal Engineering* 176.May (2020), p. 115402. DOI: 10.1016/j.applthermaleng.2020.115402 (cited on page 449).

Payri, R. et al. "Numerical Analysis of GDI Flash Boiling Sprays Using Different Fuels". In: *Energies* 14.18 (2021), p. 5925. DOI: 10.3390/en14185925 (cited on pages 271, 348, 428, 434, 437, 462).

Payri, R. et al. "Numerical Analysis of GDI Flash Boiling Sprays Using Different Fuels". In: *Energies* (2021), pp. 1–23 (cited on page 156).

Peer, J. et al. "Development of a High Turbulence, Low Particle Number, High Injection Pressure Gasoline Direct Injection Combustion System". In: *SAE International Journal of Engines* 9.4 (2016), pp. 2301–2311. DOI: 10.4271/2016-01-9046 (cited on page 48).

Pei, Y. Q. et al. "Experimental study on the particulate matter emission characteristics for a direct-injection gasoline engine". In: *Proceedings of the Institution of Mechanical Engineers, Part D: Journal of Automobile Engineering* 228.6 (2014), pp. 604–616. DOI: 10.1177/0954407013493899 (cited on page 366).

Peraza, J. E. "Experimental study of the diesel spray behavior during the jet-wall interaction at high pressure and high temperature conditions". PhD thesis. Universtitat Politècnica de València, 2020. DOI: 10.4995/Thesis/10251/149389 (cited on page 6).

Pham, P. et al. "Development of fuel metering techniques for spark ignition engines". In: *Fuel* 206 (2017), pp. 701–715. DOI: 10.1016/j.fuel.2017.06.043 (cited on pages 28, 32–34, 38).

Pickett, L. M. et al. "Transient rate of injection effects on spray development". In: *SAE Technical Papers* 6 (2013), pp. 15–16. DOI: 10.4271/2013-24-0001 (cited on page 360).

Pickett, L. et al. "Engine combustion network special issue". In: *International Journal of Engine Research* 21.1 (2020), pp. 11–14. DOI: 10.1177/1468087419882247 (cited on page 5).

Pilch, M. et al. "Use of breakup time data and velocity history data to predict the maximum size of stable fragments for acceleration-induced breakup of a liquid drop". In: *International Journal of Multiphase Flow* 13.6 (1987), pp. 741–757. DOI: https://doi.org/10.1016/0301-9322(87)90063-2 (cited on pages 83, 84).

Piock, W. F. et al. "Fuel Pressure and Charge Motion Effects on GDi Engine Particulate Emissions". In: *SAE International Journal of Engines* 8.2 (2015), pp. 464–473. DOI: 10.4271/2015-01-0746 (cited on page 48).

Piock, W. et al. "Delphi Technologies Next Generation GDi-System - improved Emissions and Efficiency with higher Pressure". In: *Internationales Wiener Motorensymposium*. 2019, pp. 1–21 (cited on pages 7, 48).

Plesset, M. et al. "Bubble Dynamics and Cavitation". In: (1974), p. 1974 (cited on pages 73, 76).

Police, G. et al. "Downsizing of SI engines by turbo-charging". In: *Proceedings of 8th Biennial ASME Conference on Engineering Systems Design and Analysis, ESDA2006* 2006.January (2006). DOI: 10.1115/esda2006-95215 (cited on page 39).

Pomraning, E. "Development of Large Eddy Simulation Turbulence Models". PhD thesis. University of Wisconsin, 2000 (cited on page 194).

Pope, S. *Turbulent Flows*. sixth. Cambridge University Press, 2009 (cited on page 373).

Pope, S. B. "An explanation of the turbulent round-jet/plane-jet anomaly". In: *AIAA Journal* 16.3 (2008), pp. 279–281. DOI: 10.2514/3.7521 (cited on pages 182, 184, 193, 461).

Postrioti, L. et al. "Experimental and Numerical Analysis of Spray Evolution, Hydraulics and Atomization for a 60 MPa Injection Pressure GDI System". In: *SAE Technical Papers* 2018-April (2018), pp. 1–17. DOI: 10.4271/2018-01-0271 (cited on page 48).

Postrioti, L. et al. "Experimental and Numerical Analysis of Spray Evolution, Hydraulics and Atomization for a 60 MPa Injection Pressure GDI System". In: *SAE Technical Papers* 2018-April (2018), pp. 1–17. DOI: 10.4271/2018-01-0271 (cited on page 155).

Povilaitis, M. et al. "Simulation of hydrogen-air-diluents mixture combustion in an acceleration tube with flamefoam solver". In: *Energies* 14.17 (2021). DOI: 10.3390/en14175504 (cited on page 190).

Pratama, R. H. et al. "Hydraulic flip in a gasoline direct injection injector and its effect on injected spray". In: *Fuel* 310.PB (2022), p. 122303. DOI: 10.1016/j.fuel.2021.122303 (cited on pages 353, 366, 404).

Price, P. et al. "Particulate Matter and hydrocarbon emissions measurements: Comparing first and second generation DISI with PFI in single cylinder optical engines". In: *SAE Technical Papers* 724 (2006). DOI: 10.4271/2006-01-1263 (cited on page 36).

Prieto, L. M. P. "CFD Modeling of Combustion and Soot Production in". PhD thesis. 2020. DOI: 10.4995/Thesis/10251/142189 (cited on pages 7, 461).

Prosperi, B. et al. "PIV Measurement of Injection Pressure Influence on Gas Entrainment in GDI Engines". In: *ILASS - Europe 2007, 21st Conference on Liquid Atomization and Spray Systems* Table 1 (2007), pp. 1–6 (cited on pages 5, 97).

Quan, S. et al. "A one-way coupled volume of fluid and eulerian-lagrangian method for simulating sprays". In: (2017), pp. 1–9. DOI: 10.1115/ICEF2016-9390 (cited on page 157).

Rahm, M. et al. "Evaluation of optical arrangements for ballistic imaging in sprays". In: *Optics Express* 23.17 (2015), p. 22444. DOI: 10.1364/oe.23.022444 (cited on page 79).

Ranz, W. E. "Some experiments on orifice sprays". In: *Can. J. Chem. Engng, August* (1958), p. 175 (cited on page 83).

Reif, K. *Gasoline Engine Management*. 2014, p. 354. DOI: 10.1007/978-3-658-03964-6 (cited on pages 24, 27).

Reitz, R. "Atomization and other breakup regimes of a liquid jet". In: 1978 (cited on pages 80, 82, 83).

Reitz, R. D. "Mechanisms of Atomization Processes in High-Pressure Vaporizing Sprays". In: *Atomization and Spray Technology* 3 (1987), pp. 309–337 (cited on page 211).

Reitz, R. D. et al. "Mechanism of atomization of a liquid jet". In: *Physics of Fluids* 25.10 (1982), pp. 1730–1742. DOI: 10.1063/1.863650 (cited on pages 80, 82).

Reitz, R. D. et al. "Mechanisms of breakup of round liquid jets". In: *Encyclopedia of Fluid Mechanics* August (1986), pp. 233–249 (cited on page 207).

Reitz, R. D. "Atomisation and other breakup regimes of a liquid jet". PhD thesis. Ph.D. Thesis, Princeton University, 1978 (cited on page 207).

Reitz, R. D. et al. "Structure of high-pressure fuel sprays". In: *SAE Paper 870598* (1987) (cited on page 88).

Reitz, R. D. et al. "IJER editorial: The future of the internal combustion engine". In: *International Journal of Engine Research* 21.1 (2020), pp. 3–10. DOI: 10.1177/1468087419877990 (cited on pages 1, 2).

Rhie, C. M. et al. "Numerical study of the turbulent flow past an airfoil with trailing edge separation". In: *AIAA Journal* 21.11 (1983), pp. 1525–1532. DOI: 10.2514/3.8284 (cited on page 226).

Richards, K. J. et al. "Convergent Science v2.4 Documentation". In: *Convergent Science Inc.* (2018), p. 1207 (cited on pages 222, 236, 254).

Sagaut, P. *Large eddy simulation for incompressible flows: an introduction.* Springer Science & Business Media, 2006 (cited on page 192).

Saha, K. et al. "Investigation of homogeneous relaxation model parameters and their implications for gasoline injectors". In: *Atomization and Sprays* 27.4 (2017), pp. 345–365. DOI: 10.1615/AtomizSpr.2017016338 (cited on page 8).

Saha, K. et al. "Modeling of internal and near-nozzle flow for a gdi fuel injector". In: *ASME 2015 Internal Combustion Engine Division Fall Technical Conference, ICEF 2015* 2 (2015), pp. 1–13. DOI: 10.1115/ICEF2015-1112 (cited on pages 138, 139).

Saha, K. et al. "Numerical simulation of internal and near-nozzle flow of a gasoline direct injection fuel injector". In: *Journal of Physics: Conference Series* 656.1 (2015), pp. 1–6. DOI: 10.1088/1742-6596/656/1/012100 (cited on page 138).

Saha, K. et al. "Modeling of Internal and Near-Nozzle Flow for a Gasoline Direct Injection Fuel Injector". In: *Journal of Energy Resources Technology* 138.5 (2016), p. 052208. DOI: 10.1115/1.4032979 (cited on pages 285, 293, 306).

Saha, K. et al. "Numerical Investigation of Two-Phase Flow Evolution of In- and Near-Nozzle Regions of a Gasoline Direct Injection Engine During Needle Transients". In: *SAE International Journal of Engines* 9.2 (2016), pp. 1230–1240. DOI: 10.4271/2016-01-0870 (cited on pages 57, 139).

Saha, K. et al. "Numerical Investigation of Two-Phase Flow Evolution of In- and Near-Nozzle Regions of a Gasoline Direct Injection Engine During Needle Transients". In: *SAE International Journal of Engines* 9.2 (2016), pp. 1230–1240. DOI: 10.4271/2016-01-0870 (cited on pages 293, 299, 324, 330, 336, 377, 430).

Saha, K. et al. "Coupled Eulerian Internal Nozzle Flow and Lagrangian Spray Simulations for GDI Systems". In: *SAE technical paper 2017-01-0834*. 2017. DOI: 10.4271/2017-01-0834 (cited on pages 140, 308).

Saha, K. et al. "Coupled Eulerian Internal Nozzle Flow and Lagrangian Spray Simulations for GDI Systems". In: *SAE Technical Papers* 2017-March.March (2017). DOI: 10.4271/2017-01-0834 (cited on pages 157, 266).

Saha, K. et al. "Investigation of Homogeneous Relaxation Model Parameters and Their Implications for Gasoline Injectors". In: *Atomization and Sprays* 27.4 (2017), pp. 345–365. DOI: 10.1615/AtomizSpr.2017016338 (cited on pages 292, 293, 296, 354).

Saha, K. et al. "Modeling of Flash Boiling Phenomenon in Internal and Near-Nozzle Flow of Fuel Injectors". In: *Energy, Environment, and Sustainability* (2018), pp. 167–181. DOI: 10.1007/978-981-10-7449-3_7 (cited on page 141).

Saha, K. et al. "Modeling the Dynamic Coupling of Internal Nozzle Flow and Spray Formation for Gasoline Direct Injection Applications". In: *SAE Technical Paper* (2018), pp. 1–13. DOI: 10.4271/2018-01-0314.Abstract (cited on pages 159, 270).

Saliba, G. et al. "Comparison of Gasoline Direct-Injection (GDI) and Port Fuel Injection (PFI) Vehicle Emissions: Emission Certification Standards, Cold-Start, Secondary Organic Aerosol Formation Potential, and Potential Climate Impacts". In: *Environmental Science & Technology* (2017), acs.est.6b06509. DOI: 10.1021/acs.est.6b06509 (cited on page 3).

Salvador, F. J. et al. "Study of the influence of the needle lift on the internal flow and cavitation phenomenon in diesel injector nozzles by CFD using RANS methods". In: *Energy Conversion and Management* 66 (2013), pp. 246–256. DOI: 10.1016/j.enconman.2012.10.011 (cited on page 61).

Salvador, F. J. et al. "Numerical analysis of flow characteristics in diesel injector nozzles with convergent-divergent orifices". In: *Proceedings of the Institution of Mechanical Engineers, Part D: Journal of Automobile Engineering* 231.14 (2017), pp. 1935–1944. DOI: 10.1177/0954407017692220 (cited on page 142).

Salvador, F. J. "Estudio teórico experimental de la influencia de la geometría de toberas de inyección Diésel sobre las características del flujo interno y del chorro". PhD thesis. Valencia: E.T.S. Ingenieros Industriales. Universidad Politécnica de Valencia, 2003 (cited on pages 6, 64, 68, 70).

Salvador, F. J. et al. "Using one-dimensional modeling to analyze the influence of the use of biodiesels on the dynamic behavior of solenoid-operated injectors in common rail systems: Results of the simulations and discussion". In: *Energy Conversion and Management* 54.1 (2012), pp. 122–132. DOI: 10.1016/j.enconman.2011.10.007 (cited on page 343).

Salvador, F. J. et al. "Complete modelling of a piezo actuator last-generation injector for diesel injection systems". In: *International Journal of Engine Research* 15.1 (2014), pp. 3–19. DOI: 10.1177/1468087412455373 (cited on pages 54, 56).

Salvador, F. J. et al. "Computational assessment of temperature variations through calibrated orifices subjected to high pressure drops: Application to diesel injection nozzles". In: *Energy Conversion and Management* 171 (2018), pp. 438–451. DOI: 10.1016/j.enconman.2018.05.102 (cited on page 22).

Sames, P. C. et al. "Application of a two-fluid finite volume method to ship slamming". In: *Journal of Offshore Mechanics and Arctic Engineering* 121.1 (1999), pp. 47–52. DOI: 10.1115/1.2829554 (cited on page 138).

Santos, F. dos et al. "Spray atomization models in engine applications, from correlations to direct numerical simulations". In: *Oil and Gas Science and Technology* 66.5 (2011), pp. 801–822. DOI: 10.2516/ogst/2011116 (cited on page 92).

Sauer, J. et al. "Unsteady cavitating flow - A new cavitation model based on a modified front capturing method and bubble dynamics". In: *American Society of Mechanical Engineers, Fluids Engineering Division (Publication) FED* 251.August (2000), pp. 1073–1079 (cited on page 142).

Schiller, L. et al. "A drag coefficient correlation". In: 77 (1935), pp. 51–86 (cited on page 202).

Schlichting, H. *Boundary-Layer Theory*. McGraw-Hill, 1978 (cited on page 62).

Schmidt, D. P. et al. "A New Droplet Collision Algorithm". In: *Journal of Computational Physics* 164.1 (2000), pp. 62–80. DOI: 10.1006/jcph.2000.6568 (cited on pages 215, 216).

Schmidt, D. P. et al. "A New Droplet Collision Algorithm". In: *Journal of Computational Physics* 164.1 (2000), pp. 62–80. DOI: 10.1006/jcph.2000.6568 (cited on page 215).

Schmidt, D. P. et al. "The Eulerian Lagrangian Mixing-Oriented (ELMO) Model". In: (2021). DOI: 10.48550/arXiv.2107.03508 (cited on page 160).

Schmitz, K. S. *Thermodynamics of the Liquid State*. 2017, pp. 203–260. DOI: 10.1016/b978-0-12-800514-9.00005-5 (cited on page 235).

Schulz, F. et al. "The influence of flash-boiling on spray-targeting and fuel film formation". In: *Fuel* 208 (2017), pp. 587–594. DOI: 10.1016/j.fuel.2017.07.047 (cited on page 97).

Schulz, F. et al. "Gasoline Wall Films and Spray/Wall Interaction Analyzed by Infrared Thermography". In: *SAE International Journal of Engines* 7.3 (2014). DOI: 10.4271/2014-01-1446 (cited on page 119).

Sciortino, D. D. et al. "A systematic approach to calibrate spray and break-up models for the simulation of high-pressure fuel injections". In: *International Journal of Engine Research* (2021), p. 146808742110507. DOI: 10.1177/14680874211050787 (cited on page 156).

Scriven, L. E. "Dynamics of a fluid interface Equation of motion for Newtonian surface fluids". In: *Chemical Engineering Science* 12.2 (1960), pp. 98–108. DOI: 10.1016/0009-2509(60)87003-0 (cited on page 74).

Senda, J. et al. "Improvement of combustion and emissions in diesel engines by means of enhanced mixture formation based on flash boiling of mixed fuel". In: *International Journal of Engine Research* 9.1 (2008), pp. 15–27. DOI: 10.1243/14680874JER02007 (cited on page 76).

Senecal, P. K. et al. "A new parallel cut-cell cartesian CFD code for rapid grid generation applied to in-cylinder diesel engine simulations". In: *SAE Technical Papers* 2007.724 (2007), pp. 776–790. DOI: 10.4271/2007-01-0159 (cited on pages 212, 253).

Senecal, P. K. et al. “Large eddy simulation of vaporizing sprays considering multiinjection averaging and grid-convergent mesh resolution”. In: *ASME 2013 Internal Combustion Engine Division Fall Technical Conference, ICEF 2013*. Vol. 2. 2013, pp. 1–16. DOI: 10.1115/ICEF2013-19082 (cited on page 438).

Seo, J. et al. “Numerical investigation of the combustion characteristics and wall impingement with dependence on split-injection strategies from a gasoline direct-injection spark ignition engine”. In: *Proceedings of the Institution of Mechanical Engineers, Part D: Journal of Automobile Engineering* 227.11 (2013), pp. 1518–1535. DOI: 10.1177/0954407013491216 (cited on page 367).

Serras-Pereira, J. et al. “An experimental database on the effects of single- and split injection strategies on spray formation and spark discharge in an optical direct-injection spark-ignition engine fuelled with gasoline, iso -octane and alcohols”. In: *International Journal of Engine Research* 16.7 (2015), pp. 851–896. DOI: 10.1177/1468087414554936 (cited on page 127).

Shahangian, N. et al. “Nozzle Flow and Spray Development One-Way Coupling Methodology for a Multi-Hole GDi Injector”. In: *SAE Technical Paper Series* (2019). DOI: 10.4271/2019-24-0031.Abstract (cited on page 392).

Shahangian, N. et al. “Spray Orientation Assessment and Correction Method for GDI Momentum Flux Measurements”. In: October (2019), pp. 231–241 (cited on pages 115, 321).

Shahangian, N. et al. “Transient nozzle flow simulations of gasoline direct fuel injectors”. In: *Applied Thermal Engineering* (2020), p. 115356. DOI: 10.1016/j.applthermaleng.2020.115356 (cited on page 383).

Shaheed, R. et al. “A comparison of standard kâepsilon and realizable kâepsilon turbulence models in curved and confluent channels”. In: *Environmental Fluid Mechanics* 19.2 (2019), pp. 543–568. DOI: 10.1007/s10652-018-9637-1 (cited on page 186).

Shao, C. et al. “Detailed numerical simulation of swirling primary atomization using a mass conservative level set method”. In: *International Journal of Multiphase Flow* 89 (2017), pp. 57–68. DOI: 10.1016/j.ijmultiphaseflow.2016.10.010 (cited on page 129).

Sharma, N. et al. “Spray Behavior of a GDI Injector at Constant Fuel Injection Pressure and Varying Engine Load”. In: *18th Annual Conference on Liquid Atomization and Spray Systems* - (2016) (cited on page 123).

Shi, J. et al. “Evidence of vortex driven primary breakup in high pressure fuel injection”. In: September (2017), pp. 6–8. DOI: 10.4995/ilass2017.2017.5707 (cited on page 387).

Shields, B. et al. “Cavitation as Rapid Flash Boiling”. In: *ILASS-Americas 23rd Annual Conference on Liquid Atomization and Spray Systems, Ventura, CA, May 2011 Cavitation*. May. 2011 (cited on page 71).

Shih, T. H. et al. “A new k-epsilon eddy viscosity model for high Reynolds number turbulent flows”. In: *Computer Fluids* 24.3 (1995), pp. 227–238. DOI: 10.1007/978-3-319-27386-0_7 (cited on page 188).

Shost, M. A. et al. “GDi nozzle parameter studies using les and spray imaging methods”. In: *SAE Technical Papers* 1 (2014). DOI: 10.4271/2014-01-1434 (cited on page 144).

Sick, V. et al. “High-speed imaging for direct-injection gasoline engine research and development”. In: *Experiments in Fluids* 49.4 (2010), pp. 937–947. DOI: 10.1007/s00348-010-0891-3 (cited on page 114).

Sirignano, W. A. *Fluid Dynamics and Transport of Droplets and Sprays*. Cambridge University Press, 1999. DOI: 10.1017/CBO9780511529566 (cited on page 180).

Smith, J. et al. “A Comparison of Spray-Guided Stratified-Charge Combustion Performance with Outwardly-Opening Piezo and Multi-Hole Solenoid Injectors”. In: *SAE International Journal of Engines* 4.1 (2011), pp. 1481–1497. DOI: 10.4271/2011-01-1217 (cited on page 52).

Smith, J. K. et al. “Thermodynamic modelling of a stratified charge spark ignition engine”. In: *International Journal of Engine Research* 21.5 (2020), pp. 801–810. DOI: 10.1177/1468087418784845 (cited on page 36).

Soteriou, C. et al. “Direct injection diesel sprays and the effect of cavitation and hydraulic flip on atomization”. In: *SAE Technical Papers* 412 (1995). DOI: 10.4271/950080 (cited on page 68).

Sou, A. et al. “Effects of Asymmetric Inflow on Cavitation in Fuel Injector and Discharged Liquid Jet”. In: *Atomization and Sprays* 26.9 (2016), pp. 939–959. DOI: 10.1615/AtomizSpr.2015013501 (cited on page 366).

Sparacino, S. et al. “Impact of different droplets size distribution on the morphology of GDI sprays: Application to multi-hole injectors”. In: *AIP Conference Proceedings* 2191.December 2019 (2019). DOI: 10.1063/1.5138872 (cited on page 155).

Sparacino, S. et al. “Impact of the primary break-up strategy on the morphology of GDI sprays in 3D-CFD simulations of multi-hole injectors”. In: *Energies* 12.15 (2019). DOI: 10.3390/en12152890 (cited on page 155).

Sparacino, S. et al. “3D-CFD Simulation of a GDI Injector under Standard and Flashing Conditions”. In: *E3S Web of Conferences* 197 (2020), pp. 1–13. DOI: 10.1051/e3sconf/202019706002 (cited on page 155).

Sphicas, P. et al. “Interplume velocity and extinction imaging measurements to understand spray collapse when varying injection duration or number of injections”. In: *Atomization and Sprays* 28.9 (2018), pp. 837–856. DOI: 10.1615/AtomizSpr.2018025956 (cited on pages 122, 364).

Sphicas, P. et al. “A Comparison of Experimental and Modeled Velocity in Gasoline Direct-Injection Sprays with Plume Interaction and Collapse”. In: *SAE Int. J. Fuels Lubr.* 10 (2017), pp. 184–201. DOI: 10.4271/2017-01-0837 (cited on pages 154, 307, 437).

Sphicas, P. et al. “Inter-plume aerodynamics for gasoline spray collapse”. In: *International Journal of Engine Research* 19.10 (2018), pp. 1048–1067. DOI: 10.1177/1468087417740306 (cited on page 97).

Spicher, U. et al. “Gasoline Direct Injection (GDI) engines - Development potentialities”. In: *SAE Technical Papers* 724 (1999). DOI: 10.4271/1999-01-2938 (cited on pages 24, 27).

Spiegel, L. et al. “Mixture formation and combustion in a spark ignition engine with direct fuel injection”. In: *SAE Technical Papers* (1992). DOI: 10.4271/920521 (cited on page 120).

Spikes, R. H. et al. “Discharge coefficient of small submerged orifices”. In: *Proceedings of the Institution of Mechanical Engineers* 173.1 (1959), pp. 661–674 (cited on page 70).

Statement, C. P. “Rail Pressure Control of Common Rail System for Gasoline Direct Injection Engines”. In: 1 (2017), pp. 1–5 (cited on pages 46, 47).

Sterling, A. M. et al. “The instability of capillary jets”. In: *Journal of Fluid Mechanics* 68.3 (1975), pp. 477–495. DOI: 10.1017/S0022112075001772 (cited on page 83).

Stralen van, S. J. D. et al. *Boiling phenomena : physicochemical and engineering fundamentals and applications*. Hemisphere, 1979 (cited on page 74).

Strek, P. et al. “X-Ray Radiography and CFD Studies of the Spray G Injector”. In: *SAE Technical Paper 2016-01-0858* (2016). DOI: 10.4271/2016-01-0858 (cited on pages 133, 238).

Suh, H. K. et al. "Effect of cavitation in nozzle orifice on the diesel fuel atomization characteristics". In: *International Journal of Heat and Fluid Flow* 29.4 (2008), pp. 1001–1009. DOI: 10.1016/j.ijheatfluidflow.2008.03.014 (cited on page 70).

Suma, S. et al. "Internal boiling atomization by rapid pressure reduction of liquids". In: *Transactions of the Japanese Society of Mechanical Engineers* 43 (1977), pp. 4608–4617 (cited on page 75).

Sun, Z. et al. "Split injection flash boiling spray for high efficiency and low emissions in a GDI engine under lean combustion condition". In: *Proceedings of the Combustion Institute* 38.4 (2021), pp. 5769–5779. DOI: 10.1016/j.proci.2020.05.037 (cited on page 127).

Takacs, G. *A Review of Production Engineering Fundamentals*. 2015, pp. 13–56. DOI: 10.1016/b978-0-12-417204-3.00002-9 (cited on page 130).

Tamim, J. et al. "A continuous thermodynamics model for multicomponent droplet vaporization". In: *Chemical Engineering Science* 50.18 (1995), pp. 2933–2942 (cited on page 91).

Tanner, F. X. "Liquid jet atomization and droplet breakup modeling of non-evaporating diesel fuel sprays". In: *SAE Technical Papers* 412 (1997). DOI: 10.4271/970050 (cited on page 85).

Taylor, G. I. "Generation of ripples by wind blowing over a viscous fluid". In: *The Scientific Papers of G.I. Taylor, vol. 3*. Ed. by G. K. Batchelor. Cambridge: Cambridge University Press, 1963. Chap. 25, pp. 244–254 (cited on page 205).

Tezduyar, T. E. "Finite Element Methods for Flow Problems with Moving Boundaries and Interfaces". In: *Archives of Computational Methods in Engineering* 8.2 (2001), pp. 83–130. DOI: 10.1007/BF02897870 (cited on page 135).

Tezduyar, T. E. "Interface-tracking and interface-capturing techniques for finite element computation of moving boundaries and interfaces". In: *Computer Methods in Applied Mechanics and Engineering* 195.23-24 (2006), pp. 2983–3000. DOI: 10.1016/j.cma.2004.09.018 (cited on page 135).

Torelli, R. et al. "Internal Nozzle Flow Simulations of Gasoline-Like Fuels under Diesel Operating Conditions Internal Nozzle Flow Simulations of Gasoline-Like Fuels under Diesel Operating Conditions". In: *29th Annual Conference on Liquid Atomization and Spray Systems* May (2017) (cited on pages 140, 141).

Torregrosa, A. J. et al. “Study of turbulence in atomizing liquid jets”. In: *International Journal of Multiphase Flow* 129 (2020), p. 103328. DOI: 10.1016/j.ijmultiphaseflow.2020.103328 (cited on page 372).

Tsui, Y. Y. et al. “Flux-blending schemes for interface capture in two-fluid flows”. In: *International Journal of Heat and Mass Transfer* 52.23-24 (2009), pp. 5547–5556. DOI: 10.1016/j.ijheatmasstransfer.2009.06.026 (cited on page 137).

Tu, P. W. et al. “Numerical Investigation of GDI Injector Nozzle Geometry on Spray Characteristics”. In: *SAE Technical Papers* 2015-Septe.September (2015). DOI: 10.4271/2015-01-1906 (cited on pages 58–60, 144).

Turton, R. et al. “A short note on the drag correlation for spheres”. In: *Powder Technology* 47.1 (1986), pp. 83–86. DOI: 10.1016/0032-5910(86)80012-2 (cited on page 86).

US Environmental Protection Agency. “Light-Duty Automotive Technology, Carbon Dioxide Emissions, and Fuel Economy Trends: 1975 Through 2016”. In: November (2018) (cited on page 3).

USCAR. “Summary Report on the Transportation Combustion Engine Efficiency Colloquium Held at USCAR, March 3 and 4, 2010”. In: (2010) (cited on page 3).

Vallet, A. et al. “Development of a Eulerian model for the "Atomization" of a liquid jet”. In: *Atomization and Sprays* 11.6 (2001), pp. 619–642. DOI: 10.1615/atomizspr.v11.i6.20 (cited on pages 151, 152).

Van Rij, J. et al. “Extreme load computational fluid dynamics analysis and verification for a multibody wave energy converter”. In: *Proceedings of the International Conference on Offshore Mechanics and Arctic Engineering - OMAE* 10.July (2019). DOI: 10.1115/omae2019-96397 (cited on page 9).

Vanegas, A. et al. “Experimental investigation of the effect of multiple injections on pollutant formation in a common-rail di diesel engine”. In: *SAE Technical Papers* 2008.724 (2008). DOI: 10.4271/2008-01-1191 (cited on page 370).

Vaquerizo, D. “Study on Advanced Spray-Guided Gasoline Direct Injection Systems”. PhD thesis. Universitat Politècnica de València, 2017. DOI: 10.4995/Thesis/10251/99568 (cited on pages 7, 56, 65, 238, 301, 304, 326, 359–364, 367, 369, 371, 379, 427, 431).

Venegas, O. “Estudio del fenómeno de la cavitación en la inyección diesel mediante la visualización del flujo interno en orificios transparentes.” PhD thesis. Universitat Politècnica de València, 2014. DOI: 10.4995/Thesis/10251/37375 (cited on page 6).

Vent, G. et al. “The new 2.0 l turbo engine from the Mercedes-Benz 4-cylinder engine family”. In: *2nd Aachen Colloquium China* (2012), pp. 137–160 (cited on page 52).

Versteeg, H. K. et al. “An introduction to computational fluid dynamics”. In: *Longman scientific and Technical* (1995) (cited on pages 179, 184, 222, 224).

Viera, A. “Effect of multiple injection strategies on the diesel spray formation and combustion using optical diagnostics”. PhD thesis. Universitat Politècnica de València, 2019. DOI: 10.4995/Thesis/10251/123954 (cited on page 6).

Wang, B. et al. “Numerical Investigation of the Deposit Effect on GDI Injector Nozzle Flow”. In: *Energy Procedia* 105 (2017), pp. 1671–1676. DOI: 10.1016/j.egypro.2017.03.545 (cited on page 145).

Wang, W. et al. “Comparison of hexahedral, tetrahedral and polyhedral cells for reproducing the wind field around an isolated building by LES”. In: *Building and Environment* 195.October 2020 (2021), p. 107717. DOI: 10.1016/j.buildenv.2021.107717 (cited on pages 259, 260).

Wang, Y. et al. “Application of Interface Area Density Modeling to Define Spray Plume Boundary Department of Mechanical and Industrial Engineering University of Massachusetts-Amherst General Motors Global R & D”. In: May (2015) (cited on page 159).

Wang, Z. et al. “Influence of deposit on spray behaviour under flash boiling condition with the application of closely coupled split injection strategy”. In: *Fuel* 190 (2017), pp. 67–78. DOI: 10.1016/j.fuel.2016.11.012 (cited on page 126).

Wang, Z. et al. “Microscopic and macroscopic characterization of spray impingement under flash boiling conditions with the application of split injection strategy”. In: *Fuel* 212.February 2017 (2018), pp. 315–325. DOI: 10.1016/j.fuel.2017.10.028 (cited on page 126).

Wei, H. et al. “Gasoline engine exhaust gas recirculation - A review”. In: *Applied Energy* 99.X (2012), pp. 534–544. DOI: 10.1016/j.apenergy.2012.05.011 (cited on page 39).

Wengle, H. et al. “Large-eddy Simulation of Turbulent Flow Over Sharp-edged Obstacles in a Plate Channel”. In: 1993, pp. 192–199. DOI: 10.1007/978-3-663-13986-7_26 (cited on page 265).

Weyand, B. et al. “Three-Dimensional Modelling inside a Differential Pressure Laminar Flow Bioreactor Filled with Porous Media”. In: *BioMed Research International* 2015 (2015). DOI: 10.1155/2015/320280 (cited on page 9).

Whitaker, P. et al. “Measures to Reduce Particulate Emissions from Gasoline DI engines”. In: *SAE International Journal of Engines* 4.1 (2011), pp. 1498–1512. DOI: 10.4271/2011-01-1219 (cited on page 32).

Wierzba, A. “Deformation and breakup of liquid drops in a gas stream at nearly critical Weber numbers”. In: *Experiments in Fluids* 9.1-2 (1990), pp. 59–64. DOI: 10.1007/BF00575336 (cited on pages 83, 84).

Wilcox, D. C. *Turbulence Modelling for CFD 3rd Edftion*. 2006, p. 536 (cited on page 186).

Winkler, A. et al. “ELECTORJECTOR. Bendix Electronic Fuel Injection System”. In: (1957) (cited on page 26).

Winklhofer, E. et al. “Comprehensive hydraulic and flow field documentation in model throttle experiments under cavitation conditions”. In: *Proceedings of the ILASS-Europe Conference, Zurich* August (2001), pp. 574–579. DOI: 10.13140/2.1.1716.4161 (cited on page 70).

Wu, J. et al. “Experimental study on flash-boiling spray structure of multi-hole gasoline direct injection injector in a constant volume chamber”. In: *International Journal of Spray and Combustion Dynamics* 12 (2020). DOI: 10.1177/1756827720932431 (cited on pages 121–123).

Wu, S. et al. “Investigation of rapid atomization and collapse of superheated liquid fuel spray under superheated conditions”. In: *Atomization and Sprays* 26.12 (2016), pp. 1361–1384. DOI: 10.1615/AtomizSpr.2016014231 (cited on pages 98, 99).

Wu, S. et al. “Experimental study of the spray collapse process of multi-hole gasoline fuel injection at flash boiling conditions”. In: *Fuel* 242.Ic (2019), pp. 109–123. DOI: 10.1016/j.fuel.2019.01.027 (cited on page 123).

Xiao, D. et al. “Experimental investigations of injector internal parameters impact on tip wetting using Laser-induced Fluorescence”. In: *15thTriennial International Conference on Liquid Atomization and Spray Systems* (2021) (cited on page 120).

Xu, M. et al. “Flash Boiling: Easy and Better Way to Generate Ideal Sprays than the High Injection Pressure”. In: *SAE International Journal of Fuels and Lubricants* 6.1 (2013), pp. 137–148. DOI: 10.4271/2013-01-1614 (cited on page 310).

Yakhot, V. et al. “Development of turbulence models for shear flows by a double expansion technique”. In: *Physics of Fluids A* 4.7 (1992), pp. 1510–1520. DOI: 10.1063/1.858424 (cited on page 186).

Yang, J. et al. "Fuel injection strategies to increase full-load torque output of a direct-injection SI engine". In: *SAE Technical Papers* 724 (1998). DOI: 10.4271/980495 (cited on page 366).

Yang, S. et al. "In-nozzle bubble formation and its effect on fuel jet breakup under cavitating and flash boiling conditions". In: *Applied Thermal Engineering* 183.P1 (2021), p. 116120. DOI: 10.1016/j.applthermaleng.2020.116120 (cited on page 118).

Yoshizawa, A. et al. "A Statistically-Derived Subgrid-Scale Kinetic Energy Model for the Large-Eddy Simulation of Turbulent Flows". In: *Journal of the Physical Society of Japan* 54.8 (1985), pp. 2834–2839. DOI: 10.1143/JPSJ.54.2834 (cited on page 194).

Youngs, D. L. "Time-dependent multi-material flow with large fluid distortion." In: January 1982 (1982) (cited on pages 137, 198).

Yu, W. et al. "Macroscopic spray characteristics of kerosene and diesel based on two different piezoelectric and solenoid injectors". In: *Experimental Thermal and Fluid Science* 76 (2016), pp. 12–23. DOI: 10.1016/j.expthermflusci.2016.03.008 (cited on page 116).

Yuan, Z. et al. "Turbulence modulation in particulate flows-A theoretical approach". In: *International Journal of Multiphase Flow* 18.5 (1992), pp. 779–785. DOI: 10.1016/0301-9322(92)90045-I (cited on page 87).

Yue, Z. et al. "Application of an Equilibrium Phase (EP) Spray Model to Multi-component Gasoline Direct Injection". In: *Submitted to Fuel* (2018), pp. 1–8. DOI: 10.1016/S0140-6736(11)61351-2 (cited on page 430).

Yue, Z. et al. "Spray characterization for engine combustion network Spray G injector using high-fidelity simulation with detailed injector geometry". In: *International Journal of Engine Research* 21.1 (2020), pp. 226–238. DOI: 10.1177/1468087419872398 (cited on pages 145, 373, 382, 383, 387).

Zamani, H. et al. "Large eddy simulation of GDI single-hole and multi-hole injector sprays with comparison of numerical break-up models and coefficients". In: *Journal of Applied Fluid Mechanics* 9.2 (2016), pp. 1013–1022. DOI: 10.18869/acadpub.jafm.68.225.22889 (cited on page 373).

Zanje, S. et al. "Development of generalized bubble growth model for cavitation and flash boiling". In: *Physics of Fluids* 33.7 (2021), pp. 1–15. DOI: 10.1063/5.0055744 (cited on page 74).

Zeng, W. et al. "Atomization and vaporization for flash-boiling multi-hole sprays with alcohol fuels". In: *Fuel* 95 (2012), pp. 287–297. DOI: 10.1016/j.fuel.2011.08.048 (cited on pages 93, 94, 100).

Zeng, W. et al. “Macroscopic characteristics for direct-injection multi-hole sprays using dimensionless analysis”. In: *Experimental Thermal and Fluid Science* 40 (2012), pp. 81–92. DOI: 10.1016/j.expthermflusci.2012.02.003 (cited on page 93).

Zeng, W. et al. “The role of spray-enhanced swirl flow for combustion stabilization in a stratified-charge DISI engine”. In: *Combustion and Flame* 168.x (2016), pp. 166–185. DOI: 10.1016/j.combustflame.2016.03.015 (cited on page 36).

Zeuch, W. “Neue Verfahren zur Messung des Einspritzgesetzes und der Einspritz-Regelmäßigkeit von Diesel-Einspritzpumpen”. In: *MTZ* 22.9 (1961), pp. 344–349 (cited on page 116).

Zhang, B. et al. “Modeling and detailed numerical simulation of the primary breakup of a gasoline surrogate jet under non-evaporative operating conditions”. In: *International Journal of Multiphase Flow* 130 (2020). DOI: 10.1016/j.ijmultiphaseflow.2020.103362 (cited on page 146).

Zhang, G. et al. “A Study of Near-field Spray Structure under Superheated Conditions of a Gasoline Fuel Spray G”. In: *ILASS Americas 26th Annual Conference on Liquid Atomization and Spray Systems* May (2014) (cited on page 118).

Zhang, G. et al. “Temporal investigations of transient fuel spray characteristics from a multi-hole injector using dimensionless analysis”. In: *Experimental Thermal and Fluid Science* 66 (2015), pp. 150–159. DOI: 10.1016/j.expthermflusci.2015.03.011 (cited on pages 93, 94).

Zhao, H. *Overview of gasoline direct injection engines*. Di. Woodhead Publishing Limited, 2020, pp. 1–19. DOI: 10.1533/9781845697327.1 (cited on pages 29, 32, 49, 52).

Zhou, J. et al. “Characteristics of near-nozzle spray development from a fouled GDI injector”. In: *Fuel* 219.92 (2018), pp. 17–29. DOI: 10.1016/j.fuel.2018.01.070 (cited on page 37).

Zhuang, H. et al. “Impact of Fuel Sprays on In-Cylinder Flow Length Scales in a Spark-Ignition Direct-Injection Engine”. In: *SAE International Journal of Engines* 10.3 (2017). DOI: 10.4271/2017-01-0618 (cited on page 179).